เอกสารแนบ

เอกสารแนบ 5.1.1

Deposition of Disinfectant Poly(methyl acrylate) Nanocapsules onto Natural Rubber Film via the Layer-by-Layer Technique

Umaporn Paiphansiri, Pramuan Tangboriboonrat

Department of Chemistry, Faculty of Science, Mahidol University, 6 Rama Road, Phyathai, Bangkok 10400, Thailand

Received 11 August 2007; accepted 30 October 2008
DOI 10.1002/app.29464
Published online 13 January 2009 in Wiley InterScience (www.interscience.wiley.com).

ABSTRACT: An aqueous core containing a disinfectant agent (chlorhexidine digluconate) was encapsulated in a poly(methyl acrylate) shell with a modified nanoprecipitation technique. After redispersion of the capsules in an aqueous medium, the remaining amount of the disinfectant agent was as high as 90%. The nanocapsules were successfully adsorbed via the layer-by-layer technique onto a γ-radiation-vulcanized natural rubber latex sheet. Water contact angle measurements and scanning electron microscopy confirmed the presence of nanocapsules on the rubber surface. © 2009 Wiley Periodicals, Inc. J Appl Polym Sci 112: 769–777, 2009

Key words: core-shell polymers; morphology; rubber; self-assembly; surfaces

INTRODUCTION

The knowledge of natural rubber (NR) films is well evolved, especially for glove production, because the use of medical gloves is highly recommended for those individuals who are exposed to the blood or bodily fluids of patients. However, the problem of needle puncture or other accidents that might take place during surgery or patient treatment that could lead to viral infections of medical personnel needs to be addressed.[1–3] Busnel and coworkers[4,5] developed a medical glove that incorporates disinfectant droplets between its rubber sheets. When a needle punctures the glove, the disinfectant agent is released and neutralizes any infectious agents carried by the needle.

Among the several types of disinfectant agents, chlorhexidine digluconate (CHD) salt, a dicationic surfactant possessing a wide spectrum of activity against Gram-positive and Gram-negative bacteria, has been widely exploited.[6–8] To incorporate the water-soluble guest molecule, a well-defined nanocapsule with an aqueous core ideally has to be prepared in a single step, and the shell that is formed should be stable and have high structural perfection. However, the available protocols are still limited to water-in-oil (w/o) or inverse interfacial polymerization.[9–11] The inverse miniemulsion process, which generally provides critically stabilized small droplets dispersed in an organic continuous phase, has been applied. By the ultrasonication of a two-phase system, stable nanodroplets including the disinfectant agent for further encapsulation have been prepared by a modified nanoprecipitation method.[12–14] The droplet size, ranging from 30 to 500 nm, is principally governed by the type and amount of the surfactant used as the compatibilizer. One key characteristic of a miniemulsion is that no effective material exchange should occur between the droplets, and this is known as the Ostwald ripening effect.[15] In the case of an inverse miniemulsion, the salt or CHD (which is an extremely hydrophilic component) in aqueous miniemulsion droplets plays an important role in building up osmotic pressure inside each droplet.[13,16]

To physically adsorb polyelectrolytes, particles, or capsules onto a solid template, the layer-by-layer (LbL) technique, concerning mainly the sequential adsorption of oppositely charged materials via electrostatic attraction, is effectively used. A multilayer thin film with precise control of the structure and thickness at the molecular level has been fabricated via the LbL process.[17] Our previous works also showed that this method could be applied to inserting anionic polystyrene particles into a cationic polyelectrolyte assembled film coated on a glass substrate.[18,19] This effectively increased the film's

Correspondence to: P. Tangboriboonrat (scptb@mahidol.ac.th).

Contract grant sponsor: The Thailand Research Fund (to P.T.).
Contract grant sponsor: Royal Golden Jubilee (through its Ph.D. program to U.P.).
Contract grant sponsor: Deutscher Akademischer Austausch Dienst.

© 2009 Wiley Periodicals, Inc.

roughness and resulted in a significant increase in the hydrophobicity of the surface with Nafion at the outermost layer. Furthermore, the deposition of hard poly(methyl methacrylate) (PMMA) particles onto NR latex sheets successfully increased the surface roughness and hardness and hence diminished the friction of the rubber surface.[20,21]

Because the simple and versatile LbL process is independent of the substrate size and topology and does not affect the bulk properties of the substrate, it was used for the deposition of disinfectant nanocapsules onto γ-radiation-vulcanized natural rubber (RVNR) latex film, a medical glove model used in this study. The disinfectant nanocapsules were prepared by the modified nanoprecipitation of poly(methyl acrylate) (PMA) from an organic continuous phase onto w/o miniemulsion droplets containing the CHD solution. The effect of the concentration of PMA on the encapsulation efficiency of the nanocapsules was determined by proton nuclear magnetic resonance (^{1}H-NMR) measurements. After the redispersion of the nanocapsules into an aqueous medium, stable nanocapsules with high encapsulation efficiency were then selected to attach onto an RVNR latex sheet. Before the deposition of the soft disinfectant PMA nanocapsules onto the RVNR latex sheet, a study employing hard PMMA particles was performed as a function of the latex concentration and immersion time. The coated surface was then characterized by contact angle measurements, attenuated total reflection/Fourier transform infrared (ATR–FTIR) spectroscopy, and scanning electron microscopy (SEM).

EXPERIMENTAL

Materials

All chemicals, including CHD (20% in water; Sigma, Steinheim, Germany), potassium persulfate (KPS; Fluka, Germany), sodium dodecyl sulfate (SDS; Fluka, GC, Japan), soybean phosphatidylcholine (PC; Sigma), dichloromethane (Fluka, purum), cyclohexane (Fluka, purum), tetrahydrofuran (THF; Fluka; purum), ethanol (Fluka; purum), methanol (Fluka; purum), hexadecane (Fluka; purum), deuterated water, Nonidet (Biochemika, Fluka), pyrazine (Merck; GC, Japan), calcium chloride (Fluka, GR, Switzerland), and RVNR latex (Siam Okamoto Co., Ltd., Pathumthani, Thailand), were used without further purification. The monomers, methyl methacrylate (Fluka; purum, Deisenhafen, Germany) and methyl acrylate (Aldrich; 99%), were purified by passage through a column packed with neutral and basic aluminum oxide (Fluka; Purum). The block copolymer emulsifier poly[(butylene-*co*-ethylene)-*b*-(ethylene oxide)] [P(B/E-EO)], with a molecular mass of 3700 g/mol for the poly(butylene-*co*-ethylene) block and a molecular mass of 3600 g/mol for the poly(ethylene oxide) (PEO) block, was synthesized with Kraton liquid (Shell, TX).[22] PMA was prepared with the miniemulsion polymerization technique.[12,23]

Nanocapsule preparation

The organic continuous phase, comprising dichloromethane (9.5 g), a known amount of P(B/E-EO) or PC [% w/v: ratio of the surfactant (g) to the drug volume (mL)], and cyclohexane (12 g), was first prepared. An antiseptic agent, a CHD solution (0.5 mL), was charged into the solvent mixture. A solution of PMA (100 or 200 mg) in dichloromethane (0.5 g) was slowly dropped into the mixture, which was subsequently ultrasonicated for 2 min at 90% amplitude with a Branson W450 sonifier (Danbury, CT) with a 1/2″ tip. Then, the temperature was raised to 50°C in an open vessel with continuous mechanical stirring overnight. During the evaporation of dichloromethane, cyclohexane was added to replace dichloromethane and also its evaporated volume.

Characterization of the nanocapsules

The size of the nanocapsules was characterized with dynamic light scattering measurements (NanoZS, Malvern, UK). For the determination of the encapsulation degree of the antiseptic agent, the nanocapsules were separated by centrifugation in a microcentrifuge (Eppendorf) and were carefully dried before dissolution in a mixture of THF and ethanol. Deuterated water and a known amount of pyrazine were applied as an external solvent and as a calibration product for the quantitative analysis of the encapsulation efficiency by ^{1}H-NMR (DRX 400 with 400.123 MHz, Bruker).[24] The mass of the drug in the nanocapsule was calculated from the area ratio of the peaks at 7.66 and 9.07 ppm corresponding to aromatic protons of the CHD and pyrazine, respectively. The morphology of the capsules, which were mounted on a copper grid before coating with carbon, was investigated with transmission electron microscopy (TEM; EM 400, Phillips, Eindhoven, The Netherlands).

The separated nanocapsules were finally redispersed in a 2% (w/v) aqueous SDS solution with stirring overnight for complete deaggregation. The characterization procedures, mentioned previously, were also exploited, and the remaining amount of the drug in the nanocapsules after redispersion in water was evaluated.

Deposition of PMMA and/or disinfectant PMA nanocapsules onto an RVNR sheet

The dried rubber sheet (1.5 × 4 × 0.1 cm^3), cast from RVNR latex at room temperature, adhered to a poly(ethylene terephthalate) film without any adhesive. The rubber surface was cleaned by the immersion of the sample into distilled methanol (100 mL)

TABLE I
Characteristics of PMA Nanocapsules with 4% (w/v) P(B/E-EO) from Cyclohexane and a 2% (w/v) SDS Aqueous Solution

	Nanocapsules in cyclohexane [4% w/v P(B/E-EO)]		Redispersion nanocapsules [2% w/v SDS aqueous solution]	
PMA content (mg)	Size (nm)	Encapsulation efficiency (%)	Size (nm)	Remaining disinfectant agent (%)
100	150	100	456	87
200	190	100	258	85

and then Milli-Q water (100 mL) for 15 min for each step during sonication in an ultrasonic cleaning bath. After drying in air, the obtained rubber sheet was kept in a desiccator.

PMMA latex was synthesized by miniemulsion polymerization.[24] An aqueous solution of Nonidet (1–8 wt % dry latex) was then added to PMMA latex [1% total solid content (TSC)] before shaking (Burell) for 12 h at room temperature. The amount of Nonidet adsorbed onto the particles was deduced from the quantity of an aqueous solution of 0.5*M* $CaCl_2$ added to provoke visible coagula.

PMMA (Nonidet) was prepared by the addition of an 8 wt % concentration of the dry latex to PMMA latex having TSCs of 0.1, 0.5, and 0.85%. The RVNR strip was then immersed into the PMMA (Nonidet) latex at pH 2 for various time intervals. The sample was subsequently washed with water via a series of three rinsing baths and finally dried at room temperature. The optimum condition of PMMA adsorption was further applied for the incorporation of a 0.85% TSC of disinfectant PMA nanocapsules.

Surface analysis of PMMA (Nonidet) and/or disinfectant PMA nanocapsules (Nonidet) deposited onto an RVNR sheet

The surface of PMMA deposited onto an RVNR sheet was characterized with ATR–FTIR spectroscopy (Equinox 55, Bruker). The spectra (32 scans at a 4-cm^{-1} resolution) were collected with a Ge crystal in a multireflection mode. The change in the characteristic absorption peaks at 1730 and 1378 cm^{-1}, corresponding to C=O stretching of the carboxylate group of PMMA and C—H bending of $—CH_3$ of NR, respectively, was investigated.

A sessile drop contact angle measurement was performed on RVNR adsorbed with disinfectant PMA nanocapsules with a contact angle goniometer (G-1, Kruss, Hamburg, Germany). The surface morphology of the modified RVNR sheet was determined by SEM (JSM 5410LV, JEOL, Tokyo, Japan).

RESULTS AND DISCUSSION

PMA nanocapsules

The characterization of PMA nanocapsules with 4% (w/v) P(B/E-EO) dispersed in cyclohexane and redispersed in a 2% (w/v) SDS aqueous solution was carried out, and the data are listed in Table I.

It was observed that the nanocapsule sizes were 150 and 190 nm with 100 and 200 mg of PMA, respectively. An encapsulation efficiency of 100% with both concentrations was detected by ^{1}H-NMR measurement. After redispersion of the PMA nanocapsules, the remaining amount of the disinfectant agent was as high as about 90%. The dissolution of a large amount of PMA (300–500 mg) in the continuous phase took more time in comparison with other polymers.[24] The high viscosity of the PMA solution caused the formation of coagulum during the evaporation of dichloromethane; consequently, probably because of the low mobility of the molecular chains, the polymer did not deposit onto the aqueous nanodroplets.[25]

Besides P(B/E-EO), the other surfactant used for the preparation of PMA nanocapsules was PC, a double-tailed zwitterionic surfactant, the chemical structure of which is shown in Figure 1. With a disinfectant agent volume of 0.5 mL and a solvent mixture volume of 22 mL and with a dichloromethane/cyclohexane ratio of 1 : 1.2, the optimum formulation of the inverse miniemulsion for the nanocapsule preparation was limited to 150 mg of PMA and 100 mg of PC (or 20% w/v with respect to the disinfectant volume).

As previously mentioned, the size of the aqueous miniemulsion droplets dispersed in the cyclohexane phase can be designed by the type and amount of the surfactant applied. In comparison with 4% (w/v) P(B/E-EO), a PC content as high as 20% (w/v) was required to obtain stable disinfectant nanodroplets, which were dispersed in a solvent mixture of dichloromethane and cyclohexane containing PMA. This might be explained in term of self-assembly characteristic of PC molecules on the nanodroplet surface.[26] Yamada et al.[27] proposed that a well-defined trilayer membrane of PC with an 8-nm

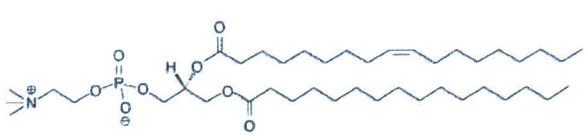


Figure 1 Chemical structure of soybean PC.

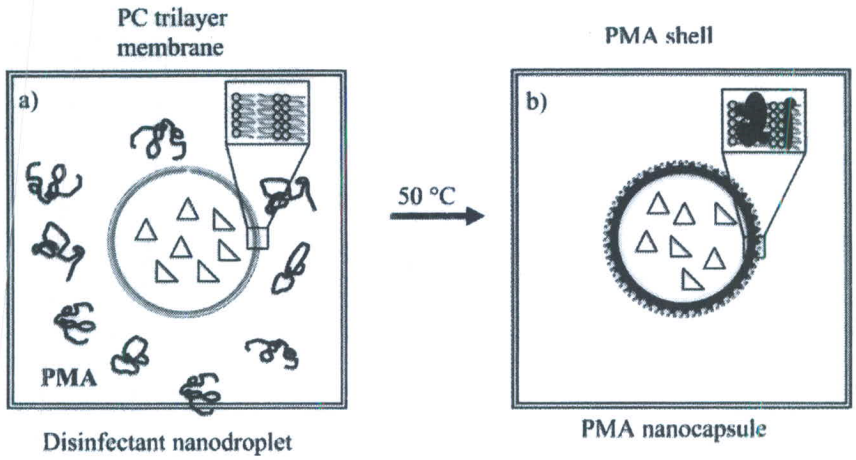


Figure 2 Schematic representation of (a) a PC-stabilized disinfectant nanodroplet in a solvent mixture of dichloromethane and cyclohexane and (b) a PMA nanocapsule dispersed in a cyclohexane phase.

thickness, organized spontaneously on a water nanodroplet, was responsible for steric stabilization in an organic continuous phase, as depicted in Figure 2(a). The internal membrane structure was constructed from the alternative orientation of each self-assembled PC layer: the first and third layers turned their hydrophilic head groups toward the nanodroplet and exposed hydrophobic alkyl chains of the third layer to the organic phase. The second layer intervened, placing alkyl chains with those of the first layer, and the head group encountered the head group of the third layer.[27] In the presence of PC's trilayer membrane, the precipitated PMA was possibly deposited onto the hydrophobic tails of PC's outermost layer or inserted within the hydrophobic part of the assembled membrane, as schematically displayed in Figure 2(b). Consequently, PMA nanocapsules about 306 nm in diameter, dispersed in the cyclohexane phase, were obtained.

After the separation of PMA nanocapsules from the cyclohexane phase by centrifugation, the nanocapsules could spontaneously redisperse into the water phase without the addition of any surfactant under continuous stirring overnight. This might be due to the reorientation of the top PC layer by the turning of its hydrophilic head group toward the aqueous continuous phase and/or migration of the PC molecules in the second layer to the nanocapsule surface so that the PMA nanocapsule would gain electrostatic stabilization.[27,28] The stable aqueous core nanocapsule dispersed in water, having an average size of 216 nm, was hence evaluated. The ζ-potential of the PMA nanocapsule against the pH was then monitored, as shown in Figure 3.

The results indicated that the PMA nanocapsule exhibited positive character when the pH was below 9.4. Above this pH, the ζ-potential was negative. This amphoteric character, having a pI of 9.4, confirmed the presence of choline [$N(CH_3)_3$] and phosphate moieties of PC, which imparted particle stability, on the nanocapsule surface. Our results agreed well with a former work[29] concerning the utilization of poly[2-(methacryloyloxy)ethyl phosphorylcholine]-*block*-poly[2-(dimethylamino)ethyl methacrylate] for stabilizing gold nanoparticles in an aqueous phase.

Morphological study of the PMA nanocapsules

TEM micrographs of air-dried nanocapsules using 100 mg of PMA with 4% (w/v) P(B/E-EO) from the cyclohexane phase were previously displayed.[25] It was observed that the size of the nanocapsules was remarkably smaller than that obtained from the dynamic light scattering measurements because the nanocapsules greatly shrank under the high-energy electron beam in TEM. However, the core–shell morphology of the nanocapsules could be clearly noted.

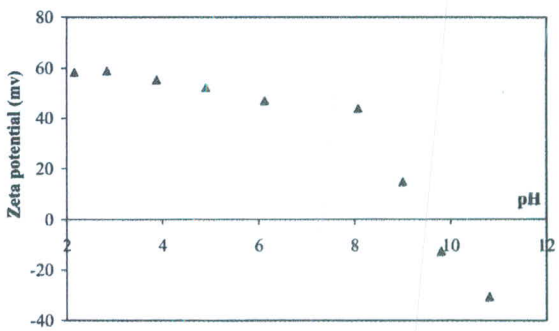


Figure 3 ζ-Potential of PMA nanocapsules prepared with 150 mg of PMA and 20% (w/v) PC versus the pH.

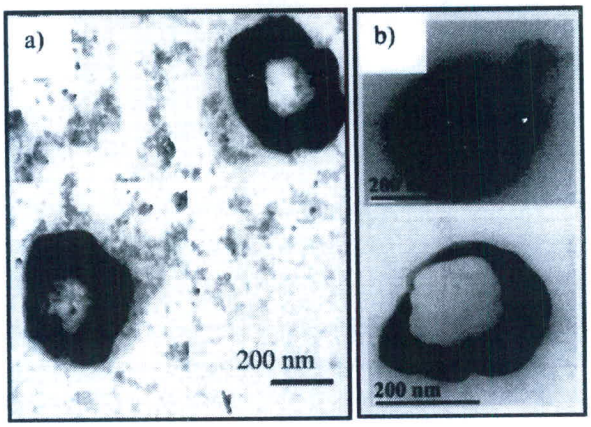


Figure 4 TEM micrographs of nanocapsules with 150 mg of PMA and 20% (w/v) PC: (a) dispersed in cyclohexane and (b) redispersed in an aqueous phase.

The morphologies of PMA nanocapsules (with 150 mg of PMA and 20% w/v PC) dispersed in cyclohexane and redispersed in an aqueous phase were evaluated, and the TEM micrographs are shown in Figure 4.

It was observed that the PMA nanocapsules possessed a spherical shape with a core–shell morphology in both cyclohexane and after redispersion into the aqueous phase. However, the PMA shell was denser than that prepared with 4% (w/v) P(B/E-EO).[24] This might be due to the fact that the PC trilayer, organizing on the disinfectant nanodroplet surface, contributed to hydrophobic vacancy. A large amount of precipitated PMA was entrapped, and this gave rise to the formation of the thick shell. The disinfectant PMA nanocapsule, prepared with 20% (w/v) PC, was used for incorporation into an RVNR latex sheet in further steps.

Deposition of PMMA latex particles onto an RVNR latex sheet

Monodisperse PMMA latex with an average size of 143 ± 0.5 nm and a TSC of 20.3 ± 0.03% was attained. The ζ-potentials at pH 2–11 were negative, and this was possibly derived from the strong acidic groups (SO_4^-) from KPS and SDS, which served as the initiator and anionic surfactant, respectively.

To determine the change from electrostatic stabilization to steric stabilization of the PMMA latex adsorbed with a nonionic surfactant, Nonidet, whose molecule contains PEO moieties, an electrolyte solution was added to provoke the visible coagula. The results showed that the volume of 0.5*M* $CaCl_2$ required for PMMA latex coagulation was increased with increasing Nonidet concentration. With less than 8% Nonidet, PMMA latex was immediately coagulated after the addition of a $CaCl_2$ aqueous solution. On the contrary, the latex remained stable at a minimum Nonidet concentration of 8%. The modification of latex stabilization from electrostatic stabilization to steric stabilization was, therefore, achieved with 8% Nonidet.

Because an LbL hydrogen-bonded film can be generated by the self-assembly of a weak polyacid and a neutral polymer at a low pH, the study of deposition of PMMA adsorbed by Nonidet [PMMA (Nonidet)] onto an RVNR latex sheet at pH 2 proceeded. The presence of PMMA (Nonidet) deposited onto an RVNR latex sheet with various immersion times at latex concentrations of 0.1, 0.5, and 0.85% was elucidated with ATR–FTIR. The spectra of RVNR sheets dipped into 0.1% PMMA (Nonidet) at different times are illustrated in Figure 5.

In the spectrum of RVNR, the characteristic peaks at 2961, 2922, and 2856 (C—H stretching), 1450 (C—H bending of $—CH_2—$), 1378 (C—H bending of $—CH_3$), and 837 cm^{-1} (C—H deformation of *cis* C=C—H) were detected. After the deposition of PMMA (Nonidet), an additional peak, a strong absorption at 1730 cm^{-1} related to C=O stretching of the carboxylate group, was observed. In addition, the intensity of the latter increased with increasing immersion time; concomitantly, the intensity of the absorbance at 1378 cm^{-1} of RVNR decreased. This implied an interpolymer complex formation between PEO groups on the PMMA surface and carboxylic

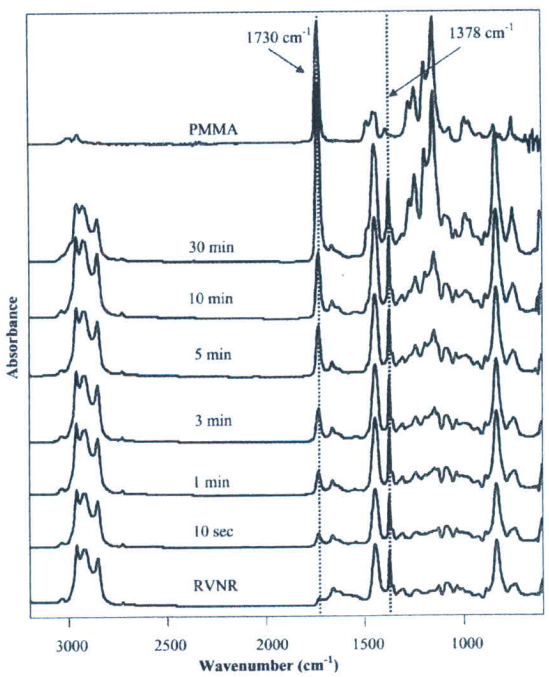


Figure 5 ATR–FTIR spectra of RVNR latex sheets immersed in 0.1% PMMA (Nonidet; pH 2) at various dipping times.

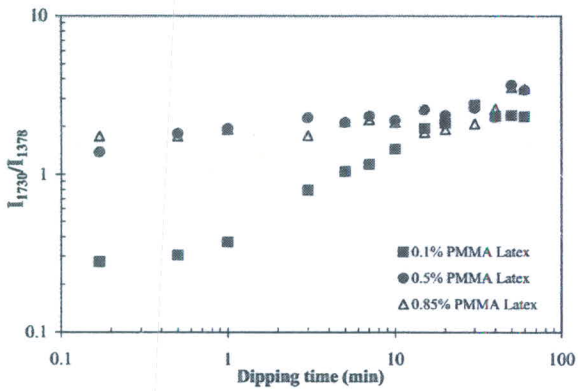


Figure 6 Absorbance ratios of 1730- and 1378-cm^{-1} peaks (I_{1730}/I_{1378}) for RVNR sheets deposited with PMMA latex (0.1, 0.5, or 0.85%) as a function of the dipping time.

groups of the residual protein substance on RVNR, which played a role in the driving force for PMMA deposition.[30,31]

To evaluate the change in the PMMA (Nonidet) content on the RVNR sheet, the absorbance ratios of the peak at 1730 cm^{-1} of PMMA to that at 1378 cm^{-1} of RVNR were calculated and plotted versus the dipping times at latex concentrations of 0.1, 0.5, and 0.85%, as depicted in Figure 6.

The results indicated that at the low latex concentration of 0.1%, the adsorption was directly proportional to the immersion time of 1–30 min and then approached a constant value after 30 min. At high latex concentrations of 0.5 and 0.85%, the deposition contents were almost constant within 1 min. Our results were in agreement with the former work, which reported that the repulsion among latex

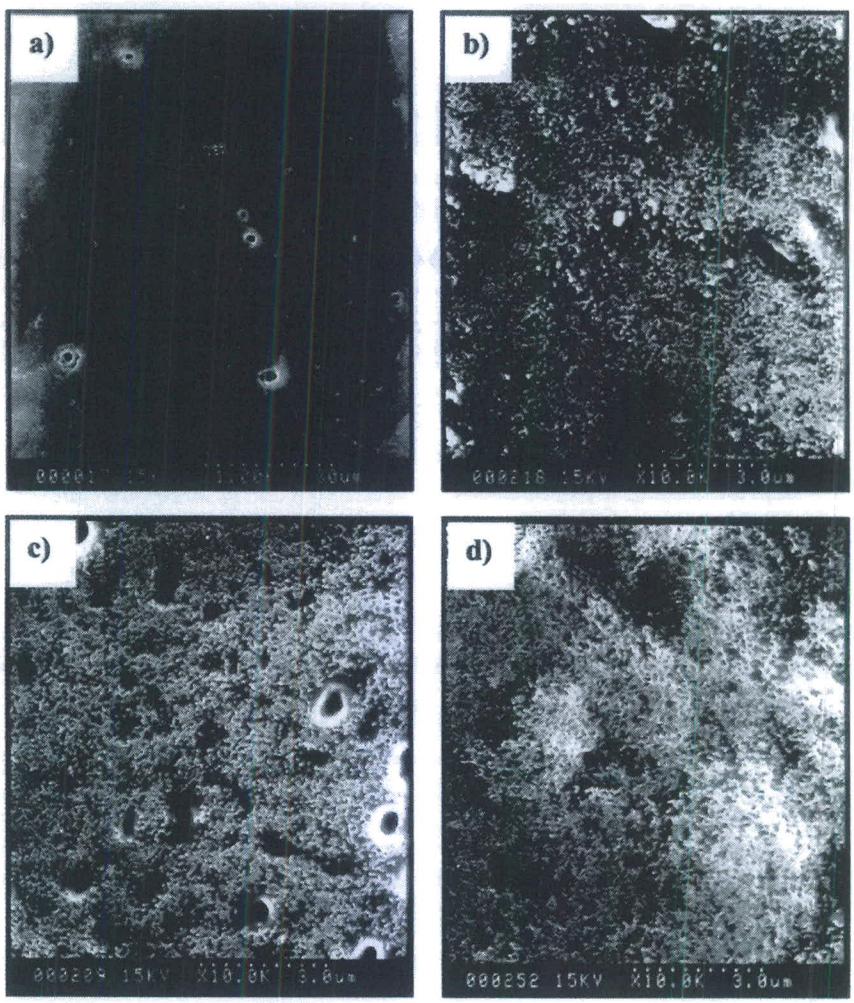


Figure 7 SEM micrographs of (a) pristine RVNR and (b–d) RVNR adsorbed with 0.1% PMMA (Nonidet) as a function of the dipping time (10 s, 1 min, and 30 min, respectively).

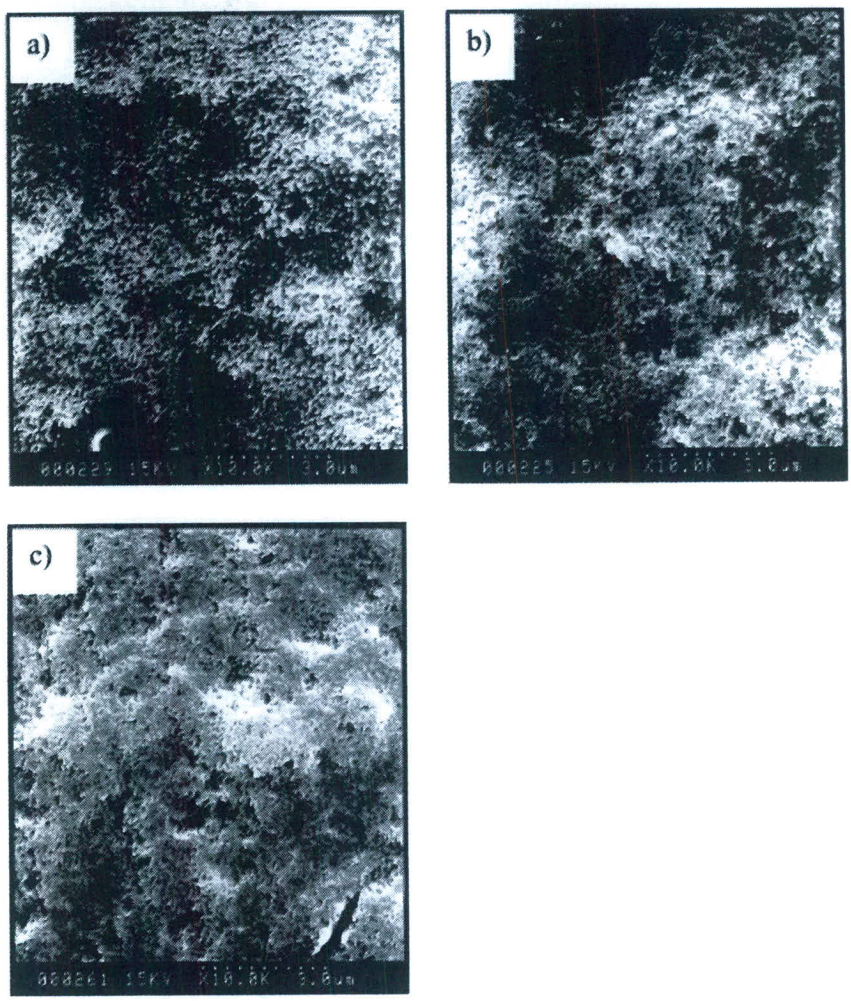


Figure 8 SEM micrographs of RVNR adsorbed with 0.85% PMMA (Nonidet) as a function of the dipping time: (a) 10 s, (b) 30 s, and (c) 30 min.

particles at high latex concentrations provided a high collision between the particles and substrate surface.[18–21] Because the adsorption rate and surface coverage depended strongly on the size of the colloidal particle,[32] the small size of PMMA, containing more active sites to attract the substrate surface, was therefore attributed to comparable deposition contents at all latex concentrations after 30 min of dipping.

The morphologies of RVNR sheets coated with PMMA (Nonidet) at different dipping times were investigated with SEM. The micrographs for 0.1 and 0.85% PMMA (Nonidet) are displayed in Figures 7 and 8, respectively.

It was noted that the pristine RVNR surface in Figure 7(a) exhibited a curvature with several voids, which might be attributed to the detachment of additives applied in the commercial latex. With the increasing immersion time of PMMA (Nonidet), as shown in Figures 7(b–d) and 8(a–c), dense particles packed onto the rubber surface were more pronounced. In comparison with the high latex concentration of 0.85% presented in Figure 8, relatively closed packing of the particles could be obtained with 30 s of dipping, as shown in Figure 8(b). Furthermore, the multilayer particles deposited onto the substrate at the immersion time of 30 min are revealed in Figure 8(c), and they might be due to the bridging formation of free latex particles that collided with the particles occupied on the rubber surface.[33,34]

Deposition of disinfectant PMA nanocapsules (Nonidet) onto an RVNR latex sheet

From the success of PMMA (Nonidet) deposition, a 0.85% TSC of PMA nanocapsules prepared with 20% (w/v) PC was adsorbed with 8% Nonidet before deposition onto RVNR at pH 2. Because the

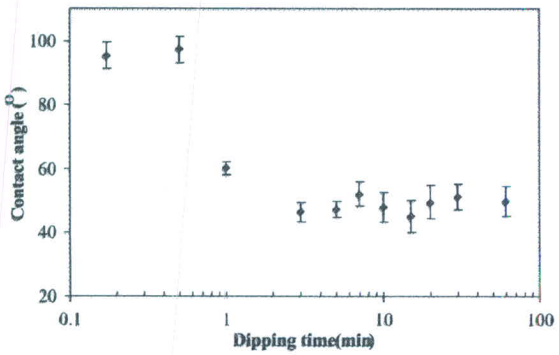


Figure 9 Water contact angle of a PMA nanocapsule (Nonidet) deposited onto an RVNR sheet as a function of the dipping time.

existence of polar groups could lower the hydrophobicity of the substrate, the water contact angle of the PMA nanocapsule (Nonidet) deposited onto an RVNR sheet as a function of the dipping time was measured. The data are presented in Figure 9.

The results indicated that the contact angles rapidly decreased from 95 ± 4 to 46 ± 2° with the immersion time of 3 min and then remained constant. The low contact angle confirmed the presence of nanocapsules, whose surface bore PC and/or Nonidet molecules, on the rubber surface. Our results agreed well with a previous work,[35] which reported that the grafting of phosphorylcholine onto a poly(ether urethane) surface exhibited a water contact angle of 43°. The insignificant change when the dipping time was greater than 3 min might be due to the limitation of the technique; that is, the contact angle measurement is sensitive only for the analysis of the outermost surface.[36] Thus, the increment of the deposition amount of the nanocapsules with increasing deposition time would not affect the contact angle.

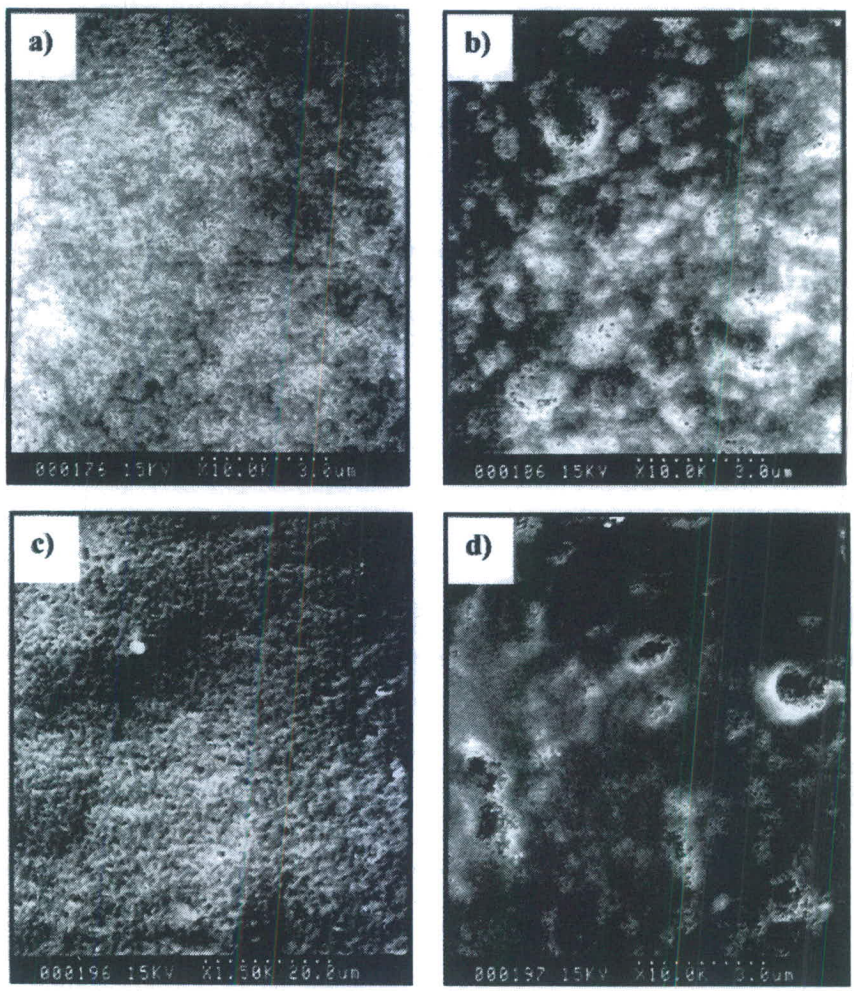


Figure 10 SEM micrographs of a PMA nanocapsule (Nonidet) deposited onto an RVNR sheet as a function of the dipping time: (a) 10, (b) 30, and (c,d) 50 min.

The surface morphologies of PMA nanocapsules (Nonidet) deposited onto rubber sheets with various dipping times were determined, and the SEM micrographs are illustrated in Figure 10. The rubber surface appeared smoother with the dipping time increasing from 10 to 50 min. The explanation was that PMA with a low glass-transition temperature formed a film at room temperature and hence covered the curvature and large voids on the pristine RVNR surface. It could therefore be assumed that the incorporation of disinfectant PMA nanocapsules into the RVNR latex sheet was achieved through the formation of an interpolymer complex driven at pH 2 as previously mentioned.

CONCLUSIONS

The formation of aqueous core nanocapsules by controlled polymer nanoprecipitation onto inverse miniemulsion droplets containing CHD has been conclusively established. The deposition of a PMA shell from an organic continuous phase onto a dispersed phase of stable nanodroplets was achieved by changes in the gradient of the solvent/nonsolvent mixture of dichloromethane and cyclohexane under mild evaporation. After the redispersion of the nanocapsules in an aqueous medium, stable nanocapsules with an aqueous core redispersed in the aqueous continuous phase were obtained. The success of the deposition of PMMA latex particles on an RVNR sheet via the LbL technique led to the development of PMA nanocapsules adsorbed onto the rubber film. The low contact angle confirmed the presence of nanocapsules, whose surface bore PC and/or Nonidet molecules, on the RVNR surface. The surface morphologies of PMA nanocapsules (Nonidet) deposited onto the rubber sheet with various dipping times were observed by SEM.

References

1. Eklund, A. M.; Ojajärvi, J.; Laitinen, K.; Valtonen, M.; Werkkala, K. A. Ann Thorac Surg 2002, 74, 149.
2. Osman, M. O.; Jensen, S. L. World J Surg 1999, 23, 630.
3. Yazdanpanah, Y.; Boelle, P. Y.; Carrat, F.; Guiguet, M.; Abiteboul, D.; Valleron, A. J. J Hepatol 1999, 30, 765.
4. Busnel, R. G.; Argy, G. U.S. Pat. 5,024,852 (1991).
5. Busnel, R. G.; Cheymol, A.; Riess, G. U.S. Pat. 5,804,628 (1998).
6. Mulberry, G.; Snyder, A. T.; Heilman, J.; Pyrek, J.; Stahl, J. Am J Infect Control 2001, 29, 377.
7. Lboutounne, H.; Chaulet, J. F.; Ploton, C.; Falson, F.; Pirot, F. J Controlled Release 2002, 82, 319.
8. Lafforgue, C.; Carret, L.; Falson, F.; Reverdy, M. E.; Freney, J. Int J Pharm 1997, 147, 243.
9. Pitaksuteepong, T.; Davies, N. M.; Tucker, I. G.; Rades, T. Eur J Pharm Biopharm 2002, 53, 335.
10. Watnasirichaikul, S.; Rades, T.; Tucker, I. G.; Davies, N. M. Int J Pharm 2002, 235, 237.
11. Wu, D.; Scott, C.; Ho, C. C.; Co, C. C. Macromolecules 2006, 39, 5848.
12. Landfester, K.; Bechthold, N.; Tiarks, F.; Antonietti, M. Macromolecules 1999, 32, 5222.
13. Landfester, K.; Willert, M.; Antonietti, M. Macromolecules 2000, 33, 2370.
14. Landfester, K.; Bechthold, N.; Tiarks, F.; Antonietti, M. Macromolecules 1999, 32, 2679.
15. Sudol, E. D.; El-Aasser, M. S. In Emulsion Polymerization and Emulsion Polymers; Lovell, P. A.; El-Aasser, M. S., Eds.; Wiley: Chichester, UK, 1997.
16. Landfester, K. Adv Mater 2001, 13, 765.
17. Decher, G. Science 1997, 277, 1232.
18. Sangribsub, S.; Tangboriboonrat, P.; Pith, T.; Decher, G. Polym Bull 2005, 53, 425.
19. Sangribsub, S.; Tangboriboonrat, P.; Pith, T.; Decher, G. Eur Polym J 2005, 41, 1531.
20. Sruanganurak, A.; Sanguansap, K.; Tangboriboonrat, P. Colloid Surf A 2006, 289, 110.
21. Sruanganurak, A.; Tangboriboonrat, P. Colloid Surf A 2007, 301, 147.
22. Schlaad, H.; Kukula, H.; Rudloff, J.; Below, I. Macromolecules 2001, 34, 4302.
23. Bechthold, N.; Landfester, K. Macromolecules 2002, 33, 4682.
24. Paiphansiri, U.; Tangboriboonrat, P.; Landfester, K. Macromol Biosci 2006, 6, 33.
25. Caruso, F. Colloids and Colloid Assemblies; Wiley-VCH: Weinheim, 2004.
26. Gupta, R.; Muralidhara, H. S.; Davies, H. T. Langmuir 2001, 17, 5176.
27. Yamada, A.; Yamanaka, T.; Hamada, T.; Hase, M.; Yoshikawa, K.; Baigl, D. Langmuir 2006, 22, 9824.
28. Schrader, W.; Kaatze, U. J Phys Chem B 2001, 105, 6266.
29. Yuan, J.-J.; Schmid, A.; Armes, S. P. Langmuir 2006, 22, 11022.
30. DeLongchamp, D. M.; Hammond, P. T. Langmuir 2004, 20, 5403.
31. Tangboriboonrat, P.; Buranabunya, U. Colloid Polym Sci 2001, 279, 615.
32. Litton, G. M.; Olson, T. M. Colloid Surf A 1996, 107, 273.
33. Zhang, L.; Liu, Y.; Liu, Z. J Appl Polym Sci 1993, 49, 1415.
34. Elimelech, M. Particle Deposition and Aggregation: Measurement, Modeling and Simulation; Colloid and Surface Engineering Series; Butterworth-Heinemann: Woburn, MA, 1995.
35. Van der Heiden, A. P.; Willems, G. M.; Lindhout, T.; Pijpers, A. P.; Koole, L. H. J Biomed Res 1998, 40, 195.
36. Castell, P.; Wouters, M.; de With, G.; Fischer, H.; Huijs, F. J Appl Polym Sci 2004, 92, 2341.

เอกสารแนบ 5.1.

Colloids and Surfaces A: Physicochem. Eng. Aspects 350 (2009) 114–120

Contents lists available at ScienceDirect

Colloids and Surfaces A: Physicochemical and Engineering Aspects

journal homepage: www.elsevier.com/locate/colsurfa

Polyethyleneimine-functionalized poly(methyl methacrylate) colloidal nanoparticles for directly coating natural rubber sheet

Panya Sunintaboon*, Sitthi Duangphet, Pramuan Tangboriboonrat

Department of Chemistry, Faculty of Science, Mahidol University, Bangkok 10400, Thailand

ARTICLE INFO

Article history:
Received 18 June 2009
Received in revised form 20 August 2009
Accepted 7 September 2009
Available online 11 September 2009

Keywords:
PMMA nanoparticle
PMMA colloid
Surface modification
Rubber
Polyethyleneimine

ABSTRACT

This work illustrated a convenient surface modification of sulphur-prevulcanized natural rubber (SPNR) sheet with poly(methyl methacrylate) (PMMA) colloidal nanoparticles without pre-treatment of the rubber. The SPNR sheet was simply immersed into the latex of PMMA core that was functionalized with polyethyleneimine (PEI) shell (PMMA/PEI) via a soap-free emulsion polymerization. The presence of PMMA/PEI nanoparticles on the SPNR sheet was revealed by Fourier transform infrared (FTIR) spectroscopy and scanning electron microscopy (SEM). It was also traced by the changes of surface roughness, adhesion force, and relative surface stiffness obtained from atomic force microscopy (AFM) analysis. The surface coverage (C_s) values depended on the variation of immersion time and particle concentration. Water contact angles on the PMMA/PEI-coated SPNR sheet decreased with increasing C_s values.

© 2009 Elsevier B.V. All rights reserved.

1. Introduction

Natural rubber (NR) latex tapped from *Hevea brasiliensis* tree, consisting mainly of *cis*-1,4 polyisoprene, has proven to be useful for fabrication of thin materials, e.g., tubing, balloons, condoms, and gloves. Although sulphur-prevulcanized natural rubber (SPNR) latex film possesses excellent inherent elastic property, its tack and high surface friction are serious drawbacks and hence limit its use in certain applications, including gloves [1]. Tightly fitting surgical or examination gloves is difficult to don because of the tendency of the glove to stick to users' skin or even to itself. Therefore, several surface treatments, without a significant change on the rubber bulk properties, have attracted much attention. In general, powder talc or cornstarch is applied for reducing the friction between the rubber film surface and the human skin [2]. However, these additives have many disadvantages, e.g., being the cause of granulomas in surgical wounds [3,4]. The powder-free gloves via a halogenation process are, therefore, of great interest [5,6]. Nevertheless, the halogenated NR gloves become hard, brittle, and dark in appearance, while their surface was slippery, and could limit their use. Apart from the approaches already mentioned, modification of NR or SPNR latex film with hard particles seems to be promising to reduce the overall surface friction coefficient, which would allow the glove to be donned more readily. However, the rubber substrate, particle surface, or both of them need some pre-treatments in order to promote the binding ability. Janssen studied the use of vinyl-functionalized beads to chemically bond to the glove's surface without the addition of binder [7]. Sruanganurak et al. used the layer-by-layer (LbL) technique to deposit PMMA particles on hydrophilic NR or SPNR film that was pre-modified with polyacrylamide (PAAm) [8].

In order to skip pre-treatment steps of SPNR sheet prior to deposition of PMMA particles, the use of PMMA (core) and polyethyleneimine (PEI) (shell) (PMMA/PEI) core–shell nanoparticles reported by Li et al. [9] was investigated in this present work. Due to the fact that PEI affixed on the nanoparticles' surface can electrostatically interact with negatively charged molecules such as enzymes or DNA [10,11], they should bind with polar non-rubber components (proteins and phospholipids) distributed on the surface of NR latex particles [12] and also on the rubber sheet. Herein, the PMMA/PEI nanoparticles were first prepared by a soap-free emulsion polymerization. Then, they were deposited directly to the rubber sheet via a simple immersion. The presence of the nanoparticles was confirmed by Fourier transform infrared (FTIR) spectroscopy, scanning electron microscopy (SEM), atomic force microscopy (AFM), and contact angle measurement. The surface coverage (C_s) values were determined from SEM images with the variation of immersion time and nanoparticle concentration. The change of surface properties, e.g., surface roughness, adhesion force, and relative surface stiffness of both uncoated and coated SPNR sheets were also derived from AFM analysis. The deposition of PMMA/PEI nanoparticles onto SPNR sheets in this work would be a model for convenient surface modification of several substrates.

* Corresponding author. Tel.: +66 2 441 9816 20x1138; fax: +66 2 441 0511.
E-mail address: scpsu@mahidol.ac.th (P. Sunintaboon).

0927-7757/$ – see front matter © 2009 Elsevier B.V. All rights reserved.
doi:10.1016/j.colsurfa.2009.09.013

2. Experimental

2.1. Materials

High ammonia-preserved NR (HA-NR) latex was purchased from Bangkok Rubber Co. Ltd., Rayong, Thailand. Sulphur, zinc oxide (ZnO), zinc diethyldithiocarbamate (ZDEC), and Lovenox used were commercially available at Lucky Four Co. Ltd., Nonthaburi, Thailand. Methyl methacrylate (MMA) monomer (Fluka, Purum) was purified by passing through a column packed with neutral and basic aluminum oxide adsorbents (Fluka, Purum). PEI, MW of 750,000 (Aldrich, 50 wt% aqueous solution) was diluted by distilled water to 10 wt% before subjected to polymerization. Other reagents, e.g., *t*-butyl hydroperoxide (TBHP) (Fluka, 70%), Potassium hydroxide (KOH) (AnalaR, pellets), Potassium laurate (Fluka, Purum), or methanol (Fisher, AR) were used as received.

2.2. Preparation of SPNR sheets

The rubber sheets used in this entire work were cast at room temperature from SPNR latex compounded from HA-NR latex with sulphur, ZnO, ZDEC, and Lovenox. Then, the compounded latex was ground by ball-milling to obtain a 50% aqueous dispersion **[13]**. Total solid content (% TSC) and dry rubber content (% DRC) of the latex were determined using the method described in ASTM D1076-97, Section 9. The amount of ingredients used for compounding SPNR latex is shown in **Table 1**.

The surface of SPNR sheet was sequentially cleaned with methanol and then water for 15 min in an ultrasonic bath (Sonorex RK 100 H, Bandelin). The rubber sheet was cut into square pieces with an approximate weight of 0.2 g each.

2.3. Synthesis and characterization of PMMA/PEI nanoparticles

PMMA/PEI nanoparticles were synthesized through a batch-wise soap-free emulsion polymerization. Distilled water (26 g) and a 10 wt% PEI aqueous solution (15 g), adjusted with concentrated hydrochloric acid (Merck) to pH 7, were charged into a 100-mL three-neck round-bottomed water-jacketed reactor. After purging nitrogen for 30 min, the MMA monomer (6 g) was added into the reactor under continuous stirring. The polymerization was then started after adding an aqueous solution of 5×10^{-3} M TBHP (3 mL) and the polymerization temperature was controlled at 80 ± 1 °C for 2 h. The resulted latex was cleaned to remove the free PEI by repeated centrifugation-redispersion, at centrifugation speed of 15,000 rpm and time of 30 min for each cycle. The conversion percentage was determined by a gravimetric method, based on the amount of MMA used and that of polymerized MMA **[9]**. Particle size was determined by the SEM image analysis (SEM 2300 s, Hitachi). ζ-potential values were obtained by using microelectrophoresis (Zetasizer 3000, Malvern Instrument, UK) in 1 mM NaCl solution at room temperature. All measurements were done at the wavelength of 633 nm at 25 °C with a scattering angle of 90°. All results reported were the average of three determinations.

Table 1
Formulations used for preparation of SPNR latex.

Ingredients	Part by weight (g)
Concentrated NR latex (60% DRC)	167
Stabilizers	
- Potassium hydroxide (KOH) solution (10% w/v)	3
- Potassium laurate solution (20% w/v)	1
- Lovenox	1
Vulcanizing ingredients (50% dispersion)	
- Sulphur	1
- Zinc diethyldithiocarbamate (ZDEC)	2
- Zinc oxide (ZnO)	0.5

2.4. Preparation and characterization of SPNR sheet deposited by PMMA/PEI nanoparticles

The SPNR sheet adhered on a poly(ethylene terephthalate) (PET) film was immersed in a glass tube, containing a PMMA/PEI nanoparticle dispersion (1–15% TSC) for 10–60 min. The immersed sample was then washed with water three times, and finally allowed to dry at ambient temperature.

After deposition, the air-dried SPNR sheet was characterized by FTIR, SEM, AFM, and water contact angle measurement. The FTIR (EQUINOX 55, Bruker) spectra (32 scans at 4 cm^{-1} resolution) of the SPNR surface were collected with a single reflection mode on a Ge crystal. Contact angles of a water droplet (approximately 5 μL) on the rubber surface were also determined (G-1, Krüss). Each value reported was the average of ten separated drops of water on a given SPNR sheet.

The images of coated SPNR sheet were clarified by SEM (SEM 2300s, Hitachi), and AFM (Model Ns3a, Digital Instrument Inc.) equipped with Nanoscope IIIa controller via the tapping mode (scan size of 10 μm × 10 μm, at six different locations). The surface coverage (C_s) values, indicating the amount of PMMA/PEI nanoparticles adsorbed per unit area of the sheet surface, were determined by the image analysis of SEM and AFM micrographs. C_s values were then calculated by the following equation **[14]**:

$$C_s(\%) = \frac{N}{N_{max}} \times 100 \quad (1)$$

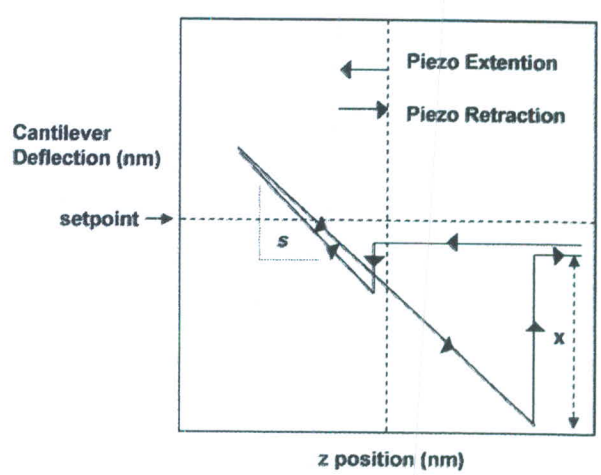
where N is the number of nanoparticles per unit area; N_{max} is the maximum number of nanoparticles on the same area assuming a hexagonal dense packing of particles **[15]**.

Surface mean roughness (R_a) was directly calculated from the Nanoscope software by using Eq. **(2)**:

$$R_a = \frac{1}{n}\sum_{j=1}^{n} |Z_j| \quad (2)$$

where Z_j is the current difference between the height and the mean plane, and n is the number of points in the image.

Relative surface stiffness and adhesion force of the sample were derived from the force or force-to-distance curve (FDC) (**Scheme 1**) obtained from a contact mode AFM measurement **[16]**. The silicon nitride tip with a spring constant of 0.58 N/m was used, and the tip frequency was set at 0.9965 Hz. In general, extending lines from FDC



Scheme 1. A typical structure of force–distance curve (FDC).

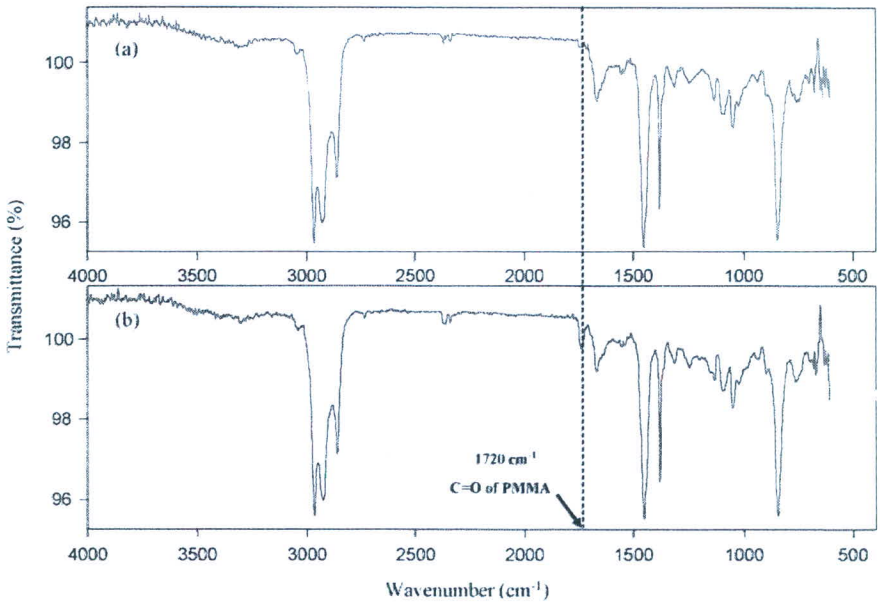


Fig. 1. FTIR spectra of (a) uncoated and (b) PMMA/PEI nanoparticles-coated SPNR sheets.

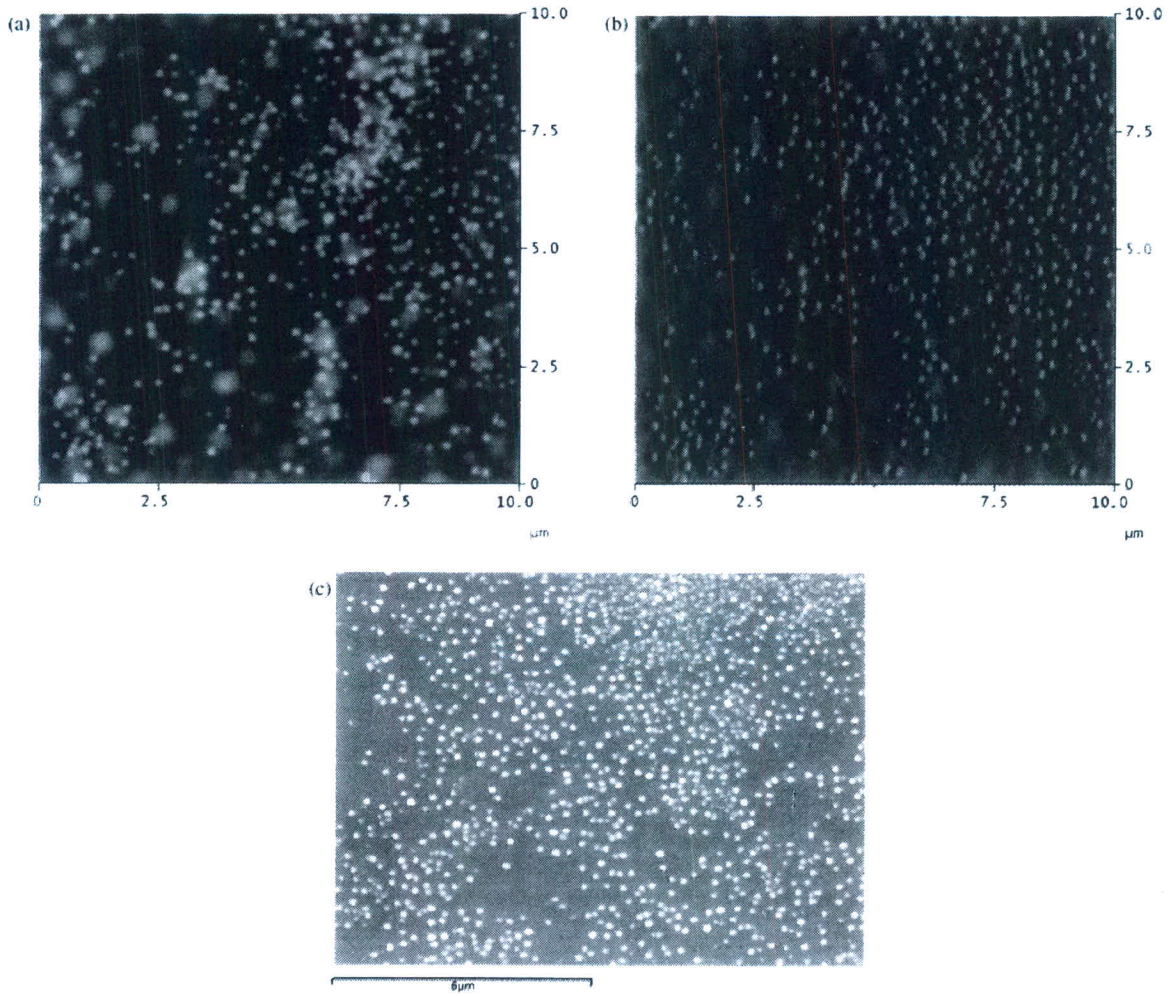


Fig. 2. Micrographs of PMMA/PEI nanoparticle-coated NR surface: (a) AFM (height), (b) AFM (amplitude), and (c) SEM (10,000X) micrographs.

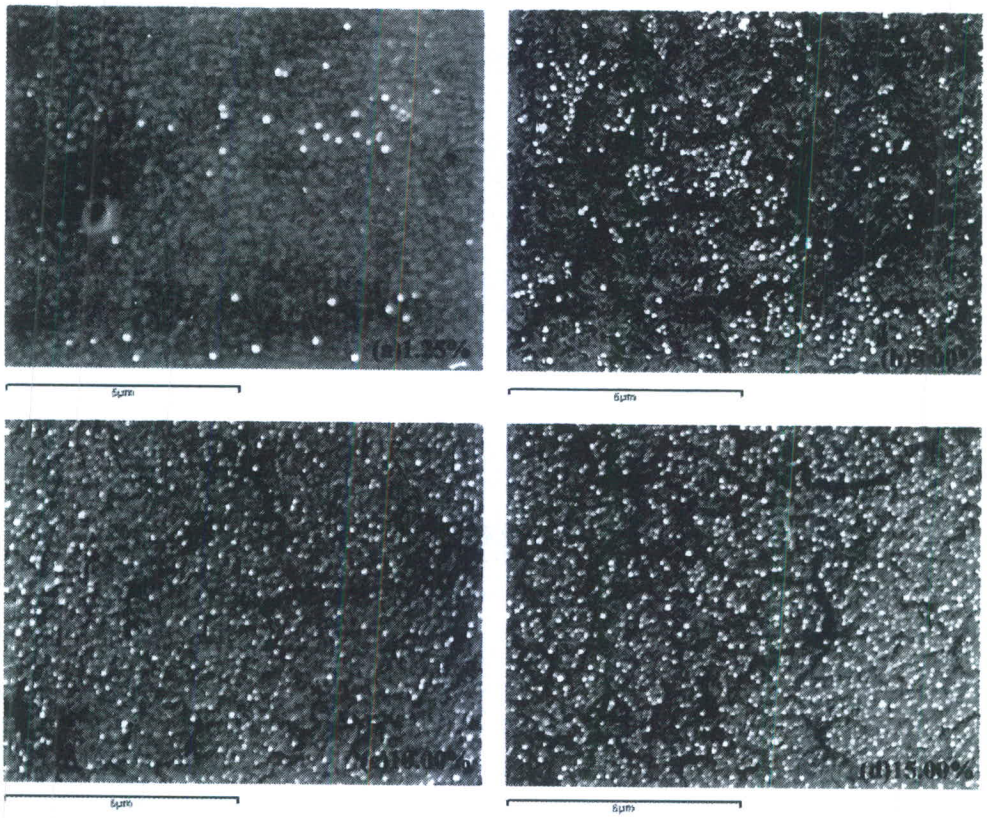


Fig. 3. SEM micrographs of PMMA/PEI nanoparticle-coated the SPNR surfaces as a function of PMMA/PEI latex concentration: (a) 1.25, (b) 5.00, (c) 10.00, and (d) 15.00% TSC at 40 min of immersion time.

reflect a surface stiffness, while retracting lines represent adhesion force between a tip and a surface. The relative surface stiffness was obtained by comparing the surface stiffness of uncoated and coated SPNR sheets to that of the reference silicon surface as shown in Eq. (3).

$$\text{Relative surface stiffness} = \frac{S_s}{S_{si}} \tag{3}$$

S_s is the slope of extending line of a tip on a sample surface, and S_{si} is the slope of extending line of a tip on the reference silicon surface.

The adhesion force is defined by the Eq. (4):

$$F = kx \tag{4}$$

where x is the deflection of the tip before pull-off in nanometers (retracting direction), and k is the spring constant of cantilever (0.58 N/m).

The scan size was the same as that determined in the tapping mode (10 μm × 10 μm). Each value reported was the average of five different areas of sample surface.

3. Results and discussion

3.1. Surface characterization of PMMA/PEI-coated SPNR sheets

The PMMA/PEI nanoparticle latex, synthesized by the emulsifier-free emulsion polymerization, was subjected to size and zeta potential measurements. Data showed that its average diameter was of 130 ± 4 nm, with narrow size distribution, and a positive zeta potential of 56 mV. It was reported by Li et al. [9,17] that PEI plays a major role for particle formation and colloidal stabilization in this polymerization system. The particle formation started when TBHP complexes with amine groups on PEI resulting in the formation of redox pairs. As a consequence of electron transfer from the redox pairs, free radicals could be generated on the PEI itself. These radicals could propagate MMA monomers leading to the amphiphilic PEI-graft-PMMA oligomers. Such oligomers aggregate to micelle-like domains, which could be the sites for further polymerization and growth of the particles. By considering the particle nucleation and growth processes as mentioned, the hydrophilic amine groups of PEI are located on the particles' surface bringing both electrostatic and steric stabilization to the particles. The protonation of PEI amine groups caused positive surface charges, which was in accordance with the zeta potential result.

After dipping the SPNR sheet in the PMMA/PEI nanoparticle latex, the alternation of chemical composition on the SPNR surface was traced by FTIR spectroscopy. The spectra of the SPNR sheets, both uncoated and coated with PMMA/PEI nanoparicles are shown in **Fig. 1**. Both spectra showed similar signals belonging to NR: at 2950–2850 cm^{-1} (C—H stretching), 1450 cm^{-1} (C—H deformation of $—CH_3$), 1375 cm^{-1} (C—H deformation of $—CH_2—$), and 836 cm^{-1} (C—H deformation of *cis* C=C—H). However, the spectrum of PMMA/PEI-coated SPNR sheet had the additional signal at 1720 cm^{-1}, assigned to a C=O stretching of grafted PMMA in the nanoparticles, which could not be detected in that of the uncoated SPNR sheet. This evidence supported the fact that the PMMA/PEI nanoparticles were deposited on the SPNR sheet.

The SPNR surface was also characterized by SEM and AFM. The SEM and AFM micrographs in **Fig. 2** revealed that PMMA/PEI nanoparticles were uniformly distributed on the SPNR sheet in a mono-layered fashion. From these results, it is proved that PMMA/PEI nanoparticles can be deposited on the SPNR sheets without any pre-treatment of their surface. PEI existing on the particles'

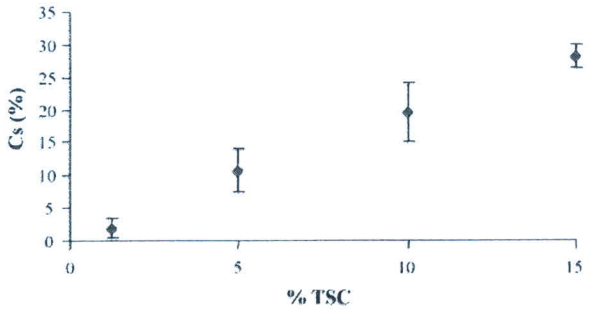


Fig. 4. Effect of PMMA/PEI nanoparticles latex concentration on C_s values for the SPNR sheets immersed for 40 min.

surface might interact electrostatically with the long-chain fatty acid soaps and polypeptides of SPNR, which enhanced a deposition of the PMMA/PEI particles on the rubber sheet [12]. In addition, it has been known that PEI itself has an adhesion promoting ability on several surfaces [18–20], which would assist the deposition.

3.2. Determination of surface coverage

3.2.1. Effect of PMMA/PEI latex concentration

The PMMA/PEI latex concentrations were varied at 1.25, 5.00, 10.00 and 15.00% TSC at dipping time of 40 min. After deposition process, the coated SPNR sheet was characterized by SEM and the resulted micrographs are shown in **Fig. 3** (a)–(d).

It was found that at low PMMA/PEI latex concentration (1.25% TSC) the adsorbed nanoparticles were uniformly distributed on the SPNR surface without aggregation. However, at higher latex concentration (10% TSC), some aggregation of PMMA/PEI nanoparticles were observed and more pronounced at 15% TSC. This lateral aggregation of PMMA/PEI core–shell nanoparticles at high % TSC was probably due to the inter-diffusion of a soft PEI shell [21], and was facilitated when the number of PMMA/PEI nanoparticles increased with latex concentration. The relationship between latex concentration and the C_s of SPNR sheet coated with PMMA/PEI particles is shown in **Fig. 4**. It was noticed that the C_s values increased with increasing latex concentration as previously reported when depositing PMMA nanoparticles on the SPNR grafted with polyacrylamide [22]. From this experiment, the highest C_s value of 27.4% was obtained.

3.2.2. Effect of immersion time

Next, the effect of immersion time on the C_s values was examined and the results are shown in **Fig. 5**. As expected, the C_s values increased with increasing immersion time in the initial period for all latex concentration levels and became almost constant after

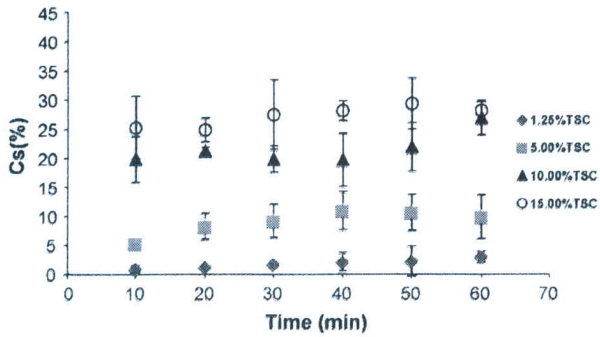


Fig. 5. Effect of immersion time on C_s values.

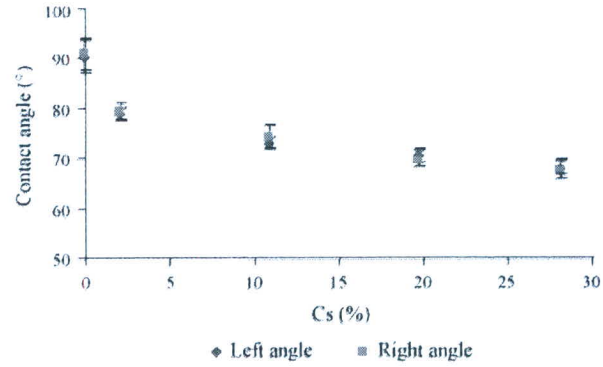


Fig. 6. Water contact angles on PMMA/PEI nanoparticle-coated NR sheets as a function of C_s values.

40 min. The constant C_s at the time longer than 40 min indicated that the deposition–detachment process might reach the equilibrium state when the rates of deposition and detachment of the particles are similar. In addition, the results showed that the higher concentrations provided the higher C_s values for each immersion time. It could be explained that the repulsion among similar charged particles provided the great collision between particle and surface of the substrate [22].

3.3. Water contact angles of PMMA/PEI-coated SPNR sheets

The effect of C_s values on the water contact angles (both left and right) of coated SPNR sheets were then investigated, and the data are presented in **Fig. 6**. The results from both left and right contact angles were similar, and it was found that the water contact angles abruptly decreased from 91° to 74° when increasing the C_s values from 0 to 10.9% and then slightly decreased when the C_s values were greater than 10.9%. The decrease of contact angle was possibly ascribed to the presence of hydrophilic groups on the rubber surface derived from PEI, which was affixed on the surface of PMMA/PEI nanoparticles as already described. This information indicated that the modification of SPNR sheet with PMMA/PEI nanoparticles affected hydrophilicity of the SPNR surface.

3.4. AFM analysis: surface roughness, adhesion force, and relative surface stiffness

The AFM micrographs of the SPNR sheets coated with PMMA/PEI nanoparticles at C_s values of 2.1, 10.9, 19.7 and 28.1%, compared with the uncoated sheet, are presented in **Fig. 7** (a)–(e). The flat and rather smooth surface of the uncoated SPNR sheet was noticed, while the coated rubber surface composed of many modules growing out of surface after the deposition of PMMA/PEI nanoparticles. The topographical images clearly showed that the PMMA/PEI particles were arranged onto the SPNR surfaces as a single layer. However, the aggregates were increasingly evident at higher C_s values. It was believed that these aggregates stemmed from a bridging attraction of PEI chain on the PMMA/PEI surface, which was formed under the action of capillary forces during drying the PMMA/PEI layer [23]. The mean surface roughness (R_a) of SPNR sheet coated with PMMA/PEI nanoparticles at various C_s values was also analyzed from the AFM micrographs, and the data are displayed in **Fig. 8**. The mean surface roughness increased from 13.9 to 31.2 nm with increasing C_s values because of the presence of adsorbed latex particles, which would have potential to reduce a surface friction of rubber sheets [7,8].

In addition to surface topography, AFM analysis provides other information such as relative surface stiffness and adhesion force.

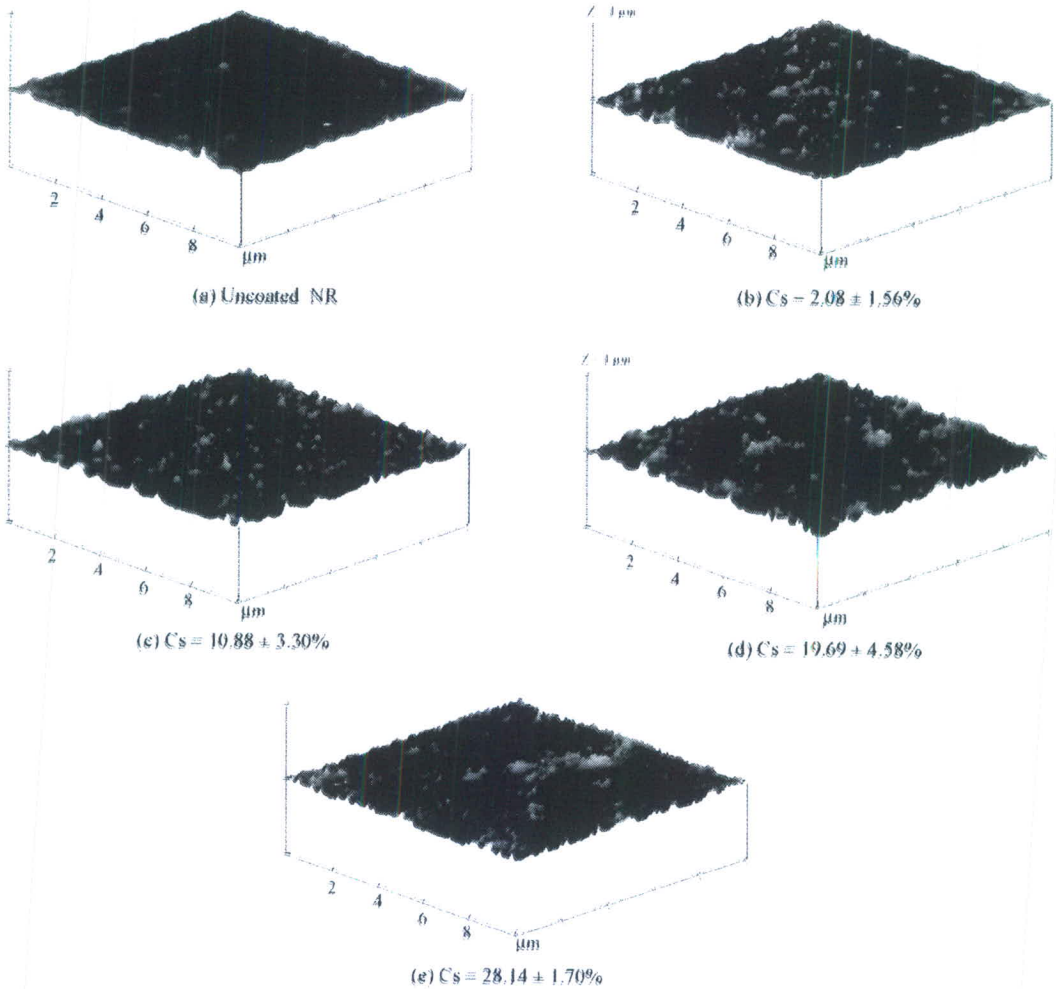


Fig. 7. AFM micrographs of (a) uncoated NR and PMMA/PEI nanoparticle-coated NR surfaces at C_s values of: (b) 2.1, (c) 10.9, (d) 19.7, and (e) 28.1%.

To obtain such information, FDC derived from a contact mode AFM was analyzed. The PMMA/PEI-coated NR sheet with the C_s value of 10.9 was selected as a representative of coated SPNR sheet, compared to that of the uncoated sample and a reference silicon wafer surface. The FDCs of silicon, uncoated, and PMMA/PEI coated SPNR surfaces are shown in **Fig. 9**. In general, the extending lines directly relate to the surface stiffness, whereas the retracting lines indicate the adhesion between a tip and a surface. The adhesion force and relative surface stiffness of all three samples, deduced from their respective FDC, are summarized in **Table 2**.

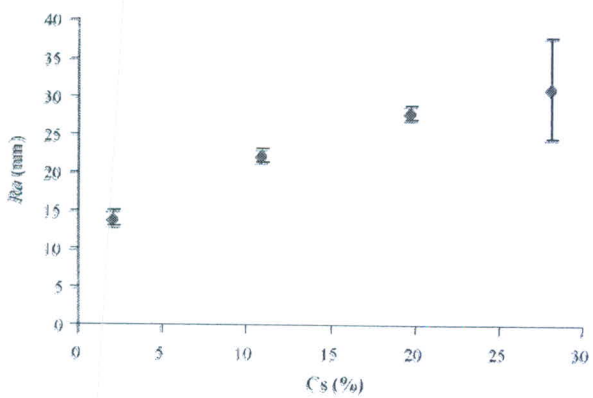


Fig. 8. Effect of C_s values on mean surface roughness (R_a) of PMMA/PEI nanoparticles-coated NR sheets.

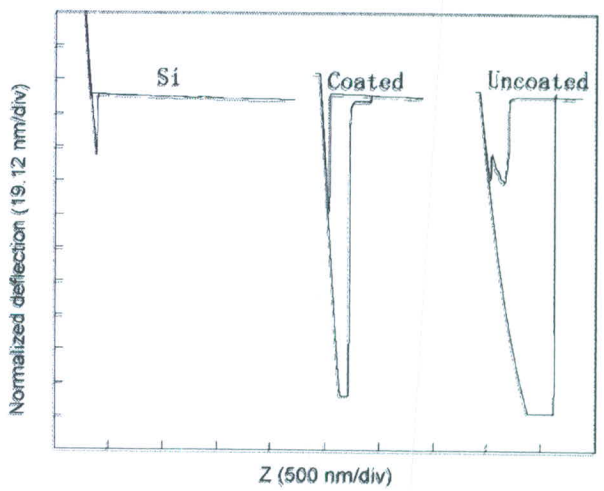


Fig. 9. FDCs of the cantilever on Si, uncoated NR, and PMMA/PEI nanoparticle-coated NR surfaces.

Table 2
Comparison of adhesion force and relative surface stiffness for Si, uncoated, and PMMA/PEI nanoparticle-coated SPNR surfaces.

Sample	Adhesion force (nN)	Relative stiffness
Silicon	20.84 ± 0.10	1.00
Uncoated NR sheet	182.86 ± 4.64	0.72 ± 0.06
PMMA/PEI-coated NR sheet	134.09 ± 2.17	0.85 ± 0.01

The adhesion force is based on the amount of force felt by the cantilever as the probe tip is brought close to a sample surface and then pulled away. It can be seen that the coated NR surface had the adhesion force of 134.1 nN, lower than that of the uncoated NR sheet (182.9 nN). This indicated that the presence of hard particles on the SPNR sheet could dramatically alter the surface properties of the rubber sheet. Moreover, it has proven that the existence of soft PEI did not affect the property of hard PMMA particles, instead promoting the particles' deposition on SPNR sheets only. The FDCs also showed that the relative surface stiffness values for the uncoated and coated SPNR sheets were 0.72 and 0.85, respectively. The increased relative surface stiffness of the coated SPNR would be the result of hard PMMA core of the particles. Therefore, the increase of relative surface stiffness and decrease of adhesion force implied that the deposition of PMMA/PEI particles on the SPNR sheets would reduce the rubber's tack property.

4. Conclusions

The convenient deposition of PMMA/PEI colloidal nanoparticles to modify the SPNR sheet surface was accomplished in this recent work. The presence of PEI on the PMMA/PEI nanoparticles' surface can enhance their deposition on SPNR sheets without pre-surface treatments of the rubber sheet. FTIR, SEM, and AFM analyses evidently revealed the deposition of PMMA/PEI nanoparticles onto the SPNR surface. C_S values were found to depend on the immersion time and the PMMA/PEI latex concentration. The presence of the PMMA/PEI nanoparticles on the surface led to the changes in SPNR surface roughness, relative surface stiffness, and adhesion force, as analyzed from AFM. Moreover, due to the ability of this synthetic method to tailor the property of the core component, i.e., being hard, soft, or brittle, therefore, a wide variety of particles with PEI shell can be prepared. This would lead to an opportunity for convenient surface modification of various substrates and various surface properties.

Acknowledgements

This work was supported by The Thailand Research Fund (TRF) (MRG4880124) and Mahidol University. P.T. is a TRF Senior Researcher (RTA5180003). Technical assistance of Dr. N. Ratanasom, Dr. S. Thanawan, and Mr. S. Radabutra is also acknowledged.

References

[1] A. Momose, Powderfree surgical gloves, US Patent, 4,597,108 (1986).
[2] M. Lundberg, K. Wrangsjö, S.G.O. Johansson, Latex allergy from glove powder—an unintended risk with the switch from talc to cornstarch, Allergy 52 (1997) 1222–1228.
[3] P. Cullinan, R. Brown, A. Field, J. Hourihane, M. Jones, R. Kekwick, R. Rycroft, R. Stenz, S. Williams, C. Woodhouse, Latex allergy: a position paper of the British society of allergy and clinical immunology, Clin. Exp. Allergy 33 (2003) 1484–1499.
[4] E.A. Field, The use of powdered gloves in dental practice: a cause for concern, J. Dent. 25 (1997) 209–214.
[5] P.E. Esemplare, D. Beeferman, Rubber articles having improved slip coating, US Patent 3,967,014 (1976).
[6] C.C. Ho, M.C. Khew, Surface characterisation of chlorinated unvulcanised natural rubber latex films, Int. J. Adhes. Adhes. 19 (1999) 387–398.
[7] R.A. Janssen, Glove having improved donning characteristics, US Patent 6,972,148 B2 (2005).
[8] A. Sruanganurak, K. Sanguansap, P. Tangboriboonrat, Layer-by-layer assembled nanoparticles: a novel method for surface modification of natural rubber latex film, Colloid Surf. A 289 (2006) 110–117.
[9] P. Li, J. Zhu, P. Sunintaboon, F.W. Harris, New route to amphiphilic core–shell polymer nanospheres: graft copolymerization of methyl methacrylate from water-soluble polymer chains containing amino groups, Langmuir 18 (2002) 8641–8646.
[10] K.M. Ho, X.P. Mao, L.Q. Gu, P. Li, Facile route to enzyme immobilization: core–shell nanoenzyme particles consisting of well-defined poly(methyl methacrylate) cores and cellulase shells, Langumir 24 (2008) 11036–11042.
[11] J. Zhu, A. Tang, L.P. Law, M. Feng, K.M. Ho, D.K.L. Lee, F.W. Harris, P. Li, Amphiphilic core–shell nanoparticles with poly(ethylenimine) shells as potential gene delivery carriers, Bioconj. Chem. 16 (2005) 139–146.
[12] C.C. Ho, T. Kondo, N. Muramutsu, H. Ohshima, Surface structure of natural rubber latex particles from electrophoretic mobility data, J. Colliod Interf. Sci. 178 (1996) 442–445.
[13] P. Tangboriboonrat, C. Lerthititrakul, Morphology of natural rubber latex particles prevulcanised by sulphur and peroxide systems, Colloid Polym. Sci. 280 (2002) 1097–1103.
[14] A. Kampes, B. Tieke, Self-assembly of carboxylated latex particles at charged surfaces: influences of preparation conditions on the state of order of the monolayers, Mat. Sci. Eng. C-Bio. S 8–9 (1999) 195–204.
[15] D.C. Blackley, Polymer Latices, vol. 1, Chapman & Hall, London, 1997.
[16] S. Thanawan, S. Radabutra, P. Thamasirianunt, T. Amornsakchai, K. Suchiva, Origin of phase shift in atomic force microscopic investigation of the surface morphology of NR/NBR blend film, Ultramicroscopy 109 (2009) 189–192.
[17] P. Li, J. Zhu, P. Sunintaboon, F.W. Harris, Preparation of tatexes with poly(methyl methacrylate) cores and hydrophilic polymer shells containing amino groups, J. Disper. Sci. Technol. 24 (3 & 4) (2003) 607–613.
[18] S. Sangribsub, P. Tangboriboonrat, T. Pith, G. Decher, Adsorption of polystyrene-poly(4-vinylpyridine) diblock copolymer on the assembled latex film, Eur. Polym. J. 41 (2005) 1531–1538.
[19] B. Ding, C. Li, S. Fijita, S. Shiratori, Layer-by-layer self-assembled tubular films containing polyoxometalate on electrospun nanofibers, Colloid Surf. A 284 (2006) 257–262.
[20] Y. Tian, Q. He, C. Tao, J. Li, Fabrication of fluorescent nanotubes based on layer-by-layer assembly via covalent bond, Langmuir 22 (2006) 360–362.
[21] P. Sunintaboon, K.M. Ho, P. Li, S.Z.D. Cheng, F.W. Harris, Formation of nanostructured materials via coalescence of amphiphilic hollow particles, J. Am. Chem. Soc. 128 (2006) 2168–2169.
[22] A. Sruanganurak, P. Tangboriboonrat, Surface modification of sulphur-prevulcanized natural rubber latex sheet via layer-by-layer assembled PMMA particles, Colloid. Surf. A 301 (2007) 147–152.
[23] J. Schmitt, P. Mächtle, D. Eck, H. Möhwald, C.A. Helm, Preparation and optical properties of colloidal gold monolayers, Langmuir 15 (1999) 3256–3266.

Copyright © 2009 American Scientific Publishers
All rights reserved
Printed in the United States of America

Journal of
Biomedical Nanotechnology
Vol. 5, 486–492, 2009

Preparation and Agglutination of Immuno-Nanolatex for Malaria Diagnosis

Duangporn Polpanich[1,2,*], Pramuan Tangboriboonrat[1], and Abdelhamid Elaissari[3,*]

[1] *Department of Chemistry, Faculty of Science, Mahidol University, Bangkok 10400, Thailand*
[2] *National Nanotechnology Center (NANOTEC), National Science and Technology Development Agency (NSTDA), Thailand Science Park, Klong Luang, Pathumthani 12120, Thailand*
[3] *Université de Lyon, F-69622, Lyon, France; Laboratoire d'Automatique et de Génie des Procédés, Université Lyon 1, CNRS, UMR 5007, Villeurbanne 69622, France*

This is the first systematic study on the adsorption of malaria antigen onto latex particles to elaborate immuno-latex for diagnostic purpose. Immuno-latex was prepared from adsorption of malaria antigen onto polystyrene (PS) or poly(styrene-*co*-acrylic acid) (St/AA) latex particles and was used for detection of antibody to *P. Falciparum* based on agglutination test. Adsorption behavior of the malaria antigen onto polymer particles as a function of incubation time, antigen concentration, pH and concentration of the medium was studied. The prepared immuno-latexes were characterized in terms of immuno-agglutination and specific bridging using patient's plasma with *P. Falciparum* infection. This evaluation was performed using photon correlation spectroscopy.

Keywords: Latex, Protein Adsorption, *In Vitro* Test, Malaria, Agglutination.

RESEARCH ARTICLE

1. INTRODUCTION

Malaria remains the most important parasitic disease having a major impact on people in tropical countries.[1] Among the four species of malaria, *P. Falciparum* deserves particular attention because of the severity of disease syndromes that it causes. The enormous variability in *P. Falciparum* proteins, which express from the multi-stage life cycle, is critical to the parasite's survival, enabling it to evade host immune defense. At the moment, there is no commercially available vaccine for the parasite. Additionally, the parasite is increasingly resistant to current antimalarial drug, i.e., chloroquine and the antifolate sulphadoxine/pyrimethamine, as are the *Anopheles* mosquito vector to insecticides.[1–3]

Besides the development of the effective vaccines and antimalarial drugs, the challenge ahead faced in diagnosis and treatment of malaria is a very important aspect of malaria control.[4,5] Generally, the presence of parasites within red blood cells (RBCs) is detected by microscopic examination. However, this technique can be problematic since it takes up to an hour of preparation time and is labor-intensive. In addition, interpretation of the result requires considerable expertise.[1,6] Several companies have recently developed diagnostic kits, based on the enzyme-linked immuno-sorbent assay (ELISA) principle, for detection of malaria such as Malaria Ag CELISA and Pan Malaria IgG CELISA.[7,8] The Malaria Ag CELISA test is applied to detect a circulating histidine rich protein II (HRP II) antigen which is secreted by blood stages of *P. Falciparum* parasites. Although the high sensitivity can be achieved, the HRP II may persist for up to fortnight even after successful therapy, a positive test result does not indicate a failed therapeutic response. While the Malaria IgG CELISA test detected *P. Falciparum* malaria antibody in the serum is used for screening of blood donor for exposure to malaria.[8] However, a negative result does not guarantee the non-transmissible malaria donor due to the fact that early in *P. Falciparum* infection antibody is not detectable and more frequently *P. Malariae, P. Vivax* and *P. Ovale* infections may not result in detectable antibody.[8]

In order to avoid the flat support, colloidal particle which provides large specific surface area is of great interest to use as a solid support of biomolecule.[9–11] Solid-phase immunoassays require latex particle with narrow size distribution and functionalized surface bearing carboxylic, amino or thiol groups for immobilization of antigen (or antibody) in order to form immuno-latex.[12] Innovations for immuno-latex development are filter separation agglutination, particles capture enzyme linked immunosorbent, dyed microsphere sandwich and latex

*Authors to whom correspondence should be addressed.

1550-7033/2009/5/486/007 doi:10.1166/jbn.2009.1037

agglutination tests.[11, 13] In the latter test, the immuno-latex, appeared as smooth polymer particles suspension, is mixed with the fluid to be analyzed. The presence of specific antibody (or antigen) in the analyte creates link between particles resulted in the *in vitro* aggregation or clumping of the microspheres that can be clearly observed with the naked eyes.[14] Not only that it is a rapid test but it is also portable and suitable for use in the field.[14, 15] The key points of this diagnostic test are based on: (i) the use of appropriate latex particle, (ii) that particle used as solid support of biomolecule for capturing step (i.e., antigen or antibody) and (iii) the complex formation with specific antibody (or antigen or target). The high efficiency and sensitivity are related to the amount and conformation of the immobilized biomolecule and the accessibility of the target.[16]

The main objective of this present work is to elaborate sensitive latexes by immobilization of malaria antigen extracted from the malaria parasites onto negatively charged sulfate polystyrene (PS) or carboxylic poly(styrene-*co*-acrylic acid) (St/AA) particles. It was important to note that many works concerning protein adsorption onto latex particles have been done by using bovine serum albumin (BSA) as a protein model.[17–19] To our knowledge, this is the first systematic study on the adsorption of malaria antigen extracted from the malaria parasites adsorbed onto the latex particles. This study was investigated as a function of incubation time, antigen concentration, pH, salinity and specific agglutination of the elaborated latex containing antigen for malaria detection was evaluated by using *P. Falciparum* patients' plasma.

2. EXPERIMENTAL DETAILS

2.1. Preparation and Characterization of Latex Particle

PS and St/AA latexes were synthesized via a batch soap-free emulsion polymerization.[20] Transmission electron microscopy (TEM) (JEOL; TEM 200-cx) was applied to investigate number average diameter ($\bar{D}_n$), weight average diameter ($\bar{D}_w$), and polydispersity index (PDI) of the latex particles. Hydrodynamic diameter ($\bar{D}_h$) of the latex particles in aqueous NaCl solution (1 mM) was measured by Coulter Counter (Coulter electronics; Hialeah) at room temperature. Conductimetric back titration and zeta potential measurement (Malvern, 3000 HS) were used to determine surface charge density (σ) and zeta potential value of the particle, respectively. The data are summarized in Table I.

Table I. Hydrodynamic diameter ($\bar{D}_h$), number average diameter ($\bar{D}_n$), weight average diameter ($\bar{D}_w$), polydispersity index (PDI), surface charge density (σ) and zeta potential values (ζ) of PS and St/AA latexes.

Latex	$\bar{D}_h$ (nm)	$\bar{D}_n$ (nm)	$\bar{D}_w$ (nm)	PDI	σ (μC/cm^2)	ζ (mV) at pH 7
PS	512±49[a]	514	515	1.0014	−4±2[a]	−70±5
St/AA	349±21[a]	335	336	1.0003	−271±9[a]	−50±5

[a]SD: Standard deviation.

2.2. Preparation and Characterization of Malaria Antigen

P. Falciparum parasites (strain AMB47) were cultured in human RBC (group O) at 5% hematocrit in RPMI-1640 medium (pH 7.2), gentamicin (40 μg/mL), HEPES (25 mM) (GIBCOBRL®) and human serum (10%). The parasites were incubated (Heraeus, Hera cell) at 37 °C in CO_2 atmosphere (5%) until reaching mature stages (>3% parasitemia). The mature parasites were enriched by gradient centrifugation (800 g, 25 min) using Percoll (60%) (Sigma). Purity and yield of the enriched pellet was determined under optical microscope (Carl Zeiss, Axiostar plus). After sonication for 25 s and then centrifugation to remove insoluble pigments, the concentration of soluble crude antigen was measured by using the Bradford method.[21]

2.3. Adsorption of Malaria Antigen onto Latex Particle

The known amounts of the polymer particle and of malaria antigen were added to an eppendorf tube and then made up to 500 μl with phosphate buffer (10 mM). The mixture was incubated, while gently stirred for a given time (10 min–3 h), at room temperature before centrifugation (12,000 rpm, 20 min). The supernatant was analyzed and the pellet of particles was resuspended in phosphate buffer (10 mM, pH 7.0) containing bovine serum albumin (BSA) (0.5 mg/ml). The adsorbed amount of protein onto the particle surface (Γ_{ads})was calculated from the following equation:

$$\Gamma_{ads} = \frac{V(C_i - C_f)}{m\Sigma} \quad (1)$$

where V (ml) is volume of the solution, C_i (mg/ml) and C_f (mg/ml) are initial and final concentrations of malaria antigen in the solution, respectively, determined by using the Bradford method, m (g) is mass of the latex particles, and Σ (m^2/g) is specific surface of the PS or St/AA particles.

In order to study effect of protein concentration, various concentrations of malaria antigen (12–50 μg/ml) and polymer particles were incubated in phosphate buffer (10 mM, pH 6.8) for 2 h. For investigation of the influence of electrostatic interaction on the protein adsorption process, the experiment was carried out at various pHs (4.8–8.8) and buffer concentrations (1, 10 and 100 mM) at constant C_i and incubation time.

2.4. Characterization of Immuno-Latex

Zeta potential value of the immuno-latex suspended in phosphate buffer (10 mM) was measured by using Zeta

Sizer in the presence of NaCl solution (1 mM). In each measurement, pH of the medium was adjusted by adding HCl or NaOH (1 M) solution. The average value of each sample was reported for at less three measurements.

2.5. Investigation of Latex Agglutination

Photon correlation spectroscopy (PCS) was conducted to monitor the agglutination reaction. The immuno-latex was diluted with filtered deionized water in order to have particle number (N_p) of about 1.62×10^{10}/l before pouring into a quartz cuvette. The recorded initial D_h was calculated from Stokes-Einstein equation. Then the immuno-latex was mixed with various concentrations of *P. Falciparum*-infected plasma (0.1–0.9 μg/ml) for 10 min before determining the presence of cluster and measuring the aggregate's size twice.

In addition, the appearance of the immuno-agglutinated particles was investigated under optical microscopy (OM). The PS or St/AA immuno-latex (0.2% w/v) (9.5 μl) was mixed with the *P. Falciparum*-infected or naïve control plasma (0.5 μl) onto a glass slide. The slide was tilted with rotating action continuously for 30 s and then covered with a cover glass. The morphology of the cluster of immuno-latex particles was immediately observed under OM at magnification of 50. The aggregate's size was then determined by using Carnoy V2.0 software.

3. RESULTS AND DISCUSSION

3.1. Adsorption of Malaria Antigen onto Latex Particle

Since most of antigen occurs predominantly in mature blood stage parasite (late trophozoite and schizont),[22] the *P. Falciparum* parasites cultured until more than 3% parasitemia of the mature stage were used to prepare malaria antigen. Due to the different density of the infected RBCs in each blood stage (densities of ring stage or uninfected RBCs = 1.10 g/ml, of trophozoite = 1.079 g/ml, and of schizont = 1.070 g/ml),[23] the mature infected RBCs were isolated by using gradient centrifugation. High purity of 94.8% (90–100%) of the enriched parasites with yielding of 60.7% (39.1–92.6%) was obtained. The concentration of malaria crude antigen quantified by Bradford method (in 10 mM phosphate buffer, pH 6.8) was equal to 5.8 mg/ml.

3.1.1. Effect of Incubation Time

The immobilization of protein onto polymeric surface has been extensively examined using various approaches. The result tendency shows that the adsorption phenomena is related to the nature of particle surface and protein, incubation time, protein concentration, pH and the salinity of the medium, and incubation temperature.[24,25] The amounts of malaria antigen adsorbed onto PS and St/AA particles (Γ_{ads}) as a function of incubation time were determined and the data are presented in Figure 1.

As shown in Figure 1, the Γ_{ads} values rapidly increased in the initial period before reaching constant value of 3.0 and 2.8 mg/m^2 for PS and St/AA latexes, respectively, within 20 min. It was believed that the protein transports toward the interface and starts the adsorption via one point attached onto the substrate's surface. This process is driven by the partial dehydration of hydrophobic parts of both protein and surface resulting in an increase in entropy from the freedom gained by water molecules which lowers the Gibbs free energy of the system and, hence, favors adsorption.[26] As the incubation time increases, the structure rearrangement of the protein takes place which encourages the increase in the number of contact points.[27] The adsorption kinetic results were in agreement with the general tendency observed in literature reported that almost all immobilized proteins could be adsorbed within 10–20 min and the adsorption was totally complete during 1–2 h.[25] This rapid adsorption process of malaria antigen might be related to high interaction between both protein and particles. This adsorption behavior is useful to point out the minimal incubation time for reaching equilibrium state.

3.1.2. Effect of Protein Concentration

The adsorption isotherms, i.e., the plot of Γ_{ads} versus the equilibrium protein concentration (C_{eq}) of malaria antigen onto both latexes, were investigated at constant pH (pH 6.8) and salinity (10 mM phosphate buffer). The results obtained are presented as shown in Figure 2. The initial slope at low C_{eq} of the curve indicated the affinity of protein for the substrate's surface.[14]

From Figure 2, it was observed that the Γ_{ads} greatly increased up to the plateau value indicating the saturated

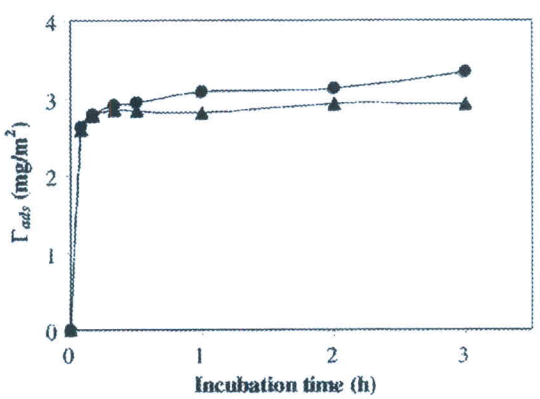


Fig. 1. Adsorption kinetics of malaria antigen onto PS (●) and St/AA (▲) latexes (pH 6.8, 10 mM of NaCl solution).

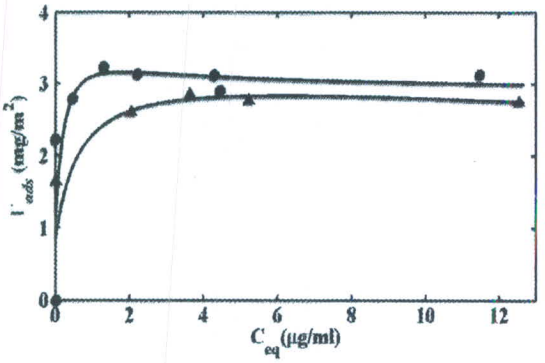


Fig. 2. Adsorption isotherms of malaria antigen onto PS (•) and St/AA (▲) latexes (pH 6.8, 10 mM of NaCl solution, incubation time 2 h).

adsorption of malaria antigen onto the particle of 3.0 and 2.8 mg/m^2 for PS and St/AA particles, respectively. The affinity of the antigen to the PS particle was slightly higher than that of the St/AA surface, which might be due to the hydrophilicity of PAA shell on polystyrene seed.[28,29] The observed low affinity between protein and PAA shell can be attributed to repulsive hydration forces, which decreased conformational entropy.

3.1.3. Effects of pH and Buffer Concentration

According to the amphoteric nature of antigen protein, the effects of pH and ionic strength of adsorption medium were considered in order to better understand the driving force involving in the adsorption process. The Γ_{ads} of malaria antigen onto PS and St/AA latex particles as function of pH (4.8–8.8) at various buffer concentrations (1, 10 and 100 mM) are given in Figure 3.

It could be presumed that the adsorption of the malaria antigen onto PS particle was not drastically sensitive to pH. On contrary, the adsorption of malaria antigen (Γ_{ads}) onto St/AA based particle greatly decreased with increasing pH to alkaline region, irrespective of buffer concentration. Since crude antigen is the mixture of proteins from malaria parasites and RBCs whose physical properties such as molecular mass and isoelectric point (pI) are different, it was difficult to identify type of protein adsorbed onto the particle surface and also to point out the real effect of ionic strength. Although the maximum Γ_{ads} of various proteins onto negatively charged particle was generally found at pH around pI of the protein due to the minimized of intra- and intermolecular electrostatic repulsions of the protein molecules.[17,30] But our results did not show this trend. The explanation of a large decrease of Γ_{ads} with increasing pH in the case of St/AA latex might be contributed by several reasons. At alkaline pH medium, the ionisation (protonation or dissociation) of amino acids along the protein chain caused the increment of net negative charges of antigen molecule. This led to the increase in the electrostatic repulsion among the approaching antigen molecules and the highly negative charged St/AA latex which did not favour the adsorption process. In addition, the increase of molecular volume of the antigen molecule with increasing pH probably attributed to the decrease on adsorption capacity.[31] While the adsorption of malaria antigen onto PS particle took place even when charges of protein and its sorbent are the same.

Additionally, Figure 3 shows that the adsorption onto PS particle was increased with increasing buffer concentration. It could be due to the fact that charges of antigen molecule were screened leading to the depletion of electrostatic repulsion in the interior of antigen and the lateral repulsion between the adsorbed antigen molecules. These caused the high amount of antigen molecules possibly adsorbed onto a given surface area of PS. In addition, as formerly reported, the increase of salt concentration could reinforce the hydrophobic interaction between protein molecule and solid support leading to the increasing the amount of adsorbed protein.[31] This behavior suggested that the hydrophobic interaction mainly governed the adsorption of malaria antigen onto the PS particle.

The opposite trend was noticed when St/AA particle was exploited as the adsorbent, i.e., the protein adsorbed amount was inversely proportional to the buffer concentration. Such results could be also explained by considering the influence of salt concentration on the PAA layer's thickness. As previously demonstrated, the hydrodynamic radius of the fully dissociated PAA chain of a spherical brush St/AA particle declined when the ionic strength was increased.[32] As shown in Figure 4, with increasing salinity, the interacting sites or $-COO^-$ groups along the shrinkage PAA chains reduced the accessible surface for malaria antigen molecule due to steric hindrance. From the results, it could be concluded that the driving force for malaria

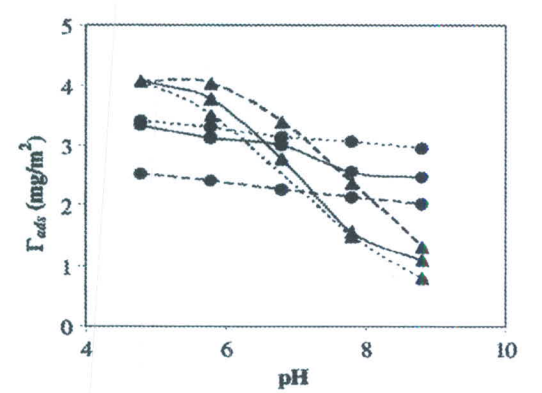


Fig. 3. Γ_{ads} of malaria antigen adsorbed onto PS (•) and St/AA (▲) latexes as a function of pH at various buffer concentrations; 1 mM (- - -), 10 mM (—) and 100 mM (···) (C_i = 29.3 μg/ml, incubation time 2 h).

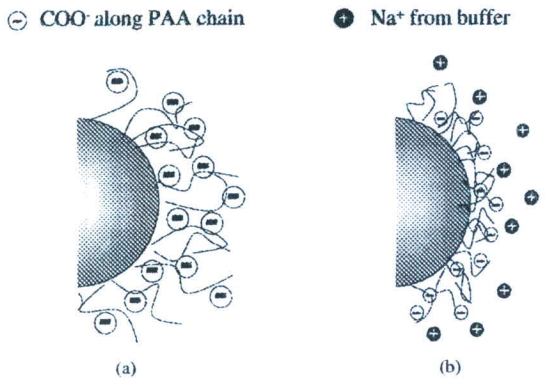


Fig. 4. Schematic illustrations of St/AA surface at (a) low and (b) high buffer concentrations.

antigen adsorbed onto the St/AA particle was electrostatic interaction.

To examine whether antigen molecule might desorb from the particle surface, after adsorption, the PS and St/AA immuno-latexes were redispersed in the phosphate buffer whose pH and concentration of medium were the same as those used in the adsorption experiment. After centrifugation and determination of the residual protein in the supernatant, no any desorption was observed in both cases. These results suggested that the adsorption of malaria antigen onto the particle surface was irreversible process.

3.2. Examination of Latex Agglutination

3.2.1. Zeta Potential of Immuno-Latex

Zeta potential measurement was applied to characterize the latex after being adsorbed with malaria antigen. The data obtained would relate to the colloidal stability of the adsorbed particles. Figure 5 shows the zeta potential values of PS and St/AA immuno-latexes at Γ_{ads} 3.0 and 2.8 mg/m^2, respectively, compared with the bare PS and St/AA particles as a function of pH.

As expected, the zeta potential values of the latex particles before and after antigen adsorption were significantly different. Bare PS and St/AA particles exhibited the negative zeta potential values in the investigated pH due to the presence of $-SO_4^-$ in the case of PS and the presence of both $-SO_4^-$ and $-COO^-$ originated from initiator (ammonium persulfate) and AA monomer, respectively, for St/AA particle. While the PS and St/AA immuno-latexes showed the positive zeta potential value at pH 3.0 and then became more negative with increasing pH. The pI value of the PS and St/AA immuno-latexes was 3.8 and 3.6, respectively. The slightly higher pI in the case of PS immuno-latex might be caused from the larger Γ_{ads}. The observed positive zeta potential was attributed to the cationic character of the adsorbed antigen at acidic pH. It was important to note that each immuno-latex particle gave the lower colloidal stability indicated by the less zeta potential (in absolute value) value compared to that of the bare one. This might provoke the nonspecific agglutination of particles which is a crucial problem for the development of latex agglutination test. Several research groups improved the colloidal stability of the immuno-latex particle by the post-treatment to cover non-occupied surface part of the immuno-latex with BSA.[33] The BSA molecule not only acted as a stabilizer but also suppressed the nonspecific agglutination. Therefore, in this study, we managed BSA post-treatment in order to reduce the nonspecific agglutination.

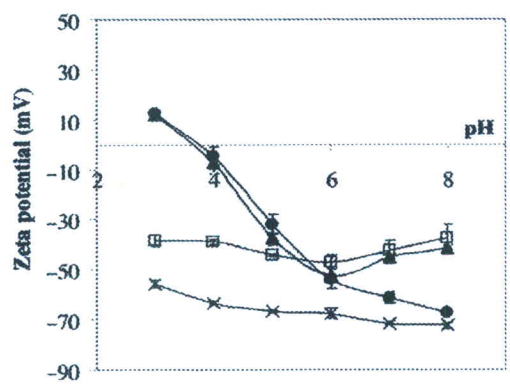


Fig. 5. Zeta potential versus pH for: bare PS (×), bare St/AA (□), PS immuno-latex (Γ_{ads}3.0 mg/m^2) (●) and St/AA immuno-latex (Γ_{ads}2.8 mg/m^2) (▲).

3.2.2. Investigation of Latex Agglutination by Using Photon Correlation Spectroscopy

Photon correlation spectroscopy (PCS) was applied to measure the hydrodynamic diameter (D_h) and average diffusion coefficient (D) of the St/AA immuno-latex particle after mixing with various concentrations of *P. Falciparum*-infected plasma. The plot of D_h values of St/AA immuno-latex versus plasma concentration demonstrated the bell-shape curve, whereas the relationship between D and plasma concentration exhibited the opposite trend.[34] It was explained that, at maximum D_h value which corresponded to plasma concentration of 0.46 μg/ml, the number of antibody in the infected plasma was equivalent to the amount of antigen adsorbed onto the particle surface. This caused the effective binding between antibody and antigen and then the largest size of immune complex.[35] The system seemed to lose the immuno-reactivity when increasing plasma concentration over 0.46 μg/ml possibly due to the saturation of the adsorbed antibody and, consequently, the bridging process was not favorable.

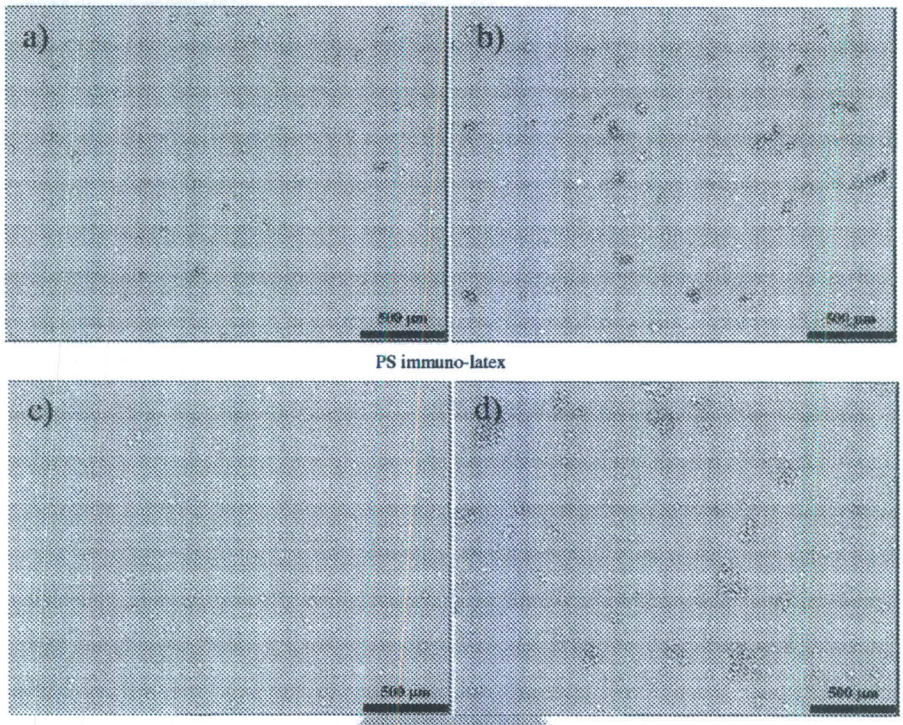


Fig. 6. Optical micrographs of PS and St/AA immuno-latexes after mixing with malaria naïve control [(a, c)] or with *P. Falciparum*-infected plasma [(b, d)].

3.2.3. *Morphology of Latex Agglutination Under Optical Microscope*

The morphology of clusters of immune complexes of PS and St/AA immuno-latexes were investigated via optical microscope. The micrographs of PS and St/AA immuno-latexes after mixing with malaria naïve control or with *P. Falciparum*-infected plasma are displayed in Figures 6(a, c) and (b, d), respectively.

It was observed in Figures 6(b) and (d) that the immune complex's size after mixing PS or St/AA immuno-latexes with *P. Falciparum*-infected plasma was 53 and 150 μm, respectively. The size of the immune complex belonging to St/AA immuno-latex when mixed with the infected plasma (Fig. 6(d)) was significantly larger than that mixed with the control sample (Fig. 6(c)). Whereas the slight difference in the immune complex's size of PS immuno-latex mixed with those plasma was noticed in Figures 6(a) and (b). The low immuno-reactivity of PS immuno-nanolatex might be caused from the loss of antigen's nature conformation while deformation or spreading onto hydrophobic PS surface during adsorption process[28] or the adsorption was performed via the active part of the antigen. On contrary, the hydrophilic St/AA surface improved the antigen-antibody interaction by extending the PAA-antigen complex into the aqueous phase allowing the accessibility of free-targeted antibody.

4. CONCLUSIONS

Well-characterized PS and St/AA particles provided a great potential to be used as a solid support for malaria *P. Falciparum* antigen extracted from parasites by using gradient centrifugation. The fast adsorption kinetics was achieved irrespective of types of latex. The Γ_{ads} values of the kinetic curves reached a constant value of 3.0 and 2.8 mg/m^2 for PS and St/AA, respectively, within only 20 min. The affinity of malaria antigen toward the St/AA particle was lower than that of the PS particle. By varying pH and concentration of adsorption medium, the adsorption of malaria antigen onto PS particle was mainly governed by hydrophobic interaction, whereas the electrostatic interaction dictated the St/AA particle adsorption with the antigen. By using photon correlation spectroscopy (PCS) and optical microscopy (OM) techniques, the occurrence of immune complexes after mixing the St/AA immuno-latex with the *P. Falciparum*-infected plasma was confirmed. This indicated that the St/AA immuno-latex might be introduced as an alternative tool for malaria diagnosis.

Acknowledgments: Research grant from The Thailand Research Fund (TRF) to Pramuan Tangboriboonrat, scholarships to Duangporn Polpanich under the TRF Golden Jubilee Ph.D. Program and French Embassy in Thailand are gratefully acknowledged. The authors would like to express sincere gratitude to Dr. R. Udomsangpetch for providing all facilities to prepare malaria antigen and insightful discussions and suggestions. Finally, the authors thank the BioMérieux Company for research support through the chemicals and equipments.

References and Notes

1. World Health Organization, World malaria report; WHO/HTM/GMP/2008.1, World Health Organization, Geneva **(2008)**.
2. R. G. Ridley, Medical need scientific opportunity and the drive for antimalarial drugs. *Nature* 415, 686 **(2002)**.
3. International Artemisinin Study Group, Artesunate combinations for treatment of malaria: meta-analysis. *Lancet* 363, 9 **(2004)**.
4. World Health Organization, Malaria rapid diagnosis: Making it work, World Health Organization, Philippines **(2003)**.
5. World Health Organization, WHO informal consultation on laboratory methods for quality assurance of malaria rapid diagnostic tests, World Health Organization, Philippines **(2004)**.
6. A. Moody, Rapid diagnostic tests for malaria parasites, *Clin. Microbiol. Rev.* 15, 66 **(2002)**.
7. C. M. Kifude, H. G. Rajasekariah, D. J. Sullivan, Jr., V. A. Stewart, E. Angov, S. K. Martin, C. L. Diggs, and J. N. Waitumbi, Enzyme-linked immunosorbent assay for detection of Plasmodium falciparum histidine-rich protein 2 in blood, plasma, and serum. *Clin. Vaccine Immunol.* 15, 1012 **(2008)**.
8. Data on http://www.cellabs.com.au, CeLLabs Pty Limited (Accessed May 2009).
9. C. Pichot, Surface-functionalized latexes for biotechnological applications. *Curr. Opinion Colloid Interface Sci.* 9, 213 **(2004)**.
10. J. Park, S. Kurosawa, J. Watanabe, and K. Ishihara, Evaluation of 2-methacryloyloxyethyl phosphorylcholine polymeric nanoparticle for immunoassay of C-reactive protein detection. *Anal. Chem.* 76, 2649 **(2004)**.
11. D. Polpanich, P. Tangboriboonrat, A. Elaissari, and R. Udomsangpetch, Detection of malaria infection via latex agglutination assay. *Anal. Chem.* 79, 4690 **(2007)**.
12. C. Wang, W. Yang, and S. Fu, Colloidal Polymers: Synthesis and Characterization, edited by A. Elaissari, Marcel Dekker Inc., New York **(2003)**, pp. 93–116.
13. L. B. Bangs, New developments in particle-based immunoassay: Introduction. *Pure Appl. Chem.* 68, 1873 **(1996)**.
14. J. A. Molina-Bolivar and F. Galisteo-Gonzalez, Colloidal Biomolecules, Biomaterials, and Biomedical Applications, edited by A. Elaissari, Marcel Dekker Inc., New York **(2004)**, pp. 53–101.
15. T. H. Abdoel and H. L. Smits, Rapid latex agglutination test for the serodiagnosis of human brucellosis. *Diagn. Microbiol. Infect. Dis.* 57, 123 **(2007)**.
16. L. Davalos-Pantoja, J. L. Ortega-Vinuesa, D. Bastos-Gonzalez, and R. Hidalgo-Alvarez, Colloidal stability of IgG- and IgY-coated latex microspheres. *Colloids Surf. B* 20, 165 **(2001)**.
17. W. Li and S. Li, A study on the adsorption of bovine serum albumin onto electrostatic microspheres: Role of surface groups. *Colloids Surf. A Physicochem. Eng. Aspects* 295, 159 **(2007)**.
18. N. Shamim, L. Hong, K. Hidajat, and M. S. Uddin, Thermosensitive-polymer-coated magnetic nanoparticles: Adsorption and desorption of bovine serum albumin. *J. Colloid Interface Sci.* 304, 1 **(2006)**.
19. D. Duracher, R. Veyret, A. Elaissari, and C. Pichot, Adsorption of bovine serum albumin protein onto amino-containing thermosensitive core-shell latexes. *Polym. Int.* 53, 618 **(2004)**.
20. D. Polpanich, P. Tangboriboonrat, and A. Elaissari, The effect of acrylic acid amount on the colloidal properties of polystyrene latex. *Colloid Polym. Sci.* 284, 183 **(2005)**.
21. M. M. Bradford, A rapid and sensitive method for the quantitation of microgram quantities of protein utilizing the principle of protein-dye binding. *Anal. Biochem.* 72, 248 **(1976)**.
22. A. E. Bianco, P. E. Crewther, R. L. Coppel, H. D. Stahl, D. J. Kemp, R. F. Anders, and G. V. Brown, Patterns of antigen expression in asexual blood stages and gametocytes of *Plasmodium falciparum*. *Am. J. Trop. Med. Hyg.* 38, 258 **(1988)**.
23. K. Y. Zhang, J. X. Zhou, J. K. Huang, B. H. Lin, Z. H. Wu, C. W. Yuan, and Q. L. Huang, Purification of isolation of different stages of *Plasmodium vivax*, *P. falciparum* and *P. berghei*. *Zhongguo Ji Sheng Chong Xue Yu Ji Sheng Chong Bing Za Zhi (Chinese Journal of Parasitology & Parasitic Diseases)* 11, 262 **(1993)**.
24. Z. G. Peng, K. Hidajat, and M. S. Uddin, Adsorption of bovine serum albumin on nanosized magnetic particles. *J. Colloid Interf. Sci.* 271, 277 **(2004)**.
25. D. Duracher, R. Veyret, A. Elaissari, and C. Pichot, Adsorption of bovine serum albumin onto amino-containing thermosensitive core-shell latexes. *Polym. Int.* 53, 618 **(2004)**.
26. C. A. Haynes and W. Norde, Globular proteins at solid/liquid interfaces. *Colloid Surf. B* 2, 517 **(1994)**.
27. H. Kawaguchi, D. Duracher, and A. Elaissari, Colloidal Biomolecules, Biomaterials, and Biomedical Applications, edited by A. Elaissari, Marcel Dekker Inc., New York **(2004)**, pp. 189–210.
28. W. Norde and J. Lyklema, Why proteins prefer interfaces. *J. Biomater. Sci. Polym. Edn.* 2, 183 **(1991)**.
29. A. Gessner, R. Waicz, A. Lieske, B. R. Paulke, K. Mader, and R. H. Muller, Nanoparticles with decreasing surface hydrophobicities: Influence on plasma protein adsorption. *Inter. J. Pharm.* 196, 245 **(2000)**.
30. J. Serra, J. Puig, A. Martin, F. Galisteo, MaJ Galvez, and R. Hidalgo-Alvarez, On the adsorption of IgG onto polystyrene particles: Electrophoretic mobility and critical coagulation concentration. *Colloid Polym. Sci.* 270, 574 **(1992)**.
31. D. Gao, D. Q. Lin, and S. J. Yao, Mechanistic analysis on the effects of salt concentration and pH on protein adsorption onto a mixed-mode adsorption with cation ligand. *J. Chromatogr. B* 859, 16 **(2007)**.
32. X. Guo, A. Weiss, and M. Ballauff, Synthesis of spherical polyelectrolyte brushes by photoemulsion polymerization. *Macromolecules* 32, 6043 **(1999)**.
33. J. L. Ortega-Vinuesa and D. Bastos-Gonzalez, A review of factors affecting the performances of latex agglutination tests. *J. Biomater. Sci. Polym. Edn.* 12, 379 **(2001)**.
34. D. Polpanich, P. Tangboriboonrat, and A. Elaissari, Colloidal Nanoparticles in Biotechnology, edited by A. Elaissari, John Wiley & Sons, Inc., Hobohen, New Jersey, USA **(2008)**, pp. 65–93.
35. J. L. Ortega-Vinuesa, J. A. Molina-Bolivar, J. M. Peula, and R. Hidalgo-Alvarez, A comparative study of optical techniques applied to particle-enhanced assays of C-reactive protein. *J. Immunol. Methods* 205, 151 **(1997)**.

Received: 31 March 2009. Revised/Accepted: 17 June 2009.

เอกสารแนบ 5.1.4

Reduction of Surface Friction of Natural Rubber Film Coated with PMMA Particle: Effect of Particle Size

Waranya Anancharungsuk,[1] Wirach Taweepreda,[2] Supa Wirasate,[1] Rattaporn Thonggoom,[1] Pramuan Tangboriboonrat[1]

[1]*Department of Chemistry, Faculty of Science, Mahidol University, Phyathai, Bangkok 10400, Thailand*
[2]*Polymer Science Program, Faculty of Science, Prince of Songkla University, Hatyai, Songkla 90112 Thailand*

Received 6 August 2009; accepted 21 September 2009
DOI 10.1002/app.31459
Published online 4 November 2009 in Wiley InterScience (www.interscience.wiley.com).

ABSTRACT: The friction coefficient of the sulphur-prevulcanized natural rubber (SPNR) film could be effectively reduced by deposition of poly(methyl methacrylate) (PMMA) particles. The nanoscale surface roughness of rubber, determined by atomic force microscope, was directly proportional to the particle size of PMMA particle at 12% surface coverage (Cs). The %Cs and surface roughness of the modified SPNR increased, while the friction coefficient decreased, with increasing PMMA latex concentration and immersion time. By using a mixture of latexes having both large and small sizes, the increase in the amount of small particles resulted in the better distribution of large particles deposited on the rubber surface. © 2009 Wiley Periodicals, Inc. J Appl Polym Sci 115: 3680–3686, 2010

Key words: emulsion polymerization; films; rubber; self-assembly; surfaces

INTRODUCTION

Friction between skin and rubber is a crucial drawback in the application of gloves made of sulfur-prevulcanized natural rubber (SPNR) latex. In general, the friction coefficient of SPNR can be decreased with powder, grease or liquid. However, the use of lubricating powder such as talc or corn starch to dust the surgical gloves can cause contamination to the patient. Moreover, it is known that talc does not help the wound healing process and corn starch causes allergic reactions.[1] Recently, the mimetic behavior has been obtained by deposition of poly (methyl methacrylate) (PMMA) nanoparticles onto the SPNR film by using the simple and versatile Layer-by-Layer (LbL) technique.[2,3] The surface charge on SPNR sheet was derived from grafted polyacrylamide (PAAm), under UV, onto the rubber surface pretreated with Ar plasma. By the electrostatic interaction between the negative PMMA latex particles and the SPNR grafted with PAAm (SPNR-*g*-PAAm), the possible loss of coated particles is, therefore, overcome. This has been proven by the insignificant change of the amount of PMMA particles on the SPNR-*g*-PAAm film after applying 7 stretched cycles.[3] These particles caused an increase in surface roughness and effectively reduced the friction coefficient of rubber, which resulted from the decrease of contact area between the bodies.[4]

It was reported that the convenient and direct route for reducing real contact area (RCA) and, hence, friction between silicon surfaces was the deposition, followed by dry etching of microparticles having different sizes on the surface.[5] Analysis of the friction of the elastomer, carried out using a friction tribometer with different sizes of spherical steel indenter, confirmed that the friction coefficient decreases with increasing surface roughness directly linked to the decrease of RCA. The model, proposed by Bowden and Tabor, showed that the friction force due to adhesion force on rough surface was determined by the distribution of the number of asperities and asperity heights or shapes in contact.[6,7] Another source of the friction attributed to deformation depends also on the surface asperities of elastic, plastic or viscoelastic material.

As variation in the particle size of coated particles randomly adsorbed on SPNR would affect the hillocks and RCA, effect of the size of PMMA particles on the surface roughness and friction of SPNR-*g*-PAAm was investigated in this present work. The different sizes of PMMA latexes were synthesized by soap-free emulsion polymerization. As in the previous case on monodispersed PMMA, the modified

Correspondence to: P. Tangboriboonrat (scptb@mahidol.ac.th).
Contract grant sponsor: The Thailand Research Fund, Commission on Higher Education; contract grant number: RTA5180003.

© 2009 Wiley Periodicals, Inc.

rubber was characterized by using scanning electron microscope (SEM), atomic force microscope (AFM), and friction test machine.

EXPERIMENTAL

Materials

Methyl methacrylate (MMA) monomer (Fluka, Purum) was purified by passing through a column packed with neutral and basic aluminum oxide (Fluka, Purum). The purified monomer was stored at 4°C until use. Acrylamide (AAm) monomer (Fluka, Purum) and methanol (Merck, AR) were used as received.

Surface modification of SPNR sheet

A dried rubber sheet, casted from SPNR latex (Dr. Boo, Chonburi, Thailand), was pretreated with Ar plasma prior to surface grafting, under UV, with PAAm.[2] The SPNR-*g*-PAAm sheet was then immersed into PMMA latex synthesized by the soap-free emulsion polymerization using potassium persulphate (KPS) as initiator. To obtain anionic PMMA particles with the size of 162, 364, 480, or 626 nm, MMA concentration of 0.18, 1.46, 2.19, or 3.28*M*, respectively, was added in the aqueous solution of KPS (0.18 g) dissolved in deionized water (137 g) and the polymerization took place at 80°C for 2 h. The remaining steps and characterizations were carried out as explained elsewhere.[2] By varying immersion time, latex concentration and ionic strength, the surface coverage (Cs), determined from the ratio of the area of the deposited PMMA particles to the selected area under SEM image (15 × 21 μm^2), could be adjusted.[8]

Characterization of SPNR sheet coated with PMMA particles

Morphology of the modified SPNR sheet surface was examined by using a Multimode AFM (Digital Instrument, Nanoscope IIIa) equipped with Nanoscope IIIa controller in tapping mode with the scan size of 20 × 20 μm^2. Because of the fact that PMMA particles were deposited onto a smooth SPNR surface, the surface mean roughness (R_a) was calculated from Nanoscope software by applying the following equation previously used by Perrin et al.[9]:

$$R_a = \frac{1}{n}\sum_{j=1}^{n} |Z_j|$$

where Z_j is current difference between the height and the mean plane and n is number of points in the image.

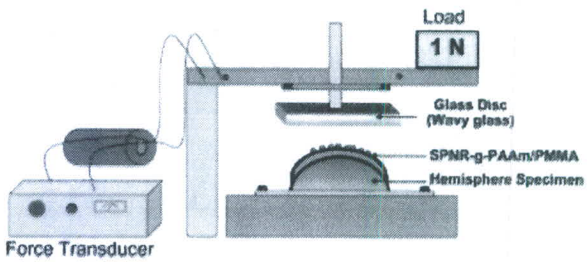


Figure 1 Schematic view of plate-on-hemisphere type friction test machine. [Color figure can be viewed in the online issue, which is available at www.interscience.wiley.com.]

In tapping mode the cantilever is driven to oscillate at near its resonance frequency by a small piezoelectric element mounted on the AFM tip holder.[10] An electronic servo uses the piezoelectric actuator to control the height of the cantilever above the sample to maintain an oscillation amplitude while the cantilever is scanned over the sample. A height image is, therefore, produced by imaging the force of the oscillating contacts of the tip with the sample surface. The friction coefficient of the SPNR-*g*-PAAm coated with PMMA particles was then measured by using a friction test machine (TE 75R, Plint) as schematically shown in Figure 1.

The device consists of a wavy glass disc, fixed on the arm of counterbalance connected to the force transducer. Load was applied by a dead weight at 1*N* on a tip of counterbalance. The specimen (2.5 × 5.0 cm^2) was clamped on a rubber hemisphere. The friction coefficient was measured by moving the glass surface against the specimen with stroke length of 5 mm at a speed of 0.25 mm/s in six cycles and four directions.

RESULTS AND DISCUSSION

Effect of NaCl on %Cs

Because of the fact that the thickness of electrical double layer or Debye length (κ^{-1}) affects the hydrodynamic volume of charge particle, the effect of ionic strength of PMMA latex, with the smallest particle size (162 nm), on %Cs was investigated. Both the zeta potential of PMMA latex and %Cs values as a function of NaCl concentration are presented in Figure 2.

As expected, the Cs increased from 7.7 to 12.3% with increasing [NaCl] from 0 to 0.1*M* which correlated well with the decrease of the absolute value of zeta potential from −40 to −30 mV. It could be explained that the presence of NaCl compressed the electrical double layer and decreased the repulsion among the charged particles which, consequently, allowed the high number of particles to deposit onto

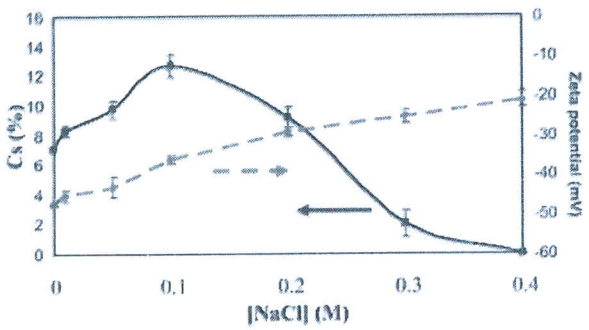


Figure 2 Effect of NaCl concentration on zeta potential of PMMA latex particle (162 nm) and on %Cs values of SPNR-*g*-PAAm sheet coated with the PMMA ([PMMA] = 3 mg/mL, pH 4, immersion time = 30 min). [Color figure can be viewed in the online issue, which is available at www.interscience.wiley.com.]

the SPNR-*g*-PAAm surface.[11] However, with increasing [NaCl] greater than 0.1*M*, the Cs values suddenly decreased and coagulation visually appeared due to the instability of particles possibly caused by screening of the surface charge on the particles by Na^+ and Cl^-. The results also agreed well with the zeta potential value which illustrated that the charged colloidal particles are unstable in the range of −30 to + 30 mV.[12]

The higher Cs value when adding 0.1*M* NaCl (12.3%) compared to that in the absence of NaCl (7.7%) was clearly observed under SEM. The micrographs of the SPNR-*g*-PAAm film surfaces coated with PMMA latex particles without NaCl and with adding 0.1*M* NaCl are, respectively, shown in Figure 3(a,b).

It has been reported that the influence of electrical double layer of small particles on the surface coverage is more significant than that of large particles,[8,13] the maximum %Cs when depositing PMMA particles with the smallest size of 162 nm was selected for further investigation. In the study of the effect of PMMA particle size on the surface roughness and friction of the modified rubber, the Cs value of SPNR-*g*-PAAm sheets adsorbed with PMMA particles having sizes of 162, 364, 480, or 626 nm was fixed at 12% by varying the latex concentration and immersion time.

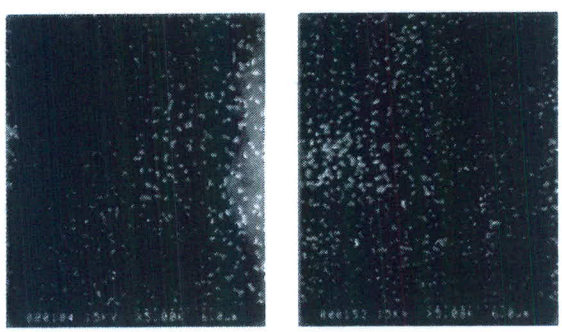


Figure 3 SEM micrographs of SPNR-*g*-PAAm surfaces adsorbed with PMMA particles; (a) without NaCl and (b) with adding 0.1*M* NaCl ([PMMA] = 3 mg/mL, pH 4, immersion time = 30 min).

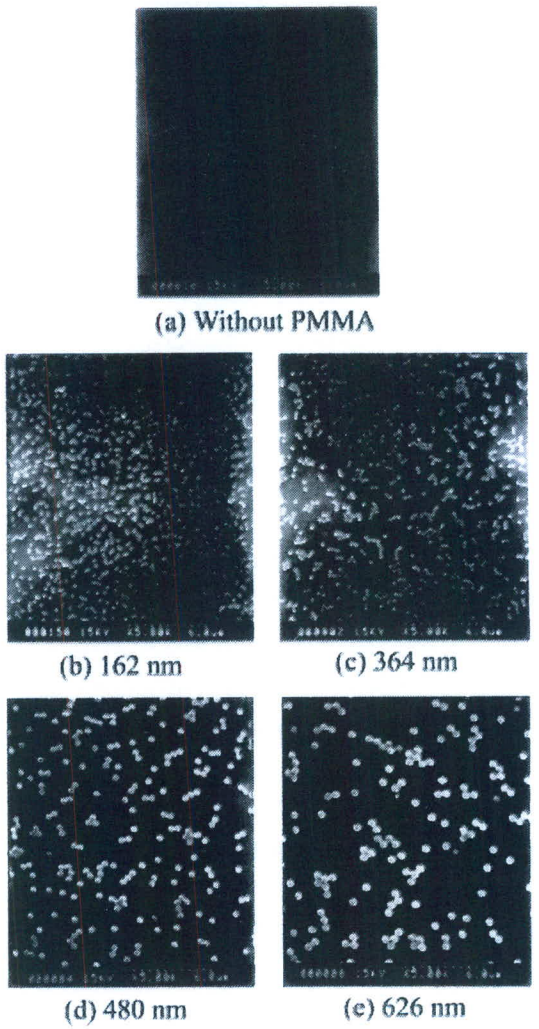


Figure 4 Surface morphology of (a) SPNR-*g*-PAAm and SPNR-*g*-PAAm surfaces coated with PMMA particles sizes of (b) 162, (c) 364, (d) 480, (e) 626 nm (Cs = 12%).

Effect of PMMA particle size

Figures 4 and 5 show the surface morphology, obtained from using SEM and AFM, of (a) SPNR-*g*-PAAm and SPNR-*g*-PAAm films after being deposited with PMMA particles having sizes of (b) 162, (c) 364 (d) 480 and (e) 626 nm at 12% Cs.

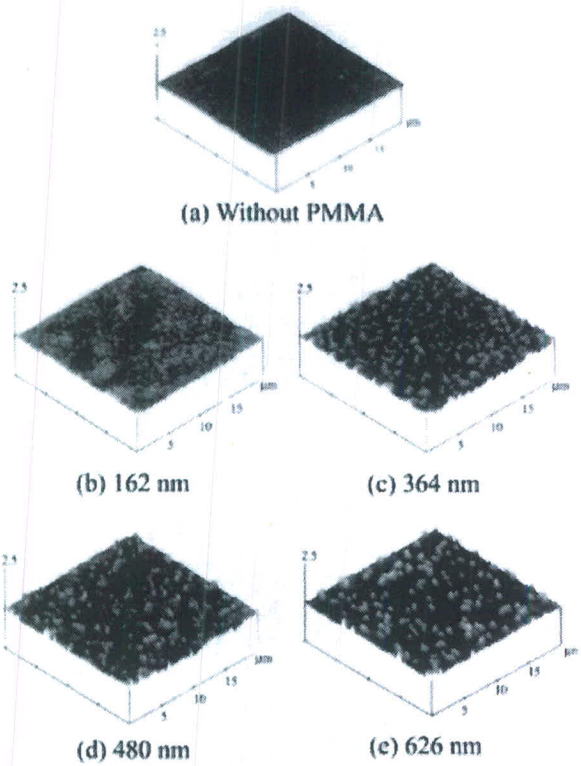


Figure 5 AFM images of (a) SPNR-*g*-PAAm and SPNR-*g*-PAAm surfaces coated with PMMA particles having sizes of (b) 162, (c) 364, (d) 480, (e) 626 nm (Cs = 12%). [Color figure can be viewed in the online issue, which is available at www.interscience.wiley.com.]

The micrographs in Figures 4 and 5 clearly showed that the PMMA particles adsorbed onto the rubber sheet in the form of monolayer possibly due to the strong repulsion between charge particles.[14] However, some aggregates were formed especially when using the large particles (626 nm). It can be explained by the effect of capillary force which is theoretically two order of magnitude higher than the electrostatic repulsive force of particles.[14,15] Moreover, the attractive capillary force between two particles during drying is proportional to the square of the diameter.

To obtain the surface mean roughness (R_a) value of the SPNR-*g*-PAAm sheets coated with PMMA particles, the AFM in tapping mode was used and the R_a values, obtained from the topographic images, plotted versus particle sizes are displayed in Figure 6.

The results clearly indicated that the R_a of SPNR-*g*-PAAm sheet coated with PMMA increased with increasing PMMA particle size at fixed *Cs*. It is likely that the decrease of contact area of the top surface of the sample is responsible for this observation. The presence of hard PMMA particles on the SPNR-*g*-PAAm surface resulted in the change in both surface chemical compositions and surface roughness. Consequently, the friction coefficient reduced from 2.2 for SPNR-*g*-PAAm (R_a = 29.7 nm) to 2.0 for SPNR-*g*-PAAm sheets coated with PMMA particles having particle size of 162 nm (R_a = 49.9 nm). However, for the rubber sheets coated with PMMA particles series, the %Cs was maintained at 12%, thus, friction force in this case is mainly dependent on the roughness, which directly linked to the real contact area. The increase in R_a from 49.9 to 72.6 nm corresponded to the decrease of the friction coefficient from 2.0 for SPNR-*g*-PAAm sheets coated with PMMA particles having particle size of 162 nm to 1.4 for the rubber sheet coated with PMMA having large particle size (626 nm) as shown in Figure 6.

Effect of %Cs

Because of the fact that the larger PMMA particle deposited onto the SPNR-*g*-PAAm provided the lower surface friction at fixed Cs, the largest PMMA particle size was selected for the study of the effect of %Cs on surface roughness and friction of the rubber. The SEM and AFM micrographs of the SPNR-*g*-PAAm surfaces coated with PMMA particles (626 nm) at various Cs values, obtained by varying dipping time and latex concentration, are presented in Figure 7.

As previously observed, the topographic images showed that these large PMMA particles, especially at high %Cs in Figure 7(e,f), arranged onto the SPNR-*g*-PAAm surface in aggregate form. Besides the capillary force, the bridging effect caused from the grafted PAAm chain which dangled into the solution and attached several latex particles might be responsible for the aggregation.[16] These aggregates

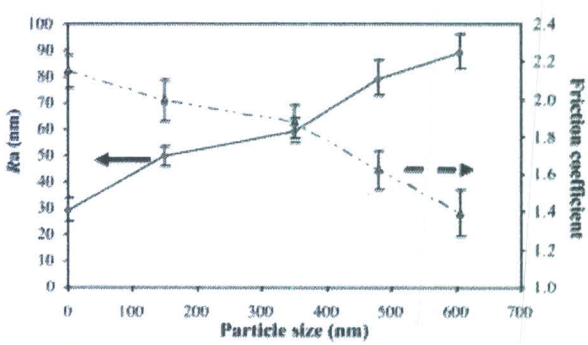


Figure 6 Surface mean roughness (R_a) and friction coefficient of SPNR-*g*-PAAm and SPNR-*g*-PAAm sheets coated with PMMA particles having various sizes (Cs = 12%). [Color figure can be viewed in the online issue, which is available at www.interscience.wiley.com.]

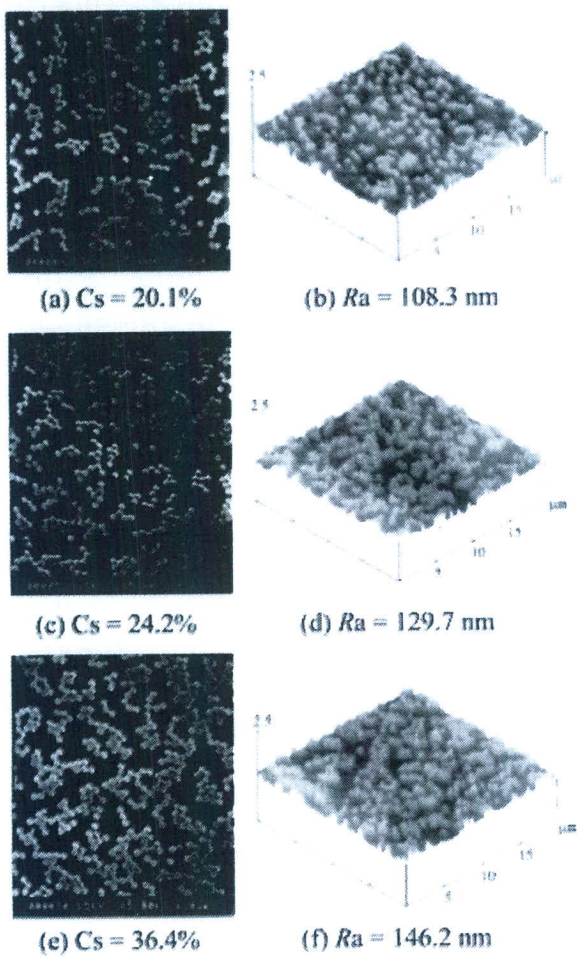


Figure 7 SEM and AFM micrographs of SPNR-*g*-PAAm surfaces coated with PMMA particles of 626 nm showing various %Cs and R_a. [Color figure can be viewed in the online issue, which is available at www.interscience.wiley.com.]

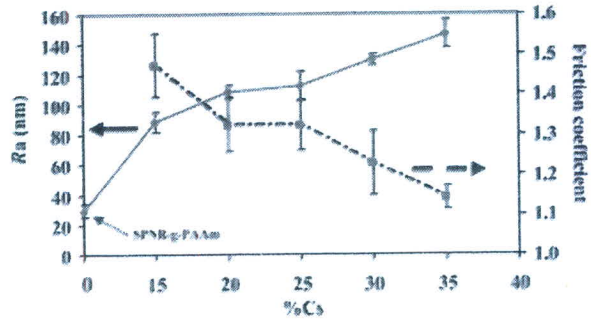


Figure 8 Effects of Cs value on R_a and friction coefficient of SPNR-*g*-PAAm surface coated with PMMA particles (626 nm). [Color figure can be viewed in the online issue, which is available at www.interscience.wiley.com.]

Effect of polydispersity of PMMA particles

The highest Cs value of 36.4% obtained from using the largest size PMMA of 626 nm was still lower than that of the calculated value using the random sequential adsorption (RSA) model (54.7%) which indicated the SPNR-*g*-PAAm surface could not be completely covered. It should be noted that the presence of various complex particle-particle, particle-surface or hydrodynamic interactions is not considered in the RSA model.[18]

To increase the amount of PMMA particles on the surface, the deposition of a mixture of latexes having both large and small particle sizes of 162 and 626 nm on the rubber substrate was, therefore, attempted. It was believed that the small particles might adsorb into the interstices between large particles.[18] The %Cs values as a function of various number ratios of the large to small particles ($N_L : N_S$) are presented in Figure 10. The SEM micrographs of

could alter the surface asperities and, consequently, the R_a value was nonlinearly proportional to the %Cs as displayed in Figure 8.[17] An increase of R_a also led to a marked reduction in friction coefficient of the modified SPNR as also shown in Figure 8.

To confirm the stability of PMMA particles deposited onto the SPNR-*g*-PAAm surface, the SEM micrographs of the modified SPNR surface before and after rubbing for six cycles in four directions under the friction test machine are shown in Figure 9. The slightly change of %Cs from 36.4 to 33.4 might be due to the grafting PAAm chains which are able to increase the interfacial adhesion between particle and matrix.[18] It was, therefore, concluded that the SPNR-*g*-PAAm coated with PMMA particles was stable under the rubbing conditions.

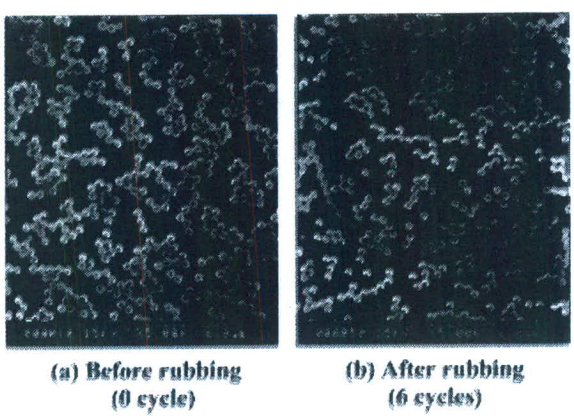


Figure 9 SEM micrographs of SPNR-*g*-PAAm surfaces coated with PMMA particles of 626 nm (a) before and (b) after rubbing for six cycles

the SPNR-*g*-PAAm surfaces at $N_L : N_S$ of 1 : 4, 1 : 12, and 1 : 17 are, respectively, displayed in Figure 11(a–c) while Figure 11(d) shows the AFM micrograph when $N_L : N_S$ was 1 : 17.

The results in Figure 10 revealed that the total Cs value decreased with increasing $N_L : N_S$ from 1 : 1 to 1 : 17. At a ratio greater than 1 : 17, the Cs approached a constant value of about 16% which might be explained by the selective deposition of the smaller particles resulting in smaller surface coverage as shown in Figure 11. The increasing number of N_S resulted in a decrease of %Cs. The reason for size selection is a combination of three mechanisms, i.e., (i) smaller particles diffuse faster to the surface from the bulk solution, (ii) small particles adsorbed on the surface may block a comparatively large area for adsorption of larger particles, and (iii) small particles can adsorb in the spaces between larger particles, not accessible for the large particles themselves.[19]

The better distribution of large particles with increasing the quantity of small particles was observed in Figure 11(c). This might be due to the high thickness of electrical double layer of the small particle which, consequently, increased the space between large particles and impeded their approach.[13,19] Similar effect of particle polydispersity on surface coverage was previously reported when a mixture of two silica particle sizes (100 and 500 nm) were adsorbed onto Si substrate having polyelectrolyte multilayer formation.[8] It should be noticed that at the Cs of 15%, the R_a obtained when using bimodal particle size in Figure 11(d) (105 nm) was greater than that obtained when using monodispersed PMMA particle (90 nm) as shown in Figure 8. The increase in R_a in the former case would increase RCA and, hence, potentially reduce the surface friction of rubber sheet.

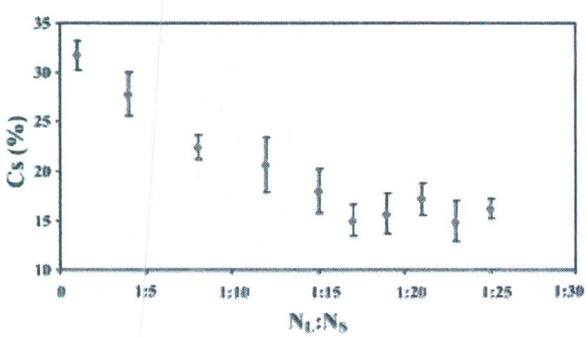


Figure 10 Effect of number ratios of the large (626 nm) to the small particles (162 nm) of PMMA latexes ($N_L : N_S$) on %Cs of the coated SPNR-*g*-PAAm surfaces. [Color figure can be viewed in the online issue, which is available at www.interscience.wiley.com.]

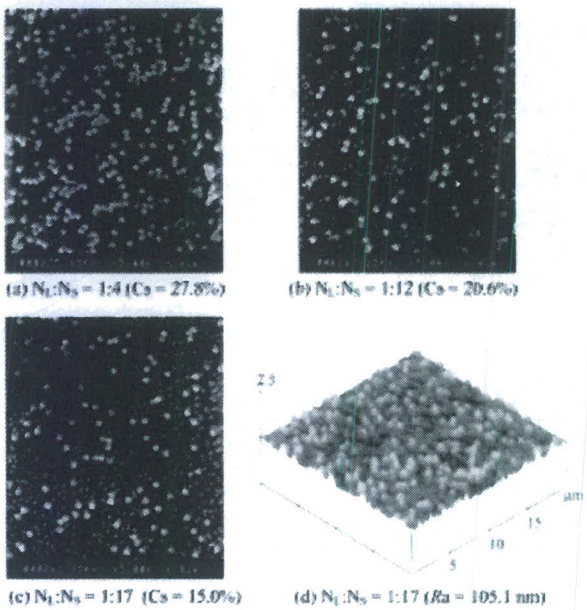


Figure 11 SEM micrographs of SPNR-*g*-PAAm surfaces deposited with a mixture of two PMMA latexes having number ratio of large (626 nm) to small (162 nm) particles ($N_L : N_S$) of (a) 1 : 4 (b) 1 : 12 and (c) 1 : 17 and (d) AFM micrograph at $N_L : N_S$ of 1 : 17. [Color figure can be viewed in the online issue, which is available at www.interscience.wiley.com.]

CONCLUSIONS

At the same %Cs value, the high surface roughness and, hence, low friction coefficient of the SPNR-*g*-PAAm sheet were obtained from coating with PMMA particle having large size (626 nm). By deposition of the large PMMA particles, both surface roughness and friction of the substrate could be further decreased with increasing %Cs. An attempt to cover the surface with the mixture of latex having both small (162 nm) and large particle sizes (626 nm) resulted in a better distribution of large particles which caused a slightly increase in R_a.

References

1. Momose, A. U.S. Pat. 4,597,108 (1986).
2. Sruanganurak, A.; Sanguansap, K.; Tangboriboonrat, P. Colloid Surface A 2006, 289, 110.
3. Sruanganurak, A.; Tangboriboonrat, P. Colloid Surface A 2007, 301, 147.
4. Tabor, D. J Lubric Technol 1981, 103, 169.
5. Zhang, Y.; Sundararajan, S. Tribol Lett 2006, 23, 1.
6. Deshpande, V. S.; Balint, D. S.; Needleman, A.; Giessen, E. V. D. Model Simul Mater Sci Eng 2007, 15, S97.
7. Bowden, F. P.; Tabor, D. Friction: An Introduction to Tribology; Anchor Press: New York, 1973; pp 23–24.
8. Qiu, H.; Lee, W.Y. J Am Ceram Soc 2006, 89, 1180.
9. Perrin, A.; Lanet, V.; Theretx, A. Langmuir 1997, 13, 2557.
10. Dufrene, Y. F. Nature 2004, 2, 451.

11. Sangribsub, S.; Tangboriboonrat, P.; Pith, T.; Decher, G. Eur Polym J 2005, 41, 1531.
12. Zhang, K.; Song, Z.; Lin, C.; Feng, S.; Chen, B. J Ceram Proc Res 2007, 8, 52.
13. Lvov, Y.; Ariga, K.; Onda, M.; Ichinose, I.; Kunitake, T. Langmuir 1997, 13, 6195.
14. Ahn, J. S.; Hammond, P. T.; Rubner, M.; Lee, I. Colloid Surf A 2005, 259, 45.
15. Kralchevsky, P. A.; Nagayama, K. Langmuir 1994, 10, 23.
16. Schmitt, J.; Mächtle, P.; Eck, D.; Möhwald, H.; Helm, C. A. Langmuir 1999, 15, 3256.
17. Klieger, P.; Lamond, J. F. Significance of tests and properties of concrete and concrete-making materials. Technology and Engineering; ASTM: Philadelphia, Pennsylvania, 1994; p. 421.
18. Semmler, M.; Ricka, J.; Borkovec, M. Colloid Surf A 2000, 165, 79.
19. Hanarp, P.; Sutherland, D. S.; Glod, J.; Kasemo, B. J Colloid Interface Sci 2001, 241, 26.

เอกสารแนบ 5.1.5

Colloids and Surfaces B: Biointerfaces 78 (2010) 328–333

Contents lists available at ScienceDirect

Colloids and Surfaces B: Biointerfaces

journal homepage: www.elsevier.com/locate/colsurfb



In vitro cytotoxicity evaluation of natural rubber latex film surface coated with PMMA nanoparticles

Waranya Anancharungsuk[a], Duangporn Polpanich[b], Kulachart Jangpatarapongsa[c], Pramuan Tangboriboonrat[a,*]

[a] Department of Chemistry, Faculty of Science, Mahidol University, Rama 6 Road, Phyathai, Bangkok 10400, Thailand
[b] National Nanotechnology Center (NANOTEC), National Science and Technology Development Agency (NSTDA), Pathumthani 12120, Thailand
[c] Department of Clinical Microbiology, Faculty of Medical Technology, Mahidol University, Bangkok 10700, Thailand

ARTICLE INFO

Article history:
Received 11 October 2009
Received in revised form 3 February 2010
Accepted 22 March 2010
Available online 27 March 2010

Keywords:
Cytotoxicity
Surface modification
Nanoparticles
Latex
Rubber

ABSTRACT

In order to increase surface roughness of the sulphur-prevulcanized natural rubber (SPNR) film and, hence, decrease the direct contact between the rubber and skin, the poly(methyl methacrylate) (PMMA) latex particles were deposited onto the SPNR film grafted with polyacrylamide (SPNR-g-PAAm). The surface coverage of PMMA particles on the SPNR-g-PAAm increased with increasing latex immersion time, particle size and concentration. Prior to the *in vitro* cytotoxicity evaluation on L-929 fibroblasts, the SPNR and SPNR-g-PAAm coated with PMMA particles were extracted by using the culture medium. Results showed that the cytotoxicity effect could be significantly reduced by coating PMMA particles onto the rubber film. At the extract concentrations of ≤12.5% for 24 h at 37 °C, no toxicity potential was detected. The study will be helpful for development of gloves designed for the hypersensitive person.

© 2010 Elsevier B.V. All rights reserved.

1. Introduction

With the aim to avoid the direct contact between hand and object, especially in biomedical and electronic applications, donning gloves is strongly recommended. Due to the good mechanical properties of the thin film, sulphur-prevulcanized natural rubber (SPNR) latex is generally used as raw material for glove manufacture. However, it has been reported that NR latex gloves give rise to certain health disorders in some sensitive individuals [1,2]. Two types of substances that may cause allergic problems are Type I, the naturally occurring non-rubbers from *Hevea brasiliensis* tree and Type IV, the chemicals added into the latex, e.g., antioxidant [2–4]. The Type I reaction is immediate hypersensitivity, mediated by immunoglobulin E (IgE) antibodies to specific proteins in the latex. The symptoms of latex allergy are thought to be due to the massive localization or systemic release of histamine upon binding of the protein allergen to the sensitized IgE-bearing mast cell [2,5–7]. The signs and symptoms may manifest from rhinitis to death. However, the prevalence of latex allergy in population is believed to be very low. Although the leachable latex proteins might be increased when sweats, no cytotoxic potentials to L-929 cells were observed when gloves were extracted with distilled water or saline (9 g/L of NaCl) at 50 °C for 72 h [8].

Besides the chemicals added into NR latex, lubricant powder is sprinkled onto the gloves to facilitate donning and to prevent the inner part of the glove from adhering to itself or to the skin [9,10]. Unfortunately, the use of talc to dust the glove can be harmful, e.g., to surgical wounds, inducing granuloma sarcoma [10]. The problems of corn starch involving allergic reactions and serving as a carrier for bacteria and germs were also reported [7,10]. Currently, the most effective method for preparing powder-free gloves is by chlorination which, however, produces the dark colored and poor ageing gloves. Alternatively, the easy route for reduction of the glove–skin contact area or the surface friction of rubber is by polymer coating [11]. However, friction, stretching or other activities may cause the coating to easily peel-off even during storage [9]. In order to improve the attachment to polymer coating and to mimic the lubricant powder, deposition of the plastic nanoparticles, i.e., poly(methyl methacrylate) (PMMA), onto SPNR film grafted with polyacrylamide (SPNR-g-PAAm) has been processed by using the simple and versatile layer-by-layer (LbL) technique [12,13]. Due to the electrostatic interaction, the monodisperse particles could be firmly adsorbed onto the rubber surface, i.e., the amount of PMMA particles on the SPNR-g-PAAm film did not significantly change after applying with 7 stretched cycles.

Since the PMMA particles' deposition reduced the direct contact area between SPNR film surface and skin, the allergic potential caused by the non-rubbers or additives would effectively decrease. An *in vitro* test using cell culture, an effective method for rapid evaluation employing standard protocols and produce quantita-

* Corresponding author. Tel.: +66 2 201 5135; fax: +66 2 354 7151.
E-mail address: scptb@mahidol.ac.th (P. Tangboriboonrat).

0927-7765/$ – see front matter © 2010 Elsevier B.V. All rights reserved.
doi:10.1016/j.colsurfb.2010.03.025

tive data, was selected for the investigation of the cytotoxicity of SPNR latex film coated with PMMA nanoparticles. Previous work has shown that the latex gloves extracted with the culture medium provided much stronger cytotoxic activity than those extracted with distilled water or saline [8]. It was explained that both polar and non-polar components are extracted by the culture medium from the sample. Therefore, the RPMI-1640 medium was employed for the extraction of SPNR-g-PAAm/PMMA and unmodified SPNR followed by testing, according to ISO 10993-5, with a mouse fibroblast L-929 cell line [14]. The proliferation of L-929 fibroblasts was investigated by counting the number of colonies forming under optical microscope. Scanning electron microscope (SEM) was used for the study of the effect of particle size of PMMA, synthesized by a soap-free emulsion polymerization, on the surface coverage of SPNR-g-PAAm.

2. Experimental

2.1. Materials

Methyl methacrylate (MMA) monomer (Fluka, Purum) was purified by passing through a column packed with neutral and basic aluminium oxide (Fluka, Purum). The purified monomer was stored at 4 °C until use. Acrylamide (AAm) monomer (Fluka, Purum), riboflavin (Sigma) and methanol (Merck, AR) were used as received.

SPNR latex (Dr. Boo Co. Ltd., Chonburi, Thailand) was filtered through a 250 mesh aluminium screen before use. The total solid content (% TSC) was determined by using the method described in ASTM D 1076-97.

2.2. Deposition of PMMA particles onto SPNR sheet

The PMMA latexes with different sizes were prepared by the soap-free emulsion polymerization process at various MMA monomer contents (0.18–3.28 M) using potassium persulfate (4×10^{-4} M) as an initiator. The reaction was carried out at 80 °C for 2 h. The particle size and polydispersity index (PDI) were measured by using dynamic light scattering while the zeta potential was measured by using a microelectrophoresis apparatus (Malvern, Zetasizer nanoZS). Particle number (N_p, per liter) was calculated from the following equation [15]:

$$N_p = \frac{6Sc}{\rho\pi D_h^3} \quad (1)$$

where Sc is the solid content (g/L), ρ is the polymer density, and D_h is the average particle diameter. The remaining steps and characterizations were described elsewhere [12].

Prior to PMMA particles' deposition, the surface of SPNR latex sheet (2.5 cm × 5.0 cm × 0.1 cm) was pretreated with Ar plasma (Basic plasma kit BP-1, Samco) for 90 s. It was then immersed into an aqueous solution of 5 wt% AAm (40 mL) and 0.05 mM riboflavin (2 mL) under UV (Mercury HPLN 1000 W, Phillips) for 30 min. After rinsing with a jet of deionized water, the sample was left in a 60 °C water bath with continuous stirring for 16 h. The SPNR grafted with PAAm (SPNR-g-PAAm) was subsequently dipped into a beaker containing PMMA latex (0.1–5 mg/mL) for 2–30 min. The sample was washed with Milli-Q water via a series of three rinsing baths and dried at room temperature [12]. SEM (S-2500, Hitachi) was used for morphological study and for determination of the surface coverage (Cs) as a ratio of the area of deposited PMMA particles to selected area under SEM image (15 μm × 21 μm) [16].

2.3. In vitro cytotoxicity test

L-929 mouse fibroblast cells were cultured in RPMI completed medium as previously described [17]. Cell viability was stained by tryphan blue exclusion technique and the number of living cells was counted with hemacytometer. The cell morphology and proliferation were observed under an optical microscope (CKX41, Olympus).

The cytotoxicity test was performed by colony-forming technique according to ISO 10993 Part 5 [14]. The samples (0.1 g) of the SPNR-g-PAAm coated with PMMA particles and the unmodified SPNR (positive control) were separately immersed into the completed medium (1 mL), i.e., RPMI-1640 supplemented with HEPES (25 mM), D-glucose (1.8 mg/mL), glutamine (2 mM), gentamicin (40 mg/mL) and 10% heat-inactivated Fetal calf serum (FCS). After incubation at 37 °C under 5% CO_2 for 24 h, the extracted fraction was serially diluted with the completed medium to attain 50, 25, 12.5 and 6.25% extracts. L-929 cells were seeded at the density of 100 cells/well in 24-well plates and incubated for 24 h. The culture medium (negative control) was then replaced by the diluted extract medium. After 6 days, the number of colonies on each well was counted under the microscope and %inhibition of cell growth was evaluated. The P-value (P) was calculated from SAS Analysis V6.12 software.

Table 1
Effect of MMA concentration on the particle size, PDI and particle number of PMMA latexes.

MMA concentration (M)	Particle size (nm)	Polydispersity index (PDI)	Particle number/mL ($\times 10^{12}$)
0.18	162 ± 5	0.017	4.4
0.36	242 ± 4	0.014	4.7
1.46	364 ± 2	0.019	4.6
2.19	480 ± 4	0.045	4.0
2.92	558 ± 6	0.033	4.1
3.28	626 ± 8	0.042	3.9

3. Results and discussion

3.1. Analysis of PMMA latex

Due to the fact that the soap-free emulsion polymerization is based on homogeneous nucleation mechanism, PMMA particles with different sizes (95–100% conversion) were obtained from varying the MMA contents. In the early stage of polymerization, the persulfate radicals initiate the MMA monomer dissolved in the aqueous phase to form oligomeric radicals. When reaching the critical chain length, which is 60–80 units for the MMA monomer, the oligomeric radicals precipitate out of the aqueous phase and the primary particles are formed [18,19]. The particles continuously grow by using monomer transported from the monomer droplet. Their stability maintained by adsorbing ionic fragment of the initiator molecules was confirmed by the negative zeta potential of −33 mV. When the particle number is kept constant, particle size of latex depends mainly on the monomer concentration.

Particle size, PDI and particle number of PMMA latex particles as a function of MMA concentrations were determined and the data are shown in **Table 1**.

From **Table 1**, particle size of PMMA latex increased with increasing MMA concentration while the particle number was almost constant. These results could be explained from the solubility of MMA in water. Since the MMA concentrations used in all cases were greater than their water solubility (0.16 M), the non-initiated MMA monomer could diffuse into the primary particles previously formed in the initial stage of nucleation [20]. Consequently, the particle diameter increased with increasing MMA concentration whereas no new particles were generated and the latex particles were kept stable [21]. The PDI and the particle number in **Table 1** correlated well with the explanation within this monomer concentration range [20].

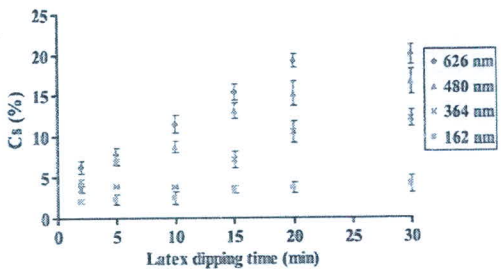


Fig. 1. %Cs values versus time used for dipping SPNR-g-PAAm films into PMMA latexes having various sizes (pH 4, [PMMA] = 0.1 mg/mL).

3.2. Effects of PMMA latex concentration and immersion time

The effect of PMMA particle size (162, 364, 480 and 626 nm), deposited onto the SPNR film, on the percent surface coverage (%Cs) was investigated. Prior to the particles' adsorption, the presence of PAAm onto the SPNR-g-PAAm surface was confirmed by ATR-FTIR spectra, showing the peaks of N–H stretching at 3357 cm^{-1} and C=O stretching of the amide group at 1665 cm^{-1}, and by the low water contact angle of 29° [12,13]. The modified SPNR film was subsequently immersed into the PMMA latex (0.1 mg/mL) at pH 4 and the Cs values plotted with dipping times are presented in Fig. 1.

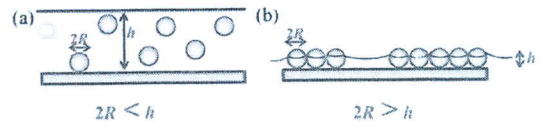


Fig. 3. Two-dimensional ordering of particles, having diameter of 2*R*, suspend in a liquid layer of thickness, *h*, on a substrate: (a) the motion of particles in the liquid layer whose thickness is much larger than the particle size and (b) the capillary forces appear and give rise to aggregation when its thickness becomes comparable or slightly smaller than the particle [26].

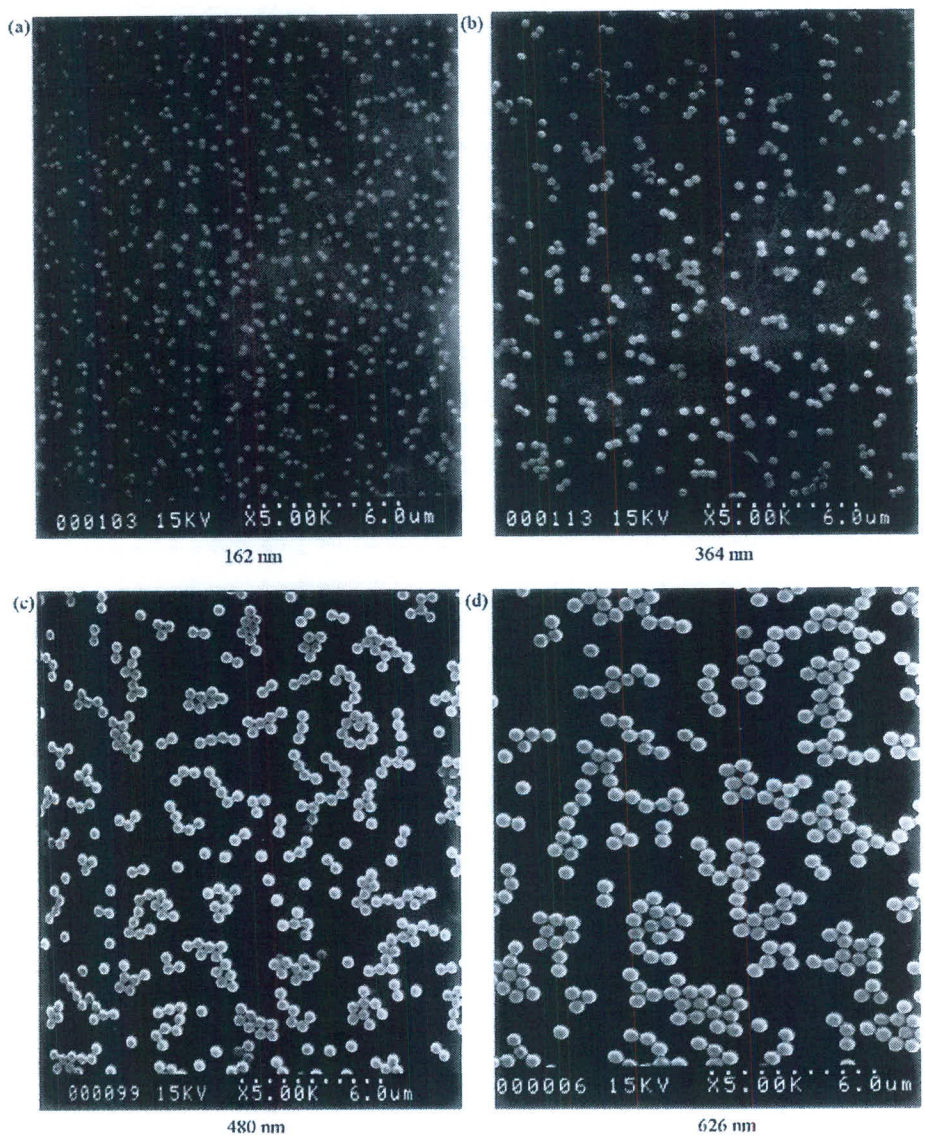


Fig. 2. SEM micrographs of SPNR-g-PAAm deposited by PMMA particles of (a) 162 nm, (b) 364 nm, (c) 480 nm and (d) 626 nm ([PMMA] = 1 mg/mL, immersion time = 10 min).

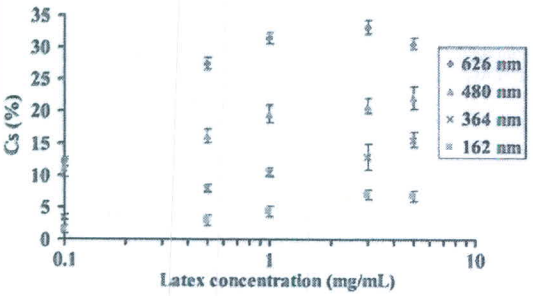


Fig. 4. Effect of concentration of PMMA latex having different particle sizes on %Cs of SPNR-g-PAAm films (pH 4, immersion time = 10 min).

It was observed that the %Cs values linearly increased with increasing immersion time from 2 to 20 min. The nearly constant %Cs, after dipping for 20 min, might be due to the repulsive force between particles in the latex and also those previously adsorbed onto the substrate [22]. Based on the random sequential adsorption (RSA) model, a geometrical jamming limit of the non-interacting particles leads to the maximum Cs of 54.7% [23]. When the particle–particle, particle–surface and hydrodynamic interactions are considered, the %Cs in the experiment is obviously lower than the RSA jamming limit [24].

Results also showed that the %Cs increased with increasing size of PMMA particles. SEM micrographs of PMMA particles with different sizes adsorbed onto the SPNR-g-PAAm surface ([PMMA] = 1 mg/mL, immersion time = 10 min) are displayed in Fig. 2.

The more uniform PMMA particle distribution on the SPNR-g-PAAm surface was observed in Fig. 2(a) when the smaller particles were used. The aggregation of larger particle might be due to the effect of capillary force which is the main contribution of structural rearrangement of particles during the drying step [25]. The rearrangement of particles, having diameter of $2R$, on a flat plate with a liquid layer of thickness, h, caused from capillary force is schematically presented in Fig. 3.

The particles in the top layer suddenly protrude from the thinning liquid films when change from disordered state, Fig. 3(a), to the ordered state in Fig. 3(b) [26]. The gravity plays the role of keeping the film surface planar by the disjoining pressure. When the film is thin enough, the capillary interactions between colloidal particles are entirely governed by the surface tension and the effect of gravity is negligible. The theoretical calculations show that the adhesion force between particle and substrate is proportional to the particle diameter, while the attractive capillary force between two particles during drying is proportional to the square of the diameter [27,28]. Therefore, with an increase in diameter, the significant capillary forces pull the particles together to form islands as observed in Fig. 2(d). However, a detailed understanding of this effect is still lacking.

In order to maximize the surface coating, the effect of PMMA latex concentration on the %Cs of SPNR-g-PAAm film was then studied (pH 4, immersion time = 10 min) and the data are displayed in Fig. 4.

Fig. 4 clearly showed that, at fixed latex concentration, the larger particle size provided the higher Cs value possibly due to the thinner electrical double layer [16,29]. Moreover, for all particle sizes, the %Cs increased with increasing the latex concentration until 5 mg/mL. It was explained that the high latex concentration favored the repulsion among similar charged particles providing the great collision between surface of the particle and that of the substrate as mentioned earlier. However, for 5 mg/mL of the PMMA latex with the largest size (626 nm), the slightly decrease of Cs value was observed. It was believed that the aggregated particles impeded the deposition of new particles on the surface [23].

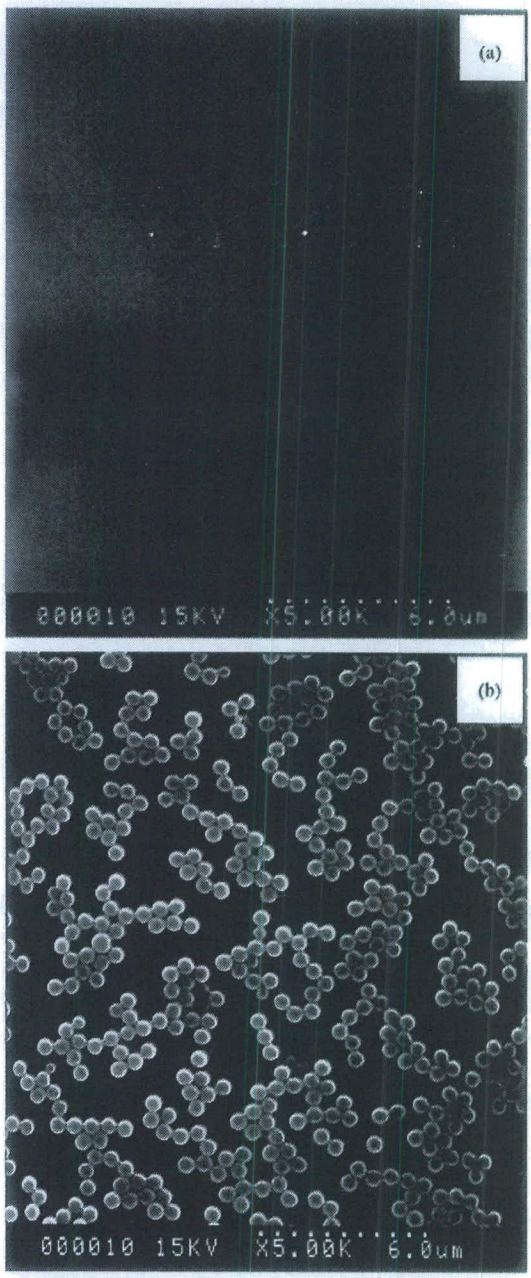


Fig. 5. SEM micrographs of (a) unmodified SPNR and (b) SPNR-g-PAAm coated with PMMA particles (size = 626 nm, Cs = 35%).

From these results, it was clearly observed that the highest Cs value of 35% was achieved when the largest PMMA particle size of 626 nm was adsorbed onto the SPNR-g-PAAm. SEM micrographs of the SPNR-g-PAAm/PMMA compared with the unmodified SPNR are shown in Fig. 5. These samples were selected for *in vitro* cytotoxic testing in the further step.

3.3. *In vitro cytotoxicity test on L-929 fibroblasts*

Similar to other materials aimed for use in biomedical applications, the toxicity of latex gloves made of the SPNR-g-PAAm/PMMA was evaluated. The recommended *in vitro* cytotoxicity test to L-

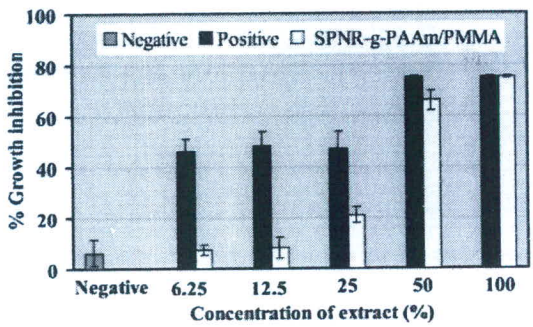


Fig. 6. Growth inhibitions of L-929 fibroblasts as a function of concentrations of the extract of SPNR-g–PAAm/PMMA films compared with that of unmodified SPNR (positive control) (extraction time 24 h, 37 °C) and of the medium without the extract (negative control).

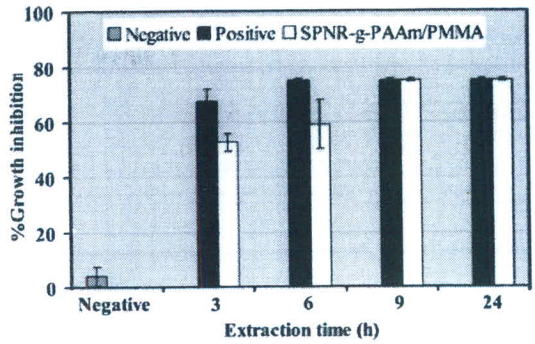


Fig. 7. Growth inhibition value of L-929 fibroblasts at various extraction times of the SPNR-g- PAAm/PMMA films compared with the unmodified SPNR film (37 °C, 100% extract concentration).

929 fibroblast cells related to hypersensitive users was performed [30].

3.3.1. *Effects of extract concentrations and time on growth inhibition*

Growth inhibition of L-929 fibroblast cells by the extract was determined by colony-forming assays (CFA) [12,31]. Cells were cultured under various concentrations of the test liquid extract comparing to that of positive (SPNR) and the negative (without the extract) controls. The number of cell colonies was examined at day 6 when cell proliferate and colonies formed were clearly observed [31] and the data are shown in Fig. 6.

As compared to the negative control, ≤12.5% diluted sample slightly affected the growth inhibition of L-929 cells ($P \leq 0.01$). The higher concentration of the extract of 25, 50 and 100%, resulted in the higher percentage of growth inhibition of the cells of 21, 66 and 75% inhibition, respectively. When compared with the unmodified SPNR at the extract concentrations ≤25%, the significant decrease of growth inhibition was clearly observed ($P = 0.02$), i.e., the cytotoxicity was effectively reduced by the surface modification of coating PMMA particles onto the SPNR-g–PAAm.

In order to mimic the physiological conditions, the extraction time of the SPNR-g–PAAm/PMMA and the unmodified SPNR was decreased from 24 to 3 h at 37 °C. The relationship between extraction time and % growth inhibition when using 100% extract concentration at day 6 is shown in Fig. 7.

It was noticed that, at short extraction times (≤6 h), the % growth inhibition of SPNR-g–PAAm/PMMA sample was lower than that of SPNR ($P \leq 0.02$). At longer extraction times (≥9 h), the growth inhibition attained the maximum value of 75% in both cases. The data indicated that the long extraction time resulted in the increase of substance released from the sample and, hence, more cells growth inhibition and toxicity [32,33]. From the results, it could be assumed that the SPNR latex gloves modified by PMMA particles' adsorption could be considered to be safe under normal conditions.

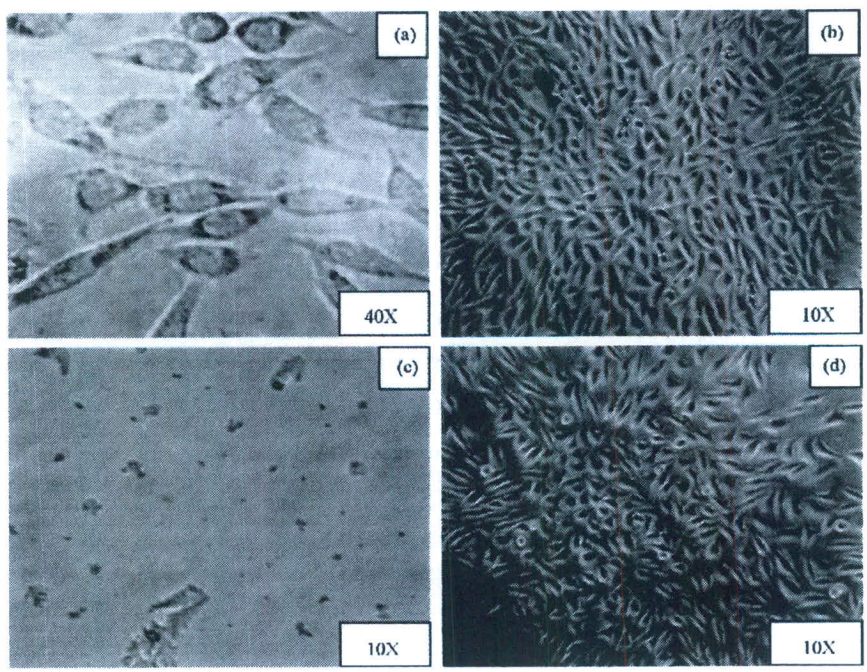


Fig. 8. Morphology of L-929 cells incubated with negative control (a) and (b), positive control (c) and SPNR-g–PAAm/PMMA sample (d) (25% extract concentration, day 6 after culturing).

3.3.2. Morphologies of L-929 fibroblasts exposed to SPNR and SPNR-g–PAAm/PMMA

The optical micrographs of L-929 cells incubated with medium extract of SPNR-g–PAAm/PMMA sample compared with the negative and positive controls are displayed in **Fig. 8**.

From **Fig. 8**(a) and (b), spindle-shaped and adherent cells growing as a confluent monolayer were observed. Similar to the negative control in **Fig. 8**(b), the SPNR-g–PAAm/PMMA extract did not affect morphology and cell proliferation as presented in **Fig. 8**(d), i.e., the cells spread out and exhibited a spindle to elongated shape which revealed normal morphology and proliferation pattern. On the contrary, the morphology of cells significantly changed, i.e., loss of spindle shape and detachment from the plate, when using the unmodified SPNR sample as shown in **Fig. 8**(c). Moreover, these cells could not continuously grow or proliferate. From these results, it could be suggested that the SPNR extracted by the culture medium had inhibitory effect on the growth of normal L-929 cell lines, while the SPNR-g–PAAm/PMMA sample effectively reduced the cytotoxicity.

4. Conclusions

When using the extract concentrations ≤25% for 24 h, the cytotoxicity of the SPNR film to L-929 mouse fibroblast cells was effectively reduced by coating its surface with PMMA latex particles. At the maximum Cs, monitored by using large particle size, long immersion time and high latex concentration, the growth inhibition of the cells increased with increasing the concentration and time of extraction. Although the maximum growth inhibition of 75% was induced by 100% extract concentration for 24 h, at the extraction time ≤6 h, the 100% extract of SPNR-g–PAAm/PMMA significantly reduced the toxicity to the cells. These findings proved valuable for further *in vivo* toxicity and more intensive allergenic investigations for developing of powder-free gloves.

Acknowledgement

Research grant (RTA5180003) from The Thailand Research Fund (TRF)/the Commission on Higher Education (CHE) to P.T. is gratefully acknowledged.

References

[1] F.W. Perrella, A.A. Gaspari, Methods 27 (2002) 77.
[2] H.M. Binkley, T. Schroyer, J. Catalfano, J Athl Training 38 (2003) 133.
[3] P. Cullinan, R. Brown, A. Field, J. Hourihane, M. Jones, R. Kekwick, R. Rycroft, et al., Clin Exp Allergy 33 (2003) 1484.
[4] K. Turjanmaa, H. Alenius, S. Makinen-Kiljunen, T. Rcunala, T. Palosou, Allergy 51 (1996) 593.
[5] A.M. Spina, H.J. Levine, L. Ky, Oral Surg Oral Med Oral Pathol 87 (1999) 5.
[6] C.R. Hamann, K. Turjanmaa, R. Rietschel, C. Siew, D. Owensby, S.E. Gruninger, K.M. Sullivan, JADA 129 (1998) 43.
[7] M.O. Osman, S.L. Jensen, World J Surg 23 (1999) 630.
[8] H.S. Baek, J.Y. Yoo, D.K. Rah, D.-W. Han, D.H. Lee, O.H. Kwon, J.-C. Park, Yonsei Med J 46 (2005) 579.
[9] W. Truscott, Methods 27 (2002) 69.
[10] A. Momose, US Patent No. 4597108 (1986).
[11] F. Hostetller, D. Rhum, M.R. Forman, M.N. Helmus, N. Ding, US Patent No. 6080488 (1986).
[12] A. Sruanganurak, K. Sanguansap, P. Tangboriboonrat, Colloid Surf A 289 (2006) 110.
[13] A. Sruanganurak, P. Tangboriboonrat, Colloid Surf A 301 (2007) 147–152.
[14] Biological evaluation of medical devices-part 5: tests for in vitro cytotoxicity, ISO 10993, 1999, pp.1–8.
[15] H. Shimizu, T. Shiraishi, R. Wada, M. Okabe, Colloid Polym Sci 285 (2006) 107.
[16] H. Qiu, W.Y. Lee, J Am Ceram Soc 89 (2006) 1180.
[17] M. Sokolsky-Papkov, A.J. Domb, J. Golenser, Biomacromol 7 (2006) 1529.
[18] R.M. Fitch, C.H. Tsai, in: R.M. Fitch (Ed.), Polymer Colloids, Plenum, New York, 1971.
[19] Y.C. Chen, C.F. Lee, W.Y. Chiu, J Appl Polym Sci 61 (1996) 2235.
[20] A. Zhang, J. Bao, J Appl Polym Sci 93 (2004) 2815.
[21] S. Gu, H. Akama, D. Nagao, Y. Kobayashi, M. Konno, Langmuir 20 (2004) 7948.
[22] A. Kampes, B. Tieke, Mater Sci Eng (1999) 195, C8–9.
[23] M. Semmler, J. Ricka, M. Borkovec, Colloid Surf A 165 (2000) 79.
[24] Y. Lvov, K. Ariga, M. Onda, I. Ichinose, T. Kunitake, Langmuir 13 (1997) 6195.
[25] H. Cong, W. Cao, Langmuir 19 (2003) 8177.
[26] P.A. Kralchevsky, K. Nagayama, Langmuir 10 (1994) 23.
[27] J.S. Ahn, P.T. Hammond, M. Rubner, I. Lee, Colloid Surf A 259 (2005) 45.
[28] P. Henarp, D.S. Sutherland, J. Glod, B. Kasemo, Colloid Surf A 214 (2003) 23.
[29] T. Serizawa, H. Takeshita, M. Akashi, Langmuir 14 (1998) 4088.
[30] J. Yun, Q. Zhong, J.Y. Kwak, W.H. Lee, Oncogene 24 (2005) 4009.
[31] A. Matsuoka, K. Isama, T. Tsuchiya, J Biomed Mater Res 75A (2005) 439.
[32] J.C. Wataha, P.E. Lockwood, S.K. Nelson, D. Rakich, J Oral Rehabil 26 (1999) 379.
[33] D. Fischer, Y. Li, B. Ahlemeyer, J. Krieglastein, T. Kissel, Biomaterials 24 (2003) 1121.

เอกสารแนบ 5.1.6

Nanocapsules Embedded in Natural Rubber Latex Gloves

Saovaree Tanpantree,[1] Pakorn Opaprakasit,[2] Surapich Loykulnant,[3] Wiyong Kangwansupamonkon,[4] Pramuan Tangboriboonrat[1]

[1]*Department of Chemistry, Faculty of Science, Mahidol University, Phyathai 10400, Bangkok, Thailand*
[2]*School of Bio-Chemical Engineering and Technology, Sirindhorn International Institute of Technology, Thammasat University, Pathumthani 12120, Thailand*
[3]*National Metal and Materials Technology Center, National Science and Technology Development Agency, Pathumthani 12120, Thailand*
[4]*National Nanotechnology Center, National Science and Technology Development Agency, Pathumthani 12120, Thailand*

Received 27 October 2009; accepted 22 January 2010
DOI 10.1002/app.32132
Published online 29 March 2010 in Wiley InterScience (www.interscience.wiley.com).

ABSTRACT: To prepare medical gloves containing disinfectant agent, poly(methyl acrylate) (PMA) with $\overline{M}_w$ of 550 K was synthesized via the iniferter technique and then used for encapsulating disinfectant agent, i.e., chlorhexidine digluconate (CHD), droplets. The CHD-PMA nanocapsules suspended in a sodium dodecyl sulfate aqueous solution having 93% encapsulation efficiency were successfully embedded between the outermost and inner layers of γ-radiation vulcanized natural rubber (RVNR) latex films by the coagulant dipping process. A RVNR/CHD-PMA nanocapsules/RVNR three-layer structure was revealed by the contact angle measurement, ATR-FTIR and SEM. Both the tensile strength and elongation at break of the three-layer film were also measured.
© 2010 Wiley Periodicals, Inc. J Appl Polym Sci 117: 1798–1803, 2010

Key words: elastomers; films; morphology; rubber; surfaces

INTRODUCTION

Natural rubber (NR) latex has been widely used for the production of gloves for medical personnel. Although NR has good mechanical properties which are unmatched by most synthetic rubbers, the gloves, especially those used by surgeons and dentists, are frequently perforated or torn during employment due to needles or sharp objects.[1,2] Medical gloves containing disinfectant droplets were, therefore, developed.[3,4] When the glove is punctured, the antiseptic agent would neutralize infectious agents carried by the needle and a significant reduction of infection rate is obtained.[5]

It is worth mentioning that gloves made of synthetic rubber are rather thick when compared with gloves made of NR latex, hence, tactile sensation and manual dexterity are decreased. The preparation of NR gloves containing chlorhexidine digluconate (CHD), possessing activity against Gram-positive and Gram-negative bacteria, in the form of nanocapsules has been studied.[6–8] Recently, precipitation of poly(methyl acrylate) (PMA) with weight average molecular weight ($\overline{M}_w$) of 470 K onto nanodroplets of a CHD aqueous solution has been applied to prepare nanocapsules by changing the gradient of dichloromethane/cyclohexane.[8] The CHD-PMA capsules were then redispersed in 2% w/v sodium dodecyl sulfate (SDS) aqueous solution before depositing onto the surface of γ-radiation vulcanized natural rubber (RVNR) latex sheet.

In this work, we report the preparation of a three-layer thin film where the outermost and inner layers were RVNR and the active middle layer containing CHD-PMA nanocapsules (RVNR/CHD-PMA nanocapsules/RVNR) by using the coagulant dipping process. To obtain the capsule's wall which is strong enough to prevent any premature release, yet delicate enough to break up under the required circumstances, the synthesis of PMA with $\overline{M}_w$ of 550 K was attempted. The thermal iniferter technique based on controlled radical polymerization under mild conditions was selected for the PMA synthesis.[9] Increases in encapsulation efficiency and capsule's size which would allow the effective release of the disinfectant agent for neutralization of infectious agents were aimed for. The water contact angle measurement,

Correspondence to: P. Tangboriboonrat (scptb@mahidol.ac.th).
Contract grant sponsor: The Thailand Research Fund/Commission on Higher Education; contract grant number: RTA5180003.
Contract grant sponsors: Thailand Graduate Institute of Science and Technology, National Science and Technology Development Agency.

© 2010 Wiley Periodicals, Inc.

attenuated total reflection-Fourier transform infrared spectroscopy (ATR-FTIR), and scanning electron microscopy (SEM) were used for characterization of the coated surfaces. The effects of coagulant ($Ca(NO_3)_2$) concentration on the thickness, tensile strength, and elongation at break of the RVNR/CHD-PMA nanocapsules/RVNR three-layer film were also investigated.

EXPERIMENTAL

Materials

Methyl acrylate (MA) monomer (Fluka, Purum) was purified by passing through a column packed with neutral and basic aluminum oxide (Fluka, Purum) and the iniferter, i.e., *N*-bromosuccinimide (Aldrich, >98%) was recrystallized and dried under vacuum before use. Other reagents, i.e., dichloromethane (Lab-scan, AR), cyclohexane (Lab-scan, AR), methanol (Lab-scan, AR), deuterated chloroform (Wimad), tetrahydrofuran (THF) (Lab-scan, AR), soybean phosphatidylcholine or lecithin (MP Biochemicals), sodium dodecyl sulfate (Fluka, GC), 20% w/v CHD (Sigma), calcium nitrate ($Ca(NO_3)_2$) (TSL chemicals, AR), and Teric 16A16 (East Asiatic, AR) were used as received. The commercial RVNR latex was kindly supplied by the Siam Okamoto Co. (Pathumthani, Thailand).

Synthesis of PMA

Polymerization of PMA using the thermal iniferter was carried out according to the method previously reported.[10] The PMA were synthesized by mixing *N*-bromosuccinimide ($0.68 \times 10^{-2}M$) with MA monomer (11.11*M*) for 300 min. The $\overline{M}_w$ of the PMA was determined by gel permeation chromatography (Waters, 150-CV) at 30°C using THF as eluent. For the chemical structure and end group analysis, PMA (10 mg) dissolved in $CDCl_3$ (2 mL) was analyzed by proton-nuclear magnetic resonance spectroscopy (^{1}H-NMR) (Bruker, DP×400).

Preparation of CHD-PMA nanocapsules

The CHD-PMA nanocapsules, stabilized by lecithin (100 mg), in cyclohexane were prepared by using the controlled nanoprecipitation technique described elsewhere.[6,8] 0.5% w/v SDS aqueous solution (10 mL) was then added into cyclohexane (10 mL) containing the nanocapsules. After evaporation of the cyclohexane by using a rotary evaporator (Buchi, Rotavapor R200) at 40°C for 15 min, the capsules suspended in SDS aqueous solution were obtained.

The sizes of the CHD nanodroplets and CHD-PMA nanocapsules were measured with a dynamic light scattering apparatus (Malvern, Zetasizer NanoZS). The charge density of the nanocapsules redispersed in SDS aqueous solution was determined by a microelectrophoresis apparatus (Malvern, Zetasizer nanoZS). The morphology of the CHD-PMA nanocapsules was examined by Transmission Electron Microscopy (TEM) (JEOL, JEM-2010). The encapsulation efficiency was determined by using ^{1}H-NMR, where deuterated water and a known amount of pyrazine were applied as an external solvent and a calibration product, respectively.[6] The mass of CHD in a nanocapsule was calculated from the area ratio of peaks at 7.66 to 9.07 ppm corresponding to aromatic-protons of CHD and pyrazine, respectively.

Preparation of RVNR/CHD-PMA nanocapsules/RVNR three-layer films

The three-layer film of RVNR/CHD-PMA nanocapsules/RVNR was prepared by the coagulant dipping process. A glass mold was first immersed for 5 s in various concentrations of $Ca(NO_3)_2$ coagulant solution (5, 10, and 15% w/v) mixed with nonionic wetting agent (0.1% w/v Teric 16A16). Thereafter, the mold was dipped in 45% total solid content of RVNR latex. The middle layer containing disinfectant agent was produced by dipping the partially dry first layer in 5% w/v $Ca(NO_3)_2$ for 5 s and, subsequently, in 1% CHD-PMA nanocapsules redispersed in SDS aqueous solution for various dipping times. The sample was washed with Milli-Q water via a series of three rinsing baths and dried at room temperature before being analyzed by water contact angle measurement (G-1, Kruss). Each value of the contact angle reported is the average of at least 10 separate drops of water on a given surface. ATR-FTIR spectra of the samples were recorded on a Bruker EQUINOX 55 spectrometer (32 scans at 4 cm^{-1} resolution) by employing a Ge ATR crystal with face angle of 45° in a single-reflection mode.

The outermost layer was subsequently prepared by following the same procedure as that used in the first step. Finally, the three-layer thin film was dried in an oven at 65°C for 15 min. The surface morphology of RVNR inner and outer layers and that of CHD-PMA nanocapsules deposited onto the rubber film was examined by SEM (Hitachi, S-2500).

The thickness of the three-layer film was measured with a digital caliper (KEIBA) at 10 different areas of each sample. The dumbbell specimens were used for tensile testing (Instron, model 5566), stamped out of the three-layer film by using a sharp die according to DIN 53504. For each sample, at least five specimens were tested with a crosshead speed of 100 mm/min using a load cell of 1000*N*.

RESULTS AND DISCUSSION

Characterization of CHD-PMA nanocapsules

The synthesized PMA having $\overline{M}_w$ of 550 K and molecular weight distribution ($\overline{M}_w/\overline{M}_n$) of 1.6 was used for the preparation of capsule's shell. The size of monodisperse CHD droplet was 251 ± 7 nm, whereas that of the nanocapsules suspended in cyclohexane and in SDS aqueous solution were 385 ± 7 and 386 ± 18 nm, respectively. The zeta potential value of the CHD-PMA nanocapsules in SDS aqueous solution which was constant at about −95 mV, confirmed the electrostatic stabilization of the capsules in the medium. From the similar size of CHD-PMA nanocapsules in both media, it can be deduced that a tight molecular interlocking of the long PMA chains effectively entrapped the CHD. The result was confirmed by the high-encapsulation efficiency of CHD-PMA nanocapsules dispersed in cyclohexane (100%) and those redispersed in SDS aqueous solution (93%), as determined by ^{1}H-NMR. A well-defined structure of nanocapsules redispersed in 0.5% SDS aqueous solution, observed under TEM, is shown in Figure 1.

Characterization of CHD-PMA nanocapsules deposited onto RVNR latex film

Water contact angles of the CHD-PMA nanocapsules deposited onto the RVNR latex film are plotted in Figure 2 versus dipping times.

The results show that the water contact angle of the RVNR surface covered with CHD-PMA nanocapsules abruptly decreased from 95° to 46° within the first 3 min of dipping time. After immersing for 3 min, the contact angle approached a constant value, which implies complete coverage of the CHD-PMA nanocapsules on the rubber surface. The low water contact angle confirms the presence of CHD-PMA nanocapsules, whose surface beared lecithin and/or SDS molecules. The present results agree with the values of water contact angle of poly(ether urethane) grafted with lecithin and the gelatin particles stabilized by SDS which were 43° and 50°, respectively.[11,12]

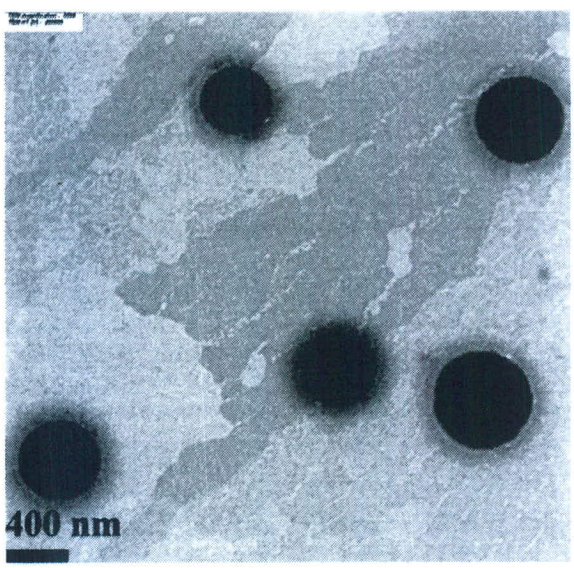


Figure 1 TEM micrograph of CHD-PMA nanocapsules redispersed in 0.5% of SDS aqueous solution.

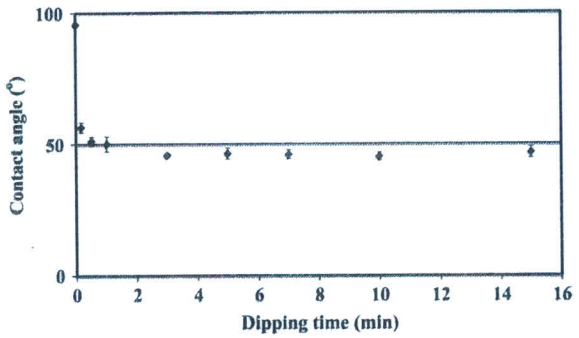


Figure 2 Water contact angles of RVNR film coated with CHD-PMA nanocapsules as a function of dipping time.

The ATR-FTIR spectra of RVNR and CHD-PMA coated-RVNR films are shown in Figure 3 as a function of dipping time.

In the spectrum of RVNR, characteristic peaks at 2961, 2922, 2856 (C—H stretching), 1450, 1378 (C—H bending of $-CH_3$) and 837 cm^{-1} (C—H deformation of *cis* C=C—H) are seen. In addition, a weak C=O stretching band is observed at 1725 cm^{-1} due to a trace amount of carbonyl groups generated during vulcanization.[13] After deposition of PMA nanocapsules, the spectra show an intense C=O stretching mode associated with carbonyl of PMA at 1730 cm^{-1}.[14] The two observable peaks related to CHD

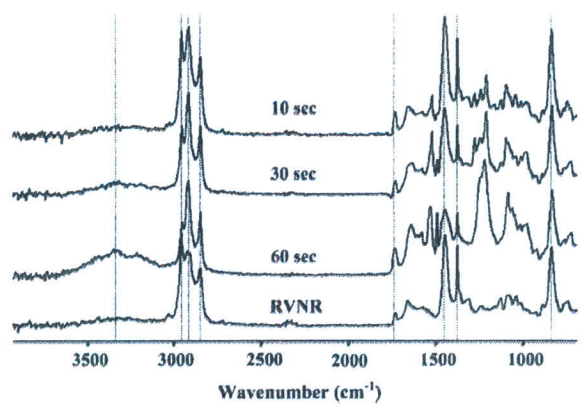


Figure 3 ATR-FTIR spectra of RVNR and CHD-PMA nanocapsules deposited onto the RVNR surface for various dipping times.

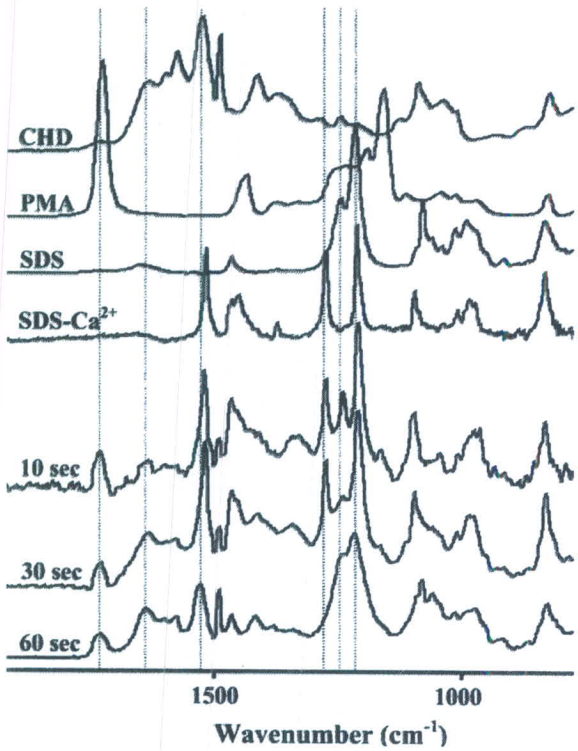


Figure 4 ATR-FTIR spectra of CHD, PMA, SDS on RVNR, SDS treated Ca^{2+} on RVNR, and CHD-PMA nanocapsules deposited on RVNR with different dipping times (10, 30, and 60 s) after subtraction of the RVNR spectrum.

appear in the spectrum of nanocapsules deposited onto RVNR sheet, i.e., (1) the broad band at 3450 cm^{-1}, possibly attributable to N—H stretching; and (2) an absorption peak at 1500–1650 cm^{-1} from C=C stretching of the aromatic moiety in the CHD molecule.[15,16] The result strongly supports that CHD-PMA nanocapsules are deposited onto the RVNR surface. However, the band characteristics of RVNR is still clearly observed in all samples with dipping times of 10, 30, and 60 s, indicating penetration of the infrared beam through the capsules layer to the RVNR base layer.

Complex vibrational modes in the region of 1600–1000 cm^{-1} are also observed in the spectra. To investigate the origin of these bands, the RVNR spectrum was subtracted from those of the capsule-coated samples to eliminate the rubber characteristics. These spectra are compared with those of PMA, CHD, SDS, and Ca^{2+}-treated SDS in Figure 4. All difference spectra show combinations of band characteristics of PMA at 1730 cm^{-1}, CHD at 1641 and 1530 cm^{-1}, and SDS at 1245 and 1214 cm^{-1} (asymmetric SO_2 stretching), respectively.[17] An increase in intensities of these vibrational modes as a function of dipping time indicates an increase in the degree of nanocapsules deposition.

Intriguingly, the spectra show changes in the vibrational modes of sulfate groups of SDS, i.e., two bands are observed at 1245 and 1214 cm^{-1} in the spectrum of the sample prepared using a dipping time of 60 s. This is similar to those found in the spectrum of the original SDS (neutralized by Ca^{2+}-cations). However, a new band is found at 1278 cm^{-1} in the spectra of the samples prepared using dipping times of 10 and 30 s. This band is probably due to sulfate groups bound with Ca^{2+}, as also observed in the spectrum of Ca^{2+}-treated SDS. The existence of this mode in the samples with dipping times of 10 and 30 s indicates the formation of electrostatic interaction between Ca^{2+} located at the RVNR surface and SDS molecules on the nanocapsules, which plays a key role in the initial stage of deposition. When the submersion time reaches 60 s, the band disappears, i.e., the interaction has diminished. This is because the nanocapsules are probably fused together and fully cover the RVNR surface, which prevents the formation of such interaction in the later stage of deposition. Nonetheless, the existence of the two lower frequency bands indicates the presence of SDS molecules in the nanocapsules layer.

The SEM micrographs of RVNR sheet and RVNR sheets covered with CHD-PMA nanocapsules as a function of dipping time are displayed in Figure 5.

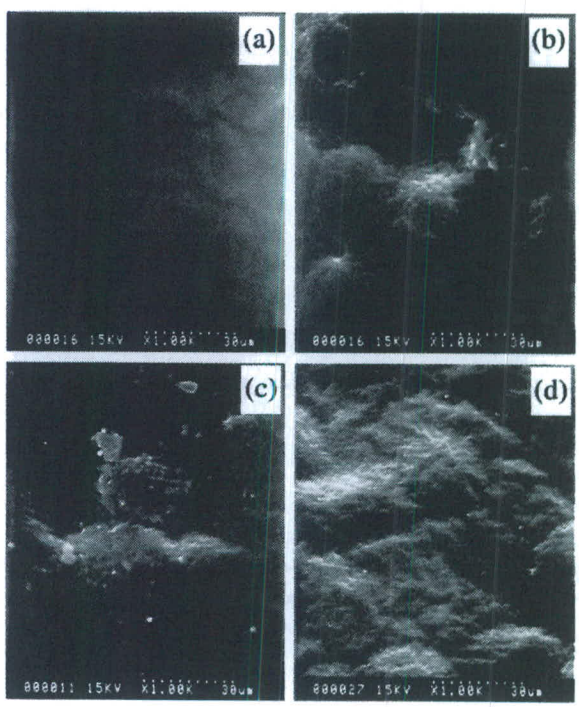


Figure 5 SEM micrographs of (a) RVNR sheet and RVNR sheets covered with CHD-PMA nanocapsules as a function of dipping time; (b) 30 s, (c) 5 min, and (d) 10 min.

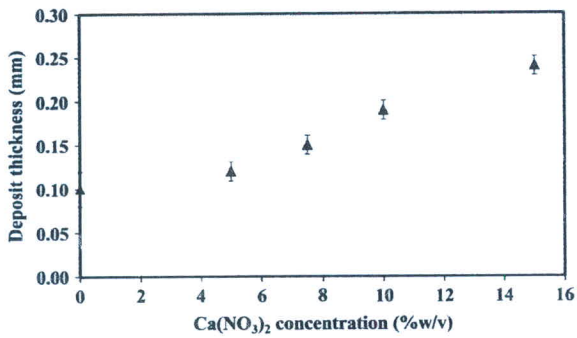


Figure 6 Effect of $Ca(NO_3)_2$ concentration on the thickness of RVNR/CHD-PMA nanocapsules (dipping time for 30 s)/RVNR three-layer film.

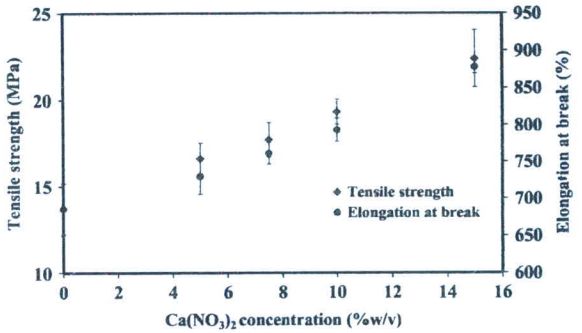


Figure 7 Effect of $Ca(NO_3)_2$ concentration on tensile strength and elongation at break of the RVNR/CHD-PMA nanocapsules/RVNR three-layer films.

A flat and smooth surface of the former is observed in Figure 5(a) when compared with the rough surface caused by the deposited CHD-PMA nanocapsules in the latter [Fig. 5(b–d)]. Because of the low glass transition temperature (T_g) of the PMA shell (15°C), the nanocapsules could fuse and form a film at room temperature.[18] From the micrographs, it can be deduced that the multilayer deposition took place by bridge formation of the nanocapsules to the rubber surface.[19]

Tensile properties and morphology of the three-layer film

Effect of coagulant concentration

The thickness of the RVNR/CHD-PMA nanocapsules/RVNR three-layer film obtained by using various concentrations of $Ca(NO_3)_2$ coagulant was measured and the data are presented in Figure 6.

The results show that the thickness of the RVNR/CHD-PMA capsules/RVNR three-layer film increased proportional to the $Ca(NO_3)_2$ concentration. This is because the higher amount of coagulant on the mold caused a higher rate of diffusion of the coagulant into the latex.[20,21] Without using coagulant, the three-layer film obtained was not uniform.

Because of the fact that some defects of the multilayer thin film might occur during the dipping process, the mechanical properties of the samples as a function of coagulant concentration were measured. The tensile strength and elongation at break of the three-layer films plotted versus $Ca(NO_3)_2$ concentrations are presented in Figure 7.

As observed in Figure 7 both tensile strength and elongation at break of the three-layer thin film linearly increase with increasing $Ca(NO_3)_2$ concentration. The high mechanical properties can be interpreted as the result of interparticle crosslinking through the Ca^{2+} and also of the high film thickness as presented in Figure 6.[22] On the other hand, the thin film obtained without using $Ca(NO_3)_2$ possessed low tensile strength and elongation at break, possibly due to defects, e.g., pinholes, generated during processing.[21]

Surface morphology

The SEM micrographs in Figure 8 show the surface morphologies of (a) the inner RVNR layer; (b) the

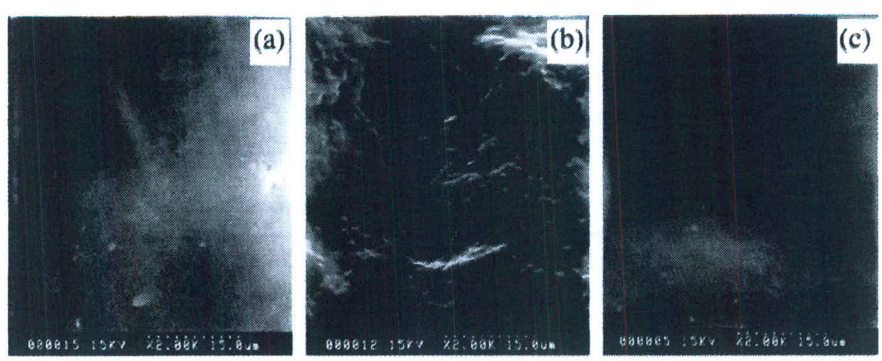


Figure 8 SEM micrographs of the surfaces of (a) inner RVNR layer; (b) RVNR film coat with CHD-PMA nanocapsules (dipping time = 30 s); and (c) the outermost RVNR layer.

RVNR film with CHD-PMA nanocapsules (dipping time = 30 s, using 5% $Ca(NO_3)_2$ as coagulant), and (c) the outermost RVNR layer.

It is observed in Figure 8(a) that the RVNR inner layer exhibits a rather smooth surface which might be attributed to slippage of the wet deposit formed on the mold. Figure 8(b) shows CHD-PMA nanocapsules deposited onto the inner RVNR layer. The multilayer of CHD-PMA nanocapsules covers the RVNR surface and the capsules are fused together due to the low T_g of the PMA shell. Finally, the outermost layer of RVNR was coated onto the nanocapsules middle layer, producing the three-layer thin film. The homogeneous and smooth surface morphology of the outer RVNR layer in Figure 8(c) confirms the advantage of multidipping where the pinholes running through the whole film, if at all existent, are absent. From the micrographs, it can be deduced that the RVNR/CHD-PMA nanocapsules/RVNR three-layer thin film has a suitable structure for further development of disinfectant medical glove's production due to the potential release of CHD for neutralization of infectious agents.

CONCLUSIONS

The size, shell thickness, and encapsulation efficiency of CHD-PMA nanocapsules were significantly improved when using a PMA shell with $\overline{M}_w$ of 550 K. The presence of nanocapsules on the RVNR latex sheet was deduced from the low contact angle value and ATR-FTIR spectra. Under SEM, multilayers of nanocapsules deposited onto the rubber with various dipping times were clearly observed. The coagulant dipping method was successfully used for preparation of the RVNR/CHD-PMA nanocapsules/RVNR three-layer thin film whose thickness and tensile properties increased with increasing concentration of coagulant. From SEM micrographs, it could be deduced that a three-layer structure was obtained, where the outermost and inner layers were RVNR and the active middle layer contained CHD-PMA nanocapsules. This structure was suitable for further development of disinfectant medical glove's preparation for the potential release of CHD for neutralization of the infectious agents carried by needles commonly used in medical practice.

References

1. Eklund, A. M.; Ojajärvi, J.; Laitinen, K.; Valtonen, M.; Werkkala, K. A. Ann Thorac Surg 2002, 74, 149.
2. Osman, M. O.; Jensen, S. L. World J Surg 1999, 23, 630.
3. Busnel, R. G.; Argy, G. U.S. Pat. 5,024,852 (1991).
4. Sonntag, P.; Hoerner, P.; Cheymol, A.; Argy, G.; Riess, G.; Rieter, G. Nat Mater 2004, 3, 311.
5. Bricout, F.; Moraillon, A.; Sonntag, P.; Hoerner, P.; Blackwelder, W.; Plotkin, S. J Med Virol 2003, 69, 538.
6. Paiphansiri, U.; Tangboriboonrat, P.; Landfester, K. Macromol Biosci 2006, 6, 33.
7. Paiphansiri, U.; Tangboriboonrat, P.; Landfester, K. Macromol Symp 2007, 251, 54.
8. Paiphansiri, U.; Tangboriboonrat, P. J Appl Polym Sci 2009, 112, 769.
9. Otsu, T. J Polym Sci Part A: Polym Chem 2000, 38, 2121.
10. Zhou, H.; Jiang, J.; Zhang, K. J Polym Sci Part A: Polym Chem 2005, 43, 2567.
11. Van Der Heiden, P. A.; Willems, M. G.; Lindhout, T.; Pijpers, A. P.; Koole, H. L. J Biomed Mater Res 1998, 40, 195.
12. Vinetsky, Y.; Magdassi, S. Colloid Polym Sci 1998, 276, 395.
13. Ratnam, T. C.; Nasir, M.; Baharin, A.; Zaman, K. Polym Int 2000, 49, 1693.
14. Chowdhury, P.; Pal, C. M. Eur Polym J 1999, 35, 2207.
15. Cortest'es, E. M.; Sinisterra, D. R.; Avilacampos, J. M.; Tortamano, N.; Rocha, G. R. J Inclsion Phenom Macrocycl Chem 2001, 40, 297.
16. Suci, A. P.; Geesey, G. G.; Bonnie, J. J Microbiol Methods 2001, 46, 193.
17. Socrates, G. Infrared Characteristic Group Frequencies: Tables and Charts; Wiley: New York, 1994.
18. Metin, B.; Blum, F. D. J Chem Phys 2006, 124, 054908.
19. Elimelechm, M. Particle Deposition and Aggregation: Measurement, Modeling and Simulation; Colloid and Surface Engineering Series; Butterworth-Heiemann: Woburn, MA, 1995.
20. Sasidharan, K. K.; Joseph, R.; Rajammal, G.; Pillai, V. P.; Gopalakrishnan, S. K. J Appl Polym Sci 2001, 81, 3141.
21. Blackley, D. C. Polymer Latices; Chapman & Hall: London, 1997.
22. Zin, W. WBM Radia Phys Chem 1998, 52, 611.

เอกสารแนบ 5.1.7

Macromolecular Research, Vol. 18, No. 9, pp 876-883 (2010)
DOI 10.1007/s13233-010-0906-1

www.springer.com/13233

Preparation of Core-Shell Particle of Disinfectant Agent Nanocapsules-Skim Rubber Particles by the Heterocoagulation Technique

Chariya Kaewsaneha and Pramuan Tangboriboonrat*

Department of Chemistry, Faculty of Science, Mahidol University, Rama 6 Road, Phyathai, Bangkok 10400, Thailand

Duangporn Polpanich

National Nanotechnology Center, National Science and Technology Development Agency, Thailand Science Park, Phaholyothin Road, Patumthani 12120, Thailand

Srung Smanmoo

Bioresources Research Unit, National Center for Genetic Engineering and Biotechnology, National Science and Technology Development Agency, Thailand Science Park, Phaholyothin Road, Patumthani 12120, Thailand

Received March 11, 2010; Revised April 26, 2010; Accepted May 12, 2010

Abstract: Sulphur-prevulcanised skim (SPVS) rubber particles were heterocoagulated on an aggregate of a disinfectant agent (chlorhexidine digluconate; CHD)-poly(methyl acrylate) (PMA) nanocapsules. The CHD-PMA nanocapsule stabilized by lecithin was prepared using the modified nanoprecipitation of PMA from an organic continuous phase onto nanodroplet containing the CHD aqueous solution. Cationic and anionic nanocapsules were produced by separately redispersing the nanocapsules into a water and 0.5% sodium dodecyl sulphate (SDS) aqueous solution, respectively. The largest aggregate, which was obtained from homocoagulation of the CHD-PMA nanocapsules with opposite charges, was selected as a core surrounded with SPVS shell particles. An interpolymer complex between poly(ethylene oxide) (PEO) moieties adsorbed on the aggregate and indigenous surfactant (protein-lipid) and/or SDS on the SPVS particle surface was the driving force for heterocoagulation. Data from the size, zeta potential measurements and TEM images of the heterocoagulated CHD-PMA/SPVS indicated the composite particle containing the CHD-PMA core.

Keywords: heterocoagulation, capsule, composite, skim, nanoparticle.

Introduction

The tri-layer glove consisting of disinfectant agent between two elastomeric layers is desired for minimising the risk of infection that might result from the glove's puncture.[1-3] For loading a disinfectant liquid in between two thin rubber layers, microcapsules comprising an inner core of active agent enveloped by polymer shell are of great interest especially in processing. The liquid-filled capsules dispersed in an aqueous medium can be easily prepared and simply incorporated into rubber films *via* a sequential dipping process.[3,4] Recently, the well-defined nanocapsules containing disinfectant agent possessing wide spectrum of activity against Gram-positive and Gram-negative bacteria, i.e., chlorhexidine digluconate (CHD) salt, have been prepared employing the controlled nanoprecipitation of poly(methyl acrylate) (PMA) onto the inverse miniemulsion droplets of CHD aqueous solution.[4-6] The deposition of PMA from the organic phase onto the CHD nanodroplets was achieved by evaporating off the solvent (dichloromethane) from the mixture of solvent/non-solvent (dichloromethane/cyclohexane). Increasing the amount and weight average molecular weight ($\overline{M}_w$) of PMA, the encapsulation efficiency of the disinfectant agent was significantly increased.[4] After the redispersion of nanocapsules ($\overline{M}_w$ of PMA = 550 K) into 0.5% w/v sodium dodecyl sulphate (SDS) aqueous solution, the maximum remaining amount of CHD in the capsules with an average size of 386 ± 18 nm was found to be as high as 93%. The incorporation of CHD-PMA nanocapsules into the γ-radiation vulcanised natural rubber (RVNR) films was achieved by using the coagulant dipping process. The nanocapsules in the middle layer were then coated with another RVNR layer to finally furnish a tri-layer film.

*Corresponding Author. E-mail: scptb@mahidol.ac.th

With the aim to increase the compatibility between disinfectant nanocapsules and sulphur-prevulcanised natural rubber (SPNR) latex film generally used for preparing the gloves, the sulphur-prevulcanised skim (SPVS) particles were applied as the CHD-PMA nanocapsule's shell in the present study. It was reported that after prevulcanisation by sulphur, the skim latex, a by-product obtained from the concentrating process of natural rubber (NR) latex, shows a uniform crosslink in each particle.[7] This would result in the formation of a coherent film with good mechanical properties. The SPVS (average diameter 134 nm) was, therefore, used as agglomerating latex in the heterocoagulation process for the preparation of composite particle containing NR core (average diameter 750 nm). This process involves agglomeration, mainly based on neutralisation, of smaller particles onto a larger particle of another polymer. Core-shell particles are obtained by heating the system at temperature above the glass transition temperature (T_g) of smaller particles. Different types of monomer pairs, even in the case of hydrophilic core and hydrophobic shell, and polymer-inorganic colloids having electronic, optics and electrochromic properties can be prepared by using this process.[8-12] The main factors controlling the core-shell particle are: i) the optimum number of smaller particles covering a larger core particle for shell formation, ii) a large contrast between the charges of larger and smaller particles provides a strong driving force to counter balance the repulsion between the similarly charged particles and, iii) the relationship of polymer surface energies of core and shell polymer particles expressed by Young's equation.[12] However, an interpolymer complex principle based on the interaction between poly(ethylene oxide) (PEO) of a nonionic surfactant (Nonidet) adsorbed on the SPVS particles and indigenous surfactant (protein-lipid) on the NR particle was also successfully

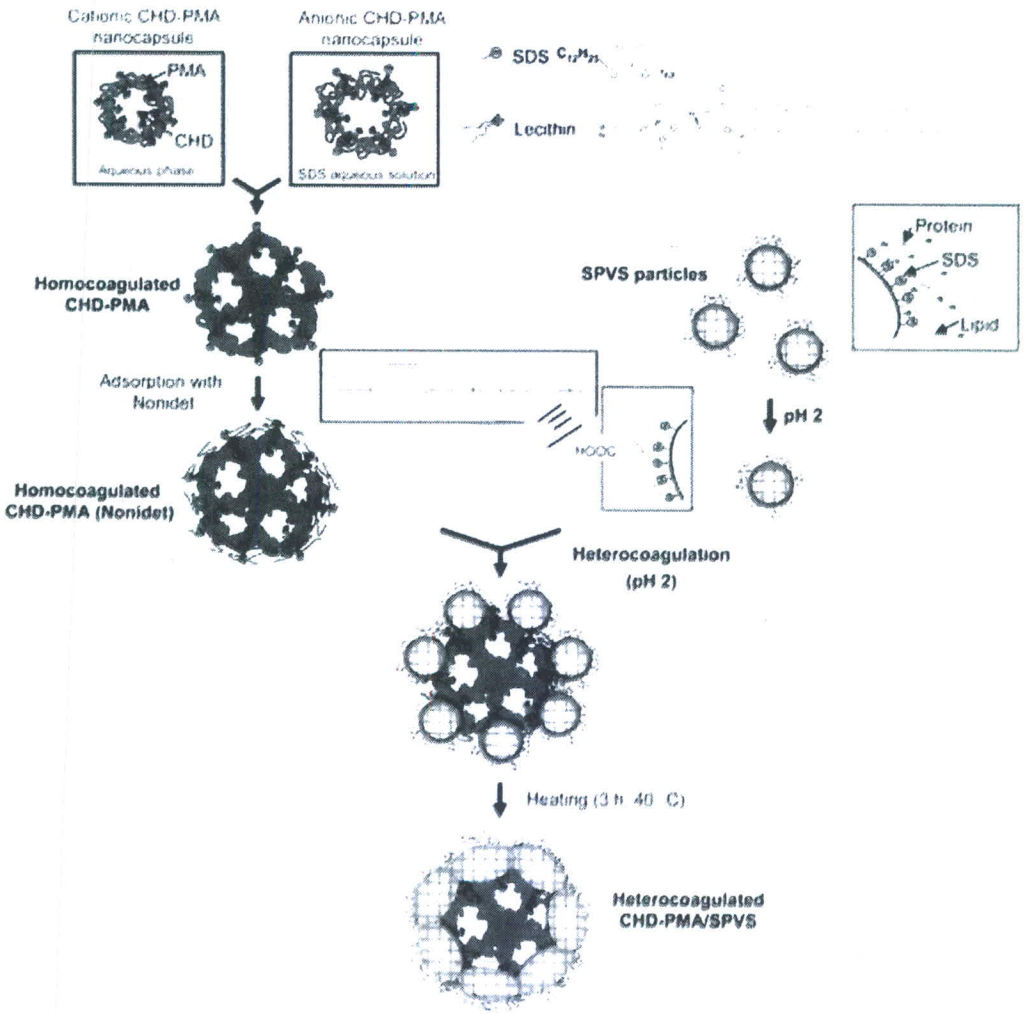


Figure 1. Schematic of the preparation of heterocoagulated CHD-PMA/SPVS.

applied to prepare the heterocoagulated NR/SPVS.[7] Results from the zeta potential measurement and toluene-resistance of the film casted from the composite latex compared with the NR film indicated the existence of SPVS at the outer layer. The heterocoagulation technique was applied for the preparation of core-shell of CHD-PMA/SPVS particle in this work. Since the size of CHD-PMA nanocapsule was similar to that of SPVS particle, the aggregate CHD-PMA nanocapsules were first prepared for further used as a core in the heterocoagulation process. Besides providing the large core size, the volume fraction of CHD in the composite CHD-PMA/SPVS particle would be increased without CHD droplet coalescence. In the process, the CHD-PMA nanocapsules, stabilised by lecithin, in cyclohexane were separately redispersed into an aqueous phase and 0.5% SDS aqueous solution to obtain the cationic and anionic nanocapsules, respectively. These two types of nanocapsules were then homocoagulated to form a large aggregate which was used as a core particle in the subsequent step. Since both the aggregate core and SPVS shell particles possessed negative charges, a nonionic surfactant (Nonidet) bearing PEO moieties was adsorbed onto the anionic aggregate and formed the complex with protein-lipid and/or SDS on the SPVS particle surface. The overall procedure is schematically presented in Figure 1. The zeta potential, size and morphology of composite particles were investigated.

Experimental

Materials. Skim latex (Pan Asia Bio Tech Co., Thailand) was prevulcanised by using sulphur (S; EMCO Intertrad Co.), zinc diethyldithiocarbamate (ZDEC; EMCO Intertrad Co.) and zinc oxide (ZnO; Global Chemical Co.) as described elsewhere.[7] Particle size and zeta potential of skim and SPVS latices were measured by using a dynamic light scattering (DLS) apparatus and a microelectrophoresis (Malvern, Zetasizer Nano ZS). The morphology of the particles mounted on a carbon-coated copper grid was studied by TEM (JEOL, JEM-2010).

Methyl acrylate (Fluka, Purum) monomer was purified by passing through a column packed with neutral and basic aluminium oxide (Fluka, Purum). Potassium hydroxide (Merck), sodium dodecyl sulphate (SDS; Fluka), acetone (Lab-scan), hydrochloric acid (Merck), sodium hydroxide (Lab-scan), chlorhexidine digluconate (20% in water, Sigma), potassium persulfate (KPS; Fluka), soybean phosphatidylcholine or lecithin (MP Biochemical), dichloromethane (Lab-scan), cyclohexane (Lab-scan), ethanol (Fluka), methanol (Lab-scan), hexadecane (Fluka), tetrahydrofuran (Lab-scan) and pyrazine (Merck) were used as received.

Preparation of CHD-PMA Nanocapsules. PMA was synthesised *via* the miniemulsion polymerisation process as previously described.[5] The weight average molecular weight ($\overline{M}_w$) of PMA was determined by a gel permeation chromatography (Waters/600/2414/600 equipped with refractive index detector).

Table I. The Formulation Used for Preparation of CHD-PMA Nanocapsules

Ingredients	Amount
PMA	0.15 g
Lecithin	0.10 g
Dichloromethane	12.0 mL
Cyclohexane	12.0 mL
CHD solution	0.5 mL

CHD-PMA nanocapsules ($\overline{M}_w$ of PMA = 250 K) were prepared by using the modified nanoprecipitation technique as described elsewhere.[4-6] The formulation used for preparation of CHD-PMA nanocapsules is shown in Table I.

For determination of the encapsulation efficiency, the nanocapsules were separated by centrifugation at 1,4000 rpm for 40 min and were carefully dried at room temperature before dissolving in a mixture of THF and ethanol. Deuterated water and a known amount of pyrazine were applied as an external solvent and a calibration product for the quantitative analysis of the encapsulation efficiency by ^{1}H NMR (Bruker, DRX 400).

$$\text{Encapsulation efficiency (\%)} = \frac{\text{Mass of CHD in nanocapsules}}{\text{Mass of CHD in formulation}} \times 100$$

Mass of CHD in nanocapsules was calculated from the area ratio of peaks at 7.66 to 9.07 ppm corresponding to aromatic-protons of the CHD and pyrazine respectively.[5]

Preparation of CHD-PMA/SPVS Core-Shell Particle. To obtain cationic and anionic nanocapsules, the CHD-PMA nanocapsules in cyclohexane were, separately, redispersed in deionised water and 0.5% w/v SDS aqueous solution (1:1), respectively. After evaporation of the cyclohexane by using a rotary evaporator (Buchi, Rotavapor R200) at 40 °C for 15 min, the nanocapsules suspended in deionised water and in SDS aqueous solution were obtained. The nanocapsules with opposite charges were then mixed in an Erlenmeyer flask under stirring for 10 min at room temperature. The weight ratios of cationic to anionic nanocapsules were varied from 90:10 to 10:90. The size and zeta potential of aggregate were examined and the morphology was investigated under TEM.

The homocoagulated CHD-PMA at the weight ratio of cationic to anionic nanocapsules of 40:60 was selected for use as the core of CHD-PMA/SPVS composite particle. Nonidet (10% by weight of dried nanocapsules) was first added into the aggregate before shaking (IKA, VIBRAX VXR basic) for 24 h. The amount of adsorbed Nonidet was deduced from the quantity of an aqueous solution of 0.5 M $CaCl_2$ added to provoke the visible coagula.[7] A known amount of 1% homocoagulated CHD-PMA (Nonidet) was

mixed with 1% SPVS latex at pH 2 in an Erlenmeyer flask at room temperature. The blending ratio was calculated from the theoretical number (N_{max}) of the shell particles required to form a closely packed particulate monolayer on a core particle from the following equation.[7-9,12]

$$N_{max} = \frac{2\pi}{\sqrt{3}}\left[\frac{R_c + R_s}{R_s}\right]^2$$

where R_c and R_s are the radii of core and shell particles, respectively. The ratios of the homocoagulated CHD-PMA (Nonidet) core to SPVS shell particles in the blends were varied from N_{max}, $N_{max}/2$, $N_{max}/4$ to $N_{max}/8$.

The size, zeta potential and morphology of the CHD-PMA/SPVS composite latex particle were examined.

Results and Discussion

General Characteristics of the Latex. Prior to using SPVS as agglomerating particles for the preparation of CHD-PMA/SPVS composite particle, the size, zeta potential, degree of crosslink and morphology of SPVS particles were investigated. The size distribution curves of skim and SPVS latices, measured by using the DLS technique, are shown in Figure 2(a).

Results showed that both skim and SPVS latices exhibited a unimodal size distribution. The average particle size of skim was 148 ± 2 nm which was in good agreement with the previous data obtained from the photon correlation spectroscopy (124 nm) and AFM images (200 nm).[13,14] For SPVS, its average particle size was found to be 164 ± 2 nm. The shift in the size distribution curve of SPVS from the skim latex was only marginal which possibly resulted from the SDS added during the prevulcanisation. It was reported that the addition of SDS in NR latex enhanced the mechanical and chemical stabilities of the latex by rearranging the indigenous soaps and making them more effective as stabilisers.[15,16] By considering the particle charge as a factor affecting the movement of the particle through a fluid, the more highly charged particles would move slower than those of the lower charge.[17] Based on the DLS technique, when a light photon hits a moving particle, the frequency of the scattered light will be different from the incident frequency, depending on whether the particle is moving towards or away from the observer. From the extent of this Doppler broadening, the diffusion coefficient (D) and the mean radius of particle (r) can be determined from $D = kT/6\pi\eta r$ where k is Boltzmann constant, T is temperature and η is viscosity of fluid medium.[18] This principle supported the fact that the size of higher charged SPVS particles was slightly larger than that of lower charge skim particles. The explanation was confirmed by the zeta potentials determined at various pHs as shown in Figure 2(b). The results indicated the amphoteric characteristic of skim and SPVS particles with an isoelectric point (pI) at about pH 2.8. The particles possessed positive charge when the pH was below 2.8 and rapidly changed to negative above this pH. This amphotericity confirmed the presence of amino acids on the rubber particle surface. However, the pI value was lower than that of normal proteins (4.0-6.0) which can be explained that, in addition to proteins, fatty acids are also present on the particle surface as generally observed in NR latex.[7,19] Results showed that the absolute value of zeta potential of SPVS was insignificantly higher than that of the skim latex. The similar effective charge on both types of particles might be responsible for the equal velocity of these colloidal particles in an electric field.

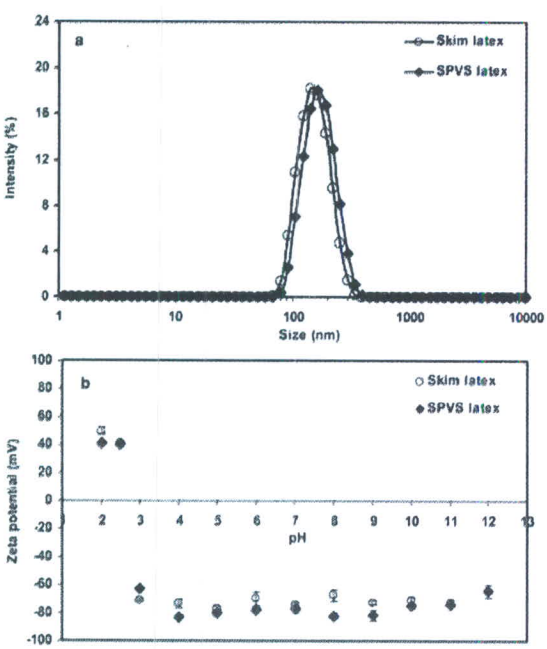


Figure 2. Characteristics of skim and SPVS latex particles (a) size distributions and (b) zeta potentials versus pH.

TEM micrographs of an air-dried skim and SPVS latex particles prevulcanised for 5 h are shown in Figures 3(a) and (b), respectively.

A clear-cut boundary or the contour of the SPVS particle in Figure 3(b) as compared to that of the skim particle in Figure 3(a) was clearly observed. Due to the fact that the diluted latices were dropped and then dried on a copper grid in the sample preparation step, the harder SPVS particle, in which chemical crosslinking of rubber chains takes place internally, would restrict the chain mobility and retain its shape. In contrast, the particle contours of non-crosslinked skim particles disappeared, resulting in blurred spots.[20] The result also agreed with the internal morphology of prevulcanised latex particles examined by the phase transfer/bulk polymerisation/TEM technique which revealed the uniform crosslink structure of SPVS particles.[7]

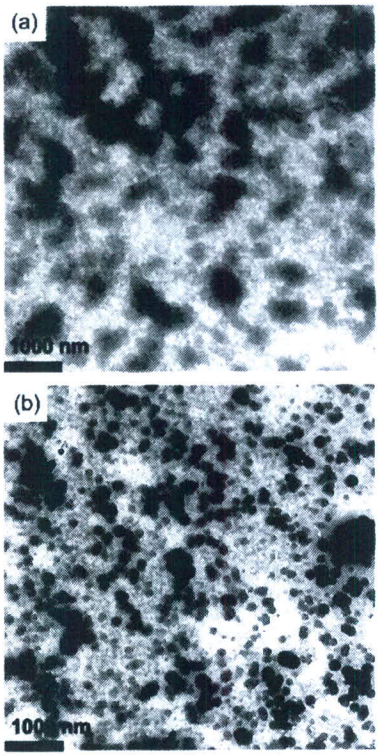


Figure 3. TEM micrographs of (a) skim and (b) SPVS latex particles prevulcanised for 5 h (%swelling ratio = 220).

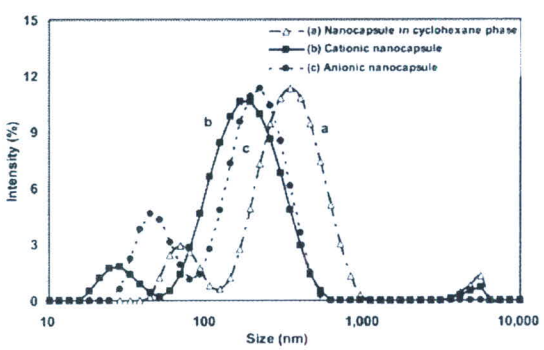


Figure 4. Size distributions of CHD-PMA nanocapsules in (a) cyclohexane phase, (b) aqueous phase (cationic nanocapsule), and (c) 0.5% w/v SDS solution (anionic nanocapsule).

Analysis of CHD-PMA Nanocapsules. The CHD-PMA nanocapsules dispersed in cyclohexane were prepared by the modified nanoprecipitation of PMA ($\overline{M}_w$ = 250 K) onto nanodroplets consisting of CHD aqueous solution. The nanocapsules suspended in cyclohexane were then redispersed in an aqueous phase and in 0.5% w/v SDS aqueous solution to produce cationic and anionic nanocapsules, respectively. The size distribution curves are presented in Figure 4.

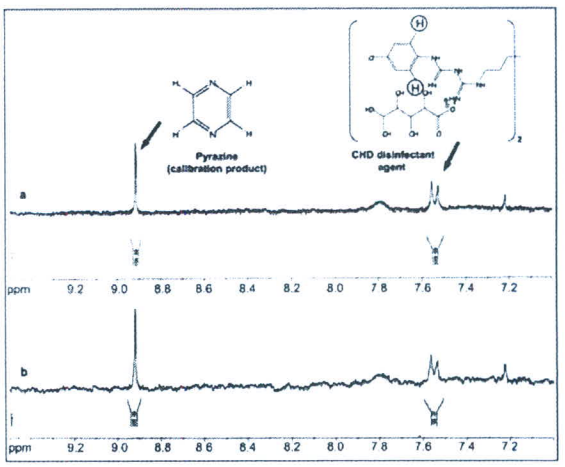


Figure 5. ^{1}H NMR spectra used for determination of the encapsulation efficiency of nanocapsules suspended in (a) cyclohexane and (b) aqueous phase.

Results showed that the average size of CHD-PMA nanocapsules in cyclohexane was 390 ± 1 nm. After the redispersion into an aqueous phase, their average size decreased to 190 ± 2 nm. The remaining amount of the CHD in nanocapsules suspended in cyclohexane and those in redispersed nanocapsules were 100 and 86% respectively. This was due to the diffusion of CHD caused by an osmotic pressure difference between the internal nanocapsule and the continuous phase.[21] The ^{1}H NMR spectra used for determination of the encapsulation efficiency in both cases are shown in Figure 5.

In addition, the average size of the nanocapsules in SDS aqueous solution (anionic nanocapules) was slightly larger (220 ± 2 nm) than those redispersed in the aqueous phase (cationic nanocapsules). This might be due to the rearrangement of lecithin on the nanocapsule's surface as previously proposed.[6] In an aqueous medium, lecithin rearranged by turning its hydrophilic positive head groups towards the continuous phase.[6,22] The zeta potential of +82 mV measured directly as prepared (pH 5.1) confirmed the role of choline [$N^+(CH_3)_3$] moieties of lecithin on the nanocapsules. On the contrary, the nanocapsules suspended in the SDS aqueous solution exhibited the negative charge with the zeta potential of -92 mV at the prepared pH (pH 4.7). This was caused by the adsorption of an alkyl chain of SDS onto the hydrophobic part of lecithin without turning the positively charged choline moieties to the top layer.[23,24] The repulsion of anionic nanocapsules resulted in the expansion of their size.

Homocoagulation of CHD-PMA Nanocapsules. Before preparing CHD-PMA/SPVS core-shell particle, the size of core was increased by homocoagulation of CHD-PMA nanocapsules. At pH of about 4-5, the difference of zeta potential values between the cationic and anionic nanocapsules was at maximum, the nanocapsules having oppositely

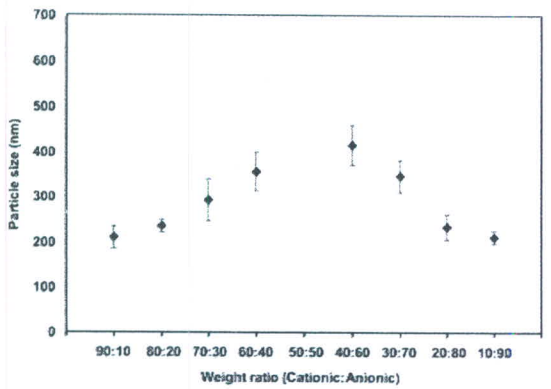


Figure 6. Sizes of homocoagulated CHD-PMA nanocapsules at weight ratios of cationic:anionic varying from 90:10 to 10:90.

charges would effectively form an aggregate at this pH. The sizes of homocoagulated CHD-PMA or aggregates at various blending ratios are presented in Figure 6.

Results showed that the size of homocoagulated CHD-PMA increased with the increasing amount of anionic nanocapsules from 10 to 60%. The largest aggregate with the average size of 415 ± 44 nm was obtained when the weight ratio of cationic:anionic nanocapsules was 40:60. It was noticed that the aggregate was not stable at the weight ratio of 50:50 which correlated well with its zeta potential value of less than +30 mV as shown in Figure 7.

Data in Figure 7 also indicated that the stable homocoagulated CHD-PMA from the weight ratio of 100:0 to 60:40 exhibited the positive character caused by lecithin. The absolute value of zeta potential decreased with the increasing amount of anionic nanocapsules due to partial neutralisation. Obviously, the zeta potentials of aggregates having a high ratio of anionic nanocapsules turned to be negative. The zeta potential of the largest aggregate prepared at the weight ratio of cationic to anionic nanocapsules of 40:60 was -54 mV.

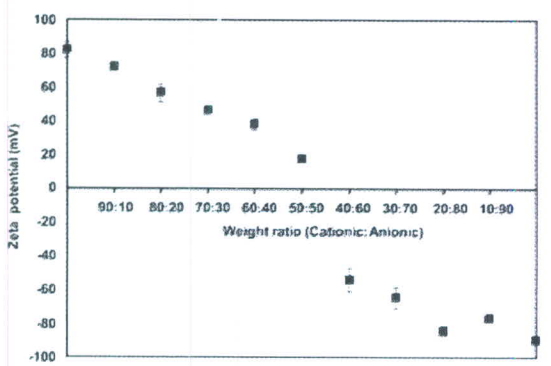


Figure 7. Zeta potentials of homocoagulated CHD-PMA nanocapsules at various weight ratios of cationic:anionic varying from 90:10 to 10:90.

Heterocoagulation of CHD-PMA/SPVS Particles. For preparation of CHD-PMA/SPVS core-shell particle using the heterocoagulation technique, the largest size of homocoagulated CHD-PMA prepared at the weight ratio of 40:60 was selected as a core. Since both the aggregate core and SPVS shell particles possessed negative charges, the driving force for the interaction between core and shell particles could not be electrostatically controlled. An interpolymer complex principle previously applied to prepare the heterocoagulated NR/polychloroprene (CR) and NR/SPVS particles with core-shell structure was, therefore, applied.[7,8] The anionic homocoagulated CHD-PMA was covered with the Nonidet having PEO moieties which then formed a complex with protein-lipid and/or SDS on the SPVS particle surface. The adsorption of Nonidet onto the homocoagulated nanocapsules was examined by the addition of an aqueous solution of 0.5 M $CaCl_2$. It was found that the volume of 0.5 M $CaCl_2$ required for coagulating the homocoagulated nanocapsules was increased with increasing Nonidet concentration. By using Nonidet less than 10% by weight of dry nanocapsules, the homocoagulated nanocapsules were immediately coagulated. After adding $CaCl_2$ aqueous solution, they remained stable at minimum Nonidet concentration of 10%. The change of stabilisation from electrostatic to steric effect was, therefore, achieved at 10 % of Nonidet. Since the zeta potential directly determines the effective charge of particles or the electrostatic potential at

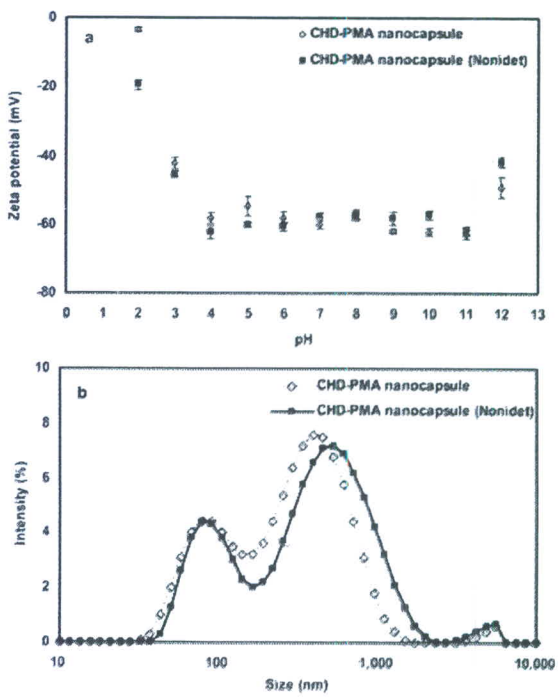


Figure 8. Homocoagulated CHD-PMA nanocapsules and those adsorbed with Nonidet (a) zeta potentials and (b) size distributions.

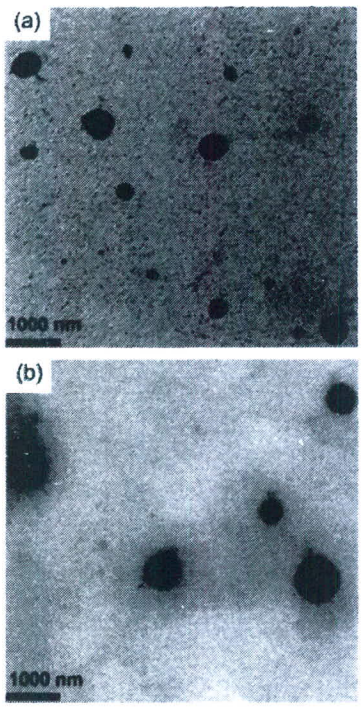


Figure 9. TEM micrographs of (a) homocoagulated CHD-PMA and (b) homocoagulated CHD-PMA (Nonidet) nanocapsules.

shear plane of electrical double layer, the zeta potential of the homocoagulated CHD-PMA (Nonidet) was not significantly different from that of the original anionic nanocapsules (Figure 8(a)). However, the hydrophilic PEO moieties of Nonidet on the aggregate oriented towards the dispersion medium. Hence, the amount of absorbed water or the hydrated layer around the aggregate increased. The boundary between the homocoagulated nanocapsules surface and the surrounding fluid was, therefore, shifted.[25] Because the hydrated PEO moved with the aggregate, the extent of the Doppler broadening and the diffusion coefficient, therefore, decreased. This resulted in an increase in their hydrodynamic volume as observed in Figure 8(b). The TEM micrographs in Figure 9 supported this explanation.

Figure 9 showed that the homocoagulated CHD-PMA, before and after adsorption with Nonidet, possessed the spherical shape. The low T_g of PMA shell (10 °C) facilitated the nanocapsules fusion or the formation of aggregate. The homocoagulated nanocapsules coated with Nonidet in Figure 9(b) confirmed the increase of aggregate's size possibly from the existence of PEO. The PEO chains on the homocoagulated CHD-PMA (Nonidet) core were allowed to form the complex *via* hydrogen bonding, at pH 2, with carboxylic groups of the protein-lipid molecules residing on the SPVS shell particles. The zeta potentials of the heterocoagulated particles at various blending ratios (N_{max}, $N_{max}/2$, $N_{max}/4$, and

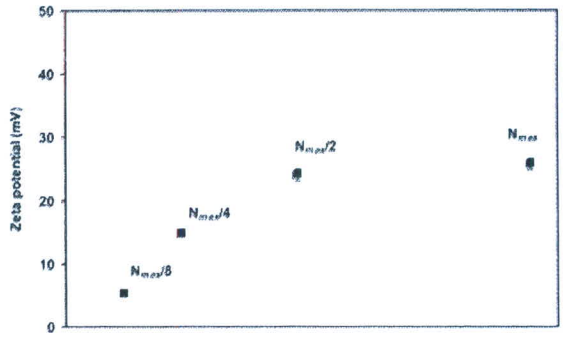


Figure 10. Zeta potentials of heterocoagulated CHD-PMA (Nonidet)/SPVS particles at various blending ratios.

$N_{max}/8$) were measured and the data are shown in Figure 10.

It was observed that the zeta potentials of all blends were positive and reached the maximum value at +25.7 mV at N_{max}. This value was vastly different from that of the core CHD-PMA (Nonidet) (-19.6 mV) but approached the zeta potential of the shell SPVS particles (+40.8 mV). The data confirmed the presence of SPVS as the outer layer of the composite particles as observed in the heterocoagulation of NR/SPVS.[7] Besides the interpolymer complex between Nonidet and the protein-lipid, the heterocoagulation between homocoagulated CHD-PMA (Nonidet) and SPVS could be driven by the complex formation of PEO and SDS on SPVS particle surface.[26,27] It was reported that the micelle of SDS molecules with a smaller aggregation number than normal was bound to the PEO coil.[27] This leads to the PEO-SDS complex that behaves like a polyelectrolyte as supported by evidences from an increase in viscosity, a decrease in the surface tension and partial special volume.

The morphology of homocoagulated CHD-PMA (Nonidet)/SPVS particles was then investigated by TEM. The micrographs of heterocoagulated CHD-PMA/SPVS particles prepared at N_{max} before and after heating for 3 h at 40 °C are shown in Figure 11.

The image in Figure 11(a) revealed that the composite particles having a raspberry-like morphology consisted of SPVS particles (light) surrounding the homocoagulated CHD-PMA (Nonidet) core (dark). The size of composite particles determined by TEM was similar to that determined by light scattering (712 ± 7 nm) although some SPVS particles could not adsorb onto the aggregate CHD-PMA. Each individual SPVS particle showed a clear-cut edge due to its high crosslink density which might prevent the interdiffusion of polyisoprene as already mentioned. Consequently, raising the temperature to 40 °C for 3 h, the SPVS particles in Figure 11(b) were partially fused to provide the aggregate CHD-PMA/SPVS core-shell-like particle. Similar to the heterocoagulation of large polypyrrole particles with small polyacrylate particles, the long period and the relatively high temperature of heat processing needed for complete

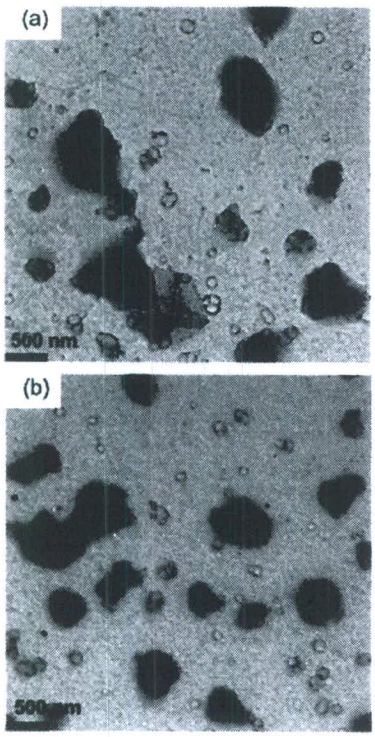


Figure 11. TEM micrographs of heterocoagulated CHD-PMA/SPVS particles prepared at N_{max} (a) before and (b) after heating for 3 h at 40 °C.

spreading of small particles (low T_g) for shell formation were not anticipated.[12] It was also believed that the difficulty in spreading of the SPVS particles on the core surface was due to the high interfacial tension and the presence of water as mentioned above. The coherent film of the outer SPVS shell would be miscible with the SPNR film used as the substrate for further gloves' preparation.

Conclusions

The small SPVS shell particles were heterocoagulated onto a large aggregate CHD-PMA core prepared from homocoagulation of CHD-PMA nanocapsules having opposite charges. The driving force of the CHD-PMA/SPVS composite particle's formation was an interpolymer complex between PEO adsorbed on the aggregate and carboxylic groups derived from indigenous surfactant (protein-lipid) and/or SDS on the SPVS particle surface. Data from size, zeta potential measurements and TEM of the composite particles indicated the CHD-PMA core enveloped by SPVS particles structure. The coherent film of SPVS would be miscible with the substrate when deposits the CHD-PMA/SPVS composite particles onto the SVNR film which would be suitable for further preparation of medical gloves.

Acknowledgements. Research grant (RTA5180003) from The Thailand Research Fund/Commission on Higher Education is gratefully acknowledged.

References

(1) R. G. Busnel and G. Argy, US. Patent 5024852 (1991).
(2) R. Jorda, P. Autant, and R. René, US. Patent 5585050 (1996).
(3) P. Sonntag, P. Hoerner, A. Cheymol, G. Argy, G. Riess, and G. Rieter, *Nat. Mater.*, **3**, 311 (2004).
(4) S. Tanpantree, P. Opaprakasit, S. Loykulnant, W. Kangwansupamonkon, and P. Tangboriboonrat, *J. Appl. Polym. Sci.*, **117**, 1798 (2010).
(5) U. Paiphansiri, P. Tangboriboonrat, and K. Landfester, *Macromol. Biosci.*, **6**, 33 (2006).
(6) U. Paiphansiri and P. Tangboriboonrat, *J. Appl. Polym. Sci.*, **112**, 769 (2009).
(7) U. Paiphansiri and P. Tangboriboonrat, *Colloid Polym. Sci.*, **284**, 251 (2005).
(8) P. Tangboriboonrat and U. Buranabunya, *Colloid Polym. Sci.*, **279**, 615 (2001).
(9) R. H. Ottewill, A. B. Schofield, J. A. Waters, and N. St. J. Williams, *Colloid Polym. Sci.*, **275**, 274 (1997).
(10) M. Okubo and Y. Lu, *Colloid Surf. A*, **109**, 49 (1996).
(11) J. Wang and X. Yang, *Colloid Polym. Sci.*, **286**, 283 (2008).
(12) H. Li and E. Kumacheva, *Colloid Polym. Sci.*, **281**, 1 (2003).
(13) P. Tangboriboonrat, T. Tanunchai, and C. Tiyapiboonchiya, *Plast. Rubber Compos.*, **28**, 357 (1999).
(14) M. M. Rippel, L. T. Lee, C. A. P. Leite, and F. Galembeck, *J. Colloid Interf. Sci.*, **268**, 330 (2003).
(15) P. Tangboriboonrat and C. Lerthititrakul, *Colloid Polym. Sci.*, **280**, 1097 (2002).
(16) D. C. Blackley, A. A. Nor Aisah, and R. Twaits, *Plast. Rubber Mater. Appl.*, **4**, 77 (1979).
(17) D. J. Shaw, *Introduction to colloid and surface chemistry*, 3rd edn., Butterworth & Co (Publishers) Ltd, Boston, 1980, pp 19-43.
(18) R. J. Hunter, *Introduction to modern colloid science*, 1st edn., Oxford Univ. Press, New York, 1993, pp 32-56.
(19) C. C. Ho, T. Kondo, N. Muramatsu, and H. Ohshima, *J. Colloid Interf. Sci.*, **178**, 442 (1996).
(20) S. Winsunthorn, F. Bonfils, C. Pochat-Bohatier, D. Bouyer, A. Deratani, and C. Dupuy, *J. Appl. Polym. Sci.*, **108**, 960 (2008).
(21) K. Landfester, N. Bechthold, F. Tiarks, and M. Antonietti, *Macromolecules*, **32**, 5222 (1999).
(22) S. J. Ryhänen, J. M. I. Alakoskela, and P. K. J. Kinnunen, *Langmuir*, **21**, 5707 (2005).
(23) N. Deo and P. Somasundaran, *Colloid Surf. A*, **186**, 33 (2001).
(24) L. Kong, J. K. Beattie, and R. J. Hunter, *Colloid Surf. B*, **27**, 11 (2003).
(25) A. Martin-Rodriguez, M. A. Cabrerizo-Vílchez, and R. Hidalgo-Álvarez, *J. Colloid Interf. Sci.*, **187**, 139 (1997).
(26) W. Brown, J. Fundin, and M. da Graça Miguel, *Macromolecules*, **25**, 7192 (1992).
(27) K. Contractor and P. Bahadur, *Eur. Polym. J.*, **34**, 225 (1998).

เอกสารแนบ 5.1.8

International Journal of Polymer Anal. Charact., 15: 524–535, 2010
Copyright © Taylor & Francis Group, LLC
ISSN: 1023-666X print
DOI: 10.1080/1023666X.2010.521294

Taylor & Francis
Taylor & Francis Group

Downloaded By: [Tearle, Jacqueline] [informa internal users] At: 15:11 8 December 2010

COMPOSITE PARTICLES OF DISINFECTANT NANOCAPSULES-SKIM RUBBER LATEX

Chariya Kaewsaneha,[1] Pakorn Opaprakasit,[2] Duangporn Polpanich,[3] Srung Smanmoo,[4] and Pramuan Tangboriboonrat[1]

[1]*Faculty of Science, Department of Chemistry, Mahidol University, Bangkok, Thailand*

[2]*School of Bio-Chemical Engineering and Technology, Sirindhorn International Institute of Technology (SIIT), Thammasat University, Pathum Thani, Thailand*

[3]*National Nanotechnology Center (NANOTEC), National Science and Technology Development Agency, Pathum Thani, Thailand*

[4]*Bioresources Research Unit, National Center for Genetic Engineering and Biotechnology (BIOTEC), National Science and Technology Development Agency, Pathum Thani, Thailand*

Skim latex, a by-product of natural rubber latex, was prevulcanized by sulfur and then used in the preparation of composite particles with disinfectant nanocapsules. Each polymeric nanocapsule contained chlorhexidine digluconate (CHD) as a disinfectant agent encapsulated with poly(methyl acrylate) (PMA) as a shell. The driving force for the heterocoagulation of CHD-PMA nanocapsule and sulfur-prevulcanized skim (SPVS) particle was the electrostatic interaction between the positive charge of lecithin residing on the surface of the nanocapsule and the negative charge from the indigenous surfactant (protein-lipid) and/or from sodium dodecyl sulfate on the surface of the SPVS latex particle. The zeta potential and morphology of heterocoagulated particles indicated the formation of the CHD-PMA/SPVS composite particles. Structures and formation mechanisms of the composite particles with different blend ratios were revealed by depth profiling confocal Raman spectra.

Keywords: Composites; Core-shell polymers; Nanoparticle; Rubber; Surfactants

INTRODUCTION

Skim latex, a by-product obtained from the concentrating process of natural rubber (NR) latex, contains small rubber particles (~5% dry rubber content) with high molecular weight of 10^6 g/mol.[1,2] This latex has been used for encapsulating urea fertilizer in a controlled-release application due to the large amount of

Submitted 7 August 2010; accepted 20 August 2010.

Research grant (RTA5180003) from The Thailand Research Fund/Commission on Higher Education is gratefully acknowledged. The authors thank Mr. Alongkot Treetong (NANOTEC) for helpful assistance on Raman experiments.

Correspondence: Pramuan Tangboriboonrat, Faculty of Science, Department of Chemistry, Mahidol University, Rama 6 Rd., Phyathai, Bangkok 10400, Thailand. E-mail: scptb@mahidol.ac.th

nonrubber substances, including proteins.[3] Similar to the case of NR latex, the prevulcanization or initial cross-linking within the rubber particle is the minimum requirement for skim rubber modification. Drying of the prevulcanized latex produces a cross-linked film without any need of further vulcanization. The physical properties of the final product can be controlled by the design of cross-linking in latex particles.[4,5] A coherent film would be achieved when each latex particle is homogeneously cross-linked. The uniform mesh structure of all sulfur-prevulcanized skim (SPVS) particles observed under transmission electron microscopy (TEM) might also be the reason for the preferred sulfur prevulcanization.[2]

Because of the small particle size (120–200 nm) and homogeneous cross-linked structure, SPVS was previously used as an agglomerating latex in the preparation of composite particles containing NR core (750 nm) by the heterocoagulation process.[2] This technique offers a good possibility for controlling the morphology of composite latex particles, particularly the core-shell type, e.g., polypyrrole/polyacrylic and poly(styrene-co-butadiene)/poly(butyl acrylate).[6,7] The interaction between the core and agglomerating particles is governed by electrostatic, hydrophobic, or hydrogen interactions.[6,8,9] However, the interpolymer complex based on the interaction between poly(ethylene oxide) adsorbed on SPVS particles and indigenous surfactant (protein-lipid) on the NR particle was employed in the preparation of heterocoagulated NR/SPVS.[2] Because of the skim's low glass transition temperature (−70°C), the NR/SPVS core-shell particles could be obtained without annealing the composite particles at high temperature.

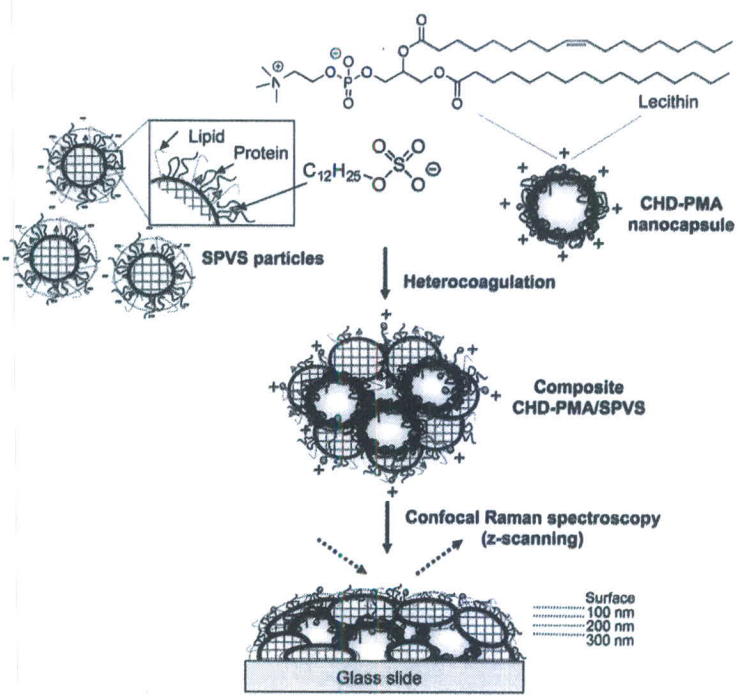


Figure 1. Schematic of the preparation and characterization of composite CHD-PMA/SPVS.

Downloaded By: [Tearle, Jacqueline] [informa internal users] At: 15:11 8 December 2010

The aim of the present study was to explore potential use of SPVS in entrapment of chlorhexidine digluconate-poly(methyl acrylate) (CHD-PMA) nanocapsules. The SPVS film with good physical properties is expected to be miscible with the substrate when the composite particles are deposited onto a sulfur-prevulcanized NR film for further preparation of disinfectant gloves, desired for minimizing the risk of infection from glove puncture.[10,11] The CHD-PMA/SPVS composite particles were produced by the heterocoagulation technique based on the electrostatic interaction between negative charges derived from indigenous surfactant and SDS on SPVS and cationic charges of lecithin on CHD-PMA nanocapsules. For the first time, structures and formation mechanisms of the composite particles obtained from different CHD-PMA/SPVS blend ratios were characterized by depth profile analysis employing confocal Raman spectroscopy, which is a powerful technique for depth profiling of materials, especially coatings, membranes, and composite materials.[12,13] The overall procedure is schematically presented in Figure 1.

Downloaded By: [Tearle, Jacqueline] [informa internal users] At: 15:11 8 December 2010

EXPERIMENTAL SECTION

Materials

Methyl acrylate (Fluka, Purum) monomer was purified by passing through a column packed with neutral and basic aluminium oxide (Fluka, Purum). Sulfur (S; Emco Intertrade Co.), zinc diethyldithiocarbamate (ZDEC; Emco Intertrade Co.), zinc oxide (ZnO; Global Chemical Co.), potassium hydroxide (Merck), sodium dodecyl sulfate (SDS; Fluka), acetone (Lab-scan), hydrochloric acid (Merck), sodium hydroxide (Lab-scan), chlorhexidine digluconate (20% in water, Sigma), potassium persulfate (KPS; Fluka), soybean phosphatidylcholine or lecithin (MP Biochemical), dichloromethane (Lab-scan), cyclohexane (Lab-scan), ethanol (Fluka), methanol (Lab-scan), hexadecane (Fluka), tetrahydrofuran (Lab-scan), and pyrazine (Merck) were used without further purification. Deionized water was used throughout the experiments.

Latex and Characterizations

Total solid content (%TSC) of skim latex (Pan Asia Bio Tech Co., Thailand) was determined using the method described in ASTM D1076:1988. Acetone was used as a rubber coagulant for determination of dry rubber content.[3]

The preparation of SPVS latex and the determination of swelling ratio of latex film were carried out as described elsewhere.[2,14] Vulcanizing ingredients, i.e., S, ZDEC, and ZnO powders, were prepared as 50% aqueous dispersion by ball milling for at least 72 h. The formula used for the preparation of SPVS latex is shown in Table I.

The particle sizes of skim and SPVS lattices were measured by a particle size analyzer (Malvern, Zetasizer Nano ZS). Their zeta potential values were determined using laser Doppler electrophoresis apparatus (Malvern, Zetasizer Nano ZS) at 25°C after adjusting pH by the addition of 0.01 M of HCl or NaOH. Polystyrene latex with known particle size and zeta potential was used as standard for calibration. For the morphological study of skim and SPVS particles, the diluted latex was dried

Table I. Formula used for the preparation of SPVS latex

Ingredients	Parts by wet weight (g)
Skim latex (5.1% DRC)	100
Stabilizers	
–10% w/v KOH solution	4.0
–25% w/v SDS solution	0.8
Vulcanizing ingredients (50% dispersion)	
–S	2.5
–ZDEC	2.0
–ZnO	0.5

Downloaded By: [Tearle, Jacqueline][informa internal users] At: 15:11 8 December 2010

on a carbon/copper grid at room temperature before investigating under TEM (JEOL, JEM-2010).

Preparation and Characterization of CHD-PMA Nanocapsules

PMA was synthesized via the mini-emulsion polymerization process as previously described.[15] The average molecular weight ($\overline{M}_w$) of PMA was determined by gel permeation chromatography (Waters/600/2414/600) equipped with refractive index detector.

CHD-PMA nanocapsules were obtained using the modified nanoprecipitation technique.[15,16] PMA (0.15 g) and lecithin (0.1 g) were first dissolved in dichloromethane (12 mL) before the addition of cyclohexane (12 mL), followed by CHD solution (0.5 mL). The mixture was ultrasonicated for 2 min at 90% amplitude (Branson Sonifier, W450 digital) and heated up to 50°C in an open vessel with continuous stirring overnight for the removal of dichloromethane. Cyclohexane was subsequently removed by rotary evaporation at 40°C, and deionized water was finally added to replace the evaporated volume. Size, morphology, and %TSC of CHD-PMA nanocapsules were examined.

For the determination of encapsulation efficiency, the CHD-PMA nanocapsules were separated by centrifugation at 14,000 rpm for 40 min and dried before being dissolved in a mixture of THF and ethanol. D_2O and known concentration of pyrazine were used as a solvent and a calibration standard in the quantitative analysis by ^{1}H-NMR (Bruker, DPX 400). The mass of drug encapsulated in nanocapsules was determined from the area ratio of proton peaks at δ 7.66–9.07 ppm, corresponding to aromatic protons of CHD and pyrazine, respectively.[16]

Preparation and Characterization of CHD-PMA/SPVS Composite Latex

In the preparation of CHD-PMA/SPVS composite latex, a known amount of SPVS latex (1% TSC) was mixed with CHD-PMA nanocapsules (1% TSC, 10 g) with continuous stirring for 10 min at room temperature. The weight ratios of CHD-PMA:SPVS were varied from 1:0.98 to 1:0.06. The zeta potential and morphology of CHD-PMA/SPVS composite latex particles were determined.

Raman spectra of the composite particles at weight ratios of 1:0.98 and 1:0.60, as a function of penetration depth, were recorded on a confocal Raman spectroscope

(NT-MDT, NTEGRA Spectra). CHD-PMA/SPVS composite latex particles were dropped onto a cover glass and dried at room temperature. Samples were then illuminated with a He-Ne laser at the excitation wavelength of 632.8 nm. Each spectrum was collected at the frequency range 80–5500 cm^{-1} over 60 s with 10 accumulations and a resolution of 2 cm^{-1}. A pinhole diameter of 50 μm was employed. Spectra were recorded at the surface of samples and at various penetration depths with 100 nm intervals.

RESULTS AND DISCUSSION

Characterizations of SPVS Particles and CHD-PMA Nanocapsules

Results from the particle size analyzer indicated that the average sizes of SPVS particles and CHD-PMA nanocapsules in an aqueous phase were 160 and 200 nm, respectively. The morphologies of skim, SPVS particles, and the CHD-PMA nanocapsules under TEM are shown in Figure 2.

The more distinct boundary of SPVS particles in Figure 2(b) compared to the unvulcanized skim particles in Figure 2(a) correlated well with the dense network structure in each SPVS particle.[2] The low swelling ratio of about 200% confirmed full cross-linking of rubber in SPVS latex. The small particle size of skim or the large particle surface area was responsible for the high degree of cross-linking.

For CHD-PMA nanocapsules ($\overline{M}_w$ of PMA = 250 K, encapsulation efficiency = 86%), spherical and well-dispersed nanocapsules with no aggregation were observed in Figure 2(c). The suspension of CHD-PMA nanocapsules in an aqueous medium resulted from the electrical stabilization of lecithin. Zeta potential values of CHD-PMA nanocapsules and SPVS particles at various pHs are presented in Figure 3.

The amphoteric character of skim and SPVS particles with the isoelectric point (pI) at pH 2.8 was observed. The amphotericity is due to the presence of amino acid moieties derived from the native proteins chemically bound to the surface of the skim particles.[14] These particles bore a negative charge at pH above pI. At pH greater than 3 for the skim and 4 for SPVS, the zeta potential values slightly changed, indicating the complete ionization of the ionogenic groupings.[2,17] Since the pI value did not fall into the normal range of protein's pI (4.0–6.0), it was believed that other compounds, e.g., fatty acids and SDS, were present on the skim particle surface.[5]

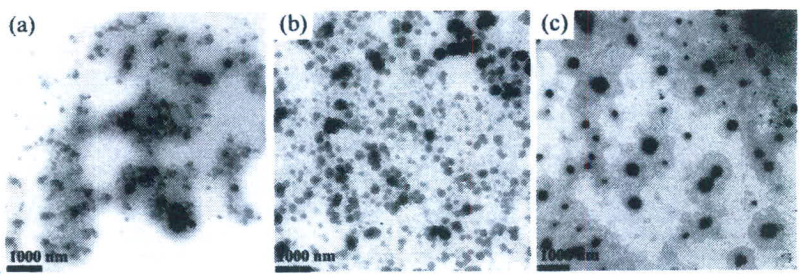


Figure 2. TEM micrographs of (a) skim, (b) SPVS, and (c) CHD-PMA nanocapsules.

Downloaded By: [Tearle, Jacqueline] [informa internal users] At: 15:11 8 December 2010

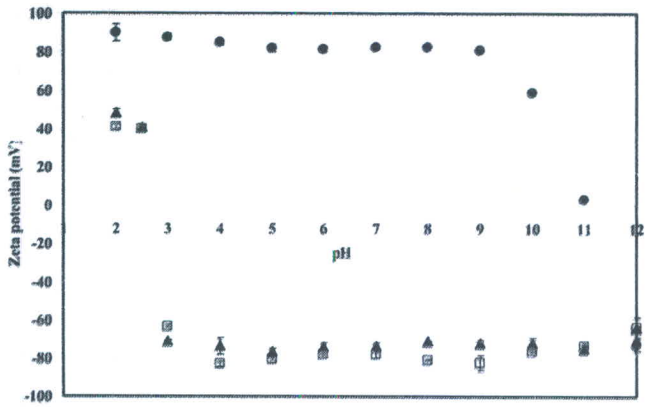


Figure 3. Zeta potential of (●) CHD-PMA nanocapsules, (◆) skim, and (□) SPVS vs. pH.

The results agreed well with the previous work, which reported that the addition of small amounts of carboxylate, sulfonate, and sulfate surfactants whose alkyl chain consisted of approximately 11 carbon atoms effectively enhanced the stability of NR latex by rearranging the indigenous soaps.[18]

For CHD-PMA nanocapsules dispersed in an aqueous medium, the zeta potentials over a range of pH 2 to 10 showed a positive value of 85 mV, derived from the protonation of choline moiety $[N^+(CH_3)_3]$ in lecithin.[15] The pI value was shown to be 11 due to the zwitterionic character of lecithin, which contains phospholipids, phosphatidyl, and quaternary ammonium moieties. At pH greater than pI, the zeta potential of CHD-PMA nanocapsules was negative. The current result is in good agreement with the pI value (10.8) obtained from TM-40 silica coated with cationic ATRP macroinitiator possessing choline group.[19]

Heterocoagulation of CHD-PMA Nanocapsules and SPVS Latex Particles

At pH 4–10, the difference in the zeta potential values of CHD-PMA nanocapsules and SPVS particles reached the maximum point. The high electrostatic interaction between both particles with opposite charges effectively provoked the heterocoagulation. The pH values of the as-prepared nanocapsules and SPVS were selected for mixing both components at various blending ratios. When the blending ratio was not greater than 1:0.2, the aggregates maintained their stability from the incomplete neutralized ionic surfactants and the repulsion from the hydrophobic part of surfactants.[20] To examine the surface charge of aggregates, their zeta potential values at various blending ratios was determined, and the data are shown in Figure 4.

It was believed that the positive value of zeta potentials of composite particles was the result of their surface charges, which were dominated by the $N^+(CH_3)_3$ moiety in lecithin. The assumption was based on the interaction between SDS on the SPVS and lecithin on the nanocapsule. Several studies argued that SDS is more surface active than lecithin and ready to form micelles, which may be trapped inside the lecithin aggregate or bind to the lecithin film. This could be the result of the absorption onto

Downloaded By: [Tearle, Jacqueline] [informa internal users] At: 15:11 8 December 2010

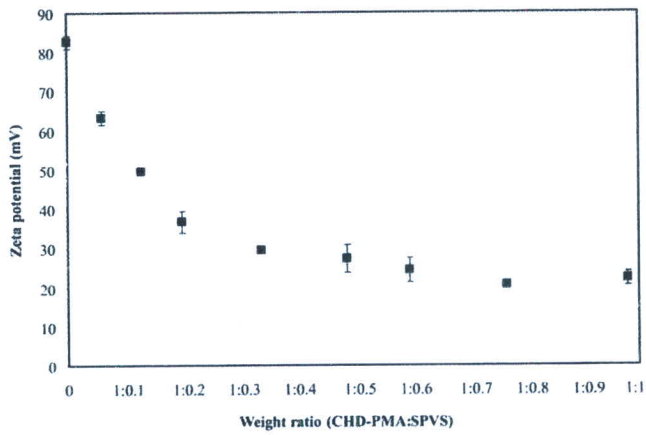


Figure 4. Zeta potential of CHD-PMA/SPVS composite particles prepared with various blending ratios.

the oil droplet surface and the formation of the complex film.[20,21] The SDS-lecithin complex formation may alter the thickness, viscosity, or density of the stabilized layer surrounding CHD-PMA nanocapsules. Although the interaction between SO_4^{2-} and $N^+(CH_3)_3$ may not be strong due to the steric hindrance of lecithin structure, SDS may also cause the lecithin molecule to unfold and change its previous interaction with the PMA or CHD droplet. The binding of SDS onto the surface decreased the electrostatic repulsion between the two components. This explained the fact that zeta potentials of the composite particles significantly decreased from 80 to 30 mV with increase of the weight ratio up to 1:0.3 before reaching to a constant value.

The morphologies of heterocoagulated CHD-PMA/SPVS particles at various blending ratios are shown in Figure 5.

It might be stated that the aggregate consists of CHD-PMA nanocapsules and SPVS particles, as represented in Figure 2 by black and white particles, respectively. Although these particles were similar in size, they were adsorbed in a random manner and formed irregular aggregates of particles.[22,23] This behavior may be due to the simultaneous adhesion of two or three consecutively dissimilar particles by interparticle bridging, which limited the adhesive area on the surface. As a consequence, it saturated more easily than in the regular heterocoagulation. Dispersive Raman spectra of CHD, lecithin, PMA, and CHD-PMA nanocapsules are shown in Figure 6.

All vibrational modes associated with the three components observed in the spectrum of the nanocapsules indicated the presence of these components. Bands due to CHD were observed at 3070, 1600, and 1500 cm^{-1} (ring modes); those of lecithin were located at 1658 (C=C stretching) and 1445 (C–O–C) cm^{-1}. Bands located at 2955 (C–H stretching), 1730 (C=O stretching), and 1454 (C–O–C) cm^{-1} were associated with PMA. The band characteristics of lecithin were very intense despite a low content of the component in the capsules. This confirmed that the molecules were densely located at the surface of the capsules. Figure 6 also shows the spectrum of SPVS, whose characteristic bands were observed at 2932 (C–H stretching), 1665 (C=C stretching), and 1445 (C–O–C) cm^{-1}.[24]

Downloaded By: [Tearle, Jacqueline] [informa internal users] At: 15:11 8 December 2010

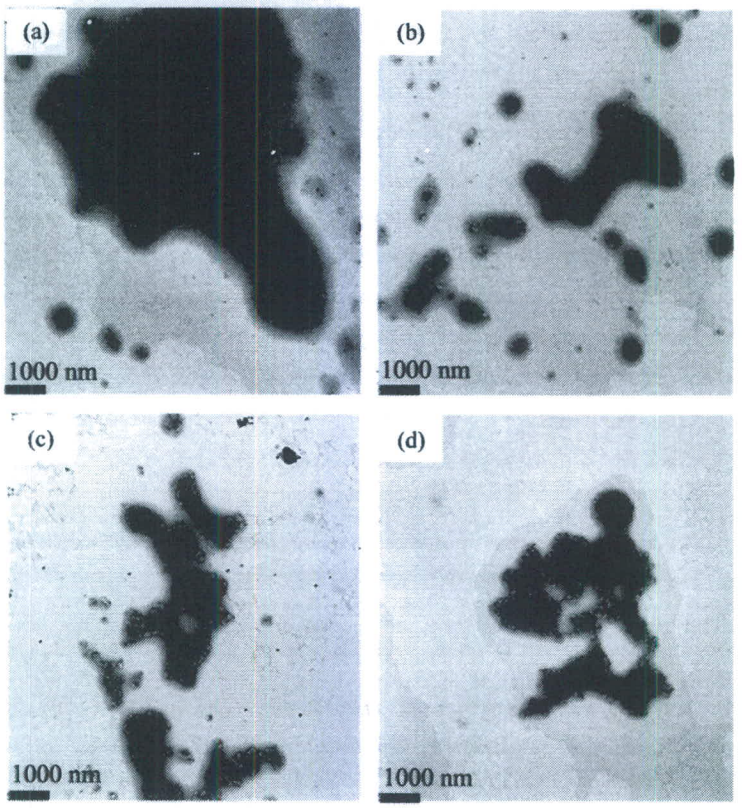


Figure 5. TEM micrographs of CHD-PMA/SPVS composite particles at ratios (a) 1:0.06, (b) 1:0.20 (c) 1:0.60, and (d) 1:0.98.

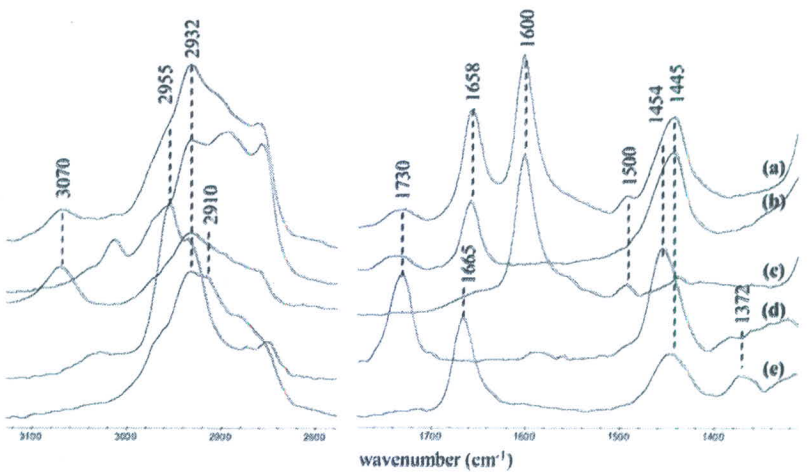


Figure 6. Dispersive Raman spectra of (a) CHD-PMA nanocapsules, (b) lecithin, (c) CHD, (d) PMA, and (e) SPVS.

Downloaded By: [Tearle, Jacqueline] [informa internal users] At: 15:11 8 December 2010

Depth profile analysis of the CHD-PMA/SPVS aggregates was studied by confocal Raman using the "z-scanning" approach, where the laser was focused on the surface or deeper inside the sample, and the spectrum was recorded at each depth.[25,26] The depth profiling spectra at 100 nm intervals from the surface of CHD-PMA/SPVS composites with a weight ratio of 1:0.98 are shown in Figure 7.

Bands due to SPVS, as denoted by S, were clearly observed from the spectra recorded at the surface and at penetration depths of up to 200 nm. When the laser was focused at 300 nm from the surface, bands due to SPVS disappeared, and those corresponding to PMA and CHD (denoted by P and C, respectively) were clearly observed. This indicated that in the composite with high content of SPVS, the skim present as shell matrix of roughly 200–300 nm thick, encapsulated the CHD-PMA nanocapsules.

On the other hand, the corresponding spectra of the composite with a weight ratio of 1:0.60, as shown in Figure 8, indicate a combination of band characteristics of SPVS, CHD, and PMA at all penetration depths. Significant differences were observed in relative intensities of the bands. As absorbencies of bands are unaffected by penetration depth, the change in band intensities indicates variations in respective functional group contents.[26] This shows that at this blend ratio the relative volume of SPVS to CHD-PMA nanocapsules was not high enough for the skim to form a continuous layer of rubber. The structure of aggregates consisting of random domains of CHD-PMA nanocapsules and SPVS was therefore obtained.

In addition, the depth profiling spectra of the CHD-PMA/SPVS composite particles prepared from both blend ratios clearly showed that the band characteristic of lecithin at 1445 cm^{-1} (denoted by L) is strong at the surface and decreases in intensity as penetration depth increases. This confirmed that the surface of

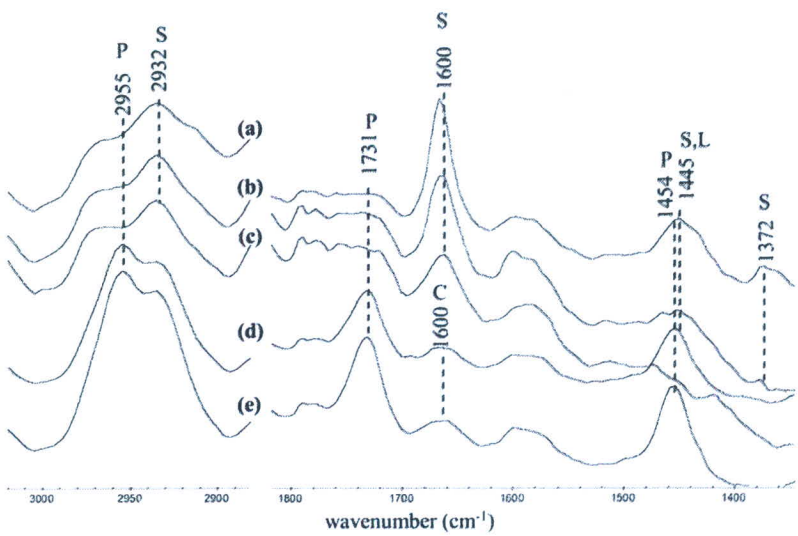


Figure 7. Confocal Raman spectra as a function of penetration depth of CHD-PMA/SPVS composites at a blend ratio of 1:0.98 recorded at: (a) surface, and at penetration depths of (b) 100, (c) 200, (d) 300, and (e) 400 nm. (S, P, C, and L denote band characteristics of SPVS, PMA, CHD, and lecithin, respectively).

Downloaded By: [Tearle, Jacqueline][informa internal users] At: 15:11 8 December 2010

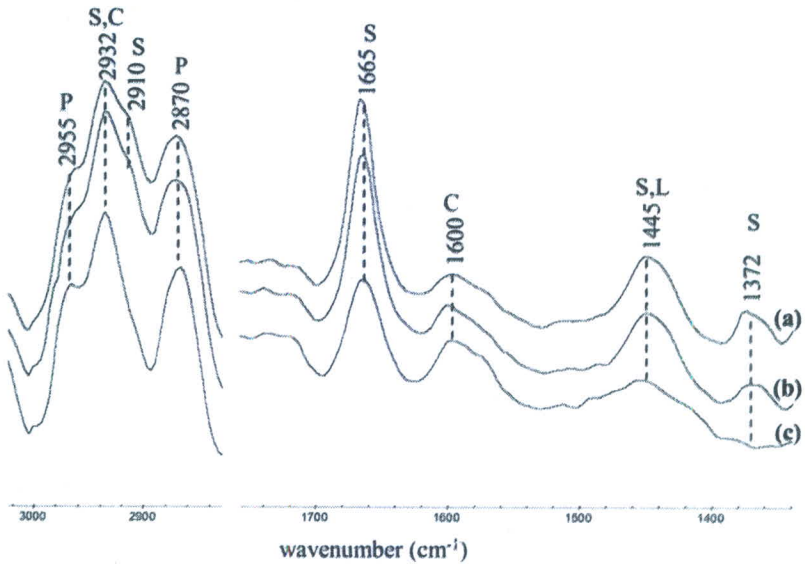


Figure 8. Confocal Raman spectra as a function of penetration depth of CHD-PMA/SPVS composites at a blend ratio of 1:0.60 recorded at: (a) surface, and at penetration depths of (b) 100 and (c) 200 nm. (S, P, C, and L denote band characteristics of SPVS, PMA, CHD, and lecithin, respectively).

CHD-PMA/SPVS composite particles was dominated by lecithin molecules. The observation is in agreement with that reported by Belaroui et al.[26] in which confocal Raman spectroscopy was employed to observe the migration of sulfate ions to the film/air interface during the formation of dry latex film.

CONCLUSION

CHD-PMA nanocapsules were prepared by the controlled nanoprecipitation of PMA onto inverse mini-emulsion droplets containing CHD. After redispersion of nanocapsules in an aqueous medium, the cationic nanocapsules were heterocoagulated with anionic SPVS latex particles. The size, zeta potential, and morphology of composite particles indicated the aggregation in which the surface charge was dominated by the $N^+(CH_3)_3$ moiety in lecithin. Confocal Raman spectra as a function of penetration depth revealed the migration of lecithin to the aggregate surface. The results also indicated that aggregations with different structures were formed, depending on the CHD-PMA/SPVS blend ratios. The corresponding composite particles will be further extended in the preparation of the disinfectant medical glove.

REFERENCES

1. Rippel, M. M., L. T. Lee, C. A. P. Leite, and F. Galembeck. 2003. Skim and cream natural rubber particles: Colloidal properties, coalescence and film formation. *J. Colloid Interface Sci.* 268: 330–340.

Downloaded By: [Tearle, Jacqueline] [informa internal users] At: 15:11 8 December 2010

2. Paiphansiri, U., and P. Tangboriboonrat. 2005. Prevulcanization of skim latex: Morphology and its use in natural rubber based composite material. *Colloid Polym. Sci.* 284: 251–257.
3. Tangboriboonrat, P., T. Tanunchai, and C. Tiyapiboonchiya. 1999. Creaming skim natural rubber latex for encapsulation of urea fertilizer. *Plast. Rubber Compos.* 28: 357–362.
4. Gorton, A. D. T. 1979. The production and properties of prevulcanized natural rubber latex. *NR Technol.* 10: 9–20.
5. Tangboriboonrat, P., and C. Lerthititrakul. 2002. Morphology of natural rubber latex particles prevulcanised by sulphur and peroxide systems. *Colloid Polym. Sci.* 280: 1097–1103.
6. Li, H., and E. Kumacheva. 2003. Core-shell particles with conductive polymer cores. *Colloid Polym. Sci.* 281: 1–9.
7. Maruyama, K., M. Kawaguchi, and T. Kato. 2001. Heterocoagulation behavior of poly(styrene-co-butadiene) and poly(butyl acrylate) at high particle concentrations. *Colloids Surf. A* 189: 211–223.
8. Yamaguchi, K., M. Ito, T. Taniguchi, S. Kawaguchi, and K. Nagai. 2004. Preparation of core-shell composite polymer particles by a novel heterocoagulation based on hydrophobic interaction. *Colloid Polym. Sci.* 282: 366–372.
9. Tangboriboonrat, P., and U. Buranabunya. 2001. Composite natural rubber-polychloroprene latex particles produced by the heterocoagulation technique. *Colloid Polym. Sci.* 279: 615–620.
10. Sruanganurak, A., and P. Tangboriboonrat. 2007. Surface modification of sulphur prevulcanized natural rubber latex sheet via layer-by-layer assembled PMMA particles. *Colloids Surf. A* 301: 147–152.
11. Busnel, R. G., and G. Argy. 1991. Process for preparation a prophylactic device made of rupturable microcapsules and layers of elastomeric material. U.S. Patent 5024852.
12. Hajatdoost, S., M. Olsthoorn, and J. Yarwood. 1997. Depth profiling study of effect of annealing temperature on polymer/polymer interfaces in laminates using confocal Raman microspectroscopy. *Appl. Spectrosc.* 51: 1784–1790.
13. Tabaksblat, R., R. J. Meier, and B. J. Kip. 1992. Confocal Raman microspectroscopy: Theory and application to thin polymer samples. *Appl. Spectrosc.* 46: 60–68.
14. Tangboriboonrat, P., C. Tiyapiboonchaiya, and C. Lerthititrakul. 1998. New evidence of the surface morphology of deproteinized natural rubber particles. *Polym. Bull.* 41: 601–608.
15. Paiphansiri, U., and P. Tangboriboonrat. 2009. Deposition of disinfectant poly(methyl acrylate) nanocapsules onto natural rubber film via the layer-by-layer technique. *J. Appl. Polym. Sci.* 112: 769–777.
16. Paiphansiri, U., P. Tangboriboonrat, and K. Landfester. 2006. Polymeric nanocapsules containing an antiseptic agent obtained by controlled nanoprecipitation onto water-in-oil miniemulsion droplets. *Macromol. Biosci.* 6: 33–40.
17. Gazeley, K. F., A. D. T. Gorton, and T. D. Pendle. 1988. Latex concentrates: Properties and composition. In *Natural Rubber Science and Technology*, ed. A. D. Roberts, Oxford: Oxford Univ. Press, pp. 63–98.
18. Blackley, D. C., A. A. N. Aisah, and R. Twaits. 1979. Effect of potassium fatty-acid soaps upon mechanical and chemical stability of natural rubber latex. *Plast. Rubber Mater. Appl.* 4: 77–86.
19. Chen, X. Y., S. P. Armes, S. J. Greaves, and J. Watts. 2004. Synthesis of hydrophilic polymer-grafted ultrafine inorganic oxide particles in protic media at ambient temperature via atom transfer radical polymerization: Use of an electrostatically adsorbed polyelectrolytic macroinitiator. *Langmuir* 20: 587–595.

Downloaded By: [Tearle, Jacqueline] [informa internal users] At: 15:11 8 December 2010

20. Deo, N., and P. Somasundaran. 2001. Mechanism of mixed liposome solubilization in the presence of sodium dodecyl sulfate. *Colloid Surf. A* 186: 33–41.
21. López, O., M. Cócera, E. Wehrli, J. L. Parra, and A. de la Maza. 1999. Solubilization of liposomes by sodium dodecyl sulfate: New mechanism based on the direct formation of mixed micelles. *Arch. Biochem. Biophys.* 367: 153–160.
22. Furusawa, K., and C. Anzai. 1992. Heterocoagulation behaviour of polymer lattices with spherical silica. *Colloids Surf.* 63: 103–111.
23. Islam, A. M., B. Z. Chowdhry, and M. J. Snowden. 1995. Heterocoagulation in colloidal dispersions. *Adv. Colloid Interface Sci.* 62: 109–136.
24. Colthup, N. B., L. H. Daly, and S. E. Wiberley. 1990. *Introduction to Infrared and Raman Spectroscopy*, 3rd ed. Boston: Academic Press.
25. Prakanrat, S., P. Phinyocheep, and P. Daniel. 2009. Spectroscopic investigation of polystyrene surface grafting on natural rubber. *Appl. Spectrosc.* 63: 233–238.
26. Belaroui, F., Y. Grohens, H. Boyer, and Y. Holl. 2000. Depth profiling of small molecules in dry latex films by confocal Raman spectroscopy. *Polymer* 41: 7641–7645.

Downloaded By: [Tearle, Jacqueline] [informa internal users] At: 15:11 8 December 2010

เอกสารแนบ 5.1.9

Copyright © 2010 American Scientific Publishers
All rights reserved
Printed in the United States of America

Journal of
Biomedical Nanotechnology
Vol. 6, 1–6, 2010

Polymeric Disinfectant Nanocapsules: Effect of Molecular Weight of Poly(methyl acrylate)

Saovaree Tanpantree[1], Pakorn Opaprakasit[2], Duangporn Polpanich[3], Srung Smanmoo[4], and Pramuan Tangboriboonrat[1,*]

[1] *Department of Chemistry, Faculty of Science, Mahidol University, Phyathai, Bangkok 10400, Thailand*
[2] *School of Bio-Chemical Engineering and Technology, Sirindhorn International Institute of Technology, Thammasat University, Pathumthani 12121, Thailand*
[3] *National Nanotechnology Center, National Science and Technology Development Agency, Thailand Science Park, Pathumthani 12120, Thailand*
[4] *Bioresources Research Unit, National Center for Genetic Engineering and Biotechnology, National Science and Technology Development Agency, Thailand Science Park, Pathumthani 12120, Thailand*

Poly(methyl acrylate) (PMA) of various weight average molecular weights ($\bar{M}_w$) were synthesized *via* the iniferter route and applied for the encapsulation of disinfectant agent (chlorhexidine digluconate; CHD) by using the controlled precipitation technique. The encapsulation efficiency of CHD-PMA nanocapsules suspended in cyclohexane increased from 70 to 100% when the $\bar{M}_w$ of PMA increased from 40 K to 550 K. After redispersing the capsules into 0.5% w/v of sodium dodecyl sulphate aqueous solution, the maximum content of CHD in the nanocapsules remained >90%. Transmission electron micrographs showed the spherical nanocapsule with continuous intact shell.

Keywords: Nanocapsule, Disinfectant Agent, Iniferter, Nanoparticle.

RESEARCH ARTICLE

1. INTRODUCTION

Wearing gloves is essential for medical personnel to avoid the infection. However, the gloves, especially those used by surgeons and dentists, are frequently perforated or torn in the case of needle prick or other similar accidents.[1,2] Recently, research attention has been focused on the development of medical gloves in which disinfectant droplets are incorporated as this would neutralize the infectious agents.[3–5] Due to the wide spectrum activity against Gram-positive and Gram-negative bacteria, chlorhexidine digluconate (CHD) salt has been widely exploited as an antiseptic agent. Among various methods used for preparation of nanocapsules, the stabilized CHD droplets dispersed in an organic continuous phase (water-in-oil; w/o) were formed by using an inverse miniemulsion process.[6–11] The CHD aqueous solution in the form of nanocapsules with polymer-based shell having different glass transition temperatures (T_g), i.e., poly(methyl methacrylate) (PMMA) ($T_g \sim 100$ °C), poly(ε-caprolactone) ($T_g \sim 60$ °C) and poly(methyl acrylate) (PMA) ($T_g \sim 10$ °C), could be prepared by the controlled precipitation of a polymer onto the w/o or inverse miniemulsion droplets.[6] The deposition of polymer from an organic continuous phase onto CHD nanodroplets was achieved by changing the gradient of the solvent/non-solvent mixture of dichloromethane/cyclohexane under mild evaporation. After being redispersed in water, an aqueous dispersion of disinfectant nanocapsules was obtained. It was reported that the remaining amount of CHD in PMMA nanocapsules was significantly decreased with the decrease in shell thickness or molecular weight of PMMA shell.

In order to obtain soft capsule's wall which is strong enough to prevent any premature releases yet delicate enough to break up under required circumstances, PMA having low T_g was investigated.[12] In the previous work, the polymer was synthesized by the miniemulsion process. Since the chain length of polymer shell was considered as an important parameter affecting the strength of the capsule wall, size of capsule and encapsulation efficiency, the effect of weight average molecular weight ($\bar{M}_w$) of this polymer on properties of nanocapsule was herein studied. PMA with various $\bar{M}_w$ was conveniently synthesized by using the thermal iniferter (*ini*tiator-trans*fer* agent-*ter*minator), based on controlled radical polymerization. The method was found to proceed under mild condition.[13] A detail synthesis of PMA and the influences of $\bar{M}_w$ on size, morphology and encapsulation efficiency

*Author to whom correspondence should be addressed.

 1550-7033/2010/6/001/006 doi:10.1166/jbn.2010.1134

of CHD-PMA nanocapsules stabilized by lecithin were presented.

2. EXPERIMENTAL DETAILS

2.1. Materials

Methyl acrylate (MA) (Purum, Fluka, Belgium) was purified by passing through a column packed with neutral and basic aluminium oxide (Purum, Fluka, Switzerland). The iniferter, i.e., *N*-bromosuccinimide (NBS) (99%, Aldrich, China), was recrystallized and dried under vacuum before use.[14] Other reagents, i.e., analytical grade dichloromethane, cyclohexane, methanol and tetrahydrofuran (THF) were purchased from Lab-scan (Thailand). Soybean phosphatidylcholine or lecithin (MP Biochemicals, USA), sodium dodecyl sulfate (SDS) (GC, Fluka, USA), pyrazine (≥98%, Fluka, Japan) and 20% w/v CHD (Sigma, Germany) were used as received.

2.2. Synthesis of PMA

PMA was synthesized *via* the controlled radical polymerization using NBS as the thermal iniferter.[14] Various $\bar{M}_w$ of PMA were obtained by employing 11.11 M of MA and 0.68, 1.37, 2.74, 11.10 or 22.23×10^{-2} M of NBS using polymerization time of 300 min. The mixture was deoxygenated by three freeze–pump–thaw cycles and then purged with nitrogen for 30 min. When the polymerization was completed at 70 °C, the reaction was terminated by cooling the flask in an ice bath. The product was obtained by precipitating the PMA solution with a large amount of methanol. The monomer conversion was gravimetrically determined. $\bar{M}_w$ and molecular weight distribution (MWD) or $\bar{M}_w/\bar{M}_n$, when $\bar{M}_n$ is number average molecular weight, of PMA were measured by gel permeation chromatography (150-CV, Waters, USA) at 30 °C using THF as an eluent. ^{1}H-NMR spectra of the PMA samples were recorded on a Bruker (DPX400, USA) using PMA (10 mg) dissolved in $CDCl_3$ (2 ml). The T_g of PMA (10 mg) was determined by differential scanning calorimeter (DSC) (DSC7, Perkin-Elmer, USA) with the heating rate of 10 °C/min.

2.3. Preparation and Characterizations of CHD-PMA Nanocapsules

In the preparation of CHD-PMA nanocapsules, a known amount of PMA and of lecithin, used as surfactant, were dissolved in dichloromethane (12 ml). Cyclohexane (12 ml) was then slowly added as a non-solvent. After charging CHD (0.5 ml) into the solution, the mixture was ultrasonicated for 2 min at 90% amplitude (W450 digital Branson, USA). The reaction mixture was heated up to 50 °C in an open vessel with continuous stirring for 22 h. During evaporation, cyclohexane was added to replace dichloromethane and also the evaporated volume. The CHD-PMA nanocapsules suspended in cyclohexane (10 ml) were then redispersed in 0.5% w/v SDS aqueous solution (10 ml). By evaporation of cyclohexane using a rotary evaporator (Rotavapor R200, Buchi, Switzerland) at 40 °C for 15 min, the capsules suspended in SDS aqueous solution were obtained.

The sizes of CHD nanodroplets and CHD-PMA nanocapsules were measured by a particle size analyzer (Zetasizer Nano ZS, Malvern, UK). The zeta potential of nanocapsules redispersed in SDS aqueous solution was determined by a microelectrophoresis apparatus (Zetasizer Nano ZS, Malvern, UK). In the determination of encapsulation efficiency, nanocapsules were centrifuged and dried before dissolving in a mixture of THF and ethanol. Deuterated water and a known amount of pyrazine were, respectively, used as an external solvent and a calibration standard in the quantitative analysis by ^{1}H-NMR.[6] Mass of drug in nanocapsules was calculated from the integrated areas of peaks at 7.66 to 9.07 ppm corresponding to aromatic-protons of the CHD and pyrazine, respectively. The morphology of the capsules, mounted on copper grid before coating with carbon, was investigated under TEM (JEM-2010, JEOL, Japan).

3. RESULTS AND DISCUSSION

3.1. Characterization of PMA

The polymerization mechanism of PMA by thermal iniferter, NBS, was proposed as shown in Scheme 1.

From Eqs. (1)–(4), the polymerization proceeded *via* the mechanism similar to that of the controlled radical polymerization in a homogeneous system.[13] The successive insertion of monomer (M) molecules into the dissociated bond took place, which produced succinimidyl (R) and bromine (R′) as the end groups of PMA chain. However, some propagating chain radicals could be irreversibly terminated according to Eq. (5).[14]

In order to confirm that NBS acted as the thermal iniferter, the end groups of PMA chain were analyzed by ^{1}H-NMR spectroscopy and the spectrum is presented in Figure 1.

The signals at 3.57 (a), 2.22 (b) and 1.41–1.84 ppm (c), corresponding to the methoxy, methine and methylene protons were observed.[15] Signal of ethylene protons of NBS appeared at 2.68 ppm (d) while that of methylene protons connected to the nitrogen atom of succinimide moiety appeared at 3.69 ppm (e). The peak at 4.12 ppm (f) of the methine protons connected to the bromine atom as the end group of PMA chain was also detected. The presence of the fragment of NBS at the end of PMA chain, therefore, confirmed that the polymerization took place through the thermal iniferter mechanism.

$$R\text{-}R' \rightleftharpoons R^{\bullet} + R'^{\bullet} \quad (1)$$

Initiation $$R^{\bullet} + M \xrightarrow{k_i} R\text{-}M^{\bullet} \quad (2)$$

Propagation $$R\text{-}M^{\bullet} + nM \xrightarrow{k_p} R\text{-}[\text{-}M\text{-}]_n\text{-}M^{\bullet} \quad (3)$$

Reversible termination $$R\text{-}[\text{-}M\text{-}]_n\text{-}M^{\bullet} + R'^{\bullet} \rightleftharpoons R\text{-}[\text{-}M\text{-}]_n\text{-}M\text{-}R' \quad (4)$$

Irreversible termination $$R\text{-}[\text{-}M\text{-}]_n\text{-}M^{\bullet} + R\text{-}[\text{-}M\text{-}]_m\text{-}M^{\bullet} \xrightarrow{k_t} R\text{-}[\text{-}M\text{-}]_{n+1}\text{-}[M\text{-}]_{m+1}\text{-}R \quad (5)$$

Scheme 1. Polymerization mechanism of PMA by using NBS iniferter technique.[13, 14]

3.1.1. Effect of Polymerization Time

The effect of polymerization time on conversion, $\bar{M}_w$ and MWD of PMA was studied. The relationship between monomer conversion and reaction time is presented in Figure 2.

It was observed that percent conversion of MA linearly increased with the increasing of reaction time, indicating that the polymerization proceeded *via* a mechanism corresponding to controlled radical polymerization.[13, 16] This implied that at the early stage, the iniferter acting as an initiator dissociated into radicals, which then reacted with MA. The long polymer chains were obtained from continuous propagation when polymerization time increased until termination. The successful insertion of monomer unit into polymer chain finally provided the high $\bar{M}_w$ of PMA. However, the conversion did not reach 100% due to the high viscosity imposed by long polymer chains produced in bulk system.

Since the initiator in the controlled polymerization system continuously reacts with monomer in the absence of terminating substance, the linear relationship between $\bar{M}_w$ and percent conversion should be observed.[13, 14] Moreover, in order to confirm the controlled radical characteristic of the bulk thermal polymerization of MA with NBS iniferter, the values of $\bar{M}_w$ and MWD of PMA determined from GPC were then plotted against the reaction time and the data are presented in Figure 3.

As expected, the results showed that $\bar{M}_w$ was directly proportional to the increased conversion.[13, 14] The iniferter which acts as an initiator, transfer agent and terminator in polymerization system, would attack the monomer to form the growing chain and finally reach the reversible termination. It was observed that the PMA obtained from using thermal iniferter technique had MWD ranging from 1.65 to 2.05. This agreed well with those (1.6 to 2.0) generally reported in the literature.[14] The MWD values of greater than 1.0 indicated that the reaction system was not a perfect living polymerization as in the case of anionic polymerization.[17, 18] This was probably because the reaction was terminated at different times, resulting in a wide distribution of polymer chain lengths.

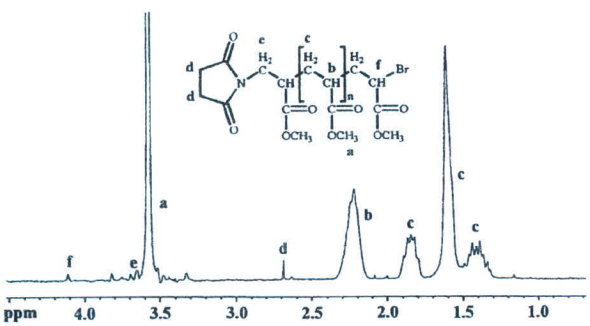


Fig. 1. ^{1}H-NMR spectrum of PMA polymerized by using NBS.

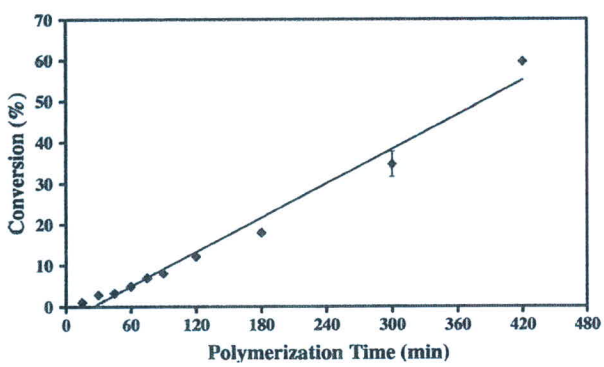


Fig. 2. Percent conversion of MA as a function of polymerization time (Polymerized at 70 °C, [MA] = 11.11 M, [NBS] = 2.74×10^{-2} M).

3.1.2. Effect of Iniferter Concentration

The effect of iniferter concentration on $\bar{M}_w$ of PMA was investigated and the results are displayed in Figure 4.

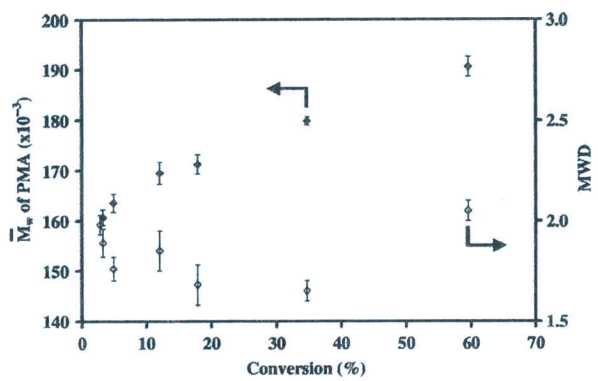


Fig. 3. $\bar{M}_w$ and MWD of PMA as a function of percent conversion from reaction conducted at 70 °C ([MA] = 11.11 M and [NBS] = 2.74×10^{-2} M).

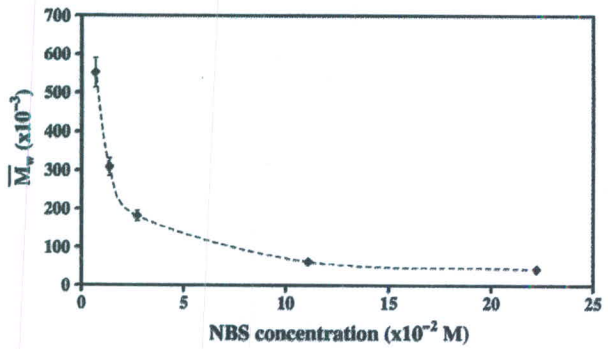


Fig. 4. $\bar{M}_w$ of PMA as a function of NBS concentration (Polymerization reaction at 70 °C, 5 h).

It was observed that the $\bar{M}_w$ of PMA increased from 40 K to 550 K with decreasing NBS concentrations from 22.23 to 0.68×10^{-2} M. This could be explained based on the principle of radical polymerization that at the high concentration of NBS, the probability of recombination of propagating chain and the primary radical was high with the low amount of monomer reacted with propagation radical.[19]

The purity of PMA homopolymer could be assumed from the DSC thermograms showing a single T_g in each sample as shown in Figure 5.

Nevertheless, samples with higher $\bar{M}_w$ showed broader transition state, which was probably resulted from their higher MWD. In addition, T_g value of PMA shifted to higher temperature with $\bar{M}_w$ increasing from 40 K to 550 K due to lower movement freedom of longer PMA chains with the higher interchain interaction.

3.2. Analysis of CHD-PMA Nanocapsules

The sizes of CHD droplets, CHD-PMA capsules dispersed in cyclohexane and then redispersed in 0.5% w/v SDS aqueous solution, prepared from using various $\bar{M}_w$ of PMA, are shown in Table I.

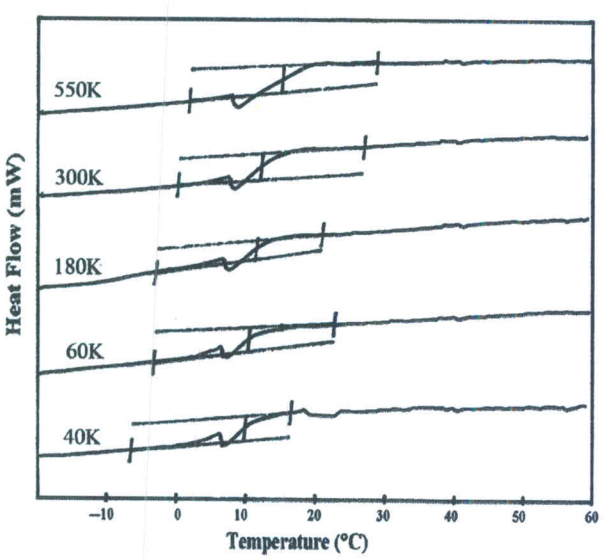


Fig. 5. DSC thermograms of PMA having various $\bar{M}_w$.

The data confirmed the monodispersed CHD nanodroplets with sizes ranging from 216 to 251 nm. As previously reported, CHD disinfectant, a lipophobe having low solubility in an oily continuous phase, plays a role in building up the osmotic pressure. As a result, the effective ingredient exchange between the droplets, i.e., Oswald ripening, can be substantially suppressed.[20] When CHD-PMA nanocapsules were formed in cyclohexane, their sizes increased from 251 to 385 nm with an increase in $\bar{M}_w$ of PMA from 40 K to 550 K.[21] This was because the longer PMA chains with higher viscosity would easily precipitate onto the CHD droplets, leading to a thicker shell formation.[22,23] The well-defined tri-layer membrane of lecithin was responsible for steric stabilization in the organic continuous phase.[24] After redispersing in SDS aqueous solution, the zeta potential value of CHD-PMA nanocapsules which remained unchanged at about −95 mV confirmed the electrostatic stabilization of the capsules in the medium. It was noticed that the size of capsules consisting of PMA with $\bar{M}_w$ of lower than 550 K in SDS aqueous solution was smaller than those suspended in cyclohexane. This might be due to the fact that the lower $\bar{M}_w$ of PMA formed a thinner capsule's wall (35–85 nm), which allowed a portion of CHD disinfectant to leak from the aqueous core to the SDS aqueous medium as previously observed in the case of CHD-PMMA.[6] Comparing the samples prepared by using different $\bar{M}_w$, it was found that the size of nanocapsules with PMA of 40 K and 60 K did not increase. This could be explained in term of the large surface area of the nanocapsules. The thickness of the low $\bar{M}_w$ PMA film over the area was very thin by taking percent ratio of core and polymer shell into account. The nanocapsules prepared from PMA with $\bar{M}_w$ of 40 K showed bimodal size distribution a result of lower T_g of short PMA chains, as shown in Figure 5, in which the soft nature led to the aggregation of capsules. However, the size of redispersed CHD-PMA nanocapsules prepared from PMA of 550 K did not significantly change. This result confirmed that the dense or thick polymeric

Table I. Effect of $\bar{M}_w$ of PMA on the size of CHD nanodroplets, CHD-PMA nanocapsules dispersed in cyclohexane, and those redispersed in SDS aqueous solution.

$\bar{M}_w$ of PMA	Size of CHD nanodroplets (nm)	Size of CHD-PMA nanocapsules in cyclohexane (nm)	Size of CHD-PMA nanocapsules redispersed in SDS aqueous solution (nm)
40 K	216 ± 4	251 ± 2	183 ± 13, 615 ± 25[a]
60 K	222 ± 9	278 ± 9	210 ± 23
180 K	236 ± 5	308 ± 9	269 ± 19
300 K	230 ± 9	315 ± 3	286 ± 23
550 K	251 ± 7	385 ± 7	386 ± 18

[a]Bimodal distribution.

shell (134 nm) could effectively entrap the CHD core. The thicker shell of nanocapsules provided a higher mass transfer resistance and thus reduced the diffusion of an aqueous continuous phase into the aqueous core.

The encapsulation efficiency of CHD-PMA nanocapsules dispersed in cyclohexane and those redispersed in SDS aqueous solution were determined by ^{1}H-NMR and the data are displayed in Figure 6.

The encapsulation efficiency of CHD-PMA nanocapsules in cyclohexane increased from 70 to 100% with increasing $\bar{M}_w$ of the polymer. The high encapsulation efficiency of the capsules coated with PMA having $\bar{M}_w$ of 300 K–550 K was probably due to the entanglement of the long polymer chains which, consequently, provided a high durability of the capsule's wall.[25] In the case of the redispersed nanocapsules, the remaining CHD increased from 55 to 80% when using PMA with $\bar{M}_w$ of 40 K–300 K, whereas the capsules prepared from PMA having $\bar{M}_w$ of 550 K retained >90% of the disinfectant agent. This pointed to the fact that the tight molecular interlocking of long PMA chains formed an effective shell which retarded the water sorption, the penetration across the polymer barrier and, thus, the reduction of diffusion of CHD through the nanocapsules' wall.[26, 27]

3.3. Morphological Study of CHD-PMA Nanocapsules

TEM micrographs of the CHD-PMA nanocapsules using PMA with $\bar{M}_w$ of 40 K and 550 K, redispersed in SDS aqueous solution, are shown in Figures 7(a) and (b), respectively.

The spherical nanocapsules with continuous intact shells, i.e., no shell rupture, was noticed especially in Figure 7(b). This confirmed that the thick shell obtained by using PMA with high $\bar{M}_w$ was due to the entanglement of long polymer chains as previously described. The soft nanocapsules with low $\bar{M}_w$ in Figure 7(a) confirmed the bimodal size distribution of nanocapsules. On a contrary, perfect structure of nanocapsules with no leakage of the

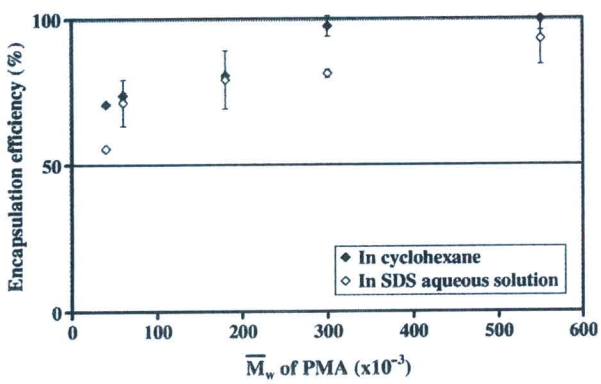


Fig. 6. Encapsulation efficiency of CHD-PMA nanocapsules, prepared from PMA with various $\bar{M}_w$, dispersed in cyclohexane, and those redispersed in SDS aqueous solution.

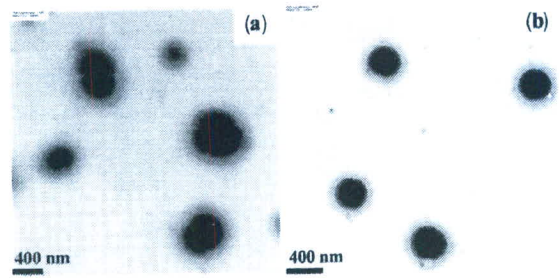


Fig. 7. TEM micrographs of CHD-PMA nanocapsules, prepared from PMA with $\bar{M}_w$ of (a) 40 K and (b) 550 K, redispersed in SDS aqueous solution.

core material was observed in Figure 7(b), when a high $\bar{M}_w$ PMA was employed. These results, therefore, emphasized the important role of high $\bar{M}_w$ of polymer shell on the nanocapsules' stability and the encapsulation efficiency. It should be noticed that the size of the dried nanocapsules prepared from PMA with $\bar{M}_w$ of 550 K (363 ± 10 nm) was slightly smaller than the hydrodynamic volume measured by the particle size analyzer (386 ± 18 nm).

4. CONCLUSIONS

PMA having various $\bar{M}_w$, synthesized by varying concentrations of thermal iniferter, were successfully used in the preparation of disinfectant (CHD) nanocapsules. Average size, shell thickness and encapsulation efficiency of the CHD-PMA nanocapsules were significantly improved when PMA with $\bar{M}_w$ of 550 K was used as shell material, i.e., the encapsulation efficiency of nanocapsules dispersed in 0.5% w/v SDS aqueous solution was greater than 90% and nanocapsules appeared to be intact. This structure is suitable for further development of disinfectant medical glove's preparation.

Acknowledgments: Research grant (RTA5180003) from The Thailand Research Fund/Commission on Higher Education to Pramuan Tangboriboonrat and the scholarship under Thailand Graduate Institute of Science and Technology (TGIST), National Science and Technology Development Agency to Saovaree Tanpantree are gratefully acknowledged.

References and Notes

1. A. M. Eklund, J. Ojajärvi, K. Laitinen, M. Valtonen, and K. A. Werkkala, Glove punctures and postoperaive skin flora of hands in cardiac surgery. *Ann. Thorac. Surg.* 74, 149 **(2002)**.
2. M. O. Osman and S. L. Jensen, Surgical gloves: Current problems. *World J. Surg.* 23, 630 **(1999)**.
3. R.-G. Busnel and G. Argy, Process for preparing a prophylactic device made of rupturable microcapsules and layers of elastomeric material. U.S. Patent 5,024,852, June 18 **(1991)**.
4. P. Sonntag, P. Hoerner, A. Cheymol, G. Argy, G. Riess, and G. Rieter, Biocide squirting from an elastomeric tri-layer film. *Nat. Mater.* 3, 311 **(2004)**.

RESEARCH ARTICLE

5. F. Bricout, A. Moraillon, P. Sonntag, P. Hoerner, W. Blackwelder, and S. Plotkin, Virus-inhibiting surgical glove to reduce the risk of infection by enveloped viruses. *J. Med. Virol.* 69, 538 **(2003)**.
6. U. Paiphansiri, P. Tangboriboonrat, and K. Landfester, Polymeric nanocapsules containing an antiseptic agent obtained by controlled nanoprecipitation onto water-in-oil miniemulsion droplets. *Macromol. Biosci.* 6, 33 **(2006)**.
7. E. Jager, C. G. Venturini, F. S. Poletto, L. M. Colome, J. P. U. Pohlmann, A. Bernardi, A. M. O. Battastini, S. S. Guterres, and A. R. Pohlmann, Sustained release from lipid-core nanocapsules by varying the core viscosity and the particle surface area. *J. Biomed. Nanotechnol.* 5, 130 **(2009)**.
8. V. Weiss-Angeli, F. S. Poletto, L. R. Zancan, F. Baldasso, A. R. Pohlmann, and S. S. Guterres, Nanocapsules of octyl methoxycinnamate containing quercetin delayed the photodegradation of both components under ultraviolet A radiation. *J. Biomed. Nanotechnol.* 4, 80 **(2008)**.
9. A. Ruebe and K. Mader, Electron spin resonance study on the dynamics of polymeric nanocapsules. *J. Biomed. Nanotechnol.* 1, 208 **(2005)**.
10. M. C. Fontana, K. Coradini, A. R. Pohlmann, S. S. Guterres, and R. C. R. Beck, Nanocapsules prepared from amorphous polyesters: Effect on the physicochemical characteristics, drug release, and photostability. *J. Nanosci. Nanotechnol.* 10, 3091 **(2010)**.
11. C. E. Mora-Huertas, H. Fessi, and A. Elaissari, Polymer-based nanocapsules for drug delivery. *Inter. J. Pharmaceut.* 385, 113 **(2010)**.
12. U. Paiphansiri and P. Tangboriboonrat, Deposition of disinfectant poly(methyl acrylate) nanocapsules onto natural rubber film via layer-by-layer technique. *J. Appl. Polym. Sci.* 112, 769 **(2009)**.
13. T. Otsu, Iniferter concept and living radical polymerization. *J. Polym. Sci. Pol. Chem.* 38, 2121 **(2000)**.
14. H. Zhou, J. Jiang, and K. Zhang, *N*-Bromosuccinimide as a thermal iniferter for radical polymerization. *J. Polym. Sci. Pol. Chem.* 43, 2567 **(2005)**.
15. M. J. Fullana, M. J. Miri, S. S. Vadhavkar, N. Kolhatkar, and A. C. Delis, Polymerization of methyl acrylate and as comonomer with ethylene using a bis(imino)pyridine iron(II) chloride/methylaluminoxane catalyst. *J. Polym. Sci. Pol. Chem.* 46, 5542 **(2008)**.
16. A. Kongkaew and J. Wootthikanokkhan, Effects of reaction conditions on poly(methyl methacrylate) polymerized by living radical polymerization with iniferter. *J. Appl. Polym. Sci.* 75, 938 **(2000)**.
17. T. Otsu, M. Yoshida, and A. Kuriyama, Living radical polymerizations in homogeneous solution by using organic sulfides as photoiniferters. *Polym. Bull.* 7, 45 **(1982)**.
18. T. Otsu, T. Matsunaga, A. Kuriyama, and M. Yoshioka, Living radical polymerization through the use of iniferters: Controlled polymers. *Eur. Polym. J.* 25, 643 **(1989)**.
19. P. Lambrinos, M. Tardi, A. Polton, and P. Sigwalt, The mechanism of the polymerization of n.butyl acrylate initiated with *N*,*N*-diethyl dithiocarbamate derivatives. *Eur. Polym. J.* 26, 1125 **(1990)**.
20. K. Landfester, N. Bechthold, F. Tiarks, and M. Antonietti, Formulation and stability mechanisms of polymerizable miniemulsions. *Macromolecules* 32, 5222 **(1999)**.
21. C. Prego, D. Torres, and M. J. Alonso, Chitosan nanocapsules as carriers for oral peptide delivery: Effect of chitosan molecular weight and type of salt on the *in vitro* behaviour and *in vivo* effectiveness. *J. Nanosci. Nanotechnol.* 6, 2921 **(2006)**.
22. G. Mittal, D. K. Sahana, V. Bhardwaj, and M. N. V. Ravi Kumar, Estradiol loaded PLGA nanoparticles for oral administration: Effect of polymer molecular weight and copolymer composition on release behavior *in vitro* and *in vivo*. *J. Controlled Release* 119, 77 **(2007)**.
23. R. A. Graves, S. Pamujula, R. Moiseyev, T. Freeman, L. A. Bostanian, and T. K. Mandal, Effect of different ratios of high and low molecular weight PLGA blend on the characteristics of pentamidine microcapsules. *Int. J. Pharm.* 270, 251 **(2004)**.
24. A. Yamada, T. Yamanaka, T. Hamada, M. Hase, K. Yoshikawa, and D. Baigl, Spontaneous transfer of phospholipid-coated oil-in-oil and water-in-oil micro- droplets through an oil/water interface. *Langmuir* 22, 9824 **(2006)**.
25. C. Yin, S. M. Chia, C. H. Quek, H. Yu, R.-X. Zhuo, K. W. Leong, and H.-Q. Mao, Microcapsules with improved mechanical stability for hepatocyte culture. *Biomaterials* 24, 1771 **(2003)**.
26. P. J. Dowding, R. Atkin, B. Vincent, and P. Bouillot, Oil core/polymer shell microcapsules by internal phase separation from emulsion droplets. II: Controlling the release profile of active molecules. *Langmuir* 21, 5278 **(2005)**.
27. W. M. Obeidat and J. C. Price, Viscosity of polymer solution phase and other factors controlling the dissolution of theophylline microspheres prepared by the emulsion solvent evaporation method. *J. Microencapsulation* 20, 57 **(2003)**.

Received: 23 March 2010. Revised/Accepted: 7 August 2010.

เอกสารแนบ 5.1.10

DNA detection of chronic myelogenous leukemia by magnetic nanoparticles†

Kulachart Jangpatarapongsa,*[a] Duangporn Polpanich,[b] Vichanan Yamkamon,[c] Yuranun Dittharot,[a] Jutharat Peng-On,[a] Raweewan Thiramanas,[b] Suradej Hongeng,[d] Saengsuree Jootar,[e] Lalida Charoenmak[f] and Pramuan Tangboriboonrat[f]

Received 4th June 2010, Accepted 19th September 2010
DOI: 10.1039/c0an00374c

A novel tool for the detection of *BCR/ABL* fusion gene in chronic myelogenous leukemia (CML) was developed by a magneto-polymerase chain reaction (PCR)-enzyme linked gene technique. The forward primers covalently bound to the surface of magnetic nanoparticles allowed a convenient separation of PCR products with high sensitivity (0.5 pg ml^{-1}) and high specificity using K562 cell line and CML patients. The results were obtained when the biotinylated-reverse primer bound to streptavidin-horseradish peroxidase (HRP) and hydrolysed the substrate. This novel readout system was approximately 1000-fold more sensitive than the conventional agarose gel electrophoresis. The present technique is practical and useful for following up CML patients and for providing appropriate treatment, particularly to patients in remote areas.

Introduction

Chronic myelogenous leukemia (CML), a common hematologic malignancy worldwide, is defined as a myeloproliferative disorder characterized by uncontrolled proliferation of myeloid lineage. The chimeric oncogene breakpoint cluster region gene and a cellular *ABL* gene (*BCR/ABL*) are traditional genes existing in almost all CML patients.[1–5] Microarray studies of mononuclear cells from CML patients reveal that most of the genes induced by *BCR/ABL* are involved in signaling transduction, cell proliferation, differentiation and apoptosis, thereby, disrupting normal hematopoietic cell regulation.[6] Therefore, the detection of *BCR/ABL* fusion gene is very important in the early diagnosis and monitoring of the disease. Quantitative assay is also necessary to determine the gene level for case follow-up studies.

Currently, several diagnostic tools for CML have been focused on the molecular level. Reverse transcriptase-polymerase chain reaction (RT-PCR) followed by gel electrophoresis is commonly performed in order to detect the specific fusion gene. However, the PCR products often disrupt the interpretation of the electrophoresis band pattern. In addition, this process is laborious and requires the use of ethidium bromide (EB), known as a carcinogenic agent, for visualizing DNA in agarose gel. Alternative techniques showing comparable sensitivity and specificity to PCR, *e.g.*, southern blot analysis and real-time PCR, are also employed. Nevertheless, these techniques are costly, more laborious, time consuming and not available at the field site or at local hospitals.

To overcome these drawbacks, we developed a novel diagnostic tool which combines the RT-PCR technology with magnetic nanoparticles (MNPs). MNPs are easily magnetized by an external magnetic field and immediately redispersed upon removal of the magnetic field. It has been widely used in various biomedical applications, *e.g.*, cell purification, immunoassay, drug delivery and as a contrast medium for magnetic resonance imaging (MRI).[7] Success in the binding of a primer onto the surface of MNPs and its application has been recently reported.[8–12] A magneto immuno-PCR (M-IPCR) technique which combined sandwich immunoassay and PCR for detection of recombinant Hepatitis B surface antigen with high sensitivity was also presented.[13,14] Here, we studied an innovative modification of the magneto-PCR-enzyme linked gene technique. It involved forward and reverse primers bound to MNPs and the labeling system (biotin), respectively, for detection of the fusion gene in the CML cell line (K562) and in patients. After RT-PCR amplification, the PCR products attached to MNPs were easily collected by an external magnetic field. By using streptavidin-horseradish peroxidase (SA-HRP), the substrate was allowed to generate the detectable colored product with high sensitivity. The overall system is summarized in Scheme 1. This technique is practical and reliable, with high sensitivity and specificity, and is useful to follow-up patients for an appropriate treatment.

Experimental

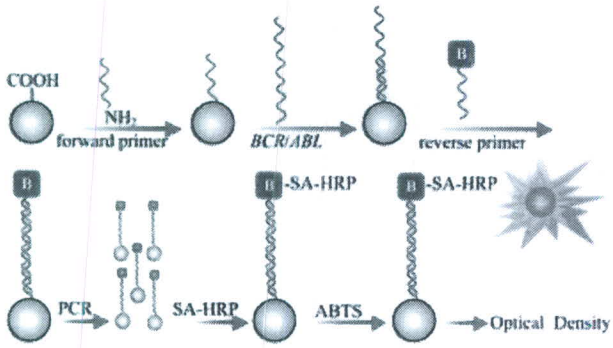
Cell culture

L929 (fibroblast cell line), K562 (t(9;22)/*BCR/ABL*) and NB4 (t(15;17)/*PML-RARα*) fusion genes were cultured in RPMI-1640 supplemented with 10% heat-inactivated fetal calf serum (FCS)

[a]*Department of Clinical Microbiology, Faculty of Medical Technology, Mahidol University, Bangkok, 10700, Thailand. E-mail: mtkjp@mahidol.ac.th; Fax: +662-441-4380*
[b]*National Nanotechnology Center, Thailand Science Park, Pathumthani, 12120, Thailand*
[c]*Department of Clinical Microscopy, Faculty of Medical Technology, Mahidol University, Bangkok, 10700, Thailand*
[d]*Department of Pediatrics, Faculty of Medicine, Ramathibodi Hospital, Mahidol University, Bangkok, 10400, Thailand*
[e]*Department of Medicine, Faculty of Medicine, Ramathibodi Hospital, Bangkok, 10400, Thailand*
[f]*Department of Chemistry, Faculty of Science, Mahidol University, Bangkok, 10400, Thailand*

† Electronic supplementary information (ESI) available: Details of magnetic nanoparticles. See DOI: 10.1039/c0an00374c

 This journal is © The Royal Society of Chemistry 2011



Scheme 1 Schematic of the detection of *BCR/ABL* fusion gene in CML by magneto-PCR-enzyme linked gene technique.

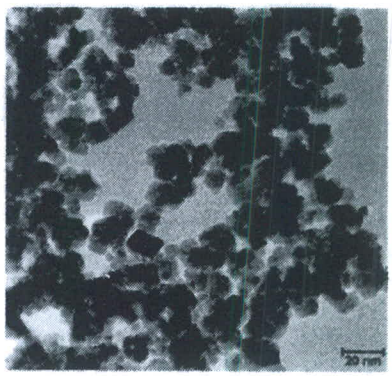


Fig. 1 TEM micrograph of MNPs.

(GIBCO, Carlsbad, USA). Viability and number of cells were determined by tryphan blue exclusion.

Sample collection

Blood samples were collected from 5 CML patients registered at Ramathibodi Hospital (Bangkok, Thailand). Diagnosis of patients was based on clinical findings, cytogenetics and RT-PCR performed using a specific primer designed as previously reported.[15] Two healthy adults living in Bangkok were considered as "healthy control" (HC) subjects. This study was approved by the Ethical Approval Committee of Biomedical Institute of Ramathibodi Hospital. Informed consent was obtained from each individual.

RNA extraction and cDNA synthesis

Total RNA was extracted from lysed cells by using Trizol® (Invitrogen, USA). Briefly, Trizol® (1 ml) was added to the cells, mixed vigorously for 15 s and then incubated for 5 min. After adding chloroform (1 ml), the mixture was centrifuged (12000 g) for 10 min at 4 °C. RNA in the colorless upper aqueous phase was precipitated by using an equal volume of isopropanol. The RNA was incubated at room temperature for 15 min before being centrifuged (14000 g) for 10 min at 4 °C. The obtained RNA pellet was washed twice with 75% ethanol (in diethyl pyrocarbonate treated distilled water (DW)) and centrifuged (14000 g) for 10 min at 4 °C. The RNA pellet was dried at ambient temperature then treated with RQ1 RNase-free DNase (Promega, USA). Afterwards, RNA (1–5 mg) was employed for cDNA synthesis by using the first strand cDNA synthesis kit including Oligo$(dT)_{12-18}$ (Invitrogen, USA) as the primer and reverse transcriptase Superscript™ III (Invitrogen, USA). The experiment was carefully handled to prevent possible contamination.[16] For example, RNA was extracted in the separation areas and the master mix with cDNA was performed before PCR amplification.

Immobilization of primers on magnetic nanoparticles

The MNPs were kindly supplied by Chemicell, Germany (see ESI†). Their morphology and size under transmission electron microscopy (JEOL, JEM-2010) are shown in Fig. 1. After washing twice with 25 mM 2-(*N*-morpholino)ethanesulfonic acid (MES) buffer (500 µl, pH 6.0), these carboxylates were immobilized with NH_2-modified BCR forward primer (5′-NH_2-C_6-CTG ACC AAC TCG TGT GTG AAA C-3′) by using the carbodiimide method. In brief, the MNPs (1000 µg) were mixed with 5.4 nmol NH_2-modified BCR forward primer and incubated for 30 min at room temperature under gently shaking. 1-ethyl-3-(3-dimethylaminopropyl)carbodiimide (EDC) solution (10 µl) (10 mg EDC in 0.25 ml MES buffer) and the MES buffer were, subsequently, added to make a final volume of 100 µl. After incubating for 10 min at room temperature, the supernatant was decanted and the immobilized MNPs were mixed with 50 mM Tris buffer (pH 7.4) to quench the unreacted carboxyl groups.[11] The immobilized MNPs were washed twice and then resuspended in Tris-EDTA buffer (10 mM Tris-HCl and 1 mM EDTA, pH 8.0) before storage at 4 °C.

RT-PCR

Specific primers for *BCR/ABL* amplification are shown in Table 1. The NH_2-modified *BCR* forward primer and the *ABL* reverse primer were 5′-labeled with the MNPs and biotin, respectively. Primers for β-actin (a house keeping gene) and DW were used as positive and negative controls, respectively. PCR was carried out in a mixture (20 µl) containing 10 mM Tris-HCl (pH 8.3), 50 mM KCl, 2.0 mM $MgCl_2$, 200 µM deoxynucleotide triphosphates (dNTP), synthesized cDNA (100 ng), 1U of Taq DNA polymerase (Intronbiotechnology, USA) and 0.3 µM unbound or MNP bound primers (3 µg MNPs content) using DNA engine PCR system (Bio-Rad Laboratories, USA). Reaction steps were done as follows: denaturation at 95 °C for 5 min, annealing at 57–65 °C for 1 min and at 72 °C for 1 min. The MNPs-bound PCR products were then separated into two parts for: (i) quantitative assay by using an enzyme-substrate system, and (ii) qualitative assay by using agarose gel electrophoresis. The MNPs-PCR products were cleaved by *Baul* enzyme (20 U) (Promega, USA) at 37 °C for 24 h before being subjected to electrophoresis.

Quantitative assay by the enzyme-substrate system

To determine the level of gene expression, the MNPs-PCR products were incubated with horseradish peroxidase-conjugated streptavidin (SA-HRP) at room temperature for 30 min. The obtained SA-biotin complexes were washed twice and simply

Published on 21 October 2010 on http://pubs.rsc.org | doi:10.1039/C0AN00574C

Table 1 Cell line, target gene, sequence and size of PCR products of fusion transcripts in the present study

Cell line	Target gene	Sequence (5′ → 3′)	Product size (base pairs)	Ref
K562	BCR-F	NH_2-C_6-CTGACC AACTCGTG TGTGAAAC	290	15
	ABL-R	Biotin-TGTGATT ATAGCCTA AGACCCGGA		
K562, L929, NB4	β-actin-F	AGAGGGAAAT CGTGCGTGAC	138	17
	β-actin-R	CAATAGTG ATGACCT GGCCGT		

separated by applying an external magnetic field. Then, 2,2′-azino-di(3-ethylbenzthiazoline-6-sulfonate) (ABTS) containing H_2O_2 (50%) (Kirkepaard & Perry Laboratories, USA) was sequentially added and the mixture was incubated for 1 h at room temperature. Enzyme activity was measured by a microplate reader (Perkin Elmer, Wallac Victor, Germany) at 405 nm.

Statistical analysis

Data were analyzed by SPSS PASW Statistics 17 (SPSS Inc., Chicago, USA) and reported as mean ± standard error of mean (sem). The difference between groups in each experiment (annealing temperature, cell line, cDNA template concentration, and CML negative and positive cells) was compared using one way ANOVA followed by Turkey HSD Post-Hoc test. Statistical significance was defined as $p < 0.05$. The reported bar graphs showed the relative ratio of *BCR/ABL* expression, calculated from the absorbance of PCR product at 405 nm from K562 cell line divided by DW. Thin lines showed the sem value.

Results and discussion

After the immobilization of primers onto the surface of the MNPs, the RT-PCR conditions, *i.e.*, annealing temperature and primer concentration, were optimized. The specificity of the technique was tested by using the K562 cell line as a CML-positive to compare with NB4 and L929 which were used as CML-negative cell lines. In the case of the K562 cell line, sensitivity was obtained by varying the concentration of the cDNA template before PCR amplification. The clinical samples were the peripheral blood collected from 5 CML patients and 2 HC donors.

Optimization of *BCR/ABL* amplification using MNPs-immobilized primer

The quality of the DNA template from the K562 cell line was investigated by using *BCR/ABL* primers and β-actin as a positive control. The bands of the PCR products at different sizes, *i.e.*, 290 and 138 base pairs when using *BCR/ABL* and β-actin as the DNA template, respectively, in Fig. 2A indicated the good quality of the extracted DNA template.

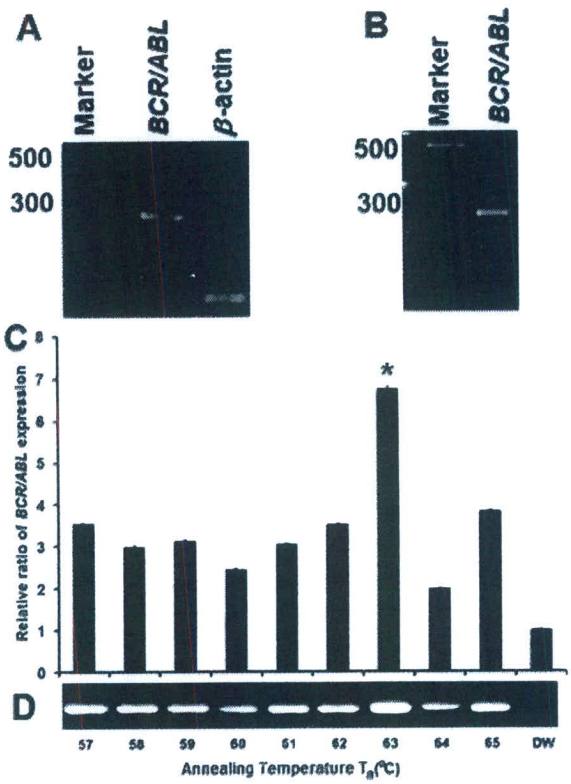


Fig. 2 Optimized conditions for the PCR product. (A) The size of *BCR/ABL* and β-actin gene product of the DNA template from the K562 cell line at T_a 63 °C. *BCR/ABL* gene expression using MNPs-bound BCR forward primer at T_a from 57 to 65 °C determined by the enzyme substrate system (C) and using primer without MNPs determined by gel electrophoresis (D). (B) The gel electrophoresis results of *Baul* enzyme cleaved products after RT-PCR. Bars show the relative ratio of *BCR/ABL* expression calculated by the absorbance of PCR product at 405 nm from K562 divided by DW. Thin lines show the value of sem. *significantly different ($p < 0.05$) from others.

To obtain a high amount of amplification product, the annealing temperature (T_a) of *BCR/ABL* amplification using MNPs-immobilized specific primers was varied from 57 to 65 °C. Fig. 2C shows the highest OD, indicated by the relative ratio of *BCR/ABL* expression (6.74 ± 0.07), when the reaction was performed at 63 °C. This OD value was significantly different from the others ($p < 0.05$) (mean ± sem at T_a 57 °C = 3.54 ± 0.02, 58 °C = 2.99 ± 0.01, 59 °C = 3.12 ± 0.01, 60 °C = 2.44 ± 0.01, 61 °C = 3.04 ± 0.02, 62 °C = 3.50 ± 0.02, 64 °C = 1.98 ± 0.02, 65 °C = 3.84 ± 0.02). Since the highest amount of PCR product was obtained at T_a 63 °C, this temperature was used to perform PCR in further steps. Results were correlated well with the band intensities obtained from gel electrophoresis. It should be noticed that the primers without MNPs and biotin tagging were employed in the latter technique as presented in Fig. 2D. The enzyme-substrate system, represented by the *BCR/ABL* gene expression, could be compared with gel electrophoresis. Moreover, this enzyme substrate assay was safer than the conventional gel electrophoresis because EB, a carcinogenic reagent, was not required.

After amplification, *Baul* restriction enzyme was used to separate the MNPs from the PCR products. Since *Baul* enzyme

This journal is © The Royal Society of Chemistry 2011

Published on 21 October 2010 on http://pubs.rsc.org | doi:10.1039/C0AN00374C

can cleave the PCR product at 5′-C↓TC GTG-3′ located on the 5′ terminal of the PCR product, the appearance of the 290 base pairs nucleotide was detected as displayed in Fig. 2B. This confirmed the presence of immobilized primers on the MNPs as previously reported.[8]

Specificity of *BCR/ABL* by the enzyme-substrate system

The specificity of *BCR/ABL* expression was determined by using a cDNA template extracted from various cell lines, *i.e.*, K562 as CML-positive cell, L929 and NB4 as CML-negative cells, and DW as a negative control. The *BCR/ABL* gene expression was quantitatively and qualitatively determined by the enzyme-substrate assay and gel electrophoresis, respectively, as presented in Figs. 3A and 3B. The data shows a significant increase in the relative ratio of *BCR/ABL* gene expression (2.70 ± 0.01) as compared to others ($p < 0.05$) and specifically detected the *BCR/ABL* gene only in the K562 cell line. The values of mean ± sem of the relative ratio of *BCR/ABL* expression from L929, NB4 and DW were 1.00 ± 0.01, 1.06 ± 0.01 and 1.00 ± 0.01, respectively. It can be observed in Fig. 3A that the relative ratio level for K562 was at least 3 fold above the average cut off from CML negative cell lines and DW. This level was also correlated well with the band appeared in the gel electrophoresis shown in Fig. 3B.

Sensitivity of the enzyme-substrate system

With the above optimized conditions, the sensitivity of detection was investigated at 63 °C by varying 10 fold dilutions of K562 cDNA template from 1 μg ml^{-1} to 0.5 pg ml^{-1}. The results in Fig. 4 show the highest relative ratio of *BCR/ABL* gene expression when using 0.05 μg ml^{-1} (7.50 ± 0.03) of cDNA. However, this level was not significantly different when cDNA was varied from 1 μg ml^{-1} to 0.5 pg ml^{-1} (level of: 1 μg ml^{-1} = 4.23 ± 0.01; 0.1 μg ml^{-1} = 4.30 ± 0.01; 0.01 μg ml^{-1} = 3.80 ± 0.01; 0.005 μg ml^{-1} = 4.31 ± 0.01; 0.001 μg ml^{-1} = 6.53 ± 0.02; 0.0005 μg ml^{-1} = 5.64 ± 0.02; 0.0001 μg ml^{-1} = 5.70 ± 0.01; 0.00005 μg ml^{-1} = 3.81 ± 0.01; 0.00001 μg ml^{-1} = 5.60 ± 0.01; 0.000005 μg ml^{-1} = 4.18 ± 0.01; 0.000001 μg ml^{-1} = 6.16 ± 0.01; 0.0000005 μg ml^{-1} = 4.04 ± 0.01; DW = 1.00 ± 0.01). On the contrary, the difference between the lowest amount of cDNA template concentration (0.5 pg ml^{-1}) and DW was clearly observed ($p < 0.05$). In addition, at lower than 0.0005 μg ml^{-1} of cDNA template concentration, no band appeared on the agarose gel as shown in Fig. 4B. This indicated that the sensitivity of the MNPs-PCR products with the enzyme-substrate system was approximately 1000-fold higher than that of the gel electrophoresis. The detection limit of our assay (in pg) was in the same scale as that of the real-time PCR, both SYBR green and *Taq*man probe as reported in other systems.[18–21]

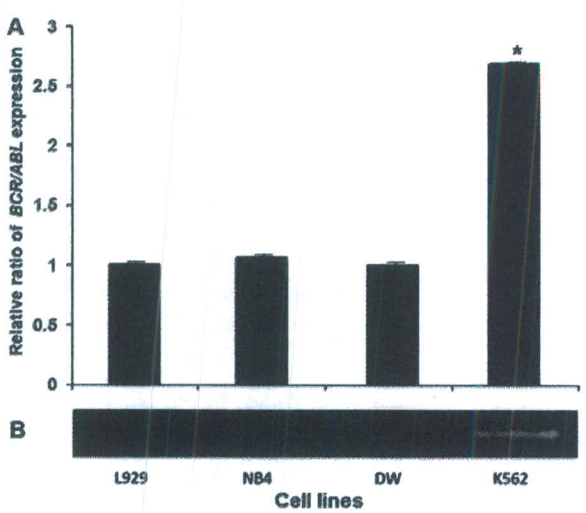


Fig. 3 The relative ratio of *BCR/ABL* gene expression in various cell lines determined by enzyme substrate system (A) and gel electrophoresis (B). Bar columns represent relative expression comparing to DW. *significantly different ($p < 0.05$) from others. Thin lines show the value of sem.

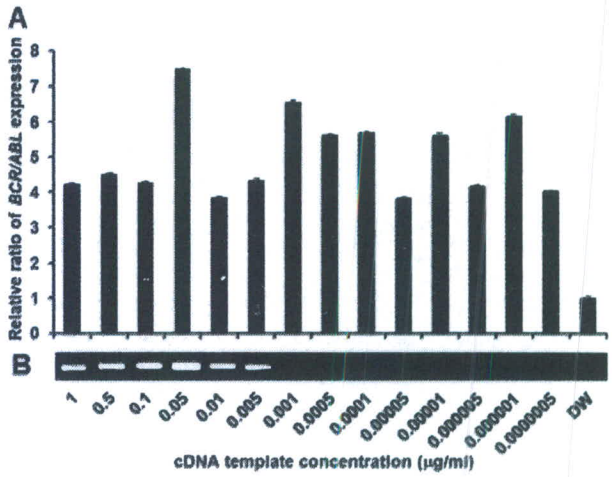


Fig. 4 Relative ratio of *BCR/ABL* gene expression (A) and gel electrophoresis (B) at various concentrations of cDNA template ranging from 1–0.0000005 μg ml^{-1}. Bar columns represent relative expression compared to DW. Thin lines show the value of sem.

Detection of the *BCR/ABL* gene in CML patients

The efficiency of the MNPs bound *BCR* forward primer and the biotinylated *ABL* reverse primers with SA-HRP system to detect the *BCR/ABL* fusion gene in clinical samples was evaluated by using blood collected from 5 CML patients and 2 HC donors. The results showed that the assay was able to detect all CML patients compared with HC subjects and the negative control. The *BCR/ABL* gene expressed by every CML patient was significantly higher than the HC; 20 fold by patient no. 1 (CML1) (21.84 ± 0.04) and 7–9 fold by patients no. 2–5 (CML2–5) (the relative ratio of *BCR/ABL* expression from CML2 = 7.64 ± 0.02, CML3 = 9.48 ± 0.03, CML4 = 8.21 ± 0.03, CML5 = 6.83 ± 0.03, HC1 = 0.99 ± 0.01, HC2 = 1.03 ± 0.01, DW = 1.00 ± 0.01) ($p < 0.05$) as presented in Fig. 5. The data correlated well with those results obtained from gel electrophoresis (data not shown). The specificity of our proposed detection system was, therefore, confirmed. Since all patients were diagnosed with the chronic phase of myelogenous leukemia, the correlation between the severity of CML patients with the level of OD could not be determined. As compared to the PCR based-gel electrophoresis, the combination of MNPs and the enzyme-substrate system brought about an enhancement in sensitivity similar to

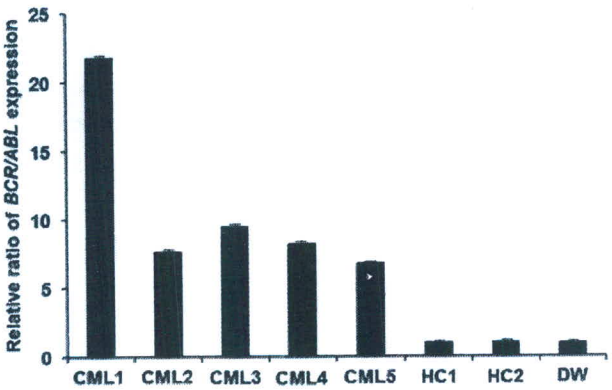


Fig. 5 Relative ratio of *BCR/ABL* gene expression in the blood from CML patients no. 1–5 (CML1–5) compared to healthy controls (HC1–2) and DW as a control.

the real-time PCR technique. Due to the fact that the proposed assay used the commonly available spectrophotometer to quantitatively determine the level of gene expression, it would be practical, especially in remote areas. Without using EB, this novel method was considered as safer than gel electrophoresis.

Conclusions

A technique for fusion gene detection of CML by combining MNPs bound to forward primer and biotinylated reverse primer for RT-PCR amplification followed by the use of an enzyme-substrate system for quantitative analysis was developed. The technique could be applied to detect *BCR/ABL* fusion gene in the CML-positive cell line with high sensitivity (0.5 pg ml^{-1} of DNA template). Also, high specificity was obtained when testing with CML-negative cell lines. This assay was successfully used to detect the *BCR/ABL* gene contained in CML patients. It could also be used as an alternative method for early diagnosis and follow-up treatment leading to a better prognosis for CML patients in clinical trials. Based on this knowledge, the detection of other genetic diseases, infectious diseases and cancers particularly in other leukemic cell types showing high prevalence among the Thai population could be investigated.

Acknowledgements

A research grant from the Thailand Research Fund/the Commission on Higher Education (RTA5180003) to PT, Mahidol University to KJ and the scholarship from National Science and Technology Development Agency under Young Scientist and Technologist Programme (YSTP) to YD and Thailand Graduate Institute of Science and Technology (TGIST) to LC are gratefully acknowledged. We also thank Dr Rachanee Udomsangpetch, Dr Pimpichaya Patamasiriwat and Dr Dalina Tanyong for technical support and Bodeeworrada Jisakul and staffs of Ramathibodi Hospital for sample collection.

References

1 W. Y. Au, P. B. Caguioa, C. Chuah, S. C. Hsu, S. Jootar, D. W. Kim, I. Y. Kweon, W. M. O'Neil, T. K. Saikia and J. Wang, *Int. J. Hematol.*, 2009, **89**, 14–23.
2 P. C. Nowell, *Exp. Cell Res.*, 1960, **19**, 267–277.
3 A. de Klein, A. G. van Kessel, G. Grosveld, C. R. Bartram, A. Hagemeijer, D. Bootsma, N. K. Spurr, N. Heisterkamp, J. Groffen and J. R. Stephenson, *Nature*, 1982, **300**, 765–767.
4 H. Pluk, K. Dorey and G. Superti-Furga, *Cell*, 2002, **108**, 247–259.
5 C. L. Sawyers, *Cancer Cell*, 2002, **1**, 13–15.
6 M. O. Nowicki, P. Pawlowski, T. Fischer, G. Hess, T. Pawlowski and T. Skorski, *Oncogene*, 2003, **22**, 3952–3963.
7 T. Osaka, T. Matsunaga, T. Nakanishi, A. Arakaki, D. Niwa and G. Iida, *Anal. Bioanal. Chem.*, 2006, **384**, 593–600.
8 H. B. Shen, M. Hu, Y. B. Wang and H. Q. Zhou, *Biophys. Chem.*, 2005, **115**, 63–66.
9 A. Fan, C. Lau and J. Lu, *Analyst*, 2008, **133**, 219–225.
10 R. Fu, T. Li and H. G. Park, *Chem. Commun.*, 2009, 5838–5840.
11 H. Li and Z. He, *Analyst*, 2009, **134**, 800–804.
12 H. Liu, S. Li, Z. Wang, M. Ji, L. Nie and N. He, *J. Biotechnol.*, 2007, **131**, 217–222.
13 M. Adler, R. Wacker and C. Niemeyer, *Analyst*, 2008, **133**, 702–718.
14 R. Wacker, B. Ceyhan, P. Alhorn, D. Schueler, C. Lang and C. M. Niemeyer, *Biochem. Biophys. Res. Commun.*, 2007, **357**, 391–396.
15 I. M. Chen, A. Chakerian, D. Combs, K. Garner and D. S. Viswanatha, *Am. J. Clin. Pathol.*, 2004, **122**, 783–793.
16 T. Hughes, M. Deininger, A. Hochhaus, S. Branford, J. Radich, J. Kaeda, M. Baccarani, J. Cortes, N. C. Cross, B. J. Druker, J. Gabert, D. Grimwade, R. Hehlmann, S. Kamel-Reid, J. H. Lipton, J. Longtine, G. Martinelli, G. Saglio, S. Soverini, W. Stock and J. M. Goldman, *Blood*, 2006, **108**, 28–37.
17 A. Giulietti, L. Overbergh, D. Valckx, B. Decallonne, R. Bouillon and C. Mathieu, *Methods*, 2001, **25**, 386–401.
18 P. Deschaght, T. De Baere, L. Van Simaey, S. Van Daele, F. De Baets, D. De Vos, J. P. Pirnay and M. Vaneechoutte, *BMC Microbiol.*, 2009, **9**, 244.
19 M. M. Lopez, P. Llop, A. Olmos, E. Marco-Noales, M. Cambra and E. Bertolini, *Curr. Issues Mol. Bio.*, 2009, **11**, 13–46.
20 E. Malinen, A. Kassinen, T. Rinttila and A. Palva, *Microbiology*, 2003, **149**, 269–277.
21 S. Yin, Y. Shang, G. Zhou, H. Tian, Y. Liu, X. Cai and X. Liu, *J. Biotechnol.*, 2010, **146**, 147–150.

This journal is © The Royal Society of Chemistry 2011

เอกสารแนบ 5.1.11

J Fluoresc (2011) 21:187–194
DOI 10.1007/s10895-010-0703-4

ORIGINAL PAPER

Selective Fluorescence Sensing of Deoxycytidine 5′-Monophosphate (dCMP) Employing a Bis (diphenylphosphate)diimine Ligand

Weerachai Nasomphan · Pramuan Tangboriboonrat · Srung Smanmoo

Received: 25 January 2010 / Accepted: 19 July 2010 / Published online: 12 August 2010
© Springer Science+Business Media, LLC 2010

Abstract A new bis(diphenylphosphate)diimine ligand (BP1) was prepared and evaluated for its ability for selective detection of deoxycytidine 5′-monophosphate (dCMP). BP1 exhibited off-type fluorescence in the presence of dCMP. The fluorescence of BP1 was significantly quenched upon the addition of 2.5×10^{-4} M dCMP and the detection limit was 1.25×10^{-5} M in MeCN-H_2O (1:1, *v/v*). The binding ratio between BP1 and dCMP was determined to be 1:1 with the binding constant of $3.98\pm0.60\times10^{-3}$ M^{-1}.

Keywords Fluorescence (FL) sensor · Deoxycytidine 5′-monophosphate (dCMP) sensor · Diimine ligand (DLs)

Introduction

Analytes are usually present in minute amounts in biological systems. Therefore, sensitive and selective detection of analytes with real-time are highly desired [1–7]. Fluorescence chemosensors have found their applications in various fields, e.g. environmental and biomedical sciences since they provide excellent degree of selectivity and sensitivity for the detection of biological and chemical analytes [8–15]. In general, the design of chemosensors bases on the incorporation of two functional moieties which are: i) ionophore (the receptor part) and ii) chromophore (the signal generating unit). The binding of the analyte to the ionophore initiates the communication between the receptor and the signaling unit to induce the change of chromophore's physical properties [16–18]. Physical changes of the chromophore can be of various types, e.g. chemiluminescence (CL), redox potentials, absorption and fluorescence (FL) [19–34]. Of these, fluorescence chemosensor receives much research attention since it provides the detection of analytes with low cost sampling and high degree of selectivity and sensitivity [35–37].

Bisphosphonate and its derivatives are well recognized for their applications as diagnostic tools in the cancer treatment [38–42]. Particularly, aminobisphosphonate (NBP) is known as an anti-cancer drug. The mode of action for an anti-cancer activity of NBP is specific for prostate cancers. Apart from its medical roles, NBP is known for its ability as a metal chelator [43–45]. Gummiena and his group demonstrated the ability of β-aminobisphosphonate derivatives as chelating agents for copper (II) ion employing electron paramagnetic spectroscopy (EPR) [46].

It is known that the bisphosphate moiety exhibits the fluorescence quenching via the photon-induced electron transfer (PET) mechanism. Diimine ligands (DLs) are known as metal chelators and also as fluorophores due to their photophysical properties [47]. Based on these facts, the incorporation of these components would emerge a new fluorescence chemosensor. Consequently, we have developed new bisphosphate derivatives based on diimine ligands and evaluated for their FL sensing towards

W. Nasomphan · S. Smanmoo (✉)
Bioresources Research Unit,
National Center for Genetic Engineering and Biotechnology (BIOTEC) Thailand Science Park,
Phaholyothin Road,
Klong Luang, Pathumthani 12120, Thailand
e-mail: srung.sma@biotec.or.th

W. Nasomphan · P. Tangboriboonrat
Department of Chemistry, Faculty of Science, Mahidol University,
Rama 6 Road,
Phyathai, Bangkok 10400, Thailand

nucleotides. The introduction of bisphosphate group into DL is aimed to facilitate the optimal hydrogen bonding between the receptor and nucleotide substrates. The detection deoxycytidine 5detection deoxycytidine-monophosphate (dCMP) is normally achieved employing high-performance liquid chromatography (HPLC) [48]. Up to date, the fluorescent (FL) chemosensor for dCMP is not yet reported. To the best of our knowledge, the chemosensor based on diimine bisphosphate has not been reported as a selective receptor for dCMP.

Experiments

Apparatus

Fluorescence measurements were carried out using a FP-6300 spectrofluorometer (JASCO) equipped with a xenon lamp source and a 1.0-cm quartz cell, and the scan speed was 600 nmmin^{-1}. ^{1}H spectrum was recorded on Bruker DPX 400 MHz spectrometer in $CDCl_3$ using TMS as the internal standard. Mass spectra were recorded on Bruker Esquire and Finnigan MAT INCOS 50 mass spectrometers.

Reagents

All reagents for the synthesis of diimine ligand phosphates obtained commercially were used without further purification. The stock solution of diimine ligand phosphates was prepared in acetonitrile with the concentration of 10 mM. The corresponding nucleotide monophosphates [deoxycytidine 5′-monophosphate (dCMP); deoxyadenosine 5′-monophosphate (dAMP); deoxycyclicadenosine 5′-monophosphate (dcAMP); deoxythymidine 5′-monophosphate (dTMP); deoxyguanosine 5′-monophosphate (dGMP); uridine 5′-monophosphate (UMP); adenosine 5′-monophosphate (AMP); guanosine 5′-monophosphate (GMP); cytidine 5′-monophosphate (CMP); thymidine 5′-monophosphate (TMP)] used in this study were purchased from Sigma Aldrich (USA) and used without further purification. Methanol was used as a HPLC grade. All other chemicals used were supplied from Sigma Aldrich (USA) as analytical grade and used without further purification. MilliQ water was used throughout this study. The concentration of stock solution of metal ions was 1 mM.

General Synthesis of Diimine Ligands

DL was synthesized from the condensation between a corresponding benzaldehyde (1 mmol) and *o*-phenylenediamine (1 mmol) in the presence of distilled water (10 mL). After the reaction mixture was left stirring for 6 h, the crude solid was collected by filtration and crystallized from methanol to obtain the final product in good yields.

3,3′-[1,2-Phenylenebis(nitrilomethylidene)]bis-phenol (DL1)

DL1 was obtained as white crystals (2.16 g, 74 %). ^{1}H NMR (DMSO-*d6*) δ_H 7.65 (d, 1H), 7.60 (m, 2H), 7.41 (q, 1H), 7.19 (m, 1H), 6.89 (d, 2H), 6.64 (d, 2H), 5.41 (s, 2H). MS (ESI) $[M+H]^+$ 317.13.

4,4′-[1,2-Phenylenebis(nitrilomethylidene)]bis-phenol (DL2)

DL2 was obtained as white crystals (2.40 g, 82 %). ^{1}H NMR (DMSO-*d6*) δ_H 8.94 (s, 2H), 7.67 (d, 2H), 7.46 (m, 4H), 7.41 (m, 4H), 6.97 (m, 4H). ^{13}C NMR δ 117.6, 119.1, 119.4, 119.8, 127.9, 132.5, 133.5, 142.6, 161.5, 163.8. MS (ESI) $[M+H]^+$ 317.35.

Synthesis of *N,N′*-Phenylenebis[2-hydroxybenzylidene-2-benzylidenealdimine] (MP)

In a flame dried round bottom flask, DL1 (0.5 g, 1.58 mmol) was added followed by addition of dry THF (5 mL). The reaction mixture was stirred until the disappearance of DL1 and the solution was brought to −80 °C followed by addition of potassium *tert*-butoxide (0.19 g, 1.74 mmol). The reaction mixture was left stirring at room temperature for 3 h before the reaction solution was cooled down to −80 °C followed by the addition of diphenyl chlorophosphate (0.33 mL, 1.58 mmol). The reaction mixture was left stirring at room temperature overnight before the addition of saturated aqueous NH_4Cl solution followed by extraction with EtOAc (3×10 mL). The organic phase was washed with brine and dried over $MgSO_4$. The solvent was removed under a vacuum and the crude product was chromatographed on a silica gel column. Elution of the column with a mixture of EtOAc and hexane (2:8) afforded the desired product as clear oil (0.54 g, 62 %). ^{1}H NMR (DMSO-*d6*) δ_H 8.40 (s, 1H), 7.70 (d, 2H, *J*=8.51), 7.39 (d, 1H, *J*=8.50), 7.30 (t, 2H, *J*= 15.77), 7.22 (m, 2H), 7.08 (t, 2H, *J*=7.81 and 15.53), 6.92 (d, 1H, 7.49), 6.61 (d, 1H, *J*=7.74), 6.48 (d, 1H, *J*=7.49), 6.38 (s, 1H), 5.45 (s, 2H).^{13}C NMR δ 111.13 (Ar*C*H), 117.47 (Ar*C*H), 119.57 (Ar*C*H), 119.74 (Ar*C*H), 119.79 (Ar*C*H), 119.88 (Ar*C*H), 119.92 (Ar*C*H), 120.54 (Ar*C*H), 121.38 (Ar*C*H), 121.70 (Ar*C*H), 122.61 (Ar*C*H), 123.22 (Ar*C*H), 123.66 (Ar*C*H), 125.54 (Ar*C*H), 125.94 (Ar*C*H), 126.04 (Ar*C*H), 126.36 (Ar*C*H), 128.77 (Ar*C*H), 129.35 (Ar*C*H), 130.04 (Ar*C*H), 130.19 (Ar*C*H), 130.28 (Ar*C*H), 130.76 (Ar*C*H), 130.89 (Ar*C*H), 131.90 (Ar*C*), 135.91 (Ar*C*), 139.37 (Ar*C*), 142.53 (Ar*C*), 149.64 (Ar*C*), 149.71 (Ar*C*), 150.17 (*C*=NH), 151.69 (*C*=NH). HRMS (ESI+) $[M+Na]^+$ found 571.1392 $[M+H]^+$, calcd for $C_{32}H_{25}N_2O_5P$

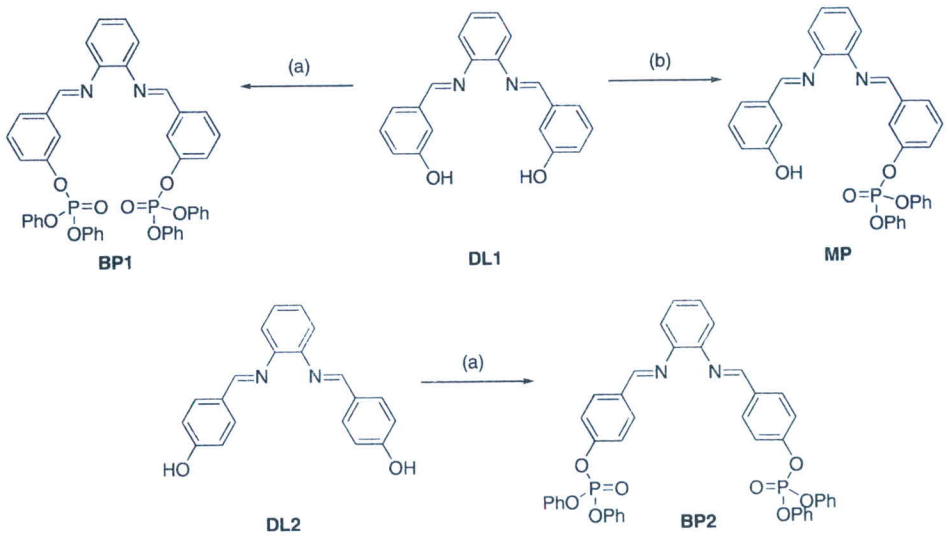


Fig. 1 Chemical structures of BP1, BP2 and MP. Conditions and Reagents; (a) (i) 2.2 equiv *tert*-BuOK, THF, room temperature, 2 hrs (ii) 2 equiv ClP(O)$(OPh)_2$, −80 °C, overnight. (b) (i) 1.1 equiv *tert*-BuOK, THF, room temperature, 2 hrs (ii) 1 equiv ClP(O)$(OPh)_2$, −80 °C, overnight

548.1501. IR (KBr, cm^{-1}) 3417, 3071, 2615, 1941, 1788, 1606, 1416, 1389, 1025, 964, 849, 777.

Synthesis of *N,N′*-Phenylenebis[2-benzylidenealdimine] phosphate (BP1)

BP1 was synthesized according to the procedure described for the synthesis of MP except 2 molar equiv of diphenyl chlorophosphate was used. ^{1}H NMR (DMSO-d6) δ_H 8.40 (s, 1H), 7.80 (d, 2H, *J*=8.67), 7.72 (d, 1H, *J*=8.96), 7.42 (m, 13H), 7.26 (m, 19H), 7.06 (d, 2H, *J*=8.61), 5.59 (s, 2H).^{13}C NMR δ 111.14 (ArCH), 115.26 (ArCH), 119.36 (ArCH), 119.91 (ArCH), 119.97 (ArCH), 120.30 (ArCH), 120.35 (ArCH), 120.41 (ArCH), 121.76 (ArCH), 122.42 (ArCH), 122.94 (ArCH), 125.97 (ArCH), 126.08 (ArCH), 128.10 (ArCH), 128.79 (ArCH), 130.24 (ArCH), 130.32 (ArCH), 130.49 (ArCH), 131.16 (ArC), 134.53 (ArC), 135.81 (ArC), 142.61 (ArC), 149.77 (ArC), 152.13 (C=NH). HRMS (ESI+) $[M+Na]^+$ found 803.1687 $[M+H]^+$, calcd for $C_{44}H_{34}N_2O_8P_2$ 780.1790. IR (KBr, cm^{-1}) 3064, 2929, 2870, 2611, 1942, 1867, 1783, 1730, 1588, 1487, 1449, 1389, 1298, 1186, 1161, 1090, 1072.

Synthesis of *N,N′*-Phenylenebis[3-benzylidenealdimine] phosphate (BP2)

BP2 was similarly prepared according to the procedure for BP1 except DL2 was used as a starting material. ^{1}H NMR (DMSO-*d6*) δ_H 7.82 (d, 2H, *J*=8.65), 7.44–7.39 (m, 15H), 7.31–7.20 (m, 14H), 7.15 (d, 2H, *J*=7.15), 5.60 (s, 2H).^{13}C NMR δ 111.14 (ArCH), 115.26 (ArCH), 119.37 (ArCH), 119.87 (ArCH), 120.36 (ArCH), 121.80 (*ArCH*), 122.41 (ArCH), 125.61 (ArCH), 126.02 (ArCH), 128.10 (ArCH), 130.14 (ArCH), 131.16 (ArCH), 135.83 (ArCH), 142.64

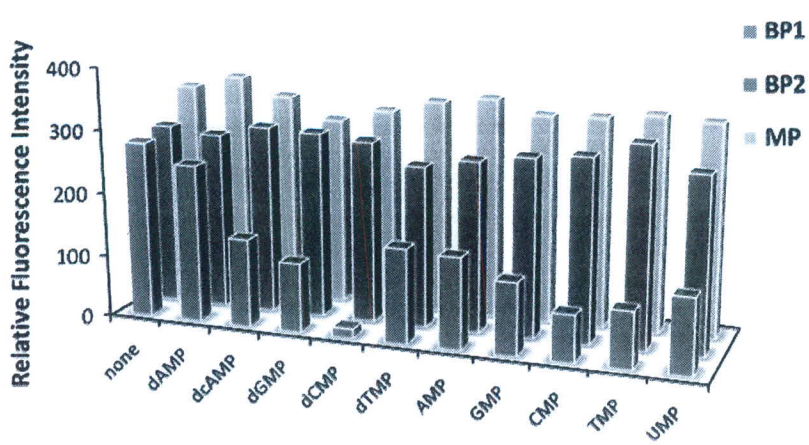


Fig. 2 The effect of various nucleotides on the FL intensities of MP, BP1 and BP2 in MeCN: H_2O (1:1; *v/v*). [receptor] = 2.5×10^{-6} M. [nucleotides] = 2.5×10^{-4} M. λ_{ex}=280 nm

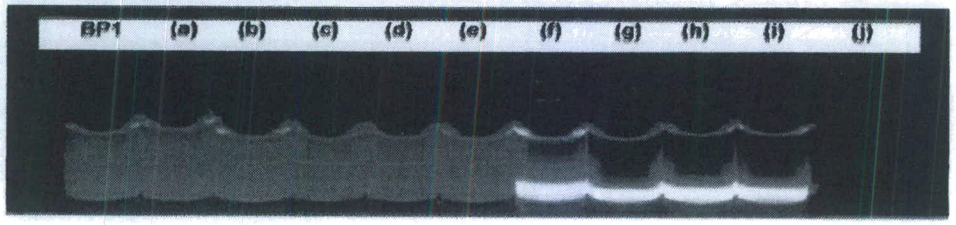


Fig. 3 FL changes of BP1 (2.5×10^{-6} M) in the presence and absence of nucleotides (a) BP1 + dAMP (b) BP1 + dcAMP (c) BP1 + dTMP (d) BP1 + dGMP (e) BP1 + AMP (f) BP1 + GMP (g) BP1 + CMP (h) BP1 + TMP (i) BP1 + UMP and (j) BP1 + dCMP. [nucleotides] = 5×10^{-4} M

(Ar*C*H), 142.77 (Ar*C*H), 149.08 (Ar*C*H), 149.83 (Ar*C*H), 150.88 (Ar*C*H), 151.51 (Ar*C*H), 152.14 (Ar*C*), 153.67 (Ar*C*), 153.95 (Ar*C*), 157.07 (Ar*C*), 159.07 (Ar*C*), 161 (*C*=NH). HRMS (ESI+) $[M+Na]^+$ found 803.1681 $[M+H]^+$, calcd for $C_{44}H_{34}N_2O_8P_2$ 780.1790. IR (KBr, cm^{-1}) 3451, 3268, 3070, 3007, 2881, 2512, 2249, 2123, 1996, 1828, 1768, 1621, 1374, 1223, 1056, 882, 759.

Results and Discussion

Syntheses of MP, BP1 and BP2

BP1 was synthesized in two steps from the reaction between DL1 with 2 equiv of diphenylchlorophosphate in the presence of potassium *tert*-butoxide as base. BP2 was also synthesized in order to investigate the positional effect of bisphosphate group. The synthesis of BP2 was similar to the procedure described for the synthesis of BP1 except DL2 was used as the starting material. After purification, BP1 and BP2 were obtained in good isolated yields (BP1= 72% and BP2=77%) (Fig. 1). Monodiphenylchlorophosphate diimine ligand (MP) was also synthesized as the control ligand for the investigation of the effect of bisphosphate group due to the fact that the presence of bisphosphate group is important for facilitating the hydrogen bonding between the receptor and analytes. The synthesis of MP was achieved by reacting DL1 with 1 equiv of diphenylchlorophosphate. BP1 was prepared in moderate yield (62%).

Fluorescence Screening of MP, BP1 and BP2 with Various Nucleotide Substrates

Obtaining BP1, BP2 and MP, FL quenching experiments of these receptors in the presence of various nucleotides were investigated. With reference to the screened nucleotides, the FL property of BP1 exhibited a significant quenching in the presence of deoxycytidine 5′-monophosphate (dCMP) (Fig. 2). It was shown that after the addition of 2.5×10^{-4} M dCMP, the FL intensity of BP1 was significantly inhibited. The presence of other nucleotides did not significantly quench the FL of BP1. BP2 and MP showed no degree of FL quenching upon treating with any nucleotides. It was shown that the presence of bisphosphate group at the *meta* position on the aromatic ring of BP1 is necessary for proper chelation between BP1 and dCMP.

In the case of MP, it lacks a phosphate group which resulted in an improper interaction between MP and dCMP. This was evident that the presence of bisphosphate group was important since no FL quenching of MP was observed in the presence of any nucleotides. BP2 possesses the

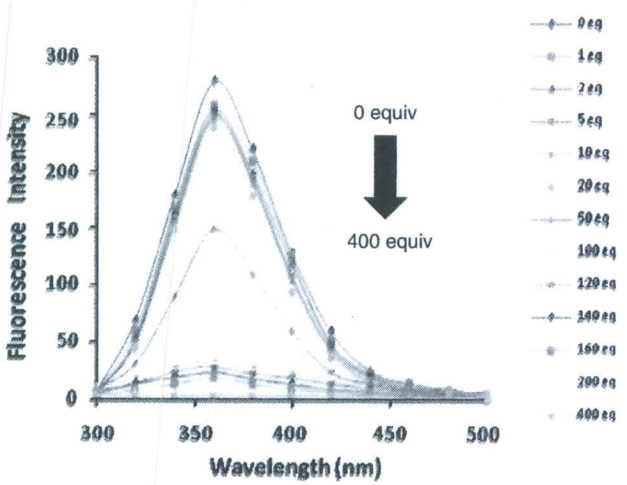


Fig. 4 FL emission spectra of BP1 (2.5×10^{-6} M) in the presence of various concentrations of dCMP

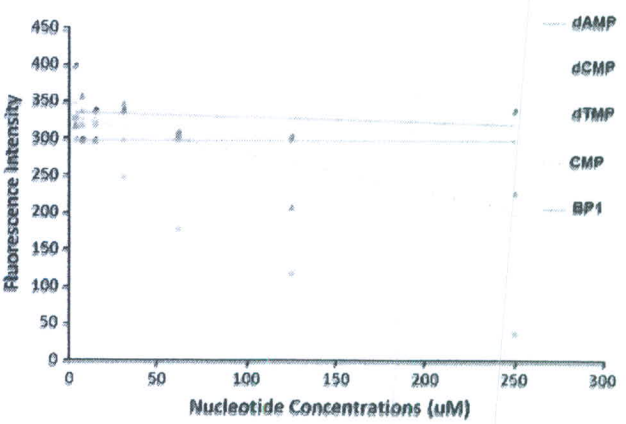


Fig. 5 FL quenching of BP1 by various concentrations of dAMP, dCMP, dTMP, and CMP

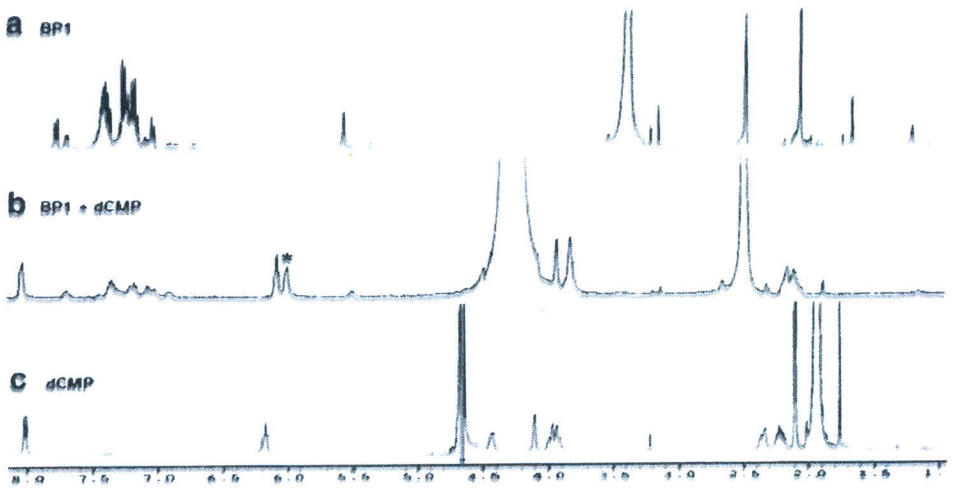


Fig. 6 ^{1}H NMR spectra (400 MHz) of (a) free BP1 (10 mM) in DMSO (top); (b) BP1 + 1 equiv of dCMP in DMSO:D_2O (1:1; *v/v*); (c) dCMP in D_2O

bisphosphate group which meets the requirement described above for the optimal interaction between the receptor and dCMP. The position of the bisphosphate group on the BP2 aromatic ring is too remote for the good binding between the receptor and dCMP. It was obvious that BP1 exhibited high degree of selectivity towards dCMP. The presence of the bisphosphate group at the *meta* position on the aromatic ring of BP1 is a prerequisite for the good recognition between the receptor and dCMP. Therefore, BP1 was used as the optimal receptor for subsequent experiments.

BP1 was shown to exhibit strong FL emission in acetonitrile. The excitation wavelength (*Ex*) of BP1 was 280 nm while the emission wavelength (*Em*) was 360 nm.

Figure 3 shows the FL changes of BP1 upon the addition of various nucleotides. The presence of various nucleotides slightly to moderately affected the FL intensity of BP1. It was clearly observed that 2.5×10^{-4} M of dCMP dramatically quenched the FL of BP1.

FL emission of BP1 was measured at different concentrations of dCMP while fixed the concentration of BP1 at 2.5×10^{-6} M (Fig. 4). Increasing concentration of dCMP resulted in the decrease of the FL emission of BP1. When the concentration of dCMP reached 2.5×10^{-4} M, the FL intensity of BP1 was significantly quenched. To investigate more precisely, the quenching effect of BP1 with dCMP and other representing nucleotides at different concentrations was studied. The FL intensity of BP1 was measured in the presence of various concentrations of four nucleotides, dAMP, dCMP, dTMP and CMP. At all concentrations of dAMP, there was a little FL quenching of BP1 (Fig. 5).

Addition of dTMP and CMP resulted in slight decrease of BP1's FL intensity. The FL intensity of BP1 was significantly inhibited in the presence of dCMP even at low concentration. Further increasing concentrations of dCMP resulted in a gradual FL quenching of BP1. When the concentration of dCMP reached 400

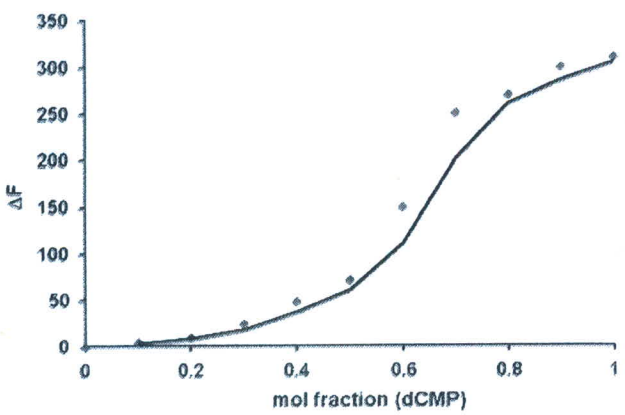


Fig. 7 Job's plot for BP1·dCMP. *Y* axis is fluorescence changes of BP1

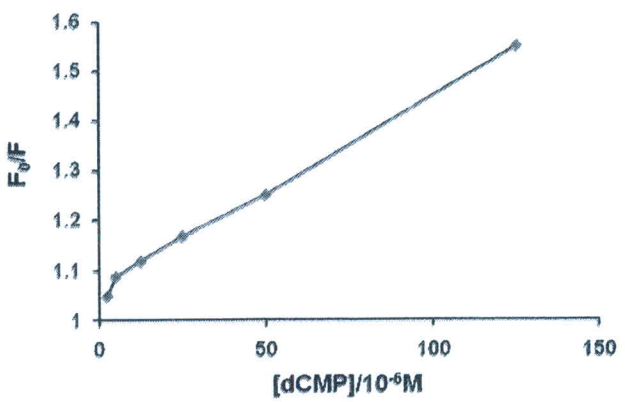


Fig. 8 Stern-Volmer plot of BP1 with increasing concentrations of dCMP. [BP1] = 2.5×10^{-6} M. [dCMP]/10^{-6} M=2.5, 5, 12.5, 25, 50, 300 (*T*=298 K)

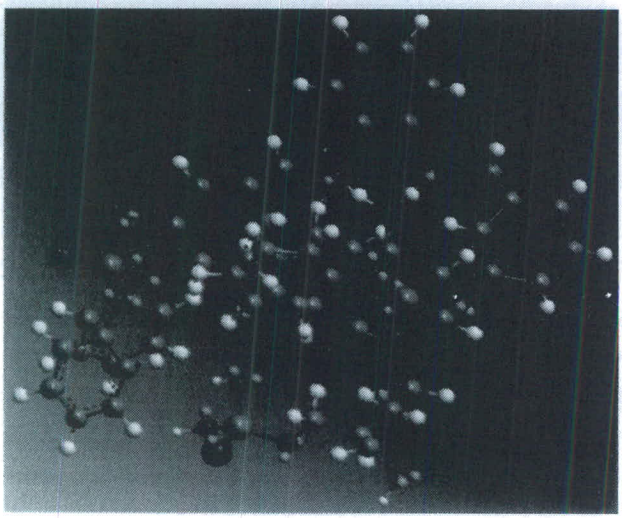


Fig. 9 Energy minimized structure of the complex between BP1 and dCMP

molar equiv of BP1, the FL intensity of BP1 was significantly quenched.

^{1}H NMR Titration of BP1 with dCMP

Of the mechanistic detail concerning interaction between BP1 and dCMP, ^{1}H NMR experiments were used for the investigation (Fig. 6). It was clearly shown that the addition of 1 equiv dCMP into BP1 solution caused a slight downfield shift of aromatic protons in BP1 indicating the disturbance of the electron density within this area. Apart from the downfield shift of protons in the aromatic region, the solution contained both BP1 and dCMP exhibited the change of the multiplicity for the designated cytosine proton. This effect was evident with the appearance of the new peak at δ 6.15 ppm (indicating as an asterisk in Fig. 6b). This new peak was the result from the perturbation for the electronic environment of the cytosine proton in dCMP due to the interaction with BP1.

Determination of the Binding Ratio and Constant for BP1 and dCMP

Attempting to obtain the binding ratio between BP1 and dCMP by mass spectrometry was unsuccessful. Therefore, Job's plot analysis was used to determine the binding ratio [49]. Job's plot analysis indicated a breaking point at 0.6 mol fraction of dCMP indicating the formation of a 1:1 complex of BP1·dCMP (Fig. 7). The binding constant between BP1 and dCMP was determined using the Stern-Volmer plot (K_{sv}). The K_{sv} was obtained from the Stern-Volmer Eq. (1) [50]

$$F_0/F = 1 + K_{SV}[Q] \quad (1)$$

Where [Q] is the concentration of the quencher (dCMP), K_{sv} is the Stern-Volmer constant. The Stern-Volmer constant indicates the constant equilibrium of BP1·dCMP complex in the static quenching process. It was shown in Fig. 8 that the Stern-Volmer plot of BP1·dCMP complex exhibited a linear relationship. The (F_0/F) was directly proportional to the increased concentration of dCMP with the correlation coefficient of 0.9953. From the plot, BP1 had a weak binding affinity to dCMP ($3.98\pm0.60\times 10^{-3}$ M^{-1}) and upon the binding between BP1 and dCMP it formed the non-fluorescent complex.

Proposed Mechanism for BP1 Binding with dCMP

The mechanistic detail for the binding between BP1 and dCMP is believed to involve the hydrogen bonding between the bisphosphate group of BP1 and the cytosine NH_2 of dCMP. The good alignment for the binding between BP1 and dCMP optimizes the interaction of these two species. Upon binding between BP1 and dCMP, the PET mechanism plays a significant role which resulted in the FL quenching of the system. The steric hindrance is also thought to play a role on the binding between BP1 and dCMP. The steric hindrance could be used to explain why the FL intensity of BP1 was not quenched upon the addition with CMP. In the case of CMP, the presence of the 2′-hydroxyl group causes the structure more bulky to fit into the receptor's pocket. Therefore, the presence of the 2′-hydroxyl group in CMP hindered proper binding between BP1 and CMP. This explained the fact that CMP is not a good substrate for BP1 due to the steric effect. The absence of the 2′-hydroxyl group in dCMP facilitates the good binding between BP1 and dCMP (Fig. 9).

Conclusions

In conclusion, we have discovered the selective FL quenching of BP1 by dCMP. The FL quenching of BP1 exhibited excellent degree of selectivity towards dCMP among various nucleotide substrates. FL and ^{1}H NMR experiments indicated the interaction between BP1 and dCMP. Job's plot analysis indicated the binding ratio between BP1 and dCMP at 1:1 with the Stern-Volmer constant of $3.98\pm0.60\times10^{-3}$ M^{-1}. It was suggested that the FL quenching of BP1 by dCMP took place via the PET mechanism. The recognition of dCMP by BP1 may be due to the extended hydrogen bonding with the proper alignment. The steric effect of the substrate also plays a determining role for good binding between BP1 and dCMP. Since BP1 shows high degree of selectivity and sensitivity to dCMP over other nucleotides it could be regarded as a new FL chemosensor for dCMP.

Acknowledgements The Thailand Research Fund (TRF)/Commission on Higher Education (CHE)'s research grant to S.S. and P.T. The Development and Promotion of Science and Technology Talents Project's scholarship to W.N. are gratefully acknowledged. We are also grateful to the partial support from National Center for Genetic Engineering and Biotechnology (BIOTEC).

References

1. Lu C, Xu Z, Cui J, Zhang R, Qian X (2007) Ratiometric and highly selective fluorescent sensor for cadmium under physiological pH range: a new strategy to discriminate cadmium from zinc. J Org Chem 72:3554
2. Tang B, Yin L, Wang X, Chen Z, Tong L, Xu K (2009) A fast-response, highly sensitive and specific organoselenium fluorescent probe for thiols and its application in bioimaging. Chem Commun 5293
3. Xue X, Wang F, Liu X (2008) One-step, room temperature, colorimetric detection of mercury (Hg^{2+}) using DNA/nanoparticle conjugates. J Am Chem Soc 130:3244
4. Kim HJ, Kim SH, Kim JH, Anh LN, Lee JH, Lee CH, Kim JS (2009) ICT-based Cu(II)-sensing 9, 10-anthraquinonecalix[4] crown. Tetrahedron Lett 50:2782
5. Maiti J, Pokhrel B, Boruah R, Dolui SK (2009) Polythiophene based fluorescence sensors for acids and metal ions. Sensors Actuat B Chem 141:447
6. Zeng X, Dong L, Wu C, Mu L, Sai-Feng X, Tao Z (2009) Highly sensitive chemosensor for Cu(II) and Hg(II) based on the tripodal rhodamine receptor. Sensors Actuat B Chem 141:506
7. Lee SJ, Lee SS, Jeong IY, Lee JY, Jung JH (2007) Azobenzene coupled chromogenic receptors for the selective detection of copper(II) and its application as a chemosensor kit. Tetrahedron Lett 48:393
8. Wu JS, Kim HJ, Lee MH, Yoon JH, Lee JH, Kim JS (2007) Anion-induced ring-opening of fluorescein spirolactam: fluorescent *OFF–ON*. Tetrahedron Lett 48:3159
9. Rieth T, Sasamoto K (1998) Detection of nitric oxide and nitrite by using a Rhodamine-type fluorescent indicator. Anal Commun 35:195
10. Soh JH, Swamy KMK, Kim SK, Sim S, Lee SH, Yoon J (2007) Rhodamine urea derivatives as fluorescent chemosensors for Hg^{2+}. Tetrahedron Lett 48:5966
11. Kikuchi K, Hashimoto S, Mizukami S, Nagano T (2009) Anion sensor-based ratiometric peptide probe for protein kinase activity. Org Lett 11:2732
12. Xue L, Liu Q, Jiang H (2009) Ratiometric Zn^{2+} fluorescent sensor and new approach for sensing Cd^{2+} by ratiometric displacement. Org Lett 11:3454
13. Wang HH, Gan Q, Wang XJ, Xue L, Liu SH, Jiang H (2007) A water soluble, small molecular fluorescent sensor with femtomolar sensitivity for zinc ion. Org Lett 9:4995
14. Xu Z, Xiao Y, Qian X, Cui J, Cui D (2005) Ratiometric and selective fluorescent sensor for Cu^{II} based on internal charge transfer (ICT). Org Lett 7:889
15. Rhee HW, Lee CR, Cho SH, Song MR, Cashel M, Choy HE, Seok YJ, Hong JI (2008) Selective fluorescent chemosensor for the bacterial alarmone (p)ppGpp. J Am Chem Soc 130:784
16. Kim NY, Chang SK (1998) Calix[4]arenes bearing two distal azophenol moieties: highly selective chromogenic ionophores for the recognition of Ca^{2+} ion. J Org Chem 63:2362
17. He X, Hu S, Liu K, Guo Y, Xu J, Shao S (2006) Oxidized bis (indolyl)methane: a simple and efficient chromogenic-sensing molecule based on the proton transfer signaling mode. Org Lett 8:333
18. Jiménez D, Martínez-Máñez R, Sancenón F, Ros-Lis JV, Benito A, Soto J (2003) A new chromo-chemodosimeter selective for sulfide anion. J Am Chem Soc 125:9000
19. Matsumoto M, Kasai D, Yamada K, Fukuda N, Watanabe N, Ijuin HK (2004) Color modulation for chemiluminescence of a dioxetane bearing a 3-(anthracen-9-yl)-5-hydroxyphenyl moiety induced by a complex of crown ether with potassium *tert*-butoxide. Tetrahedron Lett 45:8079
20. Zhu Y, Shi J, Zhang Z, Zhang C, Zhang X (2002) Development of a gas sensor utilizing chemiluminescence on nanosized titanium dioxide. Anal Chem 74:120
21. Hu X, Takenaka N, Takasuna S, Kitano M, Bandow H, Maeda Y, Hattori M (1993) Determination of ammonium ion in rainwater and fogwater by flow injection analysis with chemiluminescence detection. Anal Chem 65:3489
22. Corrales T, Abrusci C, Peinado C, Catalina F, Fluorescent sensor as physical amplifier of chemiluminescence: application to the study of poly(ethylene terephthalate). Macromolecules 37:6596
23. Kang D, Zuo X, Yang R, Xia F, Plaxco KW, White RJ (2009) Comparing the properties of electrochemical-based DNA sensors employing different redox tags. Anal Chem 81:9109
24. Cai Q, Zeng K, Ruan C, Desai TA, Grimes CA (2004) A wireless, remote query glucose biosensor based on a pH-sensitive polymer. Anal Chem 76:4038
25. Xiao Y, Qu X, Plaxco KW, Heeger AJ (2007) Label-free electrochemical detection of DNA in blood serum via target-induced resolution of an electrode-bound DNA pseudoknot. J Am Chem Soc 129:11896
26. Xiao Y, Lou X, Uzawa T, Plakos KJI, Plaxco KW, Soh HT (2009) An electrochemical sensor for single nucleotide polymorphism detection in serum based on a triple-stem DNA probe. J Am Chem Soc 131:15311
27. Watanabe S, Seguchi H, Yoshida K, Kifune K, Tadaki T, Shiozaki H (2005) Colorimetric detection of fluoride ion in an aqueous solution using a thioglucose-capped gold nanoparticle. Tetrahedron Lett 46:8827
28. Zhang C, Suslick KS (2005) A colorimetric sensor array for organics in water. J Am Chem Soc 127:11548
29. Liu J, Lu Y (2003) A colorimetric lead biosensor using DNAzyme-directed assembly of gold nanoparticles. J Am Chem Soc 125:6642
30. Zhang D, Zhang M, Liu Z, Yu M, Li F, Yi T, Huang C (2006) Highly selective colorimetric sensor for cysteine and homocysteine based on azo derivatives. Tetrahedron Lett 47:7093
31. Scrafton DK, Taylor JE, Mahon MF, Fossey JS, James TD (2008) Click-fluors: modular fluorescent saccharide sensors based on a 1, 2, 3-triazole ring. J Org Chem 73:2871
32. Yang RH, Chan WH, Lee AWM, Xia PF, Zhang HK, Li K (2003) A ratiometric fluorescent sensor for Ag^{I} with high selectivity and sensitivity. J Am Chem Soc 125:2884
33. Yao Z, Feng X, Li C, Shi G (2009) Conjugated polyelectrolyte as a colorimetric and fluorescent probe for the detection of glutathione. Chem Commun 5886
34. Mu H, Gong R, Ma Q, Sun Y, Fu E (2007) A novel colorimetric and fluorescent chemosensor: synthesis and selective detection for Cu^{2+} and Hg^{2+}. Tetrahedron Lett 48:5525
35. Hong SY, Czarnik AW (1993) A metal ion-insensitive polyanion chemosensor. J Am Chem Soc 115:3330
36. Namkung W, Padmawar P, Mills AD, Verkman AS (2008) Cell-based fluorescence screen for K^+ channels and transporters using an extracellular triazacryptand-based K^+ sensor. J Am Chem Soc 130:7794
37. Zhao J, Davidson MG, Mahon MF, Kociok-Köhn G, James TD (2004) An enantioselective fluorescent sensor for sugar acids. J Am Chem Soc 126:16179
38. Merrell MA, Wakchoure S, Ilvesaro JM, Zinn K, Gehrs B, Lehenkari PP, Harris KW, Selander KS (2007) Differential effects

of Ca^{2+} on bisphosphonate-induced growth inhibition in breast cancer and mesothelioma cells. Eur J Pharm 559:21
39. Segawa H, Kimura S, Kuroda J, Sato K, Nogawa M, Yuasa T, Yokota A, Hodohara K, Fujiyama Y, Maekawa T (2005) The anti-leukemic efficacy of the third generation bisphosphonate ONO5920/YM529. Leukemia Res 29:451
40. Cramer JA, Lynch NO, Gaudin AF, Walker M, Cowell W (2006) The effect of dosing frequency on compliance and persistence with bisphosphonate therapy in postmenopausal women: a comparison of studies in the united states, the united kingdom, and france. Clin Ther 28:1686
41. Sillero MAG, de Diego A, Silles E, Pérez-Zúñiga F, Sillero A (2006) Synthesis of bisphosphonate derivatives of ATP by T4 RNA ligase. FEBS Lett 580:5723
42. Takahashi R, Shimazaki C, Inaba T, Okano A, Hatsuse M, Okamoto A, Hirai H, Ashihara E, Nakagawa M (2001) A newly developed bisphosphonate, YM529, is a potent apoptosis inducer of human myeloma cells. Leukemia Res 25:77
43. Kamila S, Callan JF, Mulrooney RC, Middleton M (2007) A novel fluorescent chemosensor for Cu(II) in aqueous solution based on a β-aminobisphosphonate receptor. Tetrahedron Lett 48:7756
44. Matczak-Jon E, Kurzak B, Sawka-Doborwolska W, Lejczak B, Kafarski P (1998) Zinc(II) complexes of phosphonic acid analogues of aspartic acid and asparagine. J Chem Soc Dalton Trans 161
45. Gumienna-Kontecka E, Jezierska J, Lecouvey M, Leroux Y, Kozlowski HJ (2002) Bisphosphonate chelating agents: Coordination ability of 1-phenyl-1-hydroxymethylene bisphosphonate towards Cu^{2+} ions. J Inorg Biochem 89:13
46. Gumienna-Kontecka E, Galezowska J, Drag M, Latajka R, Kafarski P, Kozlowski H (2004) Coordination abilities of substituted β-aminophosphonates towards Cu^{2+} and Zn^{2+} ions. Inorg Chim Acta 357:1632
47. Jung HJ, Singh N, Jang DO (2008) Highly Fe^{3+} selective ratiometric fluorescent probe based on imine-linked benzimidazole. Tetrahedron Lett 49:2960
48. Havlis J, Madden JE, Revilla AL, Havel J (2001) High-performance liquid chromatographic determination of deoxycytidine monophosphate and methyldeoxycytidine monophosphate for DNA demethylation monitoring: experimental design and artificial neural networks optimization. J Chromatogr B 755:185
49. Schneider HJ, Yatsimirsky A (2000) Principles and methods in supramolecular chemistry. Wiley, Chichester, p 151
50. Mei X, Wolf C (2004) Enantioselective sensing of chiral carboxylic acids. J Am Chem Soc 126:14736

เอกสารแนบ 5.1.12

Inorganic Chemistry Communications 14 (2011) 351–354

Contents lists available at ScienceDirect

Inorganic Chemistry Communications

journal homepage: www.elsevier.com/locate/inoche

Highly selective fluorescent chemosensor for Fe^{3+} imaging in living cells

Srung Smanmoo [a,*], Weerachai Nasomphan [b], Pramuan Tangboriboonrat [b]

[a] Bioresources Research Unit, National Center for Genetic Engineering and Biotechnology (BIOTEC), 113 Thailand Science Park, Phaholyothin Road, Klong Luang, Pathumthani 12120, Thailand

[b] Department of Chemistry, Faculty of Science, Mahidol University, Rama 6 Road, Phyathai, Bangkok 10400, Thailand

ARTICLE INFO

Article history:
Received 24 August 2010
Accepted 18 November 2010
Available online 25 November 2010

Keywords:
Fluorescent chemosensor
Fe^{3+} sensor
Dansyl cadaverine
Fluorescence quenching
Bioimaging

ABSTRACT

2-Hydroxybenzyl dansyl cadaverine (DNSCH) was designed as a fluorescent chemosensor for Fe^{3+}. DNSCH exhibited significant FL quenching with increasing concentrations of Fe^{3+}. The presence of 15 M equiv of Fe^{3+} significantly quenched the FL intensity of DNSCH. The binding constant of DNSCH towards Fe^{3+} was determined and found to be $1.5 \pm 0.4 \times 10^{-4}$ M^{-1}. DNSCH was employed as an intracellular chemosensor for Fe^{3+}.

© 2010 Elsevier B.V. All rights reserved.

Molecular recognition of metal ions is one of active areas in supramolecular chemistry. Based on de Silva et al., the design of fluorescent (FL) chemosensor is simply achieved by the incorporation of metal-binding receptor and fluorophore via the spacer [1]. FL chemosensor receives much research attention in the field of bioanalytical science due to its high selectivity, real-time detection and simplicity [2–6]. The recognition of metals at the receptor is achieved through various modes of interactions, e.g., hydrogen bonding, van der Waals and electrostatic forces [7–9]. The binding of metal ions at the receptor initiates the communicating event with the fluorophore in which the signal obtained can be expressed as an energy transfer. Particularly, in the FL quenching type chemosensor, the quenching process involves the formation of an exciplex with charge transfer or photo-induced electron transfer.

The design of FL chemosensors exhibiting selective recognizing of Fe^{3+} receives much research attention due to Fe^{3+} is the most abundant ion in intracellular compartments. Recently, several FL chemosensors have been designed for the recognition of Fe^{3+}. Jang et al. designed a benzimidazole-based FL sensor in which the imidazole moiety presents in the sensor serves as the binding part for Fe^{3+} [10]. The sensor exhibits good binding constant with Fe^{3+}. Zheng and Huang reported an on/off chemosensor for Fe^{3+} controlled by protonation–deprotonation processes [11]. The sensor is designed based on calix[4]arene with two 3-alkoxy-2-naphthoic acids pending on the upper rim. The binding of Fe^{3+} is controlled by the deprotonation of phenolic moieties of calix[4]arene and dicarboxylic group of napthoic acid. On the contrary, the unbound state of calix[4]arene towards Fe^{3+} is driven by the protonation of calix[4]arene's phenol. Noh and his co-workers have designed an excellent chemosensor for Fe^{3+}. The sensor is based on a ferrocenyl chalcone structure which is capable in discriminating Fe^{3+} and Fe^{2+} via the selective oxidation [12]. Up to date, Fe^{3+} chemosensors for cell applications are scarcely reported and challenging for the design.

We have designed a new FL chemosensor, DNSCH, based on dansyl cadaverine. DNSCH adopts the fluorophore–spacer–receptor format. The dansyl fluorophore was attached via a pentylene spacer to the 2-hydroxybenzaldehyde receptor. DNSCH was evaluated against various metal ions and found to exhibit selective FL quenching in the presence of Fe^{3+}. DNSCH was employed as an intracellular chemosensor for Fe^{3+}.

Dansyl derivatives were extensively used as chromophores to construct a chemosensor platform [13–15]. The incorporation of 2-hydroxybenzaldehyde is expected to serve as the metal ion binding moiety and to affect the intramolecular charge transfer which induces the emission change of the sensor. 2-Hydroxybenzyl dansyl cadaverine (DNSCH) was synthesized in one step from the condensation reaction between dansyl cadaverine and 2-hydroxybenzaldehydes (Scheme 1). After reaction mixture was left stirring under nitrogen atmosphere for 24 h, DNSCH was isolated and crystallized from ethyl acetate/hexane to afford DNSCH in 81% (the spectroscopic identification for DNSCH is accomplished and can be found in Supplementary Material). The $C=N$ group formed is aimed to provide the chelation to metal ions since it is known that $C=N$ exhibits good degree of affinity towards transition and post-transition metal cations due to its electronic structure [16,17].

The selectivity of DNSCH towards metal ions was investigated (Fig. 1). Of all metal ions, DNSCH exhibited a significant degree of FL quenching in the presence of Fe^{3+}. In the presence of 15 M equiv of

* Corresponding author. Tel.: +66 2 564 6700x3560; fax: +66 2 564 6632.
E-mail address: srung.sma@biotec.or.th (S. Smanmoo).

1387-7003/$ – see front matter © 2010 Elsevier B.V. All rights reserved.
doi:10.1016/j.inoche.2010.11.025



Scheme 1. Synthesis of DNSCH.

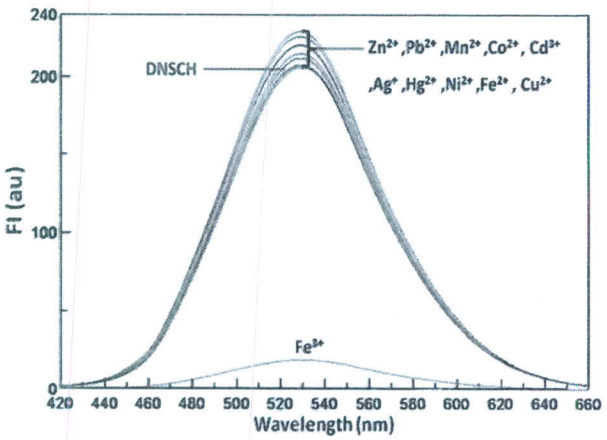


Fig. 1. Emission spectra of DNSCH (2.5×10^{-6} M) upon the addition of different metal ions (3.75×10^{-5} M) in CH_3CN-H_2O (50:50, v/v); $\lambda_{ex}=342$ nm.

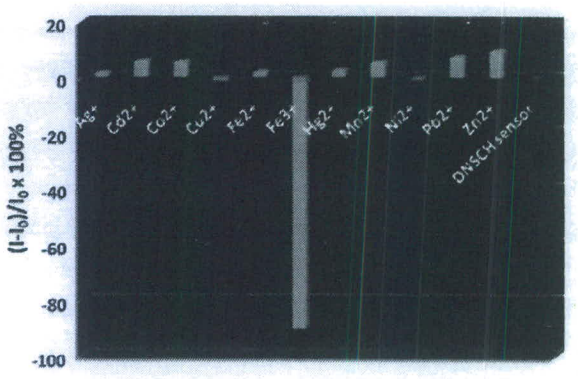


Fig. 3. FL ratio (I_0-I/I_0) of DNSCH (2.5×10^{-6} M) upon the addition of 15 M equiv (3.75×10^{-5} M) of metal guests in CH_3CN-H_2O (50:50, v/v); $\lambda_{ex}=342$ nm.

Fe^{3+}, the FL intensity of DNSCH was significantly quenched. The design of Fe^{3+} chemosensor with good discrimination between the iron valence states (Fe^{2+} and Fe^{3+}) is necessary for better understanding of various biological processes and Fenton reaction [18]. It was clearly shown that DNSCH is a selective Fe^{3+} chemosensor with the good discrimination for iron valence states. The presence of the 2-hydroxyl group in DNSCH is thought to facilitate the binding of Fe^{3+} near to the dansyl fluorophore prior to initiate the quenching process.

Fig. 2 represented the color and FL images of DNSCH in the presence of various metal ions. In the absence of metal ions, DNSCH exhibited strong yellow ($\lambda_{em}=525$ nm) FL when excited at 342 nm. The emission of DNSCH at 525 nm is the characteristic emission of dansyl fluorophore ($\lambda_{em}=520$ nm) [19]. In the addition of other metal ions except Fe^{3+}, DNSCH exhibited no color and FL changes. However, the addition of Fe^{3+} induced a slight change in color from clear to pale yellow [Fig. 2(a)], associated with the strong FL quenching [Fig. 2(b)].

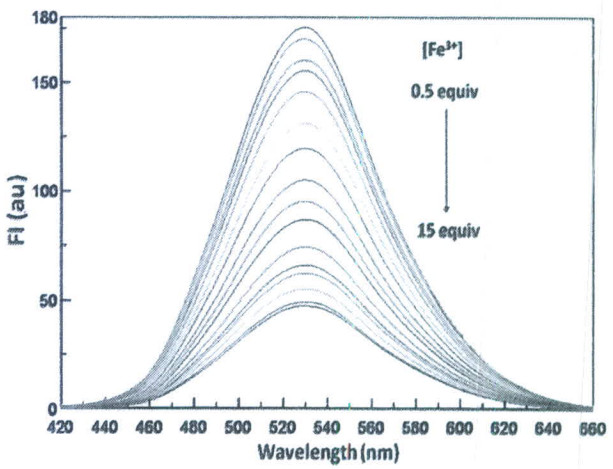


Fig. 4. FL spectra of DNSCH (2.5×10^{-6} M) titrated with (a) 0.5–15 M equiv of Fe^{3+}, in CH_3CN-H_2O (50:50, v/v); $\lambda_{ex}=342$ nm.

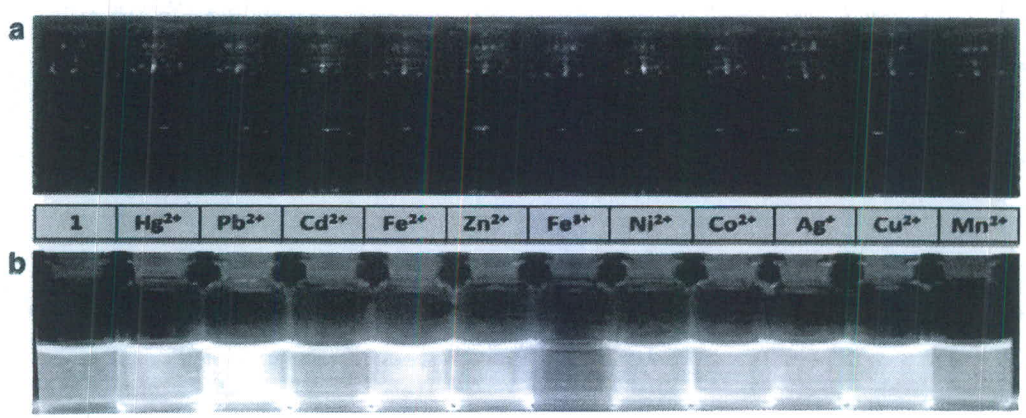


Fig. 2. (a) Images and (b) FL images of DNSCH (2.5×10^{-6} M) in the presence of various metal ions (3.75×10^{-5} M) in CH_3CN-H_2O (50:50, v/v); $\lambda_{ex}=342$ nm.

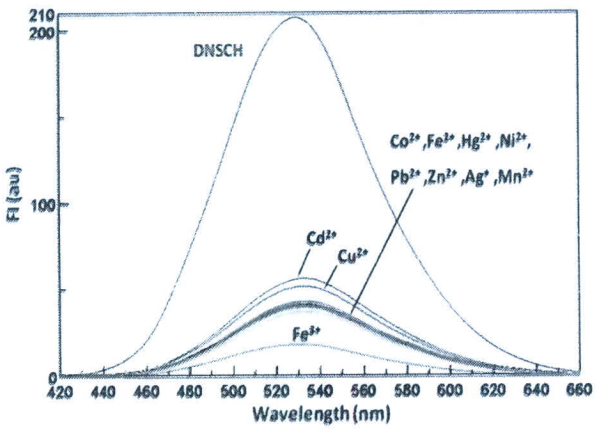


Fig. 5. FL responses of DNSCH (2.5×10^{-6} M) containing Fe^{3+} (15 M equiv) and other co-existing metal ions (15 M equiv) in CH_3CN-H_2O (50:50, v/v); $\lambda_{ex}=342$ nm.

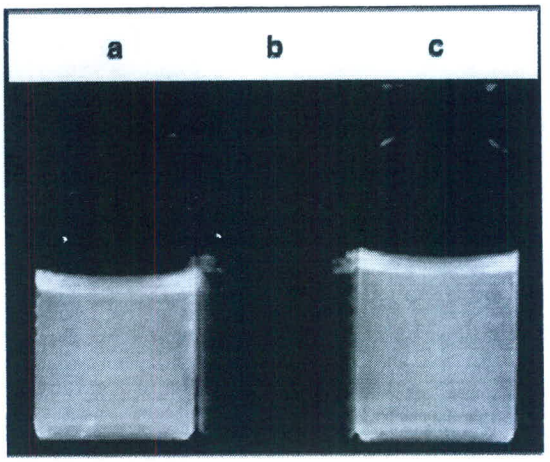


Fig. 7. FL images of (a) DNSCH (2.5×10^{-6} M). (b) DNSCH (2.5×10^{-6} M) in the presence of 15 M equiv of Fe^{3+} (3.75×10^{-5} M). (c) DNSCH (2.5×10^{-6} M) in the presence of 15 M equiv Fe^{3+} with the addition of excess EDTA.

In order to determine the degree of FL quenching of DNSCH by Fe^{3+}, the FL ratio was employed for this investigation. It was clearly shown in Fig. 3 that the degree of FL quenching for DNSCH was mostly pronounced in the presence of Fe^{3+}. There were also slight changes in FL of DNSCH in the presence of Cd^{2+}, Co^{2+}, Mn^{2+}, Pb^{2+} and Zn^{2+} ions. Comparing to other metal ions, DNSCH is highly selective in its response to Fe^{3+}.

To determine the selectivity range of DNSCH towards Fe^{3+}, the titration experiment was conducted. The FL quenching of DNSCH was investigated in the presence of various concentrations of Fe^{3+}. Fig. 4 shows that with increasing concentrations of Fe^{3+}, the FL emission intensity of DNSCH at λ_{max} 525 nm was gradually decreased. The FL

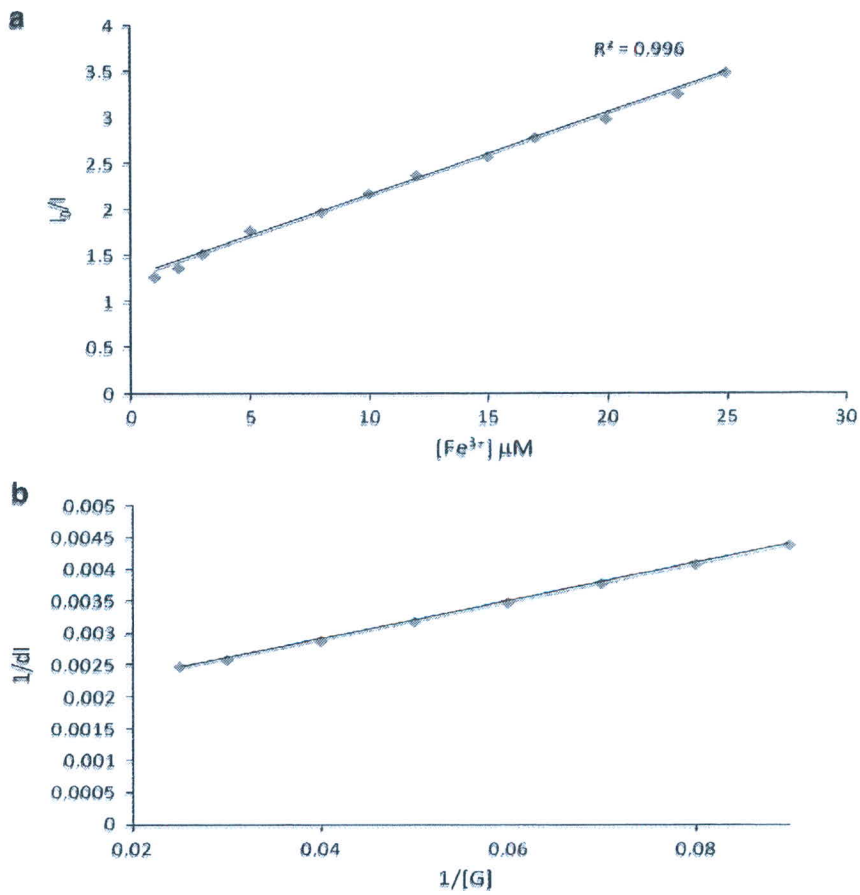


Fig. 6. (a) Stern–Volmer plot for DNSCH in the presence of various Fe^{3+} concentrations indicating 1:1 stoichiometry. (b) Benesi–Hilderbrand to determine the binding constant between DNSCH and Fe^{3+}.

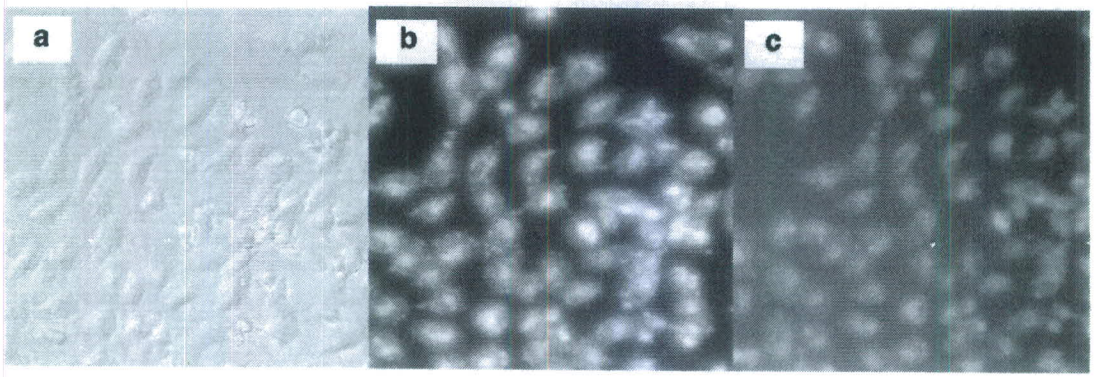


Fig. 8. Living-cell imaging of intracellular Fe^{3+} by FL microscopy: (a) Bright field transmission image of Vero cells incubated with 50 μM of DNSCH. (b) FL image of Vero cells supplemented with 50 μM of DNSCH in the growth media for 15 min at 25 °C. (c) Vero cells incubated with 50 μM of DNSCH in the growth media for 15 min at 25 °C, washed three times, and then further incubated with 100 μM $FeCl_3$ for 5 min at 25 °C.

quenching of DNSCH was mostly pronounced after the addition of Fe^{3+} at 15 M equiv (3.75×10^{-5} M). The addition of Fe^{3+} at 15 M equiv significantly quenched the FL of DNSCH.

FL responses of DNSCH towards Fe^{3+} were investigated in the presence of co-existing metal ions, e.g., Co^{2+}, Fe^{2+}, Hg^{2+}, Ni^{2+}, Pb^{2+}, Zn^{2+}, Ag^{+}, Mn^{2+}, Cd^{2+} and Cu^{2+}. It was shown in Fig. 5 that the presence of other metals did not interfere the FL quenching of DNSCH by Fe^{3+} and the FL changes caused by the addition of Fe^{3+} were not affected by the co-existing metal ions.

In order to determine the binding ratio between DNSCH and Fe^{3+}, the Stern–Volmer plot was used and found the good fit in the concentration range between 1 and 25 μM which indicated the binding ratio between DNSCH and Fe^{3+} at 1:1 stoichiometry [Fig. 6(a)]. On the basis of this binding ratio, the binding constant for DNSCH and Fe^{3+} was then calculated using the Benesi–Hilderbrand equation and found to be $1.5\pm0.4\times10^{-4}$ M^{-1} [Fig. 6(b)] [20]. The reversible binding mode of DNSCH towards Fe^{3+} was investigated. It was clear that DNSCH was a reversible FL chemosensor (Fig. 7). In the presence of 15 M equiv Fe^{3+} (3.75×10^{-5} M), DNSCH (2.5×10^{-6} M) exhibited strong FL quenching. However, the FL of DNSCH was recovered after the addition of excess EDTA. This demonstrated the potential application of DNSCH as a reversible FL chemosensor.

The mechanism for FL quenching of DNSCH by Fe^{3+} is proposed from ligand metal charge transfer (LMCT) in which the transition of the charge transfer is initiated by the binding of Fe^{3+} to the ligand (DNSCH). The chelation between DNSCH and Fe^{3+} is facilitated by the extra coordination from i) $C=N$ group which is known for the strong binding affinity to transition and post-transition metals [16,17] and ii) the 2-hydroxyl group. These functional groups are in the positions where Fe^{3+} is held close enough to the dansyl fluorophore. The electronic charge of DNSCH transfers to Fe^{3+} (d-orbital) results in the distribution of charge at the excited state. This finally causes the FL quenching of DNSCH.

For the practical application of DNSCH, it was employed as a selective intracellular chemosensor for Fe^{3+} (Fig. 8). DNSCH's ability was assessed as an intracellular FL chemosensor for Fe^{3+} by FL microscopy. As seen from the bright field image, Vero cells incubated with 50 μM of DNSCH for 15 min at 25 °C show cell viability [Fig. 8(a)] with strong intracellular background FL [Fig. 8 (b)]. After, Vero cells which pre-incubated with DNSCH were supplemented with 100 μM of Fe^{3+} in the growth medium for 5 min at 25 °C, and intracellular background FL was significantly reduced in its FL intensity [Fig. 8(c)]. Apart from its high selectivity of DNSCH towards Fe^{3+} in CH_3CN-H_2O, DNSCH was as an intracellular chemosensor for Fe^{3+}. According to this fact, DNSCH was a membrane-permeable FL chemosensor exhibiting selective FL quenching towards Fe^{3+}.

In summary, a novel FL chemosensor based on dansyl cadaverine, DNSCH, was synthesized and evaluated for its sensing ability towards metal ions. DNSCH exhibited high selectivity towards Fe^{3+} among other screened metal ions with good discrimination between different iron oxidation state (Fe^{2+} and Fe^{3+}). The 2-hydroxyl group in DNSCH facilitates the binding of Fe^{3+} prior to LMCT mechanism, which was initiated to induce the FL quenching. DNSCH exhibited a selective recognizing mode with high selectivity towards Fe^{3+}. DNSCH shows no interference from other metal ions. DNSCH was evaluated as a cell-permeable chemosensor for intracellular detection of Fe^{3+}.

Acknowledgments

The Thailand Research Fund/Commission on Higher Education's research grant to S.S. (DIG5180025) and P.T. (RTA5180003) and the Development and Promotion of Science and Technology Talents Project's scholarship to W.N. are gratefully acknowledged. We are also grateful to the partial support from National Center for Genetic Engineering and Biotechnology (BIOTEC).

Appendix A. Supplementary Material

Supplementary data to this article can be found online at doi:10.1016/j.inoche.2010.11.025.

References

[1] A.P. de Silva, H.Q.N. Gunaratne, T. Gunnlaugsson, A.J.M. Huxley, C.P. McCoy, J.T. Rademacher, T.E. Rice, Chem. Rev. 97 (1997) 1515–1566.
[2] F.-Y. Wu, S.W. Bae, J.-I. Hong, Tetrahedron Lett. 47 (2006) 8851–8854.
[3] F.-Y. Wu, Y.-Q. Zhao, Z.-J. Ji, Y.-M. Wu, J. Fluoresc. 17 (2007) 460–465.
[4] L.J. Ma, Y.-F. Liu, Y. Wu, Chem. Commun. (2006) 2702–2704.
[5] L. Ma, H. Li, Y. Wu, Sens. Actuators B Chem. 143 (2009) 25–29.
[6] H. Li, J. Xu, H. Yan, Sens. Actuators B Chem. 139 (2009) 483–487.
[7] M.H. Keefe, K.H. Benkstein, J.T. Hupp, Coord. Chem. Rev. 205 (2000) 201–228.
[8] F. Wang, Y. Xu, B.X. Ye, M.P. Song, Y.J. Wu, Inorg. Chem. Commun. 9 (2006) 797–801.
[9] L.A. Baumes, M.B. Sogo, P. Montes-Navajas, A. Corma, H. Garcia, Tetrahedron Lett. 50 (2009) 7001–7004.
[10] D.Y. Lee, N. Singh, D.O. Jang, Tetrahedron Lett. 51 (2010) 1103–1106.
[11] J.-M. Liu, Q.-Y. Zheng, J.-L. Yang, C.-F. Chen, Z.-T. Huang, Tetrahedron Lett. 43 (2002) 9209–9212.
[12] S.-K. Lee, Y.-S. Noh, K.-I. Son, D.-Y. Noh, Inorg. Chem. Commun. 13 (2010) 1343–1346.
[13] C.R. Lohani, K.-H. Lee, Sens. Actuators B Chem. 143 (2010) 649–654.
[14] Q.-Y. Chen, C.-F. Chen, Tetrahedron Lett. 46 (2005) 165–168.
[15] A. Azam, H.M. Chawla, S. Pandey, Tetrahedron Lett. 51 (2010) 4710–4711.
[16] V.K. Bhardwaj, A.P.S. Pannu, N. Singh, M.S. Hundal, G. Hundal, Tetrahedron 64 (2008) 5384–5391.
[17] S.I. Pascu, G. Balazs, J.C. Green, M.L.H. Green, I.C. Vei, J.E. Warren, C. Windsor, Inorg. Chim. Acta 363 (2010) 1157–1172.
[18] P. Wu, Y. Li, X.P. Yan, Anal. Chem. 81 (2009) 6252–6257.
[19] H. Sulowska, W. Wiczk, J. Modzianowski, M. Przyborowska, T. Ossowski, J. Photochem. Photobiol. 150 (2002) 249–255.
[20] H.A. Benesi, J.H. Hilderbrand, J. Am. Chem. Soc. 71 (1949) 2703–2707.

เอกสารแนบ 5.1.13

doi:10.1246/cl.2011.188
Published on the web January 22, 2011

Isothiocyanatoluminol as a Chemiluminescence Labeling Reagent for Amino Acids and Proteins

Srung Smanmoo,*[1] Weerachai Nasomphan,[2] and Pramuan Tangboriboonrat[2]
[1]*Bioresources Research Unit, National Center for Genetic Engineering and Biotechnology (BIOTEC), Thailand Science Park, Klong Luang, Pathumthani 12120, Thailand*
[2]*Department of Chemistry, Faculty of Science, Mahidol University, Rama 6 Road, Phyathai, Bangkok 10400, Thailand*

(Received July 22, 2010; CL-100650; E-mail: srung.sma@biotec.or.th)

Isothiocyanatoluminol (ITL) was successfully synthesized from the reaction between luminol and thiophosgene in the presence of triethylamine. The optimized conditions were extended for the preparation of isothiocyanatoisoluminol (ITIL) and phenyl isothiocyanate (PI). The chemiluminescence (CL) of ITL was comparable to luminol. ITL was used as a CL labeling reagent for amino acid and bovine serum albumin (BSA) in which the $-NH_2$ terminus of amino acid residue present in BSA acts as the labeling site.

Due to the minute amount of analytes present in biological fluids, sensitive and selective detection is highly desired.[1,2] In the past decade, there have been a number of analytical techniques available for sensitive detection, e.g., mass spectrometry, liquid chromatography, capillary electrophoresis, immune reaction, fluorescence, and chemiluminescence (CL). In particular, CL has gained research attention due to the fact that it provides the detection of biological samples with good sensitivity and selectivity.[3–5]

CL is the process in which the chemical reaction of CL compound raises its energy to the excited state and, upon returning to the ground state, releases energy in the form of light. Luminol (L) and isoluminol (IL) are well-known CL reagents in which the mechanism for CL emission is extensively studied.[6–8] CL compounds have been widely used in chromatographic techniques as a labeling reagent. In general, a CL labeling reagent consists of two reactive functionalities; i) chemiluminophore and ii) reactive functional group which serves as the attaching (labeling) site for the analyte. In order to offer (iso)luminol as CL labeling reagents, the chemical modification of their structures is required. However, chemical modifications of (iso)luminol structures generally lead to the loss of their CL capability.[9] Isothiocyanatoisoluminol (ITIL) has already been synthesized and is commercially available with a comparable degree of CL emission to isoluminol.[10] Due to the high quantum efficiency of luminol, isothiocyanatoluminol (ITL) is highly desired (Figure 1).

ITL was successfully synthesized from the reaction between luminol and thiophosgene in the presence of triethylamine. Synthetic conditions for ITL were also employed for the preparation of ITIL and phenyl isothiocyanate (PI). The kinetic profiles for CL emission of ITL and luminol were evaluated and found to be comparable (Figure 2). ITL was used as a CL labeling reagent for amino acids and proteins.

Initially, ITL was synthesized from the reaction between luminol and thiocarbonyldiimidazole (TCI) in the presence of triethylamine as base (Table 1). Various organic solvents and reaction times were investigated. Unfortunately, the starting

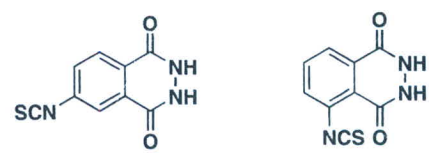


Figure 1. Chemical structures of isothiocyanatoisoluminol (ITIL) and isothiocyanatoluminol (ITL).

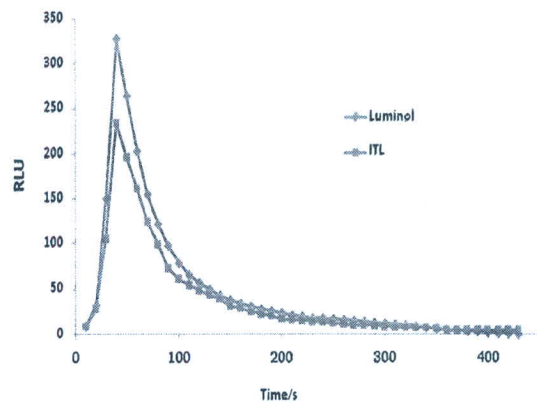
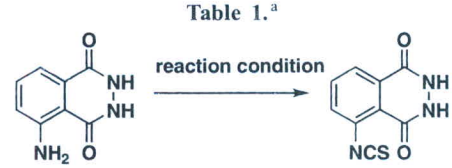


Figure 2. Time-course for CL emission of ITL and luminol.

Table 1.[a]



Entry	Reagent	Solvent	Time /h	Yield /%[b]
1	TCI	THF	6	0
2	TCI	DMF	6	5
3	TCI	DMF	12	5
4	TCI	DMF	24	5
5	Thiophosgene	DMF	6	30
6	Thiophosgene	DMF	12	45
7	Thiophosgene	DMF	24	55

[a]Reactions were performed with 1 equiv luminol, 1 equiv Et_3N, and 1 equiv TCI or thiophosgene in corresponding solvents under nitrogen atmosphere at room temperature. [b]Based on isolated product.

© 2011 The Chemical Society of Japan

material, luminol, was mainly recovered. This could be due to the low reactivity of TCI where imidazole is not a very good leaving group ($pK_a \approx 6.99$) compared to the halide substituent.[11,12] *N*,*N*-Dimethylformamide (DMF) was found to be the optimized solvent offering a high solubility of luminol. To improve the reactivity of reagent, highly reactive thiophosgene was used instead of TCI. After the reaction proceeded for 24 h, a yellow product was obtained in moderate yield (Table 1). Its molecular mass was identified by high-resolution mass spectrometry and found to correspond to the molecular weight of ITL [m/z 220 ($M + H^+$)].

It is known that chemical manipulation of (iso)luminol structures deteriorates their CL efficiency.[9] Therefore, CL emission of ITL was checked against the starting material. The CL emission obtained from ITL was comparable to luminol indicating that the introduction of isothiocyanate group into luminol did not compromise CL efficiency.

In order to ensure that these synthetic conditions could be used for the introduction of isothiocyanate group into other amine compounds, the synthetic method was employed for the preparation of ITIL and phenyl isothiocyanate. After completion, ITIL and phenyl isothiocyanate were obtained in moderate 62 and 44% yields, respectively. This demonstrated the efficiency of the protocol for the installation of isothiocyanate groups into primary amines.

In order to employ ITL as a labeling reagent for various proteins in the supersensitive CL assay, it is necessary to ensure that ITL could be used as a labeling reagent for amino acids. Since all proteins possess various amino acids which are abundant with $-NH_2$ terminus on their surfaces, the $-NH_2$ terminus is expected to serve as a labeling site for ITL. To test this hypothesis, 10 representative amino acids were used for CL labeling with ITL. The labeling of amino acids with ITL was simply achieved via the incubation of the mixture between a corresponding amino acid and ITL at 60 °C for 2 h before analyzing the product by mass spectrometry. It was found that all amino acids were successfully labeled with ITL (Table 2). The labeling mechanism is achieved via the nucleophillic addition of the $-NH_2$ group of the amino acid to the isothiocyanate group of ITL.

Since ITL could be successfully employed as a CL labeling reagent for amino acids, we targeted the ITL-labeled protein. Bovine serum albumin (BSA) was chosen as a model protein since it is widely used in various immunoassays due to its low cost and stability.[13,14] The labeling conditions (solvent) were then optimized. A mixture of DMSO and water in a ratio of 1:9 (v/v) was chosen as the solvent since both BSA and ITL were well dissolved. The optimum temperature and incubation time were found to be 60 °C for 24 h. To confirm the presence of ITL-labeled BSA, Gel-filtration liquid chromatography (GFLC) was employed for identification. After incubating BSA and ITL for 1 h, the labeled product was analyzed by GFLC. Results showed the presence of a new peak at the retention time of 15 min which was later identified as ITL-labeled BSA (Figure 3). The intensity of this peak increased with the progression of reaction time. To further confirm the identity of ITL-labeled BSA, it was spotted on a poly(vinylidene fluoride) (PVDF) membrane prior to CL detection employing a reported protocol.[15]

Kai et al. synthesized luminol-labeled dextran probe (Dex-Lu) for the CL detection of CYP3A4 protein on a solid-phase membrane. The dextran probe is highly sensitive and able to detect CYP3A4 protein at the femtomole level.[15] The signal amplication of the dextran probe originated from the multiple incorporation of luminols onto a macromolecular dextran template. In order to compare the CL efficiency of ITL-labeled BSA, Dex-Lu which was prepared according to Kai's procedure was used as a reference. The molar concentration of Dex-Lu (0.15 μM) was estimated to be the same as ITL-labeled BSA. It was found that the CL intensity of ITL-labeled BSA increased as a function of reaction time. After the reaction was left for 24 h, the CL emission of ITL-labeled BSA on a solid-phase membrane was at its highest and comparable to that of Dex-Lu (Figure 4). Comparing to the *Mr* of dextran (7×10^5) and BSA (6.6×10^4), the result from a solid-phase CL detection demonstrated a good efficiency of ITL incorporated into the smaller BSA template. The obtained CL results on a solid-phase membrane were in accordance to GFLC data. From preliminary results, ITL was successfully synthesized and employed as an effective CL labeling reagent for amino acids and proteins.

In conclusion, ITL was synthesized under optimized conditions. The introduction of an isothiocyanate group maintained its CL efficiency. The conditions were further employed for the preparation of other isothiocyanate-containing compounds, e.g., ITIL and phenyl isothiocyanate. ITL was success-

Table 2.[16]

Entry	ITL labeled amino acid	Expected *Mr*	Found (m/z)
1	Ala–ITL	308.06	309.08
2	Arg–ITL	393.12	394.13
3	Asn–ITL	337.05	360.14
4	Cys–ITL	340.03	341.08
5	Glu–ITL	366.06	367.07
6	Leu–ITL	350.10	351.11
7	Lys–ITL	365.12	366.12
8	Met–ITL	368.02	369.07
9	Phe–ITL	384.09	385.10
10	Pro–ITL	334.07	335.08

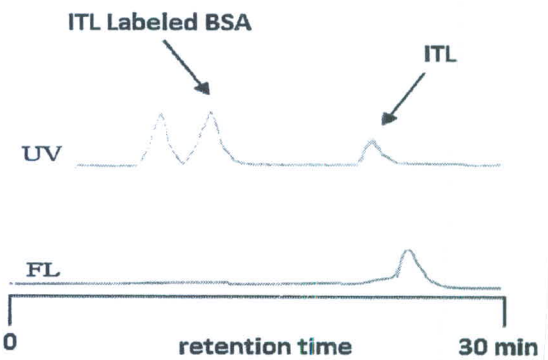


Figure 3. GFLC of ITL-labeled BSA. Conditions: injection volume, 5 μL; column, TSK gel T2000SW; eluent, 0.1% (v/v) aqueous solution of trifluoroacetic acid; flow rate, 1.0 mL min^{-1}; UV detection, lamp: 275 nm; fluorescence detection, excitation (mercury lamp)/emission (wavelength cutoff filter): 254/ >360 nm.

 © 2011 The Chemical Society of Japan

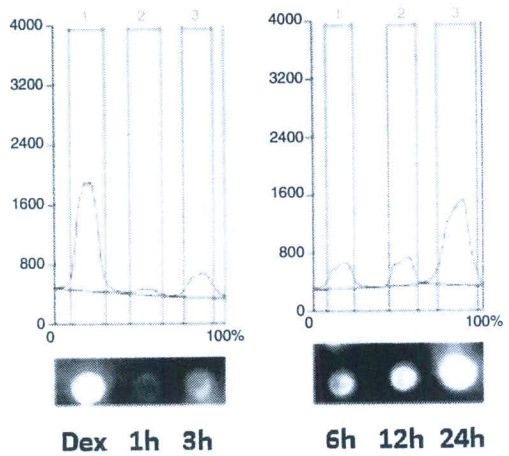


Figure 4. CL images of ITL-labeled BSA on a PVDF membrane.

fully evaluated as a CL labeling reagent for amino acids and proteins.

The Thailand Research Fund/Commission on Higher Education's research grant to S.S. and P.T., the Development and Promotion of Science and Technology Talents Project's scholarship to W.N. are gratefully acknowledged. We are also grateful to the partial support from National Center for Genetic Engineering and Biotechnology (BIOTEC).

References and Notes

1 a) A. Townshend, *Analyst* **1990**, *115*, 495. b) W. R. G. Baeyens, K. Nakashima, K. Imai, B. Ling, Y. Tsukamoto, *J. Pharm. Biomed. Anal.* **1989**, *7*, 407.
2 a) S. W. Lewis, D. Price, P. J. Worsfold, *J. Biolumin. Chemilumin.* **1993**, *8*, 183. b) K. Robards, P. J. Worsfold, *Anal. Chim. Acta* **1992**, *266*, 147.
3 a) A. C. Calokerinos, N. T. Deftereos, W. R. G. Baeyens, *J. Pharm. Biomed. Anal.* **1995**, *13*, 1063. b) M. J. Navas, A. M. Jiménez, *Food Chem.* **1996**, *55*, 7. c) K. Tsukagoshi, K. Sawanoi, M. Kamekawa, R. Nakajima, *Chem. Lett.* **2003**, *32*, 894.
4 A. R. Bowie, M. G. Sanders, P. J. Worsfold, *J. Biolumin. Chemilumin.* **1996**, *11*, 61.
5 a) A. M. García-Campaña, W. R. G. Baeyens, X. R. Zhang, E. Smet, G. Van Der Weken, K. Nakashima, A. C. Calokerinos, *Biomed. Chromatogr.* **2000**, *14*, 166. b) K. Tsukagoshi, K. Nakahama, R. Nakajima, *Chem. Lett.* **2003**, *32*, 634.
6 a) H. R. Schroeder, F. M. Yeager, *Anal. Chem.* **1978**, *50*, 1114. b) T. Fujiwara, N. Tanimoto, K. Nakahara, T. Kumamaru, *Chem. Lett.* **1991**, 1137.
7 D. F. Roswell, E. H. White, *Methods Enzymol.* **1978**, *57*, 409.
8 H. D. Albrecht, *Z. Phys. Chem.* **1928**, *136*, 321.
9 F. McCapra, I. Behesti, *Bioluminescence and Chemiluminescence: Instruments and Applications*, ed. by K. van Dyke, CRC Press, Boca Raton, FL, **1985**, Vol. 1.
10 M. Hashimoto, K. Tsukagoshi, R. Nakajima, K. Kondo, *J. Chromatogr., A* **1999**, *832*, 191.
11 S. Josse, J. L. Gal, M. Pipelier, J.-P. Pradère, R. Benhida, D. Dubreuil, *Tetrahedron Lett.* **2002**, *43*, 241.
12 *CRC Handbook of Chemistry and Physics*, CRC Press, Boca Raton, FL, **2004**.
13 A. M. Landel, *Anal. Biochem.* **1976**, *73*, 280.
14 M. Saito, L.-J. Yin, I. Kobayashi, M. Nakajima, *Food Hydrocolloids* **2006**, *20*, 1020.
15 H. Zhang, C. Smanmoo, T. Kabashima, J. Lu, M. Kai, *Angew. Chem., Int. Ed.* **2007**, *46*, 8226.
16 Supporting Information is available electronically on the CSJ-Journal Web site, http://www.csj.jp/journals/chem-lett/index.html.

 © 2011 The Chemical Society of Japan

เอกสารแนบ 5.1.14

Polylactic Acid/Ethylene Glycol Triblock Copolymers as Novel Crosslinkers for Epoxidized Natural Rubber

T.-H. Nguyen,[1] P. Tangboriboonrat,[2] N. Rattanasom,[3] A. Petchsuk,[4] M. Opaprakasit,[5] C. Thammawong,[1] P. Opaprakasit[1]

[1]*School of Bio-Chemical Engineering and Technology, Sirindhorn International Institute of Technology (SIIT), Thammasat University, Pathum Thani 12121, Thailand*
[2]*Department of Chemistry, Faculty of Science, Mahidol University, Phyathai, Bangkok 10400, Thailand*
[3]*Institute of Molecular Biosciences, Mahidol University, Salaya, Nakhon Pathom 73170, Thailand*
AQ2 [4]*National Metal and Materials Technology Center (MTEC), Pathum Thani 12120, Thailand*
[5]*Department of Materials Science, Faculty of Science, Center for Petroleum, Petrochemicals and Advanced Materials, Chulalongkorn University, Bangkok 10330, Thailand*

Received 24 September 2010; accepted 13 June 2011
DOI 10.1002/app.35088
Published online 00 Month 2011 in Wiley Online Library (wileyonlinelibrary.com).

ABSTRACT: Polylactic acid/ethylene glycol triblock copolymer ($LLA_{46}EG_{46}LLA_{46}$) was prepared and used in a crosslink process of epoxidized natural rubber (ENR) by employing a ring-opening reaction using $Sn(Oct)_2$ as a catalyst. The OH-capped copolymer acts as a macromolecular crosslinking agent in the formation of ENR networks, leading to drastic enhancement in tensile properties. Crosslink efficiency and chemical structures of the cured materials are examined by solvent fractionation, swelling experiments, XRD, ^{1}H-NMR, and ATR-FTIR spectroscopy. The efficiency of the curing process is dependent on the ENR/copolymer feed ratios. The degree of property improvement and gas permeability/selectivity behaviors of the cured materials are strongly dependent on the copolymer content and the efficiency of the curing process.
© 2011 Wiley Periodicals, Inc. J Appl Polym Sci 000: 000–000, 2011

Key words: rubber; crosslinking; gas permeation; biodegradable; block copolymers

INTRODUCTION

Natural rubber (NR) is known as a "green," sustainable, renewable, and biodegradable material.[1] However, NR latex film cannot be used without vulcanization because it is not very strong and lacks elasticity. Vulcanization is required to introduce chemical network junctures between rubber or polyisoprene chains to form crosslinked networks, which enhances their mechanical properties suitable for applications. Vulcanization is mainly classified as sulfur and nonsulfur processes. The crosslink junctures from sulfur vulcanization are derived from either single sulfur atoms or short-chain sulfur compounds with accelerators such as 2-benzothiazole disulfide.[2–4] In contrast, organic peroxides for example dicumyl peroxide[5–8] are commonly used in non-sulfur vulcanization. In addition, NR latex can be vulcanized by employing chemical-free processes, such as using electron beams,[9] γ rays,[10,11] UV radiation, and ultrasonic waves.[12]

Vulcanization by crosslinking of specially functionalized rubbers has attracted great interest in the research community. Epoxide groups are introduced and used as crosslink sites instead of allylic groups in sulfur vulcanization.[12–14] The double bonds of NR are well known to react with peracids to produce epoxide groups in the conversion of NR to epoxidized NR (ENR). This process leads to an enhancement in certain properties, such as higher hysteresis and oil resistance, and lower air permeability compared with its native NR counterpart.[13,15] Moreover, epoxide groups can readily react with many nucleophilic reagents for further modification of the material properties, such as amines,[14,16,17] phosphorus,[18] and carboxylic acids.[19] The interest of reacting hydroxyl groups with ENR has been initiated and reported by Derouet et al., where alcohols were grafted onto ENR backbone through ring-opening reaction of its epoxide.[20,21]

Polylactic acid (PLA) is a biodegradable/biocompatible polymer that is particularly attractive for use in various applications, especially in biomedical fields.[22] However, its low hydrophilicity limits its use in certain applications. Therefore, poly(ethylene

Correspondence to: P. Opaprakasit (pakorn@siit.tu.ac.th).
Contract grant sponsor: The Thailand Research Fund/Thailand Office of Higher Education Commission; contract grant number: RTA5180003.
Contract grant sponsors: National Research University Project of Thailand Office of Higher Education Commission, Thailand Toray Science Foundation, Siam Cement Foundation and SIIT, Thammasat University.

© 2011 Wiley Periodicals, Inc.

J_ID: Z8E Customer A_ID: APP35088 Date: 20-July-11 Stage: Page: 2

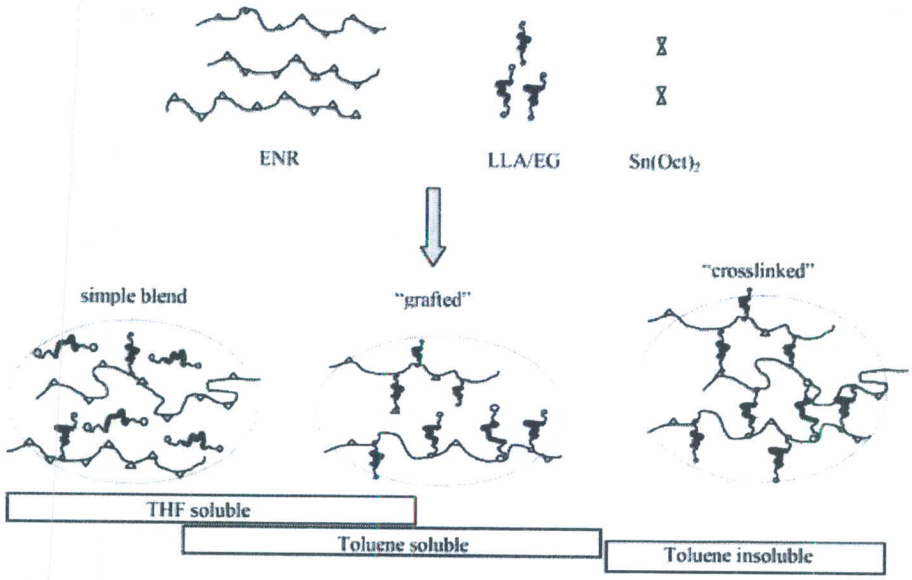


Figure 1 Proposed curing reaction of ENR by OH-capped LLA/EG/LLA block copolymers, and the possible structures of the "cured" products and their solvent solubility.

glycol) (PEG), a hydrophilic polymer with outstanding properties, i.e., nontoxicity and biocompatible characteristics, is introduced. Copolymerization of PLA and PEG at various compositions offers an opportunity to combine the advantages of these polymers to obtain biocompatible/degradable materials with tailored hydrophilicity.[23–25] Incorporation of NR with PLA has been conducted to improve its mechanical properties, especially the impact strength. It was reported that miscibility enhancement of ENR/PLA blend was achieved by a reactive mixing process at high temperature. The reaction of epoxides of ENR and ester groups of PLA was proposed as the origin of this enhancement.[26,27]

In our previous work,[28] OH-capped triblock copolymers of L-lactide (LLA) and ethylene glycol (EG) were synthesized by ring-opening polymerization of LLA using PEG as a macroinitiator. The LLA/EG/LLA copolymers with various block lengths and hence different properties were prepared by varying LLA/PEG molar ratios. In this study, the block copolymer is used as macromolecular crosslinker for ENR by utilizing the reaction of its two hydroxyl groups at the chain-ends with epoxides of ENR.[20,21] Properties of the resulting cured ENR products are then characterized. The materials are not only biocompatible and biodegradable, but also exhibit good mechanical properties comparable to conventionally cured rubber materials. Gas permeability behaviors of the cured ENR are also characterized for potential use in high-value and specific applications: membranes or medical applications such as breathable gloves or patches. Most importantly, the properties of these materials can be further modified by varying block lengths of the copolymer, epoxide content of ENR, and the copolymer/ENR feed ratios for specific applications.

EXPERIMENTAL

Materials

OH-capped $LLA_{46}EG_{46}LLA_{46}$ triblock copolymer was synthesized by the method reported in our previous work.[28] ENR with 20% epoxidation (ENR20) was synthesized from commercial high ammonia (HA)-preserved NR latex concentrate (Rayong Bangkok Rubber, Thailand) based on the methodology reported by Saendee et al.[29] $Sn(Oct)_2$ (Wako) and dried tetrahydrofuran (THF) was respectively, used as a catalyst and solvent.

Crosslinking of ENR by LLA/EG copolymer

The crosslink reaction was conducted by mixing ENR20 and the OH-capped $LLA_{46}EG_{46}LLA_{46}$ copolymer at three weight compositions (4/1, 2/1, 1/1) in dried THF (20% w/v) at 50°C. The samples are referred to as R41, R21, and R11, respectively. The mixture solution was first dried under vacuum for 1 h before purging with nitrogen gas. $Sn(Oct)_2$ catalyst (1 wt % of copolymer) was then added. The crosslink reaction was performed in a round-bottom flask equipped with magnetic stirrer at 70°C for 24 h.

The proposed chemical structures of the cured ENR products obtained from the reaction with the OH-capped copolymer are illustrated in Figure 1. When both OH end groups of the copolymer F1

ID: jaishankarn | Black Lining: [ON] | Time: 12:08 | Path: N:/3b2/APP#/Vol00000/111185/APPFile/JW-APP#111185

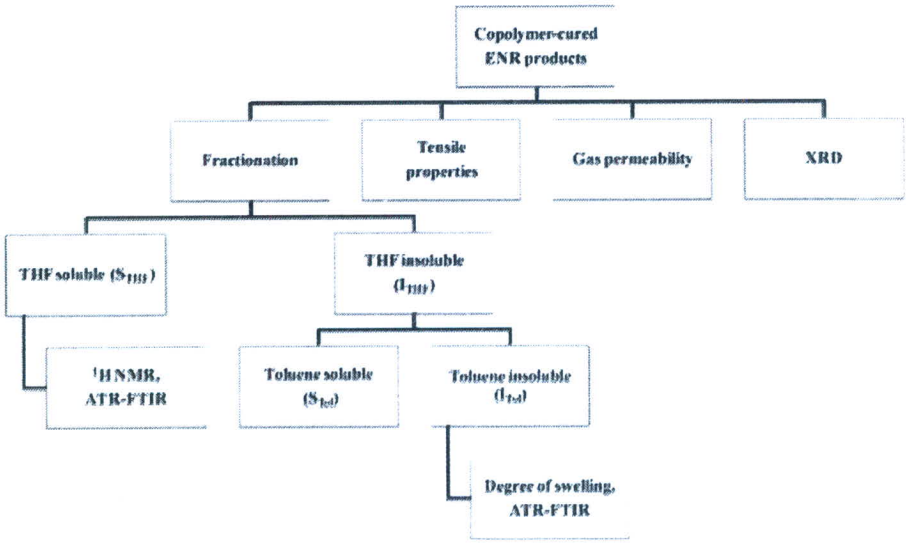


Figure 2 Overview of characterizations of the copolymer-cured ENR products.

undergo ring-opening reaction with epoxides of ENR, crosslink junctions are generated. In contrast, grafting of copolymer onto ENR backbone is achieved when only one hydroxyl per copolymer chain reacts. As ENR20 has 20% epoxide content, grafted ENR products with varied degree of grafting are generated. Additionally, unreacted copolymer chains may be present in the ENR matrix as a blended mixture, due to an excess amount of copolymer, when ENR20/copolymer ratios are varied. These possibilities will be referred to as "crosslinked," "grafted," and "free" or simple blend fractions. These fractions of products exhibit different solubility behaviors (discussed later), as summarized in Figure 1.

Characterizations

The cured ENR product, suspended in THF solvent after the crosslink reaction, was cast on a Teflon plate at room temperature. After completion of solvent evaporation, film samples (~ 0.1 mm thick) were obtained. The samples were then characterized as summarized in Figure 2. First, efficiency of the curing process in terms of weight fraction of "crosslinked," "grafted," and "free" copolymers in ENR matrix, was examined by sequential solvent fractionation, employing THF and toluene solvents. Given that ENR and the copolymer are completely dissolved in THF at 50°C, Soxhlet extraction by THF was first employed for 24 h to determine the weight content of remaining uncured ENR and "free" or unreacted copolymers in the soluble fraction (denoted by S_{THF}), which was recovered by complete evaporation of the solvent. The THF-insoluble fraction (I_{THF}) was then further extracted by toluene at room temperature for ssven days. The soluble and insoluble fractions (denoted by S_{Tol} and I_{Tol}), corresponding to "grafted" and fully "crosslinked" ENR domains, respectively, were recovered. The remaining weight of each fraction was then recorded and the weight percentage was calculated based on mass of the original sample. Chemical structures and chain compositions of each fraction were characterized by ^{1}H-NMR spectroscopy on a Bruker DRX400 using $CDCl_3$ as a solvent. ATR-FTIR spectra of each fraction were recorded on a ThermoNicolet 6700 model spectrometer. The spectra were recorded at 2 cm^{-1} resolution with 32 scans. ATR accessory equipped with ZnSe with a face angle of 45° was employed.

The crosslink density of the toluene insoluble (I_{Tol}) samples was examined by using the solvent swelling method. A piece of sample was accurately weighed and then immersed in toluene (40 mL) at room temperature in a dark cabinet. At equilibrium swelling time, where a constant solvent weight uptake was reached (about seven days), the test piece was removed, wiped with filter paper, and its weight was recorded. The swelling percentage was calculated, as follows:

$$\%\,\text{swelling} = \frac{W_{eq} - W_o}{W_o} \times 100 \qquad (1)$$

where W_o = original weight of dried sample (g)

W_{eq} = weight of swollen sample at equilibrium swelling time (g)

Tensile tests were carried out using dumbbell specimens cut from the cured rubber films (prepared from solution cast technique) with a thickness of ~ 0.1 mm by using the Type II die, in accordance with ISO 37. At the onset of testing, two extensometer clamps were set and attached to the sample 20-mm apart within the gauge region. The cross-head

J_ID: Z8E Customer A_ID: APP35088 Date: 20-July-11 Stage: Page: 4

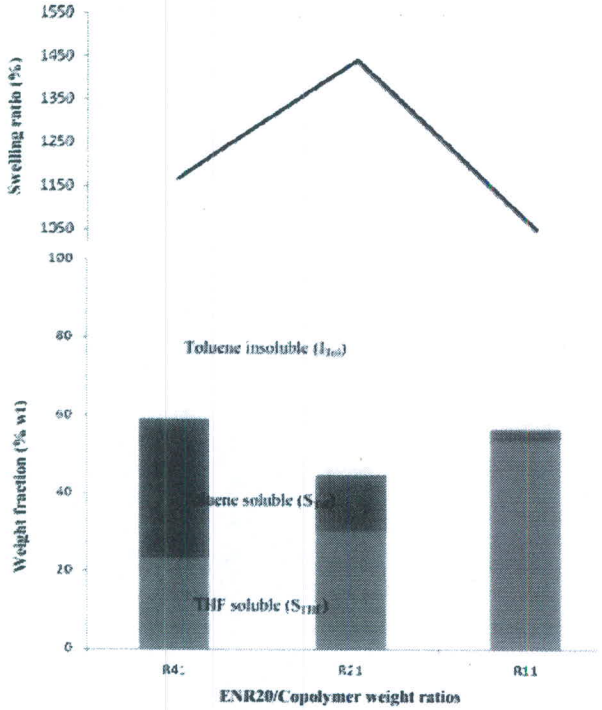


Figure 3 Solvent extraction results and swelling behaviors of cured products as a function of ENR20/copolymer feed content.

speed and full scale force used were 100 mm/min and 1 kN, respectively. The specimens were pulled in tension until rupture. The values of 100 and 300% modulus, tensile strength, and elongation at break were recorded, and the average value from three to four specimens was reported. Crystalline characteristics of the cured samples were examined by XRD on a JEOL JDX-3530 Diffractometer, using $CuK_{\alpha 1}$ radiation. The sample films were scanned from 2θ of 5–40° with 0.02 step size.

Permeability tests were also conducted on cast film samples with thickness of ~ 0.1 mm. Water vapor permeability was measured on an Illinois instrument (Model 7200), using ASTM F1249-01 at 38°C, 90% relative humidity and 1 atm pressure. Oxygen permeability was recorded on a Mocon instrument (Ox-Tran Model 2/21), following ASTM D3985 at 23°C, 0% relative humidity. Carbon dioxide permeability was measured on a Mocon instrument (Permatran-C Model 4/41) at 23°C, 0% relative humidity.

RESULTS AND DISCUSSION

Solvent fractionation

Results on weight percentage of products obtained from sequential solvent fractionation are summarized in Figure 3. As ENR20, LLA/EG copolymer, and a simple mixture of the two materials are completely dissolved in THF at 50°C, the content of S_{THF}, therefore, indicates the amount of the "free" or simple blend fraction. It is noted that slightly grafted ENR chains (copolymer-grafted ENR with low degree grafting) are also extractable by THF.[30,31] This is confirmed by NMR spectrum of the soluble material, where peaks due to copolymer dominate, with weak signals associated with ENR, as shown in Figure 4.

The content of the insoluble extracted sample (I_{THF}) represents the amount of newly formed "crosslinked" structure and "grafted" ENR domains, which are not soluble in THF solvent.[30,31] These two fractions are then further separated by toluene extraction. The "grafted" portions are soluble in toluene, while the "crosslinked" network remains insoluble. Unlike its slightly grafted counterpart, solubility behavior of the "grafted" ENR in toluene (but not THF) may be explained in terms of a decrease in epoxide content of ENR as a result of conversion to grafting points, and a large increase in the molecular weight of the "grafted" products. These two effects lead to a decrease in polarity and hence lower solubility in THF.

In the sample with low copolymer content in feed (R41), "crosslinked" and "grafted" fractions of ~ 40 and 36 wt % are observed. Unreacted "simple blend" of ~ 20 wt % is obtained. These indicate that the majority of hydroxyl groups in the copolymer chains effectively react with ENR20. When the copolymer content in feed is increased, the weight content of the "crosslinked" fraction is significantly comparable in all samples at ~ 40 wt %. In contrast, those of the "grafted" and the "simple blend" portions vary with the copolymer content. The "simple blend" (S_{THF}) content increases with an increase in the copolymer content in feed, while that of the "grafted" (S_{Tol}) fraction shows the opposite trend. Therefore, the feed ratio of ENR20/copolymer can be optimized to control the reaction efficiency. It is noted that the ENR : copolymer weight ratios of 4 : 1, 2 : 1, and 1 : 1 are equivalent to epoxide : OH molar ratios of 50 : 1, 25 : 1, and 12 : 1, respectively. The variation in the feed ratio leads to changes in two factors, i.e., the probability of copolymer's hydroxyls reacting with ENR (grafting efficiency), and the crosslinking efficiency (two hydroxyls from the same copolymer chain react with ENR to form crosslink junctions).

The increase in hydroxyls content leads to an increase in the grafting efficiency, which may reach a constant value when the limiting reagent (hydroxyl) is completely consumed. It was expected that hydroxyl groups are completely consumed in all three compositions. However, it is observed that unreacted copolymer remain in all samples even in

ID: jaishankarn | Black Lining: [ON] | Time: 12:08 | Path: N:/3b2/APP#/Vol00000/111185/APPFile/JW-APP#111185

J_ID: Z8E Customer A_ID: APP35088 Date: 20-July-11 Stage: Page: 5

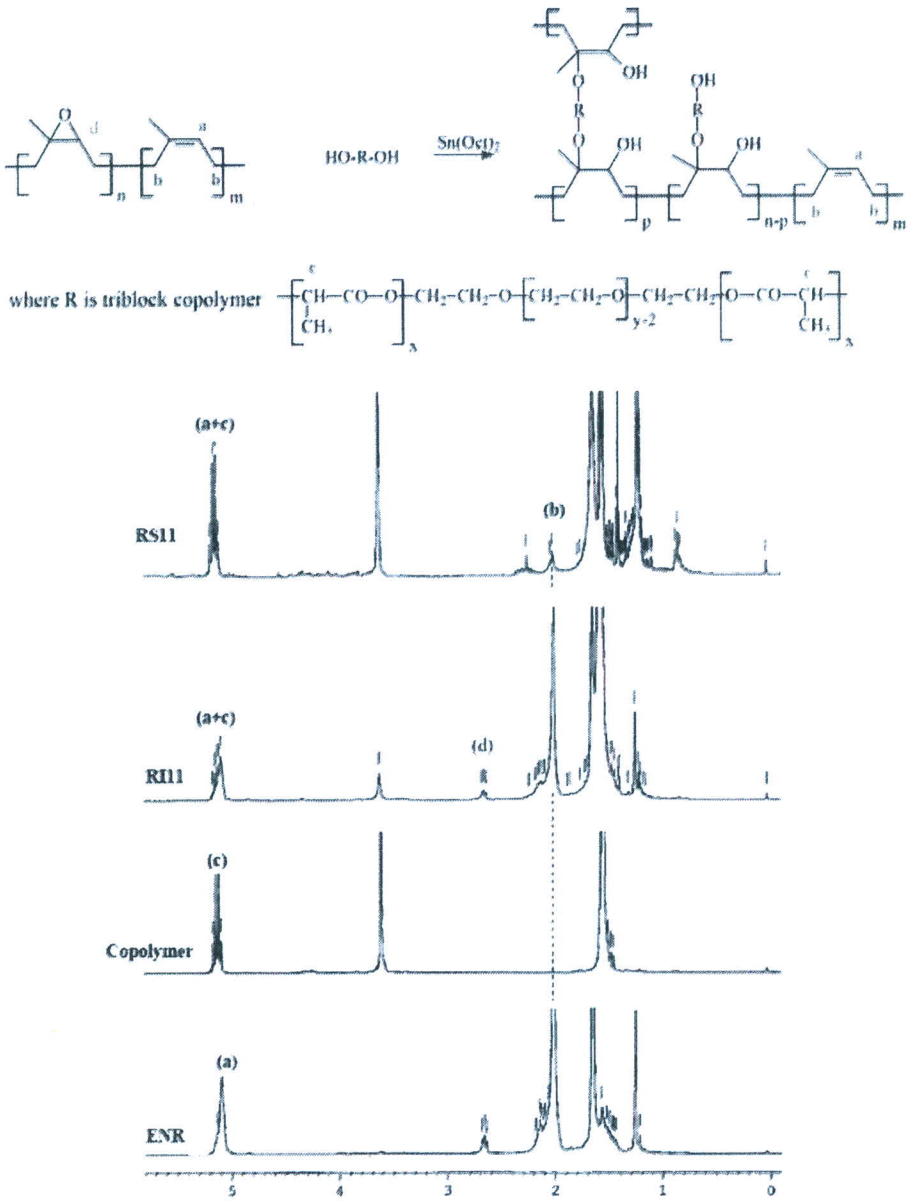


Figure 4 ^{1}H-NMR spectra and signal assignments of ENR20, $LLA_{46}EG_{46}LLA_{46}$ triblock copolymer, insoluble ($I_{THF}11$) and soluble (S_{THF} 11) fractions of the cured products after THF Soxhlet extraction.

the sample with the epoxide : hydroxyl molar ratio as high as 50 : 1. This is probably due to restriction in accessibility of the hydroxyls to epoxides, i.e., epoxide groups are spaced apart in ENR chains (20% epoxidation). In addition, steric factors and chain stiffness also play a role, as the hydroxyls are terminal groups of long copolymer chains and ENR contains double bonds in its backbone. Nonetheless, improvement of the grafting efficiency can be achieved by employing a reactive blend process, where catalyst and mechanical force are applied to aid the reaction. This will be reported in a separate communication.

In contrast, the increase in the feed hydroxyl content leads to a lower probability for two hydroxyl end-groups from the same copolymer chain, to react and form crosslink junctions, compared with that of forming grafted points. This results in a decrease in the crosslink efficiency. Figure 3 clearly indicates that the content of "grafted" fraction decreases upon increasing the feed ratio from 4 : 1 to 1 : 1. This reflects that the former effect is a dominant factor in this curing process. It is noted that solubility behavior of copolymer-grafted ENR chains varies with the degree of grafting. This may cause some uncertainties in the results obtained from the sequential

ID: jaishankarn | Black Lining: [ON] | Time: 12:08 | Path: N:/3b2/APP#/Vol00000/111185/APPFile/JW-APP#111185

solvent extraction, as "grafted" ENR with certain range of degree of grafting is likely to dissolve in both THF and toluene solvents, as indicated by an overlap area of solubility in Figure 1.

Degree of crosslinking

Degree of crosslinking of the insoluble fraction after solvent fractionation (I_{Tol}) is examined in terms of the swelling percentage in toluene. The results are also summarized in Figure 3. All samples exhibit a swelling ability, higher than 10 times their original dimensions, where the lowest swelling ratio of 1050% is observed in the sample derived from a 1 : 1 ENR20/copolymer feed ratio, indicating the highest crosslink density. This value is clearly higher ($\sim$ 2-fold) than those reported for typical sulfur-vulcanized NR samples,[32] where short sequences of sulfur bridges are employed as crosslink junctions. These results firmly support our proposed crosslink mechanism and structures that the copolymers act as long-chain junctions, which provide higher flexibility for the rubber network swelling.

^{1}H-NMR spectra

Chemical structure of the cured ENR products is illustrated in Figure 4. Formation of "crosslinked" or "grafted" structures is obtained, as a result from the variation in ENR20/copolymer feed ratio. ^{1}H-NMR spectra and signal assignments of ENR20, $LLA_{46}EG_{46}LLA_{46}$ OH-capped triblock copolymer are also compared in Figure 4, where THF soluble and insoluble fractions of the R11 cured sample are also shown. Signals located near 5.10 ppm consist of a singlet of methine proton (a) of *cis*-1,4-isoprene repeat units and a quartet of methine proton (c) of lactate units. Signals located at 2.10 (b) and 2.65 (d) ppm are assigned to methylene proton of NR units and methine proton of ENR, respectively. The strong (b) signal and a combination of signals at 5.10 ppm (a+c) in the spectrum of the THF-insoluble fraction strongly indicate that the sample consists of ENR20 matrix with the presence of the copolymer as crosslinked junctions. In contrast, a weak (b) signal in the spectrum of the soluble fraction demonstrates that the sample mainly consists of "uncrosslinked" copolymers and some copolymer-grafted ENR.[26,33]

Content of the copolymer in the THF soluble fraction of the cured products is calculated from ^{1}H-NMR spectra, as follows:

$$S_c = S_{(a+c)} - S_a \quad (2)$$

S_a = peak integration of methine proton (5.10 ppm) of ENR

TABLE I
Weight Fractions and Copolymer Content of the Extracted Products After THF Soxhlet Extraction

Samples	ENR20/copolymer feed content (wt %)	Weight fraction[a] (wt %)	Copolymer content[b] (wt %)
$S_{THF}41$	75 : 25	23	63
$S_{THF}21$	66 : 33	30	84
$S_{THF}11$	50 : 50	53	90

[a] Result from Soxhlet extraction.
[b] Calculated from ^{1}H-NMR spectra.

S_c = peak integration of methine proton (5.10 ppm) of copolymer

S_{a+c} = peak integration of methine protons of ENR and copolymer

S_b = peak integration methylene proton (2.10 ppm) of *cis*-1,4-polyisoprene unit

The weight content of the copolymer in the samples is calculated, as follows:

$$C(\%) = \frac{M_P}{M_P + \left(S_b \times \frac{U_{LA}}{S_c} \times M_{NR}\right) \times \left(\frac{100}{100 - X_{epoxy}}\right)} \times 100 \quad (3)$$

where $C(\%)$ = weight content of the copolymer,

M_P = molar mass of copolymer (8600 g/mol),

U_{LA} = average number of LLA repeat units in the copolymer chain (92 units),

M_{NR} = molar mass of *cis*-1,4-polyisoprene repeat unit (68 g/mol),

X_{epoxy} = epoxide content of ENR20 (20%).

Results on the weight fraction and copolymer content of THF-soluble samples (S_{THF}), as summarized in Table I and Figure 3, show an increasing trend, as a function of increasing copolymer content in the feed. The increase in weight fraction of S_{THF} from the Soxhlet extraction reflects an increase in (excess) unreacted copolymers, present as simple blend component or small amount of "grafted" fraction with low degree of grafting. In addition, the increase in copolymer content of S_{THF} samples, calculated from NMR spectra, with the copolymer content in the feed also reflects that the S_{THF} sample consists of a certain amount of slightly grafted ENR and an increasing quantity of unreacted copolymers.

T1

ATR-FTIR spectra

ATR-FTIR spectra of ENR20, LLA/EG copolymer, and R41 cured sample are shown in Figure 5. Characteristic bands of ENR20 are observed at 3030 (C—H stretching of epoxide), 1655 (C=C stretching of rubber unit), 1375 (C—H symmetric deformation of rubber's $-CH_3$), and 1250 cm^{-1} (C—O stretching

F5

J_ID: Z8E Customer A_ID: APP35088 Date: 20-July-11 Stage: Page: 7

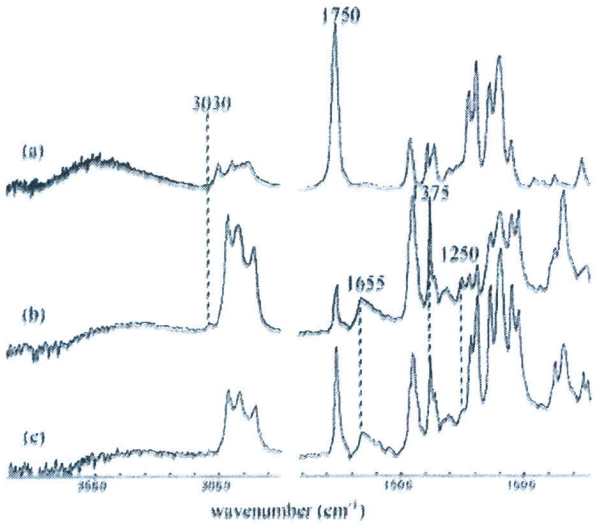


Figure 5 ATR-FTIR spectra of $LLA_{46}EG_{46}LLA_{46}$ triblock copolymer (a), ENR20 (b), and R41-cured sample (c).

of epoxide).[34] The characteristic absorption bands of LLA/EG triblock copolymer are observed at 1750 (C=O stretching), and 1375 and 1360 cm^{-1} (C—H symmetric deformation of $—CH_3$ of lactate).[34] The spectrum of R41 cured ENR sample, also shown in Figure 5, exhibits band characteristics of the two components. It is clearly observed that the epoxide bands located at 3030 and 1250 cm^{-1} decrease in band intensity upon reacting with the copolymers, indicating a reduction in epoxide content as a result from the ring-opening reaction with hydroxyl groups.

The infrared spectra of cured ENR samples prepared from different ENR20/copolymer feed ratios F6 are compared in Figure 6. Changes in relative intensities of the band characteristics of the two components as a function of feed content are clearly observed. The relative quantity of the two components can be measured by examining the intensity ratio of the 1750/1655 or 1375/1360 cm^{-1} bands. The spectra indicate the intensity ratios that are in

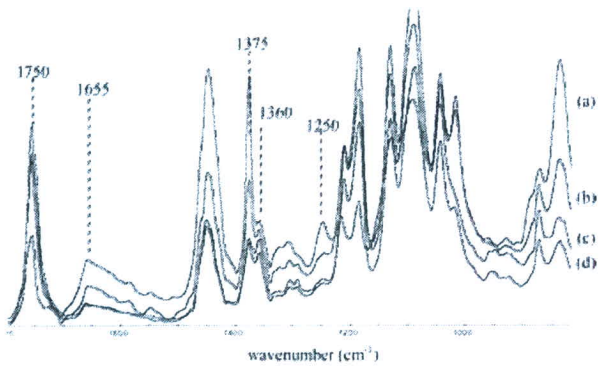


Figure 6 ATR-FTIR spectra of ENR20 (a), R41 (b), R21 (c), and R11 cured samples (d).

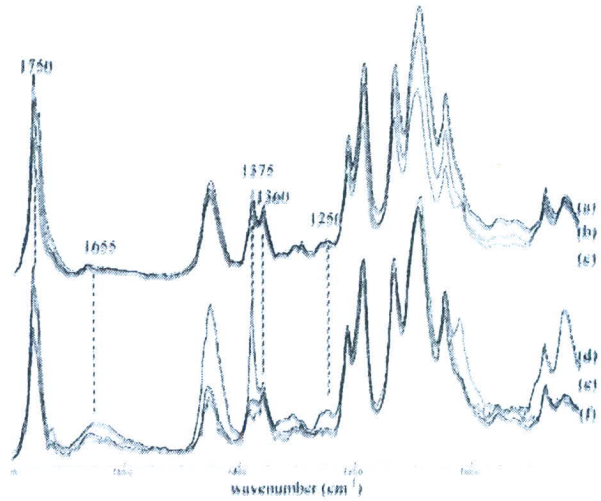


Figure 7 ATR-FTIR spectra of extracted products after THF Soxhlet extraction: $S_{THF}41$ (a), $S_{THF}21$ (b), and $S_{THF}11$ (c) soluble fractions; and $I_{THF}41$ (d), $I_{THF}21$ (e), and $I_{THF}11$ (f) insoluble fractions.

accord with the feed compositions. The efficiency of the curing process can be determined from the ATR-FTIR spectra by following the change in intensity of the 1250 cm^{-1} band, i.e., the epoxide content. The band intensity clearly decreases as the feed copolymer content increases, reflecting the conversion of epoxide groups after reaction with the hydroxyl groups. The corresponding spectra of THF extraction products, S_{THF} and I_{THF}, as a function of feed ENR20/copolymer content are compared in Figure 7. The change in relative intensity of band characteristics of the ENR and copolymer components is clearly observed, and the results are in accord with those observed from ^{1}H-NMR spectra. F7

XRD spectra

XRD traces of LLA/EG copolymer, ENR20 and the cured samples are compared in Figure 8. The spectrum of ENR20 shows a broad diffraction pattern due to its highly amorphous nature. In contrast, the spectrum of $LLA_{46}EG_{46}LLA_{46}$ copolymer show diffraction peaks at 2θ of 16.8, 19.1, and 22.4°, which correspond to crystalline domains of the LLA blocks. The diffraction patterns of EG blocks are not observed, probably because of its significantly short sequences and chain restriction imposed by the LLA terminal blocks that retards its crystallization. XRD traces of cured ENR products show diffraction peaks of the copolymer, whose intensity and sharpness increase with an increase in the copolymer in the feed. This reflects an increase in the copolymer content in the cured products, and an enhancement in crystallize ability of the copolymer, due to excess amount of copolymer chains in the ENR matrix. F8

ID: jaishankarn | Black Lining: [ON] | Time: 12:08 | Path: N:/3b2/APP#/Vol00000/111185/APPFile/JW-APP#111185

J_ID: Z8E Customer A_ID: APP35088 Date: 20-July-11 Stage: Page: 8

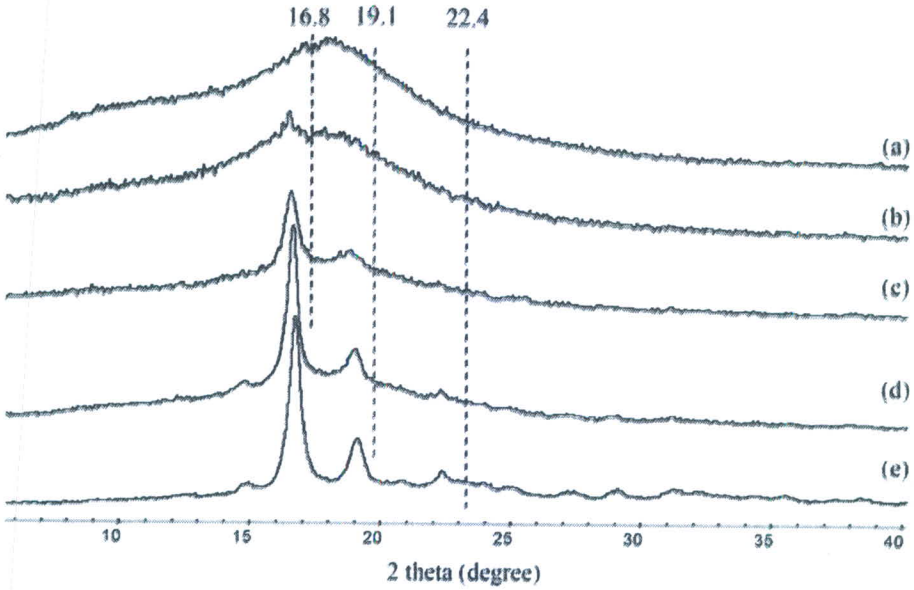


Figure 8 XRD traces of ENR20 (a), R41 (b), R21 (c), R11 (d) cured samples, and $LLA_{46}EG_{46}LLA_{46}$ triblock copolymer (e).

This is in good agreement with our previous discussion. It should also be noted that the peak position of the diffraction peaks, especially at 16.8°, shifts to lower angle along with the decrease in the peak intensity and sharpness as the feed ENR20/copolymer ratio increases from 1 : 1 to 4 : 1. This is probably due to lower degree of order arrangement of the copolymer domains, as the chains effectively react with the ENR and are present as "grafted" or "crosslink junctions." This results in mobility restriction, and hence a retardation of crystal formation.

Tensile properties

Tensile properties of R11 cured sample, a 1 : 1 ENR20/copolymer simple blended mixture without the use of catalyst (N11), and pristine ENR20 are examined and compared in Table II. It is noted that these samples do not contain ENR chains linked by conventional crosslinking junctions, i.e., reaction with double bonds. R11 and N11 show drastic improvement in 100% Modulus (M100), 300% Modulus (M300), and tensile strength, compared with those of the original ENR20. This indicates that the incorporation of LLA/EG copolymer, either by simple blending (N11) or as grafted chains and crosslink junctions (R11), leads to an enhancement in tensile properties of the samples. Given that the NMR spectrum of N11 and its extraction result (100% soluble in THF) indicate no significant chemical change in the simple blended mixture, the property improvement observed in this sample is probably attributed to interfacial adhesion of copolymer and ENR20 chains in the blend.[35] With the application of $Sn(Oct)_2$ catalyst, formation of "grafted" and "crosslinked" ENR networks by copolymer junctions is obtained in R11. This leads to further improvement in the tensile properties.

The elongation at break of R11 and N11 clearly decreases, compared to that of the original (uncured) ENR, because the incorporation of plastic materials, i.e., copolymers, into the rubber matrix leads to a decrease in elastic properties of the mixture, hence a drop in elongation at breaks. A mismatch in solubility parameter of the two components, which affects the mixture's miscibility, and the presence of excess copolymers may also play a role in the drop in the elongation at break of N11. The results also show that elongation at break of R11 is higher than that of N11. This is probably due to the existent of "grafted" ENR, which generate higher degree of chain entanglements and a closer match in solubility of the components, leading to an increase in elongation at break. In addition, the present of "crosslinked"

TABLE II
Tensile Properties of R11-Cured Sample, a 1 : 1 ENR20/Copolymer Blend (N11), and ENR20

Samples	M100 (MPa)	M300 (MPa)	Tensile strength (MPa)	Elongation at break (%)
R11	2.11 ± 0.10	3.98 ± 0.22	5.97 ± 0.31	407 ± 30
N11	1.88 ± 0.03	2.68 ± 0.04	3.14 ± 0.13	345 ± 25
ENR20	0.41 ± 0.02	0.42 ± 0.02	0.52 ± 0.04	650 ± 20

ID: jaishankarn | Black Lining: [ON] | Time: 12:08 | Path: N:/3b2/APP#/Vol00000/111185/APPFile/JW-APP#111185

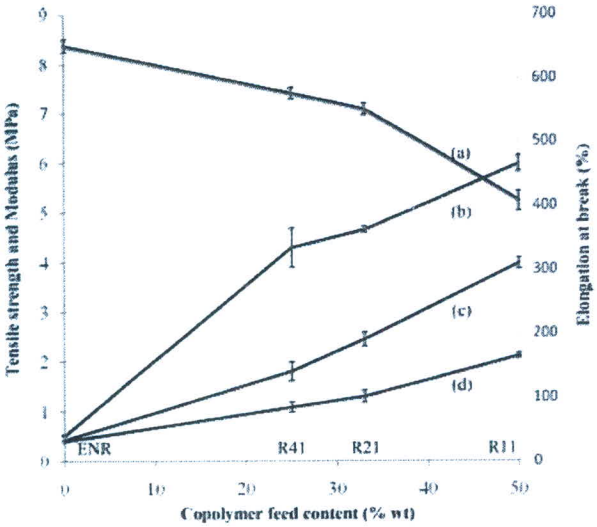


Figure 9 Elongation at break (a), Tensile strength (b), 100% Modulus, M100 (c), 300% Modulus, M300 (d) of ENR cured samples as a function of ENR20/copolymer feed content.

ENR in R11 also results in an enhancement of elongation at break.

Tensile properties of the cured samples as a function of ENR20/copolymer feed content are shown in F9 Figure 9. The degree of improvement in tensile strength, M100, and M300 is dependent on the copolymer feed content, where R11 shows an improvement of more than 10 times of those of neat ENR20. This is due to the presence of network structure and "grafted" ENR chains, leading to a mobility restriction of the cured ENR products, as previously discussed. Additionally, the increase in the content of excess copolymers in the samples is also responsible for the increase in modulus and tensile strength. It is also clearly observed that elongation at break decreases with the increase in the copolymer content in the feed, mainly due to the increase in the content of excess copolymers. As the degree of improvement of tensile properties is strongly dependent on the ENR20/copolymer ratio in the feed, cured ENR products with specific properties can be obtained by adjusting this value. Given these excellent mechanical properties and their biocompatibility, the materials can be applied in various applications, especially in biomedical fields.

Permeability behaviors

Permeability characteristics of the cured samples are examined to elucidate their potential use in membrane applications. Theoretically, the permeability of a polymer for a gas penetrant is defined as a product of solubility coefficient and diffusion coefficient, where the former is derived from the relative size of

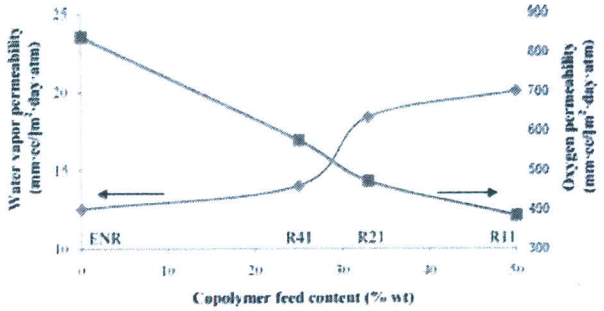


Figure 10 Water vapor and oxygen permeabilities of cured ENR samples as a function of ENR20/copolymer feed content.

penetrant and the inter/intrachain spacing of the polymer. The latter term is associated with sorption ability of the penetrant on the polymer.[36] Results of water vapor permeability of the cured samples, as summarized in Figure 10, show an increasing trend F10 with increasing feed copolymer content, compared to that of neat ENR20, at 13 mm cc/(m^2·day atm). This is mainly because the cured products contain long-chain crosslink junctions that disrupt chain arrangement of the ENR matrix (See Fig. 1), leading to an enlargement of chain spacing and hence ease of water vapor permeation. EG sequences in the block copolymer also play a key role in the enhancement of the solubility coefficient term, as its strong hydrophilic nature provides high sorption ability to the vapor. This agrees with those observed by Zenkiewicz et al.[37] that the presence of 20% of PEG in the PLLA matrix doubly increased the water permeability of the mixture.

Results on oxygen permeability, as shown in Figure 11, indicate that an increase in copolymer F11 content in the cured materials leads to a drastic reduction in the oxygen permeability. Oxygen permeability of pristine ENR25, PEG and PLLA was

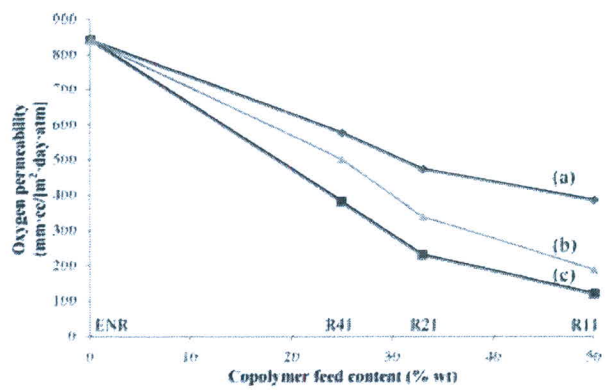


Figure 11 Experimental (a) and theoretical oxygen permeability: the free volume theory (b) and the empirical model (c), of cured samples as a function of ENR20/copolymer feed content.

J_ID: Z8E Customer A_ID: APP35088 Date: 20-July-11 Stage: Page: 10

reported as 328, 17, and 17 mm cc/(m^2 day atm), respectively.[36,38,39] Given the much lower values for PEG and PLA compared with that of ENR, a decrease in the permeability of the cured ENR samples is expected as a result from the incorporation of the copolymer. The reduction in the oxygen permeability can be explained in terms of a decrease in both diffusion and solubility coefficients, due to the relatively larger size of oxygen molecule and its nonpolar nature.

The variation in the oxygen permeability as a function of ENR20/copolymer content can be explained by the following empirical model, which was modified from that proposed by Paul et al. in the explanation of polymer blend characteristics.[40]

$$\log P_{cured} = \phi_{co} \log P_{co} + \phi_{ENR} \log P_{ENR} \quad (4)$$

where P_{cured} is gas permeability of the cured samples.

ϕ_{co} and ϕ_{ENR} are volume fractions of copolymer and ENR20 in the cured samples.

P_{co} and P_{ENR} are oxygen permeabilities of pure copolymer and ENR components.

Alternatively, the free volume model,[40] which is used to explain the transport behavior of gas in a polymer matrix, can be adopted, as described below:

$$\ln \frac{P_{cured}}{A} = \left[\frac{\phi_{ENR}}{\ln\left(\frac{P_{ENR}}{A}\right)} + \frac{\phi_{co}}{\ln\left(\frac{P_{co}}{A}\right)} \right]^{-1} \quad (5)$$

where A is parameter for free volume model at 25°C, 7.9×10^{-7} (cm^3(STP)·cm/[cm^2 sec cmHg])

Figure 11 summarizes oxygen permeability of the cured samples obtained from experiments, compared with those calculated from the empirical model and the free volume theory. Data obtained from the two models are significantly lower than the experimental results, probably because the models were designed for polymer blend systems. However, these cured ENR materials consist of full/partial crosslinked networks and blend mixtures. The free volume theory is a closer match to the experimental values, and perhaps more suitable to describe the gas permeability behavior of these materials. The higher experimental values compared to the predicted values by the free volume theory is probably due to the long-chain crosslink junctions derived from the block copolymers, which leads to formation of excess free volume in the cured network and hence, higher gas permeability.

Carbon dioxide permeability characteristics of ENR20 and R11 are compared in Table III. The values of 6142, 531, and 72 mm cc/(m^2 day atm) were reported for ENR25, PEG, and PLA, respectively.[38,39,41] Given the empirical model ($\log P_{cured} = \phi_{co} \log P_{co} + \phi_{ENR} \log P_{ENR}$), the CO_2 permeability of the cured samples is expected to decrease with increasing copolymer content. The experimental data, however, shows the reverse trend, where the cured R11 sample shows higher CO_2 permeability of more than two times, compared to that of the original ENR20. This intriguing behavior is mainly due to EG segments in the copolymer chains. It was reported that PEG can dissolve a substantial amount of sour gas.[42] Ether groups in PEG as polar moiety groups have affinity to CO_2 gas due to dipole-quadrupole interaction.[38] CO_2 is present as a strong sorbing penetrant for PEG, resulting in large solubility coefficient. The polymer matrix is subsequently plasticized by high concentration of this strong sorbing penetrant, resulting in an increase in local segment motion. Therefore, an enhancement in diffusion coefficients and permeability is achieved.[36,38,43] In addition, the presence of hydroxyl end-groups from "grafted" or "free" copolymers in the ENR matrix, and the newly formed hydroxyls from ring-opening reaction of epoxide (See Fig. 4), also favor the transport of CO_2 through the membrane because of its acidity.

TABLE III
Carbon Dioxide, Oxygen Permeability, and CO_2/O_2 Selectivity of ENR20 and Cured R11 Sample

Samples	CO_2 permeability (mm·cc/[m^2·day·atm])	O_2 permeability (mm·cc/[m^2·day·atm])	CO_2/O_2 selectivity
ENR20	6 117	841	7.3
R11	12 840	384	33.4

Results on CO_2/O_2 selectivity are also summarized in Table III. An enhancement in the CO_2/O_2 selectivity of more than four times is observed in R11 sample, compared with that of the neat ENR20. The ideal selectivity of penetrant is defined as the product of diffusivity selectivity and solubility selectivity. For rubbery polymer, it is commonly found that the selectivity is dominated by the solubility term.[36] This is firmly supported, as the solubility selectivity of the system strongly favors the transport of CO_2, as previously discussed. In addition, the permeability and selectivity of these materials may be further adjusted by varying the block length of EG sequence in the copolymer chains. Therefore, these copolymer-cured ENR samples are excellent choice for use as selective materials in membrane applications.

CONCLUSIONS

OH-capped LLA/EG/LLA triblock copolymer is used as a macromolecular crosslink agent for the ENR matrix by utilizing ring-opening reaction of epoxides and hydroxyl groups, using $Sn(Oct)_2$ as a

ID: jaishankarn | Black Lining: [ON] | Time: 12:08 | Path: N:/3b2/APP#/Vol00000/111185/APPFile/JW-APP#111185

J_ID: Z8E Customer A_ID: APP35088 Date: 20-July-11 Stage: Page: 11

catalyst. ^{1}H-NMR and ATR-FTIR spectra indicate the formation of chemical bonds between copolymer chains and ENR. Efficiency of the crosslinked reaction is varied as a function of ENR/copolymer feed ratios, which is reflected by the content of "crosslinked," "grafted," and "free" simple blend fractions of the copolymer-cured ENR samples. These are examined by ^{1}H-NMR, ATR-FTIR, XRD, solvent fractionation, and swelling experiments. The cured ENR products exhibit drastic improvement in tensile properties, suitable for use as crosslinked rubber materials for specific and high-value applications. The use of a rather high content of the biocompatible/biodegradable copolymer as a curing agent is, therefore, not a major concern. Improvement in permeability and selectivity behaviors of the materials is also achieved, where water vapor and carbon dioxide permeability increase with an increase in copolymer feed content. The opposite trend is observed for oxygen permeability. These cured materials with excellent properties show high potential for use in biomedical and membrane applications. In addition, the properties of these cured materials can be fine tuned for specific applications by varying the ENR20/copolymer ratios, the epoxide content of ENR, and the relative block lengths of the copolymer.

References

1. Bhowmick, A. K.; Stephens, H. L. Handbook of Elastomers; Marcel Dekker: New York,2001.
2. Morgan, B.; McGill, W. J. J Appl Polym Sci 2000, 76, 1413.
3. Porter, M. J Appl Polym Sci 1967, 11, 2255.
4. Craig, D.; Davidson, W. L.; Juve, A. E.; Geib, I. G. J Polym Sci 1951, 6, 1.
5. Bristow, G. M.; Moore, C. G.; Russell, R. M. J Polym Sci Part A: General Papers 1965, 3, 3893.
6. Bristow, G. M. J Appl Polym Sci 1965, 9, 3255.
7. Moore, C. G.; Scanlan, J. J Polym Sci 1960, 43, 23.
8. Dunn, J. R. J Appl Polym Sci 1963, 7, 1543.
9. Chowdhury, R. J Appl Polym Sci 2007, 103, 1206.
10. Minoura, Y.; Asao, M. J Appl Polym Sci 1961, 5, 233.
11. Minoura, Y.; Asao, M. J Appl Polym Sci 1961, 5, 401.
12. Akiba, M.; Hashim, A. S. Prog Polym Sci 1997, 22, 475.
13. Gelling, I. R. J Natural Rubber Res 1991, 6, 184.
14. Hashim, A. S.; Kohjiya, S. J Polym Sci Part A: Polym Chem 1994, 32, 1149.
15. Gelling, I. R. Rubber Chem Technol 1985, 58, 86.
16. Perera, M. C. S. J Appl Polym Sci 1990, 39, 749.
17. Jayawardena, S.; Reyx, D.; Durand, D.; Pinazzi, C. P. Die Makromolekulare Chemie 1984, 185, 2089.
18. Derouet, D.; Radhakrishnan, N.; Brosse, J.-C. Boccaccio, G. J Appl Polym Sci 1994, 52, 1309.
19. Mohanty, S.; Nando, G. B.; Vijayan, K.; Neelakanthan, N. R. Polymer 1996, 37, 5387.
20. Derouet, D.; Brosse, J.-C.; Challioui, A. Eur Polym J 2001, 37, 1315.
21. Derouet, D.; Brosse, J.-C.; Challioui, A. Eur Polym J 2001, 37, 1327.
22. Gupta, A. P.; Kumar, V. Eur Polym J 2007, 43, 4053.
23. Cohn, D.; Younes, H. J Biomed Mater Res 1988, 22, 993.
24. Deng, X. M.; Xiong, C. D.; Cheng, L. M.; Xu, R. P. J Polym Sci Part C, Polym Lett 1990, 28, 411.
25. Kulkarni, R. K.; Moore, E. G.; Hegyeli, A. F.; Leonard, F. J Biomed Mater Res 1971, 5, 169.
26. Saito, T.; Klinklai, W.; Yamamoto, Y.; Kawahara, S.; Isono, Y.; Ohtake, Y. J Appl Polym Sci 2009, 115, 3598.
27. Nghia, P. T.; Siripitakchai, N.; Klinklai, W.; Saito, T.; Yamamoto, Y.; Kawahara, S. J Appl Polym Sci 2008, 108, 393.
28. Nguyen, T.-H.; Petchsuk, A.; Tangboriboonrat, P.; Opaprakasit, M.; Sharp, A.; Opaprakasit, P. Adv Mater Res 93 2010, 94, 198.
29. Saendee, P.; Tangboriboonrat, P. Colloid Polym Sci 2006, 284, 634.
30. Derouet, D.; Tran, Q. N., Thuc, H. H. J Appl Polym Sci 2009, 114, 2149.
31. Phinyocheep, P.; Phetphaisit, C. W.; Derouet, D.; Campistron, I.; Brosse, J. C. J Appl Polym Sci 2005, 95, 6.
32. Aprem, A. S.; Joseph, K.; Mathew, T.; Altstaedt, V.; Thomas, S. Eur Polym J 2003, 39, 1451.
33. Saito, T.; Klinklai, W.; Kawahara, S. Polymer 2007, 48, 750.
34. Mathew, V.; Sinturel, C.; George, S.; Thomas, S. J Mater Sci 45, 1769.
35. Yong, M. K.; Ismail, H.; Ariff, Z. M. Polym-Plast Technol Eng 2007, 46, 1001.
36. Johnson, T.; Thomas, S. Polymer 1999, 40, 3223.
37. Zenkiewicz, M.; Richert, J. Polym Test 2008, 27, 835.
38. Lin, H.; Freeman, B. D. J Membr Sci 2004, 239, 105.
39. Bao, L.; Dorgan, J. R.; Knauss, D.; Hait, S.; Oliveira, N. S.; Maruccho, I. M. J Membr Sci 2006, 285, 166.
40. Paul, D. R. J Membr Sci 1984, 18, 75.
41. Barrie, J. A.; Becht, M.; Campbell, D. S. Polymer 1992, 33, 2450.
42. Kuehne, D. L.; Friedlander, S. K. Indust Eng Chem Proc Des Dev 1980, 19, 609.
43. Koros, W. J.; Hellums, M. W. Fluid Phase Equilibria 1989, 53, 339.

ID: jaishankarn | Black Lining: [ON] | Time: 12:09 | Path: N:/3b2/APP#/Vol00000/111185/APPFile/JW-APP#111185

เอกสารแนบ 5.1.15

Communications

Selective Sensing of L-Arginine Employing Luminol Dextran Conjugate

Weerachai Nasomphan[a,b], Pramuan Tangboriboonrat[b], Srung Smanmoo[a*]

[a]*Bioresources Research Unit, National Center for Genetic Engineering and Biotechnology (BIOTEC), 113 Thailand Science Park, Phaholyothin Road, Klong Luang, Pathumthani 12120, Thailand*

[b]*Department of Chemistry, Faculty of Science, Mahidol University, Rama 6 Road, Phyathai, Bangkok 10400, Thailand*

Abstract

Luminol dextran conjugate (LD) was synthesized by incorporating luminol into the oxidized dextran template followed by reduction with sodium borohydride. The fluorescence (FL) response of LD towards various amino acids was investigated by FL spectroscopy. The FL intensity of LD significantly quenches upon the addition of L-arginine and goes to completion after the addition of 50×10^{-5} mol L^{-1} L-arginine. Since LD is highly soluble in water, LD could be potentially used as a FL polymeric sensor for the determination of L-arginine in aqueous environment.

Introduction

Chemosensors have found their standing position in environmental and biomedical applications.[1-3] Due to the limited signal generated by molecular chemosensors, polymeric chemosensors have therefore gained their popularity due to the amplified signal output.[4-7] The effect could be due to a large number of chromophores incorporated into the macromolecular template.[8] Recently, polymeric chemosensors have been widely used for detection of explosives, volatile organic compounds, biological and chemical molecules.[9-12]

Amino acids (AAs) are important analytes present in biological fluids. It is known that many diseases are directly correlated to the deficiency of AAs.[11] Among these AAs, L-arginine is of research focus due to its various biological roles. L-arginine is a precursor for biosynthesis of a signal-transduction molecule, nitric oxide, via the enzymatic process assisted by nitric oxide synthase (NOS).[13-14] Over the past decades, AA chemosensor for L-arginine is scarcely reported. However, the specific recognition between adenosine triphosphate (ATP) and L-arginine has been recently exemplified.[15] The recognition of L-arginine by ATP proceeds via the hydrogen bonding and the charge-charge interaction between the guanidinium residue of L-arginine and the triphosphate moiety of ATP. A chemosensor based on the calix[4]pyrrole-TCBQ assembly has been carefully designed and used for the detection of AAs and amines.[16] The photophysical response of the calix[4]pyrrole-TCBQ assembly towards AAs is driven by the *n*-π charge-transfer.

Herein, we have designed a polymeric chemosensor for L-arginine based on luminol dextran conjugate (LD). Dextran, a polysaccharide consisting of a number of glucose subunits, is chosen as a polymeric template due to the fact that it exhibits strong affinity towards L-arginine via a charge-charge interaction.[17] Luminol (Lu) is selected as a chromophore because its fluorescence (FL) could be quenched in the presence of analytes via the internal charge transfer (ICT) pathway.[18] Upon binding of L-arginine to LD, ICT process is operated which quenches the FL of Lu moiety. Since LD is highly soluble in water and highly selective towards L-arginine, this offers LD as a potential chemosensor for an intracellular detection of L-arginine.

Experimental

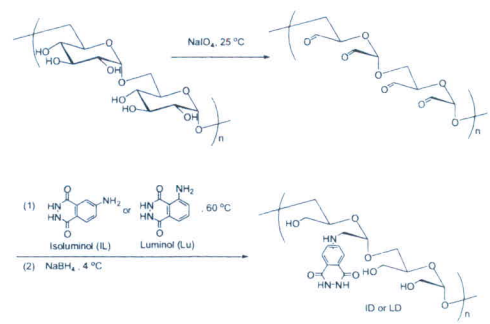
Materials. Luminol and isoluminol were purchased from Tokyo Chemical Industry (TCI), Japan. Dextran and other chemicals were supplied from Aldrich. All reagents were used without further purification.

General. ^{1}H NMR spectrum was recorded on Bruker DPX 400 MHz spectrometer in D_2O using TMS as the internal standard. Elemental analysis for the synthesized compound was analyzed by Tokyo Chemical Industry (Japan).

Luminol dextran conjugated (LD): LD was prepared according to a literature.[8] ^{1}H NMR (400 MHz, D_2O) [ppm]: 8.33 (s), 7.55-7.41 (m), 7.28-7.23 (m), 6.95 (d, J = 8.38 Hz), 4.85 (br, dextran), 4.08-3.23 (m, dextran).

Results and Discussion

Isoluminol dextran conjugate (ID) and LD were prepared according to Kai's procedure with slight modification.[8] Briefly, dextran (M*r* approx. 2×10^6 g/mol) was oxidized with sodium periodate ($NaIO_4$) to provide the oxidized dextran which was then reacted with either isoluminol (IL) or Lu, followed by reduction with sodium borohydride ($NaBH_4$) to furnish ID and LD as yellow powder (Scheme 1).



Scheme 1. The synthesis of ID and LD.

ID and LD were dried in *vacuo* before subjecting to elemental analyses performed by Tokyo Chemical Industry

Table 1. Elemental Analysis and Molecular Weight Determination of ID and LD

	%C	%H	%N	Composition of compound	Molecular weight (GPC)	Polydispersity index (M_w/M_n)
ID	43.76	5.65	5.95	$(IL)_{3262}$-$(Glc)_{12346}$	2.5×10^6 g/mol	1.59
LD	43.96	5.62	5.50	$(Lu)_{2726}$-$(Glc)_{12375}$	2.6×10^6 g/mol	1.56

IL = isoluminol unit; Lu = luminol unit; Glc= glucose unit.

(Japan). Table 1 shows %C, %H and %N of ID and LD. From the data obtained, the composition of IL, Lu and glucose (Glc) units in ID and LD were deduced. According to the data, a large number of IL (3,262 units) or Lu (2,726 units) has been incorporated into a macromolecular dextran template. This could improves the sensitivity of the polymeric sensor.[19] The molecular weight of ID and LD, determined by Gel Permeation Chromatography (GPC), were found to be 2.5×10^6 and 2.6×10^6 g/mol, respectively. Their polydispersity indexes (M_w/M_n) were 1.59 and 1.56. FL emission of ID and LD appeared at 425 nm in water which is the characteristic FL emission of IL and Lu. The thermogram obtained from thermogravimetric analysis (TGA) of LD is displayed in Figure 1. The weight loss of LD is found over three regions (0-238, 238-315 and 315-626°C) where the maximum decomposition temperature is at 626°C.

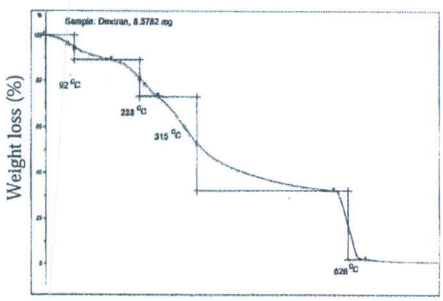


Figure 1. TGA thermogram of LD.

The selectivity of LD (25×10^{-5} mol L^{-1}) towards different concentrations of AAs was investigated. In the presence of AAs, various degrees of FL enhancement and quenching of LD were observed. However, only L-arginine significantly quenched the FL of LD. The FL quenching effect was clearly observed when 50×10^{-5} mol L^{-1} of L-arginine was added into the LD solution. FL of LD gradually decreases upon increasing concentrations of L-arginine and nearly undergoes to completion after the concentration of L-arginine reached 25×10^{-5} mol L^{-1} (Figure 2). Figure 3 shows FL quenching of ID, used here as a control, in the presence of AAs. It was clearly shown that FL enhancement and quenching of ID were also observed with different AAs. L-arginine, although, exhibited some degrees of FL quenching of ID. However, the quenching effect was less pronounced when compared to LD. This indicates that the Lu moiety in LD serves as a specific chromophore interacting with L-arginine and the interaction initiates the FL quenching of LD via the ICT process. Since IL is an isomer of Lu, it would expect to display some degrees of FL quenching.[20] The more quenching effect of LD compared to ID is presumably due to the orientation of Lu moiety in the present conformation of polymeric dextran in which the Lu moiety and L-arginine achieves the maximal interaction.

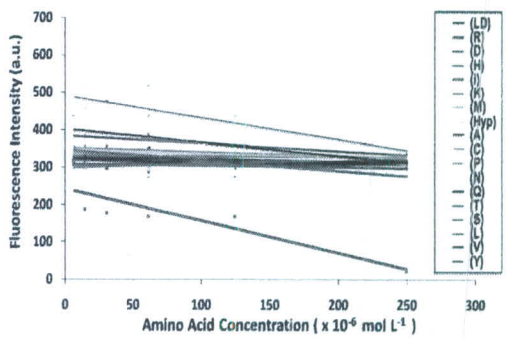


Figure 2. FL emission of LD (25×10^{-5} mol L^{-1}) in the presence of various concentrations of AAs in water. Excitation wavelength (λ_{Ex}) = 275 nm. Where LD = luminol dextran conjugate; R = L-Arginine; D = L-Aspartic acid; H = L-Histidine; I = L-Isoleucine; K = L-Lysine; M = L-Methionine; Hyp = L-Hydroxyproline; A = L-Alanine; C = L-Cysteine; P = L-Proline; N = L-Asparagine; Q = L-Glutamine; T = L-Threonine; S = L-Serine; L = L-Leucine; V = L-Valine; Y = L-Tyrosine.

Since the ICT process highly depends on the choice of donor and acceptor, the FL quenching of LD in the presence of L-arginine is presumably due to the ICT channel in which Lu and guanidinium groups are good electron donor/acceptor in this process.[21]

A curve equation is linearly obtained in the range of L-arginine concentrations from 0 to 0.1×10^{-5} mol L^{-1}, R = -0.982, N = 3. According to the equation, the FL detection of LD was determined to be as low as 1.0×10^{-5} mol L^{-1}.

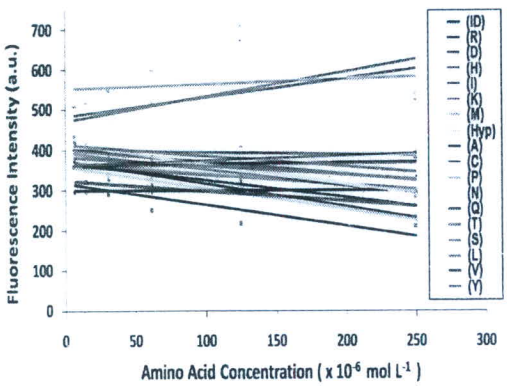


Figure 3. FL emission of ID (25×10^{-5} mol L^{-1}) in the presence of various concentrations of AAs in water. Excitation wavelength (λ_{Ex}) = 275 nm. Where ID = isoluminol dextran conjugate; R = L-Arginine; D = L-Aspartic acid; H = L-Histidine; I = L-Isoleucine; K = L-Lysine; M = L-Methionine; Hyp = L-Hydroxyproline; A = L-Alanine; C = L-Cysteine; P = L-Proline; N = L-Asparagine; Q = L-Glutamine; T = L-Threonine; S = L-Serine; L = L-Leucine; V = L-Valine; Y = L-Tyrosine.

The FL change of LD in the presence of AAs was clearly observed under UV light. When LD (1.0×10^{-5} mol L^{-1}) was added with various AAs (50×10^{-5} mol L^{-1}), only L-arginine exhibited significant FL quenching. The presence of other AAs displayed no noticeable FL change of LD (Figure 4). Increasing concentrations of L-arginine resulted in gradually FL quenching of LD and the significant FL quenching of LD was clearly observed after the addition of 50×10^{-5} mol L^{-1} of L-arginine [Figure 5(h)].

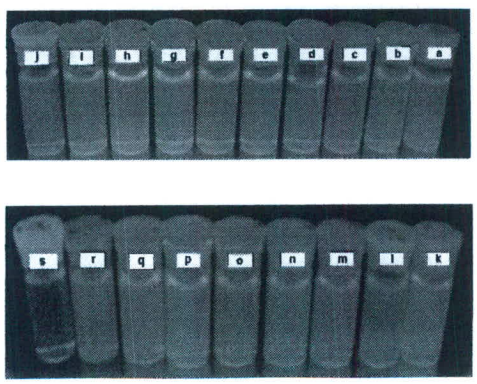


Figure 4. FL change of LD (1.0×10^{-5} mol L^{-1}) in the presence of different AAs (50×10^{-5} mol L^{-1}) in water. LD with (a) water (blank) (b) L-Methionine (c) L-Isoleucine (d) L-Histidine (e) L-Lysine (f) L-Hydroxyproline (g) L-Alanine (h) L-Cysteine (i) L-Glutamine (j) L-Tyrosine (k) L-Aspartic acid (l) L-Proline (m) L-Serine (n) L-Asparagine (o) L-Leucine (p) L-Valine (q) L-Threonine (r) L-Glutamic acid (s) L-Arginine. Excitation wavelength (λ_{Ex}) = 275 nm.

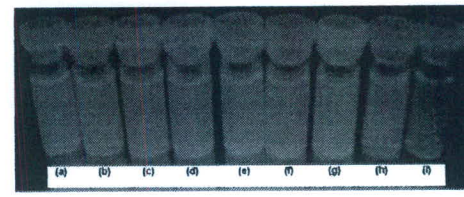


Figure 5. FL change of LD (10×10^{-5} mol L^{-1}) in the presence of various concentrations of (a) 0 (b) 0.38 (c) 0.75 (d) 1.5 (e) 3 (f) 6 (g) 12 (h) 25 (i) 50×10^{-5} mol L^{-1} of L-arginine. Excitation wavelength (λ_{Ex}) = 275 nm.

Conclusions

In summary, LD was prepared as a selective polymeric chemosensor for AAs. Among screened AAs, LD displayed high selectivity towards L-arginine. In the presence of 50×10^{-5} mol L^{-1} of L-arginine, the FL of LD undergoes to completion. Since LD is highly soluble in water, LD serves as a potential intracellular chemosensor for detection of L-arginine.

Acknowledgements The Thailand Research Fund/ Commission on Higher Education's research grants to P.T. (RTA5180003) and S.S. (TRG5380029), and the Development and Promotion of Science and Technology Talents Project's scholarship to W.N. are gratefully acknowledged. We are also grateful to the partial support from National Center for Genetic Engineering and Biotechnology (BIOTEC).

References

(1) A. P. de Silva, H. Q. N. Gunaratne, T. Gunnalaugsson, A. J. M. Huxley, C. P. McCoy, and J. T. Rademacher, Chem. Rev., **97**, 1515 (1997).

(2) B. Valeur, and L. Leray, Coord. Chem. Rev., **205**, 3 (2000).

(3) M. H. Keefe, K. D. Benkstein, and J. T. Hupp, Coord. Chem. Rev., **205**, 201 (2000).

(4) B. Adhikari, and S. Majumdar, Prog. Polym. Sci., **29**, 699 (2004).

(5) Y. Xu, L. Zheng, X. Huang, Y. Cheng, and C. Zhu, Polymer, **51**, 994 (2010).

(6) J. Meng, G. Wei, X. Huang, Y. Dong, Y. Cheng, and C. Zhu, Polymer, **52**, 363 (2011).

(7) X. Huang, J. Meng, Y. Dong, Y. Cheng, and C. Zhu, Polymer, **51**, 3064 (2010).

(8) H. Zhang, C. Smanmoo, T. Kabashima, J. Lu, and M. Kai, Angew. Chem. Int. Ed., **46**, 8226 (2007).

(9) Z. Wang, Z. Y. Wang, J. Ma, W. J. Bock, and D. Ma, Polymer, **51**, 842 (2010).

(10) J. Li, C. E. Kendig, and E. E. Nesterov, J. Am. Chem. Soc., **129**, 15911 (2007).

(11) H. O. Yoo, S. K. Chae, J. M. Kim, and D. J. Ahn, Macromol. Res., **15**, 478 (2007).

(12) E. L. Dane, S. B. King, and T. M. Swager, J. Am. Chem. Soc., **132**, 7758 (2010).
(13) G. Wu, and S. M. Morris Jr., Biochem. J., **336**, 1 (1998).
(14) R. M. Palmer, D. S. Ashton, and S. Moncada, Nature, **333**, 664 (1988).
(15) L. Xian, S. Liu, Y. Maa, and G. Lua, Spectrochim. Acta A., **67**, 368 (2007).
(16) K. Liu, L. He, X. He, Y. Guo, S. Shao, and S. Jiang, Tetrahedron Lett., **48**, 4275 (2007).
(17) K. Ohtake, H. Natsume, H. Ueda, and Y. Morimoto, J. Control. Release, **82**, 263 (2002).
(18) M. Voicescu, M. Vasilescu, T. Constantinescu, and A. Meghea, J. Luminesc., **13**, 315 (2003).
(19) J. S. A. Simpson, A. K. Campbell, M. E. T. Ryall, and J. S. Woodhead, Nature, **279**, 646 (1979).
(20) T. Burdo, and W. R. Seltz, Anal. Chem., **47**, 1639 (1975).
(21) Z. C. Wen, and Y-B. Jiang, Tetrahedron, **60**, 11109 (2004).

Subject: 7068P accepted by PPC
From: "liuvic" <vctrliu@hotmail.com>
Date: Fri, June 10, 2011 8:44 pm
To: scptb@mahidol.ac.th
Priority: Normal
View Full Header | View Printable Version | Download this as a file
Options: Block Sender
Block Sender's Domain

Dear authors:

Congratulations. Your article (7068P,
N. Kanjanathaworn, C. Kaewsaneha,
D. Polpanich, K. Jangpatarapongsa
and P. Tangboriboonrat
Composite Nanoparticles on the Natural
Rubber Latex Glove for Reduction of
Surface Friction and Cytotoxicity)
submitted to AM2011 is now accepted by PPC.

The editor will send your proof later this year
before they send it for publication.
Best wishes,
Sincerely yours,
Prof. Dr. Shiquan LIU
School of Materials Science and Engineering
University of Jinan (West Campus)
Jiwei Road 106
Jinan 250022, Shandong
China
tel:0086-(0)15953169792
fax:0086-531-87974453

Composite Nanoparticles on the Natural Rubber Latex Glove for Reduction of Surface Friction and Cytotoxicity

N. Kanjanathaworn[1,a], C. Kaewsaneha[1,a], D. Polpanich[2,b], K. Jangpatarapongsa[3,c] and P.Tangboriboonrat[*1,a]

[1]Department of Chemistry, Faculty of Science, Mahidol University, Phyathai, Bangkok, Thailand
[2]National Nanotechnology Center (NANOTEC), Thailand Science Park, Klong Luang, Pathumthani, Thailand
[3]Department of Clinical Microbiology, Faculty of Medical Technology, Mahidol University, Bangkok, Thailand
[a]scptb@mahidol.ac.th, [b]duangporn@nanotec.or.th, [c]mtkjp@mahidol.ac.th

Keywords: Composite, Surface modification, Rubber, Nanoparticle, Cytotoxicity

Abstract. Poly(methyl methacrylate) (PMMA) particles were deposited *via* the Layer-by-Layer technique onto sulphur prevulcanized natural rubber latex film grafted with polyacrylamide (SPNR-g-PAAm). Besides an increase in surface hardness and roughness, hence, decrease of the surface friction of SPNR glove, a direct contact between skin and rubber film was reduced. Consequently, it was expected that the allergic problem to certain sensitive individuals and cytotoxic potential caused by the leachable non-rubbers (proteins) and lubricant powder sprinkled onto SPNR glove would be lowered. The SPNR and SPNR-g-PAAm coated with PMMA particles were extracted by using the culture medium and subjected to the *in vitro* cytotoxicity evaluation on L-929 fibroblasts. Results showed that the cytotoxicity was effectively reduced by coating PMMA particles onto the grafted rubber film. In order to improve both the binding ability with SPNR and antimicrobial activity, the PMMA-chitosan core-shell particles were prepared for further depositing onto the non-grafted SPNR film. Moreover, the nanocapsules containing an aqueous core of disinfectant agent (chlorhexidine digluconate) and poly(methyl acrylate) or sulphur prevulcanized skim rubber shell were prepared for being embedded in SPNR glove.

Introduction

Sulphur prevulcanized natural rubber (SPNR) latex is generally used as raw material for the gloves' production due to the good physical properties of thin film. However, the high surface friction between skin and glove still causes the drawback and powder talc or cornstarch is traditionally applied to solve this problem. Unfortunately, the lubricant powder is not appropriate for the gloves used in certain applications, e.g., in electronic and biomedical fields. Therefore, the mimetic system, i.e., the deposition of hard poly(methyl methacrylate) (PMMA) particles onto SPNR film grafted with poly(acrylamide) (SPNR-g-PAAm) *via* the Layer-by-Layer (LbL) technique, was investigated [1-4]. Besides effectively roughening the film surface, the presence of PMMA particles reduced the direct contact area between SPNR film and skin. Therefore, the allergic and cytotoxic potential caused by non-rubbers or additives would effectively decrease. However, the penetration from needle or sharp objects through the glove might lead to infection for the medical personnel who contact to blood or body fluids from patients [5]. The three-layer glove consisting of disinfectant or

antiseptic agent, i.e., aqueous chlorhexidine digluconate (CHD), incorporating between two elastomeric layers is, therefore, desired [6].

In this present work, the soap-free PMMA latexes and the PMMA latex particles stabilized by chitosan (PMMA-CS) were prepared and then deposited *via* the LbL technique onto the SPNR-g-PAAm and non-grafted SPNR sheets, respectively. The modified rubber was characterized by scanning electron microscope (SEM) and atomic force microscope (AFM). An *in vitro* test on L-929 fibroblast cells was used for investigation of the cytotoxicity of rubber film coated with PMMA particles. In addition, the nanocapsules of poly(methyl acrylate) (PMA) containing an aqueous solution of CHD were synthesized [6-8]. The aggregate of CHD-PMA nanocapsules was, subsequently, used as a core for the preparation of composite particle having sulphur prevulcanized skim latex (SPVS) particles as shell *via* the heterocoagulation technique. The coherent film of SPVS is expected to be miscible with the SPNR substrate when coating with these core-shell particles for further preparation of medical gloves.

Experimental

Latexes. SPNR latex (Dr.Boo Co. Ltd., Thailand) was used for preparation of SPNR-g-PAAm [3,4]. SPVS was prepared from skim latex (5% dry rubber content) as described elsewhere [9].

Preparation of PMMA and PMMA-CS latexes. PMMA latexes with different sizes were prepared at 80°C for 2 h by the soap-free emulsion polymerization using potassium persulphate (0.18 g) dissolved in deionized water (137 g) and various MMA contents (0.18-3.28 M) [3]. The PMMA-CS particles were synthesized *via* the miniemulsion polymerization process at 80°C for 2 h by using 2,2' azobisisobutyronitrile as initiator, hexadecane as hydrophobe and oligochitosan (1% w/v in 0.1 M acetic acid) as stabilizer. The size and zeta potential of particle were measured by a Zetasizer (Malvern) while its morphology was observed under TEM (Phillips, EM 400).

Preparation of CHD-PMA/SPVS composite particle. CHD-PMA nanocapsules in cyclohexane, prepared *via* the modified nanoprecipitation technique, were redispersed in deionized water and 0.5% w/v sodium dodecyl sulphate (SDS) aqueous solution (1:1) to produce cationic and anionic nanocapsules, respectively [8]. The homocoagulated CHD-PMA at the weight ratio of cationic to anionic nanocapsules of 40:60 was used as a core of CHD-PMA/SPVS composite particle. Nonidet, a nonionic surfactant (10% w/w of dried nanocapsules) was adsorbed onto the aggregate and a known amount of 1% CHD-PMA(Nonidet) was mixed with 1% SPVS latex at pH 2 in an Erlenmeyer flask at room temperature. The blending ratio was calculated from the theoretical number (N_{max}) [8,9]. The zeta potential and morphology of the CHD-PMA/SPVS composite latex particle under TEM were examined.

Deposition of PMMA or PMMA-CS particles on rubber. A piece of SPNR-g-PAAm or SPNR sheet, was dipped into PMMA or PMMA-CS latex. The sample was washed with Milli-Q water three times and dried at room temperature before being characterized. The surface coverage, a ratio of the area of deposited PMMA particles to selected area, was determined under SEM (Hitachi, S-2500). The surface morphology and roughness of the modified rubber were examined by using AFM. The SPNR and SPNR-g-PAAm coated with PMMA particles were extracted by the culture medium and subjected to the *in vitro* cytotoxicity evaluation on L-929 fibroblasts as previously explained [4].

Results and discussion

Effect of PMMA particles. SEM and AFM techniques confirmed the adsorption of mono-dispersed PMMA particles onto the SPNR-g-PAAm surface in the form of monolayer [3]. With increasing average size of PMMA from 162, 364, 480 and 626 nm (at surface coverage of 12%), the

AFM in tapping mode indicated the increase in surface mean roughness from 50, 60, 80 and 89 nm and the decrease of friction coefficient from 2.0, 1.9, 1.6 and 1.4, respectively. Due to the decrease of contact area of the top surface of the sample, the presence of PMMA particles on the rubber surface would also cause the change in surface chemical compositions.

***In vitro* cytotoxicity test on L-929 fibroblasts.** The SPNR and SPNR-g-PAAm coated with PMMA particles were extracted at 37°C for 24 h by using the culture medium. After mixing the extracts or the culture medium (negative control) with L-929 fibroblast cells for 6 days, the number of cell colonies when cells proliferated and theirs morphologies are shown in Fig. 1.

As compared to the negative control, $\leq$ 12.5% diluted sample slightly affected the growth inhibition of cells. When compared with the positive control (unmodified SPNR) at the extract concentrations $\leq$ 25%, the significant decrease of growth inhibition indicated that the cytoxicity was effectively reduced by the coating PMMA particles onto the SPNR-g-PAAm.

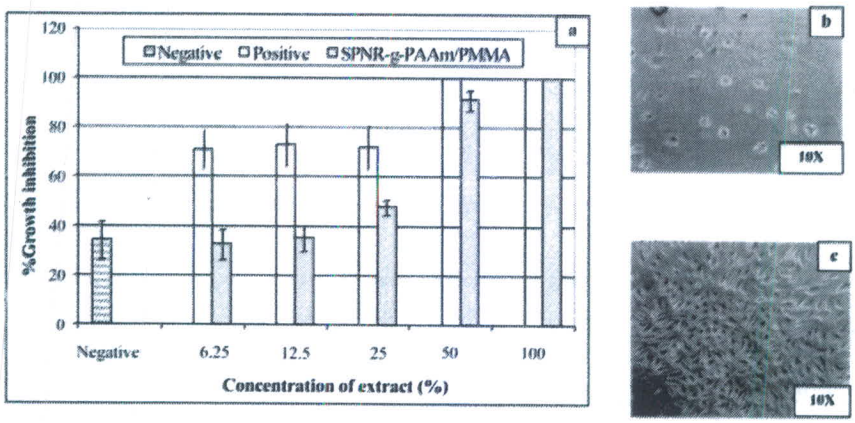


Fig. 1 Growth inhibitions of L-929 fibroblasts as a function of concentrations of the extract of SPNR-g-PAAm/PMMA films compared with that of SPNR (positive control) (extraction time 24 h, 37°C) and of the medium without extract (negative control) (a), morphology of L-929 cells incubated with the extract of SPNR (b) and with that of SPNR-g-PAAm/PMMA (c) [4].

Surface modification of SPNR film by PMMA-CS particles. TEM image of monodisperse and spherical PMMA-CS particles (average size = 380 nm) is shown in Fig. 2(a). Theirs positive zeta potentials at pH ranging from 2 to 7 in Fig. 2(b) confirmed the presence of CS as the outer layer. These cationic particles could electrostatically attract the negative charges derived from non-rubbers (protein-lipid) at the surface of SPNR sheet as observed under SEM in Fig. 2(c). The formation of aggregates was possibly caused from the attractive capillary force between these particles during drying step [3]. In order to increase particle repulsion, various CS concentrations were added into the PMMA-CS latex. The increase in hydrodynamic volume of PMMA-CS after adding different CS concentrations was observed.

Preparation of CHD-PMA/SPVS composite particles. Before preparation of CHD-PMA/SPVS core-shell particle, the size of core was increased by homocoagulation of CHD-PMA nanocapsules having oppositely charges. When the weight ratio of cationic:anionic nanocapsules was 40:60, the largest size of homocoagulated CHD-PMA or aggregate of 415 nm with their zeta potential of -54 mV were obtained. The aggregate covered with Nonidet molecules having PEO moieties could form complex *via* hydrogen bonding at pH 2 with protein-lipid and/or SDS molecules on the SPVS shell particles. The zeta potentials of all blends at various ratios (N_{max}, $N_{max}/2$, $N_{max}/4$ and $N_{max}/8$) were

positive and reached the maximum value of +25.7 mV at N_{max}. This value which was vastly different from that of the CHD-PMA(Nonidet) (-19.6 mV) but approached that of SPVS particles (+40.8 mV) confirmed the presence of SPVS as the outer layer of the composite particles. The TEM micrographs of aggregate CHD-PMA(Nonidet) and CHD-PMA/SPVS composite particles at N_{max} before and after being heated at 40°C for 3 h are shown in Fig. 3.

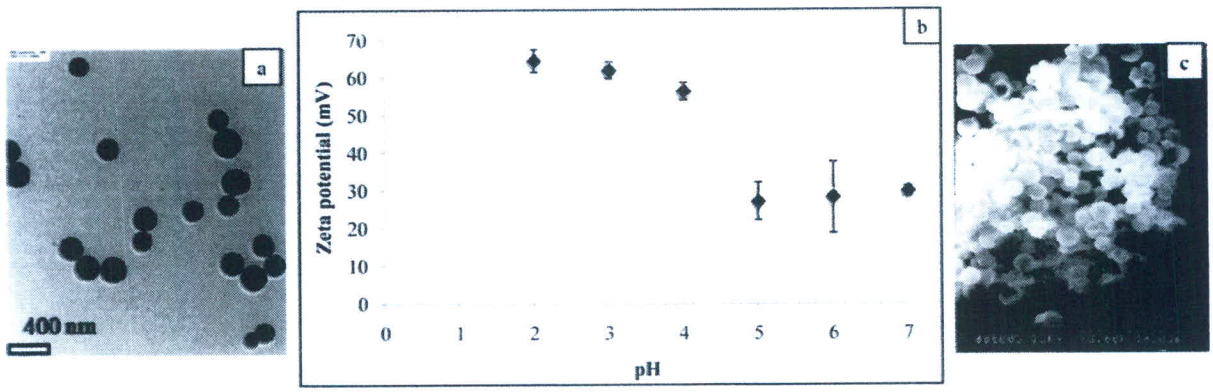


Fig. 2 TEM micrograph (a), zeta potentials of PMMA-CS particles at different pH (b) and SEM micrograph of SPNR surface coated with PMMA-CS particles (c).

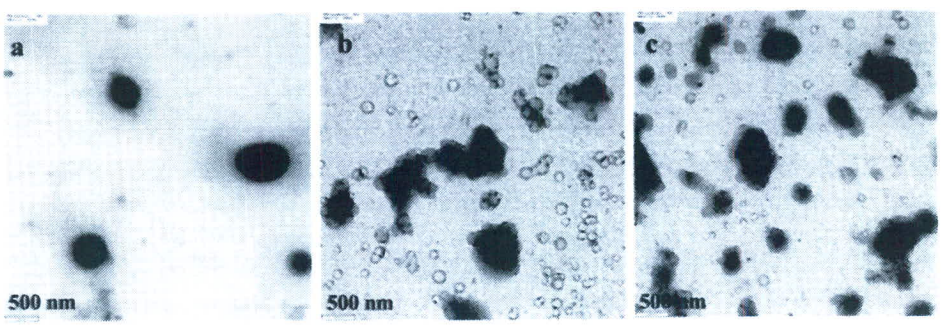


Fig. 3 TEM micrographs of aggregate CHD-PMA(Nonidet) (a), CHD-PMA/SPVS composite particles before (b) and after being heated at 40°C for 3 h (c).

In Fig. 3(b), the CHD-PMA/SPVS composite particles consisted of the SPVS particles (light) surrounding an aggregate CHD-PMA(Nonidet) core (dark) as shown in Fig. 3(a). After raising the temperature to 40°C for 3 h, the SPVS particles were partially fused to provide the composite CHD-PMA/SPVS core-shell particle as shown in Fig. 3(c). The coherent film of the outer SPVS shell would be miscible with the SPNR film used as the substrate for further gloves' preparation.

Summary

The cytotoxicity to L-929 fibroblast cells and surface friction of SPNR film were effectively reduced by coating with PMMA latex particles. With the aim to improve the binding ability with SPNR, antimicrobial and antiseptic activity, the PMMA-CS and the CHD-PMA/SPVS core-shell particles were successfully prepared. The deposition of these particles onto the non-grafted SPNR film for further gloves' preparation was under investigation.

Acknowledgement

Research grant (RTA5180003) from The Thailand Research Fund (TRF)/the Commission on Higher Education (CHE) is gratefully acknowledged.

References

[1] A. Sruanganurak, K. Sanguansap, P. Tangboriboonrat: Colloid Surf. A Vol. 289 (2006), p. 110

[2] A. Sruanganurak, P. Tangboriboonrat: Colloid Surf. A Vol. 301 (2007), p. 147

[3] W. Anancharungsuk, W. Taweepreda, S. Wirasate, R. Thonggoom, P. Tangboriboonrat: J. Appl. Polym. Sci. Vol. 115 (2010), p. 3680

[4] W. Anancharungsuk, D. Polpanich, K. Jangpatarapongsa, P. Tangboriboonrat: Colloid Surf. B Vol. 78 (2010), p. 328

[5] R.G. Busnel, G. Argy: U.S. Patent 5,024,852. (1991)

[6] S. Tanpantree, P. Opaprakasit, S. Loykulnant, W. Kangwansupamonkon, P. Tangboriboonrat: J. Appl. Polym. Sci. Vol. 117 (2010), p. 1798

[7] U. Paiphansiri, P. Tangboriboonrat, K. Landfester: Macromol. Biosci. Vol. 6 (2006), p. 33

[8] C. Kaewsaneha, P.Tangboriboonrat, D. Polpanich, S. Smanmoo: Macromol. Res. Vol. 18 (2010), p. 876

[9] U. Paiphansiri, P. Tangboriboonrat: Colloid. Polym. Sci. Vol. 284 (2006), p. 251

เอกสารแนบ 5.2.1

Editorial Manager(tm) for Macromolecular Research
Manuscript Draft

Manuscript Number: MACRO-11-499

Title: Preparation of Superparamagnetic Polystyrene-based Nanoparticles Functionalised by Acrylic Acid

Article Type: (Original) Article

Keywords: Functionalisation; Magnetic nanoparticle; Miniemulsion polymerisation; Polystyrene

Corresponding Author: Duangporn Polpanich, Ph.D.

Corresponding Author's Institution: National Nanotechnology Center

First Author: Duangporn Polpanich, Ph.D.

Order of Authors: Duangporn Polpanich, Ph.D.;Lalida Charoenmark;Raweewan Thiramanas;Pramuan Tangboriboonrat

Abstract: This work aimed to reduce the steps used for preparing homogeneous and functionalised magnetic polymeric nanoparticle (MPNP) under mild condition. Fe3O4 magnetic nanoparticle (MNP) was synthesised by the chemical co-precipitation of an aqueous Fe3+/Fe2+ solution with NH4OH at room temperature under N2 atmosphere. After dispersing MNP coated with oleic acid into a mixture of styrene (St) and acrylic acid (AA) monomers, the MPNP functionalised with AA was directly produced via the miniemulsion polymerisation without using magneto-template. When mixing a crosslinking agent (divinyl benzene; DVB) with St and AA in the polymerisation recipe, we obtained the homogeneous distribution of MNP (53%) in the PS/DVB matrix without the appearance of non-magnetic polymer particle. The superparamagnetic MPNP was, therefore, fulfilled criteria for further use in bio-related applications.

Suggested Reviewers: Gerard Riess
Laboratoire de Chimie Macromoleculaire, Ecole Nationale Superieure de Chimie, Université de Haute Alsace
G.Riess@uha.fr

Jean-Claude Brosse
Laboratoire de Chimie Organique Macromoléculaire, Faculté des Sciences
jean-claude.brosse@univ-lemans.fr

James Runt
Department of Materials Science and Engineering,Pennsylvania State University
runt@psu.edu

***Manuscript**
Click here to download Manuscript: Charoenmark L_Macromol Res.doc

Preparation of Superparamagnetic Polystyrene-based Nanoparticles Functionalised by Acrylic Acid

Lalida Charoenmark[1], Duangporn Polpanich[2,*], Raweewan Thiramanas[2] and Pramuan Tangboriboonrat[1]

[1]*Department of Chemistry, Faculty of Science, Mahidol University, Bangkok 10400, Thailand*

[2]*National Nanotechnology Center, National Science and Technology Development Agency, Thailand Science Park, Pathumthani 12120, Thailand*

*Corresponding Author: Dr. Duangporn Polpanich

E-mail: duangporn@nanotec.or.th

Tel: +66 2564 7100 ext. 6564

Fax: +66 2564 6981

Running head: Superparamagnetic Polystyrene-based Nanoparticles Functionalised by Acrylic Acid

Abstract:

This work aimed to reduce the steps used for preparing homogeneous and functionalised magnetic polymeric nanoparticle (MPNP) under mild condition. Fe_3O_4 magnetic nanoparticle (MNP) was synthesised by the chemical co-precipitation of an aqueous Fe^{3+}/Fe^{2+} solution with NH_4OH at room temperature under N_2 atmosphere. After dispersing MNP coated with oleic acid into a mixture of styrene (St) and acrylic acid (AA) monomers, the MPNP functionalised with AA was directly produced *via* the miniemulsion polymerisation without using magneto-template. When mixing a crosslinking agent (divinyl benzene; DVB) with St and AA in the polymerisation recipe, we obtained the homogeneous distribution of MNP (53%) in the PS/DVB matrix without the appearance of non-magnetic polymer particle. The superparamagnetic MPNP was, therefore, fulfilled criteria for further use in bio-related applications.

Keywords: Functionalisation, Magnetic nanoparticle, Miniemulsion polymerisation, Polystyrene.

Introduction

Magnetic nanoparticle (MNP) has attracted more and more scientific and technological interest because of its unique properties under applied magnetic field. In most applications, e.g., magnetically guided drug delivery, cell separation, protein purification and molecular diagnostics, monodisperse MNP is required in order to have uniform chemical and physical properties which depend strongly on particle size and size distribution.[1,2] To date, a range of techniques, e.g., the thermal decomposition and hydrothermal synthesis, have been developed for the preparation of MNP.[3,4] Among these techniques, the chemical co-precipitation is a cost-effective and simple method to produce the high yield of MNP.[5,6] Iron oxide MNP, i.e., magnetite (Fe_3O_4) or maghemite (γ-Fe_2O_3), is obtained from precipitating an aqueous Fe^{3+}/Fe^{2+} salt solution under base condition. The size, shape and composition of MNP can be controlled by the type of salt used, Fe^{3+}/Fe^{2+} ratio, reaction temperature, pH and ionic strength of the media.[1,6,7] The fraction of superparamagnetic components of cobalt ferrite ($CoFe_2O_4$) MNP decreased as the precipitation temperature increased with the increased particle size.[8] In addition, the selection of a proper surfactant is the key in the production of monodisperse iron oxide nanoparticle.[7] It was reported that oleic acid (OA) is an effective surfactant to stabilise Fe_3O_4 MNP. The co-precipitation method is conventional for grafting MNP with oleate or OA and for preventing the agglomeration of the ferrofluid or OA-MNP dispersed in organic solvent and non-polar monomer.[9] When a monomer, e.g., styrene (St), containing OA-MNP is polymerised, magnetic polymeric nanoparticle (MPNP), a polymer encapsulating MNP, is obtained. The stability of MPNP in an aqueous solution derived from the added ionic surfactant or hydrophilic polymer and functionalised monomer can be the conjugation site for attachment MPNP with biomolecules.[10] The MNP functionalised

by glucuronic acid was covalently attached to specific primer for detection of *BCR/ABL* fusion gene in chronic myelogenous leukemia with high sensitivity and high specificity.[11]

In order to obtain monodisperse MPNP with high magnetic content, miniemulsion polymerisation is one of the most effective methods used for encapsulating MNP.[12] By using this polymerisation technique, the stable monomer droplets with 50-500 nm in diameter are generated when applying ultrasonic. Since the particle nucleation occurs primarily within the droplets, the size of MPNP is controlled *via* the size of the initial emulsion. Moreover, the hydrophobic inorganic particles can be directly dispersed in the monomer phase. The MPNP with the magnetic content of 20–40%wt was obtained by polymerisation of St miniemulsion containing OA/sodium dodecyl sulphate (SDS) bilayer stabilised magnetite.[13] The magnetic content was increased when a two-step preparation route including ferrofluid droplet preparation and swelling of the droplets with monomer were applied.[10] Recently, the less complicated process using minidroplet of Fe_3O_4 dispersed in octane as the magneto-template miniemulsion polymerisation of St-divinyl benzene (DVB) has been applied for producing uniform-sized MPNP with high magnetic content.[12] However, the presence of octane in the Fe_3O_4 minidroplet induced the phase separation of polystyrene (PS) from the magneto-template due to the low viscosity of the polymerisation medium. The use of monomer as a dispersed phase of the MNP was found to be an effective way to solve this problem.[12,14]

With the aim of reducing the steps used for preparing homogeneous and functionalised MPNP under mild condition, we synthesised Fe_3O_4 MNP *via* the co-precipitation method at room temperature using OA as stabiliser. Then, the prepared MNP was mixed with St/AA or St/DVB/AA monomer which was subsequently

polymerised *via* the miniemulsion process without using magneto-template. The effects of OA and DVB on the final morphology of the prepared MPNP were considered. Their crystallographic structure, composition and magnetisation were determined. Distribution of the MNP into PS/AA or PS/DVB/AA was investigated under Transmission Electron Microscope (TEM). The amount of AA presented in PS/DVB/AA-MNP was also examined *via* the conductometric back titration technique.

Experimental

Materials. St (Fluka, Purum) and AA (Fluka, Purum) monomers were purified by passing through aluminium oxide column and distilled under reduced pressure. The purified monomers were stored in a refrigerator at 4°C until use. Anhydrous $FeCl_3$ (Riedle-de Haen), $FeCl_2 4H_2O$ (Fluka, Purum), NH_4OH solution (25%v/v) (Merck, AR), OA (Fluka, Natural from suet), SDS (Fluka, GC), potassium persulphate (KPS; Fluka, Puriss), hexadecane (HD; Fluka, Purum), DVB (Merck), NaOH (Lab-scan, AR), HCl (Merck, GR) and methanol (Merck, AR) were used without further purification. Deionised water was used throughout this work.

Preparation of MNP and MPNP. $FeCl_3$ (2.92 g) and $FeCl_2.4\ H_2O$ (1.76 g) were dissolved in milli-Q water (80 ml) under nitrogen atmosphere while stirring at 400 rpm. After adding NH_4OH solution (40 ml), the mixture immediately turned to black. The reaction was allowed to continue under centrifugation (Beckman; JA 20) at 5,000 rpm for 15 min. The precipitate MNP was mixed with St (15 ml) and OA (10 %v/v based on St) with stirring for 10 min. The ferrofluid (OA-MNP-St) was centrifuged at 5,000 rpm for 15 min to remove large aggregate. Then the upper phase

containing stable MNP was separated into 2 portions. The first portion of OA-MNP-St (7.0 g) was mixed with St monomer (3.0 g) whereas the second one was repeatedly washed with methanol to remove excess OA before redispersing in St (1.5 g)/DVB (1.0 g). In both cases, AA (3% wt based on St) and HD (0.3 g) were added. After sonication for 2 min, each mixture was poured into an aqueous solution of SDS (0.072 g of SDS in 24.0 g of deionised water) under continuous stirring for 1 h for pre-emulsification. It was then ultrasonicated for 10 min at 60% amplitude (Vibracell, VCX 700) in an ice bath. After raising temperature to 72°C, an aqueous solution of KPS (0.1 g KPS in 2 g of deionised water) was introduced into the reaction mixture to start the polymerisation. The reaction was left for 22 h under nitrogen atmosphere. The obtained PS/AA-MNP and PS/DVB/AA-MNP were purified by dialysis method (pore size of dialysis membrane = 25.5 mm, MWCO = 6,000-8,000 Da) before being characterised.

Characterisations of MNP and MPNP. X-ray powder diffraction (XRD; Rigaku TTRAX III, 18kW) with a high power $CuK\alpha_a$ X-ray source was used to investigate the crystallographic structure of the prepared MNP and MPNP. The phases of sample were identified through the Power Diffraction File (PDF) database (JCPDS, International Centre for Diffraction Data). The average crystallite size of MNP was calculated from the Debye-Sherrer equation,[15]

$$D = \frac{0.9\lambda}{\beta \cos\theta} \qquad (1)$$

where D is average crystallite size (Å), λ is X-ray wavelength ($CuK\alpha_a$: λ=1.5418 Å), β is the full width at half maximum (FWHM) (in radians) and θ is the Bragg diffraction angle.

Thermogravimetric analysis (TGA; Mettler Toledo, SDTA851), Fourier transform infrared spectroscopy (FTIR; Perkin Elmer, Spectrum GX) and Zetasizer (Malvern, Nano ZS) were applied to determine the magnetic content, composition and zeta potential of the prepared MNP and/or MPNP, respectively. Vibrating sample magnetometer (VSM; Lakechore, 7403) was used for recording the magnetisation curve. The magnetic moment of each sample was examined over a range of applied magnetic field from -10 to 10 kOe. Particle morphology and selected area electron diffraction (SAED) pattern of the MNPs were observed under TEM (JEOL, JEM-2010).

For determination of surface charge density (σ) representing the amount of ionised groups existing on the surface of MPNP, the conductimetric back titration was applied.[16] The PS/DVB/AA-MNP (500 µl) was dispersed in deionised water (25 ml) under stirring. Excess amount of 1 M NaOH (50 µl) solution was added into the sample before being titrated with 1 M HCl aqueous solution. The conductivity was measured by using conductimeter (ORION, 180) equipped with a glass conductivity cell (K=1). The number of microequivalent of acid groups per gram ([Acid]) were calculated by using the following equation,[17]

$$[\text{Acid}] = \frac{V_{HCl} \cdot M_{HCl} \cdot 10^3}{V_{part}(\text{ml}) \cdot \frac{SC_{part}}{100}} \quad (\mu\text{eq/g}) \qquad (2)$$

where V_{HCl} is volume of HCl at equivalent point (ml), V_{part} is sample volume (ml), M_{HCl} is concentration of HCl (M) and SC_{part} is solid content of the magnetic latex. The σ value of latex was calculated from equation (3),

$$\sigma = \frac{\rho_{part}}{6} \cdot D_h \cdot [\text{Acid}] \cdot N_A \cdot e \quad (\mu\text{C/cm}^2) \qquad (3)$$

where ρ_{part} is density of MPNP, D_h is particle diameter (cm), N_A is Avogadro's number ($6.022 \times 10^{23} \text{mol}^{-1}$) and e is electronic charge in coulombs (1.602×10^{-19} C).

Results and Discussion

MPNP functionalised by PAA was prepared in two stages: i) synthesis of initial ferrofluid or OA-MNP-St and ii) polymerisation of St/AA-MNP or St/DVB/AA-MNP. Each step was followed by characterisation of the product including crystallographic structure, morphology, chemical composition and magnetisation.

Preparation and Characterisations of MNP. Fe_3O_4 was synthesised at room temperature through the chemical co-precipitation of the mixture of Fe^{3+}/Fe^{2+} at stoichiometric ratio of 2:1 in order to avoid the formation of nonmagnetic hydroxides ($Fe(OH)_2$ and $Fe(OH)_3$).[14,18] The MNP obtained from using NH_4OH as the precipitator should have better crystallinity, smaller size and higher magnetisation than that using NaOH due to the gradual change of the reaction conditions.[2] It was observed that the resulted MNP was dense, black in colour and strongly attracted by a magnet. The critical oxidation of magnetite to maghemite was prevented by bubbling nitrogen gas through the solution. Since the as-prepared MNP could be flocculated mainly due to the Van der Waals force, its surface was subsequently modified by using OA through esterification with the hydroxyl group on the particle. After adding into OA mixed with St monomer, the brownish ferrofluid was stable due to the steric stabilisation generated from the hydrophobic tail of OA turned to the St phase while its carboxylated groups anchored on the surface of iron oxide nanoparticle.[14,19]

The crystallinity of OA-MNP was indicated in the XRD pattern shown in Figure 1(A). The position and relative intensity of the peaks at 220, 311, 400, 422,

511 and 440 matched well with the standard patterns of the magnetite Fe_3O_4 with inverse cubic spinel structure.[2,9] The results, therefore, confirmed the successful synthesis of Fe_3O_4. By using the Debye-Scherrer equation, equation (1), the calculated size of the OA-MNP was 8.9 nm which was similar to that determined by TEM (9 nm) as shown in Figure 1(B). This revealed that each individual particle was a single crystal.[20] It could be assumed from the square form of the particle that the inhibition factor for the crystal growth of the particle was absent.[21] The good dispersion of the particle resulted from the OA coated on the particle surface. In addition, the distinct rings which are the characteristics of polycrystalline sample of the SAED pattern are observed in Figure. 1(C). This indicated that the structure of the prepared MNPs composed of domains whose crystallograghic axes randomly oriented.[22] The pattern correlated well with that of XRD pattern in Figure 1(A).

Figure 1.

The chemical composition of the OA-MNP was analysed by FT-IR and the spectrum of OA-MNP compared to that of MNP is presented in Figure 2.

Figure 2.

In Figure 2(A), the characteristic absorption peaks at 437 and 582 cm^{-1} relating to the stretching vibration of Fe-O bond of Fe_3O_4 before coating with OA were observed. Whereas, the new absorption peaks at 1708 cm^{-1} corresponding to the C=O stretching vibration of ester bond appeared in Figure 2(B). This indicated that the carboxylic group of OA was esterified with the hydroxyl group on the surface of the MNP. The peaks at 2852 and 2923 cm^{-1} can be attributed to the stretching of saturated C-H bond of OA. From this analysis, it was evident that the as-prepared MNP was Fe_3O_4 which chemically bound to OA.

The magnetic and OA contents of the OA-MNP were determined by TGA and the thermograms are shown in Figure 3.

Figure 3.

In Figure 3(A), one-step decay at temperature less than 120°C was ascribed to water evaporation from the MNP. In the case of OA-MNP, the detection of two-step decay in Figure 3(B) indicated the presence of two types of OA. The first weight loss of 11.1% at less than 400°C corresponded to the physically adsorbed OA in the outer layer. The second one of 8.4% at 400-500°C was resulted from the inner layer of OA that covalently bound to the MNP surface.[9] Thus, the residual weight loss of 80.5% was owed to the magnetic content. Based on the mean diameter (9 nm) and magnetite density (5.16 g/cm^3) of the MNP, the calculated area occupied by an OA molecule

was 0.31 nm^2/molecule which was slightly less than the mean molecular area occupied by a single OA molecule (~ 0.42 nm^2/molecule).[23]

Preparation and Characterisations of MPNP. The PS/AA-MNP was prepared by polymerisation of St/AA containing OA-MNP (without removing excess OA) and HD. On contrary, the excess OA was removed by repetitive washing with methanol before preparation of PS/DVB/AA-MNP. In both cases, HD acted as hydrophobe to suppress the Oswald ripening in the miniemulsion system while DVB was used as crosslinker only in the latter case.[13,24] TEM micrographs of the prepared PS/AA-MNP and PS/DVB/AA-MNP are shown in Figures 4(A) and (B), respectively.

Figure 4.

In both micrographs, the PS/AA-MNP and PS/DVB/AA-MNP were spherical in shape with an average size of 148±38 and 117±28 nm and polydispersity index (PDI) of 1.2 and 1.1, respectively. The phase separation between magnetite and PS matrix, previously observed when using the conventional OA/octane-based ferrofluid, was suppressed.[14] However, the non-magnetic PS/AA particles (light phase), i.e., free from magnetic material (dark spot), and the inhomogeneous distribution of MNPs within each PS/AA-MNP particle are noticed in Figure 4(A). The formation of non-magnetic particle might be due to the immiscibility between the excess OA in the OA-MNP-St and PS. It was reported that the large amount of OA in the ferrofluid droplets could act as poor solvent for PS chains and the low viscosity of polymer matrix enhanced the possibility of non-magnetic PS/AA particle formation.[10,12] Therefore,

the abundant OA was removed before polymerisation of St/DVB/AA. Since DVB is a crosslinking agent of PS, the internal viscosity of the magnetic St/DVB/AA-MNP particles would increase during polymerisation. The homogeneous distribution of MNP in the PS/DVB/AA matrix without non-magnetic polymer particle was obtained accordingly. The previous work showed that the optimum concentration of DVB to produce the uniform distribution of MNP and to eliminate the non-magnetic polymer particle was about 20-40 wt% relative to total amount of monomer.[12] Hence, 40% of DVB based on St monomer was used in this present work. As expected, Figure 4(B) displays that MNPs were completely incorporated into the PS/DVB/AA, i.e., neither free magnetite nor the non-magnetic polymer particle appeared. The high viscosity caused from the presence of DVB inside the particle kept the Fe_3O_4 nanoparticle from moving outward. It was reported that, even the St monomer was replaced with methyl methacrylate, the well-dispersed MNP into polymer matrix containing DVB was still obtained.[12] The results confirmed that combination of the removal of the excess OA and the addition of DVB was the key role to produce the homogeneous distribution of MNP in the polymer matrix without pure polymer particle formation. Additionally, AA tended to be on the particle surface due to its hydrophilic nature. Consequently, poly(acrylic acid) (PAA) chain and/or oligomer that formed during the polymerisation was imparted electrosteric stabilisation. Since the AA monomer was added into the reaction at the initial period before pre-emulsification, the polymerisation step in our study was reduced when compared to the previous work.[13,25] Although, some carboxyl groups might be buried in the polymer matrix, most of them possibly remained on the particle surface and provided the colloidal stability of the PS/AA-MNP and PS/DVB/AA-MNP particles. This was supported by the zeta potential values of the particles which were -63.3±1.8 and -49.8±1.1 mV for PS/AA-MNP and PS/DVB/AA-

MNP, respectively. With increasing the amount of AA more than 3% based on monomer content, the MPNP was not stable possibly due to the bridging effect originated from long PAA chains.

Owing to its satisfied morphology, the PS/DVB/AA-MNP was systematically characterised. Figure 5(A) illustrates its XRD pattern which revealed that the crystallographic structure of MNP contained in the PS/DVB/AA matrix after polymerisation did not change compared to that in Figure 1(A). The low intensity peak at 2θ less than 25 degree, which related to the amorphous polymer matrix, was additionally observed.[18,26]

Figure 5.

The magnetic content which is a very important factor to alter the respond speed of the MPNP to an external magnetic field was determined from TGA and its thermogram is shown in Figure 6(A).

Figure 6.

In Figure 6(A), the two-step weight loss was observed. The first peak of 8.4% between 150 and 300°C was attributed to the dehydration and decomposition of residual surfactant and HD. The weight loss of 38.8% between 300 and 500°C was mainly due to the decomposition of polymer matrix.[24] Therefore, the magnetic content

deduced from the residual weight percentage of PS/DVB/AA-MNP was 53%. Due to the high magnetic content, the MPNP (10%v/v) could be completely separated from the aqueous phase under an externally applied magnetic field within only 3 min, as shown in Figure 6(B).

The magnetic properties of the PS/DVB/AA-MNP compared to those of the MNP and OA-MNP were investigated by VSM at room temperature and the magnetisation curves are displayed in Figure 7.

Figure 7.

From Figures. 7(A)-(C), the magnetisation versus magnetic field of the MNP, OA-MNP and PS/DVB/AA-MNP exhibited no hysteresis with undetectable remanence and coercivity at room temperature. This confirmed that all samples had superparamagnetic behaviour at room temperature.[6] The superparamagnetism enables the nanoparticles to respond to an applied magnetic field without any permanent magnetisation and rapidly redisperse after removal of the magnetic field.[10] Under applying a large external magnetic field, the magnetisation of the particle aligns with the field direction and reaches its saturation value. The saturation magnetisation (M_s) values of the MNP, OA-MNP and PS/DVB/AA-MNP were 47.4, 36.5 and 17.4 emu/g, respectively. The presence of OA and PS/DVB/AA matrix reduced the M_s value possibly because the surfactant and polymer substances changed the surface anisotropy of MNP, which led to the increase in surface spin disorientation resulting in the reduction of the magnetic moment.[27]

With the objective of further use of the prepared MPNP as a solid support for immobilisation of biomolecules, the amount of –COOH functional group originated from AA onto the PS/DVB/AA-MNP surface were quantified. Therefore, the surface charge density (σ) of the MPNP was determined by the conductimetric back titration technique. The titration result of the PS/DVB/AA-MNP is presented in Figure 8.

Figure 8.

In Figure 8, the three different intervals in the conductimetric back titration curve were observed. The rapid descending curve appeared in the first interval I corresponded to the neutralisation of excess OH^- ions of NaOH previously added causing a decrease in conductivity of the system to the first minimum point. Then, the increase in the volume of HCl to the second minimum point in interval II related to the titration of acidic groups (COO^- from AA and SO_4^- from KPS initiator) at the particle surface. Finally, the ascending back titration curve in the last interval III corresponded to the excess of HCl added. The difference of HCl volume between the two minimum points of the back titration curve (about 1.1 ml) was used to calculate the [Acid] and the σ value of PS/DVB/AA-MNP which were 919±97 μeq/g and 832±87 $\mu C/cm^2$, respectively. Our previous work revealed that the σ value of poly(styrene-*co*-acrylic acid) (St/AA) increased with increasing the amount of AA added in the reaction.[16] Due to the presence of the surface carboxyl group, the prepared PS/DVB/AA-MNP would potentially coupled with biomolecules for further applying in a wide variety of biological applications.

Conclusions

MNP coated with OA (OA-MNP) having an average size of 9 nm and 80.5% of the magnetic content was simply prepared by adding NH_4OH into an aqueous Fe^{3+}/Fe^{2+} (2:1) solution at room temperature. Through ultrasonication, the OA-MNP dispersed in St/AA or St/DVB/AA was directly emulsified for the synthesis of MPNP *via* the miniemulsion polymerisation. The use of DVB to crosslink the PS matrix enhanced the integrity of the MPNP and, hence, provided more uniform distribution of MNP without any non-magnetic polymer particle. The MPNP (53% of magnetic content) was superparamagnetic and, thus, appropriate for biomedical applications after suitable surface modification.

Acknowledgements.

Research grant (RTA5180003) from The Thailand Research Fund/Commission on Higher Education to P.T. and the scholarship from Thailand Graduate Institute of Science and Technology (TGIST)/National Science and Technology Development Agency to L.C. are gratefully acknowledged. The authors also thank Dr. Metha Rutnakornpituk for helpful comments and suggestions.

References

(1) S. Laurent, D. Forge, M. Port, A. Roch, C. Robic, L.V. Elst, and R.N. Muller, *Chem. Rev.*, **108**, 2064 (2008).

(2) R.Y. Hong, J.H. Li, H.Z. Li, J. Ding, Y. Zheng, and D.G. Wei, *J. Magn. Magn. Mater.*, **320**, 1605 (2008).

(3) Z.P. Chen, Y. Zhang, S. Zhang, J.G. Xia, J.W. Liu, K. Xu, and N. Gu, *Colloids Surf. A: Physicochem. Eng. Aspects*, **316**, 210 (2008).

(4) S. Xuan, L. Hao, W. Jiang, X. Gong, Y. Hu, and Z. Chen, *J. Magn. Magn. Mater.*, **308**, 210 (2007).

(5) J.H. Wu, S.P. Ko, H.L. Liu, M.-H. Jung, J.H. Lee, J.-S. Ju, and Y.K. Kim, *Colloids Surf. A: Physicochem. Eng. Aspects*, **313-314**, 268 (2008).

(6) A.-H. Lu, E.L. Salabas, and F. Schüth, *Angew. Chem. Int. Ed.*, **46**, 1222 (2007).

(7) A.K. Gupta, and M. Gupta, *Biomaterials*, **26**, 3995 (2005).

(8) Y.I. Kim, D. Kim, and C.S. Lee, *Physica B*, **337**, 42 (2003).

(9) W. Jiang, Y. Wu, B. He, X. Zeng, K. Lai, and Z. Gu, *J. Colloid Interface Sci.*, **347**, 1 (2010) .

(10) F. Montagne, O. Mondain-Monval, C. Pichot, and A. Elaissari, *J. Polym. Sci. Part A: Polym. Chem.*, **44**, 2642 (2006).

(11) K. Jangpatarapongsa, D. Polpanich, V. Yamkamon, Y. Dittharot, J. Peng-On, R. Thiramanas, S. Hongeng, S. Jootar, L. Charoenmak, and P. Tangboriboonrat, *Analyst*, **136**, 354 (2011).

(12) T. Gong, D. Yang, J. Hu, W. Yang, C. Wang, and J.Q. Lu, *Colloids Surf. A: Physicochem. Eng. Aspects*, **339**, 232 (2009).

(13) L.P. Ramírez, and K. Landfester, *Macromol. Chem. Phys.*, **204**, 22 (2003).

(14) N. Joumaa, P. Toussay, M. Lansalot, and A. Elaissari, *J. Polym. Sci. Part A: Polym. Chem.*, **46**, 327 (2008).

(15) Y.-D. Luo, C.-A. Dai, and W.-Y. Chiu, *J. Appl. Polym. Sci.*, **112**, 975 (2009).

(16) D. Polpanich, P. Tangboriboonrat, and A. Elaissari, *Colloid Polym. Sci.*, **284**, 183 (2005).

(17) S. Braconnot, C. Hoang , H. Fessi, and A. Elaissari, *Mater. Sci. Eng. C*, **29**, 624 (2009).

(18) C.-L. Lin, C.-F. Lee, and W.-Y. Chiu, *J. Colloid Interface Sci.*, **291**, 411 (2005).

(19) S. Meerod, G. Tumcharern, U. Wichai, and M. Rutnakornpituk, *Polymer*, **49**, 3950 (2008).

(20) S. Sun, H. Zeng, D.B. Robinson, S. Raoux, P.M. Rice, S.X. Wang, and G. Li, *J. Am. Chem. Soc.*, **126**, 273 (2004).

(21) L. Babes, B. Denizot, G. Tanguy, J.J. Le Jeune, and P. Jallet, *J. Colloid Interface Sci.*, **212**, 474 (1999).

(22) H. Yan, J. Zhang, C. You, Z. Song, B. Yu, and Y. Shen, *Mater. Chem. Phy.*, **113**, 46 (2009).

(23) L. Bromberg, L. Chen, E.P. Chang, S. Wang, and T.A. Hatton, *Chem. Mater.*, **22**, 5383 (2010).

(24) Z. Qian, Z. Zhang, and Y. Chen, *J. Colloid Interface Sci.*, **327**, 354 (2008).

(25) K. Landfester, and L.P. Ramírez, *J. Phys.: Condens. Matter*, **15**, S1345 (2003).

(26) C. Yang, Q. Shao, J. He, and B. Jiang, *Langmuir*, **26**, 5179 (2010).

(27) S. Wang, Y. Zhou, S. Yang, and B. Ding, *Colloids Surfaces B: Biointerfaces*, **67**, 122 (2008).

FIGURE CAPTIONS

Figure 1. (A) XRD pattern, (B) TEM micrograph and (C) SAED of the OA-MNP.

Figure 2. FT-IR spectra of (A) MNP and (B) OA-MNP.

Figure 3. TGA thermograms of (A) MNP and (B) OA-MNP.

Figure 4. TEM micrographs of (A) PS/AA-MNP and (B) PS/DVB/AA-MNP.

Figure 5. XRD pattern of PS/DVB/AA-MNP.

Figure 6. (A) TGA thermogram of PS/DVB/AA-MNP and (B) photographic images of the PS/DVB/AA-MNP before and after applying magnetic field.

Figure 7. Magnetisation curves of (A) MNP, (B) OA-MNP and (C) PS/DVB/AA-MNP measured by VSM at room temperature.

Figure 8. Conductimetric back titration curve of PS/DVB/AA-MNP.

Figure 1
Click here to download high resolution image

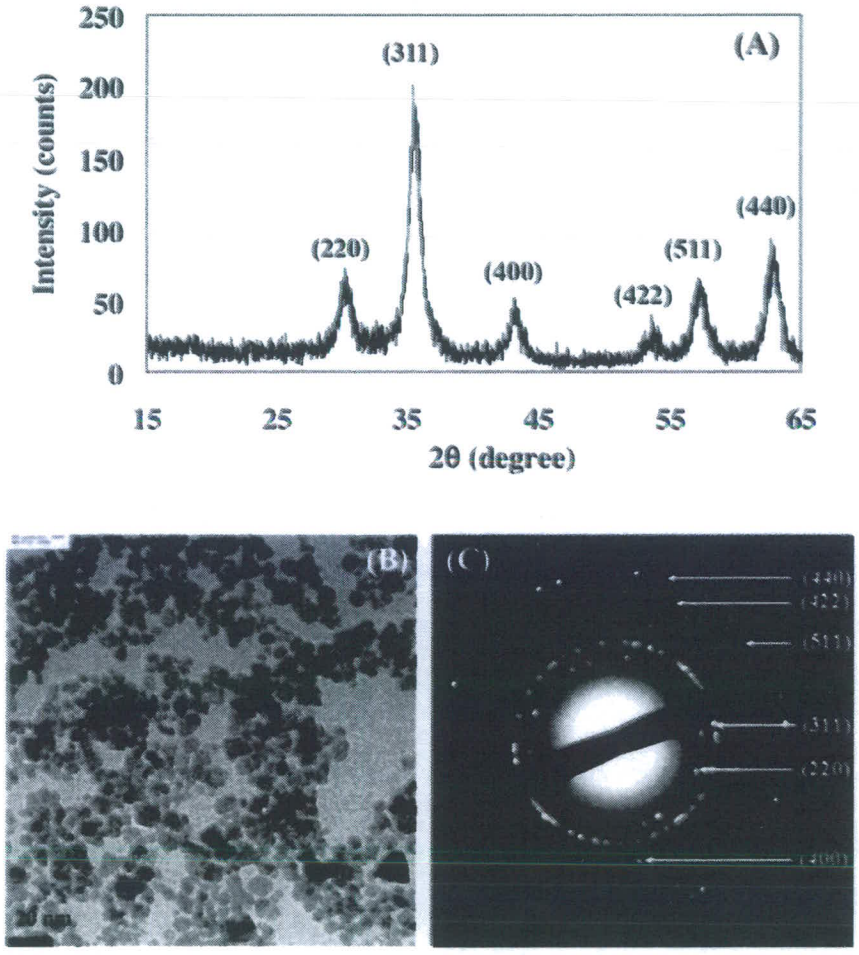


Figure 2
Click here to download high resolution image

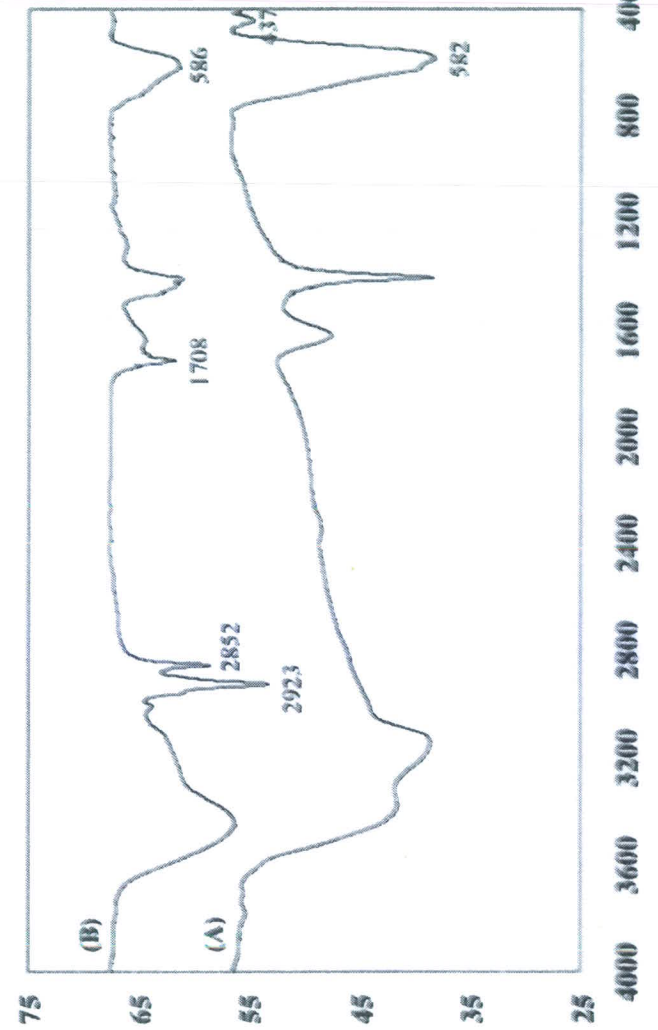


Figure 3
Click here to download high resolution image

Figure 4
Click here to download high resolution image

Figure 5
Click here to download high resolution image

Figure 6
Click here to download high resolution image

Figure 7
Click here to download high resolution image

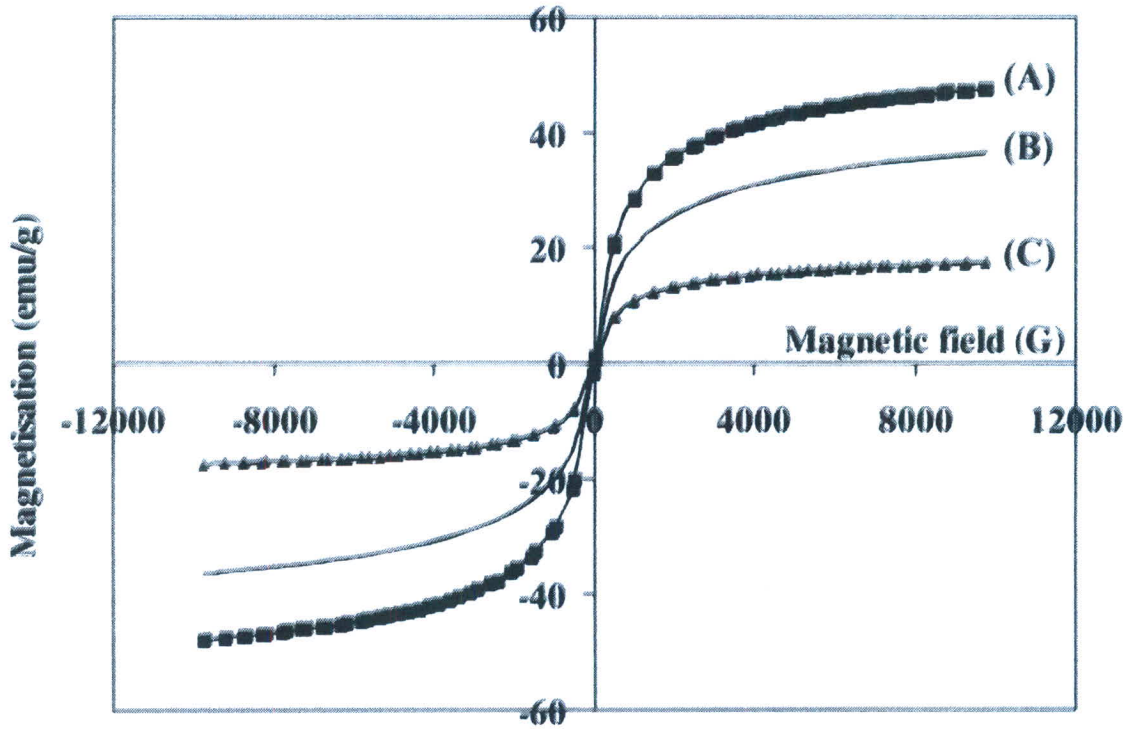
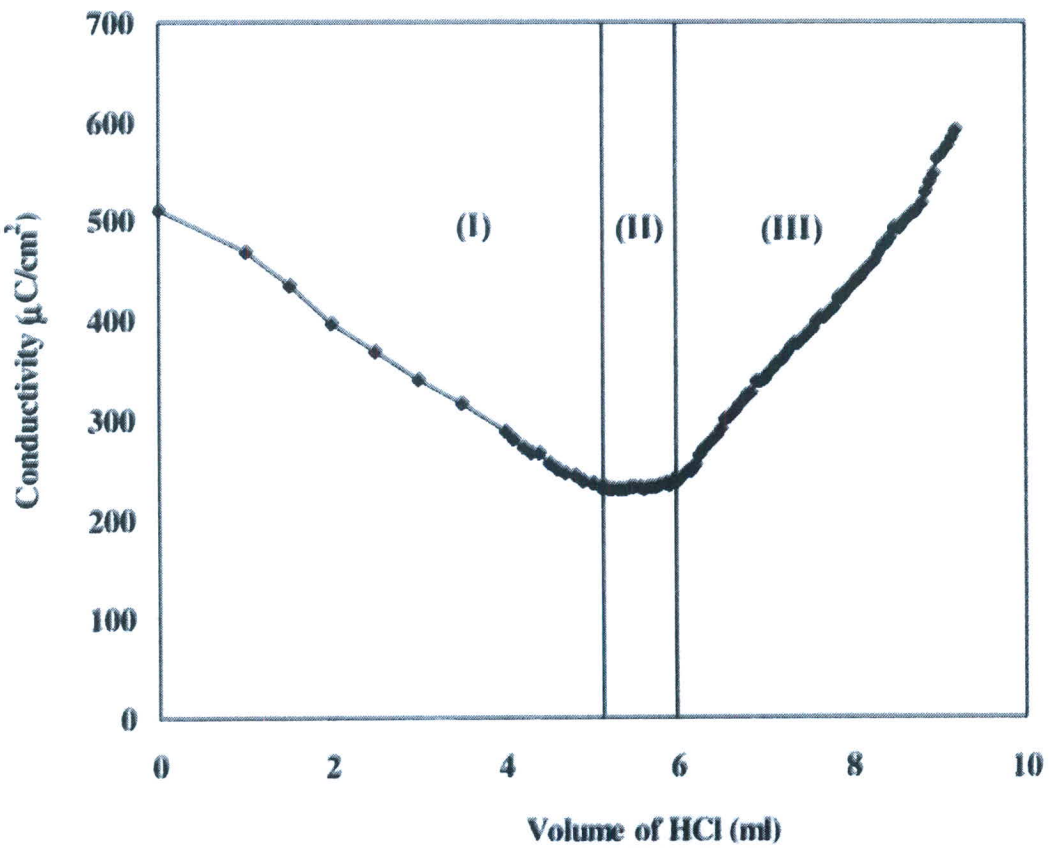


Figure 8
Click here to download high resolution image



***Cover letter**
Click here to download Cover letter: Cover letter-Polpanich D.doc

Professor Chulhee Kim
Editor-in-Chief
Department of Polymer Science and Engineering,
Inha University
Incheon, Korea
chk@inha.ac.kr

June 6, 2011

Dear Professor Chulhee Kim,

Attached please find the manuscript titled *"Preparation of Superparamagnetic Polystyrene-based Nanoparticles Functionalised by Acrylic Acid"* submitted for publication as a research article in Macromolecular research.

The manuscript aimed to reduce the steps used for preparing homogeneous and functionalised magnetic polymeric nanoparticle (MPNP) under mild condition. Magnetic nanoparticles (MNPs) coated with oleic acid (OA) were synthesised by co-precipitation technique. Then, they were incorporated into polystyrene/acrylic acid (PS/AA) or PS/divinyl benzene/AA (PS/DVB/AA) matrix by using miniemulsion polymerisation process without using magneto-template. The prepared MNP and MPNP were systematically characterised. The effects of OA and DVB on the final morphology of the prepared MPNP were considered. Results confirmed that the combination of the removal of the excess OA and the addition of DVB was the key role to produce the homogeneous distribution of MNP in the polymer matrix without pure polymer particle formation. The PS/DVB/AA-MNP (53% of magnetic content) was superparamagnetic and, thus, appropriate for biomedical applications after suitable surface modification.

The work described in the manuscript is original and has never been submitted for publication or presented elsewhere. The manuscript has been prepared according to the instructions for authors. It is believed that the work described in the manuscript would highly benefit the scientific community due to its usefulness and wide application. We sincerely hope that the manuscript will be favorably considered for publication.

Yours sincerely,

Duangporn Polpanich
Dr.
Corresponding Author
National Nanotechnology Center
National Science and Technology Development Agency
111 Thailand Science Park
Pathumthani
Thailand 12120

Tel 66 2 564 7100 ext. 6564
Fax 66 2 564 6981

A highly selective "turn-on" chemosensor based on dansyl-salicylaldehyde Schiff base for Cu^{2+} ion detection

Srung Smanmoo,*[a] Weerachai Nasomphan[b] and Pramuan Tangboriboonrat[b]

Received (in XXX, XXX) Xth XXXXXXXXX 200X, Accepted Xth XXXXXXXXX 200X
First published on the web Xth XXXXXXXXX 200X
DOI: 10.1039/b000000x

A novel "turn-on" fluorescence chemosensor based on dansyl Schiff base derivative (1) has been simply prepared for the detection of Cu^{2+} ion. 1 exhibited a remarkable blue shift of emission upon the addition of Cu^{2+} ion in CH_3CN/H_2O.

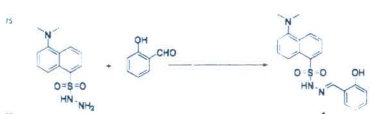
Molecular recognition of heavy metals is one of the active research areas in supramolecular chemistry. Of transition metal ions, Cu^{2+} ion is one of the important metals both in physiological and environmental systems. It involves various enzymatic processes as a cofactor. However, high concentration of Cu^{2+} ion leads to cytoxicity and many diseases, e.g. Wilson, leukemia, and dyslexia.[ref] Cu^{2+} ion is known for the correlation to Alzheimer's disease.[1]

Over the past decade, the development of selective Cu^{2+} ion fluorescence chemosensor receives much research attention. However, these sensors are usually cross-selective with other metal ions, e.g. Hg^{2+}, Ag^{+} and Pb^{2+} ions.[2] Besides, the sensors exhibit an "off-type" mode in which their fluorescence intensities are quenched by either i) an energy or electron transfer[3] or ii) an enhancement of spin-orbit coupling.[4] The disadvantages of fluorescence quenching are due to high signal output and the differentiation of spectra of similar complexes with time-resolved fluorometry.[5] For the issue of sensitivity, a chemosensor whose fluorescence emission maximum is enhanced or changed upon the complex with metal ions is highly desired. Cu^{2+} ion induced fluorescence enhancement (a "turn-on" type) chemosensors have been reported. However, those sensors require complicated synthetic manipulations and some of them are completely dissolved in organic solvents.[6]

In recent years, several dansyl-based chemosensors have been developed for the sensitive and selective detection of various metal ions. Dansyl moiety is popularly chosen as an intramolecular charge transfer (ICT) fluorophore due to its highly sensitive fluorescence response to the surrounding environment. In a polar solvent (e.g. water), dansyl fluorophore shows weak fluorescence emission while strong fluorescence and a blue shift of emission are observed in nonpolar solvents.[7]

The design of metal induced fluorescence enhancement chemosensor needs serious consideration. In general, an "on-type" chemosensor requires a minimized fluorescence quenching process while the corresponding process is in the minimization at the metal-bound state.[5] We have deliberately designed a simple yet highly selective chemosensor based on a dansyl Schiff base for Cu^{2+} ion. Imine and 2-hydroxyl groups serve not only as donors for the good coordination to Cu^{2+} ion, but they also facilitate and maximize the contact between the dansyl fluorophore and a bound Cu^{2+} ion. The intramolecular corporation of dansyl and salicylaldehyde unit is intended in such that the binding of Cu^{2+} ion with **1** induces photophysical changes of the system. To the best of our knowledge, among few "turn-on" fluorescence chemosensors for Cu^{2+} ion, none of the dansyl-salicylaldehyde Schiff base sensors has been ever reported.

1 was simply prepared in one step from the reaction between 2-hydroxybenzaldehyde and dansyl hydrazine in distilled water (Scheme 1). After the reaction mixture was left stirring under nitrogen atmosphere for 24 hours, crude dansyl receptor **1** was obtained and crystallized from ethyl acetate/hexane to afford pure **1** in 92% yield. The structure of **1** was confirmed by ^1H NMR, ^{13}C NMR and HRMS (ESI†). The imine group present in **1** is known as an active functional group which shows a strong affinity towards the transition metals.[8] This is due to the special characteristic of the imine group in providing geometric and cavity control to the metal ion complex. Consequently, the lipophilicity, selectivity and sensitivity are enhanced.[9] The presence of dansyl sulfonamide proton (C=N-N*H*) in **1** is proposed for the responsibility in stabilizing the cationic adduct resulting from the complex between **1** and Cu^{2+} ion.[10]



Scheme 1 Synthesis of **1**

The photophysical property of **1** was investigated in CH_3CN. The emission spectra of **1**, when excited at 350 nm, displayed the maximum at 547 nm which is the characteristic emission of dansyl chromophore.[11] As previously described, the fluorophore of Cu^{2+} ion sensors is generally quenched due to the paramagnetic effect via an energy or electron transfer process.[12] However, upon the addition of Cu^{2+} ion, **1** exhibited a blue shift (hypsochromic shift) of the emission maximum to 479.5 nm with fluorescence enhancement (Fig. 1a). The new blue shift of emission at 479 nm was made possible by the coordination of Cu^{2+} ion by **1**. The blue shift of **1** was evident by the emission color changing from yellow to blue (Fig. 1b). In the presence of other transition metal ions including physiological metal ions (Mn^{2+}, Cd^{2+}, Zn^{2+}, Ag^{+}, Ni^{2+}, Pb^{2+}, Co^{2+}, Fe^{2+}), the fluorescence emission of **1** exerted no change. The addition of Hg^{2+} ion resulted in a slight blue shift in **1**'s emission (to 534 nm) with fluorescence quenching. After the addition of Fe^{3+} ion, there was no hypsochromic shift of **1**'s fluorescence emission. However, a substantial decreasing of fluorescence intensity was observed.

The efficiency of a blue shift of **1**'s emission in the presence of Cu^{2+} ion was confirmed by the fluorescence intensity ratio ($F_{479nm}/F_{537.5nm}$) where F_{479nm} and $F_{537.5nm}$ are the fluorescence intensities of **1** with respect to the wavelength at 479 nm and 537.5 nm. It was shown that **1** exhibited remarkable selectivity in response to Cu^{2+} ion, while other transition metal ions displayed no response (ESI†).

Next, the quantitative data of **1** was obtained. **1** was titrated against various concentrations of Cu^{2+} ion. When it was observed that increasing in concentrations of Cu^{2+} ion resulted in a blue shift of **1**'s emission with a slight enhancement. The blue shift could be noticed when 1 equiv of Cu^{2+} ion was added. Continuing addition of Cu^{2+} ion gradually increased the fluorescence intensity of **1**. After the addition of 25×10^{-5} M Cu^{2+} ion, the fluorescence intensity of **1** reached the maxima and exhibited no significance in fluorescence enhancement (Fig. 2).

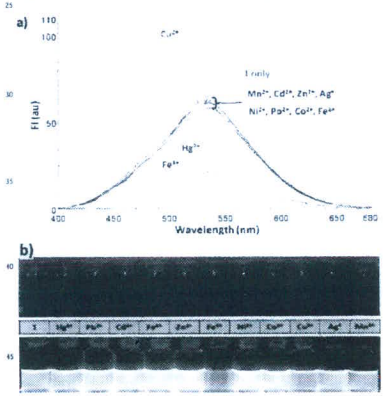


Fig. 1 Fluorescence emission spectra of **1** in the presence of various transition metal ions. [**1**] = 2.5×10^{-5} M, [ion] = 25×10^{-5} M, CH_3CN/H_2O (1:1, v/v). Excitation wavelength was 365 nm.

It is documented that some fluorescence dyes once aggregated result in either a bathochromic (J-type) or hypsochromic (H-type) shift of the emission band. Comparing to our case, the blue shift of **1** upon the addition of Cu^{2+} ion is proposed based on an ICT process.

An attempt to determine the binding ratio between **1** and Cu^{2+} ion by mass spectroscopic technique was unsuccessful. Therefore, the binding analysis by the method of continuous variations (Job's plot) which indicated the binding ratio between **1** and Cu^{2+} ion at 1:1 (ESI†). The association constant, K_{assoc} was estimated by a nonlinear curve fitting of the fluorescence titration data of **1** and found at 1.68×10^{-7} M^{-1} which demonstrated the strong affinity between **1** and Cu^{2+} ion (ESI†).[14]

The metal competing experiment was accomplished. This could provide the information on the selectivity of **1** in the presence of Cu^{2+} with other co-existing metal ions. Results from Fig. 3 indicated that the hypsochromic shift of **1** by Cu^{2+} ion was not influenced by the addition of other transition metal ions.

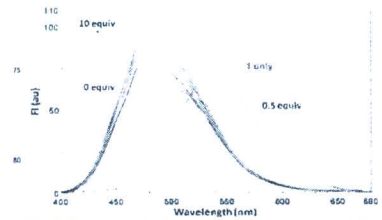


Fig. 2 Fluorescence titration of **1** with increasing concentrations of Cu^{2+} ion.

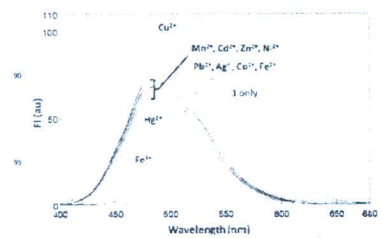


Fig. 3 Fluorescence emission spectra of **1** (2.5×10^{-5} M) and **1** in the presence of respective metal ions (10 equiv) in responses of **1** containing Cu^{2+} ion to different metal ions in CH_3CN/H_2O (1:1, v/v). Excitaiton wavelength was 366 nm.

In order to get a better insight into the coordination between **1** and Cu^{2+} ion, ^1H NMR experiment was conducted (Fig. 4). ^1H NMR spectra clearly indicated the coordination of Cu^{2+} ion since the proton on salicylaldehyde shifted upfield ($\Delta\delta = 0.10$ ppm) and broadened upon the addition of 1 equiv Cu^{2+} ion. The proton from dansyl moiety was shifted downfield ($\Delta\delta = 0.12$ ppm) due to the Cu^{2+} ion coordination which caused the decrease in electron density of dansyl unit. The proposed coordination of Cu^{2+} ion by **1** is shown in the optimized geometry (Fig. 5).

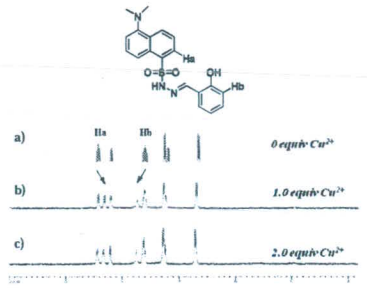


Fig. 4 Partial ^{1}H NMR spectra of **1** measured in DMSO-$d6$/D_2O (1/1, v/v): (a) without Cu^{2+} ion and with (b) 1 equiv Cu^{2+} ion, (c) 2 equiv Cu^{2+} ion.

The fluorescence enhancement of **1** upon the addition of Cu^{2+} ion could be explained via the radiationless pathway from the $\pi\pi^*$ state of the emission from imine lone-pair electrons. The photo-induced electron transfer (PET) channel is operated which suppresses the fluorescence emission of **1**.[15] In the presence of Cu^{2+} ion, the bound Cu^{2+}-**1** complex interferes with the PET pathway resulted from imine lone-pair electrons. This would raise the energy state of $n\pi^*$ while the $\pi\pi^*$ state of emission from dansyl fluorophore is minimized.[16] While the hypsochromic shift of emission is on the basis of ICT process. Therefore, the fluorescence responses of **1** towards Cu^{2+} ion operates via two channels which are the combination of i) PET (fluorescence enhancement) and ii) ICT (hypsochromic shift).[17]

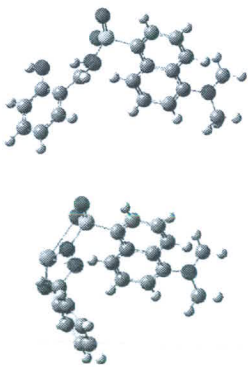


Fig. 5 Optimized geometries of **1** and **1**-Cu^{2+} ion complex.

In summary, a novel fluorescence "turn-on" chemosensor (**1**) is simply prepared and evaluated for its fluorescence response towards Cu^{2+} ion. **1** has been deliberately designed based on a combination of PET and ICT processes. The "suppressed" PET mechanism offers **1** with fluorescence enhancement upon binding to Cu^{2+} ion while the ICT process facilitates **1** with a blue shift of emission. Since **1** is quite soluble in an aqueous environment, this could offer **1** as a potential chemosensor for Cu^{2+} ion for the practical use. **1** is currently integrated into a hydrophilic polymeric template as a new polymeric sensor for a 100 % aqueous utility.

The Thailand Research Fund/Commission on Higher Education's research grant to S.S. and P.T. (RTA5180003) and the Development and Promotion of Science and Technology Talents Project's scholarship to W.N. are gratefully acknowledged. We are also grateful to the partial support from National Center for Genetic Engineering and Biotechnology (BIOTEC).

Notes and references

[a]Bioresources Research Unit, National Center for Genetic Engineering and Biotechnology (BIOTEC), 113 Thailand Science Park, Phaholyothin Road, Klong Luang, Pathumthani 12120 Thailand. Fax: 662 564 6632: Tel: 662 564 6700 ext 3560; E-mail: srung.sma@biotec.or.th

[b]Department of Chemistry, Faculty of Science, Mahidol University, Rama 6 Road, Phyathai, Bangkok 10400 Thailand. Fax: 662 354 7151; Tel: 662 201 5135; E-mail: scpth@mahidol.ac.th. (P.T.) and weerachai_na@hotmail.com (W.N.)

† Electronic Supplementary Information (ESI) available: Synthesis of **1**: Fluorescence spectra of **1**. See DOI: 10.1039/b000000x/

1 (a) L. Hesse, D. Beher, C. L. Masters and G. Multhaup, *FEBS Lett.*, 1994, **349**, 109-116; (b) G. Multhaup, A. Schlick-supp, L Hess, D. Beher, T. Ruppert, C. L. Masters and K. Beyreuther, *Science* 1996, **271**, 1406-1409; (c) C. J. Maynard, A. I. Bush, C. L. Masters, R. Cappai and Q.-X. Li, *Int. J. Exp. Path.* 2005, **86**, 147-159; (d) E. Breslow, *J. Biol. Chem.*, 1964, **239**, 3252-3259; (e) A. Zgirski and E. Frieden, *J. Inorg. Biochem.*, 1990, **39**, 137-148; (f) C. K. Luk, *Biochemistry* 1971, **10**, 2838-2843; (g) Z. L. Harris and J. D. Gitlin, *Am. J. Clin. Nutr.*, 1996, **63**, 836S-841S.

2 (a) Z. Xu, J. Yoon and D. R. Spring, *Chem. Commun.*, 2010, **46**, 2563-2565; (b) W.-C. Lin, C.-Y. Wu, Z.-H. Liu, C.-Y. Lin and Y.-P. Yen, *Talanta*, 2010, **81**, 1209-1215.

3 (a) M. B. Gholivand, P. Niroomandi, A. Yari and M. Joshagani, *Anal. Chem. Acta*, 2005, **538**, 225-231; (b) R. K. Mahajan, T. P. S. Walia and T. S. Lobana, *Anal. Sci.*, 2006, **22**, 389-392; (c) A. Mokhir, A. Kiel, D. P. Herten and R. Kraemer, *Inorg. Chem.* 2005, **44**, 5661-5666.

4 D.S. McClure, *J. Chem. Phys.*, 1952, **20**, 682-686.

5 (a) K. Rurack, U. Resch-Genger and W. Rettig, *J. Photochem. Photobiol. A. Chem.*, 1998, **118**, 143-149; (b) R. Martinez, F. Zapata, A. Caballero, A. Espinosa, A. Tarraga and P. Molina, *Org. Lett.*, 2006, **8**, 3235-3238.

6 (a) G.-K. Li, Z.-X. Xu, C.-F. Chen and Z.-T. Huang, *Chem. Commun.*, 2008, 1774-1776; (b) T. Abalos, D. Jimenez, R. Martines-Manez, J. V. Ros-Lis, S. Royo, F. Sancenon, J. Soto, A. M. Costero, S. Gil and M. Parra, *Tetrahedron Lett.*, 2009, **50**, 3885-3888.

7 (a) A. Ueno, S. Minato, I. Suzuki, M. Fukushima, M. Ohkubo, T. Osa, F. Hamada and K. Murai, *Chem. Lett.*, 1990, 605-608; (*b*) Y. Wang, T. Ikeda, A. Ueno and F. Toda, *Chem. Lett.*, 1992, 863-866; (*c*) F. Hamada, Y. Kondo, R. Ito, I. Suzuki, T. Osa and A. Ueno, *J. Incl. Phenom.*, 1993, **15**, 273-279; (*d*) Y. Wang, T. Ikeda, A. Ueno and F. Toda, *Bull. Chem. Soc. Jpn.*, 1994, **67**, 1598-1607; (*e*) M. Nakamura, T. Ikeda, A. Nakamura, H. Ikeda, A. Ueno and F. Toda, *Chem. Lett.*, 1995, 343-344; (*f*) M. Nakamura, A. Ikeda, N. Ise, T. Ikeda, H. Ikeda, F. Toda and A. Ueno, *J. Chem. Soc., Chem. Commun.*, 1995, 721-722.

8 (a) N. Aksuner, E. Henden, I. Yilmaz and A. Cukurovali, *Dyes Pigments*, 2009, **83**, 211-217; (b) H. Chen, Y. Wu, Y. Cheng, H. Yang, F. Li and P. Yang, *Inorg. Chem. Commun.*, 2007, **10**, 1413-1415; (c) C. Sousa, P. Gameiro, C. Freire and B. Castro, *Polyhedron*, 2004, **23**, 1401-1408.

9 O. Oter, K. Ertekin, R. Kihncarslan, M. Ulusoy and B. Cetinkaya, *Dyes Pigments*, 2007, **74**, 730-735.

10 Y. M. Chung, B. Raman, D.-S. Kim and K. H. Ahn, *Chem. Commun.*, 2006, 186-188.

11 (a) N. A. O'Connor, S. T. Sakata, H. Zhu and K. J. Shea, *Org. Lett.*, 2006, **8**, 1581-1584; (b) M. H. Lee, H. J. Kim, S. Yoon, N. Park and J. S. Kim, *Org. Lett.*, 2008, **10**, 213-216.

12 Y. Zheng, J. Orbulescu, X. Ji, F. M. Andreopoulos, S. M. Pham and R. M. Leblanc, *J. Am Chem. Soc.*, 2003, **125**, 2680-2686.

13 (a) K. K. Rohatgi and G. S. Singhal, *J. Phys. Chem.*, 1966, **70**, 1695-1701; (b) J. E. Selwyn and J. I. Steinfeld, *J. Phys. Chem.*, 1972, **76**, 762-774; (c) R. W. Chambers, T. Kajiwara and D. R. Kearns, *J. Phys. Chem.*, 1974, **74**, 380-387; (d) U. Rösch, S. Yao, R. Wortmann and F. Würtner, *Angew. Chem. Int. Ed.*, 2006, **45**, 7026-7030.

14 J. González-Jiménez, G. Frutos and I. Cayre, *Biochem. Pharmacol.* 1992, **44**, 824-826.

15 S. J. Qu, Z.-H. Lin, C.-Y. Duan, H.-T. Zhang, and Z.-P. Bai, *Chem. Commun.*, 2006, 4392-4394.

16 P.-J. Jiang, L. -Z. Chen, J. Lin, Q. Liu, J. Ding, X Gao and Z.-J. Guo, *Chem. Commun.*, 2002, 1424-1425.

17 Z. Xu, G.-H. Kim, S. J. Han, M. J. Jou, C. Lee, I. Shin and J. Yoon, *Tetrahedron*, 2009, **65**, 2307-2312.

Pyrazolidine luminol as a selective colorimetric receptor for Cu^{2+} in an aqueous environment

Weerachai Nasomphan[a,b], Pramuan Tangboriboonrat[b] and Srung Smanmoo[a*]

[a]*Bioresources Research Unit, National Center for Genetic Engineering and Biotechnology (BIOTEC), 113 Thailand Science Park, Phaholyothin Road, Klong Luang, Pathumthani 12120 Thailand*

[b]*Department of Chemistry, Faculty of Science, Mahidol University, Rama 6 Road, Phyathai, Bangkok 10400 Thailand*

ABSTRACT

Pyrazolidine luminol (PL) was prepared as a selective colorimetric receptor for Cu^{2+} ion. PL exhibits good selectivity and sensitivity towards Cu^{2+} over other metal cations, e.g. Cr^{3+}, Al^{3+}, Pd^{2+}, Ni^{2+}, Ce^{4+}, Sn^{2+}, Mn^{2+}, Co^{2+}, Fe^{2+}, Fe^{3+}, Mo^{2+}, and Ag^{+} ions. The colorimetric change of PL was easily observed by naked eyes in which the color of PL changed from pale yellow to dark green. The detection limit for PL was determined to be 3.75×10^{-4} M with the binding ratio between PL and Cu^{2+} of 2:1. PL was immobilized on a silica gel plate and employed for the detection of Cu^{2+} ion in an aqueous environment with good detection limit.

Keywords: Colorimetric receptor, Luminol derivatives, Copper (II) sensor

Corresponding author. Tel.: +662 564 6700 ext 3560; Fax +662 564 6632

E-mail address: srung.sma@biotec.or.th

1. Introduction

The design of the colorimetric receptor with high selectivity and sensitivity has gained chemists' attention because the detection of analyte could simply be achieved via naked eyes [1-3]. A number of colorimetric receptors play significant roles in sensing biological analytes and metal cations [4,5]. In the field of environmental sciences, colorimetric receptors have been employed for the determination of contaminated heavy metals in natural resources [6,7].

In general, the design of colorimetric receptor is based on the careful selection of an ionophore (the analyte binding unit) and a chromophore (the signaling part). The recognition of analytes at the binding unit is achieved by various modes of interactions, e.g., hydrogen-bonding, electrostatic interaction, metal-ligand coordination and Van der Waals interaction [7-9]. Upon binding of analytes to the ionophore, the communication between the binding moiety and the chromophore is initiated to alter the photopnysical property of the receptor. The measurement of the physical change of chemosensors normally relies on spectroscopic methods which sometime involve complicated sample preparation and analysis [10,11]. Therefore, the development of a portable chemosensor kit with low cost of sampling and sensitive detection is desirable.

Luminol and its derivatives are well known chemiluminescence (CL) reagents due to their high quantum yields [12]. CL emission of luminol is initiated by reacting luminol with appropriate oxidizing agents in the basic condition [13]. Recently, luminol derivative has been used as a CL sensor for metal cations [14]. The incorporation of a crown ether moiety into the luminol structure offers a CL receptor which confers the binding mode to metal cations. Upon binding to metal cations, the signal transmission between the receptor (crown ether) and the chromophore is established.

In this paper, we have synthesized a new chromogenic receptor, pyrazolidine luminol (PL). The luminol scaffold was used as the chromophore of the receptor, while the presence of the 5-membered ring of PL served as the binding unit to the metal cation. Among metal cations, PL exhibited good selectivity towards Cu^{2+} ion and showed the colorimetric change upon the addition of Cu^{2+} ion. This offers PL as a selective receptor for the detection of Cu^{2+} ion by the colorimetric mean.

ลิขสิทธิ์มหาวิทยาลัย 5.2.3

2. Experimental

2.1. Materials and instrumentations

The stock solution of the corresponding PL was prepared in DMF with the concentration of 500 μM. The metal complexes used in this study were as followed: cobalt (II) chloride, chromium (III) chloride, copper (II) chloride, nickel (II) chloride, palladium (II) chloride, manganese (II) chloride and disodium molybdate (VI), iron (II) chloride, iron (III) chloride, aluminium (III) chloride, silver (I) chloride, tin (II) chloride and cerium (IV) sulfate. Metal complexes were obtained from Aldrich or Acros and used without further purification. Solvents were used as a HPLC grade. Other chemicals used were supplied from Aldrich as analytical grade and used without further purification. MilliQ water was used throughout unless other stated. The concentration of stock solution of metal cations was 10 mM.

The reactions were monitored by thin-layer chromatography (TLC) on a commercial silica coated plates with a particle size of 60 Å. Developed plates were visualized by UV lamp (254 nm). Column chromatography was performed using 0.063 – 0.20 nm silica gel. Fluorescence measurements were carried out using a FP-6300 spectrofluorometer (JASCO) equipped with a xenon lamp source and a 1.0-cm quartz cell, and the scan speed was 600 nm min^{-1}. Absorption spectra were recorded by a Shimadzu-240 UV-vis spectrophotometer using a 1.0-cm quartz cell. ^{1}H spectrum was recorded on Bruker DPX 400 MHz spectrometer in $CDCl_3$ using TMS as the internal standard. $CDCl_3$ (77.0 ppm) were used as the internal reference for ^{13}C NMR. Mass spectra were recorded on Bruker Esquire and Finnigan MAT INCOS 50 mass spectrometers. The fluorimetric images were taken after the membrane exposed under the UV lamp (λ = 366 nm).

2.2 Preparation and characterization of pyrazolidine luminol (PL)

The preparation of PL was achieved in 2 steps as followed. In a flame dried round bottom flask, a solution of luminol (1 g, 5.64 mmol) in methanol (5 mL) was added sodium methoxide (0.91 g, 16.9 mmol) and the reaction was brought to reflux for 3 hrs. After the reaction was cooled down to room temperature, methanol was completely removed under vacuum before the obtained yellow solid was re-dissolved in ethanol folllowed by the addition of epichlorohydrin (2.21 mL, 28.2 mmol) under the N_2 atmosphere and left stirring at room temperature for 4 days. The crude product was recrystallised in water before the desired PL was obtained as a white solid; 70%; mp. 215 °C; IR ν_{max} (KBr) 1406, 1591, 1619, 3443 cm^{-1}; ESMS; Calculated for $C_{11}H_{11}N_3O_3$ $[M^+]$ = 233.080; measured mass $[M^+ + Na]$ = 256.0697; ^{1}H NMR (DMSO-*d*6): δ 3.95-4.04 (m, 2H, C*H*$_2$), 4.11 (dd, *J* = 11.8 Hz, 2H, C*H*$_2$), 4.58 (m, 1H, C*H*OH), 5.76 (br, 1H, O*H*), 6.30 (br, 2H, N*H*$_2$), 6.98 (dd, 1H, *J* = 2.36 Hz and 8.55 Hz, 1H, Ar*H*), 7.22 (s, 1H, Ar*H*), 7.81 (d, 1H, *J* = 8.56 Hz, Ar*H*) ; ^{13}C NMR (DMSO-*d*6): 54.5 (*C*H$_2$), 54.8 (*C*H$_2$), 65.0 (*C*H), 108.0 (Ar*C*H), 117.08 (Ar*C*H), 118.5 (Ar*C*H), 128.2 (Ar*C*H), 131.2 (Ar*C*H), 153.3 (Ar*C*H), 154.4 (NH*C*=O), 154.8 (NH*C*=O).

3. Results and discussion

3.1. Synthesis of pyrazolidine luminol

On the course of optimization for PL synthesis, the condition described in scheme 1 provided the best yield hence it was employed in the study throughout. The synthesis of PL was achieved in 2 steps as already mentioned. Spectroscopic data of PL agreed well with the structure shown. PL is designed as a chromogenic receptor where the luminol moiety acts as a chromophore. The 5-membered ring with the hydroxyl group is used as a chelating unit for metal cations.



Scheme 1. Synthetic procedure for PL. Reaction conditions: (i) NaOMe, MeOH, 80 °C, 3 hrs; (ii) epichlorohydrin, ethanol, RT, 4 days.

3.2. Chemiluminescence (CL) profile of PL comparing to luminol

It is known that the chemical manipulation of the luminol's phthalhydrazide ring generally leads to the loss of its CL property [15]. Therefore, the CL emission of PL was investigated and compared with luminol. Previously, we have optimized the condition for the CL emission of luminol employing Fe^{3+} catalysis [13(a)]. Therefore, the corresponding condition was used for the CL emission of PL. CL emitting reagents (CH_3CN, TPA, and $FeCl_3$) were used to initiate the CL emission of both luminol and PL. It was shown in Fig. S2 (see supplementary material) that the introduction of a 5-membered ring into the PL structure retained its CL property. Therefore, this offers PL as a newly synthesized CL reagent.

3.3. Selectivity of PL towards metal ions

The selectivity of PL over other metal cations was investigated. Various cations were added into the PL solution and the color change of the solution was observed by naked eyes in the optimized solvent (DMF:H_2O). In the presence of other metal cations (e.g. Fe^{2+}, Fe^{3+} and Mn^{2+} ions), no significant colorimetric change of PL solution was observed. It was interesting to note that in the presence of Cu^{2+} ion, the color of PL solution significantly changed from pale yellow to dark green (Fig. 1). The change was not observed when the same molar equiv of Cu^{2+} ion was added into luminol solution (see supplementary material, Fig. S3), hence the presence of hydroxyl group in PL is crucial for this interaction. The colorimetric change of PL solution upon the addition of Cu^{2+} ion indicated the interaction between PL and Cu^{2+} ion which is believed that the observed effect proceed via the intramolecular charge transfer (ICT) process. The ICT mechanism of PL is originated from the binding to Cu^{2+} ion which subsequently triggers the ICT from the receptor (the 5-membered ring moiety) to the chromophore.

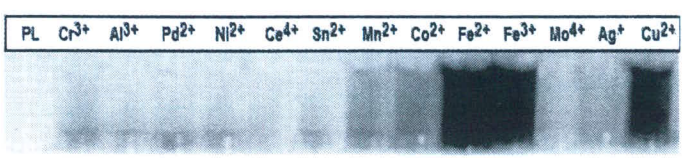


Fig. 1. Pictures of PL upon the addition of various metal cations in DMF:H_2O (9:1; v/v). [PL] = 4.5×10^{-4} M, [metal cations] = 1×10^{-3} M.

3.4. UV-vis spectra of PL upon the addition of various metal cations

The ground state absorption of PL was recorded in DMF:H_2O (9:1; v/v). It was clearly shown that in the absence and presence of other metal cations, the absorption spectra indicated three absorption maxima at 305, 350 and 375 nm. In the presence of Cu^{2+} ion, there was a new absorption observed at 425 nm (Fig. 2) which is a CT band. The colorimetric change of PL solution upon the addition of Cu^{2+} ion corresponded to the occurring of the new absorption at 425 nm. Since no absorption at 425 nm in the presence of other metal cations, the absorption at 425 nm indicated the characteristic interaction between PL and Cu^{2+} ion.

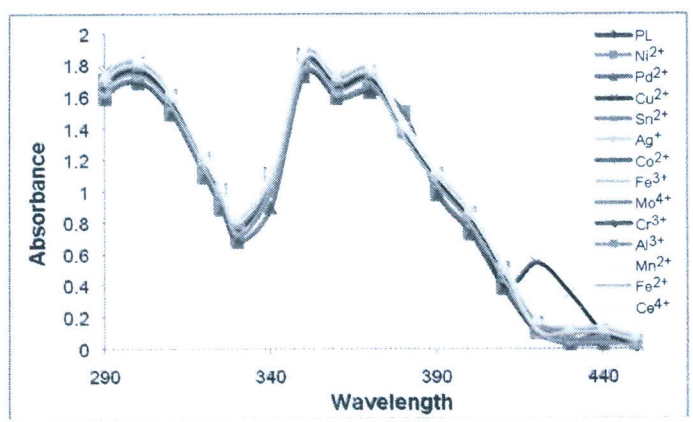


Fig. 2. UV-vis titration spectra of PL in the presence of various metal cations. [PL] = 4.5×10^{-4} M, [metal cations] = 1×10^{-3} M.

3.5. Ratiometric response of PL upon the addition of various metal cations

The change in the absorption of PL in the presence of metal cations was demonstrated with respect to two absorptions at 350 and 425 nm. The absorbance ratio at 350 and 425 nm indicates the good selectivity of PL towards metal cations. It was clearly shown that the change in the corresponding absorbance ratio (*A425/350*) of PL upon the addition of Cu^{2+} ion was more pronounced than other metal cations (Fig. 3). In the presence of other metal cations, the *A425/350* absorbance ratio did not significantly change. This shows that PL is highly selective in its response to Cu^{2+} ion in comparison to other metal cations.

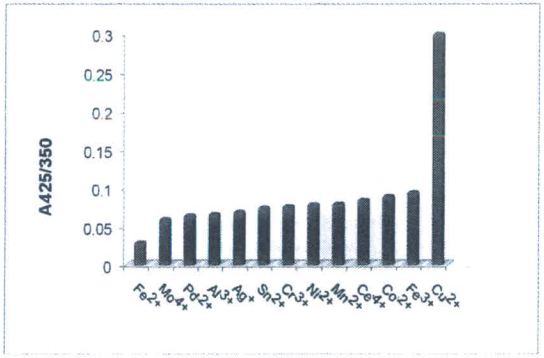


Fig. 3. Ratiometric response of PL towards different metal cations. [PL] = 4.5×10^{-4} M. [metal cations] = 1×10^{-3} M.

3.6. UV-vis titrations of PL with various concentrations of Cu^{2+} ion

It is clear that the absorption of PL is highly affected by Cu^{2+} ion. The change in the absorption spectra of PL in DMF:H_2O in the presence of various concentrations of Cu^{2+} was investigated. Fig. 4 represented the CT band (absorption at 425 nm) which selectively responded to Cu^{2+} ion. Increasing concentrations of Cu^{2+} ion resulted in the progressive incline of the absorption maxima at 425 nm, which was thought to be due to the interaction of the hydroxyl group participating in the ICT process.

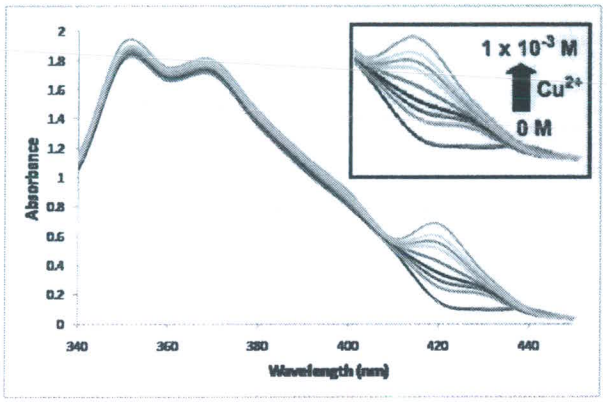


Fig. 4. UV-vis titration spectra of PL (4.5×10^{-4} M) in the presence of increasing concentration of Cu^{2+} ion in DMF:H_2O (9:1; v:v).

3.7. Colorimetric response of PL upon the addition of various concentrations of Cu^{2+} ion

Next, the colorimetric change of PL was observed in the presence of various concentrations of Cu^{2+} ion. It was noticed that the color of PL solution gradually developed more intense green color upon increasing concentration of Cu^{2+} ion (Fig. 5). From the naked eye detection, the clear cut for the color change of PL solution was observed when 3.75×10^{-4} M of Cu^{2+} ion was added into the PL solution. Further increasing concentration of Cu^{2+} ion resulted in a more intense green color. Therefore, the detection limit for the liquid-phase colorimetric detection of Cu^{2+} ion employing PL was 3.75×10^{-4} M.

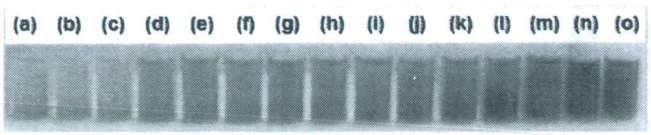


Fig. 5. Pictures of color changes of PL upon increasing concentrations of Cu^{2+} ions in DMF:H_2O (9:1; v/v). PL with Cu^{2+} ion (a) 0 M (b) 1×10^{-5} M (c) 1×10^{-4} M (d) 3.75×10^{-4} M (e) 7.5×10^{-4} M (f) 1×10^{-3} M (g) 1.5×10^{-3} M (h) 3×10^{-3} M (i) 6×10^{-3} M (j) 1×10^{-2} M (k) 1.2×10^{-2} M (l) 2.4×10^{-2} M (m) 4.8×10^{-2} M (n) 7×10^{-2} M (o) 1×10^{-1} M. [PL] = 4.5×10^{-4} M.

3.8. Mass spectroscopic spectra of PL with the addition of Cu^{2+} ion

In order to investigate the stoichiometric binding ratio between PL and Cu^{2+} ion, ESI-MS was used for the investigation. Various stoichiometric binding ratios between PL and Cu^{2+} ion were employed and subjected to the mass spectroscopic analysis. Of binding ratios, the solution containing 2:1 molar equiv between PL and Cu^{2+} ion showed the peak at m/z = 528.54 corresponded to the complex between PL and Cu^{2+} ion at 2:1 (Fig. 6).

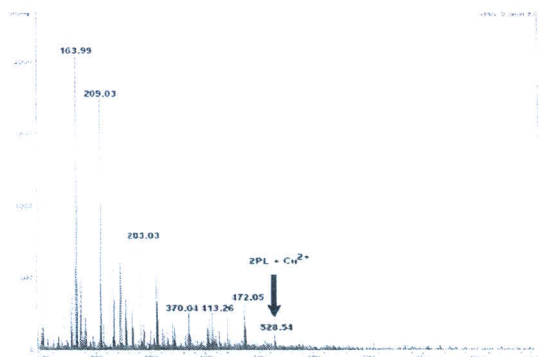


Fig. 6. Mass spectroscopic analysis of PL and Cu^{2+} ion in DMF:H_2O (9:1; v/v). The binding ratio between PL and Cu^{2+} ion was indicated as the black arrow (PL:Cu^{2+} ion = 2:1).

3.9. Proposed complex between PL and Cu^{2+} ion

From the mass spectroscopic data and the computational modeling, the proposed binding complex between PL and Cu^{2+} ion is shown in Fig. 7. It was believed that the binding mode between PL and Cu^{2+} ion is through the coordination of Cu^{2+} ion by two moles of PL. The

coordination of Cu^{2+} ion by PL is a C2 symmetry which is assisted via the chelation from the hydroxyl group present in the 5-membered ring of PL and the carbonyl group. The coordination of Cu^{2+} from the other PL adopts the same mode of binding with the opposite orientation to obtain the tetragonal complex between PL and Cu^{2+} ion. From computer modeling, the hydroxyl group of the 5-membered ring adopts the puckered conformation which facilitates the binding between Cu^{2+} ion, hydroxyl and carbonyl groups. This result demonstrates the importance of the 5-membered ring present in PL and could explain the lack of selectivity of luminol towards Cu^{2+} ion.

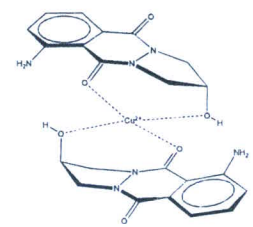


Fig. 7. MM2 energy-optimized complex between PL and Cu^{2+} ion at the binding ratio between PL and Cu^{2+} ion of 2:1.

3.10. Preliminary application of PL chemosensor kit

In order to develop PL as a chemosensor kit, a silica plate was immobilized with PL. The immobilizing process was achieved by immersing a silica plate into PL solution before drying under vacuum. It was clearly shown that the immobilized plate with PL exhibited the characteristic pale yellow. After the immersion into Cu^{2+} ion solution, PL immobilized plate showed a colorimetric change from pale yellow to green which clearly observed by naked eyes (Fig. 8). PL immobilized plate was employed for the detection of Cu^{2+} ion in an aqueous environment and found that the detection limit for Cu^{2+} ion was as low as 0.4×10^{-3} M. Therefore, this chemosensor kit has a potential to further develop as the portable detection kit for Cu^{2+} ion with the lower detection limit and will be employed as an analytical device in environmental science.

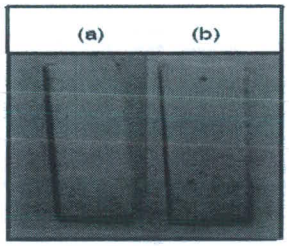


Fig. 8. Pictures of silica plates: (a) the PL immobilized silica plate. (b) the PL immobilized silica plate after immersion into the 0.4×10^{-3} M of Cu^{2+} ion solution.

4. Conclusion

We herein demonstrate a new colorimetric receptor based on the luminol scaffold, pyrazolidine luminol (PL). Its colorimetric change is clearly observed by naked eyes with selective response to Cu^{2+} ion. The color of PL solution changed from pale yellow to dark green upon the addition of Cu^{2+} ion. The detection limit of PL solution towards Cu^{2+} ion was 10^{-4} M. The binding ratio between PL and Cu^{2+} ion was determined by mass spectrometry and found to be 2:1. To the best of our knowledge, this is the first colorimetric receptor for Cu^{2+} ion based on PL. For the application, PL was immobilized on a silica plate and used for the detection of Cu^{2+} ion in an aqueous environment. The improvement of the PL sensitive chemosensor kit could facilitate applications in biological and environmental sciences.

Acknowledgements

The Thailand Research Fund (TRF)/Commission on Higher Education (CHE)'s research grant to S.S. and P.T. and the Development and Promotion of Science and Technology Talents Project's scholarship to W.N. are gratefully acknowledged. We are also grateful to the partial support from National Center for Genetic Engineering and Biotechnology (BIOTEC).

Appendix A. Supplementary data

Supplementary information associated with this article can be found, in the online version, at doi:XXXX

References

[1] S. R. Rickett, D. Douglas, Sensor. Actuat. B-Chem. 135 (2008), 46. (b) H. Jiang, Y. Wang, Q. Ye, G. Zou, W. Su, Q. Zhang, Sensor. Actuat. B-Chem. in press.

[2] H. Li, Z. Cui, C. Han, Sensor. Actuat. B-Chem. (2009), in press. (b) J. Li, H. Lin, H. Lin, J. Photoch. Photobio. B 97 (2009), 18.

[3] (a) Y.-J. Kim, H. Kwak, S. J. Lee, J. S. Lee, H. J. Kwon, S. H. Nam, K. Lee, C. Kim, Tetrahedron 62 (2006), 9635. (b) Y. Egawa, R. Gotoh, S. Niina, J.-I. Anzai, Bioorg. Med. Chem. Lett. 60 (2007), 11133.

[4] D. Zhang, M. Zhang, Z. Liu, M. Yu, F. Li, T. Yi, C. Huang, Tetrahedron Lett. 47 (2006), 7093. (b) D. Prabhakaran, H. Nanjo, H. Matsunaga, Anal. Chim. Acta 601 (2007), 108. (c) S. Shao, Y. Guo, L. He, S. Jiang, X. Yu, Tetrahedron Lett. 44 (2003), 2175.

[5] (a) I. Grabchev, P. Bosch, M. McKenna, D. Staneva, J. Photoch. Photobio. *A* 201 (2009), 75 (b) P. Kaur, S. Kaur, A. Mahajan, K. Singh, Inorg. Chem. Commun. 11 (2008), 626.

[6] (a) H. Yang, Z. Zhou, F. Li, T. Yi, C. Huang, Inorg. Chem. Commun. 10 (2007), 1136. (b) P. Buhlmann, E. Pretsch, E. Bakker, Chem. Rev. 98 (1998), 1593.

[7] (a) M. H. Keefe, K. H. Benkstein, J. T. Hupp, Coord. Chem. Rev. 205 (2000), 201. (b) F. Wang, Y. Xu, B. X. Ye, M. P. Song, Y. J. Wu, Inorg. Chem. Commun. 9 (2006), 797.

[8] (a) L. A. Baumes, M. B. Sogo, P. Montes-Navajas, A. Corma, H. Garcia, Tetrahedron Letters 50 (2009), 7001. (b) S. Chah, M. R. Hammond, R. N. Zare, Chem. Biol. 12 (2005), 323. (c) D. Saravanakumar, N. Sengottuvelan, M. Kandaswamy, P. G. Aravindan, D. Velmurugan, Tetrahedron Lett. 46 (2005), 7255.

[9] (a) D. Saravanakumar, S. Devaraj, S. Iyyampillai, K. Mohandoss, M. Kandaswamy, Tetrahedron Lett. 49 (2008), 127. (b) Y. Wan, W. Niu, W. J. Behof, Y. Wang, P. Boyle, C. B. Gorman, Tetrahedron 65 (2009), 4293. (c) P. Montes-Navajas, L. A. Baumes, A. Corma, H. Garcia, Tetrahedron Lett. 50 (2009), 2301.

[10] (a) D. A. Jose, D. K. Kumar, B. Ganguly, A. Das, Tetrahedron Lett. 46 (2005), 5343. (b) Z. Yuan, T. W. Hanks, Polymer 49 (2008), 5023. (c) K. Liu, L. He, X. He, Y. Guo, S. Shao, S. Jiang, Tetrahedron Lett. 48 (2007), 4275. (d) A. Mitra, B. Ramanujam, C. P. Rao, Tetrahedron Lett. 50 (2009), 776.

[11] (a) S. Chaure, D. Paul, P. Vadagma, A. K. Ray, J. Hard. Mater. in press. (b) D. Delmarre, R. Méallet, C. Bied-Charreton, R. B. Pansu, J. Photoch. Photobio. A 124 (1999), 23. (c) M. P. McCurdie, L. A. Belfiore, Polymer 40 (1999), 2889. (d) F. Capitelli, F. Colao, M. R. Provenzano, R. Fantoni, G. Brunetti, N. Senesi, Geoderma 106 (2002), 45.

[12] (a) H. Yoshida, R. Nakao, H. Nohta, M. Yamaguchi, Dyes Pigments 47 (2000), 239. (b) M. Nakazono, T. Hino, K. Zaitsu, J. Photoch. Photobio. A 186 (2007), 99.

[13] (a) C. Smanmoo, M. Yamasuji, T. Sagawa, T. Shibata, T. Kabashima, D.-Q. Yuan, K. Fujita, M. Kai, Talanta 77 (2009), 1761. (b) H. Chen, F. Gao, R. He, D. Cui, J. Colloid Interf. Sci. 315 (2007), 158.

[14] H. Okamoto, M. Kimura, Method. Enzymol. (2004), 183.

[15] H. R. Schroeder, F. M. Yeager, Anal. Chem. 50 (1978), 1114.

Biographies

Weerachai Nasomphan is working towards his M.Sc. degree in functionalized polymer at Mahidol University and BIOTEC.

Pramuan Tangboriboonrat obtained Ph.D. in chemistry from Université de Haute Alsace, France. She is currently professor in polymer chemistry at Mahidol University. Her research work has been focused on colloidal chemistry.

Srung Smanmoo received his Ph.D. in organic chemistry from the University of Sheffield, UK. He is now working as a researcher at bioresources unit, National Center for Genetic Engineering and Biotechnology (BIOTEC). His research interest mainly focuses on the development of new molecular sensing systems.

เอกสารแนบ 5.2.4

Polymer Composites

Physical properties of maleated sulfur prevulcanized natural rubber-g- cellulose fiber

Journal:	*Polymer Composites*
Manuscript ID:	PC-11-0402
Wiley - Manuscript type:	Research Article
Date Submitted by the Author:	22-Jun-2011
Complete List of Authors:	Riyajan, Sa-Ad; Prince of Songkla University, Material Science and Technology Intharit, Isara Tangboriboonrat, Pramuan
Keywords:	cellulose, composite

SCHOLARONE™
Manuscripts

Physical properties of maleated sulfur prevulcanized natural rubber-g- cellulose fiber

Sa-Ad Riyajan[1]*, Isara Intharit[1] and Pramuan Tangboriboonrat[2]

[1]Department of Materials Science and Technology and Natural Product Center and, Faculty of Science,

Prince of Songkla University, Songkhla 90112 Thailand

[2]Department of Chemistry, Faculty of Science, Mahidol University, Bangkok 10400 Thailand

*Corresponding author: saadriyajan@hotmail.com

Phone/Fax 660-074288398

ABSTRACT

The maleated sulfur prevulcanized natural rubber grafted cellulose (M-SPNR-g-cellulose) was prepared from SPNR latex and cellulose fiber of corn leaves by using benzoyl peroxide and potassium persulfate as thermal initiators. The chemical structure of the M-SPNR-g-cellulose was confirmed by ATR-FTIR and solid state ^{13}C-NMR. The swelling ratio of M-SPNR-g-cellulose film decreased as a function of cellulose and maleic anhydride contents. Their modulus and hardness dramatically increased with increasing cellulose content. However, the tensile strength and elongation at break decreased when compared to the unmodified SPNR. The M-SPNR-g-cellulose exhibited good thermal resistance at 90°C. The well dispersed cellulose fibers in rubber matrix was confirmed by SEM and optical microscopy. The composite film had antibacterial activity and could be easily degraded when buried in moist soil.

KEYWORDS, Natural rubber; Maleic anhydride; Cellulose; Chemical modification; Latex; Biopolymer

INTRODUCTION

The biodegradable materials, e.g., cellulose, natural rubber (NR) and starch, are used to replace the synthetic polymers due to the environmental friendly reason. Moreover, cellulose, the most abundant natural polymer, can be obtained from the 'waste' agricultural by-product, e.g., sugar beet pulp, eucalyptus kraft pulp, palm and rice husk [1-4]. Before utilization, cellulose must be treated with acid and base to remove the non-cellulose, e.g., fatty acid, wax and hemicellulose [5,6]. However, the drawbacks of the treated cellulose, i.e., high moisture absorption and high fungi attack, still exist.

In order to solve these problems, several chemical modifications, i.e., etherification, esterification, oxidization, crosslinking and graft copolymerization, through hydroxyl groups of cellulose have been carried out [7-11]. Besides reducing the moisture absorption of cellulose, these modifications enhance the adhesion between hydrophilic and hydrophobic materials. Although the cellulose grafted with polymers, e.g., polyacrylonitrile, butyl acrylate, polystyrene, β-cyclodextrin and renewable polymeric matrices, were studied, the grafting between NR and cellulose has not yet been reported [12-16]. The previous works concerned only the blend of acid treated cellulose with NR. It was found that their modulus increased depending on cellulose content due to hydroxyl group and 1,4 glycoside linkage in cellulose. However, the poor adhesion between both materials caused the slight decrease of the tensile strength and elongation at break of the blend [17-20]. The better adhesion between cellulose and NR was obtained from using cellulose grafted with allyl acrylate and allyl methacrylate [17]. The stress/strain measurement and dynamic mechanical analysis of NR/allyl acrylate and allyl methacrylate grafted cellulose composites were, therefore, improved. The modification of cellulose from banana

fiber by maleic anhydride (MA) for its use as a coupling agent was also investigated [22]. Results showed that the mechanical properties of the maleated cellulose blended with polyethylene were enhanced due to the better compatibility [22].

In this present work, MA reacted with sulfur prevulcanized natural rubber (SPNR) latex producing maleated (M) SPNR which was grafted with cellulose fiber from corn leaves. The value-added agricultural 'waste' by-product was the main goal of this study. Effects of MA and cellulose contents on the physical properties, i.e., swelling ratio in toluene, tensile strength, elongation at break and hardness, of the M-SPNR-g-cellulose film were investigated. Their antibacterial activity, thermal properties, morphology and biodegradability in soil of the composite film were also studied.

EXPERIMENTAL

Materials

High ammonia (HA) NR having 60% dry rubber content (DRC) was supplied by Chalong Latex Industry Co., Ltd (Songkhla, Thailand). Poly(vinyl alcohol) with 89% hydrolysis and vulcanizing agents, i.e., sulfur,) Zinc diethyl dithiocarbamate (ZDEC and Zinc oxide (ZnO), were purchased from Sonal Company (Songkhla, Thailand). Sodium dodecyl sulphate (SDS) was supplied from Fluka (Seelze, Germany). Maleic anhydride (MA) was supplied by Fluka (Seelze, Germany). Benzoyl peroxide (BPO) was purchased from Merck Schuchardt OHG (Seelze, Germany). Butylated hydroxytoluene (BHT) or 2,6-bis(1,1-dimethylethyl)-4-methylphenol was purchased from Kitpiboon Chemical Ltd. (Bangkok, Thailand). Teric 16, a non-ionic surfactant, was purchased from Lucky Four Company (Bangkok, Thailand). Potassium persulfate was supplied from Rankem analytical company (New delhi, India). Hydrogen

peroxide and perchloric acid were purchased from Solvay Peroxythai Ltd. (Bangkok, Thailand and Guangdong, China).

In order to prepare cellulose fiber, the corn leave was consecutively immersed in 10% NaOH for 24 h in H_2O_2 solution for 24 h and in perchloric acid for 36 h. After being washed with water until reaching neutral pH, the cellulose was dried at 80°C.

Preparation of M-SPNR-g-cellulose

First, 6%wt MA was dissolved in 10% Teric 16 aqueous solution while BHT was dissolved in toluene (2 mL). Both MA solution (10 mL) and 1.5% BHT solution (2 mL) and 1% w/w BPO were then added into SPNR latex having 30% DRC (50 mL). Then, PVA (3 g) and SDS (3 g) dissolved in distilled water (100 mL) at 80°C for 1 h were added into the mixture. 10% w/v Cellulose fiber dispersed in water (0, 5, 10, 20, 30, 50 or 100% w/w with respect to dried weight of SPNR) was then mixed at 80°C for 3 h by using a homogenizer. At the same time, the 1% w/w $K_2S_2O_8$ was added in the mixture. The M-SPNR-g-cellulose obtained was finally poured into a glass container to form a sheet with 0.5 mm in thickness after drying at ambient temperature and then at 80°C for 6 h. The sample was kept at room temperature for overnight before characterisation.

Characterizations of M-SPNR-g-cellulose

The M-SPNR-g-cellulose was characterised by using attenuated total reflection-Fourier Transform Infrared spectrophotometer (ATR-FTIR) (Equinox 55; Bruker) for 100 times of scan. CP/MAS solid-state ^{13}C-NMR spectrometer (Chemagnetics CMX100) was operated under a static field strength of 2.3 T (100 mHz, 1H) at

20±1°C. The contact time for CP was 1 ms with a proton 90° pulse of 5.5 μs and decoupling power of 75 kHz. The MAS speed was 3 kHz and the delay time 4after acquisition of the FID signal was 4 s. The chemical shifts were calibrated by using an external hexamethyl benzene standard methyl resonance at 17.3 ppm with 1600 scans. In order to study of thermal properties, thermogravimetric analysis (TGA) was performed (TGA7; Perkin Elmer). Each sample (5–6 mg) was analysed under N_2 with a flow rate of 45 mL/min. The temperature was varied from 50 to 850°C at a heating rate of 10°C/min.

For the morphological study, the sample was fractured under liquid nitrogen and then coated with platinum (12 Pa *vacuum*) before being investigated under scanning electron microscope (SEM; JMS-5800 LV, JEOL) at an accelerating voltage of 6 kV. The photograph image of the M-SPNR-g-cellulose was analyzed by optical microscopy (OM, Primo Star company, Carl Zeiss.). The tensile strength (elongation at the break) and modulus of the sample were measured according to ASTM D412-98a and JIS K6251 using the tensile tester (Strograph E-L; Toyoseiki) at a crosshead speed of 500 mm/min with a load cell of 100 and 500 N, respectively. Its tear strength was also determined according to ISO 34-1. For the study of heat aging resistance, the tensile retention value considering the respective initial tensile strength was investigated after ageing the sample in a circulating air chamber at 90°C for a week. The aged specimen was left at room temperature for at least 24 h before testing. The hardness of the vulcanizate was determined from a Shore A type durometer by using the method adopted from ISO 48. For the examination of biodegradation, the specimen (3 cm ×3 cm) was buried under soil (100 g) at 5 cm from top soil (Hat Yai, Province of Songkhla, Thailand) while water was added every week for 3 months.

Every month, the sample was carefully taken out, washed with distilled water and dried at 45°C for 2 days before being weighed.

Bacterial strain including *E. coli* ATCC25922, was used in this experiment as representative pathogenic bacteria of medical importance. All bacterial strains were cultured routinely on tryptic soy agar (TSA, Difco, France) and incubated at 35 °C for 24 h. The isolated colonies were suspended in Mueller Hinton broth (MHB, Difco, France) and then incubated for 16 h.

RESULTS AND DISCUSSION

FTIR and solid state ^{13}C-NMR analysis

The possible mechanism of grafting M-SPNR with cellulose by using BPO and $K_2S_2O_8$ is presented in Fig. 1. Free radicals from BPO attacked carbon-carbon double bonds of MA which then reacted with carbon-carbon double bonds of SPNR molecules activated by $K_2S_2O_8$ leading to the M-SPNR formation. When the M-SPNR reacted with cellulose fiber, the M-SPNR-g-cellulose was generated. In addition, the crosslink between M-SPNR and cellulose might occur through MA bridging.

Figure 1

The chemical structure of M-SPNR-g-cellulose was confirmed by ATR-FTIR. Fig. 2 shows the ATR-FTIR spectra (4000–500 cm^{-1}) of cellulose, SPNR, M-SPNR and M-SPNR-g-cellulose.

Figure 2

A broad band from 3100 to 3500 cm^{-1} in the spectrum of cellulose was assigned to OH stretching and the peaks at 896, 1046, 1382 and 2926 represented C-H deformation, C-O-C from β-1,4–glycosidic, OH bending and C-H stretching, respectively [22]. In the spectrum of SPNR, C–H and strong asymmetrical methylene group vibrations were respectively observed near 2950 and 2853 cm^{-1} while carbon-carbon double bond was observed at 1664 cm^{-1} [27]. The band at 1076 cm^{-1} mainly attributed to the symmetric C–S–C group stretching vibrations in the two C–S bonds also appeared. During vulcanization, the addition of sulfur broke the double bond between two carbon atoms and then sulfur atoms bridged two polymer chains, i.e., crosslink between polymer chains was formed. In the case of M-SPNR, the absence of unreacted MA was identified by the disappearance of the characteristic band at 698 cm^{-1} (C=C bond) of MA [2]. It should be stated that the absorption bands of unreacted MA were in the same region than those of the grafted anhydride [2,4]. The presence of grafted anhydride on SPNR molecules was confirmed by a broad and intense characteristic band at 1780–1784 cm^{-1} and a weak absorption band at 1854 cm^{-1} assigned to symmetric (strong) and asymmetric (weak) C=O stretching vibrations of succinic anhydride rings, respectively [28]. The grafted MA was also deduced from the absorbance ratio of FTIR peaks at 1780–1784 cm^{-1} and 1854 cm^{-1} to 835 cm^{-1} (–C–H stretch on *cis* C=C bonds of *cis*-1,4-polyisoprene). The weak band at 3045 cm^{-1} was attributed to an intramolecular hydrogen stretching bond from the maleate conformation. After chemical modification of M-SPNR with cellulose, the new functional group occurred. It was expected to be the carboxylic group (see Fig. 1) corresponding to the bands at 2530 cm^{-1} due to the unsaturation and 1734-1724 and 1282-1164 cm^{-1} assigned to C=O. The appearance of a new band at 821 cm^{-1} in the M-SPNR-g-cellulose spectrum was attributed to out of plane deformation of

carboxylic group. The absence of any band at 1850 and 1780 cm^{-1} also confirmed the absence of non-reacted MA. The band at 776 and 1235 cm^{-1} represented C–H and COOH plus out of plane hydroxyl bending.

The ^{13}C-NMR spectra of the cellulose, SPNR, M-SPNR and M-SPNR-g-cellulose are shown in Fig. 3.

Figure 3

For cellulose fiber, the peaks at 60-70 ppm correlated to C6 of primary alcohol group whereas those of C2, C3 and C5 appeared at 70-81 ppm. In addition, the signals at 81-93 and 102-108 ppm related, respectively, to C4 and C1, anomeric carbon as the center of a hemiketal group [29]. The appearance of three singlet peaks at 23, 26 and 32 ppm in SPNR spectrum were assigned to methyl carbon and two methylene carbons. The two peaks at 125 and 134 ppm corresponded to olefinic carbons of SPNR. After modification of SPNR with MA, the new band of carboxyl group of M-SPNR was observed at 190 ppm. The signals at 64.8 and 72 ppm referred to hydroxyl group of M-SPNR-g-cellulose. In addition, those at 40, 44, 50 and 58 ppm represented hydroxyl group of SPNR-g-cellulose. It was explained that the carbon atom beared primary hydroxyl which involved intramolecular hydrogen bonds with the hydroxyl, and intermolecular bonds with the hydroxyl in the adjacent chains. The C-O-C of β-1,4–glycosidic bond in cellulose was observed at 103 ppm. The chemical shift of SPNR molecule at 14.4, 29.7, 129.9 ppm referred to $-CH_3$, $-CH_2$, and -CH, respectively. The success of the reaction was confirmed by the signal at 192 ppm relating to carbonyl groups. However, the signals were overlapped and expected to show both ester and carboxylic groups. This upfield shifted signal was mainly due to

the conjugated system of the two different isomers. The α,β-unsaturated carbons of the modifier would shift the signal to 126 and 136 ppm [23].

Mechanical properties

The values of tensile strength of the M-SPNR-g-cellulose sheets at various cellulose contents are illustrated in Fig. 4. The tensile strength of the samples having 5, 10, 30, 50, 70 and 100% w/w of natural cellulose were 13.8, 13.5, 13.2, 12.8, 10.5 and 9.5 MPa, respectively, while that of the SPNR was 18 MPa. The lower tensile strength of the M-SPNR-g-cellulose could be explained that the incorporated cellulose retarded the stress induced crystalline of SPNR molecule.

Figure 4

Fig. 5 shows that the tear strength of M-SPNR-g-cellulose with 50% of cellulose was 32 N/mm whereas that of NR was 55 N/mm. The lower tear strength of M-SPNR-g-cellulose was observed comparing to pristine SPNR due to reduction of crystalline of SPNR molecule after chemical modification.

Figure 5

The percent elongation at break of SPNR-g-cellulose was in the range 470–350 while that of SPNR sheet was 560 as shown in Fig. 6. The elongation at break which decreased as a function of cellulose content might be attributed to the change in the hardness of SPNR sheets after grafting with cellulose. Fig.7 shows the influence of cellulose content on the hardness (Shore A) of the M-SPNR-g-cellulose sheets.

Figure 6

Figure 7

It was found that the hardness of SPNR was 36 Shore A, whereas that of the SPNR-g-cellulose was ~50 Shore A. The results indicated the change of chemical structure of SPNR after addition of cellulose. Besides grafting of MA on SPNR or cellulose, the hard sample might be caused from the crosslinked rubber chains through MA bridging [27].

The modulus of the SPNR was also enhanced after grafting with cellulose as shown in Fig. 8. The increase in modulus with adding 10, 20 or 30% of cellulose was due to the hard cellulose. However, the 50 or 100% of cellulose resulted in a decrease of the modulus. The values of 100% modulus of SPNR and of M-SPNR-g-cellulose with 50% of cellulose were 1.1 and 1.3 MPa, respectively. This result agreed well with that of the hardness in Fig.7.

Figure 8

Morphology

SEM image of cellulose fiber at magnification of 150 times is shown in Fig. 9. It was observed that the surface of untreated cellulose fiber was almost free of trenches.

The diameter of cellulose fiber was in the range of 100-250 microns. The significant change on the surface was obviously noticed when the surface of cellulose was removed after chemical modification.

Figure 9

Fig. 10 shows OM images of M-SPNR and M-SPNR-g-cellulose with 5, 10, 20, 30, 50, 70 and 100 %w/w of cellulose. At cellulose content from 50%, it was observed that the fibers well dispersed in SPNR matrix.

Figure 10

SEM micrographs of the fracture surfaces of SPNR and M-SPNR-g-cellulose are shown in Fig. 11. The cellulose fibers homogeneously distributed in the SPNR matrix were observed in all samples. At cellulose content <50%, the adhesion between SPNR and cellulose seemed to be good. However, at > 50% of cellulose, the adhesion between M-SPNR and cellulose was poor as observed from void in the M-SPNR-g-cellulose [26]. It was explained that the higher amount of cellulose fiber caused the greater surface area of the fiber while the surface of SPNR was fixed. The imbalance between the surface area of M-SPNR and cellulose fiber was responsible for the void formation.

Figure 11

Antibacterial analysis

As shown in Fig. 12, both M-SPNR-g-cellulose and SPNR suppressed pathogenic growth. The antibacterial activity, investigated by measuring diameter of the clear zone, of the composite was significantly greater than that of SPNR possibly due to the carboxylic group which was a new functional group of the M-SPNR-g-cellulose. As previously reported, phenolic hydroxyl groups in poly(styrene-alt-maleic anhydride)-4-aminophenol conjugate was responsible for its antibacterial activity [30] although the bactericidal mechanism has not yet known. Therefore, it was assumed that both hydroxyl and carboxylic groups of the M-SPNR-g-cellulose contributed to its antibacterial activity.

Figure 12

Thermal properties

TGA thermograms of the cellulose, SPNR, M-SPNR and M-SPNR-g-cellulose are shown in Fig. 13. It was observed that thermal decomposition of SPNR started at ~380 °C followed by two major losses of weight during the main volatilization and pyrolysis which were essentially completed by ~550°C. The onset degradation temperature at 265°C of the M-SPNR-g-cellulose containing 10, 25 and 50 wt% cellulose fibers was slightly lower than that of M-SPNR. When compared to SPNR, the M-SPNR-g-cellulose rapidly degraded at ~100°C due to the high thermal degradation of cellulose. The weight loss from 195 to 292°C in the TGA curve of M-SPNR-g-cellulose corresponded to water evaporation whereas that from 292 to 350°C related to the main chain of cellulose. With raising temperature to 350-400°C, the main M-SPNR molecules degraded. The weight loss at >400°C confirmed the grafting between M-SPNR and cellulose [23]. The onset degradation temperature of

cellulose at ~170°C indicated that cellulose was more sensitive to thermal degradation than rubber. Starting from ~390°C, both M-SPNR and M-SPNR-g-cellulose followed almost the same thermal degradation behavior. However, the amorphous (hemicellulose) region in cellulose fiber was easier to be degraded than that of the crystalline part [31]. It was previously reported that the mass loss stages for cellulose and hemicellulose shift towards high temperature from 330 to 430°C and from 225 to 400°C, respectively. From the more visible degradation of hemicellulose, it might be deduced that the thermal degradation of M-SPNR-g-cellulose was faster than that of SPNR due to hemicellulose.

Figure 13

Biodegradation

The reduction of weight of M-SPNR-g-cellulose degraded in soil was investigated. Results in Fig. 14 show that the biodegradation of M-SPNR-g-cellulose dramatically increased with increasing the cellulose contents. It was believed that cellulose was greatly degraded by bacteria and fungi in soil activated by moisture and heat. In the case of SPNR, the sulfur bridges and high molecular weight (~10^6) of *cis*-1,4-polyisoprene were responsible for the more difficult biodegradation [18]. The previous work reported that NR can be slowly degraded in nature by specific microorganisms. The high rate of degradation of M-SPNR-g-cellulose within 1 month and nearly constant after that was due to the low amount of cellulose in the composite.

Figure 14

CONCLUSIONS

The M-SPNR-g-cellulose was successfully prepared. Its structure was proved by the appearance of a new band at 821 cm^{-1}, in ATR-FTIR spectrum, attributing to the out of plane deformation of carboxyl group. Solid state NMR revealed the signal at 192 ppm related to carbonyl groups. At high cellulose content (over 50 phr), their tensile strength decreased from 18 MPa to range 8-14 depending on cellulose content due to the morphological change of the M-SPNR-g-cellulose film. Its optimum tensile strength of 11 MPa was found. The lowest swelling ratio of M-SPNR-g-cellulose in toluene at 50% cellulose was due to the hydrophilicity of cellulose. At this cellulose content, no phase separation was observed under SEM and OM. Both hydroxyl and carboxylic groups of the M-SPNR-g-cellulose were responsible for the antibacterial activity of the composite film. The thermal degradation and biodegradability of M-SPNR-g-cellulose were faster when compared to SPNR.

ACKNOLEDMENT

Research grant (RTA5180003) from The Thailand Research Fund (TRF)/the Commission on Higher Education (CHE) to P.T. is gratefully acknowledged.

ABBREVIATIONS

ATR-FTIR	Attenuated total reflection-Fourier Transform Infrared spectrophotometer
BPO	Benzoyl peroxide
BHT	Butylated hydroxytoluene
DRC	Dry Rubber Content
HA	High ammonia
MA	Maleic anhydride
M-SPNR-g-cellulose	Maleated sulfur prevulcanized natural rubber grafted cellulose
SDS	Sodium dodecyl sulphate
SEM	Scanning Electron Microscope
TGA	Thermogravimetric analysis
ZDEC	Zinc diethyl dithiocarbamate

REFERENCES

1. Z.Peng, L.X. Kong, S.D. Li, Y. Chen, M.F. Huang, Ind. Crop. Prod. 67, 3130 (2007).

2. H. Kang, P. Weiland, Bioresource Technol. 43,107 (1993).

3. M.C. Silva, O.R. Lopes, L.J. Colodette, A.O. Porto, J. Rieumont, D. Chaussy, M.N. Belgacem, G.G. Silva, Characterization of three non-product materials from a bleached eucalyptus kraft pulp mill, in view of valorising them as a source of cellulose fibres, Ind. Crop. Prod. 27 (2008): 288-295.

4. B. Jiang, L. Hu, C. Gao, J Shen, Acta. Biomater. 2, 9 (2006).

5.M.F.M. Zain, M.N. Islam, F. Mahmud, M. Jamil, Constr. Build. Mater. 25, 798 (2011)

6. J. Araki, M. Wada, S. Kuga, T. Okano, Colloid Surface A 142, 75 (1998)

7. F.Yaşar, H.Toğrul, N. Arslan, Food Eng. 81, (2007) 187-199.

8. A. Biswas, G. Selling, M.A.K.K. Woods, L.T. Willett, C.M. Buchanan, Carbohyd. Polym. 68, 5585 (2007).

9. Z. Ma, S. Ramakrishna, J. Membrane Sci. 319 (2008) 23-28.

10. I. Muhamad, L.S. Fen, N. Hui, N.A. Mustapha, Carbohyd Polym 83, 1207 (2011)

11.E. Khouly E, A.S. Kenawy, E. Safaan, A.A. Takahashi, Y. Hafiz, Y.A. Sonomoto, K.T. Zendo, Carbohyd. Polym. 83, 346 (2011).

12. X.M. Li, S. Chanklin, W. Zheng, A.H. Xiao, Carbohyd. Polym. 83 512 (2011).

13. N. Nishioka, M. Funakoshi, K. Inamoto, M. Uno, A. Ueda, J .Appl. Polym. Sci. 118, 2482 (2010).

14. S. Benhadi, M. Ragoubi, J.-P. Joly, S. Molina, B. George , N. Brosse, B. George, N. Brosse, J. Incl. Phenom. Macro. 48, 1 (2010) .

15 B. Thielemans, W. Dufresne, A. Chaussy, D.M.N. Belgacem, Compos. Sci. Technol. 68, 3193 (2008).

16. F. Per, S. Bengt, Brit. Polym. J. 22 (1990) 147-153.

17. A. Bendahou, Y. Habibi, H. Kaddami, A. Dufresne, J. Biobased. Mater. Bio. 3,81(2009) .

18. J. Bras, L.M. Hassan, C. Bruzesse, AE. Hassan, A. Nahla El-Wakil, A. Dufresn, Ind. Crop. Prod. 32, 627 (2010) .

19. A. Bendahou, H. Kaddami, A. Dufresne, Eur .Polym. J. 46 609 (2010).

20. D. Pasquini, D.M.E. Teixeira, A.D.S.A. Curvelo, M.N. Belgacem, A. Dufresne, Ind. Crop. Prod. 32, 486 (2010) .

21. M.H. Gabr, M.A. Elrahman, K. Okubo, T. Fujii, Compos. Part A-Appl . 41,1263 2010 (2010).

22. W. Zhanga, X. Zhanga, M. Lianga, C. Lu, Compos. Sci. Technol. 68, 2479 (2008).

23. D. Deroueta, P. Intharapata, Q.N. Trana, nF. Gohiera, C. Nakason, Eur. Polym. J. 45, 820 (2009).

24. K. Shirahama, S. Sato, M. Niino, N. Takisawa, Colloids Surfaces A 112, 233 (1994) .

25. A.I. Khalf, D.E.E.l, Nashar, N.A. Maziad, Mater. Design 31, 2592 (2010).

26. A.F. Martins, J.C.M. Suarez, L.L.Y. Visconte, J. Mater. Sci. 38, 2415 (2003).

27. M. Yoshizawa, E.Marwanta, H. Ohno, Polymer 41, 9049 (2000).

28. H. Ismail, A. Rusli, A.A. Rashid, Polym. Test. 24, 856-862 (2005).

29. J.F. Kadla; R.D. Gilbert, Chem Technol 34, 197 (2000).

30. J.H. Jeong, Y.S. Byoun, Y.S. Lee, React. Funct. Polym. 50, 257 (2002).

31. D.K. Shen, S. Gu, A.V. Bridgwater, Carbohyd. Polym. 82, 39 (2010).

Figure caption

FIG.1 Possible mechanism of grafting M-SPNR with cellulose initiated by BPO and $K_2S_2O_8$

FIG.2 ATR-FTIR spectra of cellulose, SPNR, M-SPNR and M-SPNR-g-cellulose

FIG.3 ^{13}C-NMR spectra of cellulose, SPNR, M-SPNR and M-SPNR-g-cellulose

FIG. 4 Tensile strength of SPNR and M-SPNR-g-cellulose having various cellulose contents

FIG. 5 Tear strength of SPNR and M-SPNR-g-cellulose having various cellulose contents

FIG. 6 Elongation at break of SPNR and M-SPNR-g-cellulose having various cellulose contents

FIG.7 Hardness of SPNR and M-SPNR-g-cellulose having various cellulose contents

FIG.8 Modulus of SPNR and M-SPNR-g-cellulose having various cellulose content

FIG.9 SEM image of cellulose fiber from corn leaves

FIG.10 OM images of SPNR and M-SPNR-g-cellulose having various cellulose contents

FIG. 11 SEM images of SPNR and M-SPNR-g-cellulose having various cellulose contents

FIG. 12 Antibacterial of SPNR and M-SPNR-g-cellulose (50%cellulose)

FIG.13 TGA of cellulose, SPNR, M-SPNR and M-SPNR-g-cellulose

FIG.14 Biodegradation in soil of M-SPNR-g-cellulose having various cellulose contents

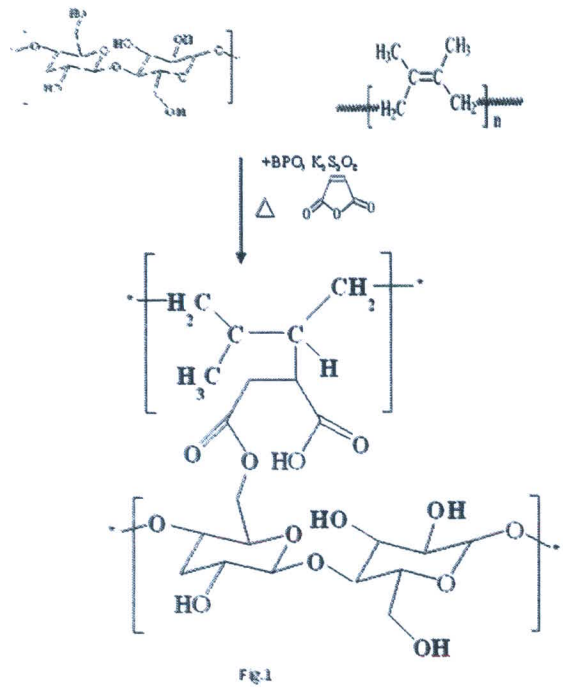


Fig.1

203x256mm (300 x 300 DPI)

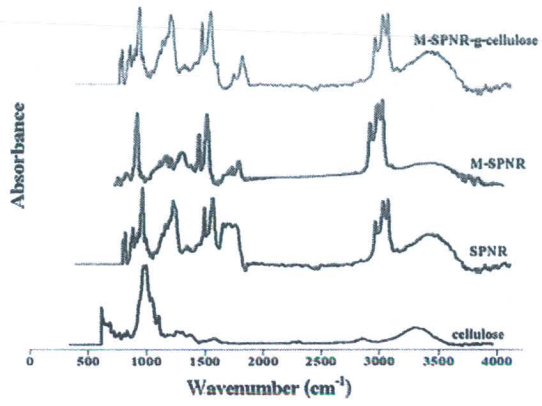


Fig.2

122x96mm (300 x 300 DPI)

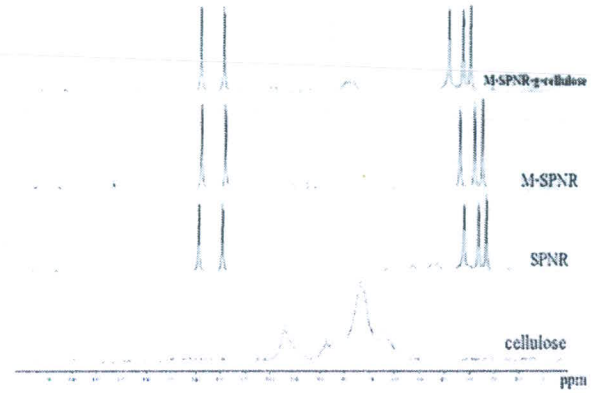


Fig.3

113x88mm (300 x 300 DPI)

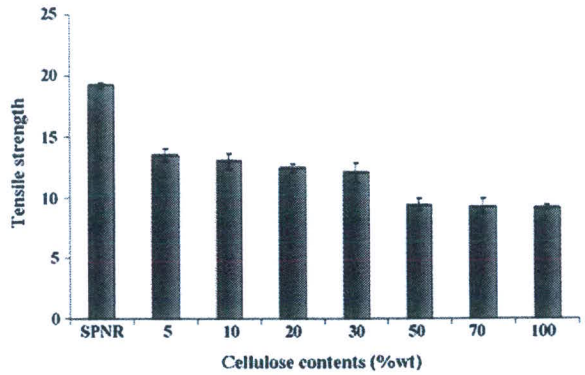


Fig.4

109x81mm (300 x 300 DPI)

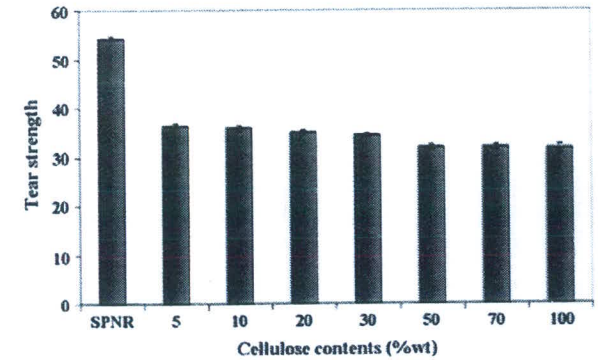


Fig.5

103x73mm (300 x 300 DPI)

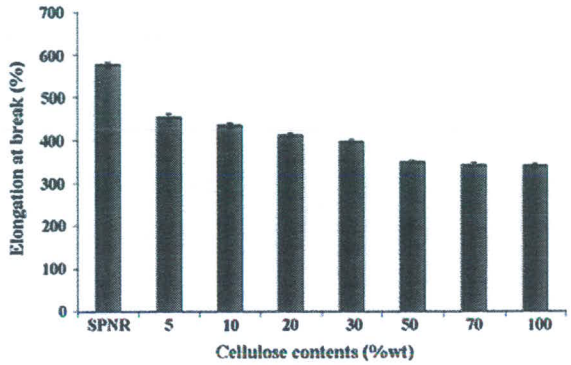


Fig.6

107x78mm (300 x 300 DPI)

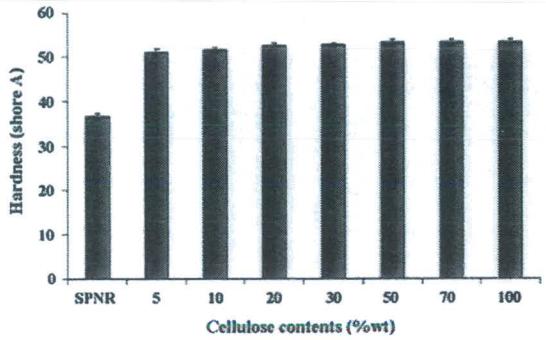


Fig.7

102x66mm (300 x 300 DPI)

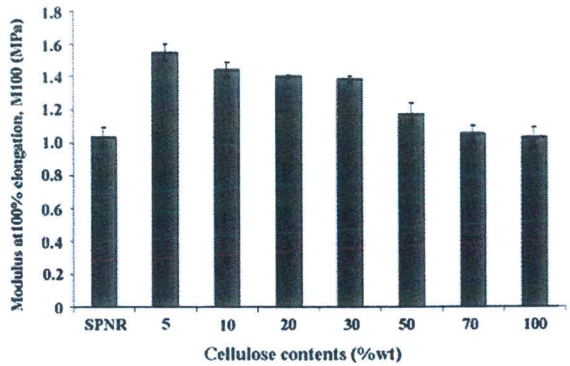


Fig.8

106x77mm (300 x 300 DPI)

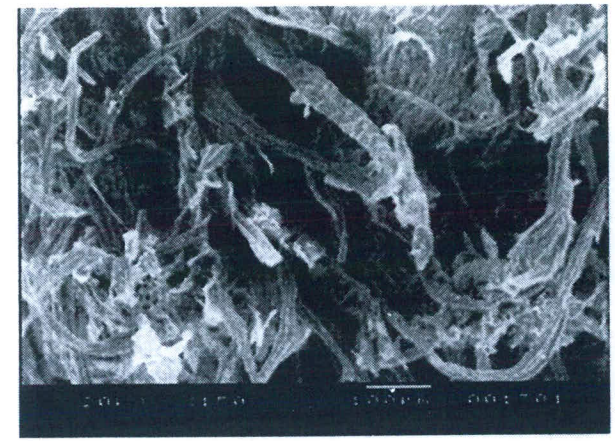


Fig.9

93x85mm (300 x 300 DPI)

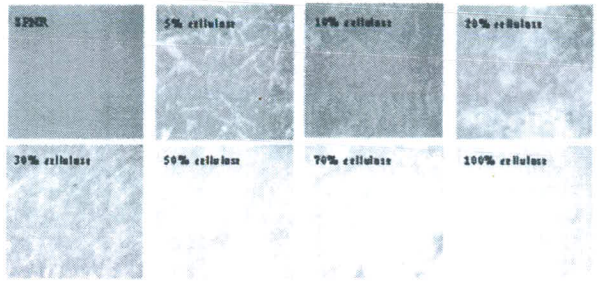


Fig.10

86x50mm (300 x 300 DPI)

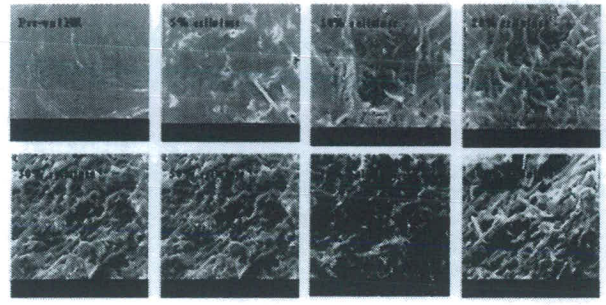


Fig.11

93x58mm (300 x 300 DPI)

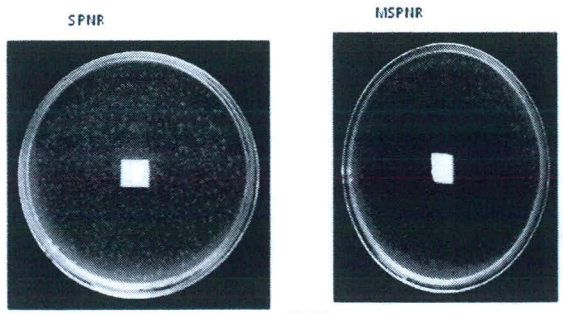


Fig.12

86x51mm (300 x 300 DPI)

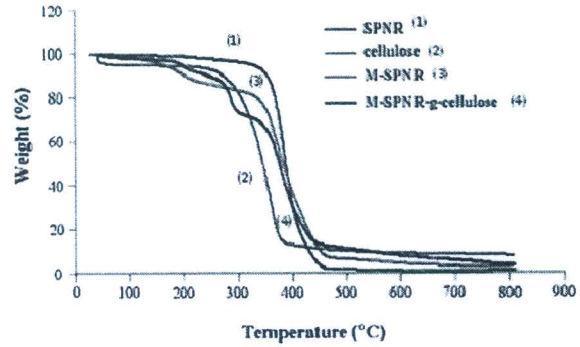


Fig.13

99x65mm (300 x 300 DPI)

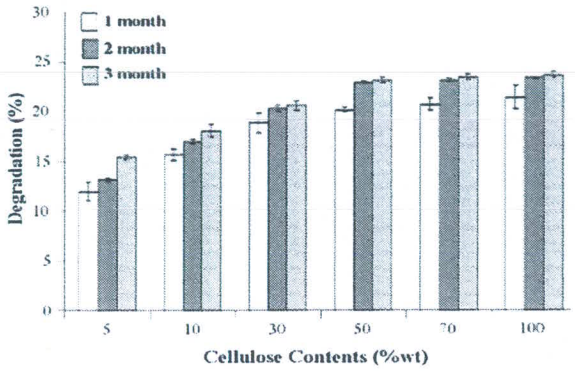


Fig.14

110x81mm (300 x 300 DPI)

เอกสารแนบ 5.2.5

Elsevier Editorial System(tm) for Industrial Crops and Products
Manuscript Draft

Manuscript Number: INDCRO-D-11-00618

Title: Physical properties of polymer composite: natural rubber glove waste/polystyrene foam waste/cellulose

Article Type: Original Research Paper

Keywords: Natural rubber; Glove; Polystyrene; Waste; Cellulose; Chemical modification

Corresponding Author: Dr. saad riyajan, Ph.D

Corresponding Author's Institution: Prince of Songkla University

First Author: saad riyajan, Ph.D

Order of Authors: saad riyajan, Ph.D; Isara Intharit ; Pramuan Tangboriboonrat

Abstract: The polymer composite was prepared from the wastes of natural rubber glove (NRG) and polystyrene foam (PSF) blended with cellulose from sugar cane leave via the laminate method. The NRG and PSF were firstly dispersed in toluene under continuous stirring. Then, maleic anhydride (MA) was added into the mixture. Effects of blend ratio and of MA content (0.5-15% w/w) on physical properties of the polymer composite were investigated. The toluene resistance of the polymer blend was improved after adding MA and cellulose. The highest toluene resistance was achieved when using 12% cellulose. The chemical reactions of MA with polymer blend and with composite were confirmed by ATR-FTIR. The hardness of the polymer blend and composite increased as a function of PSF. In addition, their impact strength increased with increasing NRG and cellulose contents.

Suggested Reviewers: Leonardo Simon PhD.
Department of Chemical Engineering , University of Waterloo
lsimon@uwaterloo.ca
He is expert in polymer characterization.

Der-Jang Liaw
Department of Chemical Engineering , National Taiwan University of Science and Technology
chem@mail.ntust.edu.tw
He is expert in polymer characterization.

Seiichi Kawahara
Prof., Department of Materials Science and Technology, Nagaoka University of Technology
kawahara@chem.nagaokaut.ac.jp
He is expert in polymer characterization.

Sabu Thomas
School of Chemical Sciences, Mahatma Gandhi University
sabuthom@vsnl.com
He is expert in naturar rubber.

Highlights

We described the influence of cellulose on properties of NR glove/PS foam blend. ► The toluene resistance and mechanical properties was improved by cellulose► It is the first polymer blend was obtained from waste from NR and PS foam. ► The advantage of this system is environment friendly.

*Manuscript
Click here to view linked References

Physical properties of polymer composite: natural rubber glove waste/polystyrene foam waste/cellulose

Sa-Ad Riyajan[1]*, Isara Intharit[1], Pramuan Tangboriboonrat[2]

[1]*Department of Materials Science and Technology, Faculty of Science, Prince of Songkla University, Songkhla 90112, Thailand*

[2]*Department of Chemistry, Faculty of Science, Mahidol University, Rama 6 Road, Bangkok 10400, Thailand*

*Corresponding author: saadriyajan@hotmail.com

Phone/Fax 660-074288398

ABSTRACT

The polymer composite was prepared from the wastes of natural rubber glove (NRG) and polystyrene foam (PSF) blended with cellulose from sugar cane leave *via* the laminate method. The NRG and PSF were firstly dispersed in toluene under continuous stirring. Then, maleic anhydride (MA) was added into the mixture. Effects of blend ratio and of MA content (0.5-15% w/w) on physical properties of the polymer composite were investigated. The toluene resistance of the polymer blend was improved after adding MA and cellulose. The highest toluene resistance was achieved when using 12% cellulose. The chemical reactions of MA with polymer blend and with composite were confirmed by ATR-FTIR. The hardness of

the polymer blend and composite increased as a function of PSF. In addition, their impact strength increased with increasing NRG and cellulose contents.

Keywords: Natural rubber, Glove, Polystyrene, Waste, Cellulose, Chemical modification

1.Introduction

At present, the demand of natural rubber glove (NRG) exponentially increases due to the health awareness. After its use, NRG is generally left as garbage which is difficult to biodegrade since polyisoprene chains of NR are crosslinked either by sulfur (Riyajan et al., 2003; Hall et al., 2009) or peroxide system. The problem of NRG waste disposal is, therefore, growing as a direct result of rapid industrialization and population growth. Especially, the infectious waste from hospital and other toxic hazardous waste might cause serious environmental problem and great health risk to public. For example, the diseases like diarrhea, leptospirosis, typhoid and cholera can be transmitted through the mismanagement of waste. Moreover, the public increasingly concerns over the handling of medical waste because of the recent acquired immune deficiency syndrome (AIDS) dilemma, severe acute respiratory syndrome (SARS) epidemic, Avian influenza and those posed by other communicable diseases such as hepatitis B.

Susceptibility of NR products towards a microbial attack is a well known phenomenon (Hall et al., 2009). The environment authority agency such as The World Health Organization (WHO) uses the landfilling or incineration (WHO, 2000) and pyrolysis process (Deng et al., 2008; Conrardy et al. 2010) to reduce the rubber waste (Hall et al., 2009). Without catalyst, the pyrolysis oil from the rubber waste consisted mainly of limonene and oligomers of polyisoprene. The presence of the Y-zeolite catalyst in the pyrolysis of rubber caused an increase in the yield of hydrocarbon gases similar to the degradation of polystyrene (PS) (Berekaa et al., 2000). The destruction of NRG waste by molten salt oxidation produced

CO_2, N_2 and water (Hsu et al., 2000). In this case, the chemical composition of the degraded glove, analyzed by thermogravimetric analysis (TGA) under N_2, played a fundamental role in pyrolytic behavior.

In parallel, the NRG waste can be reused in several applications such as mat and massive tire as well as most of the constituent parts of both passenger and truck tire (Rajan et al., 2006). In addition, the rubber waste was blended with virgin synthetic rubber and NR to improve the polymer processing. However, the blend of NRG waste with polystyrene foam (PSF) waste was not found in literature. The reports concerned only about the use of PSF waste in polymeric flocculants (Wiesław et al., 2007), ion adsorption (Long et al., 2010), polymer mortar panels (Bhutta et al., 2011) and electrolyte (Bajdur et al., 2002). The polymeric flocculant, i.e., poly(styrene sulphonate) acid, was obtained from PSF waste and virgin PS during the sulphonation process using H_2SO_4 as sulphonating agent and Ag_2SO_4 as catalyst. The effectiveness of the flocculation depended on the number of sulphonic groups per monomer unit and its molecular weight. In addition, PSF waste blended with poly(methyl methacrylate) and reinforced with steel fiber was applied in polymer mortar panels (PMPs) (Bhutta et al., 2011). Due to their high ductile and load-bearing capacity, PMPs could replace a commercial polymer-impregnated mortar panel in practical applications.

In this present work, the NRG waste was blended with PSF waste by using maleic anhydride (MA) as a crosslinker. As reported in the previous work concerning NR/ butadiene (BR)/ Ethylene Propylene Diene Monomer (EPDM) blend, it was expected that the addition of MA would improve the properties of NRG/PSF blend (Zhang et al., 2010). The NRG waste was masticated by a two-roll mill and dispersed in toluene. The NRG dispersion was mixed with PSF and MA dissolved in toluene under continuous stirring. After drying at ambient temperature, the NRG/PSF blend was laminated with cellulose from sugar cane leave by using a compression molding. Effects of polymer blend ratio, MA and cellulose

contents on the properties, i.e., tensile strength, hardness and tear strength, of polymer composite were investigated. Theirs chemical structure and morphology were studied by using attenuated total reflection-Fourier Transform Infrared spectrophotometer (ATR-FTIR) and scanning electron microscope (SEM), respectively. Toluene resistance of the polymer composite was also determined.

2. Experimental

2.1 Materials

PSF waste was received from a local company in Songkhla province, Thailand. Poly(vinyl alcohol), MA and benzoyl peroxide (BPO) were purchased from Sonal Company (Songkhla, Thailand), Fluka (Schnelldorf, Germany) and Merck Schuchardt OHG (Seelze, Germany), respectively. Hydrogen peroxide and perchloric acid were purchased from Solvay Peroxythai Ltd. (Bangkok, Thailand and Guangdong, China) while sodium hydroxide was supplied from Lab Scan Analytical Science (Bangkok, Thailand)

In the preparation of cellulose fiber, sugar cane leaves were immersed in 10% NaOH solution for 24 h and then washed with water until reaching neutral pH. The wet cellulose was cast on a glass plate and dried at ambient temperature for 3 days and, subsequently, at 50°C for 24 h. The diameter of dried cellulose fiber was determined under an optical microscopy (OM; Primo Star company, Carl Zeiss).

2.2 Preparation of polymer composite

NRG waste from Sri Trang Company (Songkhla, Thailand) was masticated by using two-roll mill (Charoenchaikarnchange; Bangkok, Thailand) at 30-32°C for 30 min. The masticated NRG was immersed in toluene for 2 days at ambient temperature and then stirred for 5 h. After stirring with a mechanical stirrer for 1 h, the size and size distribution of the NRG

suspended in toluene was measured by a Laser Particle Size Analyzer (LPSA; Beckman Coulter LS 230).

The NRG suspension with various contents was blended with 10% w/v of PSF in toluene at room temperature by using a homogenizer (PL Trading internation Co. Ltd; Bangkok, Thailand). 0.5% BPO, 5% glycerol and different MA concentrations were added into the blend under stirring. In order to form a sheet of 0.45 mm in thickness, the mixture was poured into a glass plate ($10\times10\times0.5$ cm^3) at ambient temperature. The cellulose sheet was placed between two NRG/PSF sheets. After heating at 80°C for 6 h, the dried polymer composite was compressed by compression molding (Charoenchaikarnchange; Bangkok,Thailand) at 150°C for 10 h and was kept at ambient temperature overnight. Under a hot-press, the sample was preheated at 150°C for 6 min and then compressed for 4 min before being cooled under 3 MPa at 30°C for 4 min.

2.3 Characterizations and testing of polymer composite

The chemical structure of polymer composite was investigated by using ATR-FTIR (Equinox 55; Bruker) for 100 times of scan. Its gel content was determined by immersing a known weight of specimen (2.5 cm x 2.5 cm x 0.5 mm) in toluene at 32°C for 5 days. The sample was then dried at 50°C for 24 h and weighed until a constant weight was obtained. The degree of gel content was calculated from equation (1):

$$\text{Gel content} = (W_2 - W_1) / W_1 \quad \text{.....(1)}$$

where W_1 is the original weight of the sample and W_2 is the weight of dried residual sample.

SEM (JMS-5800 LV, JEOL) was used for study of the morphology of cross-sectional sample at an accelerating voltage of 6 kV. After fracturing a specimen under liquid N_2, its cross-sectional area was coated with platinum under a 12 Pa vacuum. The storage modulus and tan δ of the polymer composite were examined by dynamic mechanical thermal analysis (DMTA V) in tension mode at 10 Hz, 0.05% strain and different temperatures. The physical testing of polymer composite was analyzed by universal testing machine (LR10K, Lloy Intruments) based on ASTM D 412 at 500 mm/min using 5 dumbbell test pieces. Its hardness was measured according to ASTM D 2240 while an Impacts-15 resilience test pendulum impact tester (Yasdu, No. 258-D) was applied for determination of impact resistance at 25-28 C

3. Results and discussion\

3.1 Analysis of polymer composite

Before mixing the masticated NRG dispersed in toluene with PSF waste solution and MA, the size and size distribution of NRG suspension are measured by a particle size analyzer and the data are shown in Fig. 1.

Figure 1

Result indicated that 75% of the dispersed NRG were in the size ranging from 250 to 500 micron. ATR-FTIR was then used for analysis of the chemical structures of the NRG/PSF blend in the presence of 10% MA and of the NRG/PSF blended with 10% MA and 5% cellulose or polymer composite. Fig. 2 shows the spectra of NRG/ PSF blended with 10% MA (a) before and (b) after immersion in toluene and those of polymer composite having 50/50 NRG/PSF blended with 10% MA and 5% cellulose (c) before and (d) after immersion in toluene.

Figure 2

The characteristic peaks at 3025 (C-H aromatic), 1610 (C-C aromatic), 2920 and 2849 (CH_2CH_2), 1490 and 1450 (C_6H_5), 905 and 697 (C-H aromatic) cm^{-1} of PS appeared in Fig. 2 (a)-(d). The bands at 1076 and 1664 cm^{-1} attributed, respectively, to the symmetric C–S–C stretching vibrations and C=C of NRG were also noticed. The grafted MA in the blend was deduced from the absorbance ratio of peaks at 1780–1784 cm^{-1} to 1835–1854 cm^{-1} (CH stretching on C=C of *cis*-1,4-polyisoprene) in (b) (Zhang et al., 2010). The characteristic peaks at 3200-3400 cm^{-1} due to OH from cellulose fiber were observed in (c) and (d). A shoulder at 1745 cm^{-1} confirmed that the small amount of ester groups remained in side chains of the polymer composite. After adding cellulose in NRG/PSF blend, the intensity of peak at 3400 cm^{-1} of polymer composite decreased. In addition, the increase of bands at 1745 and 1270 cm^{-1} due to ester C=O and C–O–C of cellulose in polymer composite was detected. The peaks at 821, 896, 1046, 1382 and 2926 corresponding to the out of plane deformation of COOH, C-H deformation, C-O-C from β-1,4–glycosidic, OH bending and C-H stretching, respectively, also appeared.

3.2 Gel content

The influence of NRG/PSF ratio on the gel content of the polymer blend containing 10% MA without cellulose is presented in Fig. 3 (a).

Figure 3

Results showed that the gel content of polymer blend having NRG/PSF of 30/70 was similar to that of 50/50 which was greatly lower than that of 70/30. It was believed that the high NRG content whose molecules were still partially crosslinked with sulphur was responsible for the high gel content. As expected, the gel contents of all NRG/PSF blends strongly increased with adding cellulose fiber as shown in Fig. 3(b). The gel contents of polymer composites containing 3, 5 and 12% were 58, 60 and 63%, respectively. It was possibly caused from the adsorption of macromolecular chains at the filler/matrix interface, filler/filler interactions and the chemical reaction between MA and polymer matrix as previously reported in the case of NR filled with cellulose (Bendahou et al., 2010).

The optical micrographs of PSF blended with 5% cellulose and various amounts of MA (0, 5, 10 and 15%) after immersion in toluene are displayed in Fig. 4.

Figure 4

The good dimensional stability of PSF/cellulose added with MA especially of 15% was observed in Fig. 4 (d). This result indicated the occurrence of chemical interaction between PSF and MA or between cellulose and MA during blending process.

3.3 SEM morphology

The morphology affecting the physical properties of polymer composite was investigated. SEM micrographs in Fig. 5 show PSF blended with 5% cellulose in the presence of (a) 0, (b) 5, (c) 10, (d) 15% w/w of MA and those of polymer composite containing 50/50 NRG/PSF, 5% cellulose and (e) 0, (f) 10% w/w of MA.

In Fig. 5 (a), it seemed that the polar cellulose fibers were hard to disperse in non-polar PSF and NRG/PSF matrix due to the difference in the surface energy of each

component (Zhange et al., 2008). The strong adhesion between PSF and cellulose was observed after addition of MA in Fig. 5 (b)-(d). A large number of voids were observed on the fracture surface of all PSF samples. When NRG was added in PSF/cellulose in the absence of MA in Fig.5 (e), the voids were also noticed due to poor interface interaction. After adding MA, the strong adhesion or chemical bond between cellulose fiber and polymer matrix occurred in Fig. 5 (f) which would affected the mechanical strength of the polymer composite.

Figure 5

3.4 Mechanical strength

Fig. 6 (a)-(d) show the effects of cellulose contents (0, 3, 5 and 12%) on tensile strength of the polymer composites having NRG/PSF of 0/100, 30/70, 50/50 and 70/30.

Figure 6

It was observed that the tensile strength of PSF was 2 MPa and that of polymer blend without cellulose in Fig. 6 (a) decreased from 3.4, 1.4 to 0.7 MPa when NRG/PSF were 30/70, 50/50 and 70/30, respectively. After addition of 3, 5 and 12% cellulose in the 30/70 NRG/PSF, the tensile strength of the polymer composites in Fig. 6 (b)-(d) increased from 5.2, 5.8 to 6.2 MPa, respectively. The results agreed well with those of NR filled cellulose previously reported (Bras, 2010). The drop in the tensile properties of the polymer composites when increasing NRG content was reasonably due to poor interaction between cellulose and the NRG/PSF matrix. Moreover, the poor dispersion and/or agglomeration of

the filler in the matrix led to the in-homogeneity of phase morphology which became the dominant process in the mixing. This effect was more pronounced with increasing filler content.

At low cellulose content of 3% w/w, the polymer composite exhibited an elastic non-linear behavior which is typical for amorphous polymer at temperature greater than glass transition temperature (Tg). At high filler content of 12%, the mechanical behavior of NRG/PSF waste was high because a considerable amount of fibers allowed the transfer of the applied load between them. The higher compatibility between cellulose fiber and the hydrophobic polymer matrix by adding MA which ensued higher filler/matrix adhesion was also responsible for this difference (Bendahou et al., 2010).

The effect of MA content on the hardness of polymer composite containing 50/50 NRG/PSF and 5% cellulose is shown in Fig. 7.

Figure 7

The presence of 5% MA significantly increased the hardness of the polymer composites from 46 to 65 shore A. With 10 and 15% of MA, the hardness values were constant, i.e., 64 and 62 shore A, respectively. The change in hardness was possibly caused from the chemical reaction between MA and NRG/PSF matrix which efficiently facilitated energy transfer process and, hence, toughened the composite (Chong et al., 2010). The influence of the both cellulose and polymer blend ratio on the hardness of the polymer blend is presented in Fig. 8 I.

Figure 8

Results showed that the hardness of the polymer composites decreased from 94 to 62 shore A when varying NRG/PSF from 30/70 to 50/50. Further increase in NRG content, the hardness of the polymer composites having 50/50 and 70/30 NRG/PSF were constant. This was due to the fact that the cellulose fiber sheet was in the center of specimen. It was confirmed by the insignificantly change of hardness of the polymer composites when changing the cellulose contents.

The data of impact strength of the polymer composites containing 30/70, 50/50 and 70/30 NRG/PSF plotted with cellulose contents are presented in Fig. 8 II.

The increase in impact strength when increasing the amount of NRG was explained from the ductile fracture initiated by the shear yielding mechanism [Mathew et al., 2001c]. Due to the low Tg of NR (-78°C), the NRG chains easily moved at room temperature and played the role of toughening agent. The dual phase continuity and phase interpenetration might also enhance the impact resistance. It was reported that the co-continuous interpenetrating polymer network (IPN) structure exhibited high impact strength of polymer composite because the uniform rubbery phase allowed the energy to be dissipated into the whole sample (Mathew et al., 2001). This effective dissipation of energy was the principal role of rubbery phase in impact resistant materials.

The effect of cellulose content on the impact strength of the polymer composites was also displayed in Fig. 8 II. At 50/50 NRG/PSF, the impact strength values of the polymer composites with 0, 3, 5 and 12% cellulose were 7, 12, 21 and 23.5 J/m^2, respectively. The reinforcement might be because a polymer chain could interact with several units of the fibers. If this chain breaks due to the impact energy, the load is transferred to many other chains providing the increase in impact strength of the material (Megiatto Jr et al., 2010).

4.Conclusions

The polymer composite was developed from the blend of NRG and PSF wastes with addition of MA and cellulose from sugar can leave. Their mechanical properties were better than those of PSF due to the chemical reaction between PSF/cellulose and MA which were confirmed by gel content and ATR-FTIR. The highest tensile strength of sample was found in 30/70 NRG/PSF blended with 10% MA and 12% cellulose. This observation was supported by SEM, toluene resistance, impact strength and hardness. The polymer composite would potentially be used in artificial wood.

Acknowledgements

The authors would like to thank The Thailand Research Fund (TRF)/ Commission on Higher Education for the research grant. P.T. is TRF Senior Researcher.

References

Berekaa, M.M., Linos A., Reichelt, R., Keller, U., Steinbüchel, A. 2000. Effect of pretreatment of rubber material on its biodegradability by various rubber degrading bacteria FEMS. Microbiology Letters 184, 199-206.

Bendahou, A., Kaddami, H., Alain Dufresne, A. 2010. Investigation on the effect of cellulosic nanoparticles' morphology on the properties of natural rubber based nanocomposites. European Polymer Journal 46, 609-620.

Beach, M.W., Rondan, N.G., Froese, R.D., Gerhart, B.B., John G. Green, Bill G. Stobby, Andrey G. Shmakov, Vladimir M. Shvartsberg, Oleg P. Korobeinichev. 2008. Studies of degradation enhancement of polystyrene by flame retardant additives. Polymer Degradation and Stability 93, 1664-1673

Bhutta, M.A.R., Ohama, Y., Tsuruta, K. 2011. Strength properties of polymer mortar panels using methyl methacrylate solution of waste expanded polystyrene as binder. Construction and Building Materials 25, 779-784

Chong, E.L., Ahmad, I., Dahlan, H.M., Abdullah, I. 2010. Reinforcement of natural rubber/high density polyethylene blends with electron beam irradiated liquid natural rubber-coated rice husk. Radiation Physics and Chemistry 79, 906-911.

Chuayjuljit, S., Boonmahitthisud, A. 2010. Natural rubber nanocomposites using polystyrene-encapsulated nanosilica prepared by differential microemulsion polymerization. Applied Surface Science 256, 7211-7216.

Conrardy, J., Hillanbrand, M., Myers, S., Nussbaum, G.F. 2010. Reducing medical waste . AORN 91, 711-721.

Dong, D., Tasaka S., Inagaki, N. 2001.Thermal degradation of monodisperse polystyrene in bean oil. Polymer Degradation and Stability 72, 345-351

Hall, W.J., Zakaria, N., Williams, P.T. 2009. Pyrolysis of latex gloves in the presence of Y-zeolite. Waste Management 29, 797-803.

Hourston, D.J., Schäfer, F.U., Gradwell, M.H.S., Song, M. 1998.TMXDI-based poly(ether urethane)/polystyrene interpenetrating polymer networks: 2. Tg behaviour, mechanical properties and modulus-composition studies. Polymer, 39, 5609-5617.

Hsu, P.C., Foster, K.G., Ford, T.D., Wallman, P.H., Watkins, B.E., Pruneda, C.O., Adamson, M.G. 2000. Treatment of solid waste with molten salt oxidation. Waste Management 20, 363-368.

Long, C., Li, Q., Li, Y., Liu, Y., Li, A., Zhang Q. 2010. Adsorption characteristics of benzene–chlorobenzene vapor on hypercrosslinked polystyrene adsorbent and a pilot-scale application study. Chemical Engineering Journal 160, 723-72

Mathew, A.P., Packirisamy, S., Thomas, S. 2001. Studies on the thermal stability of natural rubber/polystyrene interpenetrating polymer networks: thermogravimetric analysis. Polymer Degradation and Stability 72, 423-439.

Mathew, A.P., Packirisamy, S., Radusch, H.J.,Thomas, S.b. 2001. Effect of initiating system, blend ratio and crosslink density on the mechanical properties and failure topography of nano-structured full-interpenetrating polymer networks from natural rubber and polystyrene. European Polymer Journal 37, 1921-1934.

Mathew, A.P., and Thomas, S. 2001. Izod impact behavior of natural rubber/polystyrene interpenetrating polymer networks. Materials Letters 5, 154-163.

Mathew, A.P., Packirisamy, S., Stephen R., Thomas, S. 2002. Transport of aromatic solvents through natural rubber/polystyrene (NR/PS) interpenetrating polymer network membranes. Journal of Membrane Science 201, 213-227.

Madorsky, S.L., Straus, S., Thompson, D., Williamson L. 1949. Pyrolysis of polyisobutene (vistanex), polyisoprene, polybutadiene, GR-S and polyethylene in a high vacuum. Journal of Research of the National Institute of Standards and Technology *42*, 499–514.

Megiatto, Jr., Jackson,D., Ramires, E.C., Frollini, E. 2010. Phenolic matrices and sisal fibers modified with hydroxy terminated. polybutadiene rubber: Impact strength, water absorption, and morphological aspects of thermosets and composites. Industrial Crops and Products *31*, 178-184

Rajan,V.V., Dierkes,W.K., Joseph,R., Noordermeer,J.W.M. 2006. Science and technology of rubber reclamation with special attention to NR-based waste latex products. Progress in Polymer Science 31, 811-834.

Riyajan, S., Sakdapipanich, J.T., Yasuyuki, T. 2003. Controlled Degradation of Cured Natural Rubber by Encapsulated Benzophenone as a Photosensitizer. Journal of Applied Polymer Science 90, 297-305.

Riyajan, S., Chaiponban, S. 2009. Activation Energy and Thermal Behaviors of Thermoplastic Elastomer Based on Natural Rubber and Polyvinyl Alcohol. KGK-Kaustschuk Gummi Kunststoffe 63, 28-33.

Wang, S.,Liu, Q., Luo, Z., Wen, L.,Cen K. 2007. Mechanism study on cellulose pyrolysis using thermogravimetric analysis coupled with infrared spectroscopy. Front Energy Power Eng China 1, 413–419.

Wiesław, W., Agnieszka, S., Barbara, W., Wioletta. S., Bajdur, M., Sułkowska, A. 2005. Preparation and properties of flocculants derived from polystyrene waste.

pyrolysis of representative medical waste. Polymer Degradation and Stability 90, 272-280

Zhang, Y.F., Wang, Y. 2008. Thermogravimetric analysis and kinetic study pyrolysis of representative medical waste composition. Waste Management 28,1572-1580

Zhang, H., Datta, R.N., Talma, A.G., Noordermeer, J.W.M. 2010. Maleic-anhydride grafted EPM as compatibilising agent in NR/BR/EPDM blends. European Polymer Journal 46, 754-766.

Zhang,W., Zhang, X., Liang, M., Lu, C. 2008. Mechanochemical preparation of surface-acetylated cellulose powder to enhance mechanical properties of cellulose-filler-reinforced NR vulcanizates. Composites Science and Technology 68, 2479-2484.

Zhang, H., Datta, R.N., Talma, A.G., Noordermeer, J.W.M. 2010. Maleic-anhydride grafted EPM as compatibilising agent in NR/BR/EPDM blends. European Polymer Journal 46, 754-766.

Figure caption

Figure 1 Size of NRG dispersed in toluene measured by particle size analyzer

Figure 2 ATR-FTIR spectra of NRG/PSF blended with 10% MA (a) before and (b) after immersion in toluene and polymer composite containing 50/50 NRG/PSF, 10% MA and 5% cellulose (c) before and (d) after immersion in toluene

Figure 3 Effect of NRG/PSF on gel content of polymer blend

Figure 4 Photographs of PSF in the presence of 5% cellulose and (a) 0, (b) 5, (c) 10 and 15% of MA after toluene resistant test

Figure 5 SEM micrographs of PSF blended with 5% cellulose in the presence of (a) 0, (b) 5, (c) 10, (d) 15% w/w of MA and those of polymer composite containing 50/50 NRG/PSF, 5% cellulose and (e) 0, (f) 10% w/w of MA.

Figure 6 Effect of cellulose contents of (a) 0, (b) 3, (c) 5 and (d) 12%w/w on tensile strength of PSF and polymer composite containing NRG/PSF of 0/100, 30/70, 50/50 and 70/30

Figure 7 Hardness of 50/50 NRG/PSF blended with different MA contents

Figure 8 (I) Effects of cellulose contents of (a) 0, (b) 3, (c) 5 and (d) 12 % on hardness of polymer composite containing 50/50 NRG/PSF and (II)Effects of cellulose contents on impact strength of polymer composites having NRG/PSF of (a) 30/70, (b) 50/50 and (c) 70/30

Figure1
Click here to download high resolution image

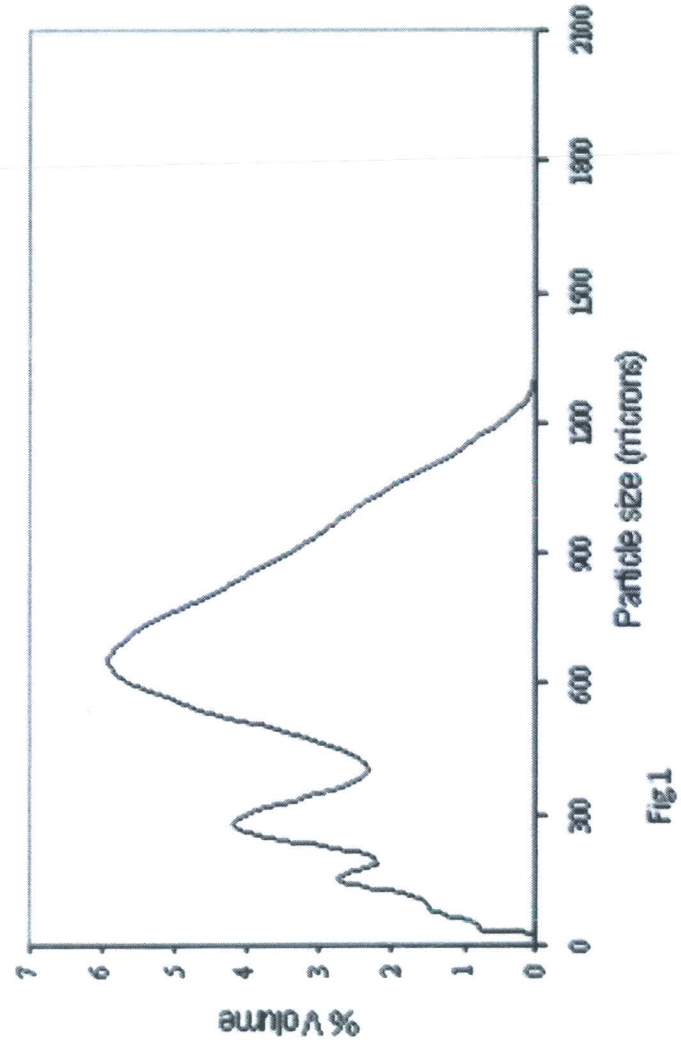


Fig.1

Figure2
Click here to download high resolution image

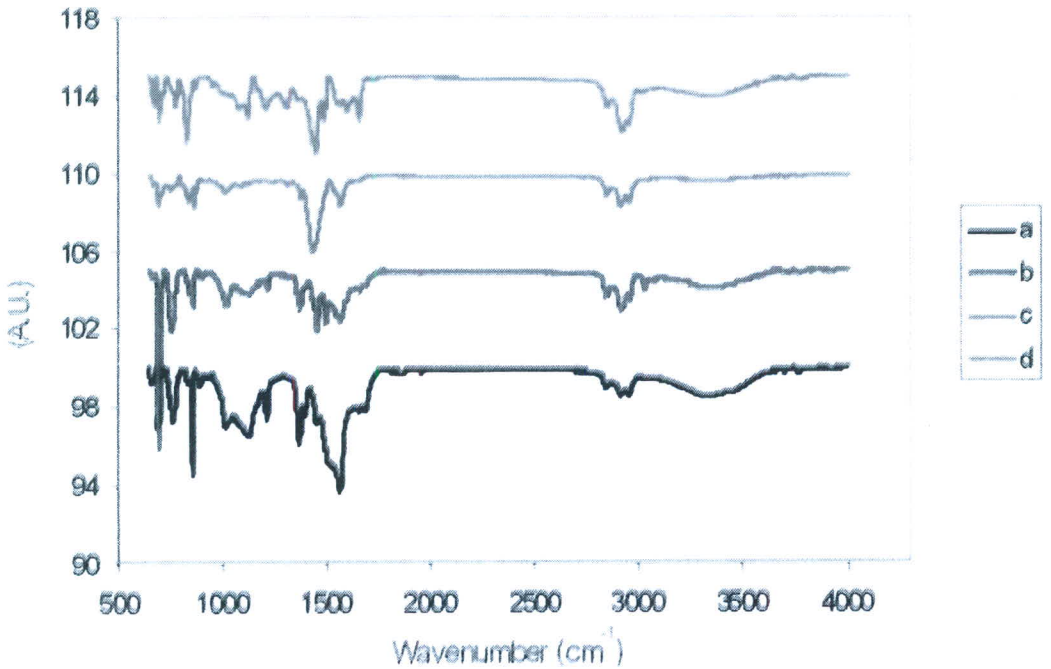


Figure3
Click here to download high resolution image

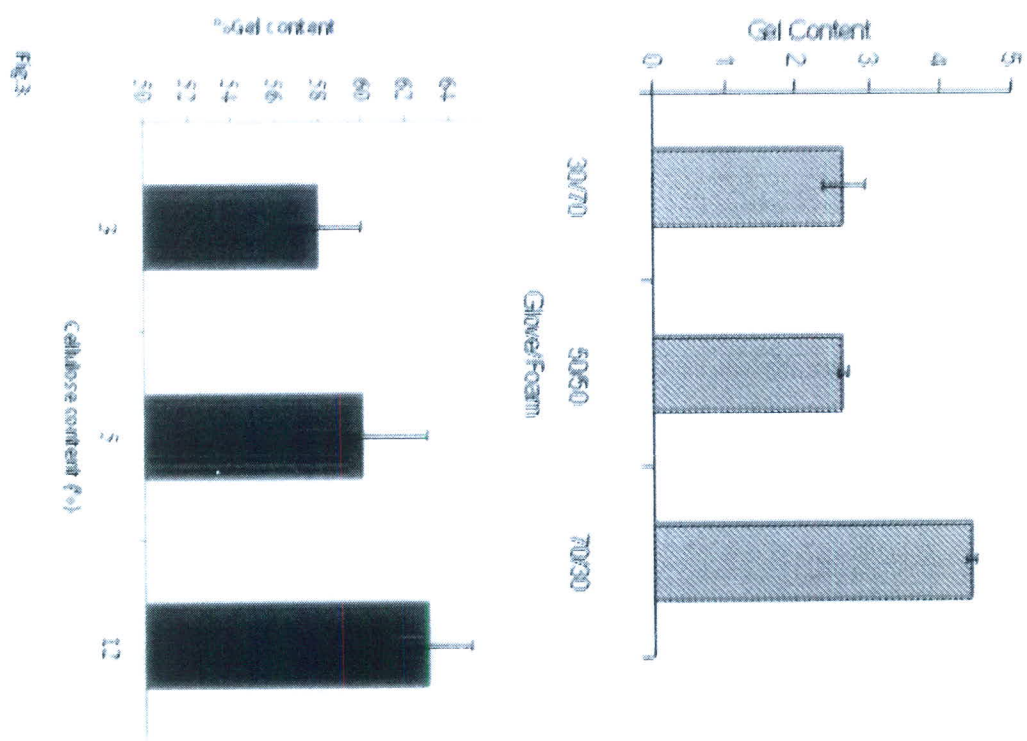


Figure4
Click here to download high resolution image

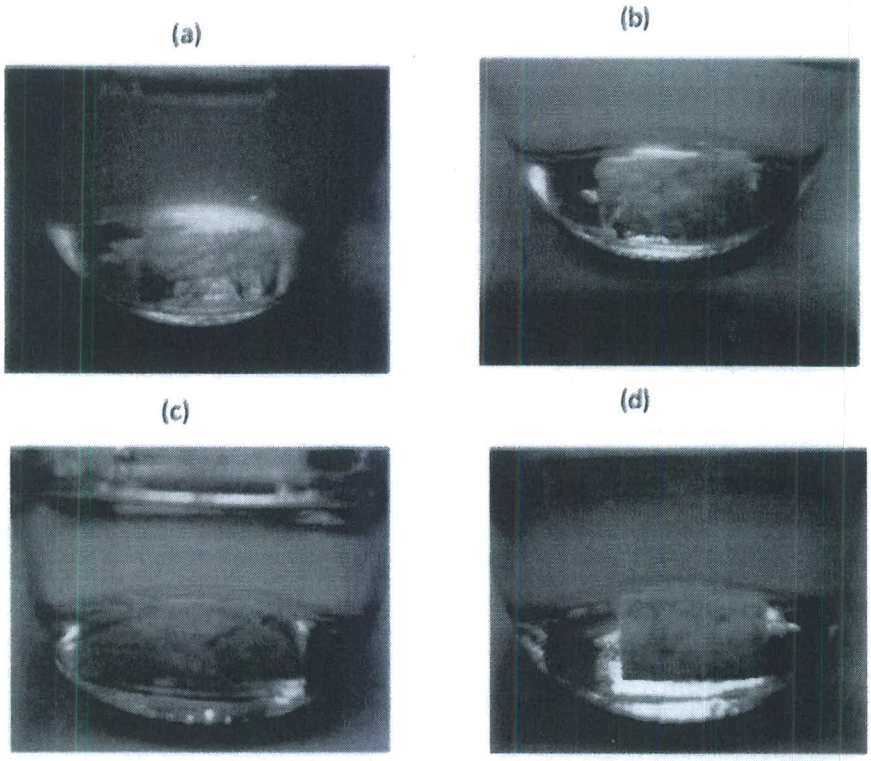


Fig.4

Figure5
Click here to download high resolution image

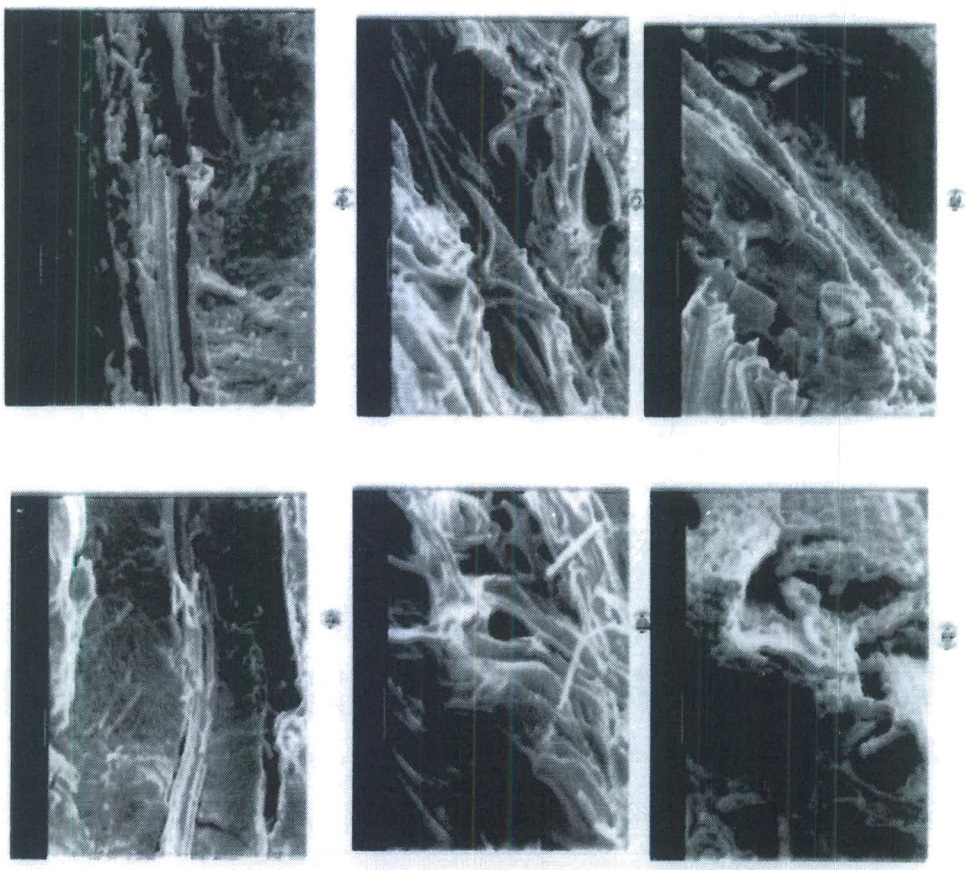


Fig.5

Figure6
Click here to download high resolution image

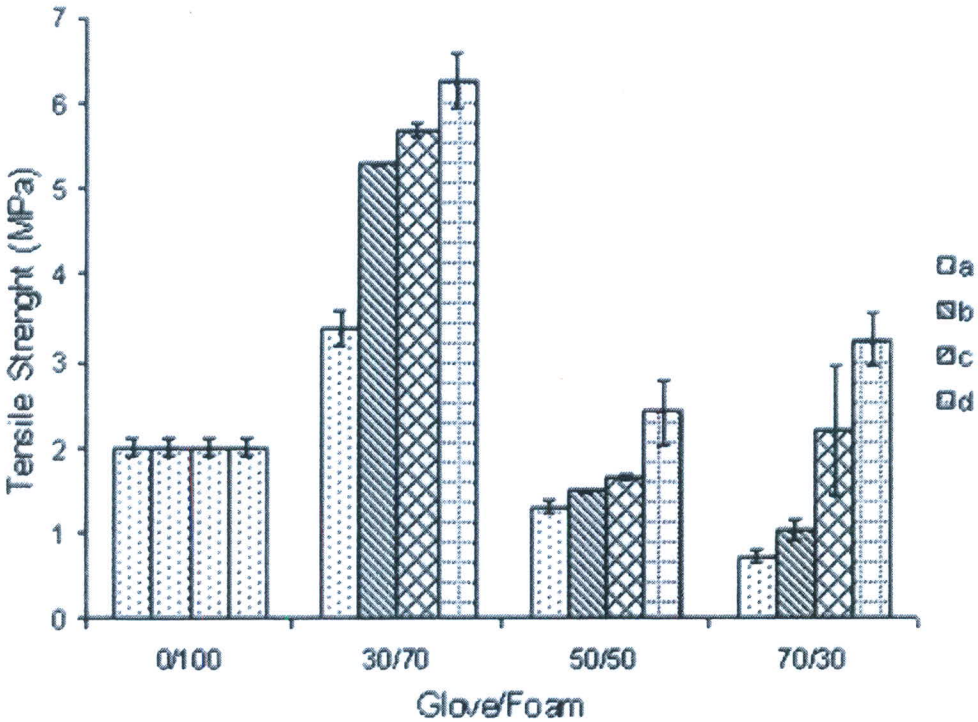


Fig.6

Figure7
Click here to download high resolution image

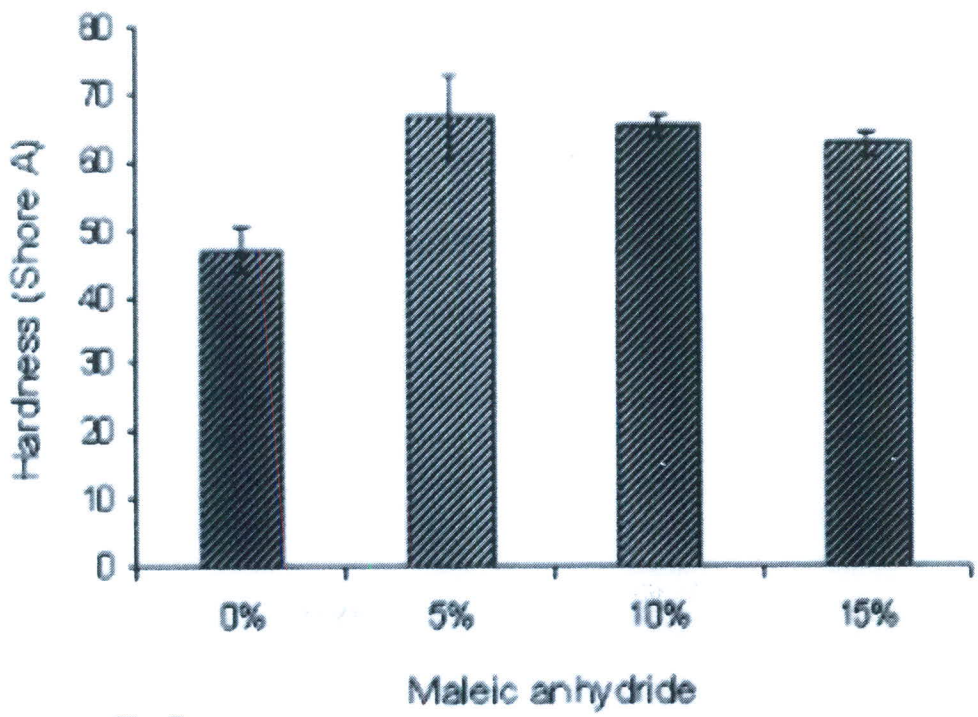


Fig.7.

Figure8
Click here to download high resolution image

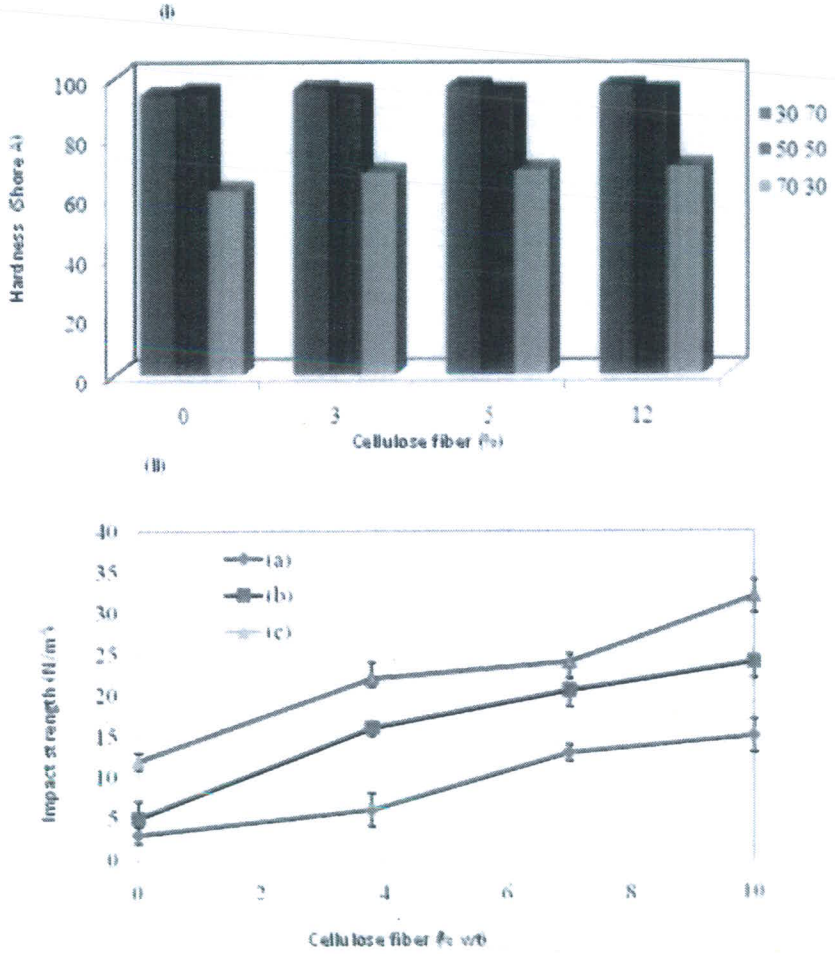


Fig 8

INBOX [scptb] Quota(163.63 / 1024 MB) Sign Out

Compose | Folders | Search | Options

Message List | Delete Previous | Next Forward | Forward as Attachment | Reply | Reply All

Subject: Journal of Applied Polymer Science - Manuscript # APP-2011-08-3054
From: appmc@wiley.com
Date: Wed, August 31, 2011 10:02 pm
To: scswr@mahidol.ac.th (more)
Priority: Normal
View Full Header | View Printable Version | Download this as a file
Options: Block Sender
Block Sender's Domain

31-Aug-2011

Greetings from the Journal of Applied Polymer Science.

You are receiving this mail because you have been listed as an author on the following paper:

"Backing-required Properties of Films based on Natural Rubber for Transdermal Patch Application"

This paper has been submitted online to the Journal of Applied Polymer Science by Dr. Supa Wirasate and has been assigned manuscript reference number APP-2011-08-3054. Please mention this reference number in all future correspondence regarding this submission.

You can view the status of your manuscript at any time by logging into http://mc.manuscriptcentral.com/app and clicking the appropriate link in your Author Center.

Thank you for submitting your manuscript to the Journal of Applied Polymer Science. Please feel free to contact us with any questions or concerns.

Sincerely,

Journal of Applied Polymer Science Editorial Office
http://mc.manuscriptcentral.com/app

This is a system-generated message.

Delete & Prev | Delete & Next

Move to: INBOX Move

Backing-required Properties of Films based on Natural Rubber for Transdermal Patch Application

S. Wirasate[1,2,3*], C. Chokbunpiam[1,2], R. Thonggoom[1,2] and P.Tangboriboonrat[1]

[1]Department of Chemistry, Faculty of Science, Mahidol University, Bangkok10400, Thailand
[2]Center for Surface Science and Engineering, Faculty of Science, Mahidol University, Salaya, Nakhorn Pathom73170, Thailand
[3]Center for Rubber Research and Technology, Faculty of Science, Mahidol University, Salaya, Nakhorn Pathom73170, Thailand

Abstract

The backing required properties, including oxygen transmission rate (OTR), water vapor transmission rate (WVTR) and Young's modulus, of natural rubber based films were investigated. Both NR and epoxidized NR (ENR) latexes with mole % epoxide ranging from 10 to 39 % were prevulcanized using *tert*-butyl hydroperoxide/fructose system. The surface of peroxide prevulcanized (PP) NR was grafted with acrylamide (PPNR-g-AAm) by dipping the PPNR strip treated with O_2 plasma into an aqueous solution of acrylamide monomer. The OTR of PPNR and PPENR films decreased with increasing theirs glass transition temperature. The WVTR of PPENR was directly proportional to mole % epoxide and the WVTR of PPENR film having 39 mole % epoxide was closed to 100 g/m^2/day. Both the OTR and WVTR of PPNR-g-AAm were slightly higher than those of PPNR. The highest Young's modulus among PPNR and PPENR films was approximately 8 times higher than that of the skin. Adhesion between PPNR or PPENR or PPNR-g-AAm and a commercial acrylate based adhesive, determined by peel test, were 1.4 N/cm for PPNR and greater than 2 N/cm for PPENR and PPNR-g-AAm.

Keywords: Backing film, Natural rubber, Epoxidized natural rubber, Transdermal patch

* Corresponding author. Address: Department of Chemistry, Faculty of Science, Mahidol University, Bangkok10400, Thailand;
Tel.: +66-2441-9817-20ext 1141; Fax: +66-2441-0511. Email address: scswr@mahidol.ac.th

1. Introduction

Transdermal drug delivery (TDD) is a promising alternative method to deliver drug into human body. By applying a transdermal patch to the skin, drug is transported across the skin to the systemic circulation. In adhesive transdermal patch, drug is typically loaded in pressure sensitive adhesive (PSA) which is sandwiched or entrapped between backing layer and release liner.With the role of protecting the drug matrix and other components of the patch from environment, backing material influences on drug delivery profile, adhesion of the patch to skin, wear ability and severity of skin irritation[1,2]. In order to allow skin movement in a natural way or to provide comfort to user and to cause less skin irritation,Young's modulus of the patch should be comparable to that of the skin(0.1-0.3 MPa) [1,3]. However, most commercial backing films and TDD patches were found to have the Young's modulus at least 100 times higher than that of the skin [1]. Other important required properties for backing materials include optimum water vapor transmission rate (WVTR) and good oxygen transmission rate (OTR). In order for skin to maintain its function, backing materials should have WVTR close to that of transepidermal water loss (5-10 g/m^2/h) [4,5]. Moreover, it was reported that transportation of moisture vapor affected adhesion of medical device to the human skin [2]. Air-filled channels, which were used as water vapor transport channels, were created on acrylic plastic disks. After that PSA was applied on the disks, which were then adhered to the human body. The disks with air-filled channels remained on the skin three times longer than the disks without the channels because of better water vapor transport.Another important factor is the adhesion between backing film and PSA, which affects the drug delivery as well as durability of the patch. For transdermal patches, adhesion between backing material and PSA is crucial because poor adhesion can lead to un-effective drug delivery as well as poor durability of the patches. The adhesive strength between the backing and the adhesive should be at lease comparable or greater than that between the patch and skin, i.e., 0.4-2.0 N/cm to be sure that the patch will stay intact during use and to be removed cleanly after use [6]. In order to increase adhesion of NR backing films and PSA like acrylate based PSA, either epoxidation reaction or plasma surface modification is required to increase polarity of NR.

Commercial backing layer can be made of single or multiple layers of synthetic plastics, such as polyethylene, polyurethane, ethylene vinyl acetate, poly(vinyl chloride) and polyester, which are known to have much higher Young's modulus than that of the skin. Published papers related to the development of backing films, especially based on natural rubber (NR) are very limited. The uses of elastomeric materials, including NR and NR

blended with polyolefins, as backing materials for transdermal patches were reported in the patent of Venkatraman *et al.*[7]. Their WVTR in a range of 2.4-480 g/m^2/day and the Young's modulus in a range of 0.001-100 MPa were reported. It should be noticed that those values were in a wide range with no specific value for each of elastomers. Among polymers that are possibly useful for transdermal patches reviewed by Sukibayashi and Morimoto [8], NR was included as a base with adhesive without providing information related to backing–required properties.

Prevulcanized NR latex is well known as a raw material that can easily be processed into thin film with good mechanical properties. An excellent in flexibility of prevulcanized NR can be benefit when applying the patch onto flexible parts of the body such as elbow. NR latex can be prevulcanized by various systems including sulfur, peroxide and γ-radiation [9]. Drawbacks for sulfur prevulcanized system for food and medical applications may cause by the use of carcinogenic nitrosamine accelerators and the smell of sulfur. Crosslinking via carbon-carbon linkage of peroxide prevulcanization (PP) and γ-radiation systems provides better compression set and heat stability of rubber products than the sulfur system [10, 11]. However, high energy of γ-radiation causes main chain scission, which resulted in deterioration of rubber properties [12].

Properties of NR and epoxidized NR (ENR) were investigated by several research groups [13-15]. Young's modulus of NR, ENR with 25 and with 50 mole % epoxide prevulcanized by sulfur were 2.15, 2.30 and 2.70 MPa, respectively whereas theirs O_2 permeabilities were 24 x10^{10}, 5 x10^{10} and 2 x10^{10} Barrer [13,14]. However, no details related to sample preparation and to backing-required properties of PPNR based films were given. Studies of PPNR and PPENR were focused on particle morphology and secant modulus [16,17]. Therefore, the main purpose of this work was to investigate backing-required properties of PPNR, PPENR and surface modified PPNR (O_2 plasma treatment of PPNR followed by grafting with AAm (PPNR-g-AAm)). Special attention was paid on OTR and WVTR since these two properties have been rarely determined. Young's moduli, obtained from tensile test, of the films were also reported and compared those of skin and of commercial backings. Moreover, adhesion between the backing film and a commercial acrylate based adhesive (DURO-TAK 87-4098) was determined by peel test.

2. Experimental

2.1Materials

High ammonia (HA) – NR latex with 60% dry rubber content (DRC) was obtained from Bangkok Rubber Co., Ltd., (Rayong, Thailand). *Tert*-Butyl hydroperoxide (t-BuHP; Purum), D-(-)-Fructose (Bacteriology) and sodium dodecyl sulfate (SDS; GC) were purchased from Fluka (Bangkok, Thailand) whereas acrylamide monomer (AAm) was purchased from Sigma-Aldrich (Bangkok, Thailand). A commercial acrylate based adhesive (DURO-TAK 87-4098), kindly supplied by Henkel Corporation (New Jersey, USA), was an acrylate-co-vinylacetate non-curing PSA without reactive functional groups.

2.2Preparation of PPNR and PPENR Latexes

PPNR latex was prepared as described elsewhere [17]. The formulation used for the preparation of PPNR is shown in Table 1.

Table 1 Formulation used for preparation of PPNR [17].

Ingredients	Part by wet weight (g)
HA-NR latex	166.7
tert- Butyl hydroperoxide(*t*-BuHP) (30%)	1.25
D-(-)-Fructose	8.5
Sodium dodecyl sulfate (SDS)	1.25
deionized (DI)water	22.4

In the first step, the peroxide emulsion was prepared by mixing *t*-BuHP solution with DI water and SDS solution. The emulsion and D-(-) - fructose solution were then added into HA-NR latex. Finally, the prevulcanization reaction was carried out at 60°C for various reaction times. During prevulcanization, the latex (about 5 g) was taken out at various time intervals and rapidly cooled down to room temperature to prevent further vulcanization and dried on a petri dish. The crosslink density of PPNR film was determined by measuring % swelling ratio of a piece of dried rubber, which was immersed into toluene for 24 h. After blotting its surface with filter paper, the swelling ratio of crosslinked rubber was calculated as follows:

$$\%\text{Swelling ratio} = \frac{W_{wet} - W_d}{W_d} \times 100$$

Where W_d is an initial weight of dried rubber (g), and W_{wet} is the weight of swollen rubber at equilibrium swelling (g).

NR latex was also used for preparation of ENR latex by using formic acid and hydrogen peroxide at 50°C as previously described [18]. The epoxide content of ENR was calculated from the spectrum of proton-nuclear magnetic resonance (^{1}H-NMR, DPX400, Bruker) spectroscopy as follows [19].

$$mole\,\%\,epoxide = \frac{I_{2.7}}{(I_{2.7} + I_{5.1})} x\,100$$

Where $I_{2.7}$ and $I_{5.1}$ are integrated area of peaks at 2.7 and 5.1 ppm, respectively.

Similar to PPNR latex, the PPENR latex was also prepared [17].

2.3 Preparation and Characterizationsof Backing Film

Rubber film (400 μm in thickness) was prepared by casting PPNR or PPENR latex on a glass plate and then dried at room temperature. In order to PPNR film with AAm, PPNR film was subjected to O_2 plasma treatment (Basic plasma kit BP-1, Samco) 100 W, 13.56 MHz under 0.5 Torr, for 15 s before being dipped into an aqueous solution of AAm monomer (5 wt%).

OTR, WVTR, glass transition temperature (T_g) and Young's moduli of all films were determined by an O_2 permeation tester, a WVTR tester, dynamic mechanical thermal analysis (DMTA) and a tensile tester, respectively.

2.3.1 Determination of OTR and WVTR

The OTR of dried rubber film was measured at 23°C using the O_2 permeation tester (Illinois 8000) according to ASTM D3985-02. After keeping in a dry test environment (0% relative humidity; RH) until equilibrium, the specimen was mounted between two chambers. One chamber was slowly purged by a stream of N_2 and the other contained O_2. As O_2 permeated through the film into N_2 carrier gas, O_2 was transported to the detector.

The WVTR was determined by Mocon Permatran-w 3/33 according to ASTM F1249-90 (reapproved 1995) at 38°C and 90% RH. Test cells were divided into two chambers, which separated by the tested film. The inner chamber was filled with N_2 gas while water vapor was in the outer. Molecules of water diffused through the film to the inside

chamber and were transported to the modulated infrared sensor by N_2 gas. This sensor measured the fraction of infrared energy absorbed by the water vapor and produced an electrical signal. The amplitude of the electrical signal was proportional to water vapor concentration and was then used to calculate the WVTR according to the formula described in the ASTM F1249-90 (reapproved 1995);

$$WVTR = C\,x\,(ES - EO)$$

where C is a calibration factor expressing rate as a function of voltage. The value of C is derived from tests of a reference film. EO is a permeation system zero level voltage, and ES is an equilibrium voltage obtained with the test specimen.

2.3.2 Determination of T_g and Young's modulus

T_g was measured using a DMTA (Explexor TM 25 N, Gabo) with a heating rate of 5°C/min from -100 to 10°C.

An Instron (model 5569) was used to determine Young's modulus of the samples at room temperature according to the procedure described in ASTM D 412-98a at a crosshead speed of 500 mm/min and the load cell of 1000N.

3. Results and Discussion

3.1 OTR and WVTR

3.1.1 PPNR Films

The swelling ratios, inversely proportional to crosslink density, of PPNR films versus prevulcanization time were determined and the data are shown in Figure 1. It was observed that the swelling ratios rapidly decreased with increasing prevulcanization time in the initial period. After prevulcanization time of 60 min, the swelling ratios reached a constant value of 1300-1400 %, which indicated the maximum crosslinking of PPNR [20].

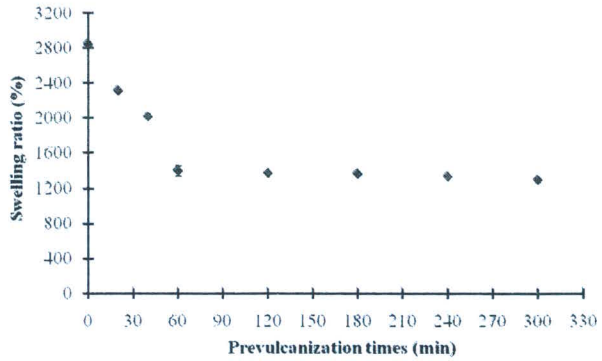


Figure 1 Swelling ratios of PPNR films as a function of prevulcanization times.

Further investigation of the extent of the crosslinking as a function of prevulcanization time was performed by measuring T_g of the PPNR films using DMTA and the data are presented in Figure 2. Since the formation of network resulted in the reduction of mobility and free volume of rubber chain molecules, it was not surprising that T_g increased from -64 to -53°C with increasing the prevulcanization time from 0 to 60 min. After 60 min, prevulcanization time had little effect on T_g, which suggested that the maximum network was obtained [20]. This result corresponded well with the swelling ratios as previously described.

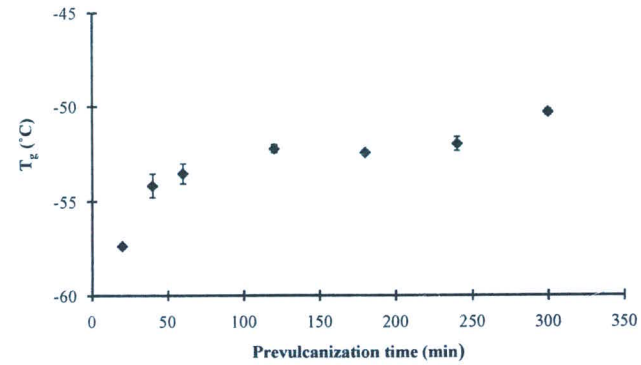


Figure 2 T_g, determined by DMTA, of PPNR films as a function of prevulcanization times.

The OTR and WVTR of PPNR films as a function of T_g are displayed in Figure 3. Results showed that both OTR and WVTR values decreased with increasing T_g of PPNR films. When T_gs of PPNR films were -57 and -50°C, the OTR were 4333 and 3968 cm^3/m^2/day whereas the WVTR were 34 and 22 g/m^2/day, respectively. It might be due to the formation of crosslinking, which reduced the mobility of rubber chains when increasing T_g and, hence, the diffusion rate of O_2 or water vapor through PPNR film decreased [13]. These WVTR values of all films were much lower than the transepidermal water loss (TEWL) of human skin), i.e., 120 – 240 g/m^2/day.

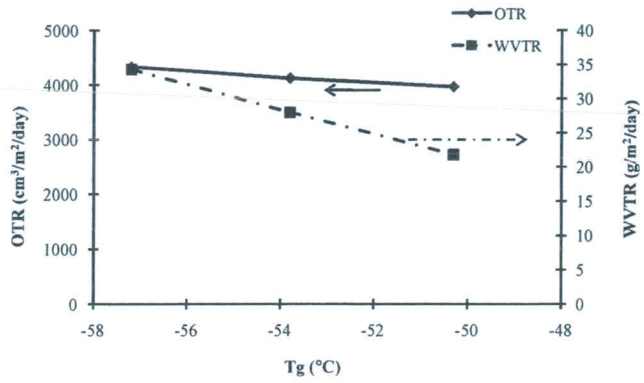


Figure 3 OTR and WVTR of PPNR films as a function of T_gs.

3.1.2 PPENR Films

By varying the reaction times from 4 to 24 h, it was found by ^{1}H-NMR that mole % epoxide was in a range of 10 – 39 % as shown in Figure 4. T_gs of PPENR latex films containing various mole % epoxide, determined by DMTA, are presented in Figure 5. It was noticed that the T_gs increased with increasing reaction times, i.e., with an increase in epoxide groups in rubber molecules because the epoxide or oxirane group reduced mobility and rotational freedom of the rubber molecules [14,18,21].

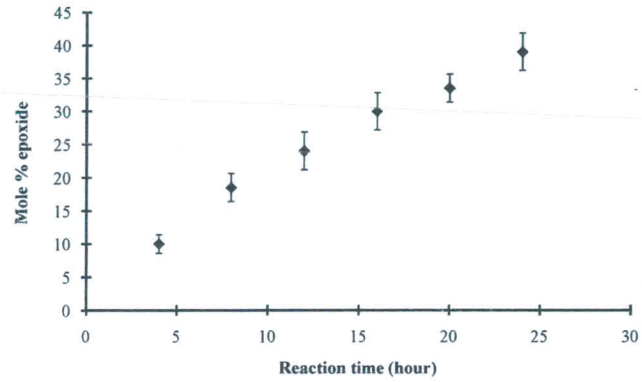


Figure 4 Mole % epoxide as a function of reaction time.

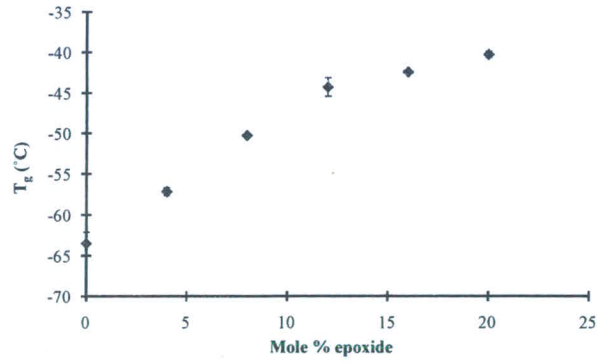


Figure 5 T_gs of PPENR films with various mole % epoxide.

The OTR and WVTR of PPENR films with prevulcanization time of 60 min as a function of mole % epoxide are shown in Figure 6. The WVTR of PPENR films increased because the epoxide group increased molecular polarity with a consequence of an increase in solubility of water vapor. The WVTR of PPENR with 39 mole % epoxide (prevulcanization time of 20 min) was 112 g/m^2/day, which was closed to TEWL of human skin. This suggested that PPENR film had a good potential to be used as a backing film that would be able to maintain the skin functions and cause less skin irritation. However, theirs OTR decreased with increasing mole % epoxide. It was explained that the insertion of oxygen atoms into the rubber molecules resulted in more polar groups in the chains, which reduced theirs mobility and free volume [14,18,21]. As previously observed, the T_g increased with increasing mole % epoxide [13,14].

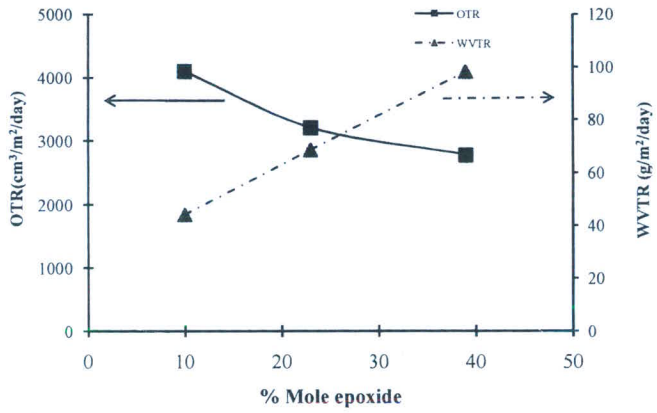


Figure 6 OTR and WVTR of PPENR films having various mole % epoxide (prevulcanization time= 60 min)

3.1.3 PPNR-g-AAm Films

The presence of acrylamide (AAm) on the surface of PPNR-g-AAm film was confirmed by the decrease of water contact angles of PPNR 91 to 40°after grafting. The OTR and WVTR of PPNR-g-AAm films compared with those of PPNR and PPENR (39 mole % epoxide) as a function of prevulcanization times are presented in Figures 7 and 8, respectively. Results showed that theirs OTR were slightly higher than those of PPNR films, although the small AAm molecules were presented on the surface of PPNR-g-AAm films. The modification of PPNR might be restricted to the outermost layer [22]. Since oxygen containing functional groups could not be detected by attenuated total reflectance infrared spectroscopy, it was assumed that the modification depth by plasma was less than a micrometer. Therefore, the diffusion of O_2 and water vapor through the bulk of the films remained unaffected. However, the high rigidity of PPENR molecules caused the much lower OTR of PPENR films with 39 mole % epoxide than those of PPNR and PPNR-g-AAm [14,18,21]. The slight increase in WVTR of PPNR-g- compared to that of PPNR film was probably due to better solubility of water vapor at the surface of PPNR-g-AAm film whose surface had higher polarity. It was also observed that the WVTR of PPENR films were 3-4 times higher than those of PPNR and PPNR-g-AAm films. As previously mentioned, the increase in molecular polarity was responsible for an increase in solubility of water vapor throughout the PPENR films.

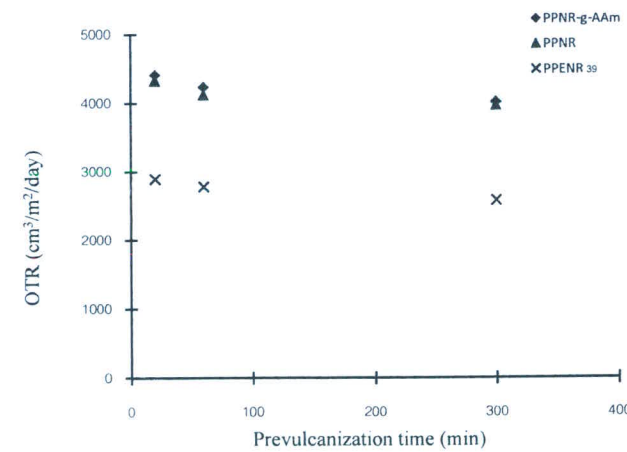


Figure 7 OTR of PPNR, PPENR(39 mole % epoxide) and PPNR-g-AAm films as a function of prevulcanization times.

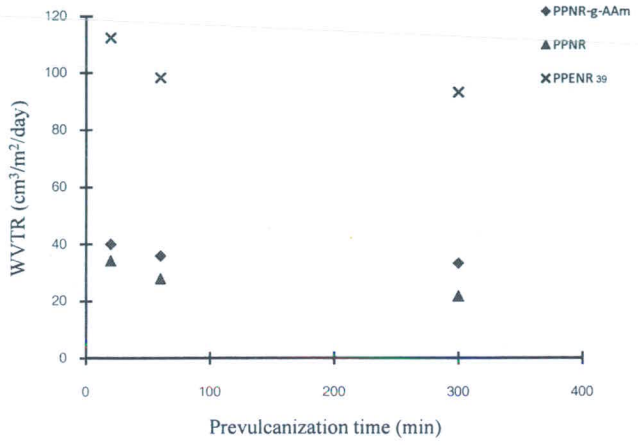


Figure 8 WVTR of PPNR, PPENR(39 mole % epoxide) and PPNR-g-AAm films as a function of prevulcanization times.

3.2 Young's Modulus and Adhesion to Acrylate Based PSA

3.2.1 Young's Modulus

The Young's moduli of PPNR films which increased with increasing prevulcanization times up to 120 min are shown in Figure 9. The highest modulus at prevulcanization time of 120 min was explained by the optimum prevulcanization, which had a suitable fuse of rubber particles [23]. As previously reported, peroxide prevulcanization of NR latex provided heterogeneous network structure inside each rubber particle, i.e., dense crosslink near the surface compared to the central region [23]. At prevulcanization time longer than 120 min, the modulus tended to decrease possibly due to highly crosslink near the surface of rubber particles, which prevented further fuse of rubber particles. It should be mentioned that the highest Young's modulus of PPNR film was approximately 8 times higher than that of the skin (i.e., 0.1–0.3 MPa). These values were much lower than those reported for commercial unlaminated backing films (77, 102 and 2128 MPa) and transdermal patches

(4-501 MPa) [1]. From these data, it could be assumed that PPNR showed promising results to be used as a backing film.

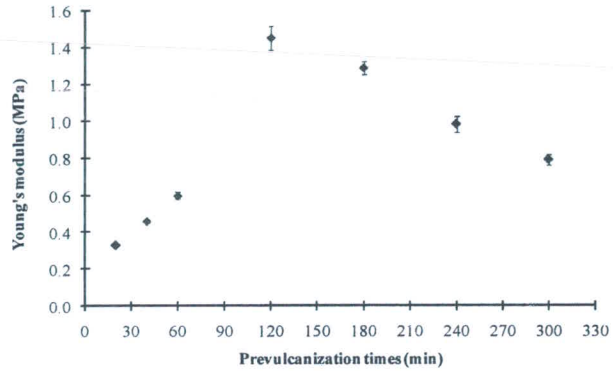


Figure 9 Young's moduli of PPNR films with various prevulcanization times.

As previously mentioned that prevulcanization time longer than 120 min resulted in poor rubber particle fusion, therefore, prevulcanization time of 60 min was selected for further investigation of PPENR films. The Young's moduli of PPENR films having various mole % epoxide are shown in Figure 10. The Young's modulus of the PPENR film was about 1.5-2.0 times higher than that of PPNR film. It might be due to coiled structure of PPNR, i.e. easily to be stretch at low strain level [14,24]. With increasing the epoxy content, the Young's moduli of PPENR increased because of increasing rigidity and reducing mobility of chains as previously explained.

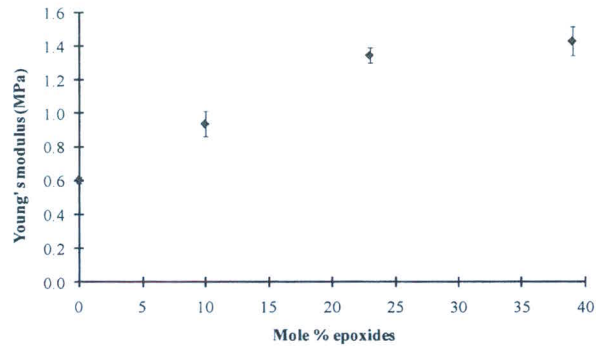


Figure 10 Young's moduli of PPENR films with various mole % epoxide (prevulcanization time = 60 min).

3.2.2 Adhesive Strength

The adhesive strength between PPNR or PPENR or PPNR-g-AAm and acrylate-co-vinylacetate adhesive (DURO-TAK 87-4098) was determined by peel test and the results are shown in Figure 11. With using PPNR and PPNR-g-AAm films, theirs peel strength values were 1.4 and 2.3 N/cm, respectively. The higher peel strength of PPNR-g-AAm compared to that of PPNR was due to the more polarity of PPNR-g-AAm surface as already reported by the water contact angle. The highest peel strength observed for PPENR (39 mole % epoxide) was also explained by the highest polarity of this rubber film.

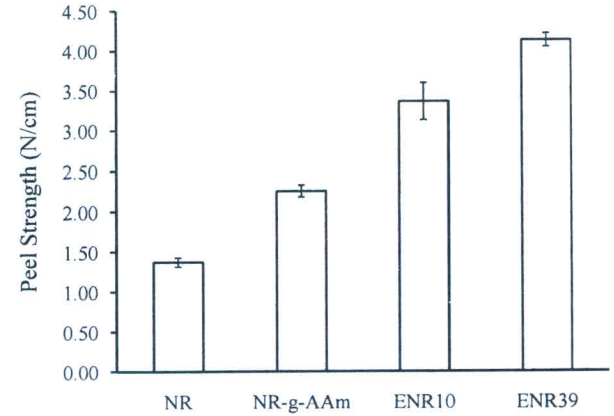


Figure 11 Peel strength between PPNR or PPENR or PPNR-g-AAm films and DURO-TAK 87-4098.

4. Conclusions

PPNR, PPENR and PPNR-g-AAm films had a potential to be used as backing films for trnasdermal patches. For both PPNR and PPENR films, as T_g increased OTR decreased due to the reduction of chain mobility and free volume. However, the lowest OTR obtained from PPENR with 39 mole % epoxide was still greater than 2500 $cm^3/m^2/day$. For WVTR of PPENR, as mole % epoxide increased WVTR increased due to more polarity. PPENR films having 39 mole % epoxide had WVTR closed to100 $g/m^2/day$, which is closed to TEWL. Both OTR and WVTR of PPNR-g-AAm were slightly higher than those of PPNR because its surface was covered with small molecules of AAm. Young's moduli of all samples were found to be at most 8 times higher than that of the skin. Adhesive strength, determined by peel test, between PPNR films and DURO-TAK 87-4098 was found to be about 1.4 N/cm whereas those for PPENR and PPNR-g-AAm were greater than 2 N/cm, which is sufficient for making the patch.

Acknowledgement

Financial support from The Thailand Research Fund /the Commission on Higher Education (MRG5380023) and the Faculty of Science, Mahidol University, Bangkok, Thailand to S.W. were gratefully acknowledged. P.T. is TRF Senior Researcher.

References

[1] C. Fauth, S. Wiedersberg, R. H. H. Neubert, and M. Dittgen, "Adhesive backing foil interactions affecting the elasticity, adhesion strength of laminates, and how to interpret these properties of braded transdermal patches", Drug Dev. Ind. Pharm., 28 (10), 1251-1259 (2002).

[2] D. D. Cunningham and M. G. Lowery, "Moisture vapor transport channels for the improved attachment of a medical device to the human body", Biomed.Microdev.,6 (2), 149-154 (2004).

[3] S. Diridollou, D. Black, J. M. Lagarde, Y. Gall, M. Berson, V. Varbe, F. Patat and L. Vaillant, „Sex- and site-dependent variations in the thickness and mechanical properties of human skin *in vivo*", Int. J. Cosmet.Sci., 22, 421-435 (2000).

[4] Y. N. Kalia, F. Pirot and R. H. Guy, "Homogeneous transport in a heterogeneous membrane: water diffusion across human stratum corneum in vivo", Biophys. J., 71, 2692-2700 (1996).

[5] Y. N. Kalia, I. Alberti, N. Sekkat, C. Curdy, A. Naik, and R. H. Guy, "Normalization of stratum corneum barrier function and transepidermal water loss *in vivo"*, Pharm. Res., 17 (9), 1148-1150 (2000).

[6] T. S. Spencer, S. E. Smith and S. Conjeevaram, "Adhesive interaction between polymers and skin in transdermal delivery systems", Polym. Mater.Sci. Eng., 63, 337-339 (1990).

[7] S. S. Venkatraman, S. E. Smith."Occlusive, elastomeric backing materials in transdermal drug delivery systems, and associated methods of manufacture and use", US Patent 5,246,705 September 21, 1993.

[8] K. Sugibayashi and Y. Morimoto, "Polymers for transdermal drug delivery systems" J. Control Release, 29, 177-185 (1994).

[9] J. T. Varkey, S. S. Rao and S. Thomas, "Effect of prevulcanization on the rheological behavior of natural rubber/styrene butadiene rubber latex blends", J. Appl. Polym. Sci., 62, 2169-2180 (1996).

[10] A. Ciesielski, An Introduction to Rubber Technology, Rapra Technology Limited Shawbury, Shrewsbury, Shropshire, SY4 4NR, UK, 1999, pp. 35-36.

[11] A. A. Basfar, M. M. Abdel-Aziz, and S. Motif, "Influence of different curing systems on the physico-mechanical properties and stability of SBR and NR rubbers", Radiat. Phys. Chem., 63, 81-87(2002).

[12] K. Makuuchi and M. Hagiwara, "Radiation vulcanization of natural rubber latex with polyfunctional monomers, J. Appl. Polym.Sci.,29, 965-976 (1984).

[13] T. Johnson and S. Thomas, "Nitrogen/oxygen permeability of natural rubber, epoxidised natural rubber and natural rubber/epoxidised natural rubber blends", Polymer, 40, 3223-3228 (1999).

[14] T Johnson and S. Thomas, "Effect of epoxidation on the transport behaviour and mechanical properties of natural rubber", Polymer 41, 7511–7522 (2000).

[15] M. Chen, N. –J Ao, B. –L. Zhang, C. –M. Den, H. –L. Qian and H. –L Zhou, Comparison and evaluation of the thermooxidative stability of medical natural rubber latex products prepared with a sulfur vulcanization system and aperoxide vulcanization system, J. Appl. Polym. Sci., 98, 591-597 (2005).

[16] P. Tangboriboonrat, D. Polpanich, T. Suteewong,K. Sanguansap, U. Paiphansiri, and C. Lerthititrakul, "Morphology of peroxide prevulcanised natural rubber latex: effect of reaction time and deprotenisation", Colloid Polym. Sci., 282, 177-181 (2003).

[17] T. Suteewong and P. Tangboriboonrat, Particle morphology of epoxidised natural rubber latex prevulcanized by peroxide system, e-Polymers, 121, 1–9 (2007).

[18] P. Saendee and P. Tangboriboonrat, "Latex interpenetrating polymer networks of epoxidized natural rubber/poly (methyl methacrylate): an insight into mechanism of epoxidation", Colloid Polym.Sci., 284, 634-643 (2006).

[19] P. Tangboriboonrat and C. Rakdee, "Effect of epoxidised natural rubber latex on carbon black-natural rubber interaction in bead masterbatch", Plast. Rubber Compos.,29, 258-262 (2000).

[20] P. Tangboriboonrat and C. Tiyapaiboonchaiya, Novel method for toughening of polystyrene based on natural rubber latex, J. Appl. Polym. Sci., 71, 1333–1345 (1999).

[21] K. Sanguansap, T. Suteewong, P. Saendee, U. Buranabunya, and P. Tangboriboonrat, "Composite natural rubber based latex particles: a novel approach", Polymer, 46, 1373-1378 (2002).

[22] C. M. Chan, T. M. Ko, H. Hiraoka, "Polymer surface modification by plasmas and photons", Surf. Sci. Rep., 24, 1–54 (1996).

[23] P. Tangboriboonrat and C. Lerthititrakul, "Morphology of sulphur and peroxide prevulcanised natural rubber latex", Colloid Polym. Sci., 280, 1097-1103 (2002).

[24] I. R. Gelling, "Modification of natural rubber latex with peracetic acid", Rubber Chem. Technol., 58, 86–96 (1985).

Advanced Materials Research Vols. 93-94 (2010) pp 198-201
Online available since 2010/Jan/12 at www.scientific.net
© (2010) Trans Tech Publications, Switzerland
doi:10.4028/www.scientific.net/AMR.93-94.198

เอกสารแนบ 5.3.1

click for feedback
consult - comment - contact

Synthesis and Characterizations of PLLA/PEG Block Copolymers

Thai Hien Nguyen[1,a], Atitsa Petchsuk[2,b], Pramuan Tangboriboonrat[3,c], Mantana Opaprakasit[4,d], Alice Sharp[1,e], and Pakorn Opaprakasit[1,f *]

[1]School of Bio-Chemical Engineering and Technology, Sirindhorn International Institute of Technology (SIIT), Thammasat University, Pathumthani 12121 Thailand

[2]National Metal and Materials Technology Center (MTEC), Pathumthani 12120 Thailand

[3]Department of Chemistry, Mahidol University, Bangkok 10400 Thailand

[4]Department of Materials Science, Chulalongkorn University, Bangkok 10330 Thailand

[a]nguyen.th.hien@gmail.com, [b]atitsp@mtec.or.th, [c]scptb@mahidol.ac.th,

[d]mantana.o@chula.th, [e]alice@siit.tu.ac.th, [f]pakorn@siit.tu.ac.th

Keywords: PLLA, PEG, copolymer, chain extending, degradable polymer

Abstract. Poly(lactic acid-co-ethylene glycol) (PLLA/PEG) copolymers were synthesized and their properties were characterized. The PLLA/PEG/PLLA triblock copolymers were synthesized by ring-opening polymerization from l-lactide (LLA) and PEG macroinitiator. Stannous octoate, $Sn(Oct)_2$ was used as a catalyst. Effects of molecular weight of PEG (600, 2000 and 4000), LLA/OH molar ratios (95:5, 98:2) and a sequence of addition of the reactants on properties of the copolymers were investigated. The triblock copolymers were subsequently used in a production of multiblock copolymers by reacting with a chain-extending agent, hexamethylene diisocyanate (HMDI). Chemical structure and molecular weight of the copolymers were characterized by ^{1}H-NMR, FTIR and GPC. The results showed that molecular weight of triblock copolymers varied from 4,500 to 10,200. After chain extension, multiblock copolymer with molecular weight of 16,490 was produced. Thermal properties of the copolymers were also examined by DSC.

Introduction

Poly(lactic acid) (PLA) is biodegradable and biocompatible polymer that is particularly attractive in scientific community to use in various applications, especially in medical applications. This aliphatic polyester is polymerized by polycondensation or ring-opening polymerization, where the latter reaction yields higher molecular weight copolymers. However, PLA is hydrophobic, which limits its use in certain applications. On the other hand, poly(ethylene glycol) (PEG) is known as hydrophilic polymer with outstanding properties, such as non-toxicity, non-ionic and biocompatible characteristics. Therefore, copolymerization of PLA and PEG offers an opportunity to combine the advantages of these polymers.

In this study, PLA/PEG copolymers are synthesized and their properties are characterized. The PLLA/PEG/PLLA triblock copolymers are synthesized by ring-opening polymerization using $Sn(Oct)_2$ as a catalyst. Effects of molecular weight of PEG, LLA:OH(PEG) molar ratios and a sequence of addition of the reactants on structure and properties of copolymer are investigated. Multiblock copolymers are then synthesized by employing a chain extending agent, HMDI. These copolymers are intended for use as biomedical materials, e.g. drug encapsulation, scaffold and controlled release applications.

Experimental

The synthesis procedure of triblock PLLA/PEG/PLLA copolymers was adopted the methodology reported by Yuqing Wan et. al.[1]. L-lactide (LLA) was synthesized in the laboratory by polycondensation of l-lactic acid (88 wt% in water, Carlo Erba), using $Sn(Oct)_2$ as catalyst. The purified LLA was stored in vacuum flask until use. PEG with M_n = 600, 2000, 4000 were supplied

consult comment contact
click for feedback

All rights reserved. No part of contents of this paper may be reproduced or transmitted in any form or by any means without the written permission of the publisher: Trans Tech Publications Ltd, Switzerland, www.ttp.net. (ID: 110.164.106.233-19/01/10,16:23:28)

by Fluka. $Sn(Oct)_2$ (Wako) was used as a catalyst. HMDI were purchased from Aldrich. The properties of copolymers were then characterized by ^{1}H-NMR (Bruker DRX400) and FTIR (ThermoNicolet 6700) spectroscopy and GPC (Waters 150 CV). Thermal properties of copolymer were characterized by Mettler Todedo DSC822^e

Effects of molecular weight of PEG and LLA/OH molar ratios. PLLA/PEG/PLLA triblock copolymers were synthesized by using PEG with different molecular weight (600, 2000, and 4000) and employing different LLA/OH molar ratios (95:5, 98:2) to yield different EG and LLA block lengths in copolymer chains. Essentially, the monomer mixture and initiator were dried by a vacuum/inert gas technique for 1 hour under dry nitrogen. The mixture was then melted at 130°C and the polymerization was taken place for 24 hours. Finally, chloroform and ethanol were used to purify the copolymer products.

Effects of sequence of adding the reactants. PEG 4000 and a LLA/OH molar ratio of 98:2 were employed in the synthesis using the same temperature and reaction time as described above. Three experiment conditions were employed. In the first experiment, LLA, PEG and $Sn(Oct)_2$ were added in the flask at the same time (a). In the second experiment, LLA and PEG were melted at 130°C and $Sn(Oct)_2$ was then added to the mixture (b). In the final experiment, PEG 4000 was melt at 80°C. Then 1%w/w $Sn(Oct)_2$ was added to PEG solution. After 1 hour, LLA was finally added to the mixture (c).

Synthesis of multiblock PLLA/PEG copolymer. The synthesis process was similar to the methodology reported by Cohn et. al.[2], except that $Sn(Oct)_2$ was used as a catalyst. PLLA/PEG multiblock copolymer was synthesized by chain extension reaction of $PLLA_{46}/PEG_{46}/PLLA_{46}$ triblock copolymer using HMDI as a coupling agent. A molar ratio of triblock copolymer:HMDI of 1.0:1.1 was employed. Triblock copolymer was first dissolved in dioxane. HMDI and $Sn(Oct)_2$ were then added to the solution, and the reaction was carried out at 80°C for 3 hours (d).

Results and Discussion

Triblock PLLA/PEG/PLLA copolymers were synthesized by ring-opening polymerization of LLA in the presence of PEG and $Sn(Oct)_2$, as presented in Figure 1. As a result, OH-capped triblock copolymers were produced.

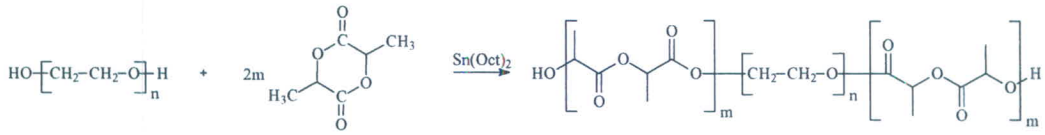


Figure 1. Copolymerisation reaction of PEG and LLA by ring-opening polymerization

The chemical structure and composition of the triblock copolymers were characterized by ^{1}H-NMR. The ^{1}H-NMR spectrum of the copolymer and signal assignments are shown in Figure 2.

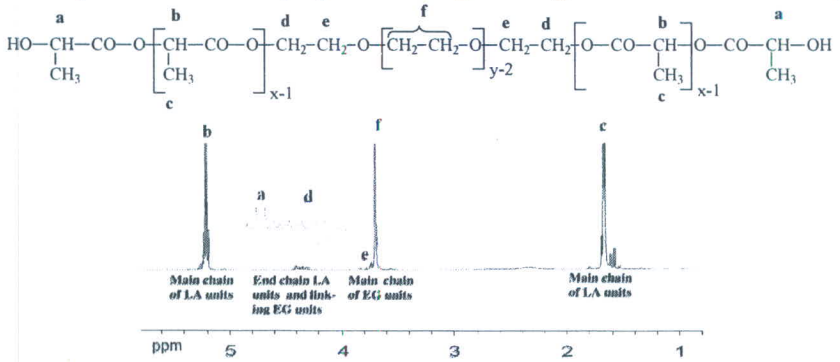


Figure 2. ^{1}H-NMR spectrum of $PLLA_{46}/PEG_{46}/PLLA_{46}$ triblock copolymer

click for feedback
consult - comment - contact

FTIR spectra of PLLA (M_n = 40,000), PEG (M_n = 2,000), and $PLLA_{46}/PEG_{46}/PLLA_{46}$ triblock copolymer are compared in Figure 3. The presence of band characteristics of PLLA and PEG were observed in the spectrum of the copolymer. Characteristic of LLA segments were observed at 1713 cm^{-1} (C=O stretching). The bands located at 3447 cm^{-1} (O-H stretching), 2872 cm^{-1} (C-H stretching) are assigned to characteristic of EG segments.

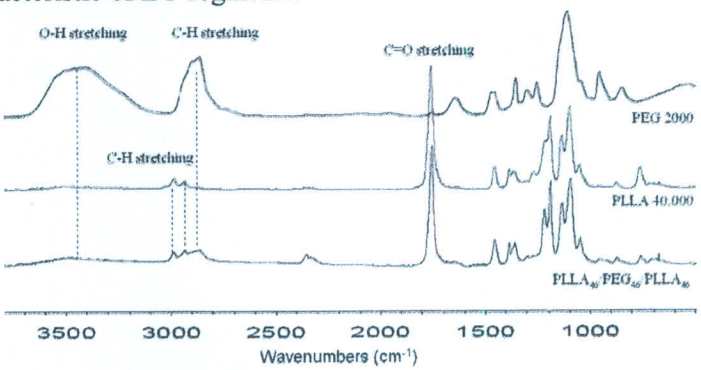


Figure 3. FTIR spectra of PEG 2,000, PLLA 40,000 and $PLLA_{46}/PEG_{46}/PLLA_{46}$ triblock copolymer

Effects of molecular weight of PEG and LLA/OH molar ratios. Triblock copolymers with wide range of molecular weight were obtained by varying molecular weight of PEG and LLA/OH molar ratios, as summarized in Table 1. The results showed that LLA/EG ratios in the products varied from 0.42:1 to 2.78:1, which are dependent on the ratios in feed.

Table 1. Effect of molecular weight of PEG and LLA/OH molar ratios

Copolymers	LLA/OH (mol/mol)	LLA/EG (in feed) (mol/mol)	LLA/EG[a] (in product) (mol/mol)	$\overline{DP}_{PEG}$[b]	$\overline{DP}_{PLLA}$[c]	M_n[d]	M_n (GPC)
$PLLA_{27}/PEG_{14}/PLLA_{27}$	95:5	2.78:1	3.90:1	14	27	4,500	5,800
$PLLA_{28}/PEG_{46}/PLLA_{28}$	95:5	0.84:1	1.26:1	46	28	6,060	6,950
$PLLA_{46}/PEG_{46}/PLLA_{46}$	98:2	2.16:1	2.04:1	46	46	8,650	10,400
$PLLA_{14}/PEG_{91}/PLLA_{14}$	95:5	0.42:1	0.31:1	91	14	6,020	10,900
$PLLA_{43}/PEG_{91}/PLLA_{43}$	98:2	1.08:1	0.95:1	91	43	10,200	12,650

[a] Calculated from the ratios of integral intensities of methyne of lactic acid at 5.0-5.3 ppm to methylene of ethylene glycol at 3.5-3.8 ppm, [b] $\overline{DP}_{PEG} = M_{nPEG} / 44$, [c] $\overline{DP}_{PLLA} = \overline{DP}_{PEG} \times (LLA / EG) / 2$, [d] $M_n = \overline{DP}_{PEG} \times 44 + \overline{DP}_{PLLA} \times 2 \times 72$

Effects of sequence of adding of the reactants. Effects of order of adding of reactants on properties of the resulting copolymers were studied to further optimize suitable synthesis conditions. The results, as shown in Table 2, indicates that comparable LLA block length were obtained from sample (a) and (b). Results from sample (c) showed copolymer with higher molecular weight than those of the former two copolymers.

Table 2. Effects of sequence of adding the reactants on properties of triblock copolymers

Copolymers	Samples	LLA/EG (in feed) (mol/mol)	LLA/EG[a] (in product) (mol/mol)	$\overline{DP}_{PEG}$[b]	$\overline{DP}_{PLLA}$[c]	M_n[d]
$PLLA_{43}/PEG_{91}/PLLA_{43}$	(a)	1.08:1	0.95:1	91	43	10,250
$PLLA_{41}/PEG_{91}/PLLA_{41}$	(b)	1.08:1	0.90:1	91	41	9,920
$PLLA_{48}/PEG_{91}/PLLA_{48}$	(c)	1.08:1	1.05:1	91	48	10,860

Synthesis of PLLA/PEG multiblock copolymer. The molecular weights of the multiblock copolymer are summarized in Table 3. As expected, the molecular weight of the resulting copolymer increased from 10,400 to 16,490, as a result from chain-linking reaction.

consult comment contact

Table 3. Molecular weight of PLLA/PEG multiblock copolymer after chain coupling reaction

Copolymers	LA/EG[a] (in product) (mol/mol)	M_n (GPC)
$PLLA_{46}/PEG_{46}/PLLA_{46}$	2.04:1	10,400
(d)	2.40:1	16,490

Thermal properties. Thermal characteristics of PLLA/PEG/PLLA triblock copolymers were examined by DSC. The results are summarized in Table 4. In copolymer with PEG length of 14 units, single T_m was observed. An increase in T_m was detected, as molecular weight of the copolymers increased. As expected, two T_m of the copolymer with $\overline{DP}_{PEG} = 46$ and $\overline{DP}_{PEG} = 91$, because each segregated block are large enough to exhibit two separate crystalline domains. On the other hand, DSC curves showed a decrease in T_g when the degree of polymerization $\overline{DP}_{PEG}$ increases from 14 to 46. T_g of copolymer with $\overline{DP}_{PEG} = 91$ was not detected because it was masked by T_m of EG block. It was difficult to determine T_g of LLA block because T_g of PLLA and T_m of PEG are very close. DSC exhibit the mutual effects of LLA and EG blocks on T_m and T_g , such as T_g of copolymers is ranging from -7 to -3°C while T_g of commercial PEG is -40°C [3]. An addition of EG block results in a decrease in T_m of PLLA blocks (118-156°C), when compared with the T_m of commercial PLLA (145-186°C) [3]

Table 4. Thermal properties of PLLA/PEG/PLLA triblock copolymers

Copolymers	T_g [°C]	T_m [°C]	
$PLLA_{27}/PEG_{14}/PLLA_{27}$	-3	129	
$PLLA_{28}/PEG_{46}/PLLA_{28}$	-7	23	129
$PLLA_{46}/PEG_{46}/PLLA_{46}$	-6	85	156
$PLLA_{14}/PEG_{91}/PLLA_{14}$	/	45	118
$PLLA_{43}/PEG_{91}/PLLA_{43}$	/	42	150

Conclusions

PLLA/PEG/PLLA triblock copolymers are synthesized at 130°C by ring-openning polymerization of lactide, PEG as a macroinitiator and $Sn(Oct)_2$ as a catalyst. Block lengths and chemical structures of the copolymers are characterized by ^{1}H-NMR and FTIR. It was found that the degree of polymerization of LLA block decreased (27, 28 and 14) when the degree of polymerization of EG block increased (14, 46 and 91). The results also indicated that a 98:2 of LLA/OH molar ratio is a suitable ratio for synthesizing high molecular weight copolymers. HMDI was used as a chain-extender to produce higher molecular weights multiblock copolymers. DSC thermograms showed the dependence of T_m and T_g on the block lengths of the copolymers.

Acknowledgements

Financial support of this work is provided by The Thailand Research Fund (TRF), The Commission on Higher Education (CHE), RTA5180003 and Thailand Toray Science Foundation. Thai Hien Nguyen is supported by a scholarship program from SCG Foundation and SIIT, Thammasat University.

References

[1] Yuqing Wan, Wenna Chen, Jian Yang, Jianzhong Bei, Shenguo Wang: Biomaterials, Vol. 24, Issue 13 (2003), p. 2196
[2] D. Cohn, A. Hotovely-Salomon: Polymer, Vol. 46, Issue 7 (2005), p. 2069
[3] James E. Mark: *Polymer Data Handbook* (1999), p.632, 545, 628

click for feedback
consult - comment - contact

click for feedback
consult - comment - contact

Functionalized and Sensing Materials
doi:10.4028/www.scientific.net/AMR.93-94

Synthesis and Characterizations of PLLA/PEG Block Copolymers
doi:10.4028/www.scientific.net/AMR.93-94.198

References

[1] Yuqing Wan, Wenna Chen, Jian Yang, Jianzhong Bei, Shenguo Wang: Biomaterials, Vol. 24, Issue 13 (2003), p. 2196

[2] D. Cohn, A. Hotovely-Salomon: Polymer, Vol. 46, Issue 7 (2005), p. 2069

[3] James E. Mark: Polymer Data Handbook (1999), p.632, 545, 628

consult
comment
contact
click for feedback

Advanced Materials Research Vols. 93-94 (2010) pp 377-380
Online available since 2010/Jan/12 at www.scientific.net
© (2010) Trans Tech Publications, Switzerland
doi: 10.4028/www.scientific.net/AMR.93-94.377

เอกสารแนบ 5.3.2

click for feedback
consult - comment - contact

Preparation and Characterizations of Electrospun Lactide-based Polymeric Nanofibers

C. Thammawong[1,a] A. Petchsuk[2,b] M. Opaprakasit[3,c]

N. Chanunpanich[4,d] P. Tangboriboonrat[5,e] and P. Opaprakasit[1,f*]

[1]School of Bio-Chemical Engineering and Technology,Sirindhorn International Institute of Technology (SIIT), Thammasat University, Pathumthani 12121 Thailand

[2]National Metal and Materials Technology Center (MTEC), Pathumthani 12120 Thailand

[3]Department of Materials Science, Chulalongkorn University, Bangkok 10330 Thailand

[4]Industrial Chemistry Department, King Mongkut's University of Technology North Bangkok, 10800 Thailand

[5]Department of Chemistry, Mahidol University, Bangkok 10400 Thailand

[a]chakrit_th@windowslive.com, [b]atisasp@mtec.or.th, [c]mantana@sc.chula.ac.th, [d]ncn@kmutnb.ac.th, [e]scptb@mahidol.ac.th, [f]pakorn@siit.tu.ac.th

Keywords: Polylactic acid; Electrospinning; Porosity; Nanofiber; Copolymer.

Abstract. Poly(L)lactide (PLLA), aliphatic polyester, and poly(LLA-co-DLLA) copolymers consisting of 2.5, 7.5, 50% of DLLA content were also synthesized. PLLA was successfully electrospun by using 15wt% solution in (1DMF:3$CHCl_3$) mixed solvent. 2.5, 7.5, 50% P(LLA-co-DLLA) copolymers were then spun at 8, 10, and 15wt% concentration in a single chloroform solvent, respective. The lactide-based polymeric nanofibers were characterized by Scanning Electron Microscope (SEM). Smooth surface morphology was observed in nanofibers produced from PLLA and 50% P(LLA-co-DLLA) copolymer. However, surface porosity was observed in the corresponding fibers from 2.5 and 7.5% P(LLA-co-DLLA) copolymers. These nanofibers have high potential for wide range of applications such as filter media, nano-sensor, drug delivery and tissue scaffold, especially, those derived from 2.5 and 7.5% P(LLA-co-DLLA) copolymers which contain high degree of porosity.

Introduction

Electrospun nanofibers have recently attracted vast attention in research community, especially in biomedical applications. Diameters of polymer nanofibers are smaller than micron (e.g. 10×10^{-3} - 100×10^{-3} μm). The materials show many interesting characteristics, i.e., very large surface area to volume ratio, flexibility, and superior mechanical performance (e.g. stiffness and tensile strength), compared to traditional materials. Polymeric nanofibers are commonly produced by an electrospinning technique from polymer solutions. There are three basic components for electrospinning process. First, a high voltage power supply is used to produce high voltage electric field to induce the charged solution jet out of the capillary tip to the metal collector. Second, a capillary is connected with a syringe. Finally, a metal collecting screen is used to collect the solution jet which has travelled along an ambient air [1]. For the experimental setup, a positive charge is placed to the capillary tube and another connected to the collector. In most case, the collector is simply grounded.

Many parameters have influences on the transformation of polymer solution into nanofibers through electrospinning [2], including (i) system parameters such as molecular weight, molecular weight distribution and architecture (branched, linear and etc.) of the polymer, and polymer solution properties (viscosity, conductivity, dielectric constant, surface tension, and charge carried by the spinning jet) and (ii) process parameters such as electric potential, flow rate and concentration, distance between capillary and collection screen, ambient parameters (temperature, humidity and air

consult comment contact

All rights reserved. No part of contents of this paper may be reproduced or transmitted in any form or by any means without the written permission of the publisher: Trans Tech Publications Ltd, Switzerland, www.ttp.net. (ID: 110.164.106.233-19/01/10,16:23:39)

velocity in the chamber) and finally motion of the target screen.

Polylactide (PLA) is aliphatic polyester, which has been widely used in medical, industrial, and agricultural applications. The advantages of this polymer are its degradability and renewable monomer resources. As PLA's repeat unit consists of chiral center, the polymer presents in two enantiomeric form, i.e. poly(L-lactide), PLLA, and poly(D-lactide), PDLA. A mixture of PLLA and PDLA results in a formation of stronger crystalline structure, a stereocomplex, compared to the homopolymer counter parts. This also leads to differences in mechanical properties of the materials. In addition, optimization of the polymer system can be achieve by copolymerization of DLA and LLA to yield poly(DL-lactide) by varying the copolymer composition with 0, 2.5, 7.5 and 50% DLLA content were synthesized. In this study, poly(LLA-co-DLLA) copolymers has a good mechanical properties as tensile strength, modulus, and elongation at break, i.e., 2.5, 7.5, and 50% [3]. The (co)polymers are then fabricated into nanofibers by an electrospinning technique. Properties and morphology of fibers are then characterized.

Experimental

Materials

All copolymers samples were synthesized by ring-opening polymerization of lactide using stannous(II) octoate as catalyst [3].

Equipments

High voltage supplier (GAMMA, High voltage research) and a syringe pump (kd Scientific, Model 781100) were employed in the electrospinning process.

Characterizations

The morphology of the electrospun nanofibers was examined by an SEM (HITASHI S3400N) after platinum coating. The average diameter and diameter distribution were examined by using image analyzer (PC SEM).

Results and Discussion

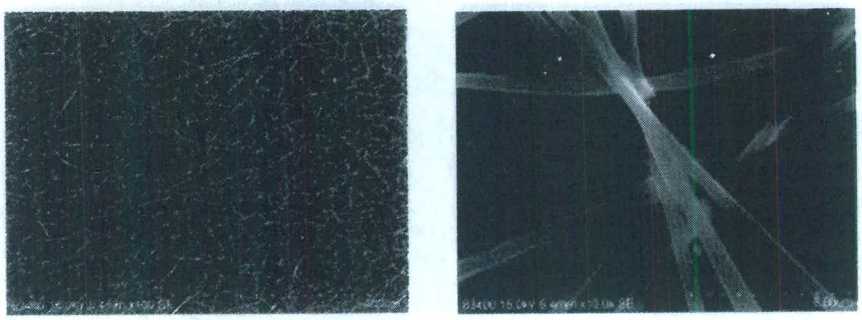
Lactide-based (co)polymers were successfully electrospun by using difference conditions, i.e., solvent system, spinning distance, applied voltage, and solution flow rate. The electrospinning conditions and properties of the resulting nanofibers are summerized in Table 1.

Table 1. Electrospinning conditions and properties of the resulting nanofibers.

Polymers	Solvents	Concentration (wt%)	Conditions			Fiber appearance	Surface morphology	Average diameter (μm)
			V (kV)	Q (ml/hr)	D (cm)			
PLLA	DMF:Chloroform (1:3)	15	5	1	10	Some beads	Smooth	0.5
2.5%P(DLLA-co-LLA)	Chloroform	8	6	1	15	Perfect fiber	Porous	7.5
7.5% P(DLLA-co-LLA)	Chloroform	10	7	1	15	Perfect fiber	Porous	7.0
50% P(DLLA-co-LLA)	Chloroform	15	5	1	12	Perfect fiber	Smooth	6.3

V = Applied voltage (kV) Q = Flow rate (ml/hr) D = Spinning distance (cm)

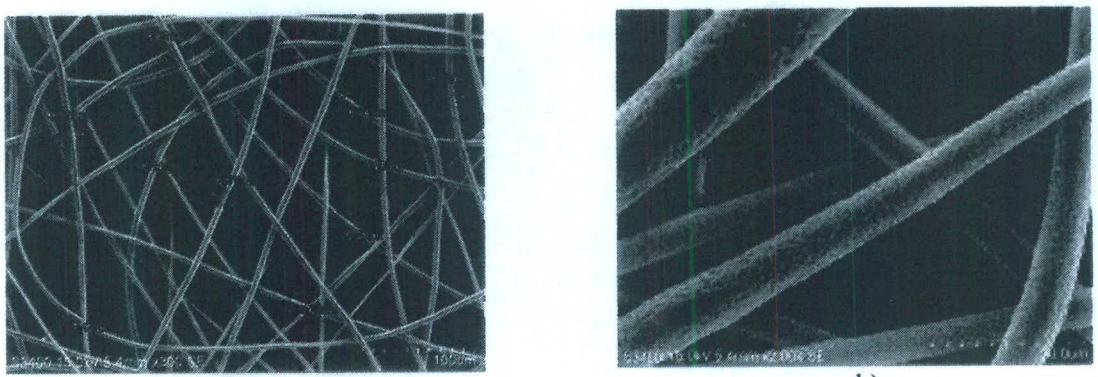
PLLA (Mn 40,000) was electrospun by using a 1DMF:3$CHCl_3$ mixed solvent at 15wt% concentration. The resulting fibers contain some beads in the fiber filaments, as can be seen in Figure 1(a). Fibers with average diameter of 0.5μm were obtained, which is the smallest compared to other samples in this lactide-based system. High magnification SEM image of the nanofibers show smooth surface morphology, as can be seen in Figure 1(b).



(a) (b)

Fig 1. SEM images of PLLA (Mn 40,000) at; (a) 100x, (b) 10,000x

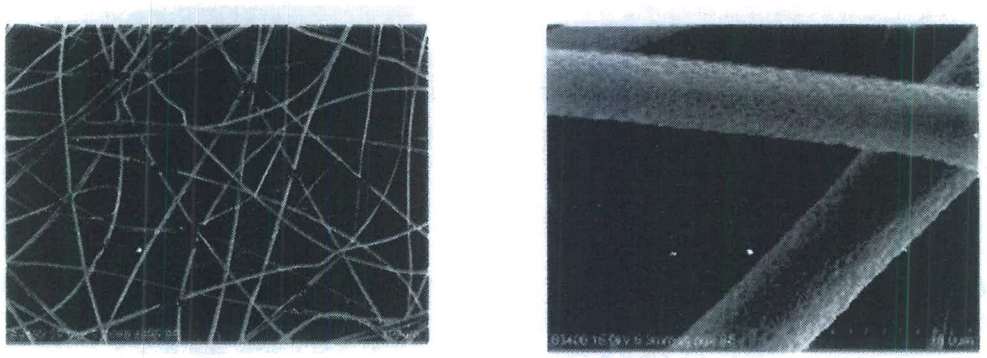
Three samples of P(LLA-co-PDLLA) copolymers were successfully electrospun by dissolving in a chloroform single solvent. Initially, 2.5% P(LLA-co-DLLA) copolymer was dissolved in a chloroform solvent at concentration of 6 wt%. Results on fibers showed some defects from beads and the fiber filaments were not uniform. Consequently, the concentration was increased to 8wt% in order to improve the chain entanglement. The resulting fibers showed no beads, as shown in SEM images in Figure2. Average fiber diameter of 7.5 μm was obtained from this copolymer.



(a) (b)

Fig 2. SEM images of 2.5% P(DLLA-co-LLA) at; (a) 300x, (b) 2000x

The corresponding fibers of a 7.5% P(LLA-co-DLLA) copolymer was spun using a chloroform solvent at concentration of 10 wt%. Perfect fibers were also produced, as shown in Figure 3.

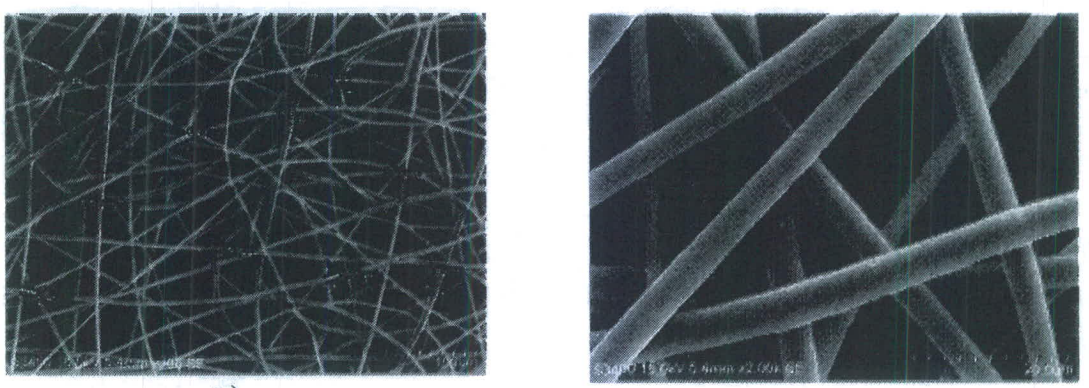


(a) (b)

Fig 3. SEM images of 7.5% P(DLLA-co-LLA) at; (a) 300x, (b) 5000x

Interrestingly, nanofibers produced from copolymers containing 2.5 and 7.5% DLLA content showed high degree of porosity on the surface, as shown in Figure 2(b) and Figure 3(b).

The corresponding nanofibers obtained from 50% P(LLA-co-DLLA) copolymer at a concentration of 15 wt% in chloroform contains no beads beads, as shown in Figure 4(a). However, surface porosity was not observed in this sample.



(a) (b)

Fig 4. SEM images of 50%P(DLLA-co-LLA) at; (a) 300x, (b) 2000x

Summary

Nanofibers of biodegradable/biocopatible lactide-based (co)polymers fabricated by an electrospinning technique were prepare for use in applications. PLLA and P(LLA-co-DLLA) copolymers containing 2.5, 7.5, and 50 % DLLA content were successfully spun by using 15 wt% in 1DMF:3$CHCl_3$, and 8, 10, and 15 wt% concentration in $CHCl_3$, respectively. Nanofibers with different surface morphology and fiber diameter were obtained. This is due to the differences in chemical structures of (co)polymers and interactions of the (co)polymers and solvents, resulting in formation of fibers with different properties.

Acknowledgements

Financial support of this work is provided by Thailand Research Fund (TRF), The commission of Higher Education (CHE), RTA5180003, and Thailand Toray Science Foundation. Chakrit Thammawong is supported by a scholarship program from SIIT, Thammasat Univesity.

References

[1] A. Frenot, I.S. Chronakis, Polymer nanofibers assembled by electrospinning, Curr. Opin. Colloid Interf. Sci. 8 (2003) 64–75.

[2] Ioannis S. Chronakis: Journal of Materials Processing Technology 167 (2005) 283–293

[3] S. Buchatip, A Petchsuk, and K Kongsuwan: Journal of Metals, Materials and Minerals. Vol.18 No.175-180, 2008.

click for feedback
consult - comment - contact

click for feedback
consult - comment - contact

Functionalized and Sensing Materials
doi:10.4028/www.scientific.net/AMR.93-94

Preparation and Characterizations of Electrospun Lactide-Based Polymeric Nanofibers
doi:10.4028/www.scientific.net/AMR.93-94.377

References

[1] A. Frenot, I.S. Chronakis, Polymer nanofibers assembled by electrospinning, Curr. Opin. Colloid Interf. Sci. 8 (2003) 64–75.
doi:10.1016/S1359-0294(03)00004-9

[2] Ioannis S. Chronakis: Journal of Materials Processing Technology 167 (2005) 283–293
doi:10.1016/j.jmatprotec.2005.06.053

[3] S. Buchatip, A Petchsuk, and K Kongsuwan: Journal of Metals, Materials and Minerals. Vol.18 No.175-180, 2008.

consult
comment
contact

เอกสารแนบ 5.3.3

Advanced Materials Research Vols. 93-94 (2010) pp 292-295
© (2010) Trans Tech Publications, Switzerland
doi:10.4028/www.scientific.net/AMR.93-94.292

click for feedback
consult - comment - contact

Improving Malaria Diagnosis via Latex Immunoagglutination Assay in Microfluidic Device

Raweewan Thiramanas[1,a], Rujira Wanotayan[2,b], Sakon Rahong[1,c], Kulachart Jangpatarapongsa[3,d], Pramuan Tangboriboonrat[4,e] and Duangporn Polpanich[1,f]

[1]National Nanotechnology Center, Thailand Science Park, Pathumthani, 12120 Thailand

[2]Department of Nanoengineering, Faculty of Engineering, Chulalongkorn University, Bangkok, 10330 Thailand

[3]Department of Clinical Microbiology, Faculty of Medical Technology, Mahidol University, Bangkok, 10700 Thailand

[4]Department of Chemistry, Faculty of Science, Mahidol University, Bangkok, 10400 Thailand

[a]raweewan@nanotec.or.th, [b]smiley_rujira@hotmail.com, [c]sakon@nanotec.or.th, [d]mtkjp@mahidol.ac.th, [e]scptb@mahidol.ac.th, [f]duangporn@nanotec.or.th

Keywords: latex immunoagglutination assay, microfluidic device, malaria diagnosis.

Abstract. Attempt to improve latex immunoagglutination assay, a rapid method in medical diagnostics, reporting as quantitative results was interested in this study by using microfluidic device. Sensitized latex was produced by physical adsorption of human polyclonal IgG antibody to *Plasmodium falciparum* malaria parasite onto carboxylated polystyrene particle. Conventional latex agglutination assay was firstly performed to verify specific interaction of antibody on the bead surface versus antigen in malaria plasma. The agglutinate size around 30 μm was observed under optical microscope. The proportion of the plasma and the particle was optimized, and an appropriate ratio was applied in microfluidic device. Three patterns of the device were used with the agglutinate size comparison after 10 min as followed: rapid mixing > U-shaped loop > straight capillary Y-junction patterns. However, compared with patient plasma, small agglutinates were also observed when using normal serum.

Introduction

Malaria is a life-threatening disease caused by parasite of the genus *Plasmodium* which causes nearly one million deaths yearly [1]. If this disease is not treated promptly with effective medicines, especially *P. falciparum* malaria can cause severe illness to death. Polpanich D and co-workers reported the success in rapid detection of malaria disease using latex agglutination assay with 90% sensitivity and 80% specificity [2]. The interaction occurred between the antibody and the antigen forming network structure resulted in the particle clumping which can be seen *via* naked eyes [2,3]. However, the assay has limitation which based the result on qualitative analysis. The combination of the assay and other devices which provide the quantitative data is the great challenge. Recently, a few researches have attempted to establish procedure using the latex agglutination assay in a Y-junction microfluidic device [4-6]. It was expected that the agglutination in the microfluidic device would be even easier than its large-sized, commercialized counter part [5]. Moreover, using the particle as mobile solid support dramatically increased surface area and allowed the device to be re-used many times [4]. However, a limited success due to the difficulty in mixing in the microchannel was reported. The ideal mixing has not properly been demonstrated so far. In this preliminary study, latex agglutination assay was applied in the microfluidic device having different channel patterns to

consult comment contact
click for feedback

All rights reserved. No part of contents of this paper may be reproduced or transmitted in any form or by any means without the written permission of the publisher: Trans Tech Publications Ltd, Switzerland, www.ttp.net. (ID: 203.185.131.97-11/12/09,02:46:50)

find the suitable mixing system for further develop a quantitative assay for malaria detection. The highly carboxylated polystyrene (PS) particle conjugated with human polyclonal IgG antibody to *P. falciparum* malaria was prepared. The agglutination reaction on the glass slide and microfluidic device was investigated under optical microscope (OM).

Experimental

Preparation of antibody: Blood samples were collected from acutely *P. falciparum* infected patients examined by Giemsa stained thick blood film at Malaria Clinic, Mae-Sod, Tak province, Thailand. Malaria naive volunteers from non-malaria endemic area were recruited as negative control. This study was approved by the Committee on Human Rights Related to Human Experimentation, Mahidol University. Informed consent was obtained from each individual.

Ammonium sulfate precipitation (33% saturation) of the malaria infected plasma was performed in an ice bath with gently stir for 2 h. The precipitate was dissolved and then dialyzed with 1x PBS (pH 7.4) at 4°C overnight by using dialysis membrane (SpectraPor®, MWCO 100kDa). After that, the human polyclonal IgG antibody was purified using Protein G column (Nunc, USA) according to manufacture's instruction. The purified antibody was checked in sodium dodecyl sulfate-polyacrylamide gel electrophoresis for purity and kept at 4°C until use.

Preparation of antibody-latex conjugate: The sensitized latex was produced by physical adsorption of the purified human polyclonal IgG antibody to *P. falciparum* onto the highly carboxylated PS particle (hydrodynamic diameter of 422 nm). Adsorption was prepared by mixing the purified antibody (30 µg/ml) and the latex (2% (w/v), 5 µl) in adsorption buffer (0.01 M) with different pHs (6.4 to 8.0) in total volume of 500 µl. The mixture was incubated at 25°C for 2 h with shaking (Thermomixer Comfort, Eppendorf, Germany). After that, the reaction was centrifuged (17,800g, 20°C for 20 min), supernatant was then collected to measure the amount of unbound BSA by Bradford assay. The adsorbed amount (Γ_{ads}) was calculated according to the previous study [7].

Latex agglutination assay: The antibody-latex conjugate (1% (w/v), 5 µl) was dropped onto a glass slide and the various amount of malaria plasma was subsequently added. The slide was swirled and the mixture was mixed thoroughly for 2 min, and then the agglutinates were investigated under an inverted OM (Body: IX71, CCD: DP71, Olympus, Japan). The PBS was used as negative control. The appropriate ratio of the particle and the malaria plasma was then applied in microfluidic device.

Microfluidic-latex agglutination assay: Microfluidic channels (200 µm (width) x 100 µm (depth)) were fabricated using standard soft lithography with the polydimethylsiloxane (PDMS) molding technique [8]. Three patterns were used namely: straight capillary Y-junction (Fig. 1(a)), rapid mixing (Fig. 1(b)) and U-shaped loop (Fig. 1(c)) patterns. The channel's inlet and outlet were attached with silicone tube (diameter 0.5 mm, Cole-Parmer, USA). Syringe pump (PHD 2000, Harvard apparatus, USA) was used to control the flow rate of the system. After the antibody-latex conjugate and the malaria plasma were injected into the microchannel and met at the Y-junction, the flow rate was reduced to 5 nl/min. The specific interaction of antigen and antibody was observed and was photographed by the OM (Body: BX51, CCD: DP71, Olympus, Japan). The experiment was repeated twice.



Figure 1. Schematic drawings of three microfluidic patterns namely: straight capillary Y-junction (a), rapid mixing (b) and U-shaped loop (c).

click for feedback
consult - comment - contact

Results and Discussion

***Preparation of antibody-latex conjugate*:** The pH of medium was optimized to find the appropriate condition for preparing the *P. falciparum* antibody-carboxylated latex conjugate. From our results, the high Γ_{ads} value of 8.96±0.08 mg/m^2 was obtained at pH 6.4, whereas the value was decreased to 6.54±0.09 and 6.63±0.08 mg/m^{2}at pH 7.0 and 8.0, respectively. Although, at pH 6.4, the highest Γ_{ads} value can be obtained, the prepared sensitized particle seemed to lose the stability during adsorption so called "spontaneous agglutination" which can be inhibited by increasing pH [9]. The conjugated particle adsorbed at pH 8.0 was more stable and was chosen for preparing antibody-latex conjugate.

***Agglutination assay on glass slide*:** Several cases of the malaria infected plasma and PBS were tested with the sensitized particle. Results showed that the 50% of the total infected cases can produce the large size of the immune complexes, whereas the rest exhibited too small size of the agglutinates. It can be pointed out that the amount of antigen and antibody play an important role in the agglutinate size [2]. The proportion of the malaria infected plasma and the prepared antibody-latex conjugate were optimized. As shown in Fig. 2(a)-(e), the size of agglutinate grew up with increasing the amount of the infected plasma, i.e., increasing the amount of antigen. The optimum ratio of the sensitized particle to the undiluted infected plasma equal to 5:1 with average agglutination size of 30 μm was chosen for further experiment.

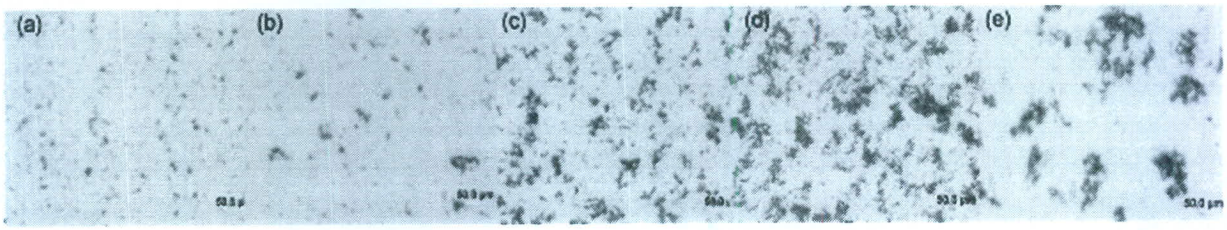


Figure 2. Immunoagglutination of the prepared antibody-latex conjugate (5 μl) in the presence of PBS (a) and the malaria infected plasma: diluted 10 times (5 μl) (b), diluted 5 times (5 μl) (c) undiluted (0.5μl) (d), undiluted (1μl) (e).

***Microfluidic-latex immunoagglutination assay*:** It was reported that the highly carboxylated particle enhanced particle mobility in the microfluidic channel and simultaneously reduce the non-specific reaction leading to the low false-positive result [5]. In our work, the agglutination of the sensitized highly carboxylated PS latex in the presence of the infected plasma in various patterns of the microchannel was investigated under OM. The boundary between the two streams of the *P. falciparum* antibody conjugated particle and the plasma was clearly observed at the beginning. After decreasing the flow rate to 5 nl/min, the agglutination reaction was then significantly occurred. Most distinguishable interaction time was about 10 min after both solutions first met. The pictures of the immune complexes with using the malaria plasma compared with the normal control were captured for each pattern and shown in Fig. 3(a)-(f). It can be seen that the small agglutinates was observed in the case of normal plasma, however, larger agglutinate size was detected in the case of the patient plasma. The comparison between three microchannel patterns were ranked from biggest agglutinate size as followed: rapid mixing, U-shaped loop and straight capillary Y-junction. Due to the low flow rate and the small dimension of the microchannel, the flow in microfluidic devices is normally laminar with slow diffusive mixing which takes place at low Reynolds number (Re), i.e., 0.01-100. Re is defined as $lU\rho/\mu$, where l is the capillary diameter (m), U is the flow velocity (m/s), ρ is the fluid density (kg/m·s) and μ is the fluid velocity (kg/m·s) [10]. To improve the diffusive mixing between two fluids, the rapid mixing (Fig. 1(b)) and U-shaped loop microchannel patterns (Fig. 1(c)) were employed. As expected the agglutinates occurred when using these patterns were larger than the straight capillary Y-junction pattern (Fig. 1(a)). However, the high curvature channel in the rapid mixing pattern might be rendered the larger size of the occurred immune complexes.

consult
comment
contact
click for feedback

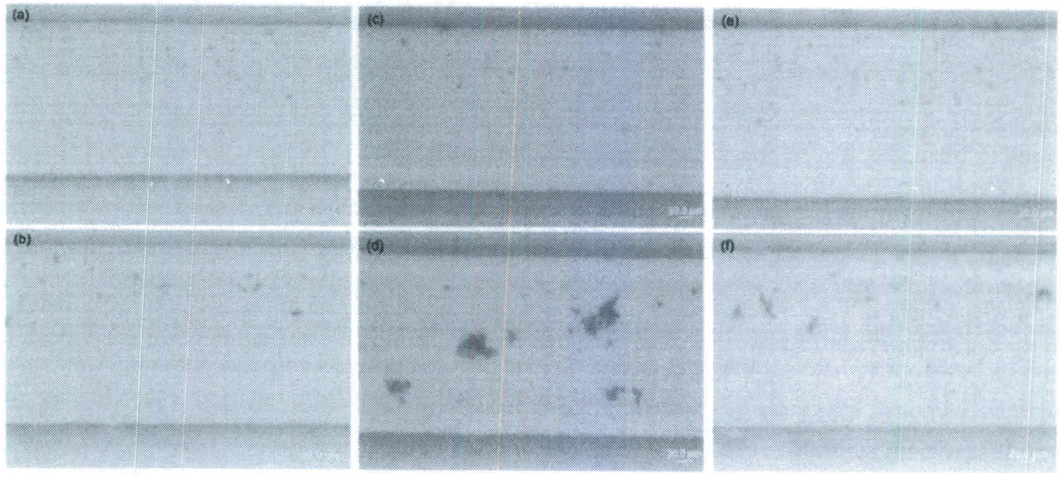


Figure 3. Microfluidic-latex immunoagglutination results for various patterns of the microchannel: straight capillary Y-junction (a,b), rapid mixing (c,d) and U-shaped loop (e,f) by using the normal plasma (a,c,e) and the malaria infected plasma (b,d,f).

Summary

The human polyclonal IgG antibody adsorbed onto the highly carboxylated PS particle was achieved by using Tris-HCl pH 8.0 (0.01M), 25°C for 2 h. The agglutination between the sensitized latex and the malaria infected plasma was clearly observed under OM with average size of 30 μm. After applying in three patterns of microfluidic device, agglutination results were compared ranking from biggest agglutinate size: rapid mixing, U-shaped loop and straight capillary Y-junction. In malaria plasma, the agglutinate size was bigger than that observed in normal plasma for all patterns. Quantitative results would be further obtained by interfacing spectrophotometer to the microfluidic device with the rapid mixing pattern to measure the optical density of agglutinate.

Acknowledgement

Research grant given by The Thailand Research Fund and Commission on Higher Education is gratefully acknowledged.

References

[1] on http://www.who.int/topics/malaria/en/ (August, 2009)

[2] D. Polpanich, P. Tangboriboonrat, A. Elaissari and R. Udomsangpetch: Anal. Chem. Vol. 79 (2007), p. 4690.

[3] L.B. Bangs: Pure Appl. Chem. Vol. 68 (1996), p. 1873.

[4] L.J. Lucas, J.-H. Han, J. Chesler and J.-Y. Yoon: Biosens. Bioelectron. Vol. 22 (2007), p. 2216.

[5] J.-H. Han, K.-S. Kim and J.-Y. Yoon: Anal. Chim. Acta Vol. 584 (2007), p. 252.

[6] J.-H. Han, B.C. Heinze and J.-Y. Yoon: Biosens. Bioelectron. Vol. 23 (2008), p. 1303.

[7] J. Revilla, A. Elaissari, P. Carriere and C. Pichot: J. Colloid Interf. Sci. Vol. 180 (1996), p. 405.

[8] Y. Xia, G.M. Whitesides: Annu. Rev. Mater. Sci. Vol. 28 (1998), p. 153.

[9] I.A. Gritskova, P.V. Nuss, I.G. Krasheninnikova, I. Grzywa-Niksińska, Ye.A. Dorokhova, S.A. Gusev and E. Grzywa: Polimery Vol. 40 (1995), p. 229.

[10] H. Song, J.D. Tice and R.F. Ismagilov: Angew. Chem. Int. Ed. Vol. 42 (2003), p.768.

click for feedback
consult - comment - contact
consult comment contact
click for feedback

เอกสารแนบ 5.3.4

August 2010, Volume 4, No.8 (Serial No.33)
Journal of Chemistry and Chemical Engineering, ISSN 1934-7375, USA

Preparation of Novel Composite from Natural Rubber, Bagasse and Plaster

Sa-Ad Riyajan [1], Isara Intharit [1], Suthikiat Thaiprasansup [1] and Pramuan Tangboriboonrat [2]

1. Department of Materials Science and Technology, Bioplastics Research Unit, Faculty of Science, Prince of Songkla University, Hat Yai, Songkhla 90112, Thailand

2. Department of Faculty of Science, Mahidol University, Bangkok 10400, Thailand

Received: February 23, 2010 / Accepted: March 8, 2010 / Published: August 30, 2010.

Abstract: The sugar cane bagasse was treated with chemical treatment including sodium hydroxide and silane. The characterization of the modified bagasse was achieved with Fourier transform infrared spectroscopy (FTIR), and scaning electron microscopy (SEM). Results showed that the presence Si-CH_3 group occurred on bagasse surface after chemical modification. In addition, the roughness of the modified bagasse was higher than that of unmodified bagasse due to chemical modification from sodium hydroxide. Two polymer composite types, namely (1) natural rubber NR/sugar cane bagasse and (2) NR/plaster via two-roll mill method, were prepared. The optimum cure (t_{90}) and torque of the NR/plaster increased with increasing plaster loading in composite. In case of NR/bagasse, the t_{90} of this sample decreased as a function of sugar cane bagasse while torque of this sample increased with increasing sugar cane bagasse. The modulus of the resulting composite increased with increasing both plaster and sugar cane bagasse, but the tensile strength and elongation at break of the composite decreased as a function of both plaster and sugar cane bagasse in composite.

Key words: Natural rubber, composite, bagasse, plaster, chemical modification.

1. Introduction

Nowadays, many works have reported the natural fibre as reinforcement of polymer matrix including both natural polymer and synthetic polymer due to environment problem [1]. The advantages of natural fiber are available in Asian country, cheap, biodegradable polymer and easily degradation in soils with many microorganisms leading to a good environment in the further. Bagasse is a solid lignocellulosic residue left after extraction of juice from the sugar cane stalk [2]. In addition, the applications of bagasse are used in burnt for energy supply in sugar cane factory, pulps, board materials and composites [3-6]. In the previous work, it was found that bagasse is a raw material blended with other polymer including poly (vinyl alcohol), PVA [2], polypropylene [4], phenol formaldehyde (PF) resin [3] waste gelatin [7] and polystyrene [8]. PVA composites sheet [2] was prepared from PVA, and lignocellulosic fillers, corn starch, presence of water and glycerol by compression molding. Results showed that the resulting polymer composite based on PVA and starch with apple wastes and sugarcane bagasse fillers were much harder than samples prepared with orange wastes. E. Chiellini, and co-worke [9, 10] reported the preparation and mechanical properties of composite films from biorelated agro-industrial waste including sugar cane and apple and orange fruit juice extraction and PVA cast from PVA aqueous solutions. They found that composite obtained from orange fruit gave to be suitable for blending in higher amounts by weight than other samples. This is the first study of its kind wherein the preparation and physical testing of polymer composite obtained from natural rubber, sugar cane bagasse and plaster. The obtained polymer

Corresponding author: Sa-Ad Riyajan, asst. Prof., research field: polymer science and technology. E-mail sa-ad.r@psu.ac.th, saadriyajan@hotmail.com.

composite from NR, sugar cane bagasse and plaster was prepared by two-roll mill method. In addition, the modified sugar cane bagasse with sodium hydroxide and silane treatment was analyzed by Attenuated Total Reflection Fourier Transform Infrared (ATR-FTIR), scanning electron microscope (SEM) and atomic force microscopy (AFM). The characterization of novel polymer composite was studied through curing properties and tensile strength.

2. Materials and Methods

2.1 Materials

Natural rubber grade STR 5L was supplied by Chalong Latex Industry Co., Ltd. Sugar cane bagasse was obtained from local in Thailand. Then, sugar cane bagasse fibers were obtained by milling using a laboratory blender. Plaster was purchased from Siam Nakarin Co., Ltd.. All other ingredients used were a commercial grade. The commercial Bis-(3-triethoxy-silyl propyl)-tetrasulfide, which is a coupling reagent, was provided by Sigma-Aldrich Company. The vulcanizing agent including zine oxide, steric acid, sulfur and tetramethyl thiuram disulfide (TMTD) were reagent grade and were obtained commercially.

2.2 Modified Sugar Cane Bagasse

The resulting sugar cane bassage was immersed in 10% sodium hydroxide solution for 24 h. After sugar cane bagasse was treated with sodium hydroxide, it was washed with water for many times and reached to neutral pH. Thus, the resulting sugar cane bagasse was coated with silane by stiring an immersion of 10 g of sugar cane bagasse in silane for 5 h.

2.3 Preparation of Polymer Composite

Formulation of mixes used for polymer composite from NR/sugar cane bagasse and NR/plaster in this the present work is shown in Table 1 and Table 2, respectively. NR was masticated on the mill for 5 min followed by addition of tphe ingredients as shown in Table 1 and Table 2. The resulting polymer composite materials were prepared in a two-roll mill. The condition of operation including the nip gap, speed ratio, mill roll and the number of passes for two-mill was controlled at the same in all the mixes at 50 ℃. The resulting samples were milled for sufficient time to disperse the sugar cane bagasse or plaster with different loading in the NR matrix at a mill opening of 1.55 mm. The silane as a coupling agent was added in NR compound during mixing to improve the interaction between sugar cane bagasse/plaster and NR matrix. Then, the resulting NR composite was kept at 28 ± 2 ℃ for overnight in a closed container before cure analysis using an Alpha Moving Die rheometer (MDR 2000). The t_{90}, cure time and max torque were measured from the MDR 2000. Then, each specimen was placed in a mold (140 × 140 × 1.5 mm) and the NR compounds were vulcanized at 150 ℃ and the pressure of 6.89 MN/m^2 for 20-30 min for a optimum cure (t = 90) or

Table 1 Formulation of polymer composite obtained from NR and sugar cane bagasse.

Chemical (phr)	Formulation			
	1	2	3	4
STR 5 CV60	100	100	100	100
Wigstay L	2	2	2	2
Sulfur	2	2	2	2
Steraric acid	2	2	2	2
ZnO	3	3	3	3
TMTD	1.3	1.3	1.3	1.3
DPG	0.7	0.7	0.7	0.7
Sugar cane Bagasse	2	5	10	20
Silane	0.5	0.5	0.5	0.5

Table 2 Formulation of polymer composite obtained from NR and plaster.

Chemical (phr)	Formulation				
	1	2	3	4	5
STR 5 CV60	100	100	100	100	100
Wigstay L	2	2	2	2	2
Sulfur	2	2	2	2	2
Steraric acid	2	2	2	2	2
ZnO	3	3	3	3	3
TMTD	1.3	1.3	1.3	1.3	1.3
DPG	0.7	0.7	0.7	0.7	0.7
Plaster	5	30	50	70	100
Silane	0	0.18	0.3	0.42	0.60

tc_{90}). The polymer composite was compressed by compression molding machine to give the polymer composite sheet.

2.4 Characterization of Modified Sugar Cane Bagasse and Testing of Polymer Composite

The chemical structure of the modified sugar cane was observed by FTIR-ATR. ATR-FTIR spectra were studied with Fourier transformed infrared; FTIR (Bruker, EQUINOX 55) spectral data, taking 100 scans for each sample with resolution 3 cm^{-1}, and raging from 400-4000 cm^{-1} and the ATR-FTIR of samples were obtained to detect any chemical interactions between silane and sugar cane bagasse. The aim of the SEM study was to obtain a topographical characterization of the modified and unmodified sugar cane bagasse. In addition, the morphology of fractured polymer composite sheet was analyzed by SEM. The sample was deposited on a brass hold and sputtered with platinum. SEM photographs were taken with a JSM 6400 Scanning Microscope (Japan) at the required magnification at ambient temperature. SEM was performed at an accelerating voltage of 20 kV. The height and deflection images were recorded with the resolution of 512 lines. Then, the resulting polymer composite was kept at 28 ± 2 ℃ for overnight in a closed container before cure analysis using an Alpha Moving Die rheometer (MDR 2000). The t_{90}, cure time and max torque were measured from the MDR 2000. The testing crosshead speed of 500 mm/min was applied with load cell of 1 kg-N. The physical testing of dried latex film was analyzed by universal testing machine Gotech brand model TCS 2000 based on ASTM D 412. Five dumbbell test pieces were cut from each film and the average thickness was calculated and then attached between the grips of a tensile testing machine and pulled at a rate of 500 mm. The thermogravimetric (TG) analysis was performed on a TGA7, PERKIN ELMER: TGA. The mass of each sample was roughly 5.00-6.00 mg. The carrier gas was air with a flow rate of 50 mL/min. The temperature rose from 50 to 800 ℃ at heating rates of 10 ℃/min.

3. Results and Discussion

3.1 Characterization of Modified Sugar Baggage

The characterization of modified sugar cane bagasse was investigated by SEM and FTIR. The chemical structure of modified sugar cane bagasse was analyzed by FTIR as shown in Fig. 1. The ester-linkage or OC=O stretching of modified sugar cane was observed at 1085 and 1238 cm^{-1}. In addition, the wavelength at 1321 cm^{-1} of modified sugar cane bagasse indicated the stretching C-O. The new peak of modified sugar cane was observed at 1180 and 1225 cm^{-1} referred to Si-O-Si and Si-O-cellulose, respectively. This result responds with this in Ref. [1]. These results revealed the successfully modified surface of sugar cane bagasse. The morphology of modified sugar cane and unmodified

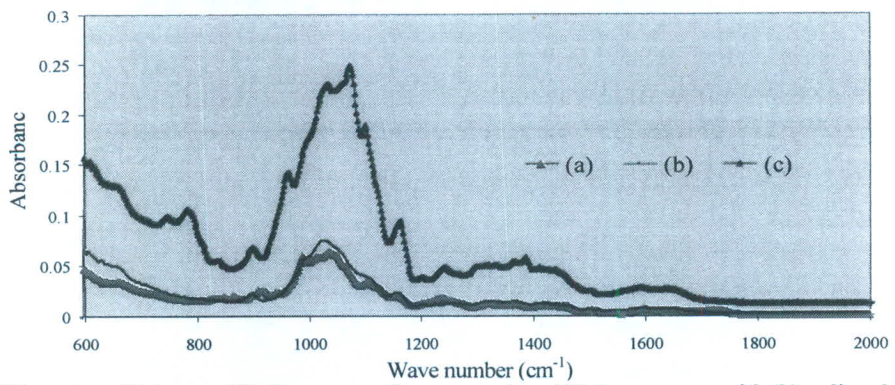


Fig. 1 ATR-FTIR spectra of (a) unmodified sugar cane bagasse, and modified sugar cane with (b) sodium hydroxide and (c) silane treatment.

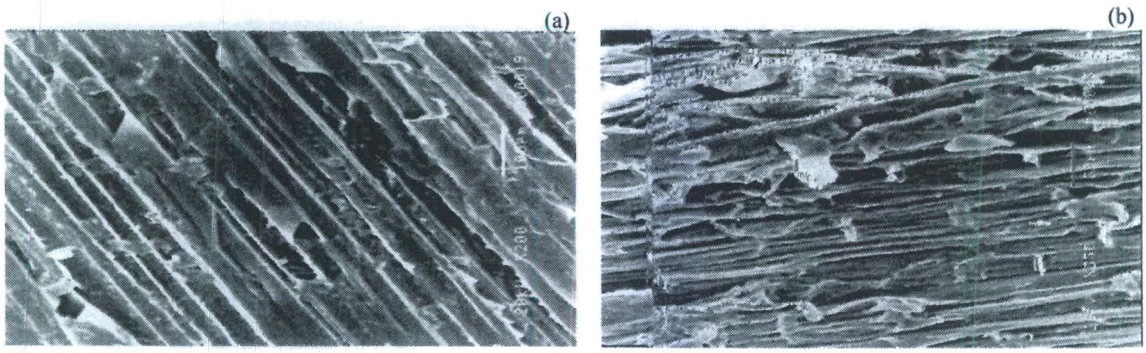


Fig. 2 SEM image of surface of (a) unmodified sugar cane and (b) modified sugar cane with sodium hydroxide.

sugar cane bagasse is shown in Fig. 2. It was found that the surface of unmofidified sugar cane bagasse showed lower roughness comparing to sample with modified with chemical treatment as shown in Fig. 2. This result indicated that the fat acid on surface of bagasse was removed by sodium hydroxide. The diameter of sugar cane was roughly 0.1 mm.

3.2 Curing Properties of Polymer Composite

When the addition of plaster in NR matrix was subjected to tc_{90} of polymer composite presence of 30, 50, 70 and 100 phr of plasters was 2.33, 2.51, 2.42 and 2.41 min, respectively as shown in Fig. 3 (a). Torque of polymer composite containing 0 phr of plaster was about 2 dNm while the torque of this polymer composite in the presence of 30, 50 and 70 phr plaster was 3, 6 and 11 dNm, respectively as shown in Fig. 3(b). Moreover, when plaster was added in polymer composite, the properties of the resulting polymer composite exhibited a hardness behavior due to elastic modulus of plaster observing from torque. In the case of bagasse, it was found that the curing time of polymer composite decreases as a function of bagasse content as shown in Fig. 4 (a). The curing time of polymer composite containing 2, 5 and 10 phr of bagasse was 1.75, 1.6 and 1.4 min, respectively. The torque of polymer composite in the presence of 2, 5 and 10 phr of bagasse was 2.6, 3 and 4.4 dNm, respectively as shown in Fig. 4 (b).

3.3 SEM of Polymer Composite

The morphology of polymer composite is a relationship with the physical properties of polymer composite. The morphology of polymer composite was obtained from NR and sugar cane bagasse contents and plaster contents as shown in Fig. 5. It is clear that the plasters and sugar cane bagasse are hard to disperse in NR matrix due to difference in surface component between NR and plaster. The morphology of polymer composite showed the more roughness as a function of amount of plaster content in polymer composite. In the case of polymer composite containing 70 phr of plaster, a large number of voids were clearly visible on the fracture surface leading to poor adhesion between NR matrix and plaster. In addition, the sugar cane bagasse is difficult to disperse in NR matrix due to difference in polar groups between sugar cane bagasse and NR matrix.

3.4 Mechanical Properties

The modulus of NR filled with plaster and bagasse increased with increasing percentage of plaster and bagasse loading as shown in Fig. 6 (a). It is noted that the maximum of modulus was observed in sample in the presence of 20 phr of sugar cane bagasse and 70 phr of plaster. Fig. 6 (b) shows the influence of both sugar cane bagasse and plaster on the tensile strength of polymer composite. The tensile strength of the polymer composite containing 70 phr of plaster was about 2 MPa. The elongation at break of polymer composite dramatically decrease after addition of more amount of sugar cane bagasse and plaster as shown in Fig. 6 (c).

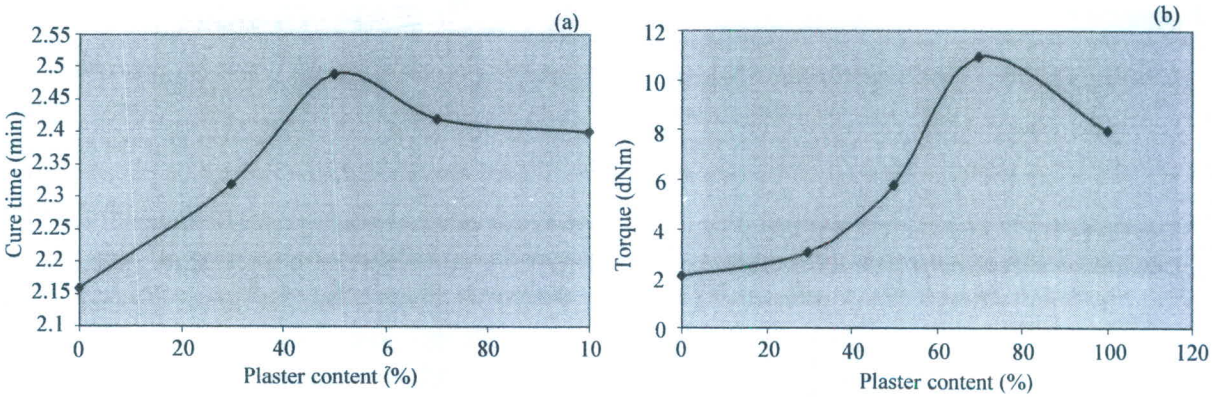


Fig. 3 Effect of plaster on (a) the cure property and (b) torque of polymer composite.

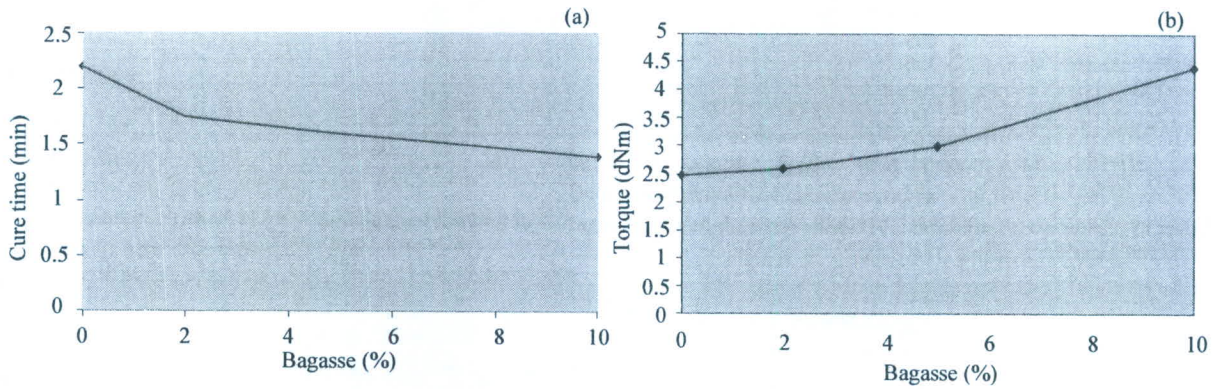


Fig. 4 Effect of bagasse on (a) the cure property and (b) torque of polymer composite.

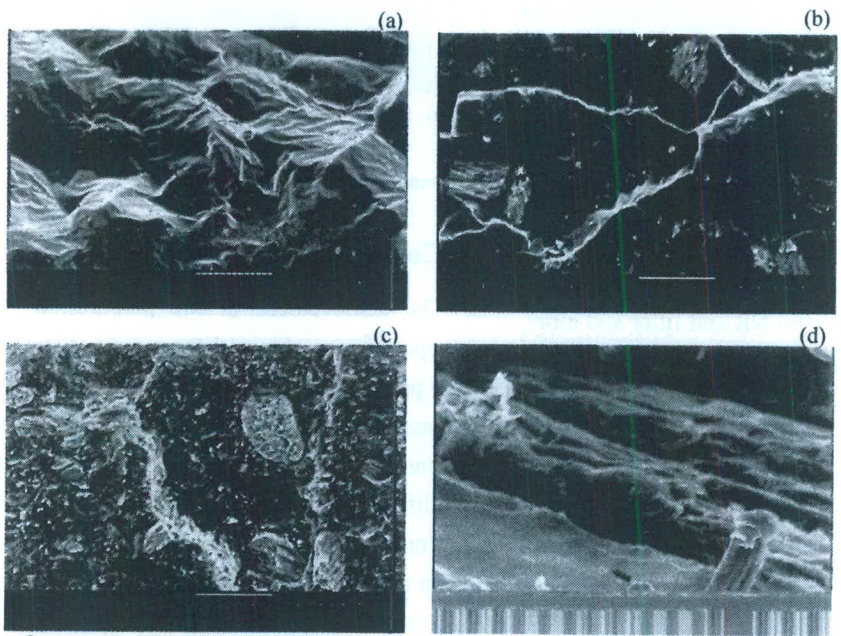


Fig. 5 Morphology of natural rubber alone (a), polymer composite in the presence of (b) 30, (c) 0 phr of plaster and (d) 20 phr of sugar cane bagasse observed from SEM.

Experimental

Materials

All molecular weights (MWs 2,000, 8,000, 12,000 and 20,000) of Poly(ethylene glycol) hydroxyl terminated (PEG), lactide monomer and stannous 2-ethylhexanoate ($Sn(Oct)_2$) were purchased from Aldrich. High ammonia NR latex was obtained from Rayong Bankok Rubber Co.,Ltd., Thailand. And all solvents such as dichloromethane and ethanol were used of AR grade and supplied by Lab Scan.

Synthesis of PELA

The PLA-PEG-PLA triblock copolymer was synthesized by ring-opening polymerization of lactide in bulk process using stannous 2-ethylhexanoate ($Sn(Oct)_2$) as a catalyst. The PEG and $Sn(Oct)_2$ were introduced into a three-necked round bottomed flask equipped with magnetic stirring. The flask was connected to a vacuum system and immersed in an oil bath. The flask was heated to 50 °C for 1 h. A predetermined content of lactide monomer (PEG:PLA molar ratio is fixed at 1:1) was added. The temperature of the reaction mixture was raised to 170 °C and maintained constant for 24 h. Then, the synthesized copolymer was dissolved in dichloromethane and precipitated in methanol and dried under vacuum. Proton nuclear magnetic resonance (^{1}H-NMR) spectra, which were taken with a Bruker DPX-300 operating at 300 MHz using $CDCl_3$ as a solvent was used to determine chemical structure and composition. Chemical shift (δ) was measured in ppm using tetramethylsilane (TMS) as an internal reference. And, the molecular weight of PELA was calculated by the following equation:

$$M_{nPLA} = LA/EO \times 72/44 \times M_{nPEG}$$

$$M_{nPELA} = M_{nPLA} + M_{nPEG}$$

where LA/EO is the molar ratio of the lactide to ethylene oxide in the copolymer determined by ^{1}H-NMR and M_n is the number-average molecular weight

Preparation of PELA modified NR film

Natural rubber (NR) latex films with a thickness about 2.0 mm were prepared from commercial NR latex concentrate (Rayong Bangkok Rubber Co., Ltd., Thailand). A dried NR film was prepared from casting the NR latex on a glass plate at room temperature. The NR strip (2x5 cm^2) was held onto a glass slide without any use of adhesive. The sample surface was cleaned by sonicating sequentially with ethanol and water for 15 minutes in each step before drying under vacuum at room temperature. A solution of 5% w/v PELA in dichloromethane was prepared. The cleaned NR strip was then immersed into the PELA solution for 24 h at room temperature. Then, the modified surface was rinsed with dichloromethane before drying under vacuum at room temperature.

Attenuated Total Reflectance Fourier Transform Infrared Spectroscopy (ATR-FTIR)

Attenuated total reflection (ATR) mode was characterized for all samples. The chemical characteristic of NR and modified NR surfaces were obtained. ATR-FTIR spectra were taken using diamond crystal for a single reflection mode and Nicolet 6700 FT-IR. The measurements were performed with sixty-four scans at resolution of 4 cm^{-1} over the range of 4,000 to 600 cm^{-1}

Atomic Force Microscopy (AFM)

The morphology of the NR and PELA modified NR sheet was determined by using a Scanning Probe Microscope (SPM) with Nanoscope IV controller (Digital Instrument) in tapping mode with the scan size of 10x10 μm^2. The surface root mean squared roughness (R_{rms}) was directly calculated from Nanoscope software using the following equation:

$$R_{rms} = \sqrt{\frac{1}{n}\sum_{i=1}^{n} Z_i^2}$$

where Z_i = current difference between the height and the mean plane

n = number of points in the image

Water Contact Angle measurement

A deionized water droplet (approximately 5 µL) was dropped on the NR and modified NR surface. And, sessile drop contact angle measurement was performed with a contact angle goniometer (G-1, Kruss). For each angle reported, at least five sample readings were averaged.

Nanoindentation testing

Nanoindentaion experiments were performed using Nano Test system (Micro Material Ltd. Wrexham, UK) with a 100 μm radius diamond spherical indenter tip manufactured by Micro Materials.

The experimental conditions for all indentation tests were as follows:

Initial load : 0.01 mN

The maximum load : 0.25 mN

Loading and unloading rate : 0.10 mN/s

Dwell time or holding time at maximum load : 60 s.

The stiffness was obtained by fitting a power law function, proposed by Oliver and Pharr [20], on the unloading curve. And, the reduced elastic modulus (E_r) was determined from average forty-eight data points using the following equation, deduced from Hertz analysis:

$$E_r = \frac{\sqrt{\pi}}{\sqrt{8R}} \frac{S}{\sqrt{P}}$$

where S is the stiffness. R and P values are the nominal radius of curvature of the spherical indenter and the applied load, respectively.

***In vitro* cytotoxicity test**

Cells

A mouse connective tissue fibroblast cell line, L929 was cultured in Dulbecco's minimum eagle medium (DMEM) supplemented with 10% fetal calf serum and 4 mM glutamine. The cultures were cultivated in an incubator at 37°C 90% r.h. and 5% CO_2, until cell monolayers attained confluence, which occurred after 24 h Then, the cultures were harvested using trypsin solution. Stock cultures were seeded in 60 mm diameter cell culture petri dishes at a density of 0.1 x 10^6 cells/cm^3 and subcultured once a week. Assays were always performed in the exponential growth phase of the cells. The cell line was periodically assayed for mycoplasma.

Extraction method

Extracts of the polymers were prepared using 0.2 g polymer per ml serum-supplemented culture medium (DMEM) containing 4 mM glutamine. The extracts were maintained in an incubator for 24 h at 37°C. If necessary, the extracts were neutralized to exclude the effect of pH and filtered through a 0.2 μm membrane filter. The cells were seeded into 96-well microtiter plates at a density of 1 x 10^4 cells/well. Then, after 24 h the culture medium (100 μl) was replaced with serial dilutions of the extracts. After an incubation period of 24 h, the viability of the cells was evaluated by the MTT assay.

MTT assay

MTT (3-(4,5-dimethylthiazol-2-yl)-2,5-diphenyl tetrazolium bromide) was dissolved in PBS (phosphate-buffered solution) at 5 mg/ml and filtered for sterilization. A total of 50 μl of this stock solution was added to each well, reaching a final concentration of 0.5 mg MTT per ml and the plates were incubated for 2 h. Unreacted dye was removed by aspiration and the purple formazan product was dissolved in 100 μl/well isopropanal and quantified by spectrophotometer at wavelengths of 570 and 650 nm. The % cell viability related to control wells containing cell culture medium without extracts was calculated by the following equation (A = absorbance):

$$\% \text{ cell viability} = \frac{[A]_{test}}{[A]_{control}} \times 100$$

Results and discussion

Synthesis and characterization of PELA

NMR spectra

Typical ^{1}H-NMR spectra of PELA is shown in Fig. 1. A series of PELA having a fixed PEG:PLA molar ratio of 1:1 were successfully synthesized by varying the PEG molecular weight (chain length) in the middle block. The obtained PELA are denoted as PELA-Xk, where X is for the number of molecular weight of PEG. By predetermination of the content of lactide monomer attached to the PEG middle block, the molar ratio of PLA:PEG could be controlled to be closely 1.0:1.0. The characteristics of PELA are presented in Table 1. The obtained PEG:PLA molar ratios were within a confined range between 1.1:1.0 and 1.2:1.0.

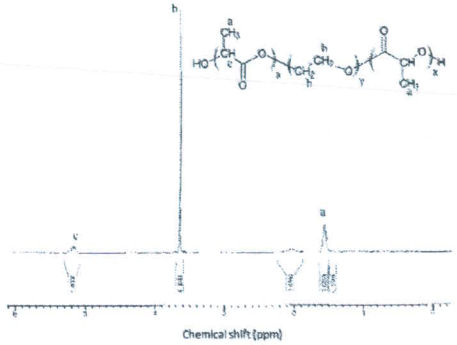


Fig.1 ^{1}H-NMR spectra of PELA-8k

Table 1 Structural characteristic and molecular weight of PLA-PEG-PLA triblock copolymer

Polymer	M_n of PEG g/mol	EG:LA (theory)	EG:LA (Exp.)	M_n (NMR)of PELA g/mol
PELA-2k	2,000	1.0 : 1.0	1.2 : 1.0	4,700
PELA-8k	8,000	1.0 : 1.0	1.1 : 1.0	22,100
PELA-12k	12,000	1.0 : 1.0	1.2 : 1.0	28,900
PELA-20k	20,000	1.0 : 1.0	1.1 : 1.0	41,000

Note: M_n is a number average molecular weight

Characterization of modified NR surface

FTIR

The presence of PELA on the surface of modified NR film was characterized by ATR-FTIR, a technique well suited for investigating surface chemical species, and the spectra are presented in Fig.2. It was apparent that the ATR-FTIR spectra of the modified NR films were different from that of the unmodified NR. The characteristic absorbance peak at 1740 cm^{-1}, corresponding to C=O stretching, was clearly observed in all NR surfaced modified with PELA indicating that PELA was introduced into the NR surface. Together with a decrease in the intensity of absorbance peak at 1380 cm^{-1} of NR, it could be inferred that the surfaces of all modified NR film were completely covered by PELA of all molecular weights. Moreover, it could be suggested that the formation of PELA onto NR surface involves only physical bonding.

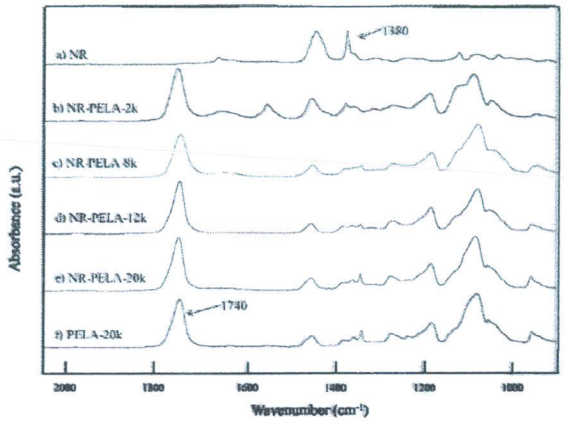


Fig.2 The ATR-FTIR spectra of of unmodified NR and modified NR with various molecular weight PELA

Morphology of modified NR surface

The surface morphologies of unmodified NR and NR modified by PELA investigated by AFM were shown in Fig. 3, with the topographic or height images on the left, and the phase images on the right. The AFM micrographs of unmodified NR are apparently different from those of PELA modified NR surfaces. The topographic image showed the relative flat and smooth surface of the unmodified NR, as seen in Fig. 3a. Whereas, globular particle like morphologies were observed on the PELA modified NR of all molecular weights, as shown in Fig 3(b-e). According to the surface root mean squared roughness (R_{rms}), the surfaces of all PELA modified NR, which are in the range of 43 to 196 nm., are slightly rougher than that of unmodified NR (R_{rms} = 29 nm). Also, the phase images of all NR modified by various PELA molecular weights, as seen in Fig.3(g-j), show no character; i.e. particularly no phase separation. This can be explained by the fact that dichloromethane is considered a good solvent for both pure PLA and PEG. Therefore, both components of PELA; namely PLA and PEG, can dissolve to form particle like morphology instead of phase-separated structure. In addition, These AFM results suggested that the orientation between PLA and PEG segment of PELA are randomly oriented, and the chain length of PELA in the scope of this study is not sufficient to induce phase separation.

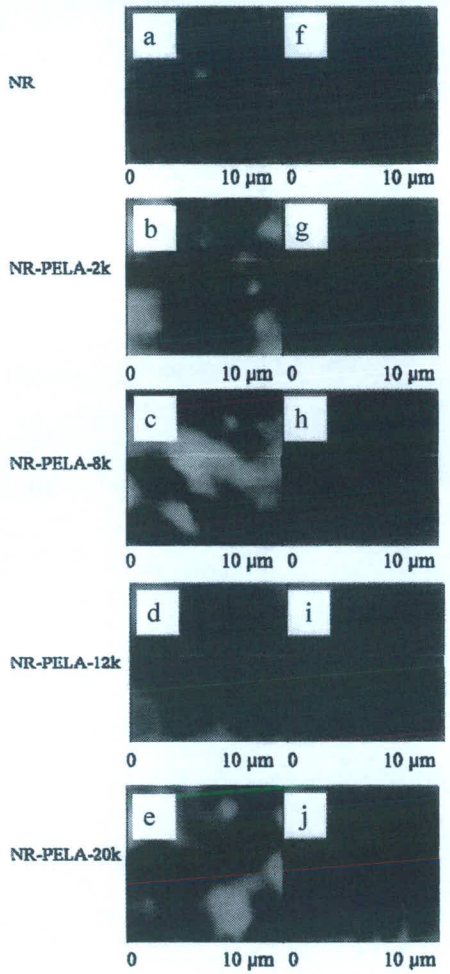


Fig.3 AFM topoghapic micrographs of (a) unmodified NR film and (b-e) modified NR with PELA-2k, PELA-8k, PELA-12k and PELA-20k, and AFM phase images of (f) unmodified NR film and (g-j) modified NR with PELA-2k, PELA-8k, PELA-12k and PELA-20k, respectively

Water Contact Angle

Table 2 Water contact angle of unmodified NR and modified NR with various molecular weight PELA

Sample	Water Contact Angle (°)
NR	87.3 ± 1.3
NR-PELA-2k	37.3 ± 2.2
NR-PELA-8k	44.8 ± 2.4
NR-PELA-12k	46.0 ± 1.7
NR-PELA-20k	46.6 ± 2.0

To determine the relative hydrophilicity of various molecular weight PELA, WCA measurements were conducted, and the results are depicted in Table 2. A decrease in WCAs on the PELA modified surfaces of NR of all molecular weight in comparison to that of unmodified NR surface indicates that the modification of NR surface by PELA can enhance hydrophilicity of NR surface.

Nanoindentation behavior

To reduce the viscoelastic or time-dependent effect, the methodology of inserting the holding period of 60 s between loading and unloading was used to determine elastic modulus in this study. Load-displacement curves of unmodified NR and PELA modified NR with various molecular weights were shown in Fig. 4. The average values of reduces modulus data extracted from the loading/unloading curves were presented in Table 3 and presented in Fig. 5. The PELA-2k exhibited the lowest reduced modulus. With an increase in the PELA molecular weight, the reduced modulus of all PELA modified NR surfaces were found to increase monotonously. It is worth noting that the PELA-20k exhibited a comparable reduced modulus to that of unmodified NR. It could be suggested that the PELA with molecular weight of PEG-20k is the best candidate for modifying the NR surface in order to enhance biocompatibility, while the mechanical property still remained intact.

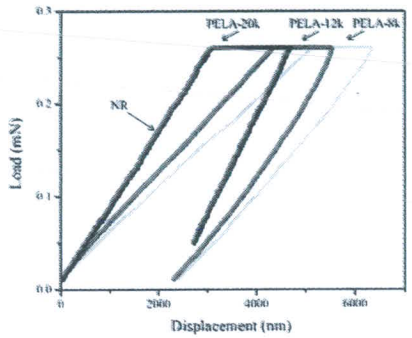


Fig. 4 Load-displacement curves of unmodified NR and modified NR with various molecular weight PELA

Table 3 Reduced modulus of unmodified NR and modified NR with various molecular weight PELA

Sample	Reduced modulus (MPa)
NR	2.45 ± 0.08
NR-PELA-2k	0.97 ± 0.04
NR-PELA-8k	1.20 ± 0.10
NR-PELA-12k	1.63 ± 0.09
NR-PELA-20k	2.35 ± 0.20

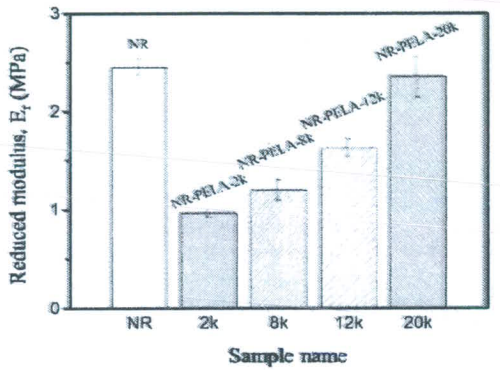


Fig. 5 The reduced modulus of unmodified NR and modified NR with various molecular weight PELA

Cytotoxicity of NR modified by PELA

The MTT assay was conducted to evaluate the cytotoxicity of all tested NR modified by PELA. This standard method was based on the colorimetric analyses of cell viability. The specimens of NR modified by PELA were tested using dimethyl sulfoxide (DMSO) as a positive control, micro covered glass as negative control, and Dulbecco's minimum eagle medium (DMEM) as a control. The results showed that % cell viability of NR was 20%, while all of those of NR modified by PELA were greater than 70%. According to the standard procedure, if cell viability was found to be greater than 70% of that of control, this tested sample was considered biocompatible material. Therefore, it was apparent that the surface modification of NR by PELA could effectively improve the biocompatibility of NR.

Conclusions

To enhance the biocompatibility of NR film, the surface modification of NR film by PELA of various molecular weights was successfully prepared, and characterized. Their nano-mechanical properties were investigated using Nanoindentation technique by taking viscoelastic effect into an account. The ATR-FTIR result suggests that the formation of PELA onto NR surface involves only physical bonding. The AFM morphologies supported ATR-FTIR result in that PELA was introduced onto NR surface and there is no phase separation between PLA and PEG segment. The

NR surfaces modified by PELA of all molecular weight exhibit enhanced hydrophilicity in comparison to that of unmodified NR, and their reduced modulus was found to increase with an increasing PELA molecular weight. In addition, the NR-PELA-20k showed a comparable reduced modulus to the unmodified NR. Finally, it was apparent that the improvement of biocompatibility of NR could be successfully achieved by the surface modification of NR by PELA.

Acknowledgement

Research grants from The Thailand Research Fund (TRF) to P.Tangboriboonrat and R.Thonggoom are gratefully acknowledged. The authors thank K.Phomphrai for valuable suggestions. Special thank to N.Promawan and N.Pancharoentavon for performing Nanoindentation.

References

[1] Chei Sara HY, Tan Peng Wang KL, Ho CC, Kang ET. Surface modification of natural rubber latex films via grafting of poly(ethylene glycol) for reduction in protein adsorption and platelet adhesion. J Mat Sci Mater Med 2001; 12: 377-384.

[2] Hoven VP, Chombanpaew K, Iwasaki Y, Tasakorn P. Improveing Blood Compatibility of Natural Rubber by UV-induced Graft Polymerization of Hydrophilic Monomers. J Appl Polym Sci 2009; 112: 208-17.

[3] Steele Terry WJ , Huang Charlotte L, Effendi Widjaja, Boey Freddy YC, Loo Joachim SC and Venkatraman Subbu S. The effect of polyethylene glycol structure on paclitaxel drug release and mechanical properties of PLGA thin films. Acta Biomater 2011; 7: 1973-83.

[4] Danquah M, Fujiwara T, Mahato RI. Self-assembling methoxypoly(ethylene glycol)-b-poly(carbonate-co-L-lactide) block copolymers for drug delivery. Biomaterials 31 (2010) 2358-70.

[5] Kumari A, Yadav SK, Yadav SC. Biodegradable polymeric nanoparticles based drug delivery systems. Colloid Surface B 2010; 75: 1-18.

[6] Nampoothiri KM, Nair NR, John RP. An overview of the recent developments in polylactide (PLA) research. Bioresource Technol 2010; 101: 8493-501.

[7] Wang H, Zhao P, Su W, Wang S, Liao Z, Niu R, Chang J. PLGA/polymeric liposome for targeted drug and gene co-delivery. Biomaterials 2010; 31: 8741-48.

[8] Rungsardthong U, Deshpande M, Bailey L, Vamvakaki M, Armes SP, Garnett MC, Stolnik S. Copolymers of amine methacrylate with poly(ethylene glycol) as vectors for gene therapy. J Control Release 2001; 73: 359-80.

[9] Barton KN, Stricker H, Kolozsvary A, Kohl R, Heisey G, Nagaraja TN, Zhu G, Lu M, Kim JH, Freytag SO, Brown SL. Polyethylene Glycol (Molecular Weight 400 DA) Vehicle Improves Gene Expression of AdenovirusMediated Gene Therapy. J Urology 2006; 175: 1921-25.

[10] Zhu J. Bioactive modification of poly(ethylene glycol) hydrogels for tissue engineering. Biomaterials 2010; 31: 4639-56.

[11] Bettahalli NMS, Steg H , Wessling M and Stamatialis D. Development of poly(L-lactic acid) hollow fiber membranes for artificial vasculature in tissue engineering scaffolds. J Membrane Sci 2011; 371: 117-26.

[12] Armentano L , Dottori M , Fortunati E, Mattioli S and Kenny JM. Biodegradable polymer matrix nanocomposites for tissue engineering: A review. Polym Degrad Stabil 2010; 95: 2126-46.

[13] Lu YC, Fulcher JT, Tandon GP, Foster DC, Baur JW. Microscale thermomechnical characterization of environmentally conditioned shape memory polymer. Polym Test 2011; 30: 563-70.

[14] Liao Q, Huang J, Zhu T, Xiong C and Fang J. A hybrid model to determine mechanical properties of soft polymers by nanoindentation. Mech Mater 2010; 42: 1043-47.

[15] Gupta S, Carrillo F, Li C, Pruitt L and Puttlitz C. Adhesive forces significantly affect elastic modulus determination of soft polymeric materials innanoindentation. Mater Lett 2007; 61: 448-51.

[16] Ebenstein Donna M and Pruitt Lisa A. Nanoindentation of biological materials. Nano Today 2006; 1: 26-33.

[17] McDaniel Dennis P, Shaw Gordon A, Elliott John T, Kiran Bhadriraju, Curt Meuse, Koo-Hyun Chung and Plant Anne L. The Stiffness of Collagen Fibrils Influences Vascular Smooth Muscle Cell Phenotype. Biophys J 2007; 92: 1759-69.

[18] Zhu J, Sabharwal T, Kalyanasundaram A, Guo L, Wang G. Topographic mapping and compression elasticity analysis of skinned cardiac muscle fibers in vitro with atomic force microscopy and nanoindentation. J Biomech 2009; 42: 2143-50.

[19] Leong PL and Morgan EF. Measurement of fracture callus material properties via nanoindentation. Acta Biomater 2008; 4: 1569-75.

[20] Oliver WC, and Pharr GM. An Improved Technique for Determining Hardness and Elastic Modulus Using Load and Displacement Sensing Indentation Experiments. J Mater Res 1992; 7: 1564-83.

[21] Rho JY, Pharr GM. Effects of Drying on the Mechanical Properties of Bovine Femur Measured by Nanoindentation. J Mat Sci Mater Med 1999; 10: 1-4.

Synthesis and Characterizations of Poly(lactic acid-co-ethylene glycol) (PLLA/PEG) Block-copolymers

Thai Hien Nguyen[a], Atitsa Petchsuk[b], Pramuan Tangboriboonrat[c], Mantana Opaprakasit[d], , and Pakorn Opaprakasit[a,*]

[a]School of Bio-Chemical Engineering and Technology, Sirindhorn International Institute of Technology (SIIT), Thammasat University, Pathumthani, 12121, Thailand
[b]National Metal and Materials Technology Center, Thailand Science Park, Pathumthani, 12120 Thailand
[c]Department of Chemistry, Mahidol University, Bangkok 10400 Thailand
[d]Department of Materials Science, Chulalongkorn University, Bangkok 10330 Thailand

Abstract. Poly(lactic acid-co-ethylene glycol) (PLLA/PEG) copolymers were synthesized and their properties were characterized. The PLLA/PEG/PLLA triblock copolymers were synthesized by ring-opening polymerization from l-lactide (LLA) and PEG. Stannous octoate, $Sn(Oct)_2$ was used as a catalyst. Effects of molecular weight of PEG (600, 2000 and 4000), LLA/OH molar ratios (95:5, 98:2) and sequence of addition of the reactants on properties of the copolymers were investigated. The triblock copolymers were subsequently used in a production of multiblock copolymers by reacting with chain-extending agents, hexamethylene diisocyanate (HMDI) and maleic anhydride (MA). Effects of chain-extending agent and reaction temperature on chain-linking reaction were studied. Chemical structure and molecular weight of the copolymers were characterized by ^{1}H-NMR, FTIR and GPC. The results showed that molecular weight of triblock copolymers varied from 4,500 to 10,200. After chain extension, multiblock copolymer with molecular weight of 16,490 was produced. Thermal properties of the copolymers were also examined by DSC. The morphology of copolymer was determine by XRD and were examined by comparing with the results from DSC.

1 Introduction

Nowadays, fossil fuel plays an important part in human living. The petroleum-based commodity plastics present everywhere from household utilities to industrial products. Most of these are non-degradable plastics which are considered as the source of environmental pollution. One of the disposing methods of these plastic wastes is landfills. However, this method presents an ugly and unhygienic seen. This littering effect on the rate of rain water percolating, results in lower of the undercurrent water level. The soil fertility deteriorates as the plastic bags form part of manure remains in the soil for years. Futhermore, the rapid increase in the demand of plastic products and the decrease of landfill site causes a formidable amount of plastic wastes. In fact, the recycling method was recommended to overcome environmental issue. This method, however, requires more manual labor, energy and time. This method, in turn, emits some toxic gases in the process. Therefore, biodegradable plastics have been considered as a new method to reduce the impact of plastic waste on the environment.

One of the biodegradable plastics is poly(lactic acid) (PLA). PLA is produced from lactic acid (2-hydroxyl propanoic acid). Lactic acid has an asymmetric carbon atom and two optically active configurations, l- and d- enantiomers. Lactic acid can be produced either by chemical synthesis or by fermentation. The chemical synthesis can procedure a racemic mixture while fermented lactic acids can be optically pure isomer [1]. PLA is considered as a renewable material because its monomer, lactic acid, is produced by fermentation from sucrose or fructose, which can be derived from agricultural product. PLA is biodegradable and biocompatible polymer that is particularly an attractive material for various applications, especially in medical applications. This aliphatic polyester is polymerized by polycondensation or ring-opening polymerization, where the later can yield high molecular weight copolymers [2]. It is a high strength and high modulus thermoplastic. PLA degrade by simple hydrolysis of the ester bond and does not require the presence of enzymes to catalyze hydrolysis. The degradation products of PLA are nontoxic to living organisms since lactic acid itself occurs in the metabolism. PLA and its copolymers have been used for applications like drug delivery system, protein encapsulation and delivery, etc [2]. PLA also finds applications in household products such as degradable rubbish bags, thermoformed trays for fruits and vegetables, disposable

DRAFT

plates and cup, toys, cutlery, fiber and composites, etc. In addition, this polymer is used in agricultural applications such as mulch films, temporary replanting pots, delivery system for fertilizers and pesticides, etc [2]. However, PLA is hydrophobic, which limits its use in certain applications.

On one hand, poly(ethylene glycol) (PEG) is known as hydrophilic polymer with outstanding properties, such as non-toxicity, non-ionic and biocompatible characteristics. Poly(ethylene oxide) (PEO), otherwise known as poly(oxide ethylene) or poly(ethylene glycol) (PEG), is synthesized form ethylene oxide or ethylene glycol. The term PEG refers to polymer chain with molecular weight below 20,000, while PEO refers to the higher molecular weight [3]. PEG is soluble in water, methanol, benzene, dichloromethane and insoluble in diethyl ether and hexane. It can be filtered through kidney when the molar mass is below 30,000[4, 5]. Especially, it lacks in antigenicity and immunogenicity, so it is suitable for drug formulations [5]. PEG is used in various biomedical applications to increase the stability of blood contacting materials [6]. It has been applied in protein pharmaceuticals as stabilizer and emulsifier to prevent aggregation and inactivation of proteins [7]. The high molecular weight PEG-grafted pericardium is used to enhance the biostability and calcium resistance of biomaterials [8]. The highly crosslinked PEG-rich networks can be produced by containing PEG bridges and PEG grafts. So the three-dimensional structure can control delivery of proteins from hydrogels containing PEG [8] and modified with galactose moieties to enhance interactions with liver cells [9]. Moreover, two hydroxyl groups at the end chain of PEG play as functional groups which can be reactive with other functional groups, especially carboxyl group. Therefore, copolymerization of PLA and PEG offers an opportunity to combine the advantages of these polymers.

Many reports in the literature focused on the synthesis and characterizations of PLLA/PEG block copolymers [4-6, 10-14]. However, to our knowledge, these reports lacked of information on the effect of reaction conditions on the structure and properties of copolymer.

In this study, PLA/PEG copolymers are synthesized and their properties are characterized. The triblock PLLA/PEG/PLLA copolymers are synthesized by ring-opening polymerization using tin(II)hexyl ethanoate, $Sn(Oct)_2$, as a catalyst. Effects of molecular weight of PEG, LLA/OH(PEG) molar ratios and a sequence of addition of the reactants on structure and properties of copolymer are investigated. Multiblock copolymers are then synthesized by employing chain extending agents, HMDI and MA. These copolymers were used as a crosslink agent in chemical modification of natural rubber.

2 Experimental

2.1 Materials

L-lactic acid (88wt% in water) was purchased from Carlo Erba. L-lactide (LLA) was synthesized according the method of Zhang et.al [15] and of Sutawan et.al [16]. First, l-lactic acid was distilled to dehydrate at 120°C. Polycondensation was then employed to convert l-lactic acid to its short chain oligomers (8-15 units) at 140°C. These oligomers were then depolymerized to form a cyclic l-lactide (LLA) by heating at 170°C in a presence of $Sn(Oct)_2$ (Wako) as a catalyst. The resulting LLA was recrystallized three times in cool ethyl acetate and was then vacuum dried at 40°C for 24 hours. The purified LLA was stored in a vacuum flask for further use. PEG with molecular weight of 600, 2000, 4000 g/mol were supplied by Fluka. Chain-linking agents, i.e. HMDI and MA, were purchased from Aldrich.

2.2 Synthesis of PLLA/PEG/PLLA triblock copolymers

The synthesized procedure of PLLA/PEG/PLLA triblock copolymers was adopted from the methodology reported by Y.Wan et. al. [11]. Effects of molecular weight of PEG, LLA/OH molar ratios, and a sequence of addition of the reactants on the properties of the resulting copolymers were investigated. PEG with different molecular weights (600, 2000, and 4000) and LLA/OH(PEG) molar ratios of 95:5, 98:2 were employed to vary PEG and PLLA block lengths in copolymer chains. Essentially, a mixture of monomer and 1%w/w catalyst were dried by a vacuum/inert gas technique for 1 hour. The mixture was then melted at 130°C and the polymerization was taken place for 24 hours.

DRAFT

Chloroform and ethanol were used to purify the copolymer products at least two times. Finally, the samples were dried under vacuum at 40°C for 24 hours.

In the study on effects of a sequence of addition of the reactants, PEG 4000 and an LLA:OH molar ratio of 98:2 were employed in the synthesis using similar reaction temperature and time, as described above. Three experiments conditions were employed. First, LLA, PEG and $Sn(Oct)_2$ were added in the flask at the same time (A). In the second experiment, LLA and PEG were melted at 130°C, and $Sn(Oct)_2$ was then added to the mixture (B). In the final experiment, PEG was melted at 80°C, followed by an addition of 1%w/w $Sn(Oct)_2$. After 1 hour, LLA was finally added to the mixture (C).

2.3 Synthesis of multiblock PLLA/PEG copolymers

Multiblock PLLA/PEG copolymers were synthesized by a chain extension reaction of triblock copolymer obtained from a reaction of PEG2000 with an LLA/OH ratio of 98:2. HMDI and MA were used as coupling agents. A 1.0:1.1 molar ratio of triblock copolymer/HMDI (or MA) was employed. Effect of synthesis conditions on properties of the copolymers was investigated by conducting reactions in bulk and by using a solvent.

Reaction in bulk was conducted by drying the triblock copolymer using vacuum/inert gas technique for 1 hour. The reactant was melted at 160°C under vacuum pressure and a coupling agent, i.e., MA (D) or HMDI (E), was added. The reaction was carried out for 1.5 hours. The mixture was then precipitated in ethanol and dried under vacuum at 40°C for 24 hours.

The synthesis procedures of reaction in solvent were similar to the methodology reported by Cohn et. al [12], except that $Sn(Oct)_2$ was used as a catalyst. The triblock copolymer was first dried by vacuum/inert gas technique for 1 hour and dissolved in dried dioxane. HMDI was then added to the mixture. The reaction temperature was kept at 80°C for 3 hours. The product was precipitated in ethanol (F). Additionally, a similar reaction was conducted with an employment of $Sn(Oct)_2$ as a catalyst (G). The sample was finally dried under vacuum at 40°C for 24 hours.

2.4 Characterizations of copolymers

Chemical structure and composition of the triblock copolymers were characterized by ^{1}H-NMR on a Bruker DRX400 using chloroform-d as a solvent. FTIR spectra were recorded on a ThermoNicolet 6700 model spectrometer in a transmission mode. A copolymer film was prepared by casting a 5% solution in chloroform on a KBr pellet. Molecular weights of the copolymers were examined by employing a Waters 150 CV Gel Permeation Chromatography (GPC). THF was used as a solvent, with a flow rate of 1 ml/min. Polystyrene standards were employed to construct a standard curve.

Thermal properties of copolymer were characterized on a Mettler Todedo DSC822^e machine. The samples were scanned from -60°C to 200°C with heating and cooling rates of 20°C/min. Glass transition temperature (T_g), melting temperature (T_m) and heat of melting (ΔH_m) were derived from the second heating thermograms. The decomposition temperatures (T_d) of copolymers were determined on a Mettler Toledo TGA/SDTA 851 instrument, under oxygen atmosphere. The temperature was increased from 50°C to 1000°C with a heating rate of 20°C/min. Differential TGA plots (DTGA) were used in the determination of degradation temperature (T_d) and degradation composition. X-ray diffraction (XRD) traces were obtained on a JEOL JDX-3530 machine, using $CuK_{\alpha 1}$ radiation. The sample films were scanned from a 2θ of 5°-50° in a 0.02 step size, 1 second step size.

3 Results and Discussion

3.1 Synthesis of PLLA/PEG/PLLA triblock copolymers

Triblock PLLA/PEG/PLLA copolymers are synthesized by a ring-opening polymerization of LLA in the presence of PEG and $Sn(Oct)_2$, as presented in **Error! Reference source not found.**. As the catalyst is more effective at high temperature to initiate the OH groups of PEG that take part in the ring opening polymerization [17], a

DRAFT

reaction temperature of 130°C is employed in this study As a result, OH-capped triblock copolymers are produced.

Figure 1

---

^{1}H-NMR spectrum of a triblock copolymer synthesized from PEG2000 with an LLA/OH ratio of 95:5 is shown in **Error! Reference source not found.**, where proton signal assignments are also shown. Signals at 5.2 ppm and 1.5 ppm are assigned to methine protons (b) and methyl protons (c) of LLA segments. The methylene protons (f) of EG repeat units are observed at 3.7 ppm. Signals located in a 4.2-4.4 ppm region are associated with the chain-end units of LLA blocks and ethylene groups of EG linked to LLA units, where the quartet signal (a) represents the methine protons (-CH-OH) of the end chain units, and the triplet signals (d) corresponds to the methylene protons of EG-connected LLA segments (-COO-CH_2-), respectively. The integration of these signals is used to calculate molecular weights and chain composition of the triblock copolymers, as discussed later.

Figure 2

FTIR spectra of PLLA (M_n = 40,000), PEG (M_n = 2,000) and copolymer synthesized from PEG2000 with an LLA/OH ratio of 95:5 are compared in **Error! Reference source not found.**. The presence of band characteristics of both PLLA and PEG are observed in the spectrum of the triblock copolymer, where the characteristic band of LLA segments is observed at 1713 cm^{-1} (C=O stretching) and bands associated with EG segments are located at 2872 cm^{-1} (C-H stretching) and 123xx (C-O-C).

Figure 3

Effects of molecular weights of PEG and LLA/OH molar ratios. Triblock copolymers with wide range of molecular weights and chain composition are obtained by varying PEG size and LLA/OH molar ratios, as summarized in **Error! Reference source not found.**. The results show that LLA/EG ratios in the copolymer chain structure range from 0.31:1 to 3.90:1, which are dependent on the ratios in feed. The effect of PEG size on chain structure and molecular weight of the copolymer is revealed in samples prepared from the 95:5 LLA/OH feeding ratio. With the use of low molecular weight PEG (samples 1 and 2), the molar ratios of LLA/EG in product are significantly higher than those in feed. However, opposite trend is observed when higher molecular weight PEG is employed (samples 4 and 5). This is probably because the bigger sized PEG leads to a reduction in reactivity of OH groups at the end chains, which act as reactive sites in the polymerization of LLA blocks. LLA/EG/LLA block lengths of the copolymer products are summarized in Table 1, and will be used to refer to the copolymers from now on.

Table 1

Effects of sequence of addition of the reactants. Effect of order of adding of reactants on properties of the resulting copolymers is studied to further optimize suitable synthesis conditions. The results, as shown in **Error! Reference source not found.**, indicates that comparable LLA block length are obtained from sample (A) and (B). Sample (C) composts copolymer chains with significantly higher molecular weight than those of the former two counterparts. This is probably because $Sn(Oct)_2$ acts as co-initiator by initiating hydroxyl groups of PEG, which readily reacts with LLA in the latter stage. On the other hand, when $Sn(Oct)_2$ is added into the mixture at the same time with LLA and

DRAFT

PEG (sample (A) and (B)), a competition in polymerization of both LLA and PEG/LLA takes place. This leads to a lowering in the molecular weight of samples (A) and (B).

Table 2

3.1.1 Synthesis of PLLA/PEG multiblock copolymers.

Results on the effects of types of chain linking agent and the reactions conditions con molecular weight of PLLA/PEG multiblock copolymer are summarized in **Error! Reference source not found.**. Molecular weight distributions plot of multiblock copolymers obtained form GPC experiments are also shown in **Error! Reference source not found.**. The results show a decrease in molecular weight of samples obtained from the reactions in bulk (samples 6 and 7), compared to the original 46/46/46 triblock copolymer. The changes in molecular weight distribution are also clearly observed in samples 6 and 7. The unimodal distribution of sample 6 shifts to the right (shorter chain), indicating chain-breaking of the copolymer structures as a result from high reaction temperature. A broader trimodal distribution observed in GPC curve of sample 7 probably indicates that both chain breaking and linking processes take place.

Table 3

Figure 4

It is likely to conclude that HMDI is more effective than MA in chain-linking process of these copolymers. In sample 7, bond breaking due to high reaction temperature (160°C), occurs in the early stage, followed by chain-linking of the resulting fragment by HMDI. However, the less effective MA may not be able to reform longer chains in sample 6. This results in a reduction in overall chain lengths. Unsurprisingly, the results indicate that reaction in solvent with the use of HMDI as a coupling agent is an effective process to increase the copolymer chain lengths, as mild reaction conditions are employed. A slight increase in molecular weight of sample 7 is observed, probably due to chain linking of some low molecular weight fractions, as seen in GPC curve. Interestingly, when $Sn(Oct)_2$ is used as a catalyst in sample 8, a large increase in molecular weight of the resulting copolymer from 10,400 to 16,490 g/mol is observed. An apparent shift in peak maximum of GPC and a disappearance of smaller sized fractions indicate an effectiveness of chain linking reaction on all copolymer chains, reflecting in an increase in average molecular weight of almost twofold.

Thermal properties of PLLA/PEG/PLLA triblock copolymers

Thermal characteristics of PLLA/PEG/PLLA triblock copolymers are examined by DSC and TGA experiments. The results are summarized in **Error! Reference source not found.**. In copolymer with PEG length of 14 units, single T_m is observed as a result from LLA segment. As expected, two T_ms are observed in copolymers with $\overline{DP}_{PEG}$ = 46 and $\overline{DP}_{PEG}$ = 91, because each segregated block are large enough to exhibit two separate crystalline domains. T_m of each component is strongly dependent on its corresponding block length. On the other hand, DSC thermograms of copolymers synthesized from PEG show T_g in the range of -3°C to -7°C, which are higher than that of pure PEG 2000 with T_g = -95°C [18, 19]. T_g of copolymer with $\overline{DP}_{PEG}$ = 91 can not be detected because it is masked by T_m of EG block in the temperature range of 42°-50°C [18]. In addition, it is difficult to determine T_g of LLA block, because T_g of PLLA and T_m of PEG were very close. DSC exhibit the mutual effects of LLA and EG blocks on T_m and T_g, such as T_g of copolymers is ranging from -7 to -3°C while T_g of PEG 2000 is -95°C [18]. An addition

DRAFT

of EG block results in a decrease in T_m of PLLA blocks (118-156°C), compared with the T_m of commercial PLLA (145-186°C) [20]. This indicates strong interaction of PEG segments with PLA segments.

TGA was used to determine decomposition temperature T_d related to change in weight of PLLA/PEG/PLLA triblock copolymers. There were two main decompositions, in there; LA chain was degraded first with T_d of PLLA blocks were observed between 270°C and 310°C, whereas T_d of PEG blocks were between 390°C and 415°C. T_d of PEG blocks increased gradually with $\overline{DP}_{PEG}$: 390°C for PEG_{14}, 410°C for PEG_{46} and 415°C for PEG_{91}. In contrast, T_d of PLLA blocks decreased when their degree of polymerization increased, as showed in **Error! Reference source not found.**. In the effect of PEG blocks, T_d of PLLA blocks (288-310°C) are quite higher than T_d of commercial PLLA (235-255°C) [20]

Thermal characteristics of PEG/PLLA multiblock copolymers. T_g and T_m of sample (G) was examined and compared with the original material, $PLLA_{46}/PEG_{46}/PLLA_{46}$ triblock copolymer. The result in **Error! Reference source not found.** showed that T_m and T_g did not change after chain linking reaction. However, ΔH_m of multibock copolymer slightly changed. For example, ΔH_m PLLA block increased to 41.12 J/g in the case of multiblock copolymer, in contrast to 40.32 J/g in the case of triblock copolymer. The increase of ΔH_m of PLLA block leaded to the higher of T_m of PLLA block, this implied that the chain of multiblock copolymer was longer due to the reaction between the original copolymers. HMDI was success in linking two PLLA blocks together to make a multiblock copolymer with longer PLLA block

Morphological Characterization by X-ray diffraction. The morphology of PEG2000 (PEG_{16}), PLLA40000 ($PLLA_{555}$) and triblock copolymers were determined by X-ray diffraction, as shown in **Error! Reference source not found.**. PEG_{46} exhibited two main diffraction peaks located at 9.6 and 11.6° whereas two main peaks of $PLLA_{555}$ were observed at 8.3 and 9.4°. PEG blocks were not always able to crystalline in copolymers. The presence of PLLA blocks in copolymer decreased the crystallizability of PEG block. This was shown through the absence of two main diffraction peaks of PEG in diffractogram ($PLLA_{27}/PEG_{14}/PLLA_{27}$). Even though $\overline{DP}_{PEG}$ was equal $\overline{DP}_{PLLA}$, the crystallizability of PLLA block still remained on advantages than that of PEG block ($PLLA_{28}/PEG_{46}/PLLA_{28}$, $PLLA_{43}/PEG_{91}/PLLA_{43}$). Only when $\overline{DP}_{PEG}$ was significant higher than $\overline{DP}_{PLLA}$, the diffraction peaks of PEG block could be observed ($PLLA_{14}/PEG_{91}/PLLA_{14}$).

The volume fraction crystallinity ϕ of each block was summarized in **Error! Reference source not found.**, based on the interpolation of XRD data. Assumed that the volumer fration crystallinity equaled with the mass fraction crystallinity ψ. The XRD data is in good agreement with DCS data, as shown in **Error! Reference source not found.**. In the case of PEG_{91}, the longer LLA blocks were, the lower the crystallinity of EG blocks were. Similar to the effect of EG blocks onto the crystallinity of LLA blocks, the longer EG blocks were, the lower the crystallinity of LLA blocks were. This can be observed in the case of $PLLA_{27}$ vs. $PLLA_{28}$ and $PLLA_{43}$ vs. $PLLA_{46}$. That is understandable because the attachment of one block reduce the chain mobility of another block. That makes the crystallinity of each block decrease when compare with that of pure PLLA or PEG.

4 Conclusions

PLLA/PEG/PLLA triblock copolymers are synthesized at 130°C by ring-opening polymerization of lactide, PEG as a macroinitiator and $Sn(Oct)_2$ as a catalyst. Block lengths and chemical structures of the copolymers are characterized by ^{1}H-NMR and FTIR. It was found that the degree of polymerization of LLA block decreased (27, 28 and 14) when the degree of polymerization of EG block increased (14, 46 and 91). The results also indicated that a 98:2 of LLA/OH molar ratio is suitable ratio for synthesizing high molecular weight copolymers. HMDI was used as a chain-extender to produce higher molecular weights multiblock copolymers.

5 Acknowledgements

Financial support of this work is provided by The Thailand Research Fund (TRF), The Commission on Higher Education (CHE), RTA5180003 and Thailand Toray Science

DRAFT

Foundation. Thai Hien Nguyen is supported by a scholarship program from SCG Foundation and SIIT, Thammasat University.

[1] N. Narayanan, P.K. Roychoudhury, A. Srivastava, L (+)lactic acid fermentation and its product polymerization, Electron. J. Biotechnol. 7(2) (2004) 167-U162.

[2] A.P. Gupta, V. Kumar, New emerging trends in synthetic biodegradable polymers - Polylactide: A critique, Eur. Polym. J. 43(10) (2007) 4053-4074.

[3] N.A. Peppas, K.B. Keys, M. Torres-Lugo, A.M. Lowman, Poly(ethylene glycol)-containing hydrogels in drug delivery, Journal of Controlled Release 62(1-2) (1999) 81-87.

[4] L. Yang, Z. Zhao, J. Wei, A. El Ghzaoui, S. Li, Micelles formed by self-assembling of polylactide/poly(ethylene glycol) block copolymers in aqueous solutions, J. Colloid Interface Sci. 314(2) (2007) 470-477.

[5] I. Rashkov, N. Manolova, S.M. Li, J.L. Espartero, M. Vert, Synthesis, Characterization, and Hydrolytic Degradation of PLA/PEO/PLA Triblock Copolymers with Short Poly(l-lactic acid) Chains, Macromolecules 29(1) (1996) 50-56.

[6] S.K. Agrawal, N. Sanabria-DeLong, J.M. Coburn, G.N. Tew, S.R. Bhatia, Novel drug release profiles from micellar solutions of PLA-PEO-PLA triblock copolymers, Journal of Controlled Release 112(1) (2006) 64-71.

[7] I.J. Castellanos, R. Crespo, K. Griebenow, Poly(ethylene glycol) as stabilizer and emulsifying agent: a novel stabilization approach preventing aggregation and inactivation of proteins upon encapsulation in bioerodible polyester microspheres, Journal of Controlled Release 88(1) (2003) 135-145.

[8] S.C. Vasudev, T. Chandy, Polyethylene glycol-grafted bovine pericardium: a novel hybrid tissue resistant to calcification, Journal of Materials Science: Materials in Medicine 10(2) (1999) 121-128.

[9] S.T. Lopina, G. Wu, E.W. Merrill, L. Griffith-Cima, Hepatocyte culture on carbohydrate-modified star polyethylene oxide hydrogels, Biomaterials 17(6) (1996) 559-569.

[10] S. Popelka, L.k. Machová, F. Rypácek, Adsorption of poly(ethylene oxide)-block-polylactide copolymers on polylactide as studied by ATR-FTIR spectroscopy, J. Colloid Interface Sci. 308(2) (2007) 291-299.

[11] Y. Wan, W. Chen, J. Yang, J. Bei, S. Wang, Biodegradable poly(-lactide)-poly(ethylene glycol) multiblock copolymer: synthesis and evaluation of cell affinity, Biomaterials 24(13) (2003) 2195-2203.

[12] D. Cohn, A. Hotovely-Salomon, Biodegradable multiblock PEO/PLA thermoplastic elastomers: molecular design and properties, Polymer 46(7) (2005) 2068-2075.

[13] M. Yuan, D. Liu, C. Xiong, X. Deng, Polymerization of lactides and lactones 6. Synthesis of poly-lactide and polyethylene glycol-co-poly-lactide copolymer with allylmagnesium chloride, Eur. Polym. J. 35(12) (1999) 2139-2145.

[14] S.M. Li, I. Rashkov, J.L. Espartero, N. Manolova, M. Vert, Synthesis, Characterization, and Hydrolytic Degradation of PLA/PEO/PLA Triblock Copolymers with Long Poly(l-lactic acid) Blocks, Macromolecules 29(1) (1996) 57-62.

[15] H.-p. Zhang, J.-m. Ruan, Z.-c. Zhou, Y.-j. Li, Preparation of monomer of degradable biomaterial poly(L-lactide), Journal of Central South University of Technology 12(3) (2005) 246-250.

[16] Sutawan Buchatip, Atitsa Petchsuk, K. Kongsuwan, Synthesis and Mechanical Properties of Poly (LLA-co-DLLA) Copolymers, Journal of Metals, Materials and Minerals 18 (2009) 175-180.

[17] H.R. Kricheldorf, I. Kreiser-Saunders, A. Stricker, Polylactones 48. SnOct2-Initiated Polymerizations of Lactide: A Mechanistic Study, Macromolecules 33(3) (2000) 702-709.

[18] H.R. Kricheldorf, S. Rost, C. Wutz, A. Domb, Stereocomplexes of Aâ^'Bâ^'A Triblock Copolymers Based on Poly(l-Lactide) and Poly(d-Lactide) A Blocks, Macromolecules 38(16) (2005) 7018-7025.

[19] R. Mladenova, T. Petrova, N. Manolova, M. Ignatova, I. Rashkov, P. Kubisa, Preparation, Characterization, and Biological Activity of Amides and Esters from 8-Hydroxyquinoline-2-Carboxylic Acid and Jeffamines ED(R) Or Poly(Ethylene Glycol)S, Journal of Bioactive and Compatible Polymers 16(4) (2001) 259-276.

[20] J.E. Mark, Polymer Data Handbook, Oxford University Press, 1999.

Enhancement of Mechanical Properties of Poly(L-lactide-*co*-D,L-lactide) Copolymers by Physical Crosslinks Derived from Configuration Interlocks

Pakorn Opaprakasit[d,*] Atitsa Petchsuk[a,*], Sutawan Buchatip[a], Mantana Opaprakasit[b], Pramuan Tangboriboonrat[c]

[a]National Metal and Materials Technology Center, Pathum Thani, 12120 Thailand

[d]Department of Materials Science, Chulalongkorn University, Bangkok 10330 Thailand

[c]Department of Chemistry, Mahidol University, Bangkok 10400 Thailand

[d]School of Bio-Chemical Engineering and Technology, Sirindhorn International Institute of Technology (SIIT), Thammasat University, Pathum Thani, 12121, Thailand

ABSTRACT— Copolymerization of enantiomeric lactides has been extensively investigated as a useful route to modify the chemical structure of PLA in order to achieve desirable properties. Various compositions of high molecular weight poly(L-lactide-co-D,L-lactide), P(LLA-co-DLLA), copolymers were successfully synthesized by ring-opening polymerization (ROP) of L-lactide (LLA) and D,L-lactide (rac-lactide, DLLA) using stannous (II) ethylhexanoate [$Sn(Oct_2)$] as a catalyst. Properties of the copolymers were investigated through thermal analysis and tensile testing. The copolymers exhibited lower glass transition temperature (T_g), melting temperature (T_m) and % crystallinity than those of PLLA homopolymer. T_g and T_m of the copolymers decreased as DLLA content increased. An enhancement in mechanical properties of the copolymers was observed, with the degree of improvement dependent on the DLLA contents. Results on Young's modulus and tensile strength showed that optimum properties were obtained when 7.5% DLLA was employed, and tended to decrease as rac-lactide composition increased. Interestingly, copolymer synthesized from 50% DLLA showed remarkable improvement in modulus, strength and elongation at break. The origin of this properties enhancement was studied by polarized FTIR spectroscopy. The result showed vibrational mode originated from a formation of point interaction between DL and LL diads of copolymer chains, which acts as a "physical crosslink" in the amorphous phase of the copolymers.

Keyword:

*Corresponding author

Introduction

Polylactide or polylactic acid (PLA) has been extensively researched and widely used in various applications, due mainly to its degradability and biocompatibility. This polymer is producible from renewable resources, very low or nontoxic in natural environments. In addition, PLA has good mechanical properties comparable to those of commodity thermoplastics. However, its rigidity and brittleness has limited its use in certain applications [1-3]. As a result, various PLA-based copolymers and blend systems have been developed to improve the materials mechanical properties [1, 4-9].

PLA is commonly synthesized by the ring-opening polymerization of lactide, its cyclic dimer derived from 2 units of lactic acid [10, 11]. Since lactic acid contains a chiral carbon, lactide occurs in three enantiomeric forms: D-lactide (DLA), L-lactide (LLA), and meso-lactide. Consequently, PLA may be synthesized in the forms of poly(L-lactide) (PLLA) or poly(D-lactide) (PDLA), which mainly consists of S or R lactate repeat units, respectively. In addition, syndiotactic polylactide may be produced when meso-lactide is employed.

It is well known that an enantiomeric mixture of PLLA and PDLA forms a stereocomplex, i.e. a stronger crystal structure that exhibits higher T_m compared to those of its single component counterparts, as a result from a formation of C-H···O=C hydrogen bonding[12-15]. Mechanical properties of the stereocomplex are also superior to those of the PLLA or PDLA single component counterparts [1, 5, 6]. This stereocomplexation is therefore used to further improve the versatile characteristics of polylactide, and to widen the materials applications[1]. In recent years, however, the applications of PLA stereocomplex have been limited because of an unavailability of PDLA in an industrial scale.

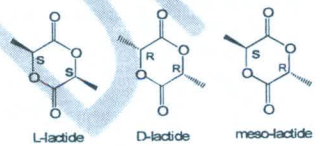


Figure 1. Structures of different stereoforms of lactide.

Copolymerization is an alternative method to modify properties of polymers for specific applications [8, 16, 17]. Polymerization of lactides with different stereoisomerism results in a formation of materials with different properties. For example, a racemic mixture of 1:1 LLA/DLA (DLLA) is used to synthesize PDLLA copolymers, which are amorphous materials. In addition, the composition of DL-lactate groups in the PDLLA copolymers can

DRAFT

be varied by using a mixture of racemic DL-lactide/L-Lactide at various compositions in order to optimize the copolymers crystalline content and hence thermal and mechanical properties [8, 16-18].

In this work, copolymers of DLLA and LLA with various DL-lactate contents are systematically synthesized by the ring-opening polymerization [19-21]. This copolymers is referred to as P(DLLA-*co*-LLA)$_x$ copolymers, where x indicates molar composition of DL-lactate groups. Intriguingly, characterization results on the synthesized copolymers reveal a drastic enhancement in mechanical properties of the copolymers consisting of certain DL-lactide compositions, especially those containing DLLA content lower than 7.5%, and the copolymer consisting of DLLA content of 50%. Insight into the origin of the mechanical properties enhancement in terms of structural conformations and interactions are investigated.

Urayama and Kimura analyzed microstructure of PDLLA copolymers in amorphous phase and found that an increase in length of L-lactate sequence resulted in an increase in helical nature, causing an increase in Tg value but a decrease in density. FTIR results indicated that band intensity of C=O stretching mode is independent on conformational change of the copolymers. Information on conformation of the chain structure can be monitored by employing the 1265 and 1210 cm^{-1} modes, corresponding to (δ_{CH}+υ_{COO}) and ($\upsilon_{as\,COC}$ + $r_{as\,CH3}$).[8]

Experimental

Materials

A racemic mixture of DL-lactide and Tin octoate [Sn(Oct$_2$)] was purchased from Wako Co., Ltd. L-lactide was synthesized in this laboratory by depolymerization of low molecular weight poly(lactic acid) using antimony (III) oxide catalyst (Sb_2O_3).

Synthesis of P(DLLA-co-LLA)$_x$ copolymers

P(DLLA-*co*-LLA)$_x$ copolymers were synthesized via a ring-opening polymerization of DLLA and LLA using 0.075 % wt. Sn(Oct$_2$) as a catalyst. The reactions were conducted at 120°C for 5 hours. Molar composition of DLLA in feed was varied from 0, 2.5, 5, 7.5, 10, 20, 30, 50 and 100%. The resulting copolymers were purified by dissolving in chloroform and precipitating in methanol.

Molecular Weight and Structural Characterizations

The average molecular weight and molecular weight distributions ($\bar{M}_n$, $\bar{M}_w$ and polydispersity) of the copolymers were measured using a Waters 150-CV gel permeation chromatography (GPC), comparative to mono-disperse polystyrene standard. Thermal properties of the copolymers were recorded on a DSC822^e Mettler Toledo DSC. The sample was scanned twice from -20 to 200°C with heating and cooling rates of 10.0 °C/min. Results on T_m and T_g were determined from the second scan thermograms. Structural information of copolymers was examined on an AVENCE 300 MHz Digital NMR spectrometer (Bruker Biospin; DPX-300). ^{13}C NMR spectra were recorded at a frequency of 75 MH$_z$. Tensile tests were carried out on an Instron tensile testing machine with a crosshead speed of 50 mm/min, using rectangular specimens with 50 mm gauge length and 15 mm width, according to ASTM D882. Copolymer films were prepared by casting from polymer solutions in chloroform. The resulting polymer film's thickness is roughly 10-60 μm. The specimens were pulled in tension until rupture. The values of modulus, tensile strength, and elongation at break were recorded, and the average value from 3-4 specimens was reported.

Density of the copolymers was measured by employing gas displacement technique on an Ultrapycnometer 1000, Quantachrome. Helium gas was employed in the measurements conducted at 23.3 ± 0.1°C. All samples were dried at 80°C overnight in a vacuum oven before measurements. The reported density values were averaged from 5 measurements.

XRD traces of the film samples were recorded on a JEOL JDX-3530 Diffractometer, using Cu$K_{\alpha 1}$ radiation. The sample films were scanned from 2θ of 5°- 40° at a 0.02 step size. FTIR spectra of the copolymer samples were recorded in transmission mode on a Fourier Transform Infrared Spectrophotometer (a NICOLET 6700 FT-IR) at a resolution of 2 cm^{-1} by coadding of 64 scans. Typical and polarized FTIR spectra were recorded.

Results and Discussion

Microstructure and Physical Properties

Microstructure of the synthesized P(DLLA-*co*-LLA)$_x$ copolymers is investigated by ^{13}C NMR spectroscopy employing resonances due to carbonyl carbons, where three signals are observed in the 169 ppm region. These signals correspond to various triad sequences in the copolymer chain, where the resonance at 169.6 ppm was assigned to the isotactic sequence of carbonyls of homo-sequence (mm triad). The signals at 169.3 and 169.1 ppm was tentatively assigned to heterotactic sequence (mr triad), and syndiotactic sequence (rr

DRAFT

triad), respectively.[8, 22-24] The percentage of these triads calculated from signals integration is summarized in Table 1. The calculated percentage of isotactic and syndiotactic sequences are comparable to those obtained from theoretical calculation employing the Bernoullian addition mechanisms[8], reflecting a success in the systematic synthesis of these random copolymers. Nevertheless, slight deviations of the values from the theory may perhaps due to racemization or intermolecular transesterification during the synthesis [8, 24]. In addition, results on molecular weight and molecular weight distribution of the P(DLLA-*co*-LLA)$_x$ copolymers are also summarized in Table 1. It is clearly seen that all copolymers have comparable molecular weight in the range of 5.8×10^4 to 11.8×10^4 g/mol, with polydispersity (PD) values ranging from 1.7-3.5. This enables a systematic comparison of copolymers properties by neglecting the effect of the copolymer molecular weight [25].

Table 1. Results on properties characterizations of P(DLLA-*co*-LLA)$_x$ copolymers.

Samples	DLLA in feed (mol %)	Chain Microstructure[1]			$\bar{M}_n$	PD	T_g (°C)	T_m (°C)	Average Density (g/cm^3)	Crystallinity[2] (%)
		% mm, $\delta_{169.0}$	% mr, $\delta_{169.3}$	% rr, $\delta_{169.1}$						
PLLA	0	99.6	0.0	0.4	91,370	1.79	68.3	169.9	1.542±0.007	48.1
P(DLLA-*co*-LLA)$_{2.5}$	2.5	92.4	6.2	1.4	83,340	3.58	59.2	159.7	1.454±0.007	30.4
P(DLLA-*co*-LLA)$_5$	5	88.6	9.2	2.2	67,870	1.99	57.4	154.2	1.304±0.005	29.7
P(DLLA-*co*-LLA)$_{7.5}$	7.5	85.9	10.6	3.5	118,250	2.68	55.9	147.6	1.537±0.007	0.7
P(DLLA-*co*-LLA)$_{10}$	10	85.8	11.1	3.1	81,140	1.98	54.0	143.7	1.530±0.007	1.7
P(DLLA-*co*-LLA)$_{20}$	20	69.1	22.9	8.0	82,660	1.85	55.5	-	1.337±0.009	-
P(DLLA-*co*-LLA)$_{30}$	30	61.6	29.2	9.2	60,660	1.99	53.4	-	1.267±0.007	-
P(DLLA-*co*-LLA)$_{50}$	50	46.1	40.6	13.3	80,880	2.23	51.1	-	1.204±0.008	-
P(DLLA-*co*-LLA)$_{100}$	100	27.9	54.2	17.9	58,920	1.79	45.3	-	1.263±0.008	-

[1] calculated from ^{13}C NMR spectra,

[2] crystallinity (%) = $\frac{\Delta H_m - \Delta H_c}{\Delta H_f^\circ} \times 100$, where $\Delta H_f^\circ = 96$ J/g [26]

Density results of the copolymers, as also summarized in table 1, show a decrease in the density values when the DLLA content of the copolymer increases from 0-5 %. However, when the DLLA content reaches 7.5%, a sudden increase in the value to 1.537±0.007 g/cm^3 is observed. Upon further increasing the DLLA content in the copolymer chain, a decreasing trend of the density values is re-observed. The former decreasing trend is probably originated from a decrease in the crystalline content of the copolymers, calculated from DSC thermograms as also summarized in Table 1. However, a sudden increase in the value and the latter decreasing trend observed in the complete amorphous copolymers series with DLLA content of higher than 7.5% is intriguing. This is probably associated with formation of different chain arrangement, which will be explained later.

Thermal properties of the copolymers derived from the second-heating cycle DSC thermograms are also summarized in Table 1. The results show that PLLA exhibits a glass transition temperature (T_g) at 68°C. As DLLA is incorporated into the copolymer chains, the T_g of the copolymers decreases with an increase in DLLA content, i.e., an increase in T_g from 59.2 to 45.3°C is observed for copolymers derived from DLLA contents of 2.5 to 100 mol%. Melting characteristic peak is only observed in thermograms of PLLA homopolymer and copolymers containing DLLA contents of less than 10 mol%, reflecting the maximum DLLA content to produce semi-crystalline copolymers. The melting temperature (T_m) of the copolymers also decreases as DLLA content increases in the copolymer chains, due to shorter sequences of LLA in the copolymer chains.

Similar trend is also observed on crystallinity of the corresponding copolymers consisting of low DLLA contents, where crystallinity decreases from 48.1% to 1.7% for PLLA and P(DLLA-*co*-LLA)$_{10}$, respectively. On the other hand, copolymers consisting of DLLA content higher than 10 mol% exhibit amorphous characteristic. This indicates that the incorporated DLLA units act as defects in LLA segments, resulting in an interruption of crystal formation that leads to reduction of T_g and T_m values, as well as crystallinity of the copolymers.

Mechanical properties

Tensile properties of P(DLLA-*co*-LLA)$_x$ copolymers as a function of DLLA contents are summarized in Figure 1. The results on modulus, tensile strength and elongation at break of PLLA and P(DLLA-*co*-LLA)$_{100}$ observed in this study are comparable to those reported earlier [1, 5, 17]. Figure 1 clearly shows that the characteristic trends of tensile strength and modulus of the copolymers as a function of DLLA content are almost identical. An enhancement of these two properties is achieved by introducing DLLA comonomer into PLLA chains at DLLA contents of up to 7.5%. This mechanical property enhancement is intriguing, given that the introduction of DLLA units causes a reduction in crystallinity, T_g,

DRAFT

and T_m of the copolymers, as previously discussed. This is coincided with the sudden increase in density of the P(DLLA-*co*-LLA)$_{7.5}$ copolymer, which may also associated with the same origin. However, further increase in the DLLA content results in a drastic drop in the copolymers strength and modulus. This is in concert with the amorphous nature of the copolymers, as discussed earlier. The drop in the properties is mainly due to a destruction of crystalline domains in the copolymer matrix. Interestingly, an unusual increase in tensile strength and modulus was re-observed in copolymer containing DLLA content of 50%, i.e. P(DLLA-*co*-LLA)$_{50}$, which are much higher than those of PLLA and P(DLLA-*co*-LLA)$_{100}$ counterparts.

Figure 1. Young's modulus, Tensile strength and Elongation at break of PLLA and P(LLA-*co*-DLLA)$_x$ copolymers as a function of DLLA composition. The dotted line indicates those of PLLA/PDLA stereocomplex [5].

In addition, Figure 1 also shows data on elongation at break of the copolymers as a function of DLLA content. The results indicate that the elongation is independent on the DLLA composition, when the content is kept lower than 20%. A drastic increase in the value is observed upon increasing the DLLA content from 30% to 50%, where the maximum elongation of 150% is achieved. The corresponding value of P(DLLA-co-LLA)$_{100}$, however, decreases to 40%. Given the mechanical properties of PDLA/PLLA stereocomplex reported by Tsuji et al.[5] (See Figure 1), it is clearly seen that the stereocomplex showed higher strength and modulus, compared to PLLA and PDLA homopolymers, and P(DLLA-*co*-LLA)$_{100}$. However, these are still inferior to those of the P(DLLA-*co*-LLA)$_{7.5}$. In addition, it is obvious that mechanical properties of these copolymers are strongly dependent on the monomer compositions. As a result, these materials are suitable candidates for producing degradable polyesters with tunable mechanical properties.

Effects of structure and interactions on mechanical properties

To obtain an insight into the origin of the enhancement in mechanical properties of P(DLLA-*co*-LLA)$_x$, XRD and FTIR spectroscopy are employed to study the nature of chain structures and interactions. XRD spectra of PLLA, PDLA/PLLA stereocomplex and the copolymers are compared in Figure 2. The spectrum of PLLA shows crystal characteristics signal at 2θ = 14.6°, 16.6°, 18.9°, which is corresponding to 110, 110α/220α, 203α planes in its 10_3 helical conformation[27]. The corresponding spectrum of PDLA/PLLA stereocomplex shows signals located at 2θ = 11.9°, 20.8° and 24°, which reflects 110, 300, and 220 planes in the 3_1 helical conformation of stereocomplex crystalline domains[27].

Figure 2. XRD traces of PLLA (a), PDLA/PLLA stereocomplex (b), P(LLA-*co*-DLLA)$_{2.5}$ (c), P(LLA-*co*-DLLA)$_{7.5}$ (d), P(LLA-*co*-DLLA)$_{50}$ (e) , and P(LLA-*co*-DLLA)$_{100}$ (f).

The corresponding spectra of P(LLA-*co*-DLLA)$_x$ copolymers show a broad pattern covering 2θ angle of 10° to 25°, reflecting the amorphous characteristics of the samples. Weak crystalline patterns are observed only in P(LLA-*co*-DLLA)$_{2.5}$, which is similar to those found in neat PLLA. This finding slightly differs from those obtained from DSC experiments, where crystalline melting peaks are observed in copolymers consisting of DLLA content of up to 10%. This is probably because the crystalline domains present in P(LLA-*co*-DLLA)$_{7.5}$and P(LLA-*co*-DLLA)$_{10}$ consists of shorter LLA sequence than the detectable limit of XRD experiments. Nevertheless, DSC thermograms of the particular copolymers show weak T_m peaks located at much lower temperature and lower ΔH_m, compared to those of neat PLLA. Interestingly, weak but sharp signals located at 2θ = 9.4°, 28.7°, and 44.4°, corresponding to d-spacing of 9.4, 3.1 and 2.0 Å, respectively, are observed in all copolymer samples. The signals are not observed in the spectra of homopolymers and the stereocomplex blend. This indicates a presence of order structures with respective d-spacings in the copolymers, which is probably an origin of the mechanical property enhancement in certain P(LLA-*co*-DLLA)$_x$ copolymers.

FTIR spectroscopy is employed to study chain structures and interactions of the copolymers. Given that polylactides and PLLA/PDLA blend can form various types of crystal structures, i.e., α, α', γ and β, this can be characterized by FTIR spectroscopy by employing vibrational modes of carbonyl, C-C backbone, C_α-H, and –CH_3 groups, as these are sensitive to chain structures and conformations [12, 13, 28, 29]. In neat PLLA or PDLA, the chains are in a 10_3 helical conformation, and dipole-dipole interaction is formed. The band characteristic of this crystal structure is observed at 921 cm^{-1} (coupling of C-C stretching with the -CH_3 rocking mode). On the other hand, a stronger C=O···H-C hydrogen bonds formed in the crystal structure of the stereocomplex blend, where the polymer chains are in a 3_1 helical conformation. This is reflected by a characteristic band located at 909 cm^{-1} [12, 13, 28-30].

DRAFT

FTIR spectra in the 1000-900 cm^{-1} region of P(LLA-*co*-DLLA)$_x$ copolymers as a function of DLLA content are shown in Figure 3, where those of PLLA and stereocomplex are also compared. The spectra of PLLA homopolymer and P(LLA-*co*-DLLA)$_x$ copolymers with DLLA contents of up to 10% exhibit a characteristic band of single crystallite at 924 cm^{-1}. A unique band characteristic of stereocomplex located at 909 cm^{-1} is not observed in all copolymers, reflecting that a formation of such structure is unlikely in these copolymers at all compositions. Intriguingly, a higher frequency band is observed at 935 cm^{-1} in copolymer samples containing DLLA contents of up to 7.5%, and at 50%. The appearance of this band in the spectra of these particular samples, which show relatively higher modulus, strength, and elongation, indicates that this vibrational mode is probably derived from structural conformations that are responsible for the improved properties, especially in P(LLA-*co*-DLLA)$_{50}$, which is an amorphous sample. Given the correlation of band position and helical structure of 10_3 and 3_1 of the homocrystalite and stereocomplex, located at 920 and 909 cm^{-1}, respectively, the new band observed here (at higher frequency) probably indicates lower strain in the helical structure.

Figure 3. FTIR spectra in the 1000-900 cm^{-1} region of PDLA/PLLA stereocomplex (a), PLLA (b), and P(LLA-co-DLLA)$_x$ copolymers with DLLA content of: 2.5% (c) , 7.5% (d), 10% (e), 30% (f) , 50% (g) , and 100 % (h).

Directional behavior of the vibrational modes in the 1000-900 cm^{-1} region is studied by examining parallel and perpendicular spectra of the copolymers, as shown in Figure 4 (lower and top spectrum, respectively). The spectra of semi-crystalline PLLA and P(LLA-co-DLLA)$_{7.5}$ show that the intensity of the 924 cm^{-1} band (due to the 10_3 helical conformations) is dependent on the measurement directions, as this is originated from anisotropic arrangement of the single crystalline domains. The 935 cm^{-1} band observed in the copolymers, however, is directional independent, as evidenced from the spectrum of P(LLA-co-DLLA)$_{50}$. This indicates that conformational structures that are origins of this vibrational mode are randomly aligned in the amorphous matrix.

Figure 4. Polarized FTIR spectra in the 1000-900 cm^{-1} region of PLLA (a), P(LLA-co-DLLA)$_{7.5}$ (b), P(LLA-co-DLLA)$_{50}$ (c) , and P(LLA-co-DLLA)$_{100}$ (d). (Top : perpendicular, lower : parallel spectrum)

Information on interactions in polylactides structure can also be derived from band position of the C-H stretching modes located in the 3000 cm^{-1} region, where three groups of band are assigned orderly from high to low frequency as $\nu(C_\alpha H)$, $\nu_s(CH_3)$, $\nu_{as}(CH_3)$, respectively. It was reported that a red shift of the three bands to lower frequency indicated formation of strong C=O··H-C hydrogen bonding in stereocomplex [30]. FTIR spectra of the P(LLA-co-DLLA)$_x$ copolymers in the C-H stretching region are shown in Figure 5. It is clearly seen that the 3 vibrational modes of the copolymers are located in the middle of that of the two extreme of PLLA and stereocomplex and dependent on copolymer compositon, which probably indicate of formation of interation

-CH_3 vibrational mode of PLLA and stereocomplex is located at 2994 and 2998 cm^{-1}, respectively. The corresponding band of the copolymers is located in between the two extremes at 2996 cm^{-1}. The relatively higher frequency of the band, compared to those of the coupled C-C backbone vibrational mode in the structures of homocrystalite and stereocomplex, indicates weaker interactions associated with the corresponding -CH_3 and C=O functional groups.

Figure 5. FTIR spectra in the –CH_3 stretching mode region of PDLA/PLLA stereocomplex (a), PLLA (b), and P(LLA-co-DLLA)$_x$ copolymers with DLLA content of: 2.5% (c) , 7.5% (d), 10% (e), 30% (f) , 50% (g) , and 100 % (h).

Interestingly, a new band centered ~3030 cm^{-1} is clearly observed in FTIR spectra of all P(LLA-*co*-DLLA)$_x$ copolymers. This unusual band is not found in those of PLLA and PDLA/PLLA stereocomplex. A close examination on the vibrational mode indicates an increase in band intensity as a function of DLLA content for copolymers with low DLLA compositions, where the most intense band is observed in P(LLA-*co*-DLLA)$_{30}$. When the DLLA content is further increased, however, the band inversely shifts to lower frequency. The presence of this band is similar to that observed in crystallization of PHBV reported by Hu et. al.[31], which were assigned to a formation of C-H OC hydrogen bonding[32]. As the

DRAFT

repeat unit of PHBV contain longer repeat unit, compared to that of PLA, and its CH3 groups is located at beta postion, it is likely that this is derived from the higher flexibility of the -CH_3 groups in the repeat units, which enables more freedom for placement of the groups in structural arrangement. In the case of copolymer it is lock conofrtmation. The formation of this band at 3030 indicate even strong interaction between the CH3 and C=O groups.

Important structural information can also be obtained from the C-O-C band located in the 1330-1290 cm^{-1} region, as shown in Figure 6 [xxx]. The spectra show that the vibrational mode is sensitive to structural conformation, where those of PLLA single crystallite show split bands located at 1304 and 1295 cm^{-1}, which is probably due to crystalline splitting. The corresponding spectrum of stereocomplex also show bands spitting, but located at higher frequency at 1307 and 1300 cm^{-1}, indicating higher strain in the helical structure. The spectrum of ...similar to those observed in methylene bridge of phenolic resin where linear and helix structure are dependent on the band location.

As relatively thick films were used in this study, quantitative information cannot be obtained from the carbonyl stretching band. However, the overtone bands of these vibrational modes can be employed. [11] Similar results to those obtained from the C-C backbone characteristics were observed. Spectrum of PLLA homopolymer shows overtone band due to single crystallite at 3508 cm^{-1}, while that of stereocomplex exibhits a band at lower frequeny at 3485 cm^{-1}, indicating stronger interaction involving C=O functional groups. The corresponding sprecta of copolymers show a broad band located at 3508cm^{-1} and a showlder at 3560 cm^{-1}. This is a mode that corresponding to probably free C=O, due to its lower interaction in the structure, probably associated with those present in the amorphous region. The spectrum of PDLLA7.5 show very sharp band at 3500 cm^{-1} and the shoulder, perhaps due to an enhancement in the arragment.

This is probably derived from a formation of segmental interactions between the -CH_3 and C=O groups of DL and LL diads in the chain structure of copolymer in the amorphous domain. The similarity of the band intensity and pattern observed in the polarized spectra reflects that these point interactions are isotropic in nature. The randomly-distributed point interactions, perhaps, act as "physical crosslink" in the amorphous domain, which collectively results in an improvement of the copolymers bulk properties. The results also indicate that the formation of such structures is strongly dependent on the DLLA content of the copolymer, where optimum value was observed at 50%. In addition, the isotropic placement of the "physical crosslinks" also improves elastic behavior of amorphous copolymers, which is reflected in superior elongation at break of the P(LLA-co-DLLA) 50, as proposed in Figure 8. A formation of such network-like structure was also observed by He et.al. in their study on effect of initial melt states of PDLA/PLLA stereocomplex on its crystallization behaviors. It was found that when PDLA/PLLA stereocomplex was melt at high temperature or longer melting time, the subsequent stereocomplex crystallization of the sample was depressed. This was because the strong $CH_3 \cdot\cdot O{=}C$ interaction between PDLA and PLLA chains was completely destroyed during the melting process, and the enantiomeric chains homogenously inter-penetrated one another in the blend matrix. This resulted in a random formation of the $CH_3 \cdot\cdot O{=}C$ strong interactions between segments of PDLA and PLLA in the melt, which subsequently prevented a crystallization of larger domain-sized stereocomplex.[24] Given its entropic driving force and its superior collective strength, the formation of such random segmental interactions is able to prevent melt crystallization of stereocomplex. It is therefore likely that similar structure is present in the structure of PDLLA copolymers, where a random formation of segmental interaction is also responsible for the enhancement in the materials properties, especially their high elongation at break.

Conclusions

P(LLA-co-DLLA) copolymers have been synthesized by ring-opening polymerization of L-lactide and D,L-lactide using Sn(II)-ethylhexanoate [$Sn(Oct_2)$] as a catalyst. The resulting high molecular weight copolymers have Mn in the range of $5.8x10^4$ to $11.8x10^4$. The incorporation of DLLA units results in a modification of thermal and mechanical properties of the copolymers. T_g and T_m of the copolymers decreased with an increase in DLLA comonomer in copolymer chains. The Young's modulus and tensile strength were obviously improved upon addition of DLLA comonomer units, where an optimum value was achieved in copolymer with 7.5 mol% monomer in feed. In addition, elongation at break of the copolymers is also affected by the DLLA content, where the largest improvement was observed in copolymer with 50 mol% of DLLA. The origin of this properties enhancement was investigated by polarized FTIR spectroscopy. The result indicated a formation of point interaction between DL and LL diads of the copolymer chain, which acts as a "physical crosslink" in the amorphous phase of the copolymers.

Acknowledgement

Financial support of this work is provided by The Thailand Research Fund (TRF)/ The Commission on Higher Education (CHE), RTA5180003, and Thailand Toray Science Foundation.

DRAFT

DRAFT

References

[1] Albertsson AC, Stridsberg KM, Ryner M. Controlled Ring-Opening Polymerization: Polymers with designed Macromolecular Architecture. Advances in Polymer Science 2002; 157: 41-65.

[2] Jacobsen S, Degee PH, Fritz, HG, Dubois PH, Jerome R. Polylactide(PLA)-A new way of production. Polymer Engineering and Science 1999; 39:1311-1319.

[3] Ouchi T, Ichimura S, Ohya Y. Synthesis of branched poly(lactide) using polyglycidol and thermal, mechanical properties of its solution-cast film. Polymer 2006; 47: 429-434.

[4] Tsuji H, Ikada Y. Stereocomplex formation between enantiomeric poly(lactic acid)s. XI. Mechanical properties and morphology of solution-cast films. Polymer 1999; 40: 6699-6708.

[5] Kimura Y, Fukushima K. Stereocomplexed polylactide (Neo-PLA) as high-performance bio-based polymers: their formation, properties, and application. Polymer International 2006; 55: 626-642.

[6] Chen GX, Kim HS, Kim ES, Yoon JS. Synthesis of high-molecular-weight poly(L-lactic acid) through the direct condensation polymerization of L-lactic acid in bulk state. Europian Polymer Journal 2006; 42: 468-472.

[7] Lima LT, Aurasb R, Rubinob M. Processing technologies for poly(lactic acid). Progress in Polymer Science 2008 (article in press).

[8] Zhang J, Sato H, Tsuji H, Noda I, Ozaki Y. Infrared spectroscopic study of $CH_3\cdots O{=}C$ interaction during poly(L-lactide)/poly(D-lactide) stereocomplex formation, Macromolecules 2005; 38: 1822-1828.

[9] Zhang J,Tashiro K, Tsuji H, Domb AJ. Investigation of phase transitional behavior of poly(L-lactide)/poly(D-lactide) blend used to prepare the highly-oriented stereocomplex. Macromolecules 2007; 40: 1049-1054.

[10] Meaurio E, Zuza E, Lopez-Rodrıguez N, Sarasua JR. Conformational behavior of poly(L-lactide) studied by infrared spectroscopy. Journal of Physical Chemistry B 2006; 110: 5790-5800.

[11] Opaprakasit P, Opaprakasit M, Tangboriboonrat P. Crystallization of polylactide and its stereocomplex investigated by two-dimensional Fourier Transform Infrared correlation spectroscopy employing carbonyl overtones. Applied Spectroscopy 2007; 61: 1352-1358.

1. Fukushima, K. and Y. Kimura, *Stereocomplexed polylactides (Neo-PLA) as high-performance bio-based polymers: Their formation, properties, and application.* Polymer International, 2006. **55**(6): p. 626-642.
2. Lindblad, M.S., et al., *Polymers from renewable resources*, in *Advances in Polymer Science*. 2002. p. 139-161.
3. Lim, L.T., R. Auras, and M. Rubino, *Processing technologies for poly(lactic acid).* Progress in Polymer Science (Oxford), 2008. **33**(8): p. 820-852.
4. Tsuji, H., *Poly(lactide) stereocomplexes: Formation, structure, properties, degradation, and applications.* Macromolecular Bioscience, 2005. **5**(7): p. 569-597.
5. Tsuji, H. and Y. Ikada, *Stereocomplex formation between enantiomeric poly(lactic acid)s. XI. Mechanical properties and morphology of solution-cast films.* Polymer, 1999. **40**(24): p. 6699-6708.
6. Brizzolara, D., et al., *Mechanism of the stereocomplex formation between enantiomeric poly(lactide)s.* Macromolecules, 1996. **29**(1): p. 191-197.
7. Urayama, H., T. Kanamori, and Y. Kimura, *Properties and biodegradability of polymer blends of poly(L-lactide)s with different optical purity of the lactate units.* Macromolecular Materials and Engineering, 2002. **287**(2): p. 116-121.
8. Urayama, H., S.I. Moon, and Y. Kimura, *Microstructure and thermal properties of polylactides with different L- and D-unit sequences: Importance of the helical nature of the L-sequenced segments.* Macromolecular Materials and Engineering, 2003. **288**(2): p. 137-143.
9. Ouchi, T., S. Ichimura, and Y. Ohya, *Synthesis of branched poly(lactide) using polyglycidol and thermal, mechanical properties of its solution-cast film.* Polymer, 2006. **47**(1): p. 429-434.
10. Stridsberg, K.M., M. Ryner, and A.C. Albertsson, *Controlled ring-opening polymerization: Polymers with designed macromolecular architecture*, in *Advances in Polymer Science*. 2002. p. 41-65.
11. Jacobsen, S., et al., *Polylactide (PLA) - a new way of production.* Polymer Engineering and Science, 1999. **39**(7): p. 1311-1319.
12. Opaprakasit, P., M. Opaprakasit, and P. Tangboriboonrat, *Crystallization of polylactide and its stereocomplex investigated by two-dimensional Fourier transform infrared correlation spectroscopy employing carbonyl overtones.* Applied Spectroscopy, 2007. **61**(12): p. 1352-1358.
13. Zhang, J.M., et al., *Infrared spectroscopic study of CH3 center dot center dot center dot O=C interaction during poly(L-lactide)/poly(D-lactide) stereocomplex formation.* Macromolecules, 2005. **38**(5): p. 1822-1828.
14. Zhang, J.M., et al., *Structural changes and crystallization dynamics of poly(L-lactide) during the cold-crystallization process investigated by infrared and two-dimensional infrared correlation spectroscopy.* Macromolecules, 2004. **37**(17): p. 6433-6439.
15. Zhang, J.M., et al., *Weak intermolecular interactions during the melt crystallization of Poly(L-lactide) investigated by two-dimensional infrared correlation spectroscopy.* Journal of Physical Chemistry B, 2004. **108**(31): p. 11514-11520.
16. Fukuzaki, H., et al., *Synthesis of copoly(d,l-lactic acid) with relatively low molecular weight and in vitro degradation.* European Polymer Journal, 1989. **25**(10): p. 1019-1026.
17. Ferguson, S., D. Wahl, and S. Gogolewski, *Enhancement of the mechanical properties of polylactides by solid-state extrusion. II. Poly(L-lactide), poly(L/D-lactide), and poly(L/DL-lactide).* Journal of Biomedical Materials Research, 1996. **30**(4): p. 543-551.
18. Bigg, D.M., *Polylactide copolymers: Effect of copolymer ratio and end capping on their properties.* Advances in Polymer Technology, 2005. **24**(2): p. 69-82.
19. Albertsson, A.C. and I.K. Varma, *Aliphatic polyesters: Synthesis, properties and applications*, in *Degradable Aliphatic Polyesters*. 2002. p. 1-40.
20. Stridsberg, K.M., M. Ryner, and A.C. Albertsson, *Controlled ring-opening polymerization: Polymers with designed macromolecular architecture*, in *Degradable Aliphatic Polyesters*. 2002. p. 41-65.
21. von Schenck, H., et al., *Ring-opening polymerization of lactones and lactides with Sn(IV) and Al(III) initiators.* Macromolecules, 2002. **35**(5): p. 1556-1562.
22. Chabot, F., et al., *Configurational structures of lactic acid stereocopolymers as determined by 13C{1H} n.m.r.* Polymer, 1983. **24**(1): p. 53-59.
23. Chen, G.X., et al., *Synthesis of high-molecular-weight poly(l-lactic acid) through the direct condensation polymerization of l-lactic acid in bulk state.* European Polymer Journal, 2006. **42**(2): p. 468-472.
24. He, Y., et al., *Unique crystallization behavior of poly(l-lactide)/poly(d-lactide) stereocomplex depending on initial melt states.* Polymer, 2008. **49**(26): p. 5670-5675.
25. Pan, P., et al., *Polymorphous crystallization and multiple melting behavior of poly(L-lactide): Molecular weight dependence.* Macromolecules, 2007. **40**(19): p. 6898-6905.
26. Lin, Y., et al., *Study of Hydrogen-Bonded Blend of Polylactide with Biodegradable Hyperbranched Poly(ester amide).* Macromolecules, 2007. **40**(17): p. 6257-6267.
27. Fujita, M., et al., *Stereocomplex Formation through Reorganization of Poly(l-lactic acid) and Poly(d-lactic acid) Crystals.* Macromolecules, 2008. **41**(8): p. 2852-2858.
28. Meaurio, E., et al., *Conformational behavior of poly(L-lactide) studied by infrared spectroscopy.* Journal of Physical Chemistry B, 2006. **110**(11): p. 5790-5800.
29. Zhang, J., et al., *Investigation of phase transitional behavior of poly(L-lactide)/poly(D-lactide) blend used to prepare the highly-oriented stereocomplex.* Macromolecules, 2007. **40**(4): p. 1049-1054.
30. Sarasua, J.R., et al., *Stereoselective crystallization and specific interactions in polylactides.* Macromolecules, 2005. **38**(20): p. 8362-8371.
31. Hu, Y., et al., *C-HΠ_nO=C hydrogen bonding and isothermal crystallization kinetics of poly(3-hydroxybutyrate) investigated by near-infrared spectroscopy.* Macromolecules, 2006. **39**(11): p. 3841-3847.
32. Zhang, J., et al., *Conformation rearrangement and molecular dynamics of poly(3-hydroxybutyrate) during the melt-crystallization process investigated by infrared and two-dimensional infrared correlation spectroscopy.* Macromolecules, 2005. **38**(10): p. 4274-4281.

Property Modification of Epoxidized Natural Rubber: Crosslinking by Reactive Blend Technique of Poly(L-Lactic Acid-co-Ethylene Glycol) Block Copolymers

Thai-Hien Nguyen[1], Pramuan Tangboriboonrat[2], Nittaya Rattanasom[3], Atitsa Petchsuk[4], Mantana Opaprakasit[5], Pakorn Opaprakasit[1]*

[1] School of Bio-Chemical Engineering and Technology, Sirindhorn International Institute of Technology (SIIT), Thammasat University, Pathum Thani 12121, Thailand

[2] Department of Chemistry, Mahidol University, Bangkok 10400 Thailand

[3]Institute of Molecular Biosciences, Mahidol University, Salaya, Nakhon Pathom 73170, Thailand

[4] National Metal and Material Technology Center (MTEC), Pathum Thani 12120, Thailand

[5] Department of Materials Science, Chulalongkorn University, Bangkok 10330, Thailand

Tel: +66 (0) 2986 9009 Ext. 1806

Fax: +66 (0) 2986 9009 Ext. 1801

E-mail: pakorn@siit.tu.ac.th

* Corresponding author

Abstract

Property modification of epoxidized natural rubber (ENR) was studied by croslinking with Poly(L-Lactic Acid-co-Ethylene Glycol) Block Copolymers ($PLLA_{46}/PEG_{46}/PLLA_{46}$) using a Moving Rheometer (MDR, TechPro MD+). Chemical structure and properties of the products were characterized by ^{1}H-NMR. Curing characteristic, swelling behavior and thermal properties of the blends cured using ENR and $PLLA_{46}/PEG_{46}/PLLA_{46}$ triblock copolymer were investigated. Results indicate that the maximum elastic and viscous torque increased as a function of increasing copolymer content. However, a reverse trend was observed for tanδ. The swelling ratio increased with decreasing ENR composition in the blend. Thermal stability property was determined by TGA.

Keywords: Epoxidized natural rubber, PLLA/PEG copolymer, blend, curing characteritics

DRAFT

1. Introduction

Epoxidized natural rubber (ENR) is chemical modified natural rubber (NR) product obtained from the introduction of epoxide groups into NR backbone to enhance its properties such as higher hysteresis, oil resistance and lower air permeability [1-3]. ENR contains both epoxide and unsaturated sites, in which epoxide groups are reactive toward nucleophilic reagents, while the double bond is conventionally use as typical crosslink points by using various curing agents [4-14]. Reaction through epoxide groups were carried out by reactive blending of ENR with other polar components such as carboxylated nitrile rubber [4,5], chlorosulfonated polyethylene rubber,[5,6] polychloroprene rubber [4,7], polypropylene [8], ethylene vinyl acetate [9,10], *p*-phenylenediamine [11-13], butylphosphate [14].

LLA/EG/LLA triblock copolymers are materials that combine good characteristics of PEG and PLLA polymers, biocompatibility and biodegradability [15-22]. Moreover, OH-capped in chain-end of triblock copolymer play as nucleophilic reagents to react with epoxide groups of ENR. There are several papers in the literature regarding to addition of hydroxyl groups onto ENR has been initiated for recent years and some accomplishments have been achieved so far [23-25]. Elastomeric rubber-plastic materials have become a great interest in rubber industry nowadays because they have properties of rubber and thermoplastic material [26]. Thus, this study focuses on the use of PLLA/PEG block copolymer with the OH-capped at the chain-end as a macromolecular crosslink agent for ENR to obtain elastomeric materials, which exhibits biocompatible and biodegradable properties for use in biomedical applications. Thus, crosslinking of ENR-PLLA/PEG block copolymer by a reactive blend process was conducted to obtain elastomeric material. In this process mixtures of ENR and the copolymer and catalyst were prepared and then subjected to elastic torque measurement to study its *in situ* crosslinking characteristics. In this study, the mixing torque value, swelling ratio as well as thermal properties of ENR-PLLA/PEG blend were investigated.

2. Experimental

2.1 Materials

$LLA_{46}/EG_{46}/LLA_{46}$ triblock copolymer was synthesized by the methodology reported in the previous study [27]. ENR with 20% epoxidation was synthesized from commercial high ammonia (HA)-preserved NR latex concentrate (Rayong Bangkok Rubber, Thailand). Epoxidation procedure was similar to that reported by Saendee et al. [28]. Dried tetrahydrofuran (THF) was used as a solvent in a mixing process. $Sn(Oct)_2$ (Wako) was used as a catalyst in the curing of the materials.

2.2 Crosslinking of ENR by LLA/EG copolymer

Crosslinking of ENR by OH-capped LLA/EG copolymer was conducted by a reactive blend process. This is achieved by reactions of OH groups of copolymer with epoxide groups of ENR through ring opening reaction with $Sn(Oct)_2$ as a catalyst [29]. A mixture of ENR/copolymer and the catalyst was first prepared. Essentially, ENR and copolymer were separately dissolved in dried THF at 50°C. ENR solution was then cooled to 30°C. $Sn(Oct)_2$ catalyst was added in the copolymer solution and stirred for 1 hour. The solution of copolymer and catalyst was slowly added into the ENR solution. Finally, homogeneous mixtures of ENR, copolymer and catalyst were obtained by evaporation of the solvent under vacuum pressure. Compositions of ENR and copolymers of various mixtures, 4/1, 2/1, 1/1 by weight, are referred to as T41, T21, and T11, respectively.

The cure characteristics of ENR-LLA/EG sample in the reactive blend process were assessed *in situ* by using a moving die rheometer (MDR, TechPro MD+) at 80 °C in accordance with ISO 6502. Elastic and viscous torques were measured as function of curing time.

Soxhlet extraction experiments were carried out to determine the content of soluble and insoluble fractions by using THF at 110°C for 24 hours. The insoluble (denoted by "I") and soluble fractions (denoted by "S") of each sample were recovered by evaporation of the solvent and dried in a vacuum oven at room temperature until a constant weight was reached.

DRAFT

Chemical structure and chain composition of the triblock copolymers were characterized by ^{1}H-NMR on a Bruker DRX400 using $CDCl_3$ as a solvent. Decomposition temperatures (T_d) of the cured samples were determined on a Mettler Toledo TGA/SDTA 851, using nitrogen atmosphere. The samples were scanned from 50°C to 1000°C with a heating rate of 20°C/min.

The crosslink density was measured by using the swelling method. A piece of crosslinked sample (approximately 0.2 g) was accurately weighed and immersed in toluene (40ml) at room temperature in a dark cabinet. At equilibrium swelling time (about 7 days), the test piece was removed from toluene, wiped with filter paper, and its weight was recorded. The swelling ratios were calculated as follows:

$$\%\text{Swelling} = \frac{W_{eq} - W_o}{W_o} \times 100$$

where W_o = original weight of dried sample (g)

W_{eq} = weight of swollen sample at equilibrium swelling time(g)

Solvent taken up by the swollen samples after equilibrium swelling was then completely removed by air dry at room temperature for at least 1 month until a constant weight was reached. The remaining weight was recorded, and the weight loss of the sample, which reflect weight fractions of sample dissolved into toluene solvent during the swelling experiment were calculated, as follows:

$$\%\text{ weight loss} = \frac{W_o - W_d}{W_o} \times 100$$

where W_o = weight of original dried sample before swelling experiment (g)

W_d = remaining weight of dried sample after swelling experiment (g)

3. Results and Discussion

In previous study, OH-capped LLA/EG triblock copolymer is used as crosslinking agent for ENR by using $Sn(Oct)_2$ as a catalyst with chemical reaction technique. ^{1}H-NMR spectra indicate formation of chemical bond between copolymer and ENR by ring opening reaction of epoxide groups by OH end chain of copolymer [29]. With the application of $Sn(Oct)_2$ catalyst, formation of crosslinked ENR with the copolymer takes places, resulting in further increase in the tensile properties [29].

3.1 Curing characteristics of samples during reactive blending process

The steady-state elastic torques of ENR/copolymer mixture as a function of compositions are shown in Figure 1. The maximum torque increases with an increase in the copolymer content, reflecting an increase in modulus of the mixtures. This is probably because the presence of the copolymer in the rubber matrix results in a mobility restriction of ENR molecules and consequently increases the elastic torque of the mixture. In addition, epoxide of ENR is able to react with the hydroxyl end groups of copolymer to form crosslinked network. This significantly contributes to the decrease in chain flexibility and the increase in the elasticity of the structure with increasing copolymer content.

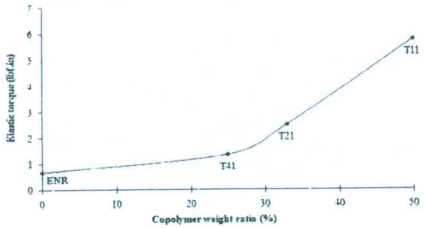


Figure 1 Maximum elastic torques as a function of ENR/copolymer compositions

Figure 2 shows that the maximum viscous torques also increase with an increase in the copolymer composition. This is surprising, as it was expected that the formation of crosslinked ENR by using LLA/EG block copolymer should lead to a decrease in viscous

torques. This is probably due to a combination of crosslinking and simple blending characteristic of ENR and copolymer in the mixtures. Although increasing of copolymer composition in the mixture provides higher amount of OH groups for enhancements of improves crosslinking reaction, this may lead to an excess amount of copolymers which are not crosslinked. It is likely that some copolymer chains may react with ENR only one end (grafting) or may not react (simple blend), as the copolymer is macromolecule crosslinker. This results in an increase in the flow characteristics of the mixture and, in turn, increases the viscous torques or damping behavior of the material.

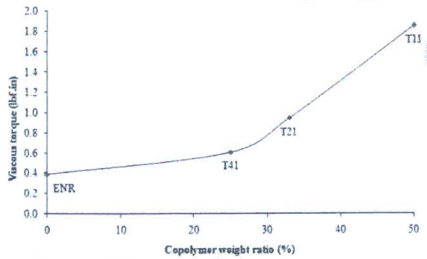


Figure 2 Maximum viscous torques as a function of ENR/copolymer compositions

Loss tangent (tan δ) at maximum elastic torque of samples at various ENR/copolymer compositions is shown in Figure 3. Tan δ is the ratio of viscous to elastic torque, indicating relative viscous/elastic behaviors. A decrease in tan δ with an increase in copolymer content indicates that the relative elastic behavior of the crosslinked samples improves with an increase in copolymer composition. This indicate a higher effectiveness of crosslinking process as a function of copolymer content, as this results in an improvement in elasticity of the material, compared to damping behavior derive from simple blend.

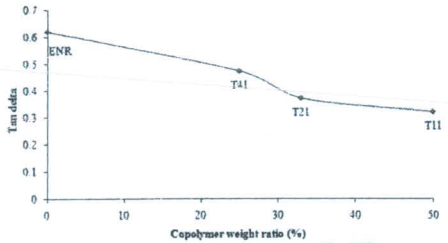


Figure 3 Maximum tan δ as a function of ENR/copolymer compositions

3.2 *^{1}H-NMR characterization*

Results on copolymer composition of samples after reactive blend process are summarized in Table 1. The results indicate that the presence of copolymer in insoluble samples TI, decreases with increasing ENR content. The disappearance of copolymer in TI11 can be explained base on its hard crosslink network because of high concentration of copolymer. This hard crosslink network cannot dissolve in $CDCl_3$ which is the solvent for ^{1}H-NMR. Therefore, the ^{1}H-NMR cannot detect integrated peak area value of one methine proton (5.10 ppm) of monomer of copolymer in rubber network.

Table 1 Weight compositions of copolymers in extracted products of samples after reactive blending process

	C(%)	wt (%)
TI11	N/A	25
TS11	100	72
TI21	21	35
TS21	86	62
TI41	19	47
TS41	42	42

3.3 *Degree of crosslinking*

Degree of crosslinking of T and TI samples were carried out in toluene based on the completely soluble characteristic of ENR and LLA/EG/LLA triblock copolymer and the insoluble behavior of cured sample after crosslinking at room temperature. Figure 4 shows

DRAFT

that the swelling ratios of crosslinked samples decrease with increasing copolymer composition. T and TI represent the original samples before THF Soxhlet extraction and the THF insoluble fraction of sample after extraction, respectively. The swelling ratio of both T and TI fraction are more than 400 %. Aprem et al. reported that the swelling ration of sulfur vucalnization of natural rubber is less than 550 % [30]. It is probably because the copolymer acts as long chain-linking junction that creates more vacance in the rubber network. In the sample with higher copolymer content, the crosslink reaction is dominant and a high crosslinked network is formed, leading to a decrease in the swelling ratio. This confirms the result on ^{1}H-NMR spectra, where no signal due to copolymer is observed, as previously discussed in Table 1. TI11 sample has a hard crosslinked network because of high concentration of copolymer, so it cannot be dissolved in $CDCl_3$ which is the solvent for ^{1}H-NMR experiment. Therefore, the ^{1}H-NMR cannot detect integrated peak area value of one methyne proton (5.10 ppm) of monomer of copolymer in rubber network.

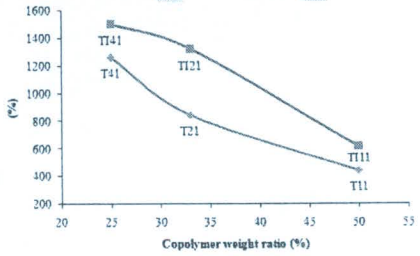


Figure 4 Swelling behavior of samples from reactive blend process as a function of ENR/copolymer composition

The weight losses of samples after swelling experiments are shown in Figure 5. The weight losses decrease as a function of increasing copolymer content. This confirms the results on swelling ratio, where the composition of 1/1 gives the highest crosslink density, lowest swelling ratio, or weight loss whereas the composition of 4/1 gives the lowest crosslink density, highest swelling ratio, or highest weight loss. This also confirms the presence of copolymer either as grafted or crosslinked copolymer on the ENR backbone. In samples with

lower copolymer content, 2/1 and 4/1, the grafting reaction is dominant, leading to a higher weight loss values because simple grafting or lightly crosslink can dissolve in toluene.

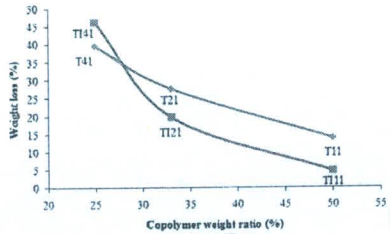
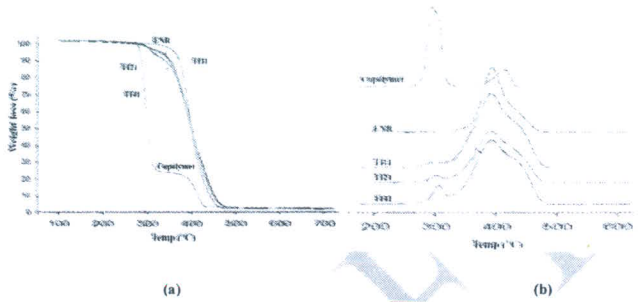


Figure 5 Weight losses after swelling ratio experiments

3.4 TGA thermogram

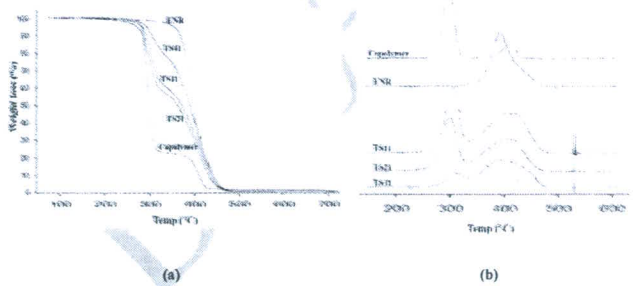
Thermal stability of samples as a function of ENR/copolymer composition is examined. Figure 6 (a) and Figure 7 (a) show TGA curves of THF insoluble (TI) and soluble fractions (TS) after Soxhlet extraction. It is clearly seen that the degradation temperatures of TI and TS start at 287°C and complete at 490°C. Thermal degradation temperatures of copolymer and ENR, T_{dC} and T_{dE}, are conveniently determined from DTGA curves, as shown in Figure 6 (b) and Figure 7 (b). The degradable characteristics of sample are summarized in Figure 8, where four steps of degradation are observed from the second derivative TGA curve. LLA block in copolymer chain that react with ENR only with ENR only with one chain end (grafted LLA) and unreacted LLA blocks degrade first in the early stage at the temperature $T_{d\ LLAg,f}$ approximately 300°C. It was observed that T_d of LLA in pure LLA/EG copolymer showed T_d at 298°C [31]. The second degradation step is associated with junction LLA block. This presence of this degradation temperature ($T_{d\ LLAc}$) at approximately 350°C indicates formation of ENR crosslinked network, leading to a higher thermal stable LLA blocks. ENR then degrades in the third step with $T_{d\ ENR}$ closer to 400°C. The results show that crosslinked LLA junction degrades at the temperature close to that of ENR matrix. This is clearly visible in the subtracted thermogram. The close temperature indicates the link of the two

components by strong covalent bonds. Final step is the degradation of EG block ($T_{d\ EG}$) at higher temperature around 470°C.



(a) (b)

Figure 6 (a) TGA thermograms of ENR, copolymer, and THF insoluble products after Soxhlet extraction of cured sample and (b) the corresponding DTGA plots



(a) (b)

Figure 7 (a) TGA thermograms of ENR, copolymer, and THF soluble products after Soxhlet extraction of cured sample and (b) the corresponding DTGA plots

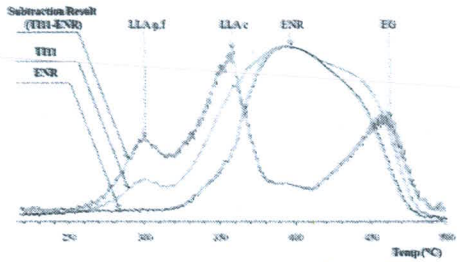


Figure 8 Illustration of degradable temperature (T_d) from DTGA thermograms

Weight percentage of each component in the cured samples in calculated form curve resolved DTGA thermogram, as illustrated in Figure 9. Peak integrations of each component are as follows. $A_{LLA\ g.f}$: unreacted and grafted LLA blocks, A_{EG}: EG block, $A_{ENR+LLA\ c}$: ENR and crosslinked LLA block which are overlapped and hardly determined separately.

Percentage of LLA block of copolymer is therefore calculated as follows:

$$A_{LLA} = \frac{2.04}{1} \times \frac{A_{EG}}{44} \times 72$$

where $\frac{2.04}{1}$ is the $\frac{LLA}{EG}$ molar ratio of $LLA_{46}/EG_{46}/LLA_{46}$. 44 is the molecular weight of EG unit. 72 is the molecular weight of LLA unit.

Percentage of copolymer in the sample, C(%), is calculated as follows:

$$C(\%) = A_{EG} + A_{LLA}$$

Percentage of crosslinked copolymer in the sample, $C_{crosslink}(\%)$, is calculated as follows:

$$C_{crosslink}(\%) = (A_{LLA} - A_{LLAg.f}) + \frac{1}{2.04} \times \frac{(A_{LLA} - A_{LLAg.f})}{72} \times 44$$

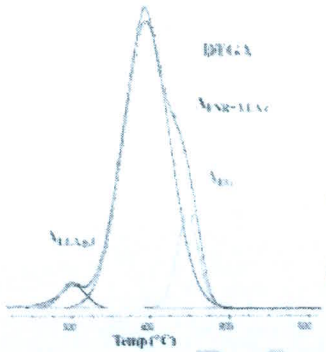


Figure 9 Curve fitting and band assignment of DTGA thermogram of TI11

The thermal degradable properties obtained from TGA are summarized in Table 2. The results show that the percentages of crosslinked copolymer in samples prepared from the reactive blend process improve with an increase in copolymer content, especially in THF insoluble fraction (TI). These results are in good agreement with those from swelling experiments and ^{1}H-NMR characterizations, as shown in Figure 4 and Table 1, respectively. The drastic reductions in percentage of copolymer and crosslinked copolymer indicate that the copolymers do not completely react with ENR as crosslinked blocks, but partially present as grafted copolymer on ENR backbone or stay unreacted, especially for samples of THF soluble part.

Table 2 Degradable temperatures of THF insoluble parts (TI) and THF soluble parts (TS) of blends

Samples	T_{dC} (°C)			T_{dE} (°C)	C (%)	$C_{crosslink}$ (%)
ENR	-			394	0	0
Copolymer	LA block		EG block	-	100	0
	293		410			
	$T_{dLLAg,f}$	T_{dLLAc}				
TI11	298	356	459	394	56	42
TI21	303	356	457	394	30	23
TI41	304	356	457	394	26	18
TS11	308	359	430	398	56	8
TS21	301	-	425	397	47	0
TS41	305	356	459	392	26	2

4. Conclusions

In situ crosslink network of ENR and PLLA/PEG triblock copolymer were prepared by using reactive blending technique. Higher value of elastic torque and lower value of tangent δ were observed in an increase in copolymer composition.

Results from ^{1}H-NMR indicate formation of chemical bond between copolymer and ENR. After the incorporation of ENR and copolymer, crosslink density of rubber matrix increase with increasing copolymer composition. . Moreover, these crosslinked samples exhibit better thermal stability, compared to the original copolymer constituents.

5. Acknowledgements

Financial support of this work is provided by The Thailand Research Fund (TRF), The Commission on Higher Education (CHE), RTA5180003 and Thailand Toray Science Foundation. Thai Hien Nguyen is supported by a scholarship program from Siam Cement Foundation and SIIT, Thammasat University.

References and Notes

1. Gelling IR. MODIFICATION OF NATURAL RUBBER LATEX WITH PERACETIC ACID. *Rubber Chemistry and Technology*, 58(1), 86-96 (1985).

2. Gelling IR. Epoxidised Natural Rubber. *Journal of Natural Rubber Research*, 6(3), 184-205 (1991).

3. Akiba M, Hashim AS. Vulcanization and crosslinking in elastomers. *Progress in Polymer Science*, 22(3), 475-521 (1997).

4. Alex R, De PP, De SK. Self-vulcanizable ternary rubber blend based on epoxidized natural rubber, carboxylated nitrile rubber and polychloroprene rubber: 1. Effect of blend ratio, moulding time and fillers on miscibility. *Polymer*, 32(13), 2345-2350 (1991).

5. Roychoudhury A, De PP, Bhowmick AK, De SK. Self-crosslinkable ternary blend of chlorosulphonated polyethylene, epoxidized natural rubber and carboxylated nitrile rubber. *Polymer*, 33(22), 4737-4740 (1992).

6. Park CY, Kim BK. Self-Vulcanization of ENR/CSM Blends. *Polymer (Korea)*, 17(5), 537-542 (1993).

7. Bandyopadhyay S, De PP, Tripathy DK, De SK. Dynamic mechanical spectroscopic studies on the miscibility of polychloroprene--epoxidized natural rubber blend in presence of carbon black filler. *Polymer*, 36(10), 1979-1984 (1995).

8. Nakason C, Wannavilai P, Kaesaman A. Effect of vulcanization system on properties of thermoplastic vulcanizates based on epoxidized natural rubber/polypropylene blends. *Polymer Testing*, 25(1), 34-41 (2006).

9. Yong MK, Ismail H, Ariff ZM. Comparison Properties of Natural Rubber (SMR L)/Ethylene Vinyl Acetate (EVA) Copolymer Blends and Epoxidized Natural Rubber (ENR-50)/Ethylene Vinyl Acetate (EVA) Copolymer Blends *Polymer-Plastics Technology and Engineering*, 46(4), 361 - 366 (2007).

10. Yong MK, Ismail H, Ariff ZM. The Effect of Epoxidized Natural Rubber (ENR-50) or Polyethylene Acrylic Acid (PEA) as Compatibilizer on Properties of Ethylene Vinyl Acetate (EVA)/Natural Rubber (SMR L) Blends. *Polymer-Plastics Technology and Engineering*, 46(10), 1001 - 1009 (2007).

11. Hashim AS, Kohjiya S. Curing of epoxidized natural rubber with *p*-phenylenediamine. *Journal of Polymer Science Part A: Polymer Chemistry*, 32(6), 1149-1157 (1994).

12. Jayawardena S, Reyx D, Durand D, Pinazzi CP. Synthesis of macromolecular antioxidants by reaction of aromatic amines with epoxidized polyisoprene, 3. Reaction of 4-anilinoaniline with epoxidized 1,4-polyisoprene. *Die Makromolekulare Chemie*, 185(10), 2089-2097 (1984).

13. Perera MCS. Reaction of aromatic amines with epoxidized natural rubber latex. *Journal of Applied Polymer Science*, 39(3), 749-758 (1990).

14. Derouet D, Radhakrishnan N, Brosse J-C, Boccaccio G. Phosphorus modification of epoxidized liquid natural rubber to improve flame resistance of vulcanized rubbers. *Journal of Applied Polymer Science*, 52(9), 1309-1316 (1994).

15. Popelka S, Machová Lk, Rypácek F. Adsorption of poly(ethylene oxide)-block-polylactide copolymers on polylactide as studied by ATR-FTIR spectroscopy. *J. Colloid Interface Sci.*, 308(2), 291-299 (2007).

16. Yang L, Zhao Z, Wei J, El Ghzaoui A, Li S. Micelles formed by self-assembling of polylactide/poly(ethylene glycol) block copolymers in aqueous solutions. *J. Colloid Interface Sci.*, 314(2), 470-477 (2007).

17. Agrawal SK, Sanabria-DeLong N, Coburn JM, Tew GN, Bhatia SR. Novel drug release profiles from micellar solutions of PLA-PEO-PLA triblock copolymers. *Journal of Controlled Release*, 112(1), 64-71 (2006).

18. Wan Y, Chen W, Yang J, Bei J, Wang S. Biodegradable poly(-lactide)-poly(ethylene glycol) multiblock copolymer: synthesis and evaluation of cell affinity. *Biomaterials*, 24(13), 2195-2203 (2003).

19. Cohn D, Hotovely-Salomon A. Biodegradable multiblock PEO/PLA thermoplastic elastomers: molecular design and properties. *Polymer*, 46(7), 2068-2075 (2005).

20. Yuan M, Liu D, Xiong C, Deng X. Polymerization of lactides and lactones 6. Synthesis of poly-lactide and polyethylene glycol-co-poly-lactide copolymer with allylmagnesium chloride. *Eur. Polym. J.*, 35(12), 2139-2145 (1999).

21. Li SM, Rashkov I, Espartero JL, Manolova N, Vert M. Synthesis, Characterization, and Hydrolytic Degradation of PLA/PEO/PLA Triblock Copolymers with Long Poly(l-lactic acid) Blocks. *Macromolecules*, 29(1), 57-62 (1996).

22. Rashkov I, Manolova N, Li SM, Espartero JL, Vert M. Synthesis, Characterization, and Hydrolytic Degradation of PLA/PEO/PLA Triblock Copolymers with Short Poly(l-lactic acid) Chains. *Macromolecules*, 29(1), 50-56 (1996).

23. Derouet D, Brosse J-C, Challioui A. Alcoholysis of epoxidized polyisoprenes by direct opening of oxirane rings with alcohol derivatives 1. Modelization of the reaction. *European Polymer Journal*, 37(7), 1315-1326 (2001).

24. Derouet D, Brosse J-C, Challioui A. Alcoholysis of epoxidized polyisoprenes by direct opening of oxirane rings with alcohol derivatives 2. Study on epoxidized 1,4-polyisoprene. *European Polymer Journal*, 37(7), 1327-1337 (2001).

DRAFT

25. Nakason C, Kaesaman A, Sainamsai W, Kiatkamjonwong S. Rheological behavior of reactive blending of epoxidized natural rubber with cassava starch and epoxidized natural rubber with natural rubber and cassava starch. *Journal of Applied Polymer Science*, 91(3), 1752-1762 (2004).

26. Bhowmick AK, Stephens HL. Handbook of Elastomers. (2001).

27. Nguyen T-H, Petchsuk A, Tangboriboonrat P, Opaprakasit M, Sharp A, Opaprakasit P. Synthesis and Characterizations of PLLA/PEG Block Copolymers. *Advanced Materials Research* 93 - 94, 198-201 (2010).

28. Saendee P, Tangboriboonrat P. Latex interpenetrating polymer networks of epoxidised natural rubber/poly(methyl methacrylate): an insight into the mechanism of epoxidation. *Colloid & Polymer Science*, 284(6), 634-643 (2006).

29. Nguyen T-H, Tangboriboonrat P, Rattanasom N, Petchsuk A, Opaprakasit M, Opaprakasit P. Property Modification of Epoxidized Natural Rubber by Polymerization of Poly(L-Lactic Acid-co-Ethylene Glycol) Block Copolymers. (Ed.^(Eds) (2010)

30. Aprem AS, Joseph K, Mathew T, Altstaedt V, Thomas S. Studies on accelerated sulphur vulcanization of natural rubber using 1-phenyl-2, 4-dithiobiuret/tertiary butyl benzothiazole sulphenamide. *European Polymer Journal*, 39(7), 1451-1460 (2003).

31. Nguyen TH, Thammawong C, Tangboriboonrat P *et al.* L-Lactide/Ethylene Glycol Block Copolymers and Their Applications: Nanofibrous Materials and Surface Modification of Epoxidized Natural Rubber. *Express Polymer Letters*, (2010).

DRAFT

Morphology and Interactions of Naproxen-loaded Fe_3O_4 magnetic nanoparticles coated PLA-co-PEG block copolymer

1. Introduction

Owing to the magnetic properties and the ability to function at the cellular and molecular level of biological interactions of magnetic nanoparticles (MNP), they have a number of potentials to be used in medical applications such as contrast agents for magnetic resonance imaging (MRI) [1-4], cell engineering [1-3], and carriers for drug delivery [1, 2]. Especially, in the last decade, nanostructure mediated drug delivery or nanomedicine has been realized with the potential to enhance drug bioavailability, improve the timed release of drug molecules, enable precision drug targeting, reduce drug toxicity, and increase the efficiency in drug distribution [5, 6]. That is, the technology has developed so that it is possible to synthesize, characterize and tailor the functional properties of magnetic nanoparticles for medical applications.

Many methods have been proposed for the synthesis of iron oxide nanoparticles. These includes co-precipitation, reactions in constrained environments, hydrothermal and high-temperature reactions, sol-gel reactions, polyol methods, flow injection syntheses, electrochemical methods, aerosol/vapor methods, and sonolysis [7-9].

For drug delivery application, the use of magnetic nanoparticles, magnetite (Fe_3O_4) can give rise to a precise drug delivery to a specific target site by application of external magnetic fields [10]. However, there are some limitations that are needed to be overcome in using nanoparticles in the drug delivery applications—especially the short blood circulation time due to rapid elimination of the nanoparticles from the blood stream, poor cell internalization, poor biocompatibility, and any other processes that might affect their behaviors *in vivo* [6].

To overcome these limitations, it is necessary that some adjustments for suitable composition, size, morphology, and surface chemistry are carried out before being used in order to avoid those limitations and thereby achieve the utmost effectiveness. For the simplest approach to increasing the blood circulation time, the magnetic nanoparticles are coated with hydrophilic polymers as many recent researches have focused on [7, 11-13] such as poly(ethylene glycol) or PEG to disperse particles, increase blood circulation time, biocompatibility, and improve cell internalization [6]. In addition to a simple hydrophilic polymer coating, it is also possible to coat MNPs with copolymer such as PEG-co-PLA with the help of hydrophobic compounds such as oleic acid, as shall be the formulation used in this work.

Tapan K. Jain, *et al.* reported using Pluronic F-127 to coat oleic acid (OA) pre-stabilized MNP and encapsulate an anticancer agent, doxorubicin [7]. As a result of this study, the obtained particles, mean particle size measured by TEM being 9-13 nm, can be loaded easily with high doses of water insoluble anticancer agents. In addition, the sustained release behavior of the encapsulated drug is observed over 2 weeks under *in vitro* conditions. Similarly, Rutnakornpituk, M., *et al.* employed OA to stabilized the MNP, before using different block length mPEG-PCL diblock copolymers to coat the drug delivery system [11]. The particles obtained had the diameter of 9 nm measured by TEM. Furthermore, it was found that increase of Mn of hydrophilic mPEG blocks in the enhanced the particle dispersability in water, while increase of Mn of hydrophobic PCL blocks improved their adsorbing ability to the hydrophobic inner layer of the particles. Nonetheless, particle size and magnetic properties did not depend on copolymer coating. For the particle stability, they were stable in water for one month period before aggregation was observed..S. Kayal and R.V. Ramanujan successfully coated the MNP with a conjugate of doxorubicin (DOX) and PVA and the average particle size was 10 nm analyzed by TEM [13]. DOX loading and release profiles showed that up to 45% of adsorbed drug was released in 80 h. Another different polymer is used by Bakandritsos, A., *et al.* in their research [12]. They apply PLA or PEG-PLA diblock copolymer to the MNP where the magnetic nanoparticles are organized in superclusters inside the hydrophobic core of the polymers. As a result, they found that the hydrodynamic diameter of MNPs-loaded PLA is approximatelt 250 nm, while that of MNPs-loaded PLA-PEG micelles is much lower (around 100 nm) and thus suitable with applications where prolonged blood circulation is required. Moreover, PLA-PEG magnetic hybrids showed remarkable colloidal stability in human blood plasma. However, no drug encapsulation was mentioned in this report.

PEG-PLA block copolymers are interesting in the use to coat magnetic nanoparticles. This is because the PLA part, with the help of hydrophobic compounds such as oleic acid, would serve as the hydrophobic area excellent for encapsulation of hydrophobic drugs [12] while the PEG part of the polymer chain offers hydrophilic properties to the complex, which is useful in stabilizing MNP in water. According to the work of Bakandritsos, A., *et al.*, they employed diblock PLA-PEG copolymer with PLA and PEG molecular weight 10,000 and 5,000 Da, respectively, to coat the MNP. This drug delivery complex is also similar to the system of water-dispersible oleic acid (OA)-Pluronic-coated iron oxide magnetic nanoparticle illustrated in the work of Tapan K. Jain, *et al.* except the polymer in their work is Pluronic [7]. The schematic representation is shown in Fig 1.

DRAFT

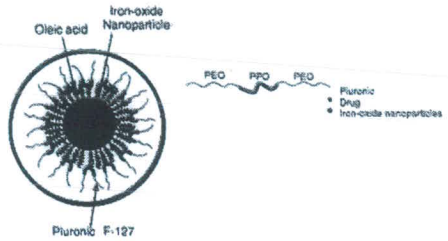


Fig. 1 Schematic representing formulation of iron oxide nanoparticles with oleic acid (OA) and pluronic (PEO-PPO-PEO) [7]

Modified MNP have a potential to act as drug carriers for a variety of therapeutic agents such as etoposide, doxorubicin, methotrexate, etc. The design of structural features, such as coating material, interaction between drug and coating, etc, determines the characteristics such as loading capacities and drug release profiles [14].

Naproxen is a hydrophobic anti-inflammatory agent. Liversidge G. and Conzentino P. has demonstrated that having high concentration of this drug can trigger gastric mucosal damage. They have also proven that lowering the drug particle size by suspension of drug in pluronic F-68 has lower the damaging effects [15]. Another experiment done be Maver U., *et al.*, synthesized a novel magnetic nanoparticle complex incorporated with naproxen which can readily be released [16]. The coating substance is, however, inorganic silica and drug encapsulation is done by incorporation into the porous silica area, not by hydrophobic and hydrophilic interaction.

In this work, oleic acid (OA)-PLA-PEG-PLA-coated magnetic iron oxide nanoparticles is successfully synthesized with and without drug encapsulation. The magnetic nanoparticle core is completed using the conventional co-precipitation method. Different weight ratio of polymer to MNP was used to find a suitable amount for coating. Also, incorporation of the therapeutic agent naproxen into the delivery complex is achieved.

2. Experiment

2.1 Materials

Iron(II) chloride tetrahydrate ($FeCl_2.4H_2O$) and iron(III) chloride anhydrous ($FeCl_3$) were purchased from Acros Organics. Oleic acid, n-hexane and methyl alcohol were from Carlo Erba Reagents. Ammonia solution 25% (NH_4OH) was bought from Merck. THF is obtained from Fischer Scientific. Chloroform is from Lab-Scan analytical sciences. Naproxen drug is purchased from Andenex-Chemie GmbH; Germany. PLA-PEG-PLA triblock copolymer (MW=) was obtained from... All solvents are of analytical grades. All reagents and solvents are used without further purification. Reversed Osmosis (RO) water was used throughout the experiment.

2.2 Preparation of oleic acid stabilized Fe_3O_4 magnetic fluid

Magnetic nanoparticles were synthesized using the co-precipitation method reported by Rutnakornpituk, M., *et al.* with slight modification. That is 3 g of $FeCl_2.4H_2O$ and 4.98 g of $FeCl_3$ were separately dissolved in 40ml of water. The mixtures were then sonicated using an ultrasonic bath, with interval stirring, for 1 hour. Finally, they were mixed together with stirring followed by rapid addition of ammonium hydroxide solution (25 vol%; 20 mL) to stimulate a basic environment for reaction I.

$$Fe^{2+} + Fe^{3+} + 8OH^- \longrightarrow Fe_3O_4 + 4H_2O \qquad \text{(I)}$$

Oleic acid (9 mL) was subsequently added dropwise to the black liquid with stirring which continued for a further 30 minute. Afterwards, the oleic-coated magnetic nanoparticles were separated by magnetic decantation using a neodymium magnet. They were washed with water 5 times to remove excess oleic acid. Finally, the particles were suspended in THF.

2.3 Surface modification of oleic acid stabilized Fe_3O_4 with PLA-PEG-PLA copolymer

The surface modification was carried out with a few number of steps. The solution of polymer (PLA-PEG-PLA) in THF was prepared (10%, 25%, 50% and 100%, wt polymer/wt oleic acid coated magnetic nanoparticles). The suspension of magnetic nanoparticles was added into the polymer solution prior to ultrasonic bath sonication for 30 minutes. Then, deionized water was added, followed by further sonication until 2 hours is reached. The mixture was undergone rotary evaporation (vacuum, 50 °C) to change medium—from THF to water. Afterwards, suspended nanoparticles in water were sonicated for 5 minutes using (strong sonicator). Lastly, the surface-modified magnetic nanoparticles suspended in water were centrifuged at 4000 rpm for 5 minutes to precipitate large aggregates. The supernatant was filtered and collected.

2.4 Drug encapsulation

For drug incorporation in nanoparticles, naproxen is primarily the represent of hydrophobic drug. Naproxen 10 mg was dissolved in 5 ml of methyl alcohol. The prepared drug solution is added

dropwise to 15 ml of (OA)-PLA-PEG-PLA-coated magnetic iron oxide nanoparticles suspended in water with stirring and heating at 60°C. The stirring and heating is continued for 20 minutes to evaporate the methyl alcohol. The mixture is sonicated using the (strong sonicator) for 2 minutes. Excess drug is removed by centrifugation at 3000 rpm for 5 minutes followed by filtration.

2.5 Characterization

2.5.1 Transmission Electron Microscope (TEM)

2.5.2 Scanning Electron Microscope (SEM)

2.5.3 Environmental Scanning Electron Microscope (ESEM)

2.5.4 RAMAN Spectroscopy: NTEGRA Spectra. Helium neon laser (λ = 632.8 nm). Objective lens 100x

2.5.5 Confocal RAMAN Spectroscopy:

2.5.6 Thermogravimetric Analysis (TGA)

2.5.7 Dynamic Light Scattering (DLS)

The morphology of the magnetic nanoparticles was characterized using transmission electron microscope (TEM) model JEOL JEM – 2010, (200kV) and scanning electron microscope (SEM) model JEOL JSM 6301F. For TEM, the nanoparticle suspended in water is drop onto a carbon coated copper grid and left overnight. As for the SEM preparation, the samples are drop onto aluminum foil and heated overnight. Structure of the samples were observed using confocal RAMAN spectroscopy (NTEGRA Spectra, Helium neon laser (λ = 632.8 nm), Objective lens 100x), Fourier Transform infrared spectroscopy (FTIR) NICOLET 6700 FTIR and thermogravimetric analysis (TGA) METTLER TOLEDO TSO801RO. Samples are dried on a glass slide for confocal RAMAN spectroscopy. Dried powder samples are employed for TGA. Particle size distribution and colloidal stability (zeta potential) is done using dynamic light scattering (DLS) Zetasizer Nanoseries ZS Model 3600 (Malvern, UK). Nanoparticles suspended in water are sonicated before measurement.

Also have VSM and XRF left

3. Result and Discussion

X-ray Fluorescence (XRF) was used to confirm the existence of iron oxide. Fig.2 illustrates the intensity in the range of 60 to 120 degree of 2 thetas in which the synthesized magnetic nanoparticles show the peak whereas the medium—water—has no peak of iron. Thus, it reassures the presence of iron oxide suspended in water. There are other different compounds including silicon, phosphate and calcium ion exist in the synthesized nanoparticles; however, these impurities already present in water used in the experiment as shown in Table 1.

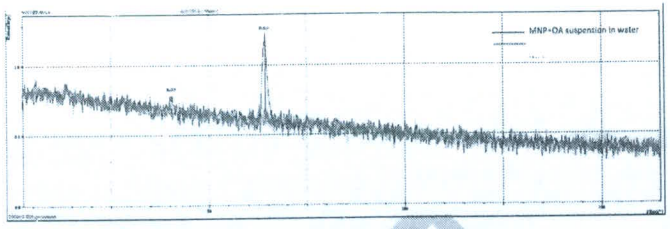
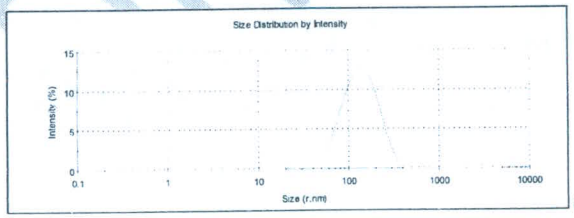


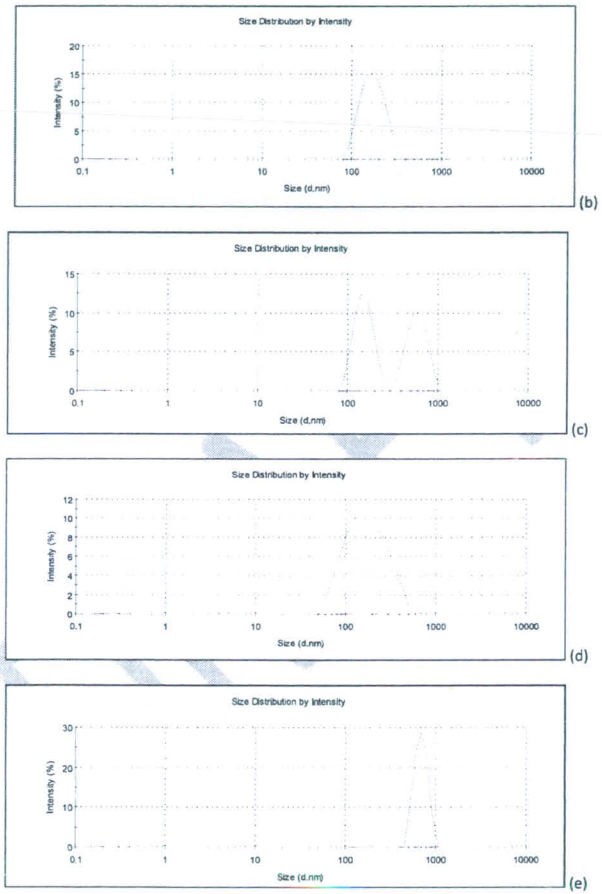
Fig. 2 XRF spectra of MNPs+OA in comparison with the medium (water)

Table 1. XRF Quantification of water and MNPs+OA suspended in water

Compound	Concentration (%)	
	Water	MNPs+OA suspended in water
Si	0.02	0.02
P	0.13	0.17
Ca	0.13	0.12
Fe	-	0.14



(a)



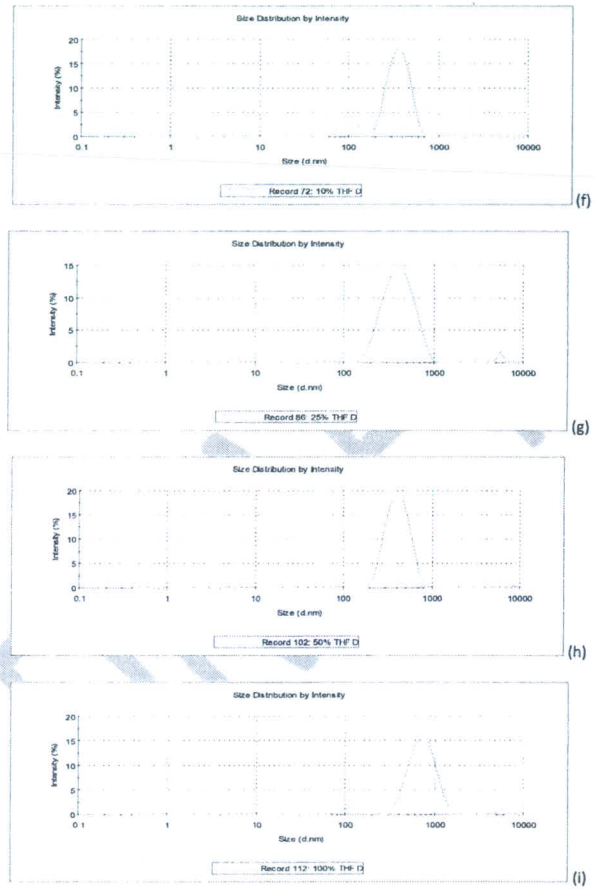
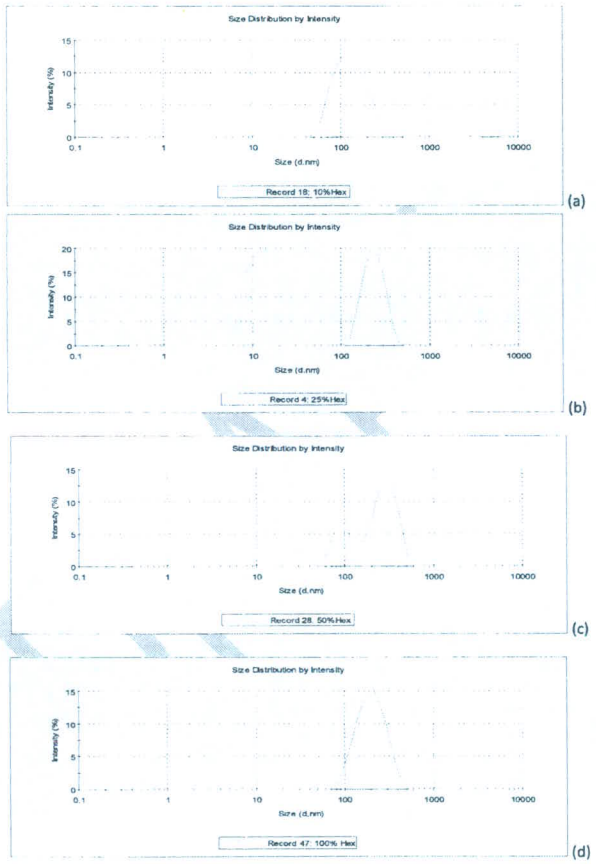


Fig. 3 Size distribution of PLA-PEG-PLA loaded magnetic nanoparticles synthesized in THF suspended in water
(a) no polymer coating (b) 10 wt% polymer (c) 25 wt% polymer
(d) 50 wt% polymer (e) 100 wt% polymer (f)) 10 wt% polymer with drug (g) 25 wt% polymer with drug
(h) 50 wt% polymer with drug (i) 100 wt% polymer with drug



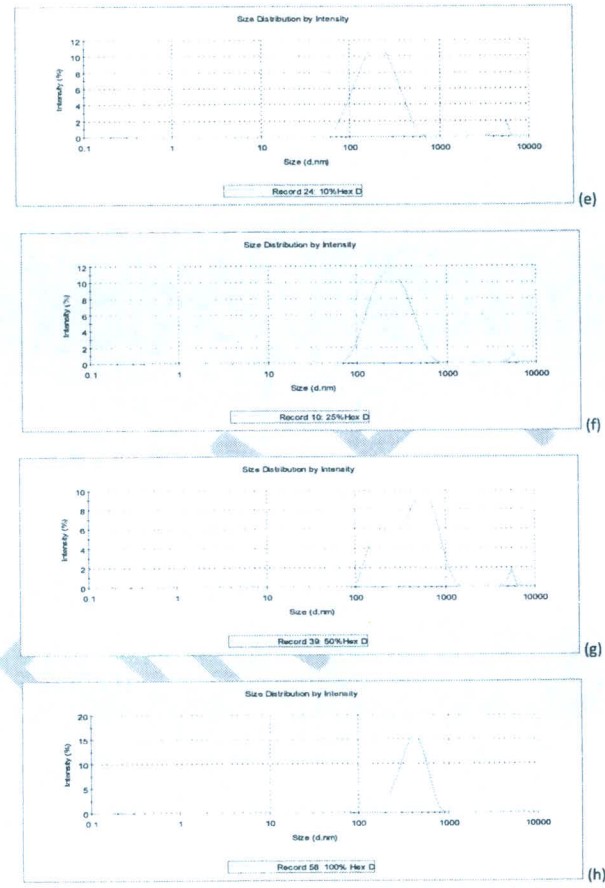


Fig. 3 Size distribution of PLA-PEG-PLA loaded magnetic nanoparticles synthesized in hexane suspended in water
(a) 10 wt% polymer (b) 25 wt% polymer
(c) 50 wt% polymer (d) 100 wt% polymer (e)) 10 wt% polymer with drug (f) 25 wt% polymer with drug
(g) 50 wt% polymer with drug (h) 100 wt% polymer with drug

Table 2. Summary of hydrodynamic size and zeta potential

Solvent	Concentration (wt%)		hydrodynamic size (nm)	zeta potential (mV)
Hexane	No drug	10	145.07	-23.27
		25	332.00	-26.20
		50	227.27	-26.60
		100	228.00	-27.70
	Drug	10	232.30	-17.73
		25	252.53	-17.67
		50	423.00	-12.20
		100	509.00	-13.03
THF	No drug	10	390.00	-52.2
		25	302.00	-29.23
		50	216.00	-16.18
		100	285.00	-22.77
	Drug	10	404.00	-20.37
		25	441.00	-15.77
		50	499.00	-15.53
		100	780.00	-14.23

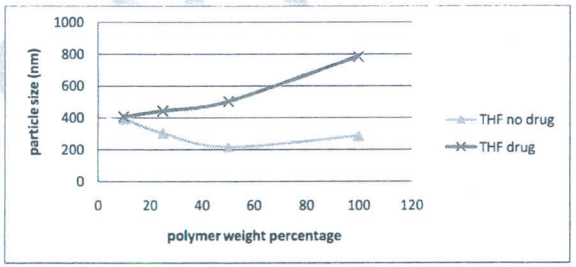


Fig x, summary of DLS synthesized in THF

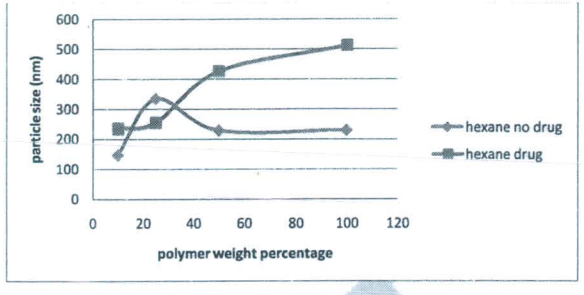
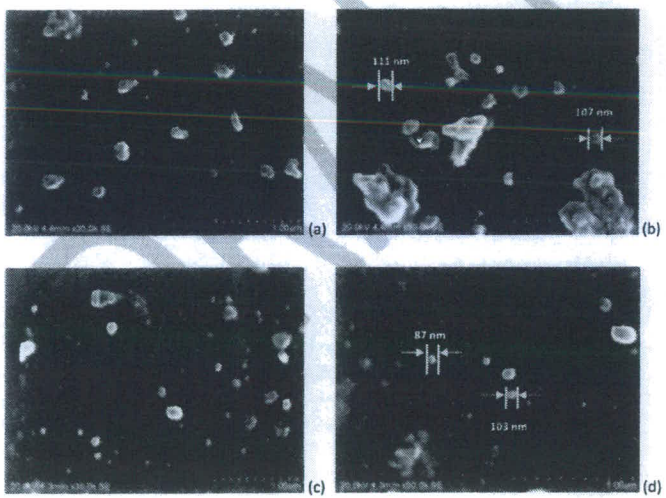


Fig x, summary of DLS synthesized in Hex



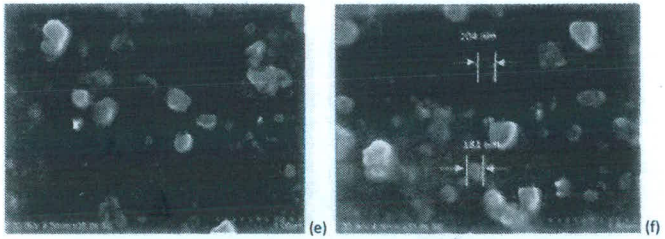


Fig. 4 SEM pictures of PLA-PEG-PLA loaded iron oxide nanoparticles
(a) 25 wt% polymer without drug encapsulation (35k magnification)
(b) 25 wt% polymer without drug encapsulation (50k magnification)
(c) 50 wt% polymer without drug encapsulation (35k magnification)
(d) 50 wt% polymer without drug encapsulation (50k magnification)
(e) 50 wt% polymer with drug encapsulation (35k magnification)
(f) 50 wt% polymer with drug encapsulation (50k magnification)

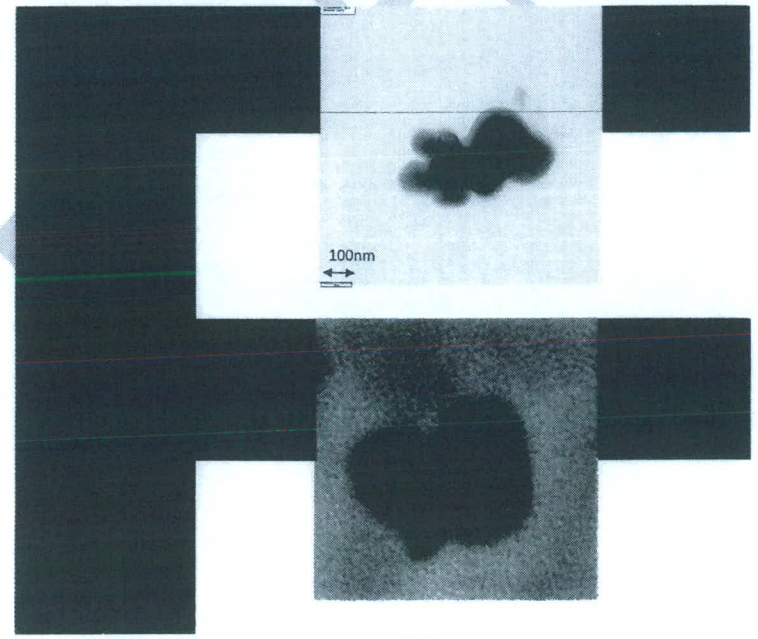


Fig 5. TEM pictures of PLA-PEG-PLA loaded iron oxide nanoparticles
a) 50 wt% polymer without drug encapsulation
b) 50 wt% polymer with drug encapsulation
c) TEM showing iron oxide nanoparticle grain
d) Zoomed region illustrating the lineup of atomic lattice of iron oxide

The pictures from TEM (Fig.5) illustrate the feature of the particles and size as well as SEM pictures do. Both pictures of particles of 50 wt% polymer with and without drug encapsulation show that there are some agglomerations. The scale bar on the bottom left hand side is 100 nm showing that the size of each particle is around 100-150 nm and 120-200 nm for particles without and with drug encapsulation, respectively. In addition, Fig 5c and d represents the atomic lattice of the iron oxide nanoparticles. The texture of the nanoparticles can be seen to be distinct from other surfaces.

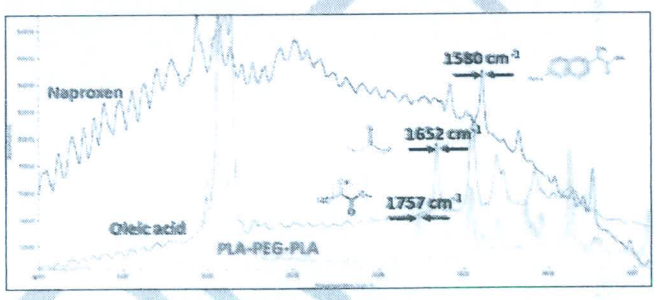


Fig. 6 RAMAN Spectra for pure oleic acid, drug, and polymer

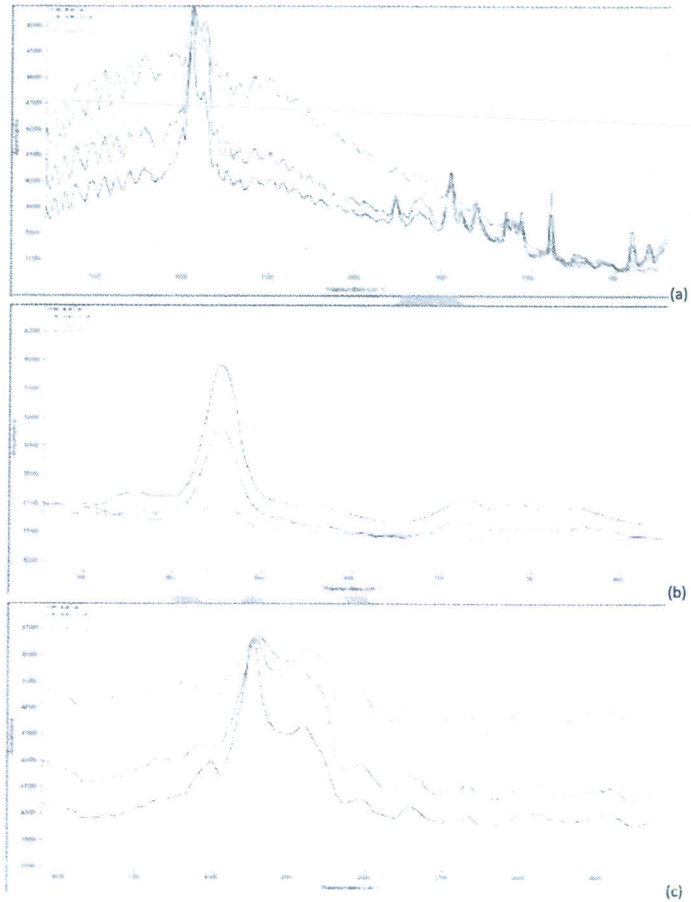


Fig. 7 RAMAN Spectra of PLA-PEG-PLA loaded iron oxide nanoparticles prepared by drug encapsulation together with polymer

a) Overall spectrum

b) Peak at wavenumber 875 cm^{-1} coresponding to polymer

c) Peaks at wavenumber 2880cm^{-1} and 3040cm^{-1} corresponding to oleic acid and naproxen, respectively

Figure 7 illustrate the coating morphology of the magnetic nanoparticle with drug encapsulation simultaneously with polymer coating. The peak present at wavenumber 875, 2880 and 3040cm^{-1} corresponds to the polymer, oleic acid and naproxen, respectively. It can be seen from figure 7b that the intensity of the polymer peak decreases with the increase in dept into the MNP. The same can be said for the profile of the naproxen drug. However, an opposite trend is observed with the oleic acid peak (figure 7c). The further into the nanoparticle results in an increase in oleic acid peak intensity. From this information, it can be modeled that this drug delivery complex is composed of different layers in the same way that has been reported by others, with the magnetic nanoparticles surrounded by an oleic acid and polymer layer in succession with the drug partitioning in the oleic acid layer [7, 11]. The schematic representation is shown in figure 8.



Fig. 8 Schematic representation of PLA-PEG-PLA loaded iron oxide nanoparticles prepared by drug encapsulation together with polymer

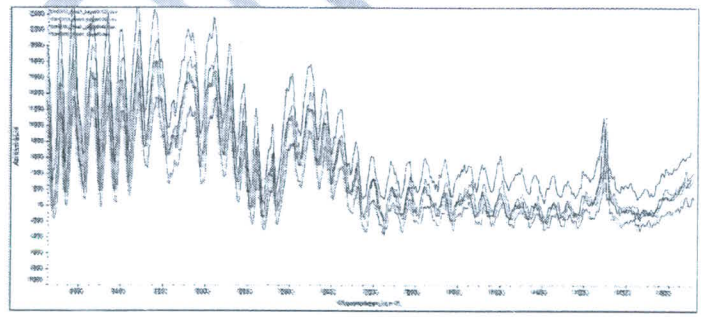


Fig. 9 RAMAN Spectra of PLA-PEG-PLA loaded iron oxide nanoparticles prepared by drug encapsulation after polymer coating

Figure 9 shows the RAMAN spectrum of the complex with drug encapsulation after polymer encapsulation. Unlike the other drug encapsulation method, where drug is mixed and entrapped together with the polymer, this method gives different nanoparticle morphology. It is seen that all peaks change in the same trend with relatively the same quantity. This indicates that instead of a bilayer coating consisting of oleic acid and polymer, the magnetic nanoparticles are coated with a mixed single layer of polymer and oleic acid. The schematic representation of this morphology is shown in Fig 10.

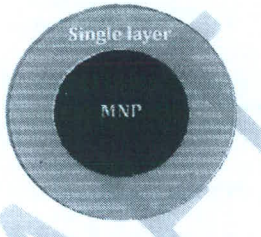


Fig. 10 Schematic representation of PLA-PEG-PLA loaded iron oxide nanoparticles prepared by drug encapsulation after polymer coating

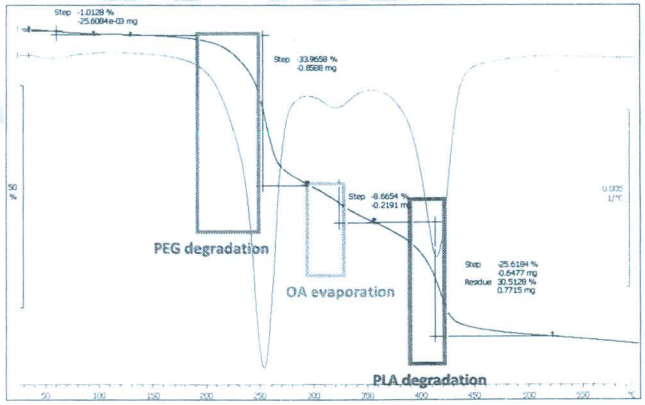


Fig.9 TGA result for the sample coated with oleic acid and 50 wt% polymer

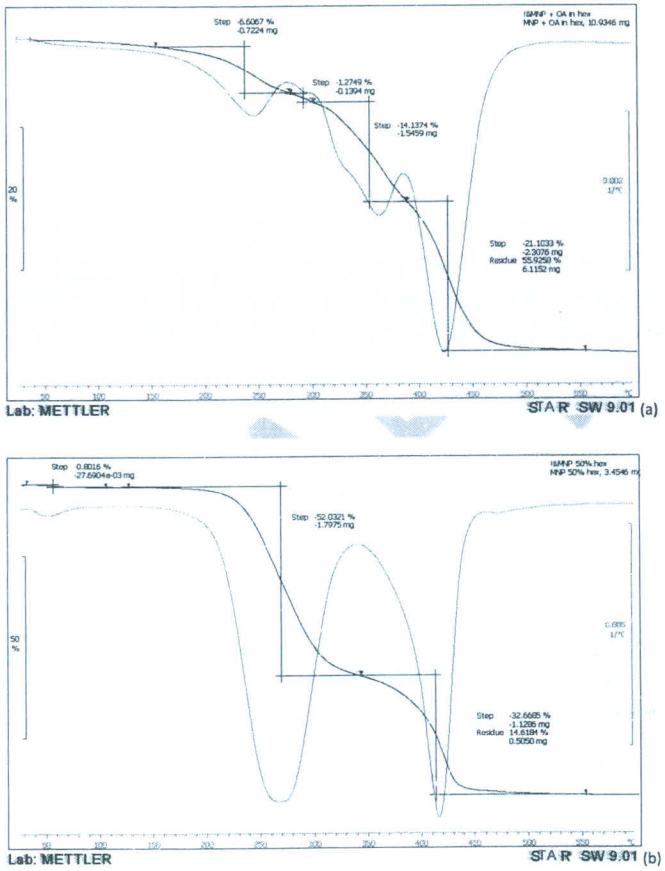


Fig.10 TGA result for (a) MNP+OA in hexane (b) MNP coated with 50% polymer

References

1. Gupta, A.K. and M. Gupta, *Synthesis and surface engineering of iron oxide nanoparticles for biomedical applications.* Biomaterials, 2005. **26**(18): p. 3995-4021.
2. Mahmoudi, M., et al., *Superparamagnetic Iron Oxide Nanoparticles with Rigid Cross-linked Polyethylene Glycol Fumarate Coating for Application in Imaging and Drug Delivery.* The Journal of Physical Chemistry C, 2009. **113**(19): p. 8124-8131.
3. Suh, W.H., et al., *Nanotechnology, nanotoxicology, and neuroscience.* Progress in Neurobiology, 2009. **87**(3): p. 133-170.
4. Corot, C., et al., *Recent advances in iron oxide nanocrystal technology for medical imaging.* Advanced Drug Delivery Reviews, 2006. **58**(14): p. 1471-1504.
5. Ajay K. Gupta, A.C., *Surface Modification of Superparamagnetic Iron Oxide Nanoparticles and Their Intracellular Uptake.* European Cells and Materials, 2002. **4**(Suppl.2): p. 101-102.
6. Sun, C., J.S.H. Lee, and M. Zhang, *Magnetic nanoparticles in MR imaging and drug delivery.* Advanced Drug Delivery Reviews, 2008. **60**(11): p. 1252-1265.
7. Jain, T.K., et al., *Iron Oxide Nanoparticles for Sustained Delivery of Anticancer Agents.* Molecular Pharmaceutics, 2005. **2**(3): p. 194-205.
8. Zhang, X., et al., *Synthesis and characterization of the paclitaxel/MPEG-PLA block copolymer conjugate.* Biomaterials, 2005. **26**(14): p. 2121-2128.
9. Laurent, S., et al., *Magnetic Iron Oxide Nanoparticles: Synthesis, Stabilization, Vectorization, Physicochemical Characterizations, and Biological Applications.* Chemical Reviews, 2008. **108**(6): p. 2064-2110.
10. Venkatraman, S.S., et al., *Micelle-like nanoparticles of PLA-PEG-PLA triblock copolymer as chemotherapeutic carrier.* International Journal of Pharmaceutics, 2005. **298**(1): p. 219-232.
11. Rutnakornpituk, M., et al., *Magnetic core-bilayer shell nanoparticle: A novel vehicle for entrapmentof poorly water-soluble drugs.* Polymer, 2009. **50**(15): p. 3508-3515.
12. Bakandritsos A, M.G., Zboril R, Bouropoulos N, Tucek J, Fatouros DG, Avgoustakis K., *Preparation, stability and cytocompatibility of magnetic/PLA-PEG hybrids.* Nanoscale, 2010. **2**(4).
13. Kayal, S. and R.V. Ramanujan, *Doxorubicin loaded PVA coated iron oxide nanoparticles for targeted drug delivery.* Materials Science and Engineering: C, 2010. **30**(3): p. 484-490.
14. Yasugi, K., et al., *Preparation and characterization of polymer micelles from poly(ethylene glycol)-poly(,-lactide) block copolymers as potential drug carrier.* Journal of Controlled Release, 1999. **62**(1-2): p. 89-100.
15. Liversidge, G.G. and P. Conzentino, *Drug particle size reduction for decreasing gastric irritancy and enhancing absorption of naproxen in rats.* International Journal of Pharmaceutics, 1995. **125**(2): p. 309-313.
16. Maver, U., et al., *Incorporation and release of drug into/from superparamagnetic iron oxide nanoparticles.* Journal of Magnetism and Magnetic Materials, 2009. **321**(19): p. 3187-3192.

Preparation and characterizations of Fe_3O_4 magnetic nanoparticles coated PLA-grafted Chitosan copolymer as potential drug delivery material for naproxen

1. Introduction

Magnetic nanoparticles possess special physical and chemical properties suitable for use in many industrial and biomedical applications. Fe_3O_4 iron oxide nanoparticles can be dispersed in various solvents by using surfactants to assist its suspension present as magnetic nanoparticles colloid in selected media. Many research has been focused on the materials potential use, such as magnetic drug targeting, pigment, recording material, magnetic sensing, and separation, etc [1-4]. Various methods of Fe_3O_4 nanoparticles preparation have been reported in the literatures, such as microemulsions [5], laser ablation [6], high temperature decomposition of organic precursor [7], etc. However, one of the convenient and economical technique is chemical coprecipitation, due to the well-dispersed in water-base solution of Fe_3O_4 (magnetite) nanoparticles, which offers low temperature processing.

Chitosan, β-(1-4) linked 2-amino-2-deoxy-D-glucose, is linear cationic polysaccharide obtained by deacetylation of chitin, which is derived from crab and shrimp shells. This polymer is known to be non-toxic, good biocompatible, highly flexible, and low cost material [8]. As a result, this biopolymer is widely use in many applications, especially in biomedical and agricultural fields. Polylactide (PLA) is aliphatic polyester derived from agricultural sources, such as corn and starch. PLA has attracted vast attention due to its good mechanical properties, bio-degradability and biocompatibility [9]. However, its hydrophobicity limits its use in certain biomedical applications. Combining of PLA and chitosan by copolymerization produces copolymers with improved mechanical properties, adjustable crystallinity and hydrophilicity. In addition, a variation in PLA/Chitosan composition in the copolymer chain results in the change in amphiphilic property of the copolymer, which behave as polymeric surfactant.

Naproxen is a non-steroidal anti-inflammatory drug (NSAID), which possess a very poor water-solubility (0.025mg/ml at 25°C). Several approaches have been attempted to improve the naproxen dissolution properties. Encapsulation is one of the effective procedures. This technique not only provides an enhancement in water solubility of drug by the encapsulation material, but also reduces the irritation of gastrointestinal and provides long lasting release of selected drug as controlled release drug delivery [10]. Chitosan and its derivative have demonstrated as an efficient material to promote dissolution of naproxen [11].

In this study, magnetic nanoparticles coated PLA/Chitosan copolymers are prepared for use as potential drug delivery material for naproxen. The drug–encapsulated magnetic nanoparticles are prepared by one step coating of Fe_3O_4 magnetic nanoparticles synthesized via chemical coprecipitation using ammonium hydroxide ($NH_3.H_2O$) solution. This material is obtained without the use of external surfactant as the PLA/Chitosan copolymer (low molecular weight) functions as encapsulation and coating material and as well as a surfactant. Properties of the drug-encapsulated materials are then characterized.

2. Experimental

2.1. Materials

Ferric chloride anhydrous ($FeCl_3$) and ferrous chloride tetrahydrate ($FeCl_2.4H_2O$) were purchased from Acros organics. Chitosan oligomers (97.0% deacetylation) were obtained from Taming Enterprises Co., Ltd., Thailand. Lactic acid (commercial grade, 10% weight water), n-hexane, and ammonium hydroxide (NH_4OH, 25% of ammonia) were acquired from Carlo Erba reagents. Tin (II) chloride was received from Sigma Aldrich. Naproxen was purchased from Andenex-Chemie GmbH, Germany. All chemicals were analytical grade reagents, and were used without further purification. Deionized water was used throughout this work.

2.2. Synthesis of PLA/Chitosan copolymer

PLA/Chitosan copolymer was synthesized by grafting of PLA chain from hydroxyl groups of chitosan structure employing condensation reaction of lactic acid. Essentially, 100 mL of lactic acid was heated to 120°C for 1 hour. The temperature was increased to 140°C for 1hour, and 1.1 g chitosan (1 wt% of pure lactic acid) was then added to the system. The temperature of the mixture was kept at 140°C for 1 hour, then 0.55 g $SnCl_2$ catalyst (0.2 mol % pure lactic acid) was added. The temperature was kept at 140°C for 3 hours. Vacuum system was applied for 1 hour to remove small molecular weight by products. Consequently brown copolymer in viscous liquid form was obtained.

2.3. Preparation of Fe_3O_4 nanoparticles coated PLA/chitosan copolymer with loaded naproxen

Magnetic nanoparticles were prepared by chemical coprecipitation, where 1 g (0.005 mol) $FeCl_2.4H_2O$ and 1.66 g (0.01 mol) $FeCl_3$ were dissolved in 40 ml of deionization water, then stirred at 350 rpm for 10 min. Ammonium hydroxide (NH_4OH, 25% of ammonia) was then added dropwise to the iron salt solution. Precipitate was observed and the mixture was vigorously stirred for 30 min at room temperature. The Fe_3O_4 precipitate was then washed twice with ethyl alcohol and deionization water. In a separate container, naproxen was dissolved in viscous PLA/Chitosan copolymer and the mixture was heated at 60°C to form a homogeneous phase mixture. The mixture was then added dropwise to the Fe_3O_4 with slowly stirred motion. Subsequently, 20 ml of n-hexane was added to the system as a dispersing medium. Deionized water (100 ml) was added and the mixture was stirred for 30 min to evaporate n-hexane. The resulting magnetic nanoparticles colloid was centrifuged at 2500 rpm for 15 min, and the liquid supernatant was kept as the magnetic nanoparticles dispersed in the water medium.

DRAFT

9.4.5 ณัฐวุฒิ ชนะวงศ์

2.4. Characterizations

2.4.1. X-Ray diffraction

The crystal structure of the magnetic nanoparticles was characterized by X-ray diffraction (XRD) recorded by using a Rigaku TTRAX III diffractometer with CuKα radiation (1.5418 Å). The conditions are $\theta/2\theta$ scan, 50 kV, 300 mA, 0.2°/ step, 2°/min, Ds = Ss = $(\frac{1}{2})°$, fix monochomator, and focusing beam method were used.

2.4.2. TEM and particle size analyzer

The morphology and size of the magnetic nanoparticles were investigated by using transmission electron microscope (JEOL, JEM-2010) at accelerating voltage of 200 keV. The samples were prepared by placing drops of diluted medium dispersed of the nanoparticles on the copper grids. Size distribution was determined by Particles Size Analyzer (ZETA-SIZER, MALVERN Nano-Zs90). The real and imaginary reflective indexes were used at 1.59 and 0.0, respectively. The following parameters were used for the experiment: medium refractive index 1.330, medium viscosity 1.0 mPa.s and a dielectric constant of 80.4. The size analysis of each sample consisted of 30 measurements.

2.4.3. Raman spectroscopy

The liquid sample was dropped on the glass slide and placed into the vacuum oven at room temperature for 24 hours. Then, the magnetic nanoparticles were characterized by using Raman spectroscopy (NT-MDT NTEGRA Spectra). Laser light source is 632.8 nm and confocal raman scanning mode were applied.

2.4.4. Fourier transform infrared spectroscopy (FTIR)

FTIR spectra of the PLA/Chitosan copolymer and naproxen drug were investigated using Fourier Transform Infrared Spectrophotometer (Nicolet 6700 FT-IR).

2.4.5. Vibrating Sample Magnetometer

The magnetic properties were investigated by using room temperature vibrating sample magnetometer (VSM, Lakeshore 7400, Lakeshore) at an applied maximum field of 10,000 G.

3. Results and Discussion

3.1. Particle size distribution and zeta potential

Preliminary study on preparation of Fe_3O_4 magnetic nanoparticles, coated by PLA/chitosan copolymer as a surfactant was conducted by varying MNP/copolymer compositions. Effect of the mixture compositions on average particles size and surface charge of the nanoparticles are shown in Figures 1and 2. Figure 1 shows that average size of the copolymer-coated magnetic nanoparticles increases when Fe_3O_4 contents increases. This reveals that the decrease in copolymer content compared to Fe_3O_4 leads to less effective coating of the copolymer on the nanoparticles surface, resulting in agglomeration of the magnetic particles to form larger particles. Figure 2 shows results from zeta potential of the resulting nanoparticles as a function of pH and weight ratio of Fe_3O_4/ copolymer. The result show that copolymer-coated nanoparticles prepared from different weight ratio contains significantly similar values of surface charge at all composition range, accept at acidic pH of 3, where those prepared from a 1:1 ratio show much higher positive value. Moreover, results on zeta potential of the nanoparticles as a function of pH show moderate negative value at pH 7, indicating appreciable stability of the particles however base solution exhibits more stable particles than acidic and neutral solution. This probably, the charge of the basic solution can assist particles to stabilize in the medium.

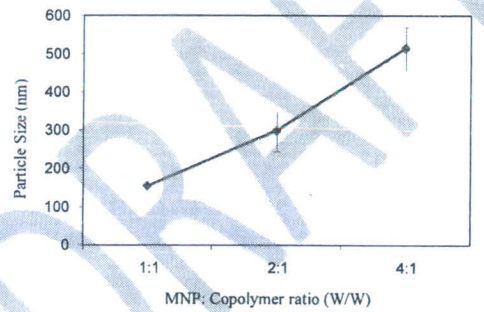


Figure 1. Average size of copolymer-coated magnetic nanoparticles as a function of Fe_3O_4 to copolymer ratios.

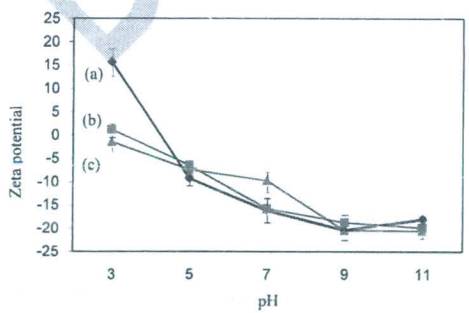


Figure 2. Effect of pH on surface charge of copolymer-coated magnetic nanoparticles prepared from various Fe_3O_4/copolymer ratio: (a) 1.1, (b) 2:1, and (c) 4:1

DRAFT

PLA/Chitosan copolymer-coated MNP with loaded naproxen is then prepared by the same procedure as previous discussed, except that 3 wt% of naproxen is mixed with the copolymer before the coating process. Results on average diameters, yield, and surface charge of the resulting drug-loaded nanoparticles are shown in Figures 3 and 4. The results show that the average size of the nanoparticles decrease from 351 nm to138 nm with an increase in Fe_3O_4/copolymer ratios from 1:1 to 4:1. This is intriguing, as this is opposite to those previously observed in the system not containing naproxen. This is probably due to the presence of naproxen along with PLA/Chitosan copolymer, which prevents the magnetic nanoparticles to aggregate. Yield of suspended magnetic nanoparticles is also determined from weight percentage of suspended particle per original magnetic particle. The yield results show an increasing trend with increasing MNP and the surface charge with loaded naproxen, which enable the particles to be more stable in the neutral solution, compared to the MNP without naproxen. This can be explain in term of naproxen perform as the co-surfactant [12], resulting in the smaller sizes and also make the MNP well disperse in the neutral medium. It has been clearly seen that the magnetic nanoparticles is stable at basic solution (pH>7), from this result, 2:1 ratio was prepared the basic medium in order to study the affect of the particles size and the yield product as a function of pH. Consequently, the results show that percent yield of 2:1 ratio of MNP: PLA/Chitosan with naproxen in basic solution was increased from 59 to 79 percent, and particles size was slightly decreased from 225 nm to 185 nm with the standard deviation is 11.

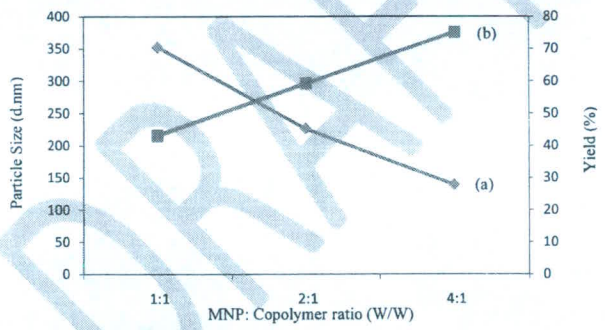


Figure 3. Average size and yield of naproxen-encapsulated magnetic nanoparticles as a function of MNP/copolymer ratios; (a) average particle size and (b) yield.

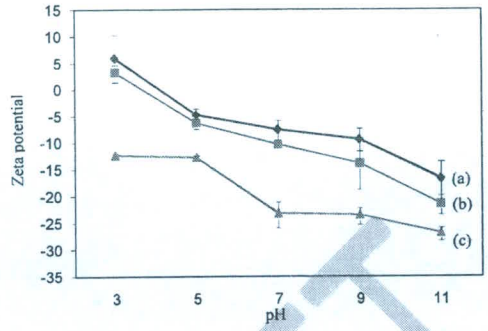


Figure 4. Effect of pH on surface charge of naproxen loaded PLA/Chitosan-MNP; (a) 1.1, (b) 2:1, and (c) 4:1

DRAFT

3.2. Morphology of naproxen loaded PLA/Chitosan-MNP.

TEM images of naproxen-loaded PLA/chitosan-MNP prepared at various MNP/copolymer ratio, shown in Figure 5. The images reveals that at 1:1 MNP/copolymer ratio, cluster of magnetic Fe3O4 nanoparticles are represent in the bulk polymer matrix as shown in Figure 5(a). However, when the 2:1 and 4:1 ratios are used, smaller particles are obtained, especially 4:1 shows the diameters smaller than 20 nm (Figure 5(c)). Moreover, the core shell of 2:1 ratio of MNP: PLA/Chitosan with naproxen in basic medium is also observed, as shown in Figure 5(d). It should be noted that all the pictures that show in Figure 5, the sizes are smaller than the results from the size distribution because of the swelling of the organic phase in the solution we obtained.

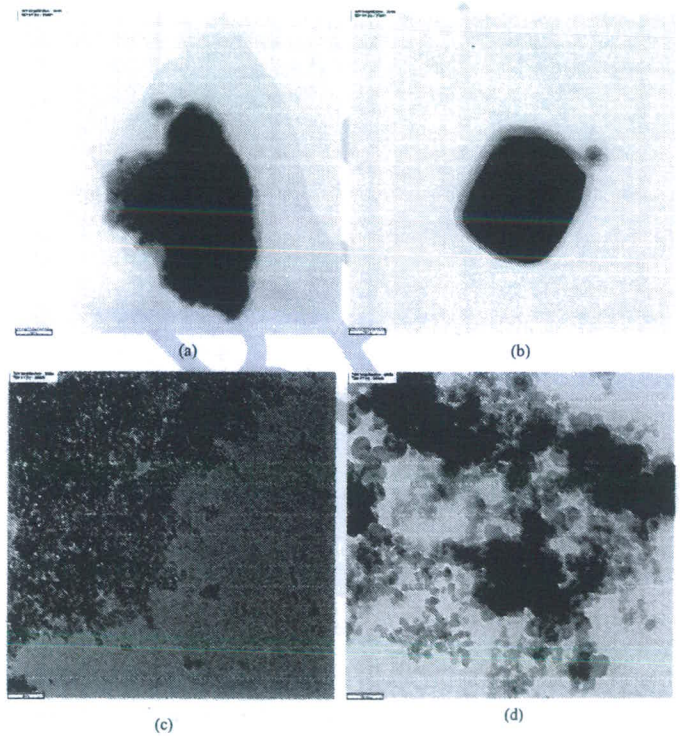


Figure 5. The TEM images of PLA/Chitosan-MNP with naproxen (a) 1:1, (b) 2:1, (c) 4:1 (d) 2:1 in pH 11.

3.3. Confocal Raman spectroscopy of PLA/Chitosan-Fe3O4 with loaded naproxen.

PLA/chitosan-MNP (4:1) with naproxen was investigated by using confocal Raman. Figure 6 shows, the spectra show the pattern of naproxen on PLA/Chitosan-MNP at approximately 2490 cm^{-1}. Depth profile does not clearly show the increasing of naproxen's intensity while increasing of percent penetration as y-axis. Similarly, chitosan intensity does not decrease as increasing the penetration into the samples. This may confirm the idea that naproxen works as co-surfactant for the nanoparticles. It reveals that PLA/Chitosan copolymer and naproxen drug cum together as one phase mixing. Moreover, a model picture for these magnetic nanoparticles as showed in Figure 7.

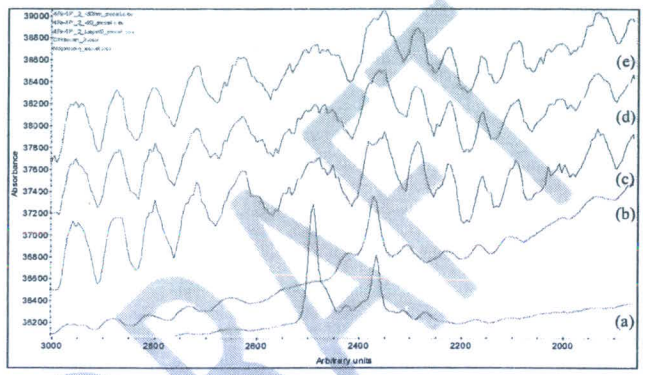


Figure 6. Raman spectra of MNP: Chitosan (4:1) showed: (a) naproxen, (b) chitosan, and confocal spectra of (c) 80 nm, (d)30 nm, and (e) at the surface

Figure 7(a), shows practical spherical core shell as PLA/Chitosan-MNP with loaded naproxen (co-surfactant), one phase mixing of PLA/chitosan and naproxen is observed. However, ideally bilayer outer shell of naproxen in between Fe3O4 and PLA/Chitosan copolymer is not observed.



Figure 7. Model for PLA/Chitosan-MNP with loaded naproxen, (a) one phase mixing, (b) bilayer outer shell.

3.4. Confirmation of unchanged naproxen drug properties by using Fourier transform infrared spectroscopy (FT-IR).

There is not much changed in the spectra of the mixing of PLA/Chitosan and naproxen together as shown in Figure 8(a). However, small shift to the lower wavelength of carbonyl (C=O) peak of PLA/Chitosan at 1750 cm^{-1} was observed. This probably represents the interaction between OH- group of naproxen and the C=O group of PLA/Chitosan copolymer. Therefore, this can be concluded that the properties of naproxen drug are not

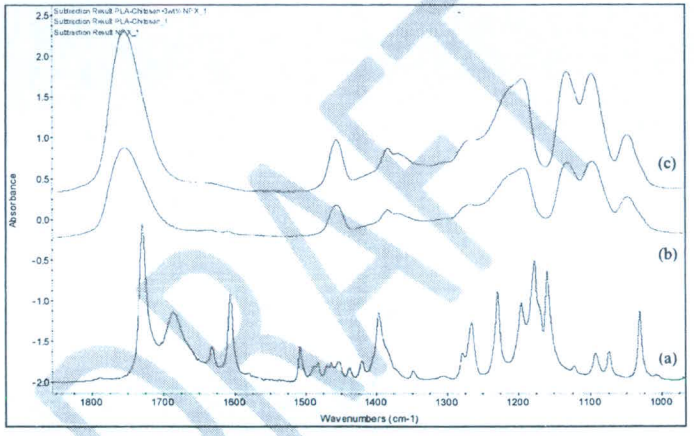


Figure 8. FT-IR spectra of: (a) naproxen, (b) PLA/Chitosan copolymer, and (c) PLA/Chitosan mixed with naproxen drug

3.5. X-ray diffraction

XRD spectra of the resulting nanoparticles are examined. Naproxen-loaded PLA/Chitosan-MNP prepared at a 4:1 ratio clearly shows similar crystallinity characteristics to that of the origin Fe_3O_4 magnetite material, as shown in Figure 9. This reveals that modified MNP with PLA/Chitosan and drug does not changed the form of the magnetite.

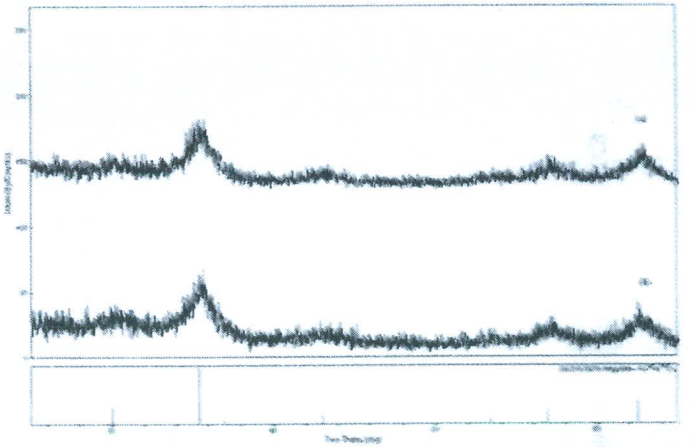


Figure 9. XRD pattern of magnetic nanoparticles of (a) Fe3O4 without coating PLA/Chitosan copolymer and (b) Fe3O4 with coating PLA/Chitosan copolymer and naproxen

DRAFT

3.6. Magnetic properties of PLA/Chitosan-MNP with naproxen.

The magnetization curve of naproxen-loaded Fe_3O_4 nanoparticles is shown in Figure 10. The magnetization curve of 4:1 ratio of PLA/Chitosan-MNP with naproxen is to be without hysteresis, coercivity field and remnant magnetization can be found from the curve. This confirms that PLA/Chitosan-Fe_3O_4 with loaded naproxen shows superparamagnetic properties. The magnetization curve indicates that the saturation magnetization (Ms) of the prepared magnetic nanoparticles is 0.88 emu/g, which is much lower than that of the oleic acid coated MNP (MS of OA-MNP = 32 emu/g), reported in the literature [13]. This probably due to the highly coating thickness by copolymer, this leads to stronger shield effect on the magnetic properties of the nanoparticles. Nonetheless, this material is suitable for use in biomedical applications, as this is conveniently prepared in a one-step process without the use of external surfactant, in which the copolymer acts as both surfactant and biocompatible coating materials.

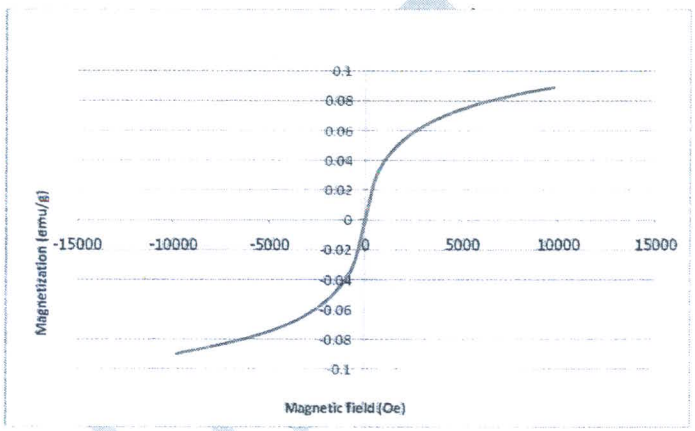


Figure 10. Magnetization curve of 4:1 PLA/Chitosan-MNP with





การประชุมประจำปีเมธีวิจัยอาวุโส สกว. ครั้งที่ 1

ทุนส่งเสริมกลุ่มวิจัย *(ศาสตราจารย์ ดร. ประมวล ตั้งบริบูรณ์รัตน์)*

วันศุกร์ที่ 24 กรกฎาคม 2552

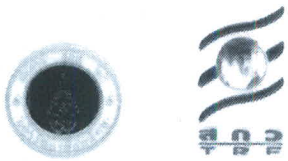
ณ ห้องทวีวัฒนา ชั้น 6 โรงแรมศาลายาพาวิลเลียน มหาวิทยาลัยมหิดล ศาลายา จ.นครปฐม

เวลา	
08.50 - 09.00	เปิดประชุม **ฝ่ายวิชาการ สกว.**
09.00 - 09.10	**แนะนำโครงการวิจัย RTA 5180003 และคณะผู้วิจัย** การปรับแต่งพื้นผิวของพอลิเมอร์และอนุภาคคอลลอยด์เพื่อการประยุกต์ในทางชีวการแพทย์ Surface Modification of Polymers and Colloidal Particles for Biomedical Applications โดย ***เมธีวิจัยอาวุโส สกว. (ศ.ดร.ประมวล ตั้งบริบูรณ์รัตน์)***
09.10 - 09.40	การปรับแต่งพื้นผิวของแผ่นฟิล์มที่เตรียมจากน้ำยางธรรมชาติด้วยอนุภาคนาโน เพื่อพัฒนาการเตรียมถุงมือทางการแพทย์ Surface Modification of Natural Rubber Latex Film by Using Nanoparticles for the Development of Medical Gloves' Preparation โดย ***ศ.ดร.ประมวล ตั้งบริบูรณ์รัตน์*** *วรัญญา อนันต์จรุงสุข (1A) เสาวรีย์ ตันพันตรี (1B)* *จริยา แก้วเสน่หา และณัฐกุล กาญจนถาวร (1C) คณะวิทยาศาสตร์ มหาวิทยาลัยมหิดล*
09.40 – 10.00	การเกิดฟิล์มจากลาเทกซ์ของอนุภาคพอลิเมอร์ผสมและการเชื่อมขวางที่ผิว Film Formation of Latex Blends and Cross-linking at Interface โดย ***ดร.วิรัช ทวีปรีดา*** *คณะวิทยาศาสตร์ มหาวิทยาลัยสงขลานครินทร์* *ชลดา อมรชัยยาพิทักษ์ (1D) คณะวิทยาศาสตร์ มหาวิทยาลัยมหิดล*
10.00 – 10.30	พอลิเมอร์ที่มีหมู่ฟังก์ชันสำหรับใช้ในการตรวจจับยีนและโปรตีนด้วยวิธีทางเคมีลูมิเนสเซนต์บนวัฏภาคของแข็งที่มีความไวสูง Functionalized Biopolymer for Supersensitive Luminescent Detection of Genes and Proteins on a Solid-Phase Membrane โดย ***ดร.สรวง สมานหมู่*** *ศูนย์พันธุวิศวกรรมและเทคโนโลยีชีวภาพแห่งชาติ สวทช.* *วีระชัย นาสัมพันธ์ (1E) คณะวิทยาศาสตร์ มหาวิทยาลัยมหิดล*
10.30 – 10.50	***** พัก อาหารว่าง*****

10.50 – 11.20	การสังเคราะห์และการดัดแปรพื้นผิวอนุภาคนาโนที่มีสมบัติแม่เหล็ก Synthesis and Surface Modification of Magnetic Nanoparticle โดย ***ผศ.ดร.เมธา รัตนากรพิทักษ์*** *คณะวิทยาศาสตร์ มหาวิทยาลัยนเรศวร*
11.20 – 11.50	อนุภาคพอลิเมอร์ขนาดนาโนที่มีสมบัติแม่เหล็กสำหรับใช้ในการตรวจวินิจฉัย Magnetic Polymeric Nanoparticle for Rapid Diagnosis โดย ***ดร.ดวงพร พลพานิช*** *ศูนย์นาโนเทคโนโลยีแห่งชาติ สวทช.* *ลลิดา เจริญมาก (4A) คณะวิทยาศาสตร์ มหาวิทยาลัยมหิดล*
11.50 – 12.20	การแยกแอนติบอดีที่จำเพาะต่อเชื้อมาลาเรียด้วยอนุภาคพอลิเมอร์ขนาดนาโนที่มีสมบัติแม่เหล็ก Magnetic Polymeric Nanoparticle for Separation of Malaria Antibody โดย ***ดร.กุลชาติ จังภัทรพงศา*** *คณะเทคนิคการแพทย์ มหาวิทยาลัยมหิดล* *อฏิชญา จิวะพงศ์วิทูรย์ (4B) คณะวิทยาศาสตร์ มหาวิทยาลัยมหิดล*
12.20 – 13.30	***** อาหารกลางวัน*****
13.30 – 14.00	โคพอลิเมอร์ย่อยสลายได้จากแลคไทด์และการประยุกต์ใช้ประโยชน์ Degradable Lactide-based Copolymers and Their Applications โดย ***ผศ.ดร.ปกรณ์ โอภาประกาสิต*** *ภรณี ศรีรมรื่น (2A) ไท เฮียน เหวียน (2B)* *ชาคริต ธรรมวงศ์ (2C) สถาบันเทคโนโลยีนานาชาติสิรินธร มหาวิทยาลัยธรรมศาสตร์*
14.00 – 14.50	เส้นใยนาโนพอลิเมอร์เพื่อการเลี้ยงเซลล์เนื้อเยื่อ Polymeric Nanofibers for Cell Culture โดย ***รศ.ดร.นพวรรณ ชนัญพนิช*** *ชลลดา สุวรรณบูรณ์ (2D)* *คณะวิทยาศาสตร์ประยุกต์ มหาวิทยาลัยเทคโนโลยีพระจอมเกล้าพระนครเหนือ* ***รศ.ดร.สำรี มั่นเขตกรณ์*** *คณะเทคนิคการแพทย์ มหาวิทยาลัยเชียงใหม่*
14.50 – 15.40	การพัฒนาแผ่นปิดชนิดไวต่อแรงกดที่ทำจากยางธรรมชาติเพื่อประยุกต์ใช้ในทางการแพทย์ Natural Rubber-based Pressure Sensitive Adhesive Patch for Medical Applications โดย ***ดร.สุภา วิรเศรษฐ์*** *ชมพูนุช โชคบุญเปี่ยม (3A) คณะวิทยาศาสตร์ มหาวิทยาลัยมหิดล* ***ดร.รัฐพร ทองกุม*** *นฤดม ศรีสว่าง (3B) คณะวิทยาศาสตร์ มหาวิทยาลัยมหิดล*
15.40 – 17.00	อาหารว่าง และ **Poster Session**

<u>หมายเหตุ</u> **ผู้ที่แจ้งความประสงค์เข้าร่วม ณ 17 กค. 52 จำนวน 106 คน**





การประชุมประจำปีเมธีวิจัยอาวุโส สกว. ครั้งที่ 2

ทุนส่งเสริมกลุ่มวิจัย *(ศาสตราจารย์ ดร. ประมวล ตั้งบริบูรณ์รัตน์)*

วันศุกร์ที่ 30 กรกฎาคม 2553

ณ ห้อง N 101 คณะวิทยาศาสตร์ มหาวิทยาลัยมหิดล พญาไท กรุงเทพมหานคร

08.45 - 09.10	***ลงทะเบียน***
09.10 - 09.30	**Overview โครงการวิจัย Surface Modification of Polymers and Colloidal Particles for Biomedical Applications** ***ศ.ดร.ประมวล ตั้งบริบูรณ์รัตน์*** *คณะวิทยาศาสตร์ มหาวิทยาลัยมหิดล*
09.30 - 09.50	**IL1: R&D on Skim Rubber Latex** ***ดร.สุรพิชญ์ ลอยกุลนันท์*** *ศูนย์เทคโนโลยีโลหะและวัสดุแห่งชาติ สวทช.*
09.50 - 10.05	**OP1: Composite Particle of Disinfectant Nanocapsules – Skim Rubber Latex** ***จริยา แก้วเสน่หา*** *คณะวิทยาศาสตร์ มหาวิทยาลัยมหิดล*
10.05 – 10.25	**IL2: R&D on Epoxidized Natural Rubber** ***ผศ.ดร.นิตยา รัตนโสม*** *สถาบันชีววิทยาศาสตร์โมเลกุล มหาวิทยาลัยมหิดล* P1) *ชนิดา อาภรณ์วิชานพ / พลอยไพลิน น้ำประสานไทย*
10.25 – 10.45	**IL3: Development and Characterization of Backing Film based on Natural Rubber for Transdermal Drug Delivery Patch** ***ดร.สุภา วิรเศรษฐ์*** *คณะวิทยาศาสตร์ มหาวิทยาลัยมหิดล* P2) *ชมพูนุช โชคบุญเปี่ยม*
10.45 – 11.00	******* พัก ... อาหารว่าง*******
11.00 – 11.20	**IL4: Novel Polymer from Natural Rubber and Cellulose** ***ผศ.ดร.สอาด วิยะจันทร์*** *คณะวิทยาศาสตร์ มหาวิทยาลัยสงขลานครินทร์ หาดใหญ่* P3) *อิศรา อินทฤทธิ์*
11.20 – 11.40	**IL5: R&D on Functionalized Colloidal Nanoparticles** ***ดร.พันธ์ญา สุนินทบูรณ์*** *คณะวิทยาศาสตร์ มหาวิทยาลัยมหิดล* P4) *ณัฐกุล กาญจนถาวร*
11.40 – 12.00	**IL6: DNA Detection of Chronic Myelogenous Leukemia by Magnetic Nanoparticles** ***ดร.กุลชาติ จังภัทรพงศา*** *คณะเทคนิคการแพทย์ มหาวิทยาลัยมหิดล*
12.00 – 12.20	**OP2: Primer Bound Magnetic Nanoparticles for Colorimetric Detection of *Vibrio Cholerae*** ***รวีวรรณ ถิรมนัส*** *ศูนย์นาโนเทคโนโลยีแห่งชาติ สวทช.* P5) *ลลิตา เจริญมาก*
12.20 – 13.30	******* อาหารกลางวัน*******
13.30 – 13.50	**IL7: Supersensitive Polymeric Luminescent Probes for Detection of Proteins and DNA on a Solid-Phase Membrane** ***ดร.สรวง สมานหมู่*** *ศูนย์พันธุวิศวกรรมและเทคโนโลยีชีวภาพแห่งชาติ สวทช.*
13.50 – 14.10	**OP3: Selective Fluorescence Sensing of Deoxycytidine 5'-monophosphate (dCMP) employing a bis(diphenylphosphate)diimine ligand** ***วีระชัย นาสัมพันธ์*** *คณะวิทยาศาสตร์ มหาวิทยาลัยมหิดล* P6) *ศมน ตรังคธาร / ณัฐพงษ์ หริวงศานุภาพ*
14.10 – 14.40	**IL8: Lactide-based Copolymers and Their Applications** ***ผศ.ดร.ปกรณ์ โอภาประกาสิต*** *สถาบันเทคโนโลยีนานาชาติสิรินธร มหาวิทยาลัยธรรมศาสตร์* P7) *ภรณี ศรีร่มรื่น* P8) *ชาคริต ธรรมวงศ์* P9) *วิไลรัตน์ ทรัพย์มาก*
14.40 – 15.00	**IL9: PLA-PEG-PLA Triblock Copolymer as Potential Drug Carriers** ***ดร.รัฐพร ทองกุม*** *คณะวิทยาศาสตร์ มหาวิทยาลัยมหิดล* P10) *นฤดม ศรีสว่าง*
15.00 – 16.30	**Poster Session: *ดร.ธรรมสิทธิ์ วงศ์เศรษฐสกุล*** และ P1) - P10)

ผู้เข้าร่วม 134 คน


การประชุมประจำปีมหาวิทยาลัย

รายชื่อกลุ่มวิจัย

เมธีวิจัยอาวุโส สกว. ศาสตราจารย์ ดร. ประมวล ตั้งบริบูรณ์รัตน์ (ณ วันที่ 20 มิย. 2554)

ชื่อ-นามสกุล	เริ่มเข้าร่วมโครงการ			ปัจจุบัน		
	ตำแหน่งวิชาการ	สังกัด	ตำแหน่งในโครงการ	ตำแหน่งวิชาการ	สังกัด	สถานภาพปัจจุบัน
1. ดร.รัชนีย์ อุดมแสงเพ็ชร	ศาสตราจารย์	ภาควิชาพยาธิชีววิทยา คณะวิทยาศาสตร์ มหาวิทยาลัยมหิดล	ที่ปรึกษา	ศาสตราจารย์	ภาควิชาพยาธิชีววิทยา คณะวิทยาศาสตร์ มหาวิทยาลัยมหิดล	ยังอยู่ในโครงการ
2. ดร.เมธา รัตนากรพิทักษ์	ผู้ช่วยศาสตราจารย์	ภาควิชาเคมี คณะวิทยาศาสตร์ มหาวิทยาลัยนเรศวร	ที่ปรึกษา	รองศาสตราจารย์	ภาควิชาเคมี คณะวิทยาศาสตร์ มหาวิทยาลัยนเรศวร	ยังอยู่ในโครงการ
3. นพ.สุรเดช หงส์อิง	รองศาสตราจารย์	ภาควิชากุมารเวชศาสตร์ คณะแพทยศาสตร์ รามาธิบดี มหาวิทยาลัยมหิดล	ที่ปรึกษา	รองศาสตราจารย์	ภาควิชากุมารเวชศาสตร์ คณะแพทยศาสตร์ รามาธิบดี มหาวิทยาลัยมหิดล	ยังอยู่ในโครงการ
4. Dr.Paul E. Orndorff	Professor	Public Health and Pathobiology, College of Veterinary Medicine, North Carolina State University	ที่ปรึกษา	Professor	Public Health and Pathobiology, College of Veterinary Medicine, North Carolina State University	ยังอยู่ในโครงการ
5. Dr.Masaaki Kai	Professor	Faculty of Pharmaceutical Sciences, Nagasaki University	ที่ปรึกษา	Professor	Faculty of Pharmaceutical Sciences, Nagasaki University	ยังอยู่ในโครงการ
6. ดร.นพวรรณ ชนัญพานิช	รองศาสตราจารย์	ภาควิชาเคมีเทคนิค คณะวิทยาศาสตร์และเทคโนโลยี สถาบันเทคโนโลยีพระจอมเกล้า พระนครเหนือ	ที่ปรึกษา	รองศาสตราจารย์	ภาควิชาเคมีเทคนิค คณะวิทยาศาสตร์และเทคโนโลยี สถาบันเทคโนโลยีพระจอมเกล้า พระนครเหนือ	ยังอยู่ในโครงการ

เอกสารแนบ 5.9

7. ดร.นิตยา รัตนโสม	ผู้ช่วยศาสตราจารย์	สถาบันวิจัยและพัฒนา วิทยาศาสตร์และเทคโนโลยี มหาวิทยาลัยมหิดล	ที่ปรึกษา	ผู้ช่วยศาสตราจารย์	ภาควิชาเคมี คณะวิทยาศาสตร์ มหาวิทยาลัยมหิดล	ยังอยู่ในโครงการ
1. ดร.ประมวล ตั้งบริบูรณ์รัตน์	ศาสตราจารย์	ภาควิชาเคมี คณะวิทยาศาสตร์ มหาวิทยาลัยมหิดล	หัวหน้ากลุ่มวิจัย	ศาสตราจารย์	ภาควิชาเคมี คณะวิทยาศาสตร์ มหาวิทยาลัยมหิดล	ยังอยู่ในโครงการ
2. ดร.ปกรณ์ โอภาประกาสิต	ผู้ช่วยศาสตราจารย์	ภาควิชาวิศวกรรมและเทคโนโลยีเคมีชีวภาพ สถาบันเทคโนโลยีนานาชาติสิรินธร (SIIT) มหาวิทยาลัยธรรมศาสตร์	นักวิจัย	รองศาสตราจารย์	ภาควิชาวิศวกรรมและเทคโนโลยีเคมีชีวภาพ สถาบันเทคโนโลยีนานาชาติสิรินธร มหาวิทยาลัยธรรมศาสตร์	ยังอยู่ในโครงการ
3. ดร.อทิตย์สา เพ็ชรสุข	-	ศูนย์เทคโนโลยีโลหะและวัสดุแห่งชาติ สำนักงานพัฒนาวิทยาศาสตร์และเทคโนโลยีแห่งชาติ	นักวิจัย	-	ศูนย์เทคโนโลยีโลหะและวัสดุแห่งชาติ สำนักงานพัฒนาวิทยาศาสตร์และเทคโนโลยีแห่งชาติ	ยังอยู่ในโครงการ
4. ดร.มัณฑนา โอภาประกาสิต	อาจารย์	ภาควิชาวัสดุศาสตร์ คณะวิทยาศาสตร์ จุฬาลงกรณ์มหาวิทยาลัย	นักวิจัย	ผู้ช่วยศาสตราจารย์	ภาควิชาวัสดุศาสตร์ คณะวิทยาศาสตร์ จุฬาลงกรณ์มหาวิทยาลัย	ยังอยู่ในโครงการ
5. ดร.ไพบูลย์ ศรีอรุโณทัย	อาจารย์	ภาควิชาวิศวกรรมและเทคโนโลยีเคมีชีวภาพ สถาบันเทคโนโลยีนานาชาติสิรินธร มหาวิทยาลัยธรรมศาสตร์	นักวิจัย	อาจารย์	ภาควิชาวิศวกรรมและเทคโนโลยีเคมีชีวภาพ สถาบันเทคโนโลยีนานาชาติสิรินธร มหาวิทยาลัยธรรมศาสตร์	ยังอยู่ในโครงการ
6. ดร.สรวง สมานหมู่	-	ศูนย์พันธุวิศวกรรมและเทคโนโลยีชีวภาพแห่งชาติ สำนักงานพัฒนาวิทยาศาสตร์และเทคโนโลยีแห่งชาติ	นักวิจัย	นักวิจัย 1	ศูนย์พันธุวิศวกรรมและเทคโนโลยีชีวภาพแห่งชาติ สำนักงานพัฒนาวิทยาศาสตร์และเทคโนโลยีแห่งชาติ	ยังอยู่ในโครงการ

7. ดร.สอาด ริยะจันทร์	ผู้ช่วยศาสตราจารย์	ภาควิชาวิทยาศาสตร์และเทคโนโลยีวัสดุ คณะวิทยาศาสตร์ มหาวิทยาลัยสงขลานครินทร์	นักวิจัย	ผู้ช่วยศาสตราจารย์	ภาควิชาวิทยาศาสตร์และเทคโนโลยีวัสดุ คณะวิทยาศาสตร์ มหาวิทยาลัยสงขลานครินทร์	ยังอยู่ในโครงการ
8. ดร.รัฐพร ทองกุม	อาจารย์	ภาควิชาเคมี คณะวิทยาศาสตร์ มหาวิทยาลัยมหิดล	นักวิจัย	ผู้ช่วยศาสตราจารย์	ภาควิชาเคมี คณะวิทยาศาสตร์ มหาวิทยาลัยมหิดล	ยังอยู่ในโครงการ
9. ดร.สุภา วิรเศรษฐ์	อาจารย์	ภาควิชาเคมี คณะวิทยาศาสตร์ มหาวิทยาลัยมหิดล	นักวิจัย	อาจารย์	ภาควิชาเคมี คณะวิทยาศาสตร์ มหาวิทยาลัยมหิดล	ยังอยู่ในโครงการ
10. ดร.ดวงพร พลพานิช	-	ศูนย์นาโนเทคโนโลยีแห่งชาติ สำนักงานพัฒนาวิทยาศาสตร์และเทคโนโลยีแห่งชาติ	นักวิจัย	นักวิจัย 1	ศูนย์นาโนเทคโนโลยีแห่งชาติ สำนักงานพัฒนาวิทยาศาสตร์และเทคโนโลยีแห่งชาติ	ยังอยู่ในโครงการ
11. ดร.กุลชาติ จังภัทรพงศา	อาจารย์	ภาควิชาจุลชีววิทยาคลินิก คณะเทคนิคการแพทย์ มหาวิทยาลัยมหิดล	นักวิจัย	ผู้ช่วยศาสตราจารย์	ศูนย์วิจัยพัฒนานวัตกรรมและถ่ายทอดเทคโนโลยี คณะเทคนิคการแพทย์ มหาวิทยาลัยมหิดล	ยังอยู่ในโครงการ
12. ดร.วิชนันท์ แย้มกมล	อาจารย์	ภาควิชาจุลทรรศนศาสตร์คลินิก คณะเทคนิคการแพทย์ มหาวิทยาลัยมหิดล	นักวิจัย	อาจารย์	ศูนย์วิจัยพัฒนานวัตกรรมและถ่ายทอดเทคโนโลยี คณะเทคนิคการแพทย์ มหาวิทยาลัยมหิดล	ยังอยู่ในโครงการ
13. นางสาวรวีวรรณ ถิรมนัส	-	ศูนย์นาโนเทคโนโลยีแห่งชาติ สำนักงานพัฒนาวิทยาศาสตร์และเทคโนโลยีแห่งชาติ	ผู้ช่วยนักวิจัย	ผู้ช่วยนักวิจัย 2	ศูนย์นาโนเทคโนโลยีแห่งชาติ สำนักงานพัฒนาวิทยาศาสตร์และเทคโนโลยีแห่งชาติ	ยังอยู่ในโครงการ

14. ดร.วิรัช ทวีปรีดา	อาจารย์	สาขาวิชาวิทยาศาสตร์พอลิเมอร์ คณะวิทยาศาสตร์ มหาวิทยาลัยสงขลานครินทร์	นักวิจัย	อาจารย์	สาขาวิชาวิทยาศาสตร์พอลิเมอร์ คณะวิทยาศาสตร์ มหาวิทยาลัยสงขลานครินทร์	ไม่อยู่ในโครงการ
1. นางสาวชลลดา อมรชัยยาพิทักษ์	-	ภาควิชาเคมี (สาขาวิทยาศาสตร์และเทคโนโลยีพอลิเมอร์) คณะวิทยาศาสตร์ มหาวิทยาลัยมหิดล	นักศึกษาปริญญาโท	-	ศูนย์เทคโนโลยีโลหะและวัสดุแห่งชาติ สำนักงานพัฒนาวิทยาศาสตร์และเทคโนโลยีแห่งชาติ	สำเร็จการศึกษา
2. นางสาววรัญญา อนันต์จรุงสุข	-	ภาควิชาเคมี (สาขาวิทยาศาสตร์และเทคโนโลยีพอลิเมอร์) คณะวิทยาศาสตร์ มหาวิทยาลัยมหิดล	นักศึกษาปริญญาโท	-	หจก. เหรียญทองการพิมพ์	สำเร็จการศึกษา
4. นางสาวเสาวรีย์ ตันพันตรี	-	ภาควิชาเคมี (สาขาวิทยาศาสตร์และเทคโนโลยีพอลิเมอร์) คณะวิทยาศาสตร์ มหาวิทยาลัยมหิดล	นักศึกษาปริญญาโท	-	บริษัท Siam Modified Starch	สำเร็จการศึกษา
5. นางสาวลลิดา เจริญมาก	-	ภาควิชาเคมี (สาขาวิทยาศาสตร์และเทคโนโลยีพอลิเมอร์) คณะวิทยาศาสตร์ มหาวิทยาลัยมหิดล	นักศึกษาปริญญาโท (ได้รับทุน TGIST จาก สวทช.)	-	*อยู่ระหว่างการสมัครงาน*	สำเร็จการศึกษา
6. นายอิศรา อินทฤทธิ์	-	ภาควิชาวิทยาศาสตร์และเทคโนโลยีวัสดุ คณะวิทยาศาสตร์ มหาวิทยาลัยสงขลานครินทร์	นักศึกษาปริญญาโท	-	ประกอบอาชีพอิสระ	สำเร็จการศึกษา
7. นางสาวเหงียน ไท เฮียน	-	ภาควิชาวิศวกรรมและเทคโนโลยีเคมีชีวภาพ สถาบันเทคโนโลยีนานาชาติสิรินธร	นักศึกษาปริญญาโท (ได้รับทุน	-	กลับประเทศเวียดนาม	สำเร็จการศึกษา

		มหาวิทยาลัยธรรมศาสตร์	จาก SIIT มูลนิธิ SCG)			
8. นายอรรถพล กอเดช	-	ภาควิชาวิศวกรรมและเทคโนโลยีเคมีชีวภาพ สถาบันเทคโนโลยีนานาชาติสิรินธร มหาวิทยาลัยธรรมศาสตร์	นักศึกษาปริญญาโท	-		สำเร็จการศึกษา
9. นายสิทธิวัฒน์ กิจเสถียรกุล	-	ภาควิชาวิศวกรรมและเทคโนโลยีเคมีชีวภาพ สถาบันเทคโนโลยีนานาชาติสิรินธร มหาวิทยาลัยธรรมศาสตร์	นักศึกษาปริญญาโท	-		สำเร็จการศึกษา
10. นางสาวจริยา แก้วเสน่หา	-	ภาควิชาเคมี (สาขาวิทยาศาสตร์และเทคโนโลยีพอลิเมอร์) คณะวิทยาศาสตร์ มหาวิทยาลัยมหิดล	นักศึกษาปริญญาโท	-	ภาควิชาเคมี (สาขาวิทยาศาสตร์และเทคโนโลยีพอลิเมอร์) คณะวิทยาศาสตร์ มหาวิทยาลัยมหิดล	สำเร็จการศึกษาปริญญาโท แล้วศึกษาต่อเป็นนักศึกษาปริญญาเอก (ได้รับทุน คปก.) ยังอยู่ในโครงการ
11. นายวีระชัย นาสัมพันธ์	-	ภาควิชาเคมี (สาขาวิทยาศาสตร์และเทคโนโลยีพอลิเมอร์) คณะวิทยาศาสตร์ มหาวิทยาลัยมหิดล	นักศึกษาปริญญาเอก (ได้รับทุน พสวท.)	-	ภาควิชาเคมี (สาขาวิทยาศาสตร์และเทคโนโลยีพอลิเมอร์) คณะวิทยาศาสตร์ มหาวิทยาลัยมหิดล	นักศึกษาปริญญาเอก ยังอยู่ในโครงการ
12. นางสาวสุกัญญา เหนือแสน	-	ภาควิชาเคมี คณะวิทยาศาสตร์ มหาวิทยาลัยมหิดล	นักศึกษาปริญญาเอก	-	ภาควิชาเคมี คณะวิทยาศาสตร์ มหาวิทยาลัยมหิดล	นักศึกษาปริญญาเอก จะขอรับทุน คปก. ยังอยู่ในโครงการ

13. นายนฤดม ศรีสว่าง	-	หลักสูตรวิทยาศาสตร์ และวิศวกรรมวัสดุ คณะวิทยาศาสตร์ มหาวิทยาลัยมหิดล	นักศึกษา ปริญญาโท	-	หลักสูตรวิทยาศาสตร์ และวิศวกรรมวัสดุ คณะวิทยาศาสตร์ มหาวิทยาลัยมหิดล	Transfer เป็น นักศึกษาปริญญาเอก ยังอยู่ในโครงการ
14. นางสาวภฤษฎี สุขพ่วง	-	ภาควิชาวัสดุศาสตร์ คณะวิทยาศาสตร์ จุฬาลงกรณ์มหาวิทยาลัย	นักศึกษา ปริญญาเอก	-	ภาควิชาวัสดุศาสตร์ คณะวิทยาศาสตร์ จุฬาลงกรณ์มหาวิทยาลัย	นักศึกษา ปริญญาเอก ยังอยู่ในโครงการ
15. นางสาวศิริพร บุญพา	-	ภาควิชาวิศวกรรมและเทคโนโลยี เคมีชีวภาพ สถาบันเทคโนโลยี นานาชาติสิรินธร มหาวิทยาลัยธรรมศาสตร์	นักศึกษา ปริญญาเอก (ได้รับทุน จาก JGSEE)	-	ภาควิชาวิศวกรรมและเทคโนโลยี เคมีชีวภาพ สถาบันเทคโนโลยี นานาชาติสิรินธร มหาวิทยาลัยธรรมศาสตร์	นักศึกษา ปริญญาเอก ยังอยู่ในโครงการ
16. นายทวีศักดิ์ บุญสด	-	ภาควิชาวิศวกรรมและเทคโนโลยี เคมีชีวภาพ สถาบันเทคโนโลยี นานาชาติสิรินธร มหาวิทยาลัยธรรมศาสตร์	นักศึกษา ปริญญาเอก (ได้รับทุน จาก JGSEE)	-	ภาควิชาวิศวกรรมและเทคโนโลยี เคมีชีวภาพ สถาบันเทคโนโลยี นานาชาติสิรินธร มหาวิทยาลัยธรรมศาสตร์	นักศึกษา ปริญญาเอก ยังอยู่ในโครงการ
17. นางภารณี ศรีรมรื่น	-	ภาควิชาวิศวกรรมและเทคโนโลยี เคมีชีวภาพ สถาบันเทคโนโลยี นานาชาติสิรินธร มหาวิทยาลัยธรรมศาสตร์	นักศึกษา ปริญญาเอก (ได้รับทุน จาก สกอ.)	-	ภาควิชาวิศวกรรมและเทคโนโลยี เคมีชีวภาพ สถาบันเทคโนโลยี นานาชาติสิรินธร มหาวิทยาลัยธรรมศาสตร์	นักศึกษา ปริญญาเอก ยังอยู่ในโครงการ
18. นายมนตรี นามขจร	-	ภาควิชาวิศวกรรมและเทคโนโลยี เคมีชีวภาพ สถาบันเทคโนโลยี นานาชาติสิรินธร มหาวิทยาลัยธรรมศาสตร์	นักศึกษา ปริญญาโท	-	มหาวิทยาลัยมหิดล	สำเร็จการศึกษา ปริญญาโท แล้วศึกษาต่อเป็น นักศึกษาปริญญาเอก
19. นายชาคริต ธรรมวงศ์	-	ภาควิชาวิศวกรรมและเทคโนโลยี เคมีชีวภาพ สถาบันเทคโนโลยี	นักศึกษา ปริญญาโท	-	ภาควิชาวิศวกรรมและเทคโนโลยี เคมีชีวภาพ สถาบันเทคโนโลยี	นักศึกษา ปริญญาโท

		นานาชาติสิรินธร มหาวิทยาลัยธรรมศาสตร์			นานาชาติสิรินธร มหาวิทยาลัยธรรมศาสตร์	ยังอยู่ในโครงการ
20.นางสาววิไลรัตน์ ทรัพย์มาก	-	ภาควิชาวิศวกรรมและเทคโนโลยี เคมีชีวภาพ สถาบันเทคโนโลยี นานาชาติสิรินธร มหาวิทยาลัยธรรมศาสตร์	นักศึกษา ปริญญาโท	-	ภาควิชาวิศวกรรมและเทคโนโลยี เคมีชีวภาพ สถาบันเทคโนโลยี นานาชาติสิรินธร มหาวิทยาลัยธรรมศาสตร์	นักศึกษา ปริญญาโท ยังอยู่ในโครงการ
21. นางสาวชมพูนุช โชคบุญเปี่ยม	-	ภาควิชาเคมี (สาขาวิทยาศาสตร์ และเทคโนโลยีพอลิเมอร์) คณะวิทยาศาสตร์ มหาวิทยาลัยมหิดล	นักศึกษา ปริญญาโท	-	ภาควิชาเคมี (สาขา วิทยาศาสตร์ และเทคโนโลยี พอลิเมอร์) คณะวิทยาศาสตร์ มหาวิทยาลัยมหิดล	นักศึกษา ปริญญาโท ยังอยู่ในโครงการ
22. นางสาวณัฐกุล กาญจนถาวร	-	ภาควิชาเคมี (สาขาวิทยาศาสตร์ และเทคโนโลยีพอลิเมอร์) คณะวิทยาศาสตร์ มหาวิทยาลัยมหิดล	นักศึกษา ปริญญาโท	-	ภาควิชาเคมี (สาขา วิทยาศาสตร์และเทคโนโลยี พอลิเมอร์) คณะวิทยาศาสตร์ มหาวิทยาลัยมหิดล	นักศึกษา ปริญญาโท ยังอยู่ในโครงการ
23. นางสาวศมน ตรังคธาร	-	ภาควิชาเคมี (สาขาวิทยาศาสตร์ และเทคโนโลยีพอลิเมอร์) คณะวิทยาศาสตร์ มหาวิทยาลัยมหิดล	นักศึกษา ปริญญาโท	-	ภาควิชาเคมี (สาขา วิทยาศาสตร์และเทคโนโลยี พอลิเมอร์)คณะวิทยาศาสตร์ มหาวิทยาลัยมหิดล	นักศึกษา ปริญญาโท ยังอยู่ในโครงการ
24. นางสาวธนิดา อาภรณ์วิชานพ	-	ภาควิชาเคมี คณะวิทยาศาสตร์ มหาวิทยาลัยมหิดล	นักศึกษา ปริญญาตรี	-	ภาควิชาเคมี (สาขา วิทยาศาสตร์และเทคโนโลยี พอลิเมอร์) คณะวิทยาศาสตร์ มหาวิทยาลัยมหิดล	สำเร็จการศึกษา ปริญญาตรี แล้วศึกษาต่อเป็น นักศึกษาปริญญาโท ยังอยู่ในโครงการ
25. นายณัฐพงษ์ หริวงศานุภาพ	-	ภาควิชาเคมี คณะวิทยาศาสตร์	นักศึกษา ปริญญาตรี	-	ภาควิชาเคมี (สาขา วิทยาศาสตร์และเทคโนโลยี	สำเร็จการศึกษา ปริญญาตรี

		มหาวิทยาลัยมหิดล	(ได้รับทุน YSTP จาก สวทช.)		พอลิเมอร์) คณะวิทยาศาสตร์ มหาวิทยาลัยมหิดล	แล้วศึกษาต่อเป็นนักศึกษาปริญญาโท ยังอยู่ในโครงการ
26. นายณัฐพงศ์ พรหมะวัน	-	ภาควิชาเคมี คณะวิทยาศาสตร์ มหาวิทยาลัยมหิดล	นักศึกษาปริญญาตรี	-	หลักสูตรวิทยาศาสตร์และวิศวกรรมวัสดุ คณะวิทยาศาสตร์ มหาวิทยาลัยมหิดล	สำเร็จการศึกษาปริญญาตรี แล้วศึกษาต่อเป็นนักศึกษาปริญญาโท ยังอยู่ในโครงการ
27. นายเธียรรัตน์ ตั้งไชยคีรี	-	ภาควิชาจุลชีววิทยาคลินิก คณะเทคนิคการแพทย์ มหาวิทยาลัยมหิดล	นักศึกษาปริญญาตรี	-	ศูนย์วิจัยพัฒนานวัตกรรมและถ่ายทอดเทคโนโลยี คณะเทคนิคการแพทย์ มหาวิทยาลัยมหิดล	สำเร็จการศึกษาปริญญาตรี แล้วศึกษาต่อเป็นนักศึกษาปริญญาโท ยังอยู่ในโครงการ
28. นางสาวญาณภัทร แม้นถาวรศิริ	-	ภาควิชาปรสิตวิทยา คณะเทคนิคการแพทย์ มหาวิทยาลัยมหิดล	นักศึกษาปริญญาตรี	-	ศูนย์วิจัยพัฒนานวัตกรรมและถ่ายทอดเทคโนโลยี คณะเทคนิคการแพทย์ มหาวิทยาลัยมหิดล	สำเร็จการศึกษาปริญญาตรี แล้วศึกษาต่อเป็นนักศึกษาปริญญาโท (ได้รับทุน TGIST จาก สวทช.) ยังอยู่ในโครงการ
29. นายชัชชนก ชูสวัสดิ์	-	ภาควิชาวิศวกรรมและเทคโนโลยีเคมีชีวภาพ สถาบันเทคโนโลยีนานาชาติสิรินธร มหาวิทยาลัยธรรมศาสตร์	นักศึกษาปริญญาตรี	-	ภาควิชาวิศวกรรมและเทคโนโลยีเคมีชีวภาพ สถาบันเทคโนโลยีนานาชาติสิรินธร มหาวิทยาลัยธรรมศาสตร์	นักศึกษาปริญญาตรี ยังอยู่ในโครงการ

30. นายภวิศ ตั้งวิรุฬห์	-	ภาควิชาวิศวกรรมและเทคโนโลยีเคมีชีวภาพ สถาบันเทคโนโลยีนานาชาติสิรินธร มหาวิทยาลัยธรรมศาสตร์	นักศึกษาปริญญาตรี	-	ภาควิชาวิศวกรรมและเทคโนโลยีเคมีชีวภาพ สถาบันเทคโนโลยีนานาชาติสิรินธร มหาวิทยาลัยธรรมศาสตร์	นักศึกษาปริญญาตรียังอยู่ในโครงการ
31. นายณัฐพล สมานุกูล	-	ภาควิชาวิศวกรรมและเทคโนโลยีเคมีชีวภาพ สถาบันเทคโนโลยีนานาชาติสิรินธร มหาวิทยาลัยธรรมศาสตร์	นักศึกษาปริญญาตรี	-	ภาควิชาวิศวกรรมและเทคโนโลยีเคมีชีวภาพ สถาบันเทคโนโลยีนานาชาติสิรินธร มหาวิทยาลัยธรรมศาสตร์	นักศึกษาปริญญาตรียังอยู่ในโครงการ
32. นายปฐมพงศ์ เวศอุไร	-	ภาควิชาปรสิตวิทยา คณะเทคนิคการแพทย์ มหาวิทยาลัยมหิดล	นักศึกษาปริญญาตรี (ได้รับทุน YSTP จาก สวทช.)	-	ภาควิชาชีวเคมี คณะวิทยาศาสตร์ มหาวิทยาลัยมหิดล	สำเร็จการศึกษาปริญญาตรีแล้วศึกษาต่อเป็นนักศึกษาปริญญาโท (ได้รับทุน TGIST จาก สวทช.)
33. นางสาวอัจฉราวลัย พรเจริญ	-	ศูนย์วิจัยพัฒนานวัตกรรมและการถ่ายทอดเทคโนโลยี คณะเทคนิคการแพทย์ มหาวิทยาลัยมหิดล	นักศึกษาปริญญาตรี	-	ศูนย์วิจัยพัฒนานวัตกรรมและการถ่ายทอดเทคโนโลยี คณะเทคนิคการแพทย์ มหาวิทยาลัยมหิดล	นักศึกษาปริญญาตรี (ได้รับทุน YSTP จาก สวทช.)
34. นายยุรนันท์ ดิษฐโรจน์	-	ภาควิชาจุลชีววิทยาคลินิก คณะเทคนิคการแพทย์ มหาวิทยาลัยมหิดล	นักศึกษาปริญญาตรี (ได้รับทุน YSTP จาก สวทช.)	-	ภาควิชาจุลทรรศนศาสตร์คลินิก คณะเทคนิคการแพทย์ มหาวิทยาลัยมหิดล	สำเร็จการศึกษาปริญญาตรีแล้วศึกษาต่อเป็นนักศึกษาปริญญาโท
35. นางสาวจุฑารัตน์ เพ็งอ้น	-	ภาควิชาจุลชีววิทยาคลินิก คณะเทคนิคการแพทย์ มหาวิทยาลัยมหิดล	นักศึกษาปริญญาตรี	-	ภาควิชาจุลทรรศนศาสตร์คลินิก คณะเทคนิคการแพทย์ มหาวิทยาลัยมหิดล	สำเร็จการศึกษาปริญญาตรีแล้วศึกษาต่อเป็น

						นักศึกษาปริญญาโท (ได้รับทุน TGIST จาก สวทช.)
36. นางสาวศศิธร พรหมวัลย์	-	ภาควิชาจุลชีววิทยาคลินิก คณะเทคนิคการแพทย์ มหาวิทยาลัยมหิดล	นักศึกษาปริญญาตรี (ได้รับทุน YSTP จาก สวทช.	-	มหาวิทยาลัยศิลปากร	สำเร็จการศึกษาปริญญาตรี แล้วศึกษาต่อเป็นนักศึกษาปริญญาโท
37. นายภูเบศร์ นิ่มปุญญกำพงษ์	-	ภาควิชาวิศวกรรมและเทคโนโลยีเคมีชีวภาพ สถาบันเทคโนโลยีนานาชาติสิรินธร มหาวิทยาลัยธรรมศาสตร์	นักศึกษาปริญญาตรี	-	ศึกษาต่อปริญญาโท University of Manchester	สำเร็จการศึกษาปริญญาตรี แล้วศึกษาต่อเป็นนักศึกษาปริญญาโท
38. นางสาวชลกาญจน์ ศุภสุธีกุล	-	ภาควิชาวิศวกรรมและเทคโนโลยีเคมีชีวภาพ สถาบันเทคโนโลยีนานาชาติสิรินธร มหาวิทยาลัยธรรมศาสตร์	นักศึกษาปริญญาตรี	-	ศึกษาต่อปริญญาโท University of Manchester	สำเร็จการศึกษาปริญญาตรี แล้วศึกษาต่อเป็นนักศึกษาปริญญาโท
39. นางสาวกุลจิรา อิทธิอมรกุล	-	ภาควิชาวิศวกรรมและเทคโนโลยีเคมีชีวภาพ สถาบันเทคโนโลยีนานาชาติสิรินธร มหาวิทยาลัยธรรมศาสตร์	นักศึกษาปริญญาตรี		ศึกษาต่อปริญญาโท ประเทศอังกฤษ	สำเร็จการศึกษาปริญญาตรี แล้วศึกษาต่อเป็นนักศึกษาปริญญาโท
40. นายสุพัฒน์ กัมมาระบุตร		ภาควิชาวิศวกรรมและเทคโนโลยีเคมีชีวภาพ สถาบันเทคโนโลยีนานาชาติสิรินธร มหาวิทยาลัยธรรมศาสตร์	นักศึกษาปริญญาตรี		ศึกษาต่อปริญญาโท ประเทศอังกฤษ	สำเร็จการศึกษาปริญญาตรี แล้วศึกษาต่อเป็นนักศึกษาปริญญาโท

41. นายปกรณ์ ไตรประเสริฐพงศ์		ภาควิชาวิศวกรรมและเทคโนโลยี เคมีชีวภาพ สถาบันเทคโนโลยี นานาชาติสิรินธร มหาวิทยาลัยธรรมศาสตร์	นักศึกษา ปริญญาตรี		บริษัทปูนซิเมนต์ไทย	สำเร็จการศึกษา
42. นางสาวกิรศิกานท์ ดาบคำ	-	ภาควิชาจุลชีววิทยาคลินิก คณะเทคนิคการแพทย์ มหาวิทยาลัยมหิดล	นักศึกษา ปริญญาตรี	-	โรงพยาบาลเปาโล	สำเร็จการศึกษา
43. นางสาวภาวิณี โตดเครือ	-	ภาควิชาจุลชีววิทยาคลินิก คณะเทคนิคการแพทย์ มหาวิทยาลัยมหิดล	นักศึกษา ปริญญาตรี	-	โรงพยาบาลนครธน	สำเร็จการศึกษา
44. นายสรยุทธ ฉัตรากาญจน์	-	ภาควิชาปรสิตวิทยา คณะเทคนิคการแพทย์ มหาวิทยาลัยมหิดล	นักศึกษา ปริญญาตรี	-	สถาบันวิจัยจุฬาภรณ์ (ในตำแหน่งผู้ช่วยวิจัย)	สำเร็จการศึกษา
45. นายสุธีรพล ปิงใจ	-	ภาควิชาปรสิตวิทยา คณะเทคนิคการแพทย์ มหาวิทยาลัยมหิดล	นักศึกษา ปริญญาตรี	-	โรงพยาบาลธนบุรี	สำเร็จการศึกษา
46. นางสาวอธิษฐาน ยศสงคราม	-	ภาควิชาจุลทรรศนศาสตร์คลินิก คณะเทคนิคการแพทย์ มหาวิทยาลัยมหิดล	นักศึกษา ปริญญาตรี	-	สถาบันแห่งชาติเพื่อ พัฒนาเด็กและครอบครัว มหาวิทยาลัยมหิดล	สำเร็จการศึกษา
47. นางสาววราภรณ์ เที่ยงธรรม	-	ภาควิชาจุลทรรศนศาสตร์คลินิก คณะเทคนิคการแพทย์ มหาวิทยาลัยมหิดล	นักศึกษา ปริญญาตรี	-	ประกอบอาชีพอิสระ	สำเร็จการศึกษา
48. นายนิติกร อ่อนหวาน	-	ภาควิชาเคมี คณะวิทยาศาสตร์ มหาวิทยาลัยมหิดล	นักศึกษา ปริญญาตรี	-	บริษัท ทีโอเอ	สำเร็จการศึกษา

49. นางสาวชนิตา แสงสุขวาว	-	ภาควิชาเคมี คณะวิทยาศาสตร์ มหาวิทยาลัยมหิดล	นักศึกษา ปริญญาตรี	-	เข้าร่วมโครงการแลกเปลี่ยน ประสบการณ์ที่ต่างประเทศ	สำเร็จการศึกษา
50. นางสาวอัญชนา นิ่มอนุสสรณ์กุล	-	ภาควิชาเคมี คณะวิทยาศาสตร์ มหาวิทยาลัยมหิดล	นักศึกษา ปริญญาตรี	-	ได้รับทุน สควค. หลักสูตร ประกาศนียบัตรบัณฑิตวิชาชีพ ครู (ป.บัณฑิต) มหาวิทยาลัย ศรีนครินทรวิโรฒ	สำเร็จการศึกษา
51. นายดลยา สาบวช	-	ภาควิชาวิทยาศาสตร์และเทคโนโลยี วัสดุ คณะวิทยาศาสตร์ มหาวิทยาลัยสงขลานครินทร์	นักศึกษา ปริญญาตรี	-	ทำงานโรงงานยาง จ.สงขลา	สำเร็จการศึกษา

หมายเหตุ

สังกัด ให้ใส่รายละเอียดที่อยู่ต้นสังกัด เช่น ภาควิชา/คณะ/มหาวิทยาลัย

สถานภาพปัจจุบัน - ยังอยู่ในโครงการหรือไม่ หากไม่อยู่ในโครงการแล้ว ให้ระบุหน่วยงานใหม่ด้วย

- หากเริ่มเข้าร่วมโครงการเป็นนักศึกษาปริญญาเอก ปริญญาโท หรือปริญญาตรี ให้ระบุว่าปัจจุบันสำเร็จการศึกษาหรือยังไม่สำเร็จการศึกษา